Advances in Mechanical and Materials Engineering

SPIS TREŚCI

Original Research

Experimental Research on the Influence of Structural Modifications of Adherends on the Load-Bearing Capacity of Lap Joints of S235JR Steel Sheets

Władysław Zielecki [1] , **Katarzyna Łabno [2], Ryszard Perłowski [1,*]** ,
Łukasz Bąk [3] , **Tomáš Katrňák [4]**

[1] Department of Manufacturing and Production Engineering, Rzeszow University of Technology, al. Powst. Warszawy 8, 35-959 Rzeszów, Poland

[2] Zakłady Mechaniczne Tarnów S.A., ul. Kochanowskiego 30, 33-100 Tarnów, Poland

[3] Department of Materials Forming and Processing, Rzeszow University of Technology, al. Powst. Warszawy 8, 35-959 Rzeszów, Poland

[4] Institute of Aerospace Engineering, Brno University of Technology, Antonínská 548/1, 601 90 Brno, Czech Republic

* Correspondence: ryszard.perlowski@prz.edu.pl

Abstract

The paper presents the results of the research determining the impact of structural modifications of adherends on the load capacity of the joints determined in the static shear test. Tests of adhesive lap joints of S235JR steel sheets bonded with Araldite 2014-2 epoxy adhesive are described. The influence of technologically simple structural modifications was investigated; it consisted in making notches and holes at the leading edge of the adherends. These modifications were aimed at bringing about local flexibility of the joint in the sensitive area of stress concentration. Based on experimental studies, it was shown that there is a possibility of increasing the load-bearing capacity of the joint due to the applied modifications; in the most favorable variant, an increase in the load-bearing capacity by 15.9% compared to the base variant was demonstrated. The tests confirmed that the notches filled with the adhesive in the front part of the adherends can significantly improve the strength properties of joint, while the considered modifications in the form of holes do not have a significant impact on the properties of the adherends.

Keywords: adhesive joints, structural modification, static shear test, S235JR steel

1. Introduction

Structural adhesive joints are becoming more and more widely used, as they enable joining materials with different properties. They are used in composite structures combining various material properties (Davis et al., 1999). The type of joints considered is commonly used in the construction of the means of transport, especially in the automotive, aviation or railways, because they enable the production of structures with a relatively low weight. Adhesive joints are not only used in manufacturing of new products, but are also widely used in repairs, including aviation structures (Davis et al., 1999).

The strength of adhesive bonds depends on many factors, such as the method of surface preparation of adherends, the conditions of bonding and hardening the adhesive, and the thickness of the adhesive layer (Bartczak et al., 2013; da Silva et al., 2009; Davies et al., 2009; Kadioglu & Adams, 2015; Karachalios et al., 2013).

The factors influencing the properties of joints also include the geometric features of the adherends (da Silva et al., 2011; Zhao et al., 2011). The most important of them are the geometrical dimensions and the shape of the joint, which translates into the way it is loaded and the stiffness of the adherends (Zhao et al., 2011).

A general recommendation for the design of adhesive joints determines the shape of the joints so that they are dominated by shear stresses.

In reality, however, there is usually no pure shear in lap joints. Usually there appears a complex state of stresses, in which an important role is also played by normal stresses, causing an unfavourable state of peeling (da Silva et al., 2009).

At the front edges of the loaded lap joint, a stress concentration occurs (da Silva et al., 2009), which usually initiates the failure of the joint. The amount of accumulation depends primarily on the stiffness of the adherends and the properties of the adhesive.

In the literature, there are various methods aimed at limiting stress concentration at the leading edges of the joint. Godzimirski (2002) suggests making a groove (undercut) along the edge of the adhesive joint as one of the methods of reducing the concentration of stresses. Such a procedure, despite weakening the adherends, reduces the value of stresses in the joint and moves the maximum stress away from the edge of the joint.

In the adhesive joining technology, if there is no such requirement, it is recommended not to remove the adhesive flashes. Many authors have shown that flashes have a positive effect on stress distribution (Belingardi et al., 2002; Godzimirski, 2002). They unify and reduce the maximum stress values in the near-edge zone of the joint. The authors of research works (Belingardi et al., 2002; Lang and Mallick, 1998; Rispler et al., 2000; Wang et al., 1998) showed that the additional application of adhesive beyond the outline of the main lap joint, which increases the spew, increases the strength.

An additional method of reducing the near-edge stress concentration in lap joints is to increase the thickness of the adhesive layer in this zone. A number of scientific works raise the issue of the appropriate shaping of adherends, which aims to increase the thickness of the adhesive layer locally in the area of stress concentration (da Silva & Adams, 2007; Kaye & Heller, 2002; Kim et al., 2001; Lang and Mallick, 1999; Mazumdar & Mallick, 1998). These modifications may include, inter alia, the application of chamfer or fillet on the leading edge of adherend (Belingardi et al.2002; You et al., 2007; Zielecki et al., 2017). Thanks to this, local flexibility of the joint in the sensitive area is introduced.

The authors of the work (Belingardi et al., 2002) conducted FEM analyzes for bevelled edges of adherends. The analyzes concern the influence of the bevel angle on the distribution of tangential and normal stresses in a single-fold joint of adherends of different thickness. With the proposed modifications, clear benefits can be noticed, related not only to the lowering of the maximum tangential stresses, but also to the uniformity of the distribution in the sensitive zone.

Similar analyzes were carried out by You et al. (2007), who supported these considerations with experimental research. They confirmed the possibility of improving the strength of adhesive lap joints with structural modifications. In the most preferred cases, an increase in the shear strength of about 20% (You et al., 2007) is obtained.

Structural modifications consisting in making a radius in the joint near-edge zones were considered by Lucas (2011). Considerations from the publication (Lucas, 2011) also apply to the shear lap joint. Various dimensions of the radius were considered here, together with adhesives with different modulus of elasticity. In the most preferred variants, an increase in the shear strength of about 40% was demonstrated.

On the basis of the literature review, it what was noticed was the need for relatively simple ways of introducing structural changes that do not require a significant increase in technology costs, which would contribute to the improvement of the properties of the joints.

In this paper, experimental tests were carried out on structural adhesive joints with structural modifications of the front part of the adherends. The modifications consisted in introducing simple notches and holes at the edges of sheets of various sizes. The aim of the study was to show whether this type of relatively technologically simple modification of joints can contribute to the local flexibility of the adhesive joint in the sensitive zone, where stress concentration occurs.

2. Material and methods

The research on the impact of structural modifications aimed at reducing stress concentration in the frontal area of the adhesive joint was carried out for adhesive lap joints with the dimensions shown in Fig. 1a. Both adherends were made of S235JR sheet steel with a thickness of 2 mm. The shape and dimensions of the considered structural modifications in the form of notches at the leading edge of the adherend are shown in Fig. 1b, while the modifications in the form of holes are shown in Fig. 1c. As structural modifications, variants with the indentations of 1 mm, 2 mm and 3 mm widdt and lengths: 1

mm, 2 mm, 3 mm and 4 mm were used. Modifications in the form of holes with the diameters of 2 mm, 3 mm and 4 mm were also tested. A detailed specification of the modification dimensions at the leading edge of the adherends is presented in Table 1. As part of the research, only symmetrical joints were tested, i.e. in each variant, both adherends had identical modifications.

Notches and holes in the front part of the adherends were made by machining. The notches were made using disc cutters with the thickness corresponding to the width of the notches, while the holes were made using drills.

The joint was made using the epoxy adhesive Araldite 2024-2 (supplied by Huntsman Corporation, Texas USA).
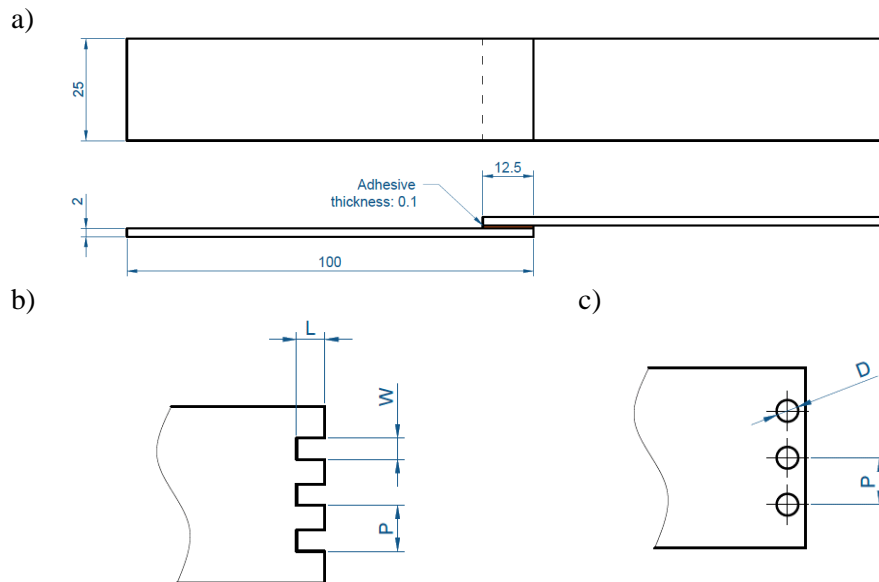
Fig. 1. The shape and dimensions of the samples of adhesive lap joints used in the tests in the basic version (a) and the shape and dimensions of structural modifications in the front part of the adherends in the form of notches (b) and holes (c)

The same methods of surface preparation and hardening conditions of the adhesive composition were applied to all joint variants. Each surface to be joined was subjected to abrasive blasting with aloxite 95A, which contains 96% aluminium oxide (Al_2O_3), ~3% titanium dioxide (TiO_2) and 1-2% other admixtures. Abrasive blasting was performed under the following conditions: grain size $w_z = 0.27$ mm, air pressure $p = 0.8 \pm 0.1$ MPa, and blasting time $t = 60$ s.

Table 1. Summary of dimensions of structural modifications for individual variants of samples

	Variant	Notch width (W in mm)	Notch length (L in mm)	Hole diameter (D in mm)	Pitch (P in mm)	Location of the holes (L in mm)
	Base	-	-	-	-	-
Narrow notch	N-1x1	1	1	-	6.5	-
	N-1x2	1	2	-	6.5	-
	N-1x3	1	3	-	6.5	-
	N-1x4	1	4	-	6.5	-
Medium notch	N-2x1	2	1	-	6.5	-
	N-2x2	2	2	-	6.5	-
	N-2x3	2	3	-	6.5	-
	N-2x4	2	4	-	6.5	-
Wide notch	N-3x1	3	1	-	6.5	-
	N-3x2	3	2	-	6.5	-
	N-3x3	3	3	-	6.5	-
	N-3x4	3	4	-	6.5	-
Hole	H-2	-	-	2	6.5	2
	H-3	-	-	3	6.5	2.5
	H-4	-	-	4	6.5	3

Surface morphology of the adherends was measured with the Talysurf CCI Lite 3D optical profiler (Taylor Hobson Ltd., Leicester, United Kingdom). Figure 2 presents surface morphology of the adherends after the sand blasting process.
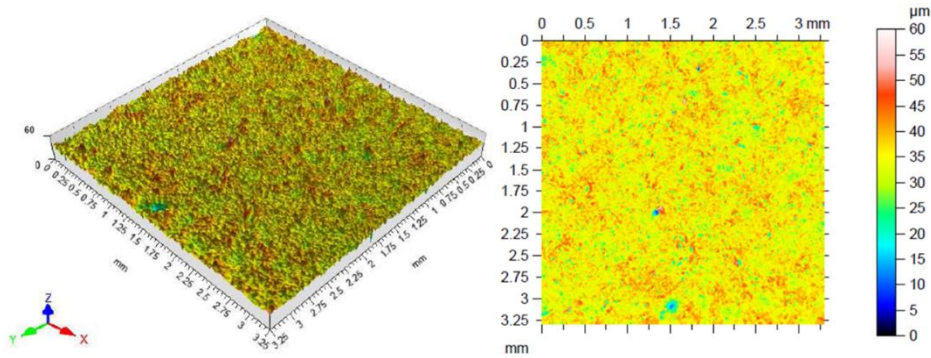
Fig. 2. Surface morphology of the adherends after the sand blasting process

The values of basic surface roughness parameters are as follows: arithmetical mean height Sa = 1.55 µm, root mean square deviation Sq = 3.92 µm, kurtosis Sku = 4.98, skewness Ssk = -0.447, maximum profile peak height Sp = 24.6 µm, maximum height Sz = 60.0 µm and maximum profile valley depth Sv = 35.4 µm.

The hardening process of the adhesive-bonded joints lasted for 24 h at room temperature 20 ± 3 °C under a constant pressure of 0.1 MPa applied to the joint area.

The investigation of the load capacity of the joint by tensile/shear tests was carried out using a ZWICK Roell Z-100 universal testing machine (Zwick/Roell GmbH & Co. KG, Ulm, Germany) with the constant crosshead speed of 5 mm/min at ambient temperature. The research was carried out for five repetitions of each variant.

The morphologies of the fracture surfaces of the adhesive joints were examined using an scanning electron microscope (SEM) Phenom ProX (Nanoscience Instruments, Phoenix, AZ, USA).

3. Results and discussion

Figs. 3a-c show representative curves from static shear tests of joints for each of the variants of the applied modifications in comparison to the basic variant. In Fig. 3a the shear curves of the samples from narrow notch of different lengths were related to the base variant. Herein, in selected cases, a higher load capacity of the joints was observed, and in each variant with a modification, a slightly higher stiffness of the joint in relation to the base variant was also observed. Similar phenomena were demonstrated for the variants of medium notch and wide notch.

On the other hand, in the case of structural modifications consisting in making holes, no significant differences were revealed in the strength and stiffness of joints in relation to the base variant.

The discussion of the possible mechanisms of failure of joints affecting the nature of the mechanism of static shear curves for individual variants will be carried out on the basis of fractographic analyzes.

Diagram shown in Fig. 4 summarizes the individual test results for individual samples along with the mean value for each variant and the value of the standard deviation. The highest increase in the load capacity of the joint in relation to the base variant was demonstrated for the notch medium, specifically for the N-3x1 variant. In this case, the average value of the load capacity of the joint increased by about 15.9%, as for the variant under consideration it was 8634.04 N, while for the base variant, this value is 7446.95 N. It should be noted that the dispersion of the load capacity results was also increased here, because for the variant N-3x1 the standard deviation value was 381.6 N, while for the base variant, the standard deviation was 201.5 N. The increase in the spread of strength results was observed for most variants with structural modifications. The largest scattering of results in relation to the base variant was shown for the variant with holes, namely H-3, where the standard deviation was 982.9 N and the average value of the load capacity for this variant was 7033.12 N.

It should be noted that from the technological point of view, accurate filling of the notches with adhesive is difficult to obtain, hence in many cases quite significant scattering of the strength results was demonstrated. Additionally, filling certain volumes with adhesive mass creates the possibility of the occurrence of voids, air bubbles in these volumes, which may be random, and undoubtedly affect the repeatability of the test results.

a)

b)

c)

d)
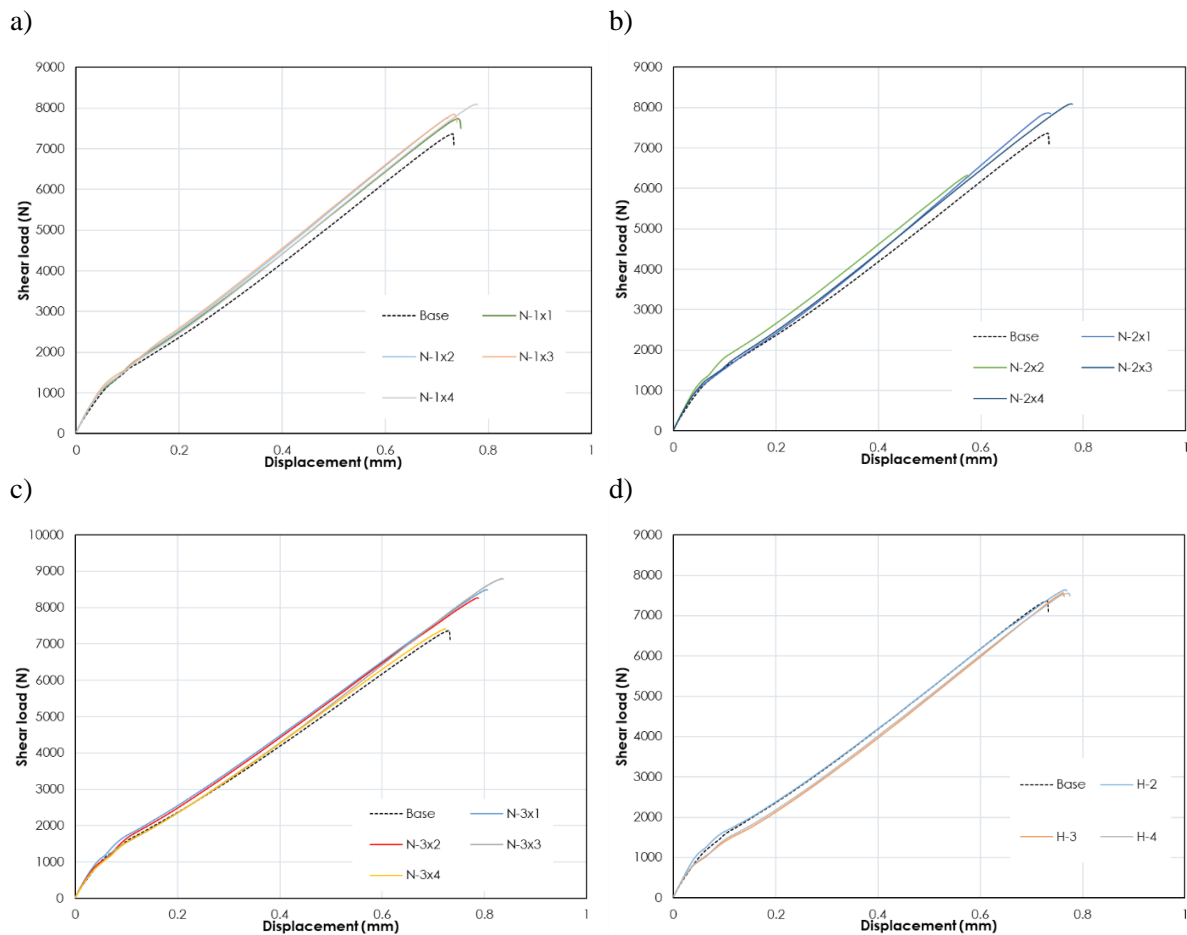
Fig. 3. Shear load-displacement representative static test curves of adhesive joints with structural modifications in relation to the base variant, for the following types of modifications: narrow notch (a), medium notch (b), wide notch (c) and hole (d)
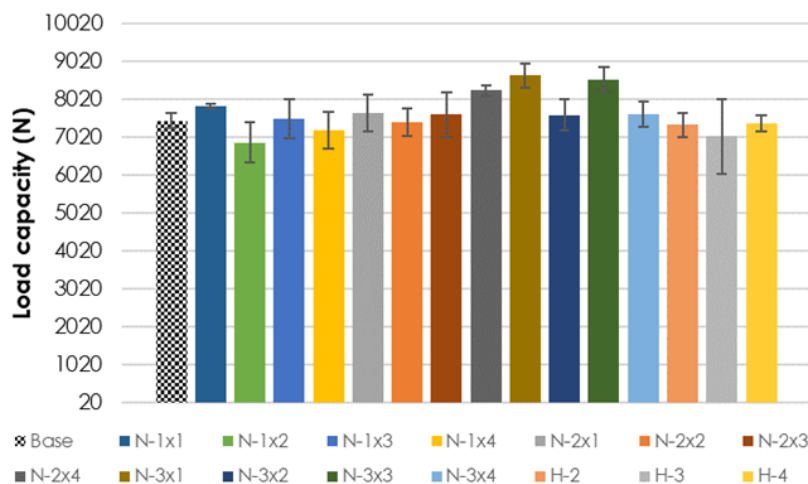
Fig. 4. Effect of the geometry of structural modifications on load capacity of adhesive joints

However, in the case of one of the variants with a structural modification, namely N-1x1, high repeatability of the results was demonstrated during the tests, because in this case the average load capacity of the joint was 7834.13 N with the standard deviation equal to 61.62 N. It should be noted that this is the variant with the smallest notch dimensions that were considered, namely the volume of the notches which is filled with the adhesive, has the dimensions of 1×1×2 mm. With such a small volume, it is easy to completely and repetitively fill the space with adhesive; the probability of defects

such as voids occurring in these volumes is reduced, hence the high repeatability of the test results is ensured.

On the basis of fractographic analyzes, an attempt was made to determine the phenomena influencing the increase in strength of the selected joint variants. The analyzes were started with the notched variants, as this modification resulted in a significant increase in the strength of the joint. Fig. 5 shows images of the fracture surface for the N-2x4 variant showing the border between the sheet surface and the notch filled with adhesive. The SEM micrograph shows a clear difference in the nature of the fracture of the adhesive in the area of the notch and the sheet surface. In the case of failure of the joint in the area of the sheet, a typical failure of the adhesive joint was observed due to shearing of a thin layer of adhesive of about 0.1 mm thickness. In this case, there is essentially cohesive failure, although fragments of adhesive failure can also be seen in small areas at the leading edge of the sheet. A similar character of failure occurs with the basic variant (Fig. 6a), while in this case no areas of adhesive failure were observed. A completely different character of the cracking takes place in the notch area; in this case the fracture is characterized by a failure mechanism typical for the stretching of thermosets, where the fracture of adhesive a brittle character. In the area of the notch, the hardened adhesive has a thickness that is much greater than that of the adhesive joint, i.e. close to the thickness of the sheet, i.e. 2 mm. In the considered areas formed by the adhesive-filled notches, a different, lower joint stiffness occurs locally, which results in a change in the stress distribution. The local flexibility of the front joint area is advantageous due to the stress concentration typical of this type of joint. It is in this phenomenon that the increase in strength for variants with notches should be seen. At the same time, as previously observed, the technological problem of uniform filling of the volume of notches and holes with adhesive may translate into an increase in the scatter of test results. On the one hand, the greater the volumes formed by the notches, the greater the flexibility of the joint, but on the other hand, the larger volumes filled with the adhesive mass increase the likelihood of the aforementioned drawbacks, such as air bubbles, voids, etc.

In the case of structural modifications consisting in making round holes at the front edges of the adherends, no significant effect on the strength of the joint was demonstrated. Fig. 6b shows the micrographs of the fracture surface for the H-4 variant. Based on the SEM image, it can be concluded that in this case there was no significant difference in the mechanism of failure of the joint in the area of the sheet surface and the hole filled with adhesive. In the case of notches, the adhesive that fills the notch volume has one degree of freedom, i.e. it stretches in the direction of the joint loading. On the other hand, the adhesive closed in a hole made in steel having significantly higher stiffness than the hardened adhesive material, has no possibility of stretching. Therefore, such a structural modification does not have a significant impact on the stress distribution at the leading edge of the joint - the adhesive filling the holes is sheared in the joint plane.
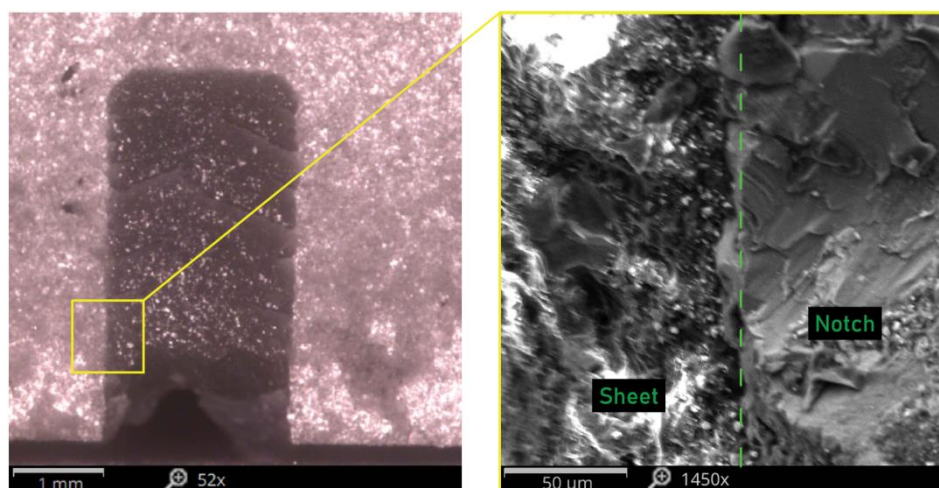
Fig. 5. Micrographs of the fracture surfaces for variant: medium notch 4 mm length

To sum up, a significant potential to increase the static strength of the adhesive joint by several percent thanks to making the front part of the joint more flexible has been demonstrated. The issue requires further optimization studies aimed at indicating the optimal dimensions and shapes of notches. The issue of technology also requires development, because in order to ensure the repeatability of

the strength of joints, it is necessary to fill the space in the notches in such a way so as to ensure uniform mechanical properties.
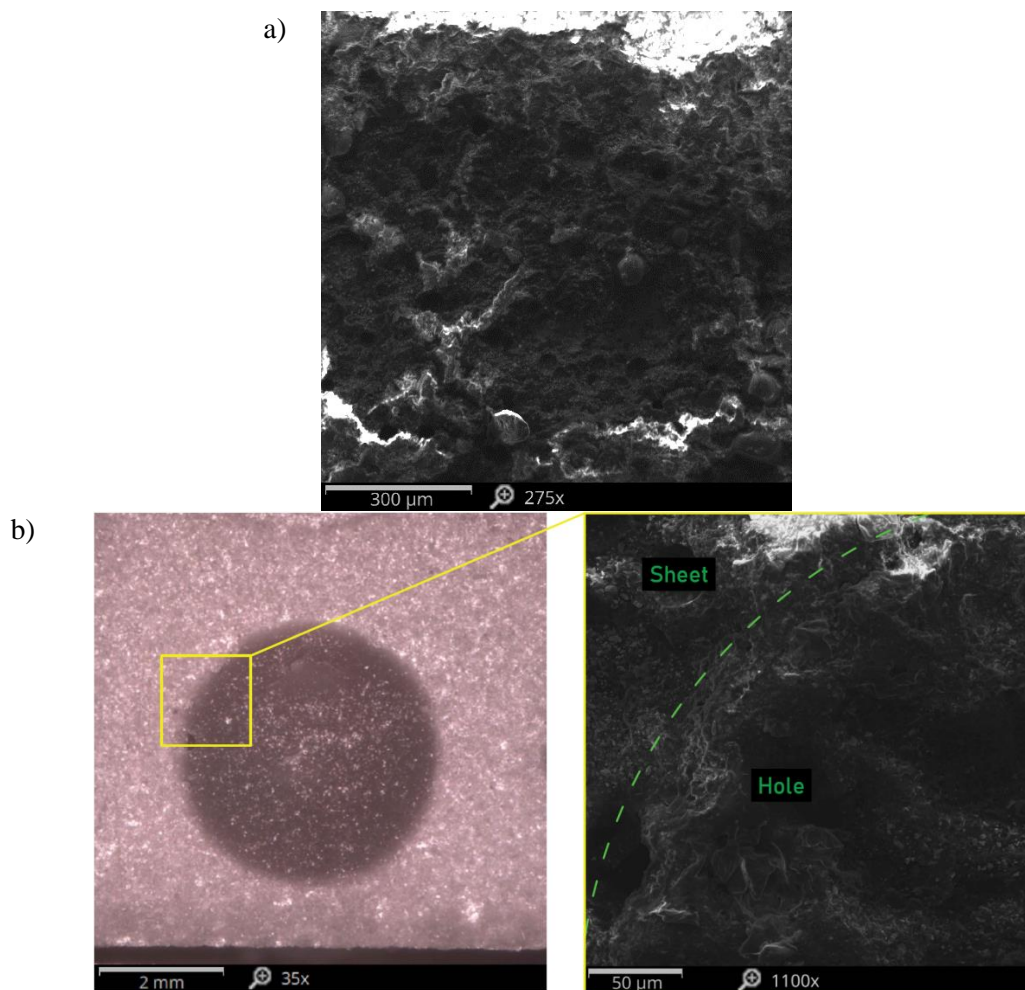
Fig. 6. Micrographs of the fracture surfaces for base (a) and hole with a diameter of 4 mm (b)

4. Conclusions

The aim of the work was to demonstrate, on the basis of experimental studies, the possibility of increasing the structural load-bearing capacity of S235JR steel adhesive joints by making relatively easy structural modifications to the adherends. Based on the research work carried out, the following conclusions were drawn:

- Due to the application of relatively easy-to-implement structural modifications, the load-bearing capacity of adhesive lap joints can be improved. As part of the research, the highest increase was shown for the variant with 3 mm wide and 1 mm long notches. In this case, the average value of the load capacity of the joint increased by about 15.9%, as for the variant under consideration it was 8634.04 N, while for the base variant, this value is 7446.95 N.
- The increase in the load capacity of the joints was demonstrated only for the variants with notches, while no significant changes in the load capacity were observed for the variants with openings at the leading edge of the adherends.
- The increase in load capacity for variants with structural modifications in the form of notches is caused by the local elasticity of the front part of the joint, where stress concentration occurs. In the area of the notches, the adhesive filling undergoes a different destruction mechanism than the thin layer of adhesive sheared between the sheet surfaces.
- In most cases, for variants with structural modifications, the standard deviation of the test results was increased. The largest dispersion of results in relation to the base variant was shown for the variant with holes with the diameter of 3 mm, where the standard deviation was 982.9

N and the average value of the load capacity was 7033.12 N, while for the base variant the value of the standard deviation was 201.5 N for the average value of the load capacity of the joints equal to 7446.95 N.

- Increasing the dispersion of the results is caused by a technological problem, because filling the notches and holes with adhesive mass creates the possibility of the occurrence of voids, air bubbles in these volumes, which may be random and has a significant impact on the repeatability of the test results.

Acknowledgements

References

Bartczak, B., Mucha, J., & Trzepieciński, T. (2013). Stress distribution in adhesively-bonded joints and the loading capacity of hybrid joints of car body steels for the automotive industry. *International Journal of Adhesion and Adhesives*, *45*, 42–52. https://doi.org/10.1016/j.ijadhadh.2013.03.012

Belingardi, G., Goglio, L., & Tarditi, A. (2002). Investigating the effect of spew and chamfer size on the stresses in metal/plastics adhesive joints. *International Journal of Adhesion and Adhesives*, *22*(4), 273–282. https://doi.org/10.1016/S0143-7496(02)00004-0

Davies, P., Sohier, L., Cognard, J. Y., Bourmaud, A., Choqueuse, D., Rinnert, E., Créac'hcadec, R. (2009). Influence of adhesive bond line thickness on joint strength. *International Journal of Adhesion and Adhesives*, *29*(7), 724–736. https://doi.org/10.1016/j.ijadhadh.2009.03.002

Davis, M. J., & Bond, D. (1999). Principles and practise of adhesive bonded structural joints and repairs. *International Journal of Adhesion and Adhesives*, *19*(2-3), 91–105. https://doi.org/10.1016/S0143-7496(98)00026-8

Godzimirski, J. (2002). *Wytrzymałość doraźna konstrukcyjnych połączeń klejowych [Ultimate strength of structural adhesive joints]*. Wydawnictwa Naukowo-Techniczne.

Kadioglu, F., & Adams, R. D. (2015). Flexible adhesives for automotive application under impact loading. *International Journal of Adhesion and Adhesives*, *56*, 73–78. https://doi.org/10.1016/j.ijadhadh. 2014. 08.001

Karachalios, E. F., Adams, R. D., & da Silva, L. F. M. (2013). The behaviour of single lap joints under bending loading. *Journal of Adhesion Science and Technology*, *27*(16), 1811–1827. https://doi.org/10.1080/01694243.2012.761926

Kaye, R. H., & Heller, M. (2002). Through-thickness shape optimisation of bonded repairs and lap-joints. *International Journal of Adhesion and Adhesives*, *22*(1), 7–21. https://doi.org/10.1016/S0143-7496(01)00029-X

Kim, J. S., Kim, C. G., & Hong, C. S. (2001). Practical design of tapered composite structures using the manufacturing cost concept. *Composite Structures*, *51*, 285–299. https://doi.org/10.1016/S0263-8223(00)00145-8

Lang, T., & Mallick, K. (1998). Effect of spew geometry on stresses in single lap adhesive joints. *International Journal of Adhesion and Adhesives*, *18*(3), 167–177. https://doi.org/10.1016/S0143-7496(97)00056-0

Lang, T., & Mallick, K. (1999). The effect of recessing on the stresses in adhesively bonded single-lap joints. *International Journal of Adhesion and Adhesives*, *19*(4), 257–271. https://doi.org/10.1016/S0143-7496(98)00069-4

Lucas, F. M. (2011). Design Rules and Methods to Improve Joint Strength. Springer-Verlag. https://doi.org/10.1007/978-3-642-01169-6_27

Mazumdar, S. K., & Mallick, K. (1998). Static and fatigue behavior of adhesive joints in SMC-SMC composites. *Polymer Composites*, *19*(2), 139–146. https://doi.org/10.1002/pc.10084

Rispler, A. R., Tong, L., Steven, G. P., & Wisnom, M. R. (2000). Shape optimisation of adhesive fillets. *International Journal of Adhesion and Adhesives*, *20*(3), 221–231. https://doi.org/10.1016/S0143-7496(99)00047-0

da Silva, L. F. M., das Neves P. J. C., Adams R. D., Spelt, J.K. (2009). Analytical models of adhesively bonded joints – Part I: literature survey. *International Journal of Adhesion and Adhesives, 29*, 319–330. https://doi.org/10.1016/j.ijadhadh.2008.06.005

da Silva, L. F. M., Ochsner, A., & Adams R. D. (Eds.). (2011). *Handbook of adhesion technology*. Springer-Verlag.

da Silva, L. F. M., & Adams, R. D. (2007). Techniques to reduce the peel stresses in adhesive joints with composites. *International Journal of Adhesion and Adhesives*, *27*(3), 227–235. https://doi.org/10.1016/j.ijadhadh.2006.04.001

Wang, C. H., Heller, M., & Rose, L. R. F. (1998). Substrate stress concentrations in bonded lap joints. *Journal of Strain Analysis for Engineering Design*, *33*(5), 331–346. https://doi.org/10.1243/0309324981513039

You, M., Yan, Z., Zheng, X., Yu, H., & Li, Z. A. (2007). A numerical and experimental study of adhesively bonded aluminium single lap joints with an inner chamfer on the adherends. *International Journal of Adhesion and Adhesives*, *28*(1-2), 71–76. https://doi.org/10.1016/j.ijadhadh.2007.06.001

Zhao, X., Adams, R. D., da Silva, L. F. M. (2011). Single lap joints with rounded adherend corners: experimental results and strength prediction. *Journal of Adhesion Science and Technology*, *25*(8), 837–856. https://doi.org/10.1163/016942410X520880

Zielecki, W., Kubit, A., Kluz, R., & Trzepieciński, T. (2017). Investigating the influence of the chamfer and fillet on the high-cyclic fatigue strength of adhesive joints of steel parts. *Journal of Adhesion Science and Technology*, *31*(6), 627-644. https://doi.org/10.1080/01694243.2016.1229521

Badania Eksperymentalne Wpływu Modyfikacji Konstrukcyjnych Materiałów Klejonych na Nośność Złącza Zakładkowego Blach Stalowych S235JR

Streszczenie

W artykule przedstawiono wyniki badań określających wpływ modyfikacji konstrukcyjnych elementów klejonych na nośność złączy wyznaczoną w statycznej próbie ścinania. Opisano badania połączeń klejowych zakładkowych blach stalowych S235JR sklejonych klejem epoksydowym Araldite 2014-2. Zbadano wpływ prostych technologicznie modyfikacji konstrukcyjnych, polegających na wykonaniu nacięć i otworów na krawędzi natarcia elementów klejonych. Modyfikacje te miały na celu doprowadzenie do miejscowego uelastycznienia połączenia we wrażliwym obszarze koncentracji naprężeń. Na podstawie badań eksperymentalnych wykazano, że istnieje możliwość zwiększenia nośności złącza dzięki zastosowanym modyfikacjom. W najkorzystniejszym wariancie zaobserwowano wzrost nośności o 15,9% w stosunku do wariantu niemodyfikowanego konstrukcyjnie. Badania potwierdziły, że wypełnione przez klej nacięcia w przedniej części elementów klejonych mogą znacząco poprawić właściwości wytrzymałościowe złącza, natomiast rozważane modyfikacje w postaci otworów nie mają istotnego wpływu na właściwości elementów klejonych.

Słowa kluczowe: połączenia klejowe, modyfikacja konstrukcyjna, statyczna próba ścinania, stal S235JR

Original Research

Analysis of the Technological Position in Relation to Aluminium Casting Production

Andrzej Pacana * iD**, Karolina Czerwińska** iD

Department of Manufacturing Processes and Production Engineering, Rzeszow University of Technology, al. Powst. Warszawy 8, 35-959 Rzeszów, Poland

* Correspondence: app@prz.edu.pl

Abstract

The dynamically developing production market, and in particular the metallurgic industry, enforces constant improvement of the level of production efficiency and product quality, which influences company position on the market and the level of its competitiveness. Therefore, the aim of the study was to determine the current position of the foundry enterprise, taking into account the aluminium gearbox casting, in the context of technological capabilities and market position, as well as to identify critical factors and, finally, to indicate the conditions for its strengthening. The study used a 3x3 matrix. The company under study, in the context of manufacturing the analysed product, is classified in the area of "marketing improvement". This area demonstrates the need to take measures to establish a marketing and development department and the need to make better use of the company's identified technological potential. The method presented in the study can be useful for analysing the position of manufacturing and service companies in various industries, in order to select an appropriate development strategy.

Keywords: metal industry, mechanical engineering, quality management, 3x3 matrix, aluminium casting

1. Introduction

Productivity growth in the modern world is perceived as one of the key sources of social improvement, social progress and economic growth. This approach has contributed to the fact that productivity growth in many countries has become a goal pursued in almost all enterprises, regardless of the type of products manufactured or services provided (Pacana et al., 2019; Piętowska–Laska, 2015). In industry, a manufacturing system that enables production of high-quality products with minimum inputs is important. This can be achieved with an increase in the productivity of enterprises (Hys, 2014; Ligarski, 2018; Wolniak & Skotnicka–Zasadzień, 2010). Productivity is a category depicting the efficiency of the inputs incurred. As such, it has a significant impact on the competitiveness of economic units. It is crucial that the development of productivity reflects all types of inputs incurred. Productivity is an important issue in the context of analysing the performance of manufacturing enterprises, as it allows assessing their development, paying particular attention to the resources involved in the production process (Klimecka–Tatar, 2018; Ulewicz & Novy, 2019; Wolniak, 2020). In an era of increased market volatility, technology development and significant competition, the manufacturing process requires continuous improvement. Seemingly small improvements can affect the success of a company, which indicates that the production process should be subjected to constant monitoring, analysis and improvement, in order to eliminate imperfections and to increase technological efficiency, competitiveness, and, thus, improve market position (Pacana & Czerwińska, 2020).

Technology can be understood as the science relating to the processes of processing raw materials and producing semi-products and products from input materials. In such an approach, technology refers to the fixed assets of the sub-entity and including the equipment of production lines. Technology can refer to the results of research and development and production-engineering functions of an enterprise (Chiu et al., 2010). The effective use of technology is significantly influenced by a variety of

measures. A significant number of factors determining its level depend directly on the enterprise, but also on its suppliers and environment. A failure to ensure an adequate level of these resources and factors not infrequently results in a loss of competitiveness (Ligonenko, 2016).

Competitiveness is the process by which one entity strives to outperform another. For manufacturing firms, competitiveness indicates the ability to produce products in a timely and cost-effective manner that meets buyers' demands and market needs (Zhamoida, 2009; Zhou & Zhu, 2005). The activities undertaken by enterprises are carried out with the aim of gaining and expanding market share, which determines their profits, i.e. achieving the main objective of any manufacturing enterprise (Pacana & Czerwińska, 2017).

The aim of the study is to clarify the current position of the foundry company, taking into account aluminium gearbox casting, in terms of technological capabilities and market position, as well as to identify critical factors and, ultimately, to identify conditions for its strengthening. It is important to take appropriate action in relation to the identified position in the 3x3 matrix.

2. Analysis

2.1. Aim and subject of the study

The main objective of the study was to analyse the technological strategies followed by the selected foundry company. The study will make it possible to assess the existing technology and compare it with similar technologies on the market. Achieving the objective will enable to make changes within critical areas of the strategy.

The gearboxes are manufactured in series at one of the companies located in the south-eastern Poland. The gearboxes in question, measuring 600 x 500 x 150 mm, are used in light-duty vehicles. The gearboxes are responsible for changing the gear ratios, thus effectively utilising the power generated by the engine within the combustion of the fuel-air mixture. Figure 1 shows an illustrative model of the test object.
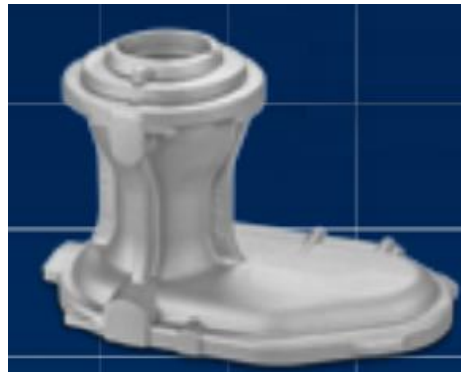
Fig. 1. Model of the subject of research – gearbox

The gearboxes are cast from the AlSi7Mg0.3 alloy, by using gravity sand moulds. The chemical composition and mechanical properties of the alloy used are shown in Table 1.

Table 1. The chemical composition and mechanical properties of the alloy

Chemical composition									
Element	Fe	Si	Mn	Ti	Cu	Mg	Zn	Others	Al
Min., %	-	6.50	-	-	-	0.45	-	each:0.03; total: 0.01	remainder
Max, %	0.19	7.50	0.10	0.25	0.05	0.70	0.07		

Mechanical properties								
Property Name	Tensile strength R_m		Yield strength $R_{0.2}$			Elongation at break A		Brinell hardness
Min, %	300		320	240	240	4	6	100 / 151
Max, %	350			280		6		151
Unit of measure	N/mm^2		N/mm^2	N/mm^2	MPa	%	%	HB / HB

Source: Own elaboration based on (PN-EN 1706:2011. Aluminium and aluminium alloys Castings. Chemical composition and mechanical properties, 2011, Warszawa: PKN)

The AlSi7Mg0.3 alloy (EN AC-42200) used by the company is used to manufacture castings of moderately loaded engine parts with complex shapes. Thanks to the presence of such elements as silicon and magnesium, the alloy exhibits relatively good mechanical properties (Briol, 2010; Mueller et al. 2016). The alloy has exceptional corrosion resistance and very good machining and welding properties (Julis et al., 2011; Pereira et al., 2020; Salomon et al., 2017). For this reason, the alloy is used in automotive, architectural, aerospace (Brungs, 1997; Cavaliera et al., 2004), food and chemical industries, mechanical engineering and in shipbuilding and moulds and models (Chokkalingam et al., 2017; Pysz et al., 2014).

2.2. Research methodology

The volume-driven orientation of the economy has resulted in a concomitant high material, labour and energy intensity, resulting in increased technology development. This mainly concerns highly processed aluminium alloy products. The level of technological capabilities influences the company's position on the market. When building a stable competitive position, it is important to identify the relationship between the characteristics of the technology used and the company's market position.

The study uses a 3x3 matrix, which presents the correlation that occurs between technological capabilities (X axis) and the company's market position (Y axis). A 9-point Parker scale was used, with indications of 1-3 weak, 4-6 medium, 7-9 strong impact on technological capabilities and market position (Konstanciak, 2021). The matrix is divided into 9 areas, which indicate the technological position of the analysed company. This makes it easier to indicate future technology development activities and define a development strategy. Enterprises should strive to achieve the field numbered 1 - "Focus on the revealed Chance", i.e. the field whose component values achieve high parameters. A field marked with this number indicates a very good market position and significant technological opportunities (Borkowski et al., 2014; Borkowski et al., 2021).

The first stage of the study consisted in identifying two groups of factors: those reflecting technological capabilities and factors influencing market position, i.e. factors that represent the functioning of the company. Factors that do not fit into either of the identified groups were not included in the study. The factors were assessed on a 9-point scale. In the next step, the average value for both categories of factors was calculated. The values obtained were placed in a 3x3 matrix in order to determine the technological position of the company and identify the factors that influenced it.

3. Analysis

The listed factors determining the technological capabilities and market position of the foundry company, as well as their evaluations, are presented in Table 2. 13 characteristics of the company influencing the evaluation of the technological level and 13 characteristics determining the market position were distinguished.

Table 2. List of highlighted factors

No	Factors indicative of technological capabilities	Evaluation	Factors indicative of market position	Evaluation
1.	Availability of information on good foundry practices	6	Location	6
2.	Motivation system	4	Regular customers	7
3.	Modern means of transport	7	Competition	2
4.	Ability to transport large parts	7	New markets	4
5.	Extensive network of distribution channels	6	Exports	5
6.	Flexibility in production	8	Unemployment	6
7.	Technical equipment	6	Company image	7
8.	Machinery park	6	Demand for products	7
9.	Production technology	6	Product prices	8
10.	Accessibility of services on the Internet	8	Labour costs	5
11.	High quality of manufactured products	5	Charges	7
12.	Qualified personnel	7	Marketing and advertising	4
13.	Implemented management systems	7	Customer service	8
	Average value	6.38	Average value	5.85

Based on the data in Table 1, a 3x3 matrix was developed (Fig. 2). The average values of the assessed factors indicate that the studied foundry company is located in the field number 2 - "improvement of marketing".

Fig. 2. A general treatment of the 3x3 matrix for the foundry company under study

The factors determining the technological level of the enterprise reached an average value of 6.38, while its position on the market reached 5.85 (Fig. 2). The achieved position indicates that the examined enterprise should pay more attention to improving the factors related to its position on the market.

In order to better understand the distribution of the analysed enterprise characteristics, a map of the number of assessments was drawn up against a 3x3 matrix (Fig. 3a). It can be seen that the distribution of assessments is not even. The pairs of assessments are concentrated at the junction of areas 8 and 9.

From a substantive point of view, it is advisable to draw up a graphical representation of the data in the form of an axis-radar diagram to complement the interpretation of the data (Fig. 3b). Based on the characteristics of the 3x3 matrix (Fig. 1), the analysis of Figure 3b clearly shows that five pairs of factors are located in area 8, while areas: 4, 5, 6 and 7 do not contain pair ratings.
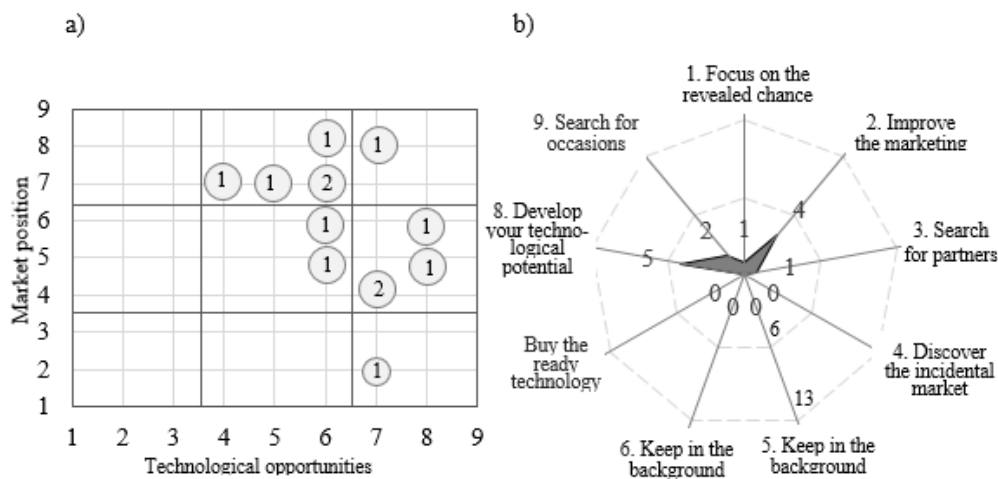
Fig. 3. Presentation of test results a) map of evaluations b) radar chart

Among the features determining the technological capabilities in the context of manufacturing the product - aluminium gearboxes, special attention should be paid to the flexibility of production, which is an important factor in the casting industry and the area under analysis. In the company, castings are often made to order, according to customer needs, hence the high rating. Another factor rated at level 8 was the availability of services on the internet. This factor plays an important role due to its ability to showcase a wide range of products in offer and to reach a wide range of customers from different industries. 4 factors received a score of 7, which also indicates their strong influence on technological capabilities. This group included a factor indicating: modern means of transport, the ability to transport bulky parts, qualified personnel and the implemented management systems. Modern means of transport enable timely transport of products meeting individual customer requirements, often with

large and unusual dimensions. In addition to periodic training, the company provides additional training in quality assurance. The company's employees are mainly people with long working experience in the foundry industry, most of them well educated. The research company has implemented in a quality management system and industry standardised systems appropriate to the product range offered, which has a positive impact on the quality of processes and products.

It should be noted that among the factors determining the technological level of the analysed product (gearbox) in the enterprise, the motivation system was rated the lowest. With regard to the evaluations of technological equipment and machinery park, it can be concluded that despite a modern machinery park operating without major breakdowns and with significant efficiency, the employees do not make full use of the technological potential through an inadequate level of motivation.

Among the factors determining the market position, the factors relating to: product price and customer service deserve special attention. It should be remembered that in Poland there are many companies involved in the foundry industry, so from the company's perspective, the indicated factors are an important issue. The company has signed long-term contracts with several customers, which makes it possible to realise production also in times of lower demand.

The study also identified factors that negatively affect the company's position on the market. These are definitely competition, but also the issue of marketing and advertising, as well as new markets. In Poland, and in particular in the analysed region - the south-eastern part of Poland, there are many foundry companies offering aluminium alloy products for many industries. So far, there is no separate marketing department in the company under analysis. No advertising campaigns are conducted, only the information about products and services appears in trade magazines, which certainly influences a limited number of sales markets and the limited possibility of entering new markets.

It is worth noting that many of the factors influencing market position and the level of technological capabilities are internal. The company should undertake improvement actions in the identified, critical areas so that the result of the evaluation of the analysed factors could prove the achievement of a stable and satisfactory position on the foundry market. The action to be taken first is the creation of a marketing and advertising department and the development of a new incentive system.

Due to the dynamically changing environment and the constant increase in requirements for structures and construction materials, the issue addressed in the study is topical. The method presented in the study can be used to analyse the positioning of manufacturing and service companies in various sectors in order to select an appropriate development strategy.

4. Conclusions

The technology used by individual foundry companies determines the quality of the finished products. It also influences the level of customer satisfaction. On the other hand, the position on the market largely depends on the broadly understood market competitiveness. Therefore, it is important to determine an appropriate strategy that will determine the further development of the company. The research carried out and the analysis of the results contributed to the achievement of the objective of the study, which was to specify the current position of the foundry enterprise, taking into account the aluminium gearbox casting, in the context of technological capabilities and market position, as well as to identify critical factors and, finally, to indicate the conditions for its strengthening. It is important to take appropriate action in relation to the identified position in the 3x3 matrix.

The company's position has been identified as 'improving marketing' (box 2 within the 3x3 matrix). Flexibility in production and availability of online services, as well as the availability of modern means of transport, the ability to transport large parts, qualified staff and implemented management systems were found to be key determinants of technological performance in the analysed company. On the other hand, factors with a strong impact on market position were product prices and customer service. The analysis shows that many of the factors influencing market position and the level of technological capabilities are internal to the foundry company. The company should undertake improvement actions in the identified, critical areas so that the result of the evaluation of the analysed factors could prove the achievement of a stable and satisfactory position on the foundry market.

The method presented in the study may be useful for analysing the position of production and service enterprises from various branches in order to select an adequate development strategy. Further research directions will concern the analysis of the position of a selected aluminium alloy casting product manufactured in the analysed company.

References

Borkowski, S., Ingaldi, M., & Jagusiak–Kocik, M. (2014). The use of 3x3 matrix to evaluate a manufacturing technology of chosen metal company. *Management Systems in Production Engineering*, *3*(15), 121-125. https://doi.org/10.12914/MSPE-06-03-2014

Borkowski, S., Ulewicz, R., Selejdak, J., Konstanciak, A., & Klimecka–Tatar D. (2021). The use of 3x3 matrix to evaluation of ribbed wire manufacturing technology. *Procedings of the 21st International Conference on Metallurgy and Materials*, Czech Republic, 1-6.

Briol, Y. (2010). Effect of solution heat treatment on the age hardening capacity of dendritic and globular Al-Si7Mg0.6 alloys. *International Journal of Materials Research*, *101*(3), 439-444. https://doi.org/10.3139/146.110293

Brungs, D. (1997). Light weight design with light metal castings. *Materials & Design* 18, *4*(6), 285-291. https://doi.org/10.1016/S0261-3069(97)00065-4

Cavaliere, P., Cerri, E., & Leo, P. (2004). Effect of heat treatment on mechanical properties and fracture behavior of a thixocas A356 aluminum alloy. *Journal of Materials Science*, *39*, 1653-1658. https://doi.org/10.1023/B:JMSC.0000016165.99666.dd

Chiu, Y. C., Lai, H. C., Liaw, Y. C., & Lee, T. Y. (2010). Technological scope: diversified or specialized. *Scientometrics*, *82*, 37-58. https://doi.org/10.1007/s11192-009-0039-5

Chokkalingam, B., Raja, V., Anburaj, J., Immanual, R., & Dhineshkumar, M. (2017). Investigation of shrinkage defect in castings by quantitative Ishikawa diagram. *Archives of Foundry Engineering*, *17*(1), 174-178. https://doi.org/10.1515/afe-2017-0032

Hys, K. (2014). Tools and methods used by the Polish leading automotive companies in quality management system. Results of empirical research. *Journal of Achievements in Materials and Manufacturing Engineering*, *63*(1), 30-37.

Julis, M., Pospisilova, S., Zapletal, J., & Podrabsky, T. (2011). Study of microstructure and mechanical properties of aluminum alloy AlSi7Mg0.6 after different cooling methods. *Chemicke Listy*, *105*, S812 - S813.

Klimecka–Tatar D. (2018). Contemporary quality management model of professional services in B2C and B2B systems cooperation. *Proceedings of the 10th International Scientific Conference Business And Management*, Lithuania, 371-380. https://doi.org/10.3846/bm.2018.41

Konstanciak, M. (2021). Analysis of technological strategies on the example of the production of the tramway wheels. *Archives of Materials Science and Engineering*, *57*(2), 69-74.

Ligarski, M. J. (2018). Methodology of problem analysis in the quality management system with the use of systems approach. *Management Systems in Production Engineering*, *26*(3), 157-161. https://doi.org/10.1515/mspe-2018-0025

Ligonenko, L. O. (2016). Theoretical and methodological foundations of technological management. *Marketing and Management of Innovations*, *3*, 145-160. https://doi.org/10.21272/mmi.2016.3-11

Mueller, M.G., Fornabaio, M., Zagar, G., & Mortensen, A. (2016). Microscopic strength of silicon particles in an aluminium-silicon alloy. *Acta Materialia*, *105*, 165-175. https://doi.org/10.1016/j.actamat.2015.12.006

Pacana, A., & Czerwińska, K. (2017). Wykorzystanie metody 8D do rozwiązania problemu jakościowego, *Zeszyty Naukowe Politechniki Częstochowskiej*, *2*(28), 73-86. http://dx.doi.org/10.17512/znpcz.2017.4.2.07

Pacana, A., & Czerwińska, K. (2020). Comparative tests of the quality of the piston combustion chamber for a diesel engine. *Tehnicki Vjesnik-Technical Gazette*, *27*(3), 1021-2024. https://doi.org/10.17559/TV-20190112193319

Pacana, A., Czerwińska, K., & Dwornicka, R. (2019). Analysis of non-compliance for the cast of the industrial robot basis, *Proceedings of the 28th International Conference on Metallurgy and Materials*, Czech Republic, 644-650. https://doi.org/10.37904/metal.2019.869

Pereira, J. C., Gil, E., Solaberrieta, L., San Sebastián, M., Bilbao, Y., & Rodríguez, P. P. (2020). Comparison of AlSi7Mg0.6 alloy obtained by selective laser melting and investment casting processes: Microstructure and mechanical properties in as-built/as-cast and heat-treated conditions. *Materials Science and Engineering A*, *778*, 139124. https://doi.org/10.1016/j.msea.2020.139124

Piętowska–Laska, R. (2015). Produktywność systemów logistycznych – ujęcie teoretycznopraktyczne. *Logistyka*, *4*, 5315-5324.

PN-EN 1706:2011 (2011). Aluminum and aluminum alloys Castings. Chemical composition and mechanical properties. Warszawa: PKN.

Pysz, S., Maj, M., & Czekaj, E. (2014). High-strength aluminium alloys and their use in foundry industry of nickel superalloys. *Archives of Foundry Engineering*, *14*(3), 71-76. https://doi.org/10.2478/afe-2014-0065

Salomon, A., Voigt, C., Fabrichnaya, O., Aneziris, C., & Rafaja, D. (2017). Formation of corundum, magnesium titanate, and titanium(III) oxide at the interface between rutile and molten Al or AlSi7Mg0.6 alloy. *Advanced Engineering Materials*, *19*(9), 1700106. https://doi.org/10.1002/adem.201700106

Ulewicz, R., & Novy, F. (2019). Quality management systems in special processes. *Transportation Research Procedia*, *40*, 113-118. https://doi.org/10.1016/j.trpro.2019.07.019

Wolniak, R. (2020). Main functions of operation management. *Production Engineering Archives*, *26*(1), 11-14. https://doi.org/10.30657/pea.2020.26.03

Wolniak, R, Skotnicka–Zasadzień, B. (2010). *Zarządzanie jakością dla inżynierów*. Wydawnictwo Politechniki Śląskiej.

Zhamoida, O. A. (2009). Methodical peculiarities of estimating competitiveness of industrial enterprises. *Actual Problems of Economics*, *91*, 110-118.

Zhou, S., & Zhu, A. M. (2005). Comprehensive evaluation of enterprise technological competitiveness. *Proceedings of the 2005 International Conference on Management Science and Engineering*, 9-11.

Analiza Pozycji Technologicznej w Odniesieniu do Produkcji Odlewów Aluminiowych

Streszczenie

Dynamicznie rozwijający się rynek produkcyjny, a w szczególności przemysłu metalurgicznego, wymusza stałe doskonalenie poziomu efektywności produkcji, jakości wyrobów, co wpływa na pozycję przedsiębiorstwa na rynku oraz na poziom jego konkurencyjności. Z tego względu celem opracowania było określenie aktualnej pozycji przedsiębiorstwa odlewniczego biorąc pod uwagę aluminiowy odlew skrzyni biegów, w kontekście możliwości technologicznych i pozycji na rynku, a także identyfikacja newralgicznych czynników i finalnie wskazanie warunków jej umocnienia. W badaniu wykorzystano macierz 3x3. Badane przedsiębiorstwo w kontekście wytwarzania analizowanego wyrobu zlokalizowane jest w obszarze „poprawa marketingu". Lokalizacja ta świadczy o konieczności podjęcia działań związanych z utworzeniem działu marketingu i rozwoju oraz konieczności lepszego wykorzystania zidentyfikowanego potencjału technologicznego przedsiębiorstwa. Przedstawiona w opracowaniu metoda może być przydatna do analizy pozycji przedsiębiorstw produkcyjnych oraz usługowych z różnych branż, celem obrania adekwatnej strategii rozwojowej.

Słowa kluczowe: przemysł metalurgiczny, budowa maszyn, zarządzanie jakością, macierz 3x3, odlew aluminiowy

Original Research

Numerical Simulation of Mechanical Joining of Three DP600 and DC06 Steel Sheets

Denis Cmorej *, Ľuboš Kaščák

Department of Technology, Materials and Computer Supported Production, Technical University of Košice, Mäsiarska 74, 04001 Košice, Slovak Republic

* Correspondence: denis.cmorej@tuke.sk

Abstract

There are many reasons to utilize various grades of steel in car body production. Automotive producers tend to choose steels with great formability and the capacity to absorb impact energy. The dominant method used for joining car body sheets has for many years been resistance spot welding, but the use of various steel sheets leads to research into alternative joining methods. Mechanical joining - clinching, is the innovative method to join these materials. Numerical simulation tools are used to optimize the joining of materials. Simufact Forming software was used to analyse the clinching joining of three sheets of material DP600 and DC06. According to the axisymmetric character of the mechanical joining process, the simulation was stream-lined to a 2D representation. The results of the simulation of the mechanical joining process were compared with the real samples prepared for metallographic observation.

Keywords: DC06, DP600, clinching, FEM analysis

1. Introduction

The main issue in the automotive industry are the solutions for improving the lightweight of the cars and improved crash reaction of explicit car-body structures. Achieving these aims leads to the use of different grades of steel sheets in different parts of the car body (Kaščák et al., 2016). Materials from extra deep-drawing grades to ultra-high strength grades are therefore utilized. The dual-phase steel sheets are distinguished by the combination of high strength and good formability because of their specific microstructure (the hard martensitic or bainitic phase is dispersed in a ferritic matrix). This specific type of material is characterized by an acceptable ability to redistribute stress and improve mechanical properties (Bzowski et al., 2018; Qin et al., 2020; Spena et al., 2019). Extra deep-drawing grades are characterized as cold rolled steel and are mostly designed for cold forming, suitable for multifaceted large scale presswork of automobile bodies (Behrouzi et al., 2014; Livatyali et al., 2010; Neto et al., 2017). Resistance spot welding is used as the primary method of joining of steel sheets, but the use of various grades of materials leads to research into other joining methods.

Clinching, as one of a mechanical joining methods, is an innovative technique to join various grades and thicknesses of materials. In general, the principle of the process of clinching consists of interlocking the sheets together using a specially shaped punch and die. At the stage of contact of the material and the specially shaped die, the material flows to the sides and creates a clinched joint. The resulting interlocking between the joined materials is an important factor for the creation of a high-quality clinched joint with sufficient load-bearing capacity (Kaščák et al., 2017; Lambiase, 2013; Shi et al., 2020). To optimize the joining of materials, the means of numerical simulation are advantageously used. They make it possible to predict the behaviour of materials during the joining process (Pater et al., 2021; Potgorschek et al., 2020).

Most of the research is aimed at evaluating the properties of joints formed on two sheets. Only a few studies concern the evaluation of joints formed on three sheets. The paper deals with the simula-

tion of the process of clinching DP600 and DC06 steel sheets, and by comparing the results of the simulation with the clinched joints that were created.

2. Methodology of the research

2.1. Used materials

In the experimental part of this article, two types of materials were used – DP600 (dual-phase high-strength grade) and DC06 (extra deep-drawing grade) steel sheets. The thickness of both steel sheets was 0.8 mm. Table 1 shows the basic mechanical properties of the DC06 and DP600 steel sheets, which were used on basis of the material list. The samples were prepared to a size of 40 x 90 mm (overlap length of 30 mm). Since it is a mechanical joining, it was not necessary to clean the surfaces of the samples.

Table 1. Basic mechanical properties of the observed materials

Material	E, GPa	A_{80}, %	$R_{p0.2}$, MPa	R_m, MPa	Strain hardening exponent n90 min.
DC06	210	41	142	330	0.220
DP600	206	23	407	633	0.216

2.2. Principle of clinching

Mechanical joining - clinching is an innovative technique to join progressive materials. The principle of the process of clinching consists of interlocking the sheets together using a specially shaped punch and die. At the stage of contact of the material and the specially shaped die, the material flows to the sides and creates a clinched joint. The interlocking creation is important for the creation of mechanically clinched joints to carry the load. The process of clinching is demonstrated in Fig. 1. A specially shaped punch with the diameter of ø5 mm and a die with the diameter of ø8 mm were used. Specially shaped punch and die were made of material grade 1.3343. Grade 1.3343 is the HSS-type steel. HSS refers to high-speed steel grade. The grade is defined in ISO 4957. The parameters of the clinching process are described in Table 2.
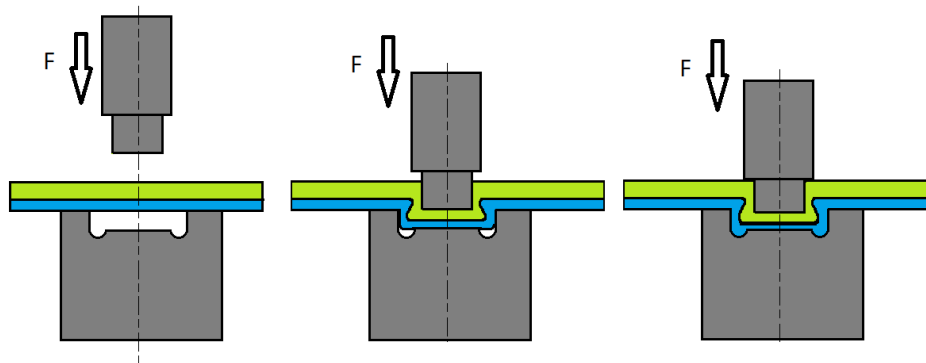
Fig. 1. Process of the mechanical joining – clinching

Table 2. Parameters of the clinching process

Material	Joined sheets	Pressing force F, kN	Punch diameter, mm	Die diameter, mm
DP600 (0.8 mm)	3	70	ø5	ø8
DC06 (0.8 mm)	3	70	ø5	ø8

2.3. Metallographic observation

During the stage of metallographic observation, changes in the microstructure of DP600 and DC06 steel sheets after the process of mechanical joining - clinching were observed. Interlocking, the value of the thickness of the bottom of the joint, the value of the thickness of the neck of the joint as well as the defects of the joints formed by the process of mechanical joining - clinching were observed as well. Microscopic observation was realized by KEYENCE VHX- 5000 light optical microscope (Fig. 2).
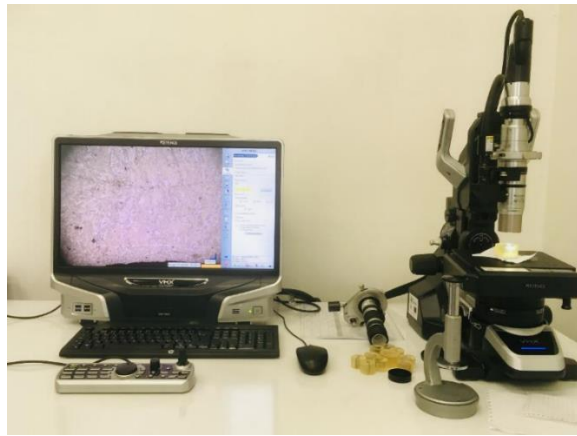
Fig. 2. KEYENCE VHX- 5000

2.4. Simufact Forming software

Simufact Forming software is a simulation tool for optimizing forming technology. This software includes a module of mechanical joining, specifically designed for simulation of mechanical joining processes. Simufact Forming enables the use of both two-dimensional (axisymmetric and planar) and three-dimensional simulations in the same specific graphical user interface. Different types of materials specific to the process of forming technology can be simulated. Joining different thicknesses of the materials can be simulated as well. In practice, simulation software is used to optimize the joining processes before the values of parameters are implemented in the process (optimal values are selected) (Lambiase, 2013; Shi et al. 2020). The software environment of Simufact is shown in Fig. 3.
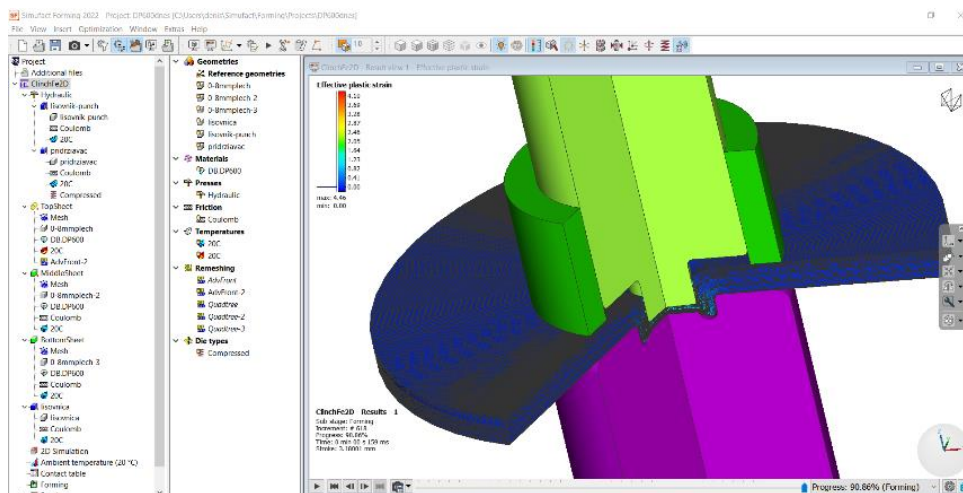
Fig. 3. The software environment of Simufact

The Simufact Forming was used for the mathematical representation of the solved problem and optimization of the joining process of mechanical joining – clinching of DP600 and DC06 steel sheets. As a part of the optimization of the mechanical joining process - clinching, different values of the punch stroke were evaluated with the simulation. Figure 4 shows the development of plastic deformation during the process of mechanical joining – clinching three DC06 steel sheets in the four characteristic joining steps.

The overall solution to the problem was simplified on a 2D model because the specially shaped tools and the created joint itself are axially symmetrical. The basic parameters necessary when defining the simulation itself include the friction coefficient, the holding force, and the specific distance of the punch stroke. During the simulation of the process of mechanical joining, the specially shaped punch can only be moved in the vertical position, with the punch making a vertical downward movement at a punch stroke. In the process of simulation, the punch can only be moved in the vertical position, with the punch making a vertical downward movement at the punch stroke of 1.8 mm, 2.2 mm, 2.5 mm, and 3 mm.

1. drawing   2. compression

3. upsetting   4. punch
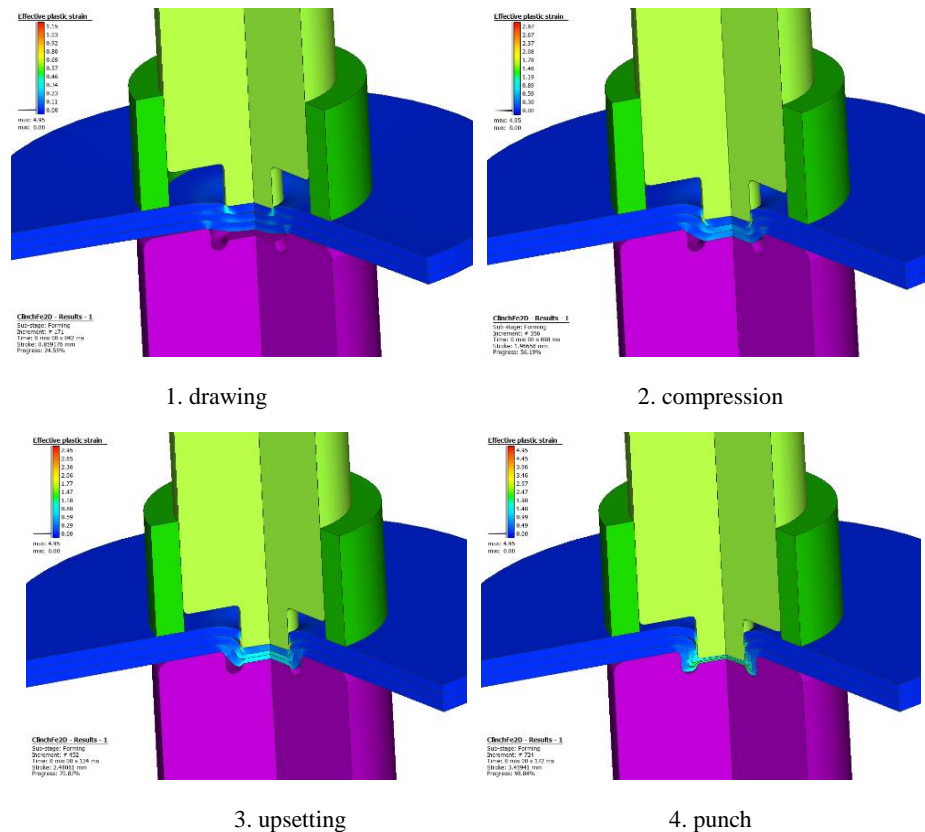
Fig. 4. Development of plastic deformation during the joining process

The contacts between the specially shaped tools and joined steel sheets (DP600 and also for DC06) as well as the contacts between the joined materials were defined as frictional contacts. Between specially shaped punch/die and sheets was defined as a friction coefficient of 0.12 and between three sheets was defined special friction coefficient of 0.2. The important and last boundary condition is the sheet holder force of 100 N that acts on the upper sheet to fix the joined materials during the process of the simulation. At the exact moment, the prescribed distance of the stroke height is reached, the special-shaped punch performs a backward movement to the starting position. At the same time, the special force of the sheet holder stops to work. The specially shaped punch, specially shaped die, and sheet holder were specified as perfectly stiff and non-deformable bodies. The joined sheets - a combination of three steel sheets for material DP600 and a combination of three steel sheets for material DC06 were defined as deformable bodies.

3. Results and discussion

When numerical simulation of three DP600 steel sheets was performed, a crack occurred at the value of punch stroke of 2.5 mm, in the area of interlocking (Fig. 5). On the other hand, numerical simulation of clinching of the three DC06 steel sheets was successfully completed at the value of punch stroke of 3 mm (Fig. 6). The critical area during the clinching process is the sheet metal on the punch side in the interlocking area. The maximum value of plastic deformation during the mechanical joining process of clinching is located just in the upper sheet at a certain point where it is excessively thinned. This area is known as the neck area of the clinched joint and is considered critical in terms of the process of mechanical joining. It is possible to verify the simulation to compare it and then verify the results with a real joining process. The experiments with real samples confirmed the results of the numerical simulation. When joining three steel sheets of DP600, the clinch joint did not form at all. There was a failure of the top sheet (from the punch side) in the interlocking area. The clinching of three steel sheets was successfully performed. The well-formed quality clinched joints were created. No defects were observed in the joints. The effect of the high stroke of the punch has a significant impact on the maximum effective plastic strain. The Simufact simulation software predicted the effective plastic strain for joints of DP600 sheets to the maximum value of 5.2%. For joints of DC06 sheets, the value of effective plastic strain was predicted to be max. 4.75%.
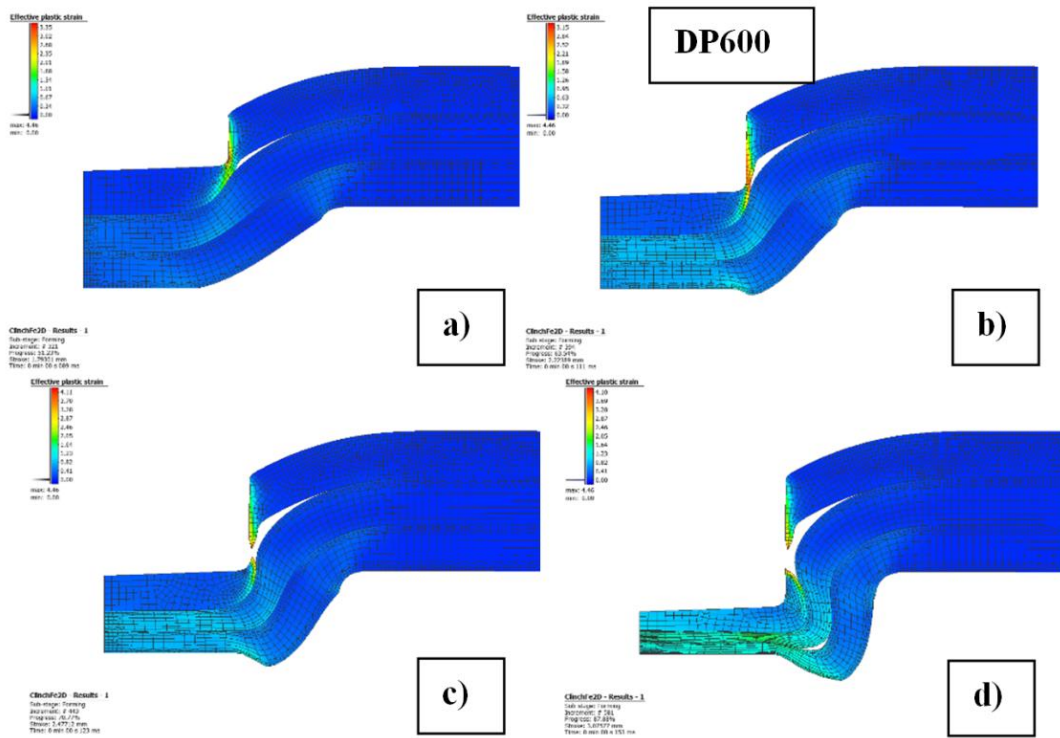
Fig. 5. Clinching of DP600 steels – punch stroke distance: a) 1.8 mm b) 2.2 mm c) 2.5 mm and d) 3 mm
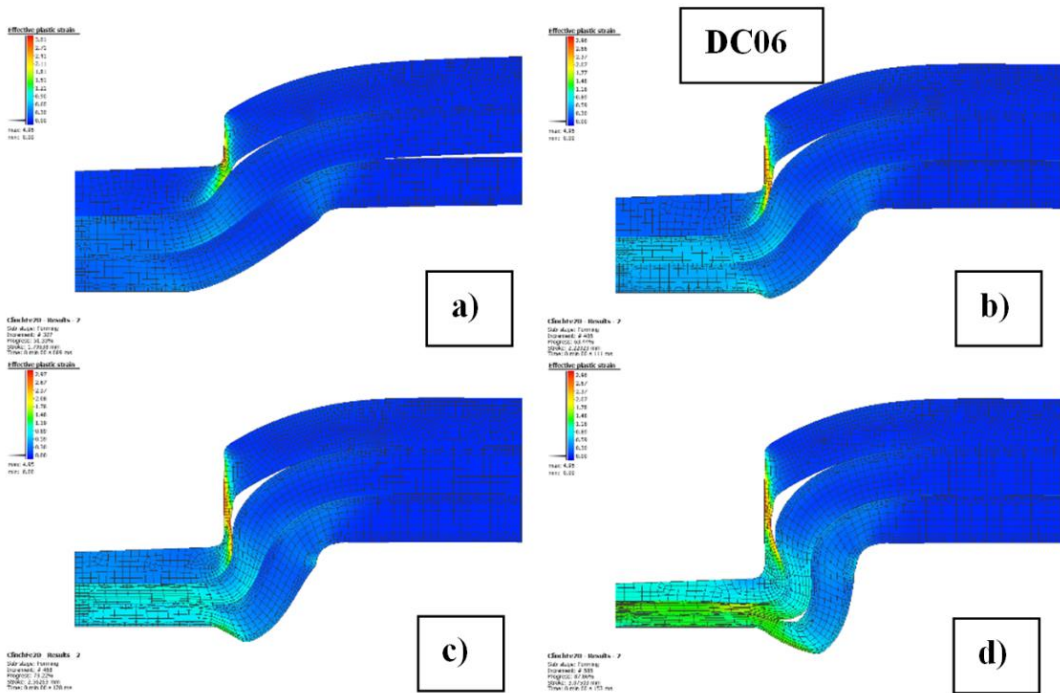
Fig. 6. Clinching of DC06 steels - punch stroke distance: a) 1.8 mm b) 2.2 mm c) 2.5 mm and d) 3 mm

Figure 7 shows a comparison of the cross-sections between the real joint created by the mechanical joining process - clinching (left side) and the joint resulting from the numerical simulation process (right side). The dimensions in the neck area of the joint were different; the simulation showed a large gap between the top and middle sheet (Fig. 7 – location A). Figure 8 shows the comparison of clinching joint parameters of real and simulated joints. The values in the area of the joint were within a certain tolerance identical for both the simulated joint and the real joint. Metallographic cut of the joint made of DP600 material was not realized, because the joint did not occur (which was also predicted by the simulation).
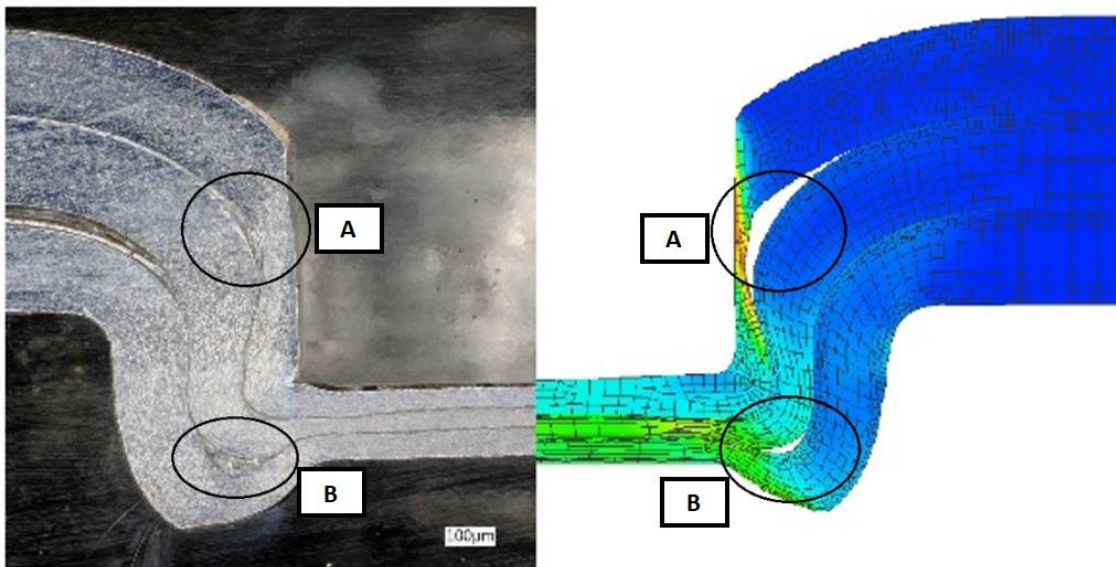
Fig. 7. Comparison of the cross-sections between the real joint created by the mechanical joining process of material DC06 - clinching (left side) and the joint resulting from the simulation (right side)
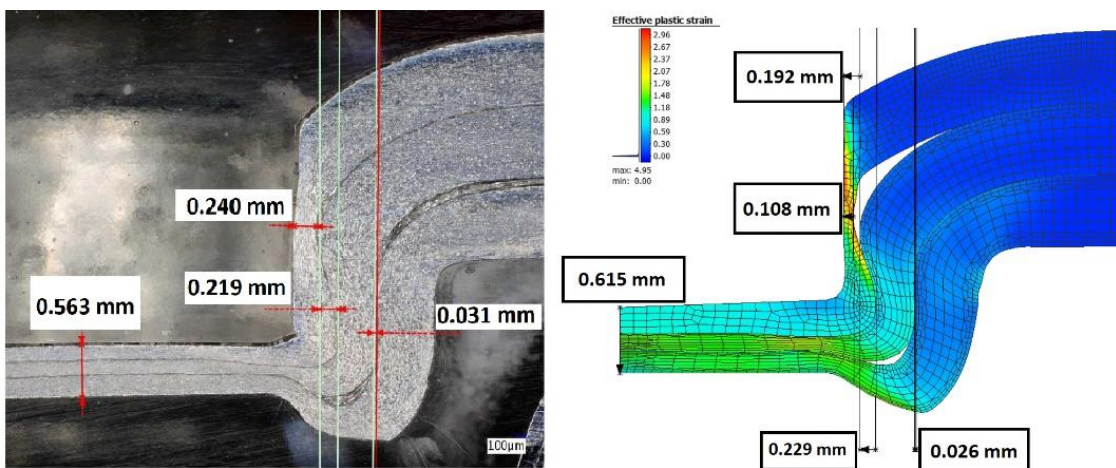
Fig. 8. Comparison of clinching joint parameters: a) real joint, b) simulated joint

4. Conclusions

The paper dealt with the numerical simulation of the clinching process of three steel sheets of various grades. The calculation of the simulation was simplified into 2D conditions based on the axial symmetry of the entire process of mechanical joining. The resulting simulation of the joining process in the form of the representation of the plastic deformation in the joining of three steel sheets (DP600 and DC06) during the individual mechanical joining stages was verified with the results of the real experiments.

The results from the experiments confirmed the results from the numerical simulation. When joining three steel sheets of DP600 quality, clinch joints were not successfully created. However, the joining of three DC06 grade steel sheets was successfully realized as was predicted by the numerical simulation.

Acknowledgments

References

Behrouzi, A., Soyarslan, C., Klusemann, B., & Bargmann, S. (2014). Inherent and induced anisotropic finite visco-plasticity with applications to the forming of DC06 sheets. *International Journal of Mechanical Sciences*, *89*, 101-111. https://doi.org/10.1016/j.ijmecsci.2014.08.025

Bzowski, K., Rauch, L., & Pietrzyk, M. (2018). Application of statistical representation of the microstructure to modeling of phase transformations in DP steels by solution of the diffusion equation. *Procedia Manufacturing*, *15*, 1847-1855. https://doi.org/10.1016/j.promfg.2018.07.205

Kaščák, Ľ, et al. (2016). *Aplication of modern joining methods in car production*. Processes Examples Strength. Rzeszów, pp.143.

Kaščák, Ľ., Spišák, E., Kubík, R., & Mucha, J. (2017). Finite element calculation of clinching with rigid die of three steel sheets. Strength of Materials, 49, 488–499. https://doi.org/10.1007/s11223-017-9892-2

Lambiase, F. (2013). Influence of process parameters in mechanical clinching with extensible dies. *The International Journal of Advanced Manufacturing Technology*, *66*, 2123–2131. https://doi.org/10.1007/s00170-012-4486-4

Livatyali, H., Firat, M., Gurler B., & Ozsov, M. (2010). An experimental analysis of drawing characteristics of a dual-phase steel through a round drawbead. *Materials & Design*, *31*(3), 1639-1643. https://doi.org/10.1016/j.matdes.2009.08.030

Neto, D.M., Oliveira, M. C., Santos, A. D., Alves, J. L., & Menezes, L. F. (2017). Influence of boundary conditions on the prediction of springback and wrinkling in sheet metal forming. *International Journal of Mechanical Sciences*, *112*, 244-254. https://doi.org/10.1016/j.ijmecsci.2017.01.037

Pater, Z., Tomczak, J., Bulzak, T., Knapiński, M., Sawicki, S., & Laber, K. (2021). Determination of the critical damage for 100Cr6 steel under hot forming conditions. *Engineering Failure Analysis*, *128*, 105588. https://doi.org/10.1016/j.engfailanal.2021.105588

Potgorschek, L., Domitner, J., Hönsch, F., Sommitsch, C., & Kaufmann, S. (2020). Numerical simulation of hybrid joining processes: self-piercing riveting combined with adhesive bonding. *Procedia Manufacturing*, *47*, 413-418. https://doi.org/10.1016/j.promfg.2020.04.322

Qin, S., Lu, Y., Sinnott, S. B., & Beese, A. M. (2020). Influence of phase and interface properties on the stress state dependent fracture initiation behavior in DP steels through computational modeling. M*aterials Science and Engineering: A*, *776*, 138981. https://doi.org/10.1016/j.msea.2020.138981

Shi, C., Yi, R., Chen, C., Peng, H., Ran, X., & Zhao, S. (2020) Forming mechanism of the repairing process on clinched joint. *Journal of Manufacturing Processes*, *50*, 329–335. https://doi.org/10.1016/j.jmapro.2019.12.025

Spena, P. R., Angelastro, A., & Casalino, G. (2019). Hybrid laser arc welding of dissimilar TWIP and DP high strength steel weld. *Journal of Manufacturing Processes*, *39*, 233-240. https://doi.org/10.1016/j.jmapro.2019.02.025

Symulacja Numeryczna Mechanicznego Łączenia Trzech Blach Stalowych DP600 oraz DC06

Streszczenie

Istnieje wiele powodów dla których warto wykorzystywać różne gatunki stali do produkcji karoserii. Producenci motoryzacyjni wykorzystują blachy stalowe o dużej plastyczności i zdolności pochłaniania energii uderzenia. Od wielu lat dominującą metodą łączenia blach karoserii samochodowej jest punktowe zgrzewanie oporowe. Zastosowanie różnych blach stalowych prowadzi do badań nad alternatywnymi metodami łączenia. Łączenie mechaniczne – przetłaczanie, to innowacyjna metoda łączenia tych materiałów. Numeryczne narzędzia symulacyjne służą do optymalizacji łączenia materiałów. Oprogramowanie Simufact Forming zostało wykorzystane do analizy łączenia przez przetłaczanie trzech arkuszy materiałów DP600 i DC06. Zgodnie z osiowosymetrycznym charakterem procesu łączenia mechanicznego, symulacja została uproszczona do reprezentacji 2D. Wyniki symulacji procesu łączenia mechanicznego porównano z rzeczywistymi próbkami przygotowanymi do obserwacji metalograficznych.

Słowa kluczowe: DC06, DP600, przetłaczanie, analiza MES

Original Research

Assessment of the Tribological Performance of Bio-Based Lubricants Using Analysis of Variance

Marek Szewczyk [ID]**, Krzysztof Szwajka** *[ID]

Department of Integrated Design and Tribology Systems, Faculty of Mechanics and Technology, Rzeszow University of Technology, ul. Kwiatkowskiego 4, 37-450 Stalowa Wola

* Correspondence: m.szewczyk@prz.edu.pl

Abstract

The purpose of this article is to determine the coefficient of friction of a DC04 steel sheet using a specially designed flat-die strip drawing test. Four different bio-based lubricants, edible (sunflower and rape-seed) and non-edible (karanja and moringa) were used in the study. The experiments were carried out for different contact pressure values. The as-received specimens were pre-strained with strains of 7, 14, and 21%. The values of the coefficient of friction as a ratio of the friction force to the normal force were determined. The influence of the viscosity of the lubricant and the contact pressure on the value of the coefficient of friction has been investigated using ANOVA. A tendency to a decrease in the coefficient of friction with increasing contact pressure was observed. Significance results obtained after the ANOVA analysis confirmed the influence of normal pressure and oil viscosity on the value of the coefficient of friction. At the same time, the hypothesis about the influence of the sheet pre-straining on the value of the coefficient of friction was not confirmed by the significant interactions.

Keywords: analysis of variance, ANOVA, friction, plastic working

1. Introduction

The metal forming industry is one of the largest sectors of *a* nation's economy. Chipless forming will ensure the production of finished products without material loss and is much faster than machining methods. For the correct course of the forming process, the parameters of the machining process and the friction conditions need to be properly selected (Dou & Xia, 2019; Wu et al., 2021). Lubrication is a basic and effective way to reduce friction and ensure a proper surface finish (Lachmayer et al., 2022). Surface texturing has also attracted great attention as a geometrical modification approach to improving tribological performance (Shimizu et al., 2019). In cold forming processes, in which the material is subjected to large deformations and high contact pressures, the lubricant is also responsible for cooling the tools (Evin & Tomáš, 2022; Folle et al., 2022). The basic criteria for the division of lubricants are the consistency of the lubricant, the origin (mineral or organic) and the intended use. Due to their consistency, the following types of lubricants are distinguished: solid lubricants, liquid lubricants (oils), emulsions (oil mists) and greases (Alaboodi, 2020). From their origin, lubricants are divided into natural (animal and vegetable), refined and synthetic. The selection of a specific type of grease depends on the conditions of the forming process, that is, contact pressures, surface topography of the tool and workpiece, sliding speed and temperature (Nagendramma & Kaul, 2012; Singh et al., 2022).

During the last decade, due to the tendency to manufacture products in environmentally friendly processes, the engineering industry focused on introducing lubricants with a high degree of biodegradability (Bobzin et al., 2009; Klocke et al., 2005). These are mainly lubricants of animal and vegetable origin (edible and non-edible). A chemical feature of vegetable oils is that they consist mainly of triglycerides of fatty acids, which can vary greatly depending on the plant cultivation conditions (Ilyin et al., 2022). The most advantageous utility feature of vegetable oils from the point of view of environ-

mental protection is the ability to biodegrade, that is, self-decomposition to carbon dioxide (CO_2) and water (H_2O) (Zajezierska, 2016). Compared to petroleum oils and even synthetic esters, vegetable oils show the highest biodegradability (80–100%) (Zajezierska, 2016). Vegetable lubricants are modified by antiwear additives. Antiwear additives (phosphoric acid, zinc dialkyldithiophosphates, nano-particulate potassium borate, etc.) form a lubricious sacrificial coating that protects the metal from wear under boundary lubrication conditions (Stolte et al., 2012).

Due to the large number of parameters affecting friction in sheet metal forming, many analytical techniques are used to determine the influence of process parameters on the value of the coefficient of friction. Bhaumik and Pathak (2016) used the analysis of variance (ANOVA) to predict the significant factors affecting the tribological properties of neat castor oil in a boundary lubrication regime. From the ANOVA it has been observed that the normal load is the significant factor while determining frictional force. Mirahmadi et al. (2015) investigated the coefficient of friction in a ring compression test. The effect of platen speed and temperature on the coefficient of friction was analysed using ANOVA. Carvalho and Lukács (2021) used ANOVA to analyse the friction propeties of austenitic chromium-nickel stainless steel determined using a strip drawing test. It was found that higher velocity resulted in a decreasing coefficient of friction. An increase in contact pressure caused decreasing friction. Dilmec and Arap (2016) investigated the effects of the surface roughness of tools, drawing speed, and lubrication on the dynamic coefficient of friction by using ANOVA. The coefficient of friction in the die radius region was found to be significantly different from that in the flange region. Basavaraj et al. (2014) investigated the friction performance of a metal matrix composite using ANOVA. It was observed that sliding speed and normal pressure influence the coefficient of friction of an LM6 aluminium alloy that has been reinforced with SiC. The purpose of this article is to determine the coefficient of friction of a DC04 steel sheet using the flat-die strip drawing test. Four different bio-based lubricants were used in the study. The influence of the viscosity of the lubricant and the contact pressure on the value of the coefficient of friction has been investigated using ANOVA. The drive to eliminate synthetic and mineral oils, which are difficult to recycle, from the manufacturing process has opened up opportunities for the use of vegetable-based bio-lubricants (Sayhir et al., 2017). This article presents a comparison of the lubrication performance of two non-edible oils (moringa and karanja) with the most frequently tested edible oils. Due to the global food crisis, it seems desirable to replace edible oils with non-edible bio-based oils. Environmentally friendly bio-based lubricants have been found to exhibit superior lubricant properties over the conventional mineral lubricants, with renewability and biodegradability being their strongest suit. There is a need to explore the potential of bio-based lubricants for various applications. In this regard, the aim of this paper is to highlight the potential of non-edible oils for applications in sheet metal forming.

2. Material and installation

2.1. Test sample

Cold-rolled DC04 steel sheet was used as the test material. The sheet thickness was 0.83 mm. The chemical composition of the DC04 steel sheet according to the EN 10130:2009 is as follows: $C \leq 0.1$ wt.%, $Mn \leq 0.45$ wt.%, $P \leq 0.035$ wt.%, $S \leq 0.035$ wt.%, Fe – remainder. The mechanical properties of the test material according to the EN 10130:2009 standard are listed in Table 1.

Table 1. Basic mechanical parameters of the DC04 steel sheet according to the EN 10130:2009 standard

Yield stress Re, MPa	Ultimate tensile stress Rm, MPa	Elongation A80, %	Anisotropy coefficient r90
140-240	270-370	≥ 34	≥ 1.6

The topography of the sheet surface in the as-received state (Fig. 1) was determined using a Hommel-Etamic T8000RC stationary profilometer. The values of basic surface roughness parameters are as follows: Sq = 2.29 μm, Sku = 2.70, Ssk = −0.022. The basic height parameters of the geometric structure of the countersamples' surface were also determined: maximum profile valley depth Sv (5.11 μm), arithmetical mean height Sa (0.636 μm), kurtosis Sku (3.76), skewness Ssk (-0.544), maximum height Sz (10.0 μm), maximum profile peak height Sp (4.89 μm) and root mean square deviation Sq (0.81 μm). The average hardness was found to be 215 HV10.
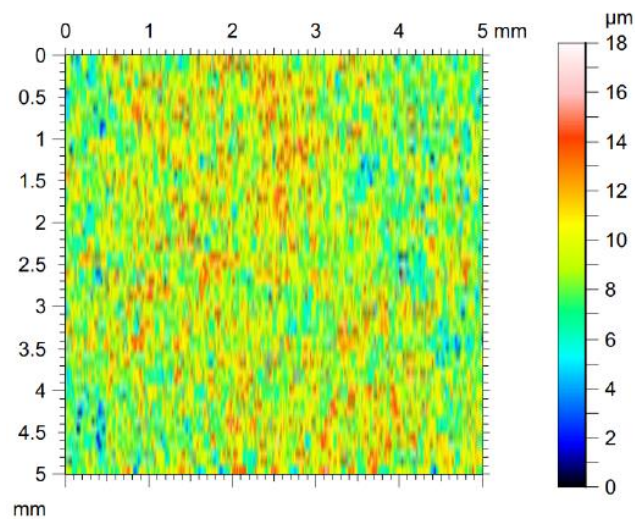
Fig. 1. Topography of the sheet surface in the as-received state

2.2. Test procedure

The coefficients of friction of low-carbon DC04 steel sheets have been determined using the flat-die strip drawing test (Fig. 2). The test involves pulling a strip of sheet metal between two flat counter-samples. Friction tests were carried out using a specially designed tester (Fig. 3) which was mounted in the lower grip of a Zwick/Roell Z100 testing machine. Countersamples were made of 145Cr6 cold-work tool steel.
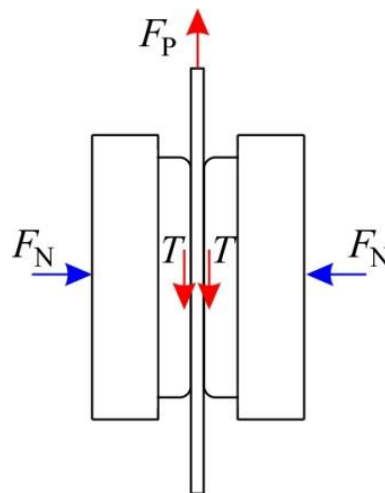
Fig. 2. Schematic diagram of the strip drawing test
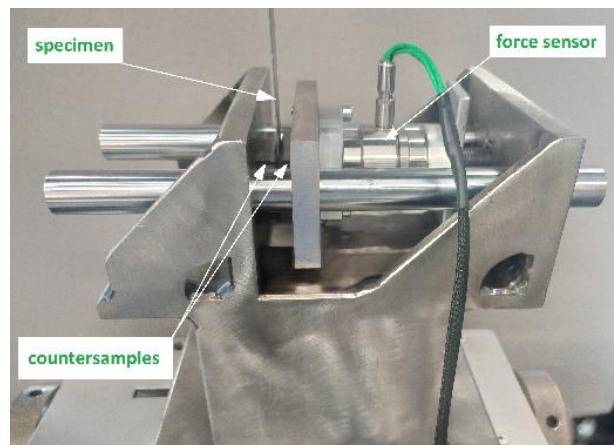
Fig. 3. Photograph of the friction tester

Specimens (130 mm long and 20 mm wide) were cut from a sheet of metal. The tests were carried out for four nominal pressures of 3, 6, 9 and 12 MPa. The as-received specimens were pre-strained with strains of 7, 14, and 21%. The specimens pre-straining was performed using a Zwick Roell Z030 standard tensile machine. The sliding speed of the specimen was 2 mm/s. The contact (normal) force F_N was recorded using the Labview program and a Kistler type 9345B force sensor. The pulling (friction) force F_T was recorded using the measuring system of a uniaxial tensile testing machine. The value of the coefficient of friction was determined according to the relationship:

$$\text{coefficient of friction} = \frac{F_P}{2F_N} \tag{1}$$

One specimen was tested for each conditions. However, the sheet was drawn for a distance of about 50 mm. For each of tests, we obtained about 9000–9500 discrete values of the coefficient of friction. The average coefficient of friction was determined using the Eq. (1).

Vegetable oils (edible and non-edible) are extensively used in incremental sheet metal forming (Diabb et al., 2017). Karthik (2016), Carcel et al. (2005) and Syahrullail & Afifah (2017) indicated the usefulness of edible oils in conventional sheet metal forming. However, they can not be used as lubricants if high load magnitudes are applied during forming process (Syahrullaila et al., 2013). The usefulness edible oils (rape-seed oil, olive oil, sunflower oil) has been confirmed by Więckowski & Dyja (2017) in the process of Grade 2 titanium sheet metal forming. In the face of the growing food crisis, more emphasis should be placed on non-edible oils of vegetable origin. The tests were carried out in conditions of dry friction and lubrication of the sheet surface with edible and non-edible oils. The basic physical parameters of the oils used are listed in the Table 2.

Table 2. The basic physical properties of the vegetable oils

Oil	Kinematic viscosity mm²/s	Density, g/cm³	Flash point, °C
karanja	75	0.936	212.0
moringa	73	0.897	268.5
rape-seed	51	0.914	314.0
sunflower	58	0.920	319.1

2.3. ANOVA

For the experiment presented, an analysis of variance was performed in the STATISTICA 13 (StatSoft Inc.) program in which the significance of the influence of the controlled factors on the friction phenomenon was determined. In order to trace the influence of nominal pressure, viscosity and sample pre-strain on the examined feature, a three-factor classification model was adopted.

3. Results and discussion

Table 3 shows the influence of individual input parameters and their products on the value of the coefficient of friction. In addition to the impact of individual factors, there is an additional interactional source of variability, that is, the combined effect of input parameters. The interaction shows to what extent the influence of one factor depends on the level of the other factor. As a result of the analysis (Fig. 4 and Table 3), the hypothesis of no influence of the nominal pressure on the value of the coefficient of friction is rejected at the significance level of $p = 0.002$. Furthermore, the hypothesis of no influence of the lubricant viscosity on the value of the coefficient of friction is also rejected at the significance level of $p = 0.000$. It can therefore be concluded that the value of nominal pressure and oil viscosity significantly affect the coefficient of friction.

Table 3. Significance of the input parameters determined using ANOVA

Parameter	Significance level ($p \leq 0.05$)
pressure	0.002
viscosity	0.000
sample pre-strain	0.307
pressure · viscosity	0.951
sample-pre-strain · pressure	0.966
pressure · viscosity · sample pre-strain	0.987
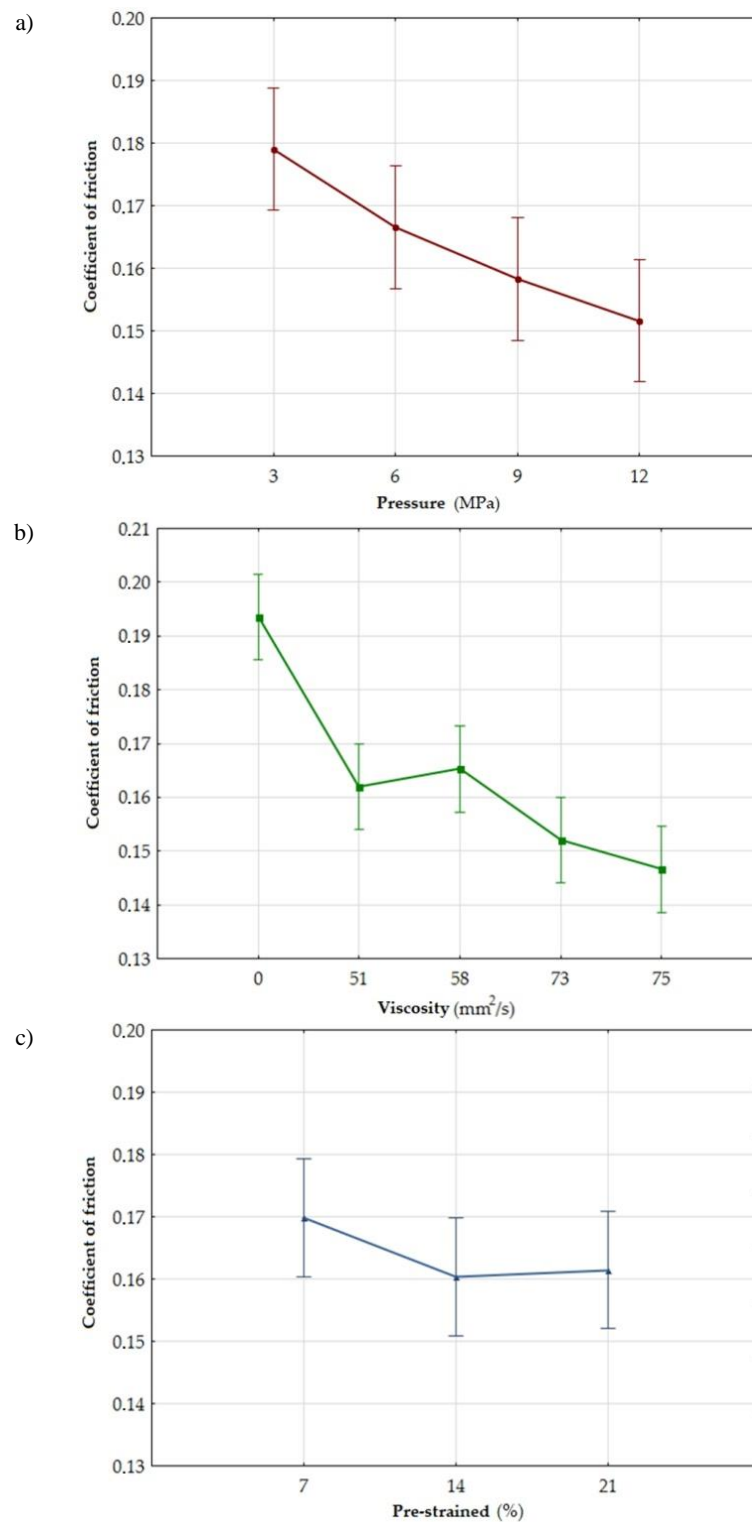
Fig. 4. Effect of (a) nominal pressure, (b) lubricant viscosity and (c) sample pre-strain on the value of the coefficient of friction

The results presented in Table 3 and Fig. 5 make it possible to unequivocally state that in the conducted statistical analysis concerning the occurrence of interactions, no statistically significant interactions between the tested factors were observed. In the tests, it was observed that the value of the coefficient of friction decreased with increasing pressure in the range of 3 to 12 MPa. It was found that at relatively low normal pressures, the friction force does not change proportionally to the normal force.

a)

b)
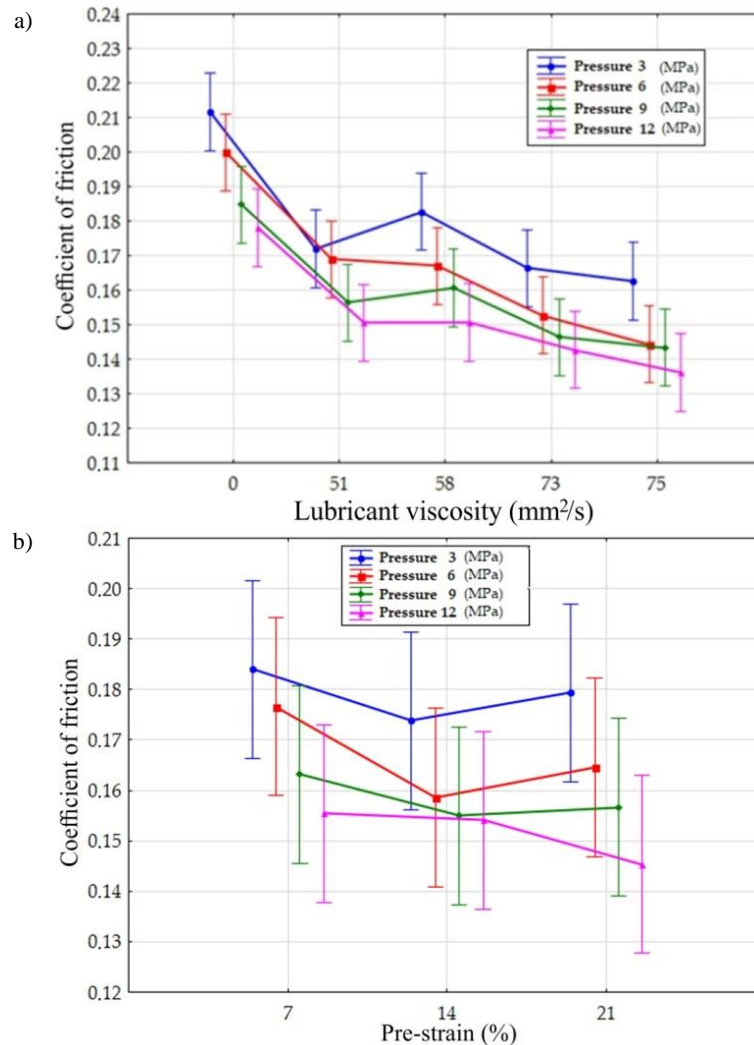
Fig. 5. Interactions between (a) viscosity and (b) sample pre-strain and the coefficient of friction

As expected, the coefficient of friction was highest in dry friction conditions. All the tested oils showed a similar effect of reducing the coefficient of friction depending on the degree of sample pre-strain. In the dry friction conditions for the pre-strained samples with the smallest degree of deformation (7%), an initial decrease in the value of the coefficient of friction was observed, followed by continuously increasing at the highest nominal pressures. Similarly, the curves of the lubrication efficiency of the pre-strained sheets at 14% showed a certain minimum, beyond which the value of the coefficient of friction began to increase. This can be explained by the fact that the additional plastic deformation of the sheet changes the mechanical properties of the sheet material through the work hardening effect. The SEM micrographs of the sheet surface after friction tests were carried out under nominal pressure of 12 MPa (Fig. 6). The sheet surface revealed frictional occurrences of the alignment mechanism. There are also visible grooves in the surface of the sheet, which are oil pockets. In general the flattening mechanism has been revealed in the surface of all specimens tested.

4. Conclusions

In this article, the assessment of the tribological performance of bio-based lubricants using the analysis of variance is presented. Based on the results, the following conclusions can be drawn:
- There is a dominant influence of the nominal pressure and lubricant viscosity on the value of the coefficient of friction in the sheet metal forming process. Both an increase in nominal pressure and oil viscosity result in a decrease in the value of the coefficient of friction for the range of pressures considered.
- The most significant impact on the value of the coefficient of friction was observed for changes in the viscosity value.

- No statistically significant interactions between the analysed factors in the sheet metal forming process were observed.
- All the oils tested showed a similar effect of reducing the coefficient of friction depending on the value of the sample pre-strain.
- Bio-lubricants based on moringa and karanja oils achieved the lowest values of the coefficient of friction.
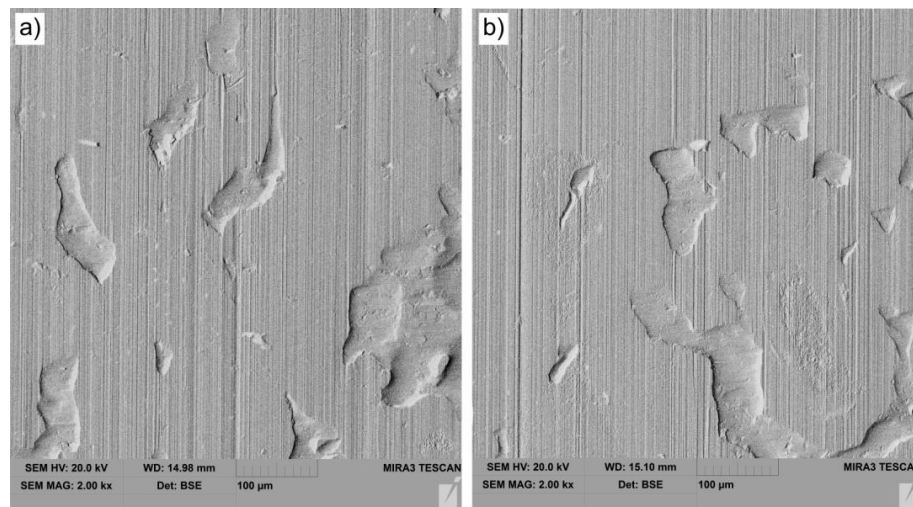
Fig. 6. The SEM micrographs of the sheet surface after friction tests under nominal pressure of 12 MPa: a) moringa and b) karanja oil

Flat-die strip drawing test is used to model friction condition in metal forming, i.e., between the punch and the die wall as well as between the blankholder and flange area of the drawpiece. This article is a part of the authors' effort to the application of artificial neural networks and machine leaning algorithms to understand the effect of the most important parameters on the coefficient of friction. The results obtained will constitute the knowledge base for training the artificial neural network.

References

Alaboodi, A.S. (2020). Natural oils as green lubricants in forming processes. Encyclopedia of Renewable and Sustainable Materials, 3, 122-128. https://doi.org/10.1016/B978-0-12-803581-8.10849-5

Basavaraj, Y., Kumar, P.B.K., Hiremath, P. (2014). Analysis of friction performance of LM6-SiC metal matrix composite by using design of experiments. *International Journal of Mechanical and Industrial Technology*, *2*(1), 28-34.

Bhaumik, S., & Pathak, S.D. (2016). A comparative experimental analysis of tribological properties between commercial mineral oil and neat castor oil using Taguchi method in boundary lubrication regime. *Tribology in Industry*, *38*(1), 33-34.

Bobzin, K., Bagcivan, N., Immich, P., Warnke, C., Klocke, F., Zeppenfeld, C., & Matfeld, P. (2009). Advancement of a nanolaminated TiHfN/CrN PVD tool coating by a nano-structured CrN top layer in interaction with a biodegradable lubricant for green metal forming. *Surface and Coatings Technology*, *203*(20-21), 3184-3188. https://doi.org/10.1016/j.surfcoat.2009.03.053

Carcel, A.C., Palomares, D., Rodilla, E., & Pérez Puig, M.A. (2005). Evaluation of vegetable oils as pre-lube oils for stamping. *Materials and Design*, 26, 587–593. https://doi.org/10.1016/j.matdes.2004.08.010

Carvalho, L.A., & Lukács, Z. (2021). The role of friction in the sheet metal forming numerical simulation. *IOP Conference Series: Materials Science and Engineering*, 1246, 012021. https://doi.org/10.1088/1757-899X/1246/1/012021

Diabb, J.; Rodríguez, C.A., Mamidi, N., Sandoval, J.A., Taha-Tijerina, J., Martínez-Romero, O., & Elías-Zúñiga, A. (2017). Study of lubrication and wear in single point incremental sheet forming (SPIF) process using vegetable oil nanolubricants. Wear, 376-377, 777-485. https://doi.org/10.1016/j.wear.2017.01.045

Dilmec, M., & Arap, M. (2016). Effect of geometrical and process parameters on coefficient of friction in deep drawing process at the flange and the radius regions. *International Journal of Advanced Manufacturing Technology*, 86, 747-759. https://doi.org/10.1007/s00170-015-8225-5

Dou, S., & Xia, J. (2019). Analysis of sheet metal forming (stamping process): A study of the variable friction coefficient on 5052 aluminum alloy. *Metals, 9(8),* 853. https://doi.org/10.3390/met9080853

Evin, E., & Tomáš, M. (2022). Influence of friction on the formability of Fe-Zn-coated IF steels for car body parts. *Lubricants*, *10(11),* 297. https://doi.org/10.3390/lubricants10110297

Folle, L. F., Caetano dos Santos Silva, B., Sousa de Carvalho, M., Zamorano, L .G. S., & Coelho, R. S. (2022). Evaluation of the friction coefficient for TRIP1000 steel under different conditions of lubrication, contact pressure, sliding speed and working temperature. *Metals, 12(8),* 1299. https://doi.org/10.3390/met12081299

Ilyin, S.O., Gorbacheva, S.N., & Yadykova, A.Y. (2022). Rheology and tribology of nanocellulose-based biodegradable greases: wear and friction protection mechanisms of cellulose microfibrils. *Tribology International*, 108080. https://doi.org/10.1016/j.triboint.2022.108080

Karthik, A.V. (2016). Vegetable oil as a forming lubricant for deep drawing of AA6061. *International Journal of Engineering Science and Computing*, 2016, 6, 1580–1582.

Klocke, F., Mabmann, T., & Gerschwiler, K. (2005). Combination of PVD tool coatings and biodegradable lubricants in metal forming and machining. *Wear*, *259*(7-12), 1197-1206. https://doi.org/10.1016/j.wear.2005.01.041

Lachmayer, R., Behrens, B. A., Ehlers, T., Müller, P., Althaus, P., Oel, M., Farahmand, E., Gembarski, P. C., Wester, H., & Hübner, S. (2022). Process-integrated lubrication in sheet metal forming. *Journal of Manufacturing and Materials Processes, 6(5),* 121. https://doi.org/10.3390/jmmp6050121

Mirahmadi, S.J., Hamedi, M., & Cheragzadeh, M. (2015). Investigating friction factor in forging of Ti-6Al-4V through isothermal ring compression test. *Tribology Transactions*, *58*(5), 778-785. https://doi.org/10.1080/10402004.2015.1019598

Nagendramma, P., & Kaul, S. (2012). Development of ecofriendly/biodegradable lubricants: An overview. *Renewable and Sustainable Energy Reviews, 16*(1), 764-774. https://doi.org/10.1016/j.rser.2011.09.002

Sayhir, A.Z., Zulkifli, N.W.M., Masjuki, H.H., Kalaam, MA, Alabdulkarem, A., Gulzar, M.; Khuong, L.S., & Harith, M.H. (2017). A review on bio-based lubricants and their applications. *Journal of Cleaner Production*, 168, 997-1016. https://doi.org/10.1016/j.jclepro.2017.09.106

Shimizu, T., Kobayashi, H., Vorholt, J., & Yang, M. (2019). Lubrication analysis of micro-dimple textured die surface by direct observation of contact interface in sheet metal forming. *Metals*, *9(9),* 917. https://doi.org/10.3390/met9090917

Singh, J., Chatha, S. S., & Bhatia, R. (2022). Behaviour and applications of ionic liquids as lubricants in tribology: A review. *Materials Today: Proceedings*, 56, 2659-2665. https://doi.org/10.1016/j.matpr.2021. 09.228

Stolte, S., Steudte, S., Areitioaurtena, O., Pagano, F., Thöming, J., Stepnowski, P., & Igartua, A. (2012). Ionic liquids as lubricants or lubrication additives: An ecotoxicity and biodegradability assessment. *Chemosphere*, *89*(9), 1135-1141. https://doi.org/10.1016/j.chemosphere.2012.05.102

Syahrullail, S. & Afifah, Z.N. (2017). Bio-lubricant for metal forming. *Mytribos Symp.*, *2*, 54–56.

Syahrullail, S., Kamitani, S., & Shakirin, A. (2013). Performance of vegetable oil as lubricant in extreme pressure condition. *Procedia Engineering*, 68, 172–177. https://doi.org/10.1016/j.proeng.2013.12.164

Więckowski, W., & Dyja, K. (2017). The effect of the use of technological lubricants based on vegetable oils on the process of titanium sheet metal forming. *Archives of Metallurgy and Materials,* 62, 489-494. https://doi.org/10.1515/amm-2017-0070

Wu, Y., Recklin, V., & Groche, P. (2021). Strain induced surface change in sheet metal forming: numerical prediction, influence on friction and tool wear. *Journal of Manufacturing and Materials Processes, 5(2),* 29. https://doi.org/10.3390/jmmp5020029

Zajezierska, A. (2016). Biodegradowalne smary plastyczne. Instytut Nafty i Gazu - Państwowy Instytut Badawczy.

Ocena Właściwości Tribologicznych Smarów Pochodzenia Naturalnego za Pomocą Analizy Wariancji

Streszczenie

Celem artykułu jest wyznaczenie współczynnika tarcia blachy stalowej DC04 za pomocą specjalnego przyrządu do realizacji testu przeciągania pasa blachy. W badaniach wykorzystano cztery różne smary pochodzenia naturalnego: jadalne (oleje słonecznikowy i rzepakowy) oraz niejadalne (karanja i moringa). Eksperymenty przeprowadzono dla różnych wartości nacisku. Próbki w postaci pasów blachy wstępnie odkształcono do wartości 7, 14 i 21%. Wartości współczynnika tarcia wyznaczono jako stosunek siły tarcia do siły normalnej. Wpływ lepkości środka smarnego i nacisku kontaktowego na wartość współczynnika tarcia określono za pomocą analizy ANOVA. Zaobserwowano tendencję do zmniejszania się współczynnika tarcia wraz ze wzrostem nacisku. Wyniki istotności otrzymane po przeprowadzonej analizie ANOVA, potwierdziły zależność współczynnika tarcia od nacisku normalnego i lepkości oleju, jednocześnie zaprzeczając hipotezę o wpływie odkształcenia wstępnego na wartość współczynnika tarcia oraz możliwość wystąpienia istotnych interakcji.

Słowa kluczowe: analiza wariancji, ANOVA, tarcie, obróbka plastyczna

Original Research

Application of the Finite Element Method to Simulate the Friction Phenomenon in a Strip Drawing Test

Romuald Fejkiel [1],* , Patryk Goleń [2]

[1] Department of Mechanics and Machine Building, Carpatian State School in Krosno, Rynek 1, 38-400 Krosno, Poland

[2] BWI Poland Technologies Sp. z o.o., ul. Generała Leopolda Okulickiego 7, 38-400 Krosno, Poland

* Correspondence: romuald.fejkiel@kpu.krosno.pl

Abstract

Friction is an undesirable phenomenon in the flange area of the drawpiece in sheet metal forming processes, causing a deterioration in surface finish and a decrease in the formability limits of the sheet metal. The aim of this work is numerical analysis using the finite element method of the strip drawing test with two rounded countersamples. This test simulates friction conditions in the flange area of the drawpiece. The results of the experimental research on the influence of surface roughness on the value of the friction coefficient of S235 steel samples were used to verify the numerical results. The relation between the real contact area and the mean roughness Ra of the countersamples was determined. The real contact area increases with the increase of the mean roughness Ra. In sheet metal forming processes, the coefficient of friction depends on the real contact area, and its value increases with the increase of the real contact area.

Keywords: coefficient of friction, finite element method, friction, sheet metal forming

1. Introduction

Sheet metal forming processes require the establishment of appropriate process conditions, that is, forming speed, temperature and contact conditions. Friction is one of the basic phenomena that should be considered when designing the deep drawing processes (Sigvant et al., 2019). A quantitative indicator of the friction phenomena is the coefficient of friction, the value of which depends on many parameters related to the workpiece material, tool material, contact conditions, forming temperature and lubricants used (Xu et al., 2020; Zabala et al., 2022). Due to the variety of pressure values occurring in different areas of the drawpieces formed, it is necessary to use various tribological tests to assess the friction and lubrication conditions. These tests include the drawbead test, the bending under tension test and the strip drawing test. Among the many tribological tests used to assess friction conditions in sheet metal forming processes, the strip drawing test is the most common method (Schell et al. 2022). It consists of pulling the sheet metal between two countersamples with different profiles (flat or rounded). The strip drawing test is used to determine the friction and wear of sheets under cold or hot forming conditions (Venema et al., 2022).

In addition to conventional friction testing methods, in recent years dynamic development of computer techniques has been observed, among which the finite element method (Pop et al., 2011), the boundary element method (Lu et al., 2020) and the extended finite element method (Khoei & Nikbakht, 2019) are the leaders. The most important problems subjected to numerical simulations are determination of the real contact area (Buchner et al., 2009), determination of the character of cooperation between rough bodies (Wang & Schipper, 2019; Zhai et al., 2016) and analysis of the lubrication conditions (Guiggiani, 2020).

Modelling and simulation of the behaviour of tribological systems in the areas of cooperating surfaces, the modelling of damage and wear, the flow dynamics of lubricating fluids, and the behaviour of non-Newtonian lubricating fluids pose serious methodological difficulties, resulting from a very

large number of factors influencing the lubrication conditions and the wear process (Korzyński and Sęp, 2007). Using numerical methods also allows modelling of the friction in concentrated contact, where significant plastic deformations occur (Abo-Elkhier, 1997; Karpenko and Akay, 2001). Mahrenholtz et al. (2005) and Zhang et al. (2003) developed a numerical model describing the phenomenon of the deformation of the asperities of surface roughness of a friction pair. The use of the developed model allowed the authors to determine the coefficient of friction associated with the surface roughness of materials. Forecasting the wear of rubbing elements based on analysis of the conditions prevailing in the friction pair is also possible using the finite element method. Numerical models are extensively described in the works of Pereira et al. (2008) and Yan et al. (2000), who found that the wear rate of tools depends on the values of the maximum pressures. Numerical studies using the finite element method, the aim of which was to determine the value and distribution of contact pressure on the rounded surfaces of the punch and die, are the subject of works by Boher et al. (2005), Coubrough et al. (2002) and Eriksen (1997).

Based on the results of the bending under tension tests, a numerical simulation of the flow of the material at the draw bead and at the edge of the punch was carried out (Chabrand, 1996). The numerical results confirmed that it is possible to predict the value of the coefficient of friction, ensuring high consistency of the predictions of experimental results. An extensive review of scientific papers on the application of numerical methods in tribology, including finite element methods is provided by Popov and Psakhie (2007).

This article presents a finite element numerical analysis of a strip drawing test between two rounded countersamples. This test simulates friction conditions in the flange area of the drawpiece. The results of experimental investigations into the influence of the surface roughness of countersamples on the value of the coefficient of friction of S235 steel samples were used to verify the numerical results.

2. Material and experimentation

2.1. Test sample

The test material consisted of 20 mm wide and 300 mm long strips made of 1-mm-thick S235 steel sheet. S235 is a non-alloy structural steel that meets the requirements of the EN 10025-6:2019 standard. S235 grade steel is a weldable low carbon manganese steel with good impact resistance. This steel is used for welded, load-bearing and dynamically loaded structures, such as columns, beams and extension arms. The mechanical properties of test material are shown in Table 1.

Table 1. The basic mechanical parameters of steel tested (Ansys, 2019)

Density, kg/mm³	Young's modulus, MPa	Poisson's ratio	Bulk modulus, MPa	Shear modulus, MPa	Yield stress, MPa
$7.85 \cdot 10^{-6}$	200000	0.3	166670	76923	260

2.2. Experiment setup

The strip drawing test is used to describe the friction phenomenon occurring between the sheet metal and the blankholder in the sheet metal forming process. It involves pulling the specimen between two stationary rollers with a diameter of 20 mm, which are pressed against the specimen with a constant force F_N. The diagram of the test device is shown in Fig. 1.
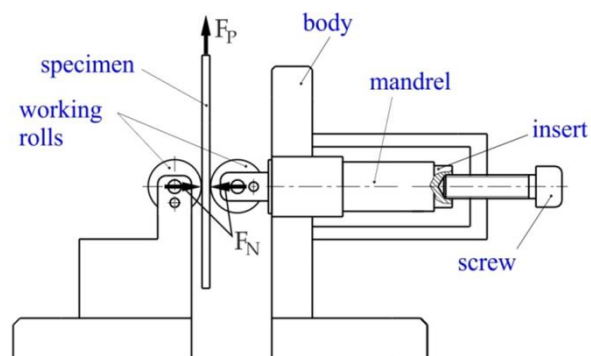
Fig. 1. Diagram of the strip drawing test

During the test, the pulling force F_T is measured using the control system of a Zwick/Roell Z100 uniaxial tensile testing machine. The tests were carried out at the Laboratory of Strength of Materials and Tensometry at the Carpathian State School in Krosno. Three sets of countersamples with a mean roughness Ra of 1.36 μm, 1.53 μm and 1.83 μm were used. During the friction tests of the sheet metal (1 mm thick, 20 mm wide and a 300 mm long), the value of the pulling force F_P was measured.

2.3. Numerical modelling

The 3D finite element method (FEM) model of the strip drawing test was prepared in the Solid-Works program. In the next step, the model was saved in the STEP format and launched in the AN-SYS program (Fig. 2). The countersample material was steel NL with bilinear isotropic hardening (tangent modulus 1450 MPa) which was selected from the ANSYS program library.
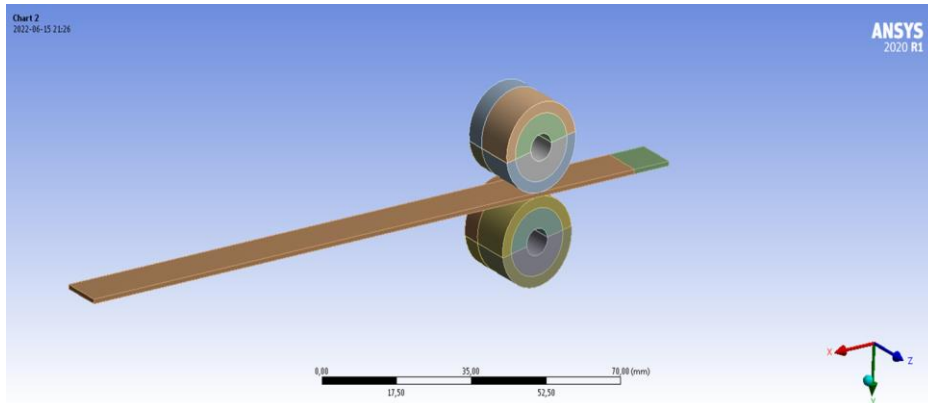
Fig. 2. Model of the strip drawing test prepared in the ANSYS program

A clamping force of 2654 N was applied to the countersamples. The analysis was carried out with several different values for the real contact area, a function of the surface roughness $A_n = f(Ra)$. The measured value was the pulling force F_P applied to the end of the sheet metal strip. The boundary conditions are defined in Fig. 3. To discretise the model of countersamples and sheet metal, brick-type spatial elements were used (Fig. 4).
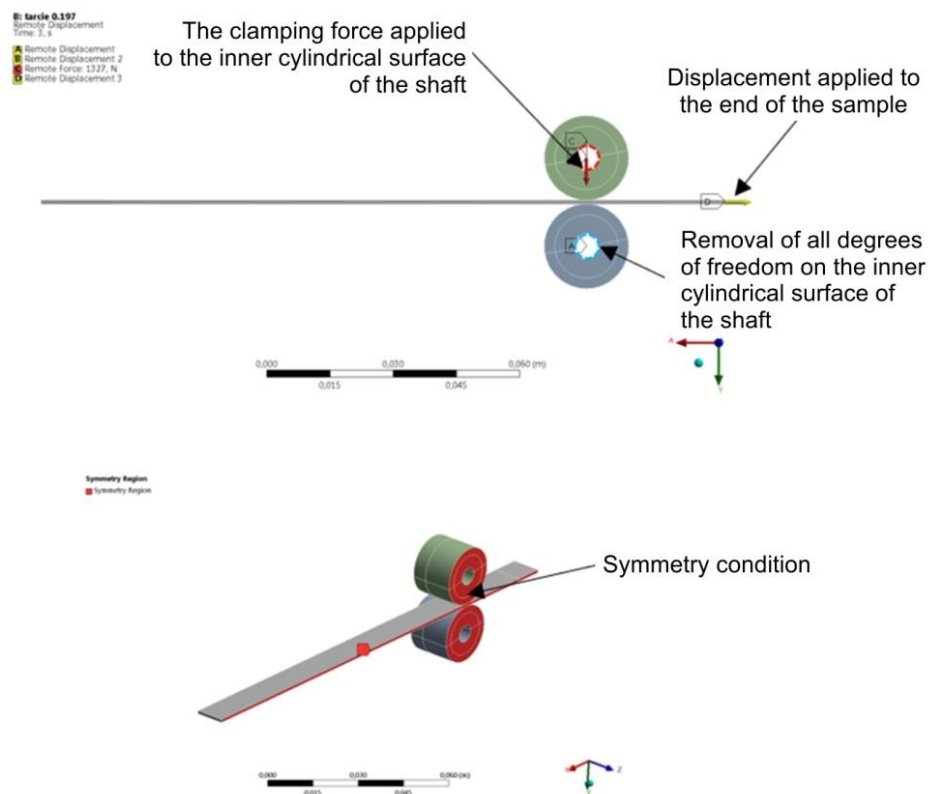
Fig. 3. The boundary conditions for the FEM model of the strip drawing test
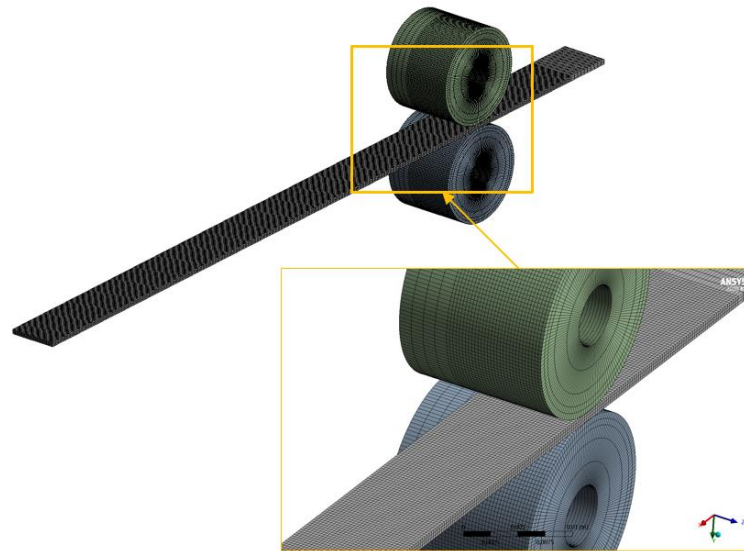
Fig. 4. Finite element mesh

In the ANSYS program, it is not possible to introduce a variable surface roughness value, therefore the relationship resulting from the Bowden and Tabor friction theory was used. According to the Bowden and Tabor (1950) model of friction, the friction force T is not proportional to the normal load, but depends on the contact area A_n and the shear strength R_t of the softer metal of the friction pair:

$$T = A_n \cdot R_t \tag{1}$$

3. Material and experimentation

In the first stage of the FEM analyses, the average values of the pulling force (Table 1) for the individual mean roughness Ra values were determined based on the results of the experimental tests.

Table 2. Average value of pulling force for the selected mean roughness Ra

Mean roughness Ra, μm	Mean value of pulling force, N
1.83	1160
1.53	725
1.36	670

Since the friction force T is equivalent to the pulling force F_P, the results of the experimental tests presented in Table 2 were used to determine the real contact area A_n, which in the FEM model is a dependent variable $A_n = f(Ra)$. Hence:

$$A_n = \frac{F_P}{R_t} \tag{2}$$

where R_t is the shear strength equal to 0.65 R_m (R_m – ultimate tensile strength).

For the tested S235 grade sheet, R_m equal to 360 MPa was assumed in the calculations, therefore $R_t = 0.65 \cdot R_m = 234$ MPa. After substituting into Eq. (2), the results shown in Table 3 were obtained for each Ra value.

Table 3. Real contact areas for the selected mean roughness Ra

Mean roughness Ra, μm	Real contact area A_n, N
1.83	4.96
1.53	3.1
1.36	2.86

For the values of the real contact surface area listed in Table 4, friction analyses were performed in the ANSYS program. Changes in the value of the pulling force with a specific clamping force were obtained. An exemplary graph of the changes in the pulling force for the contact area of $A_n = 2.86$ mm^2 is shown in Fig. 5.
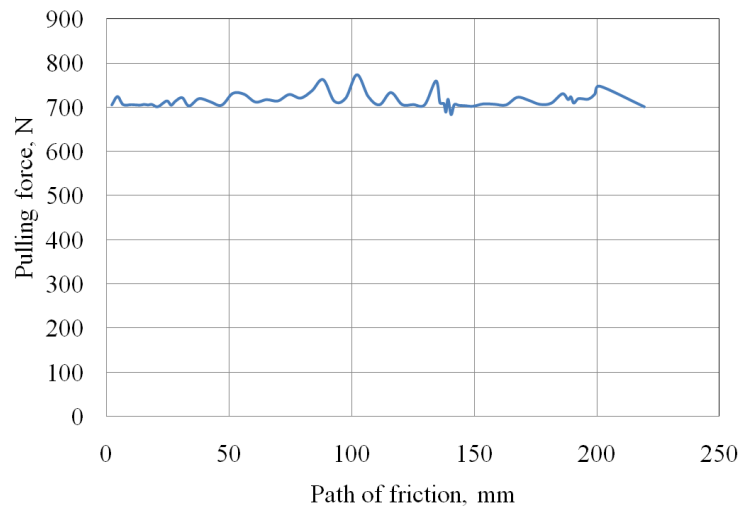
Fig. 5. Variations of pulling force for the contact area $A_n = 2.86$ mm^2

In addition, on the basis of the test results, it is possible to determine the interpolation of the relationship between the real contact area A_n and the mean roughness Ra. The interpolation graph is shown in Fig. 6. The red points indicate the values of the real contact area determined on the basis of the experiment, and the white points indicate the values determined by the approximation. From the graph obtained, it is also possible to see the extrapolated values of $A_n = f(Rt)$ for selected values of the mean roughness Ra (Table 4).
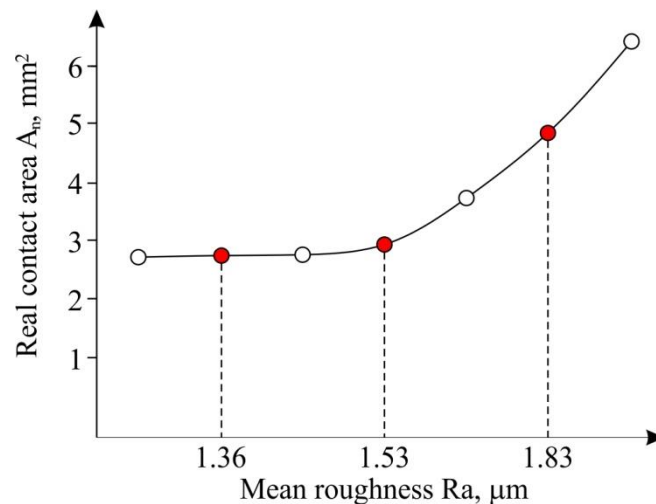
Fig. 6. Variation of the real contact area A_n

Table 4. The value of the real contact area A_n (experimental results)

Mean roughness Ra, µm	Real contact area A_n, N
1.26	2.7
1.46	2.95
1.68	3.9
2	5.8

FEM simulations were carried using the real contact values presented in Table 4. The value of the coefficient of friction was calculated from the relationship:

$$\mu = \frac{A_n R_t}{2 F_N} \tag{3}$$

where F_N is the clamping force of the countersamples.

A clamping force of 2654 N was assumed for the calculations. The value of the coefficient of friction for the individual mean roughness Ra is shown in Table 5. The coefficient of friction increases with the increase in the real contact area (Fig. 7).

Table 5. Values of the coefficient of friction for individual mean roughness Ra

Mean roughness Ra, μm	Real contact area A, mm^2	Coefficient of friction
1.26	2.7	0.12
1.36	2.86	0.126
1.46	2.95	0.13
1.53	3.1	0.14
1.68	3.9	0.17
1.83	4.96	0.21
2.0	5.8	0.26
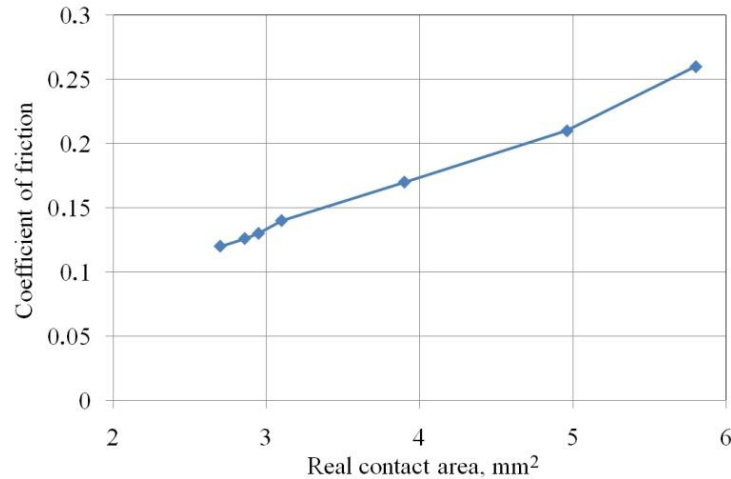
Fig. 7. Effect of the real contact area on the coefficient of friction

Unlike friction in machine nodes, in sheet metal forming there is contact between a relatively soft metal sheet and a hard tool. Under these conditions, the friction force is the result of severe mechanical cooperation between the surface asperities. In machine nodes, there is cooperation between a friction pair characterised by similar mechanical properties. Coulomb's law then remains valid.

4. Conclusions

Based on the results of the numerical and experimental investigations, it was found that the real contact area increases with the increase in the initial mean roughness of the sheet surface. In plastic working processes, two materials with significantly different mechanical properties, especially hardness, come into contact. Under these conditions, one of the rubbing pair bodies is subjected to plastic deformation caused by high normal pressures. Under these conditions, the mechanisms of mechanical interaction of the summits of the asperities and the continuous evolution of the surface topography are intensified. The influence of sheet material properties and countersample roughness on changes to the sheet surface roughness of sheet metals caused by the friction process and normal pressures need to be further studied. The use of numerical modelling makes it possible to carry out analyses that are limited by expensive and time-consuming experimental research.

References

Abo-Elkhier, M. (1997). Elasto-plastic finite element modelling of strip cold rolling using Eulerian fixed mesh technique. *Finite Elements in Analysis and Design*, *27*(4), 323-334. https://doi.org/10.1016/S0168-874X(97)81966-X

Ansys (2019). ANSYS Workbench. Product Release Notes 18. Ansys, Inc.

Boher, C., Attaf, D., Penazzi, D., & Levaillant C. (2005). Wear behaviour on the radius portion of a die in deep-drawing: Identification, localisation and evolution of the surface damage. *Wear*, *259*(7-12), 1097–1108. https://doi.org/10.1016/j.wear. 2005.02.101

Bowden, F. P., & Tabor, D. (1950). *The friction and lubrication of solids*. University Press.

Buchner, B., Buchner, M., & Buchmayr, B. (2008). Determination of the real contact area for numerical simulation. *Tribology International*, *42*(6), 897-901. https://doi.org/ 10.1016/j.triboint.2008.12.009

Chabrand P., Dubois F., & Gelin J. C. (1996). Modelling drawbeads in sheet metal forming. *International Journal of Mechanical Sciences*, *38*(1), 59-77. https://doi.org/10.1016/0020-7403(95)00033-T

Coubrough, G. J., Alinger, M. J., & Van Tyne C. J. (2002). Angle of contact between sheet and die during stretch-bend deformation as determined on the bending under-tension friction test system. *Journal of Materials Processing Technology*, 130–131, 69–75. https://doi.org/10.1016/S0924-0136(02)00781-1

Eriksen, M. (1997). The influence of die geometry on tool wear in deep drawing. *Wear*, *207*(1-2), 10–15. https://doi.org/10.1016/S0043-1648(96)07461-3

Guiggiani, M. (2020). Lubrication problems solved by the boundary element method. Engineer*ing Analysis with Boundary Elements*, 119, 183-188. https://doi.org/ 10.1016/j.enganabound.2020.07.011

Karpenko, Y. A., & Akay, A. (2001). A numerical model of friction between rough surfaces. *Tribology International*, *34*(8), 531–545. https://doi.org/10.1016/S0301-679X(01)00044-5

Khoei, A. R., & Nikbakht, M. (2006). Contact friction modeling with the extended finite element method (X-FEM). *Journal of Materials Processing Technology*, *177*(1-3), 58-62. https://doi.org/10.1016/j.jmatprotec.2006.03.185

Korzyński, M., & Sęp J., (2007). Komputerowe wspomaganie badań tribologicznych. *Zagadnienia Eksploatacji Maszyn*, 42, 57-72.

Lu, K., Coombs, W. M., Auearde, C. E., & Hu, Z. (2020) An implicit boundary finite element method with extension to frictional sliding boundary conditions and elasto-plastic analyses. *Computer Methods in Applied Mechanics and Engineering*, 358, 112620. https://doi.org/10.1016/j.cma.2019.112620

Mahrenholtz, O., Bontcheva, N., & Iankov, R. (2005). Influence of surface roughness on friction during metal forming processes. *Journal of Materials Processing Technology*, *159*(1), 9-16. https://doi.org/10.1016/j.jmatprotec.2003.10.009

Pereira, M. P., Yan, W., & Rolfe, B. F. (2008). Contact pressure evolution and its relation to wear in sheet metal forming. *Wear*, *265*(11-12), 1687-1699. https://doi.org/10.1016/j.wear.2008.04.042

Pop, N., Cioban, H., & Horvat-Marc, A. (2009). Finite element method used in contact problems with dry friction. *Computational Materials Science*, *50*(4), 1283-1285. https://doi.org/10.1016/j.commatsci.2010.03.018

Popov, V. L., & Psakhie, S. G. (2007). Numerical simulation methods in tribology. *Tribology International*, *40*(6), 916-923. https://doi.org/10.1016/j.triboint.2006. 02.020

Schell, L., Emele, M., Holzbeck, A., & Groche, P. (2022). Investigation of different lubricant classes for aluminium warm and hot forming based on a strip drawing test. *Tribology International*, 168, 107449. https://doi.org/10.1016/j.triboint.2022.107449

Sigvant, M., Pilthammar, J., Hol, J., Wiebenga, J. H., Chezan, T., Carleer, B., & van den Boogaard, T. (2019). Friction in sheet metal forming: influence of surface roughness and strain rate on sheet metal forming simulation results. *Procedia Manufacturing*, 29, 512-519. https://doi.org/10.1016/j.promfg.2019.02.169

Venema, J., Hazrati, J., Atzema, E., Matthews, D., & van den Boogaard, T. (2022). Multiscale friction model for hot sheet metal forming. *Friction*, *10*(2), 316-334. https://doi.org/10.1007/s40544-021-0504-6

Wang, C., & Schipper, D. J. (2020). A numerical-analytical approach to determining the real contact area of rough surface contact. *Tribology - Materials, Surfaces & Interfaces*, *14*(3), 166-176. https://doi.org/10.1080/17515831.2020.1720382

Xu, Z., Huang, J., Mao, M., Peng, L., & Lai, X. (2020). An investigation on the friction in a micro sheet metal roll forming processes considering adhesion and ploughing. *Journal of Materials Processing Technology*, 285, 116790. https://doi.org/ 10.1016/j.jmatprotec.2020.116790

Yan, W., Busso, E. P., & O'Dowd, N. P. (2000). A micromechanics investigation of sliding wear in coated components. *Proceedings of the Royal Society A: Mathematical, Physical and Engineering Sciences*, 456, 2387–2407. https://doi.org/ 10.1098/rspa.2000.0617

Zabala, A., de Argandoña, E. S., Cañizares, D., Llavori, I., Otegi, N., & Mendiguren, J. (2022). Numerical study of advanced friction modelling for sheet metal forming: Influence of the die local roughness. *Tribology International*, 165, 107259. https://doi.org/10.1016/j.triboint.2021.107259

Zhai, C. P., Gan, Y. X., & Hanaor, D. (2016). Numerical analysis of normal contact stiffness of rough surfaces. *Applied Mechanics and Materials*, 846, 300-305. https://doi.org/10.4028/www.scientific.net/AMM.846.300

Zhang, S., Hodgson, P. D., Cardew-Hall, M. J., & Kalayanasundaram, S. (2003). A finite element simulation of micro-mechanical frictional behaviour in metal forming. *Journal of Materials Processing Technology*, *134*(1), 81-91. https://doi.org/10.1016/S0924-0136(02)00926-3

Zastosowanie Metody Elementów Skończonych do Symulacji Zjawiska Tarcia w Teście Przeciągania Pasa Blachy

Streszczenie

Tarcie jest zjawiskiem niepożądanym w strefie kołnierzowej wytłoczki w procesach kształtowania blach powodującym obniżenie jakości powierzchni wyrobu i zmniejszenie odkształceń granicznych blachy. Celem

pracy jest analiza numeryczna metodą elementów skończonych testu przeciągania pasa blachy pomiędzy dwoma zaokrąglonymi przeciwpróbkami. Test ten symuluje warunki tarcia w strefie kołnierza wytłoczki. Do weryfikacji wyników numerycznych wykorzystano wyniki badań eksperymentalnych wpływu chropowatości powierzchni na wartość współczynnika tarcia próbek ze stali S235. Wyznaczono zależności pola rzeczywistej powierzchni kontaktu od parametru chropowatości przeciwpróbek Ra. Rozmiar rzeczywistej powierzchni kontaktu zwiększa się wraz ze zwiększeniem wartości parametru Ra. W procesach kształtowania blach współczynnik tarcia zależy od pola rzeczywistej powierzchni kontaktu, wraz ze wzrostem pola powierzchni styku rośnie jego wartość.

Słowa kluczowe: współczynnik tarcia, metoda elementów skończonych, tarcie, kształtowanie blach

Original Research

Mechanical Properties of Aluminium/Copper Bimetallic Sheets Subjected to Cyclic Bending

Krzysztof Żaba [1],* ⓘ, Sandra Puchlerska [1] ⓘ, Stanislav Rusz [2] ⓘ
Romuald Fejkiel [3] ⓘ

[1] Department of Metal Working and Physical Metallurgy of Non-Ferrous Metals, AGH—University of Science and Technology, al. Adama Mickiewcza 30, 30-059 Cracow, Poland

[2] Department of Mechanical Technology, Faculty of Mechanical Engineering, VŠB—Technical University of Ostrava, 17 listopadu 15, CZ 708 33 Ostrava–Poruba, Czech Republic

[3] Department of Mechanics and Machine Building, Carpatian State School in Krosno, Rynek 1, 38-400 Krosno, Poland

* Correspondence: krzyzaba@agh.edu.pl

Abstract

The aim of this study is to evaluate the influence of the roll bonding (RB) process on the mechanical properties of Al/Cu bimetallic strip specimens. A specially designed test instrument for the cyclic bending test of strip specimens produced by RB has been proposed. The test consists of repeated pulling of a strip of sheet metal through a system of cylindrical countersamples. Samples cut along and across the sheet rolling direction were tested. The specimens were subjected to preliminary microstructural tests using an optical microscope with Nomarski contrast and scanning electron microscopy. The tests showed a slight influence of the orientation of the samples on changes to the mechanical properties of the bimetallic sheets in the cyclic bending process. For samples oriented along the sheet rolling direction, discontinuities in the transition layer were found. The samples oriented perpendicularly to the rolling direction were free of this defect.

Keywords: bimetallic sheet, cycling bending, hardness, work hardening

1. Introduction

Bimetallic sheets are a composite material with properties that are the result of the properties of the joined sheets (Khan et al., 2021; Vini et al., 2017). The main advantage of bimetallic sheets is the acquisition of the different physical and mechanical specifications of both materials at the same time, such as thermal expansion, electromagnetic conductivity, corrosion resistance and mechanical strengths. Several methods of joining bimetal sheets are commonly used, that is, surfacing, roll bonding (RB) and explosive plating. RB is used to produce bimetallic sheets in which the combined thickness is reduced. RB changes the shape of plastically processed materials as a result of the impact of external forces. The geometrical dimensions of the rolled sheet, internal microstructure and mechanical properties change as a result of the RB process (Stradomski et al., 2022; Walnik et al., 2021). Accumulative roll bonding is a technique used to produce laminates because the rolling pressure can create a mechanical bond between metals, such as Al/Cu (Vini et al., 2017), Al/Zn (Dehsorkhi et al., 2011), Al/Fe (Tang et al., 2015), and Al/Ni (Mozafarri et al., 2011).

The analysis of the influence of the rolling process on the properties of bimetallic sheets was the subject of investigations by Pan et al. (1989). They found that the use of the cross-shear cold rolling technique results in a significant reduction in the rolling load. Furthermore, the cold roll cladding of aluminium–stainless steel, copper–stainless steel, and mild steel–stainless steel led to the conclusion that the incorporation of an optimum final heat treatment considerably decreases the requirement for rolling. Polyzou et al. (2017) investigated the suitability of cold rolling processes for the formation and improvement in the properties of explosively welded bimetallic Al/Cu samples. Examination of the

bimetallic sheets with regards to their microstructure and the hardness of the intermetallic layer on the bonding surface proved that cold rolling improves the hardness of both layers of explosively welded bimetallic Al/Cu specimens. Athar and Tolaminejad (2015) calculated the weldability criteria which should be met in order to achieve a good welding quality for an Al/Cu/Al explosively welded bimetallic sandwich. The effect of a cold rolling process on the bond strength and the mechanical properties of Al/Cu/Al sandwich sheets fabricated by explosive welding has been studied by Asemabadi et al. (2012). The results of the tensile, tensile-shearing and hardness tests along the thicknesses of the sheets indicate that the amount of hardness has increased in different layers, and the largest hardness increase can be observed in the copper layer. Fabrication of an Al/Cu bimetallic sheet by explosive welding and cold rolling process was performed by Mamalis et al. (1994). They concluded that the application of cold rolling as a post-cladding forming operation requires careful selection of the lubricants, rolling variables, and the roll-pass schedule.

Obtaining precise adhesion of two plates and their connection is possible only when the oxides and adsorbed gases are removed from the surfaces of the metallic sheets. Sometimes post-welding processes are necessary to improve the properties of the bimetal sheet (Polyzou et al., 2017). Sheets that are a combination of aluminium and copper layers are the most commonly used in the electronics, automotive, chemical and shipbuilding industries.

The materials of the bimetallic sheet layers should be characterised by high plasticity and crack resistance. The decisive mechanical property determining the suitability of a given sheet for the rolling process is susceptibility to work hardening (Paul et al., 2011). When rolling bimetallic sheets, it is sometimes necessary to use the asymmetric rolling process as a method of reducing the curvature of the double-layer strip (Sun et al., 2020). During the rolling process, structural and dynamic changes may occur in the sheets (Dyja & Wilk, 1998; Salimi & Sassani, 2002; Vini et al., 2017). When rolling two-layer sheets with a large difference in the properties of the joined layers, one of the layers may not deform or deform only to a small extent. Increasing the uniformity of the deformation of bimetallic sheets is obtained by using the asymmetry of the circumferential speed of the working rollers (Sun et al., 2020; Yu et al., 2013). Sometimes dynamic recrystallisation of the workpiece subjected to the rolling process may be eliminated (Stradomski et al., 2022).

One of the methods for testing the resistance of bimetallic sheets is the continuous bending test (Poulin et al., 2019). The test consists of repeated pulling of a strip of sheet metal through a system of cylindrical countersamples. As a result of the deformation process, the plastic properties of the sheet change because of the work hardening phenomenon. This article presents a specially designed test instrument for the cyclic bending test of strip specimens produced by roll bonding. The aim of this study is to evaluate the influence of the RB process on the mechanical properties of Al/Cu strip specimens. Samples cut along and across the sheet rolling direction were tested.

2. Experimental

2.1. Material

Cu/Al bimetallic strips in a z6 state (after rolling) and a ratio for the Cu and Al layers equal to 1:1 have been used in this study. The bimetallic sheets with a thickness of 1 mm were produced by the roll bonding method in industrial conditions by Walcowania Metali Dziedzice S.A in Gliwice (Poland). The input materials for the production of Al/Cu bimetallic sheets were sheets of technical grade aluminium EN AW-1050A and sheets of electrolytic copper M1E. The chemical compositions of the layers of test material are shown in Tables 1 and 2.

Table 1. The chemical composition of EN AW-1050A aluminium alloy (wt.%)

Al	Mg	Mn	Fe	Si	Cu	Zn	Ti	rest
99.43	0.025	0.027	0.23	0.17	0.028	0.033	0.029	0.028

Table 2. The chemical composition of M1E copper (wt.%)

Cu	Bi	O	Pb	rest
99.93	0.0004	0.036	0.004	0.029

2.2. Cyclic bending process

Experimental tests for drawing sheet metal with bending were carried out on a device shown in Fig. 1. A strip of the sheet is bent and straightened many times when passing through the working rollers

(1), (2) and (3). With freely rotating rollers, the pulling force overcomes the deformation resistance of the sheet, because the frictional forces are negligible. The guide roller (4) counteracts the deflection of the end of the sheet metal at the entrance to the working roller (3). The body (5) of the device is mounted on the lower gripper of the Zwick/Roell Z100 uniaxial tensile testing machine (Fig. 2a). The strip specimen (6) with width $w_s = 10$ mm was mounted in the upper gripper of the testing machine. The pulling force was measured using the testing machine's measuring system. The position of the central roller (2) in relation to the working rollers (1) and (3) is regulated by the nut (7).
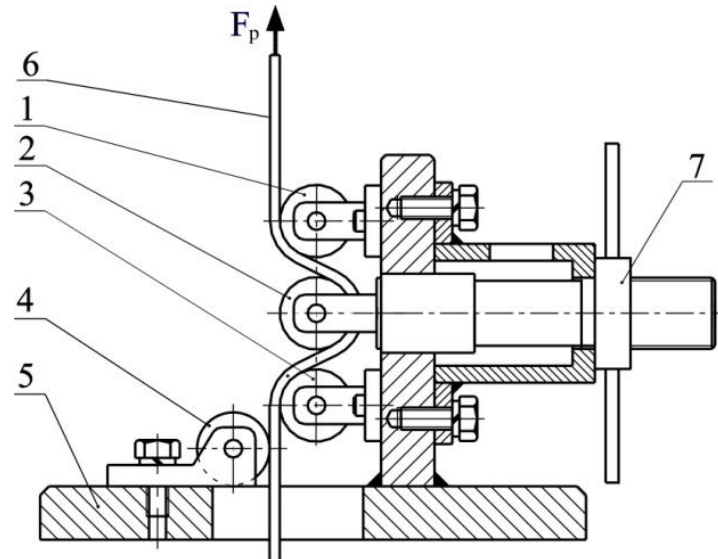
Fig. 1. Diagram of the test device for cyclic bending: (1), (2) and (3) – working rollers; (4) – guide roller; (5) – body; (6) – specimen; (7) – nut

During the maximum penetration h_r (Fig. 2b) of the middle roller (2), the angle of contact α is greatest. However, it does not reach the value of the angle $\alpha = 180°$ due to the clearance c_l between the rollers. During the tests, adequate side clearance c_l should be ensured between the rollers to prevent blocking of the sheet strip between the rollers (Kręcisz, 2005).

The samples were pulled through the roller system at a speed of 10 mm/s. Before the tests, the penetration of the central roller (2) was determined to be $h_r = 18$ mm. Changes in the pulling force F_p were recorded at a frequency of 50 Hz. The scheme of the cyclic bending process of Cu/Al bimetallic sheets is shown in Fig. 3. Cycling bending parameters and sample markings are listed in Table 3. The sample was pulled ten times for each layer setting and sample orientation.
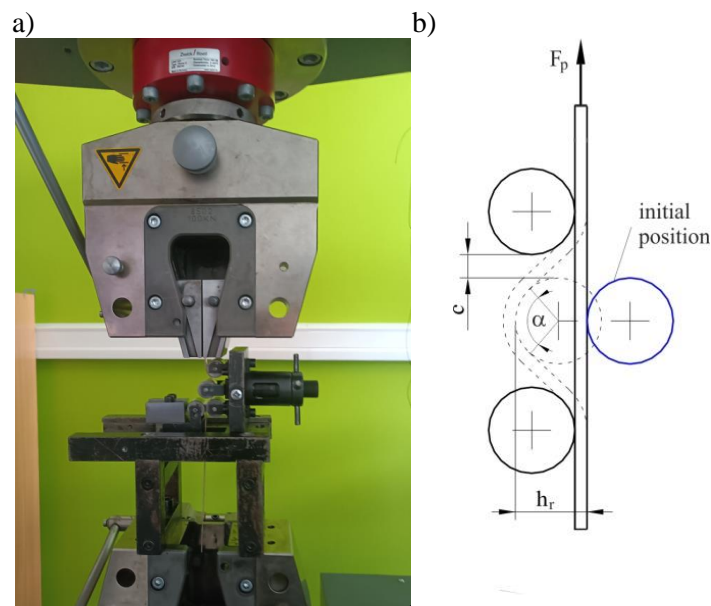
Fig. 2. a) photograph of the device for the cyclic bending process and b) the geometrical parameters of the cyclic bending process
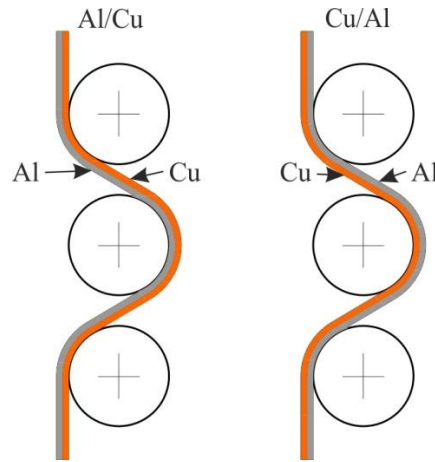
Fig. 3. The diagram of the bending process and the marking of Cu/Al sheets

Table 3. The process parameters and the determination of the samples

Indication	Layering	Specimen orientation	Number of passes	Penetration h_r, mm
Al/Cu-0	Al-Cu	0°	10	18
Al/Cu-90	Al-Cu	90°	10	18
Cu/Al-0	Cu-Al	0°	10	18
Cu/Al-90	Cu-Al	90°	10	18

2.3. Microstructural analysis

The sheets were subjected to preliminary structural tests using an optical microscope with Nomarski contrast. The microstructure of the specimens was examined using a scanning electron microscope (SEM) HITACHI S-3400N along with analysis of the chemical composition by energy dispersion spectroscopy (EDS). The thickness of the individual layers was measured using the measurement methods available in the microscope software. Hardness was measured with a load of 10g (HV0.01) using a Shimadzu HMV-C microhardness tester.

3. Results and discussion

The mean thickness and mean microhardness of the layers of the bimetallic sheets are shown in Figs. 4a and 4b, respectively. The microhardness analysis showed that its value varies depends on the measurement point, which is shown in Figure 5. These differences are not insignificant, but it can be seen that the microhardness of the copper layer at the contact boundary with aluminium decreases compared to measurements at a longer distance. Meanwhile, the microhardness of the aluminium layer in the boundary zone with the copper layer increases.
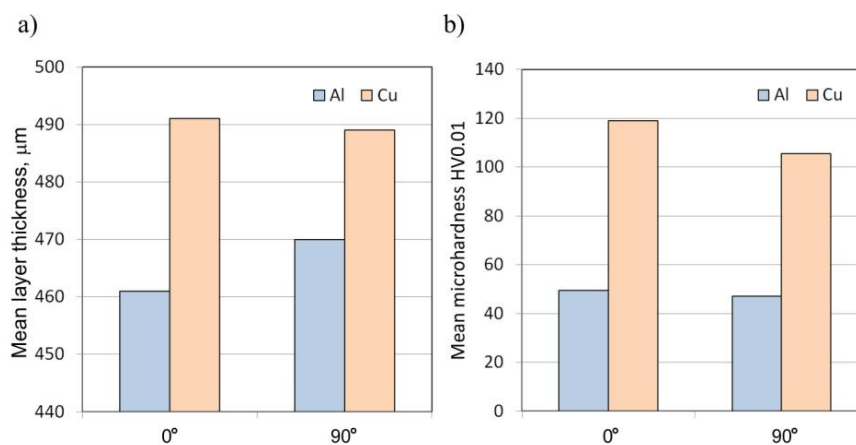
Fig. 4. a) mean thickness and b) mean microhardness of specific layers of samples oriented at 0° and 90°

The microstructural analysis showed that for the material denoted as Al/Cu-0, there is a lack of good bonding between the individual metals (Fig. 6). Analysis of the chemical composition in this

area showed the presence of an increased amount of oxygen (Fig. 7, Table 4). It should be noted that this discontinuity occurs in fragments along the entire length of the test material. For the sample denoted as Al/Cu-90, this type of discontinuity was not observed (Fig. 8). In addition, in this case, the SEM micrographs showed an area parallel to the sheet surface in which an increase in the aluminium content was identified (Fig. 9, Table 5). In the transition layer of the Cu/Al-0 sheet, the copper content was about 76 wt.%. Meanwhile, in the same place on the Cu/Al-90 sheet, the content of copper is about 81wt%. Similarly, the aluminium content in this zone is almost twice as high for the Cu/Al-90 material compared to Cu/Al-0. In the EN AW-1050A layer, the aluminium content is 50% higher than for the Cu/Al-90 bimetal sheet. On the other hand, in the layer of the M1E sheet, the copper content is similar for both sheet orientations considered.
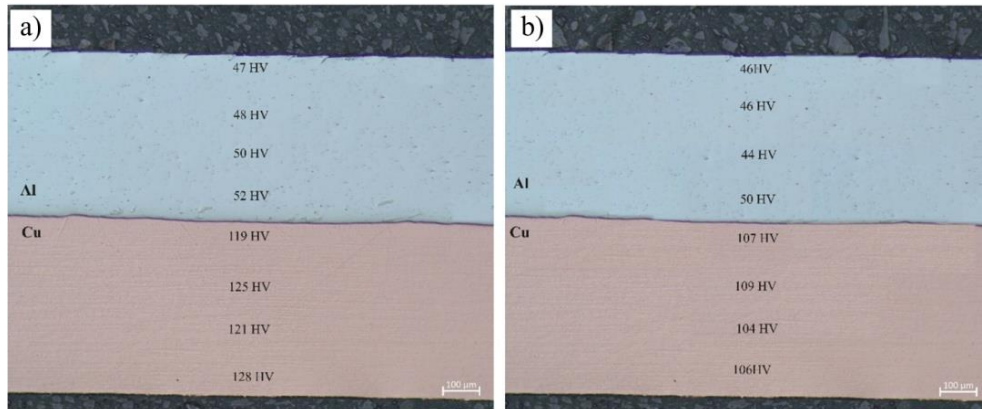
Fig. 5. Microstructure of the Al/Cu bimetallic sheet, including the microhardness measurement results: a) Al/Cu -0, b) Al/Cu-90
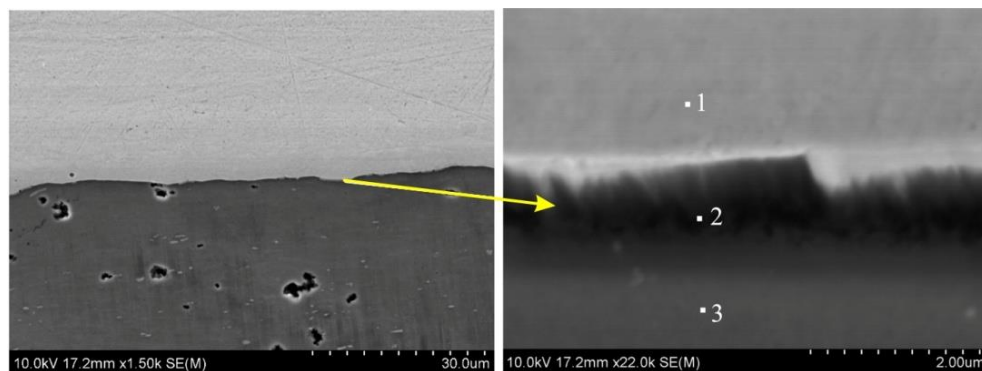
Fig. 6. SEM micrographs of the Cu/Al-0 bimetallic sheet
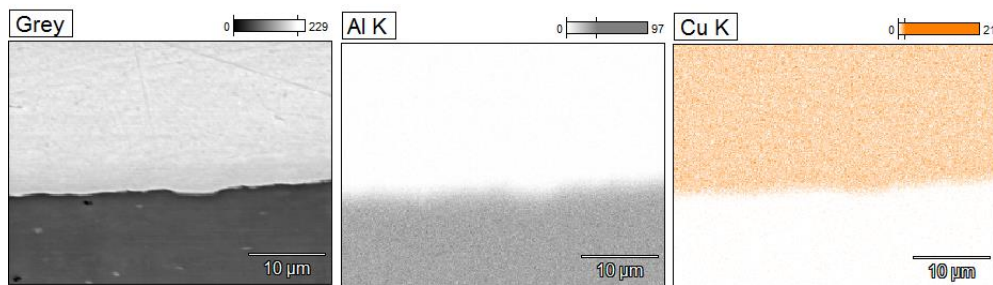
Fig. 7. EDS elemental mapping of the interface area of Cu/Al-0 bimetallic sheet

Table 4. EDS point scanning of the interface area of Cu/Al-0 bimetallic sheet (wt.%)

Point	O-K	Al-K	Cu-L
1	0.37	0.29	99.34
2	14.76	8.59	76.64
3	4.95	89.54	5.50
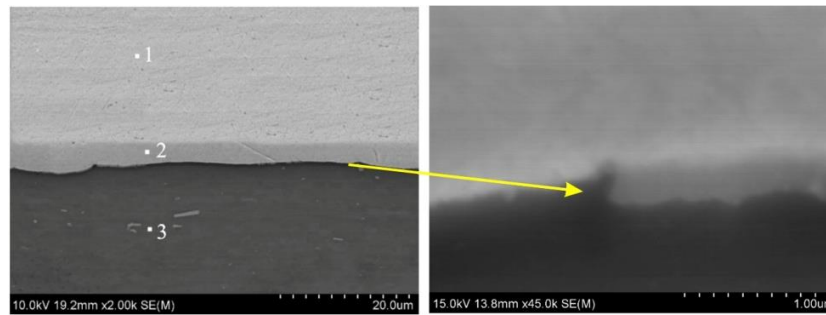
Fig. 8. SEM micrographs of the Cu/Al-90 bimetallic sheet
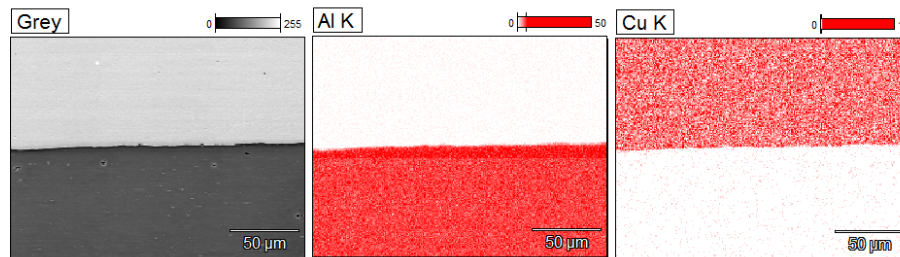
Fig. 9. EDS elemental mapping of the interface area of Cu/Al-90 bimetallic sheet

Table 5. EDS point scanning of the interface area of Cu/Al-90 bimetallic sheet (wt.%)

Point	O-K	Al-K	Cu-L
1	0.39	0.75	98.85
2	0.99	17.80	81.20
3	5.22	62.02	32.76

Fig. 10 shows the variation in the pulling force F_p at the tenth bending. Due to the large plastic deformation of the sheet during the cyclic bending process, the mechanical properties of the sheet change as a result of the work hardening phenomenon.
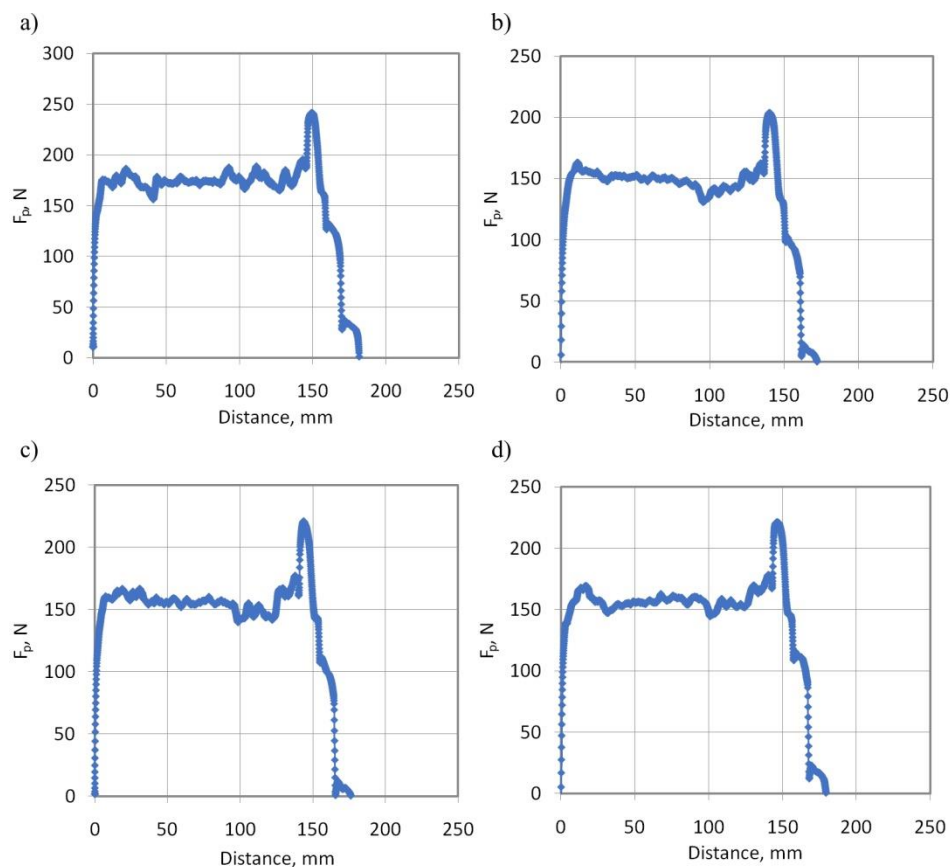
Fig. 10. Variation in the pulling force F_p at the tenth bending: a) Al/Cu-0, b) Cu/Al-0, c) Al/Cu-90 and d) Cu/Al-90

The strength of the sheet metal increases and at the same time the material is susceptible to cracking. The EN AW-1050A aluminium alloy is characterised by very high plasticity. On the other hand, M1E copper shows better strengthening properties. This is visible in the form of a higher average pulling force of the Al/Cu-0 sheet (Fig. 10a) by about 17% compared to the Al/Cu-90 sample (Fig. 10c). This indicates a clear influence of the orientation of the sample in relation to the direction of sheet rolling on the tendency of the bimetallic material to strain hardening. A different character of the force occurs for the Cu/Al-0 (Fig. 10b) and Cu/Al-90 (Fig. 10d) samples. The average pulling force values for both cases are almost the same.

4. Conclusions

This article presents the results of preliminary research on the cyclic bending of Al/Cu bimetallic sheets. The results allow the following conclusions to be drawn:
- The microhardness of the copper layer at the contact boundary with the aluminium alloy decreases in comparison to measurements at a longer distance, while the microhardness of the aluminium layer at the boundary with the copper layer increases.
- The orientation of the sample affects the occurrence of discontinuities on the interface between the layers of the bimetallic sheet.
- Significant differences in element content were observed in samples oriented in the direction along the sheet rolling direction and in the perpendicular direction.
- The influence of the cyclic bending process on the mechanical properties of the sheet is not unambiguous. When testing Al/Cu-0 and Al/Cu-90 bimetallic sheets, a higher pulling force was observed for the Al/Cu-0 sheets compared to Al/Cu-90. Meanwhile, for the Cu/Al-0 and Cu/Al-90 sheets, the average value of the pulling force was similar and amounted to about $F_p = 150$ N.

Future works should focus on understanding the layer-wise bonding mechanism, the extent of the bonding between subsequent layers and the bond variation throughout the joint. The effect of cyclic bending on the fatigue properties of the layer-wise bond should be further investigated for different degrees of sheet strain and strain rates.

Acknowledgments

References

Asemabadi, M., Sedighi, M., & Honarpisheh, M. (2012). Investigation of cold rolling influence on the mechanical properties of explosive-welded Al/Cu bimetal. *Materials Science and Engineering A*, 558, 144-149. https://doi.org/10.1016/j.msea. 2012.07.102

Athar, M. H., & Tolaminejad, B. (2015). Weldability window and the effect of interface morphology on the properties of Al/Cu/Al laminated composites fabricated by explosive welding. Materials and Design, *86*, 516–525. https://doi.org/ 10.1016/j.matdes.2015.07.114

Dehsorkhi, R. N., Qods, F., & Tajally, M. (2011). Investigation on microstructure and mechanical properties of Al–Zn composite during accumulative roll bonding (ARB) process. *Materials Science and Engineering A*, 530, 63–72. https://doi.org/10.1016/j.msea.2011.09.040

Dyja, H. & Wilk, K. (1998). Asymetryczne Walcowanie Blach i Taśm, Seria; Metalurgia. Politechnika Częstochowska.

Khan, H. A., Asim, K., Akram, F., Hameed, A., Khan, A., & Mansoor, B. (2021). Roll bonding processes: State-of-the-art and future perspectives. *Metals*, *11*, 1344. https://doi.org/10.3390/met11091344

Kręcisz, D. (2005). The study of the flange resistance caused by the action of draw beads in the sheet metal forming. Ph.D. Thesis. Wrocław University of Technology.

Mamalis, A. G., Vaxevanidis, N. M., Szalay, A., & Prohaszka, J. (1994). Fabrication of aluminium/copper bimetallics by explosive cladding and rolling. *Journal of Materials Processing Technology*, *44*(1-2), 99–117. https://doi.org/10.1016/0924-0136(94)90042-6

Mozaffari, A., Danesh Manesh, H., & Janghorban, K. (2011). Evaluation of mechanical properties and structure of multilayered Al/Ni composites produced by accumulative roll bonding (ARB) process. *Journal of Alloys and Compounds*, *489*(1), 103–109. https://doi.org/10.1016/j.jallcom.2009.09.022

Pan, D., Gao, K., & Yu, J. (1989). Cold roll bonding of bimetallic sheets and strips. *Materials Science and Technology*, 5(9), 934-939. https://doi.org/10.1179/mst. 1989.5.9.934

Paul, H., Faryna, M., Prażmowski, M., & Bański, R. (2011). Changes in the bonding zone of explosively welded sheets. Archi*ves of Metallurgy and Material*s, *56*(2), 463–474. https://doi.org/10.2478/v10172-011-0050-8

Polyzou, A. K., Seretis, G. V., Vaxevanidis, N., Provatidis, C. G., & Manolakos, D. E. (2017). On the cold rolling of explosive welded Al/Cu bimetallic sheets. *Material Science and Engineering with Advanced Research*, 34-44. https://doi.org/10. 24218/msear.2017.5S

Poulin, C. M., Korkolis, Y. P., Kinsey, B. L., & Knezevic, M. (2019). Over five-times improved elongation-to-fracture of dual-phase 1180 steel by continuous-bending-under-tension. *Materials and Design*, 161, 95-105. https://doi.org/10.1016/ j.matdes.2018.11.022

Salimi, M., & Sassani, F. (2002). Modified slab analysis of asymmetrical plate rolling. *International Journal of Mechanical Sciences*, *44*(9), 1999–2023. https://doi.org/ 10.1016/S0020-7403(02)00043-7

Stradomski, G., Rydz, D., Garstka, T., Pałęga, M., Dyl, T., Szarek, A., Szarek, J. Ł., & Dembiczak, T. (2022). Influence of asymmetric rolling process on the microstructure properties of bimetallic sheet metals. *Materials*, *15(6),* 2013. https://doi.org/ 10.3390/ma15062013

Sun, X. K., Liu, X. H., Wang, J., & Qi, J. (2020). Analysis of asymmetrical rolling of strip considering percentages of three regions in deformation zone. *International Journal of Advanced Manufacturing Technology*, 110, 763–775. https://doi.org/ 10.1007/s00170-020-05690-3

Tang, C., Liu, Z., Zhou, A. D., & Wu, S. (2015). Surface treatment with the cold roll bonding process for an aluminium alloy and mild steel. *Strength of Materials*, 47, 150–155. https://doi.org/10.1007/s11223-015-9641-3

Walnik, B., Woźniak, D., Nieszporek, A., & Adamczyk, M. (2021). Study on mechanical properties and microstructure of 42CrMo4/NANOS-BA® high-strength clad plates after the process of hot rolling and two-stage heat treatment with isothermal transformation. *Journal of Metallic Materials*, 73, 22–31.

Vini, M. H., Daneshmand, S., & Forooghi, M. (2017). Roll bonding properties of Al/Cu bimetallic laminates fabricated by the roll bonding technique. *Technologies*, *5*,(2), 32. https://doi.org/10.3390/technologies5020032

Yu, H., Lu, C., Tieu, A.K., Godbole, A., Su, L., Sun, Y., Liu, M., Tang, D., & Kong, C. (2013). Fabrication of ultra-thin nanostructured bimetallic foils by accumulative roll bonding and asymmetric rolling. *Scientific Reports*, 3, 2373. https://doi.org/ 10.1038/srep02373

Właściwości Mechaniczne Blach Bimetalowych Aluminium/Miedź Poddanych Procesowi Gięcia

Streszczenie

Celem artykułu jest ocena wpływu procesu walcowania na właściwości mechaniczne próbek w postaci pasów blachy bimetalowej Al/Cu. Zaproponowano specjalnie zaprojektowany przyrząd do cyklicznego gięcia próbek wytwarzanych metodą walcowania. Test polega na wielokrotnym przeciąganiu paska blachy przez układ cylindrycznych przeciwpróbek. Badaniom poddano próbki cięte wzdłuż i w poprzek kierunku walcowania blachy. Próbki poddano wstępnym badaniom mikrostrukturalnym przy użyciu mikroskopu optycznego z kontrastem Nomarskiego oraz skaningowego mikroskopu elektronowego. Badania wykazały niewielki wpływ orientacji próbek na zmianę właściwości mechanicznych blach bimetalicznych w procesie cyklicznego zginania. W przypadku próbek zorientowanych wzdłuż kierunku walcowania blachy stwierdzono nieciągłości w warstwie przejściowej. Próbki zorientowane prostopadle do kierunku walcowania były wolne od tej wady.

Słowa kluczowe: blacha bimetalowa, gięcie cykliczne, twardość, umocnienie odkształceniowe

Original Research

Analysis of Tribological Performance of New Stamping Die Composite Inserts Using Strip Drawing Test

Krzysztof Żaba [1],* [iD]**, Łukasz Kuczek [1]** [iD]**, Sandra Puchlerska [1]** [iD]**,
Marcel Wiewióra [2], Marek Góral [3]** [iD]**, Tomasz Trzepieciński [4]** [iD]

[1] Department of Metal Working and Physical Metallurgy of Non-Ferrous Metals, AGH—University of Science and Technology, al. Adama Mickiewcza 30, 30-059 Cracow, Poland
[2] ERKO sp. z o.o. sp.k., Czeluśnica 80, 38-204 Tarnowiec, Poland
[3] Research and Development Laboratory for Aerospace Materials, Rzeszow University of Technology, Powstancow Warszawy 12, 35-959 Rzeszow, Poland
[4] Department of Manufacturing Processes and Production Engineering, Rzeszow University of Technology, al. Powstańców Warszawy 12, 35-959 Rzeszów, Poland

* Correspondence: krzyzaba@agh.edu.pl

Abstract

This article assesses the tribological performance of new composite tool sets for stamping dies. Four sets of composite countersamples were tested. These consisted of polyurethane resin with mineral filler (base variant) and modified with aluminium powder (10wt%) and roving fabric (5wt%). Strip samples for the strip drawing tests were cut from AMS5599 (Inconel 625) corrosion-resistant nickel alloy, AMS5510 (321) corrosion and heat-resistant steel and AMS6061-T4 heat treatable aluminium alloy sheet metals. The influence of the type of sample material on the coefficient of friction (COF) was observed. The smallest values of the COF over the entire range of clamping force values used on AMS5599 and AMS5510 sheets were observed during tests with countersamples made of the base variant of composite. When testing the AMS6061-T4 aluminium alloy sheet, the countersamples modified with roving fabric provided the lowest value of COF, which stabilised at a value of about 0.197 as pressure was increased.

Keywords: friction, coefficient of friction, composite tool, stamping tool

1. Introduction

Plastic working is a manufacturing technique in which the shape and dimensions of the workpiece change under the influence of applied external forces, causing the metal to undergo a plastic deformation. Plastic working techniques also permit give the appropriate performance properties to be given to the material, which depend on the rheological conditions of the forming process and on the thermo-plastic treatments carried out during or immediately after the end of processing (Birkhold et al., 2013). Plastic forming processes involve high unit pressures. The condition of the surface layer of the product determines its operational and functional features, such as durability and reliability (Ersoy-Nürnberg et al., 2008). Uncontrolled tool wear reduces the quality of components and increases the total cost of production (Domitner et al., 2021). As a result of heat exchange between the deformed material and the tools, their temperature increases, which results in a decrease in their strength. The designer has many means and methods to design the optimal tool in order to increase the efficiency and reliability of the forming process. In particular, it is possible to select the parameters of plastic working with which, under conditions of normal tool wear, the required probability of meeting all the quality requirements of the workpiece is ensured, and the reliability of the process is conditioned by the desired tool life (Groche et al., 2019).

The operating conditions of plastic forming tools depend primarily on the temperature, the contact pressures and the history of loading (Hol et al., 2012). Friction is the basic factor that determines

the flow character of the workpiece and enables an element to be manufactured with the desired dimensions and shape (Vierzigmann et al., 2011). One way to ensure appropriate friction conditions is the selection of the tool material (Schmoeckel et al., 1986). Because of the requirements regarding wear resistance and form stability, deep drawing tools are mainly made of tooling steel or cast iron (Liewald & de Souza, 2008). In addition to commonly used metal tools, it is possible to use tools made of elastomers or composites based on metals and plastics (Bergweiler et al., 2021). Liewald and de Souza (2008) investigated tribological and tool design aspects for the use of polymeric materials (polyurethane with Al hydroxide and Al powder fillers) in sheet metal forming. They developed a new test method for measuring polymer/sheet wear. Using polymeric materials with a minimal Young's modulus of 11,000 MPa and compressive strength of 110 MPa, it is possible to produce prototype-series using high strength steels. Polymeric materials (resins filled with steel powder or sand) can be used in the manufacture of prototype tools or in the production of small size series (Park & Colton, 2003). Schuh et al. (2020) investigated the application of additively manufactured functional elements made by fused filament fabrication (FFF) polymer additive manufacturing in deep drawing tools. They concluded that 3D printed polylactic acid tools are sufficiently stable and provide results that are similar and as good as metal tools in terms of formability. Bergweiler et al. (2019) developed the use of polymer based additive FFF manufactured tools to shorten development cycles and respond to increasing individualisation of forming tools. Frank (1999) used cast polyurethane tools and proved that this tool material shows extraordinarily good friction behaviour. To improve the mechanical properties of laminated object manufacturing-tools Schell (2005) infiltrated the tools with epoxy resin. Selective laser melting and sintering are other methods of producing stamping tools (Leal et al., 2017; Levy et al., 2003).

This article presents the results of investigations into the tribological performance of new materials for the production of tools for sheet metal forming of AMS5599 nickel alloy, AMS5510 corrosion and heat resistant steel and AMS6061-T4 aluminium alloy sheets. The new tool materials include base composites consisting of polyurethane resin and mineral filler as well as composites modified with aluminium powder and roving fabrics. The evaluation of the frictional properties was carried out using a strip drawing test under dry friction conditions.

2. Experimental

2.1. Test material

Friction tests were carried out on four sets of composite countersamples containing polyurethane resin (PR) consisting of two components (isocyanate + polyol) and mineral filler (powdered aluminium hydroxide $Al(OH)_3$). This base variant was modified by adding aluminium powder (10wt.%) and roving fabric (5wt.%). Countersamples were cut from commercial materials in the form of sheets produced by rolling. Cuboid-shaped countersamples with a working surface radius of R = 200 mm (Fig. 1) were coded according to the symbols listed in Table 1. Specimens were fabricated from AMS5599 nickel alloy, AMS5510 corrosion and heat resistant steel and AMS6061-T4 aluminium alloy sheets with a thickness of 1 mm, 1 mm and 2 mm, respectively.
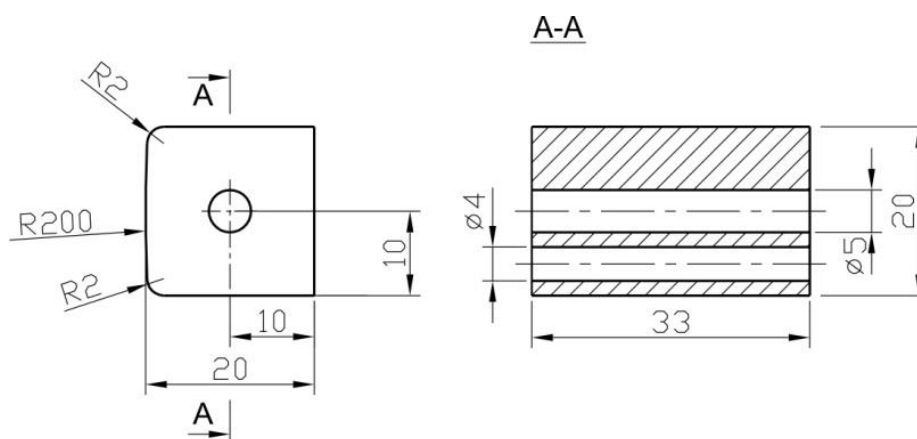
Fig. 1. Shape and dimensions of the countersamples

Table 1. Designation and composition of the countersample material

Countersample type	Aluminium powder, wt.%	Roving fabric, wt.%
F1 (base variant)	-	-
F2	-	5
F3	10	-
F4	10	5

The surface topography of the countersamples (Fig. 2) and sheet metals (Fig. 3) was measured with a Hommel-Etamic T8000RC stationary profilometer in accordance with the requirements of the ISO 25178 standard. The values of the basic surface roughness parameters of the sheets and countersamples are listed in Table 2.
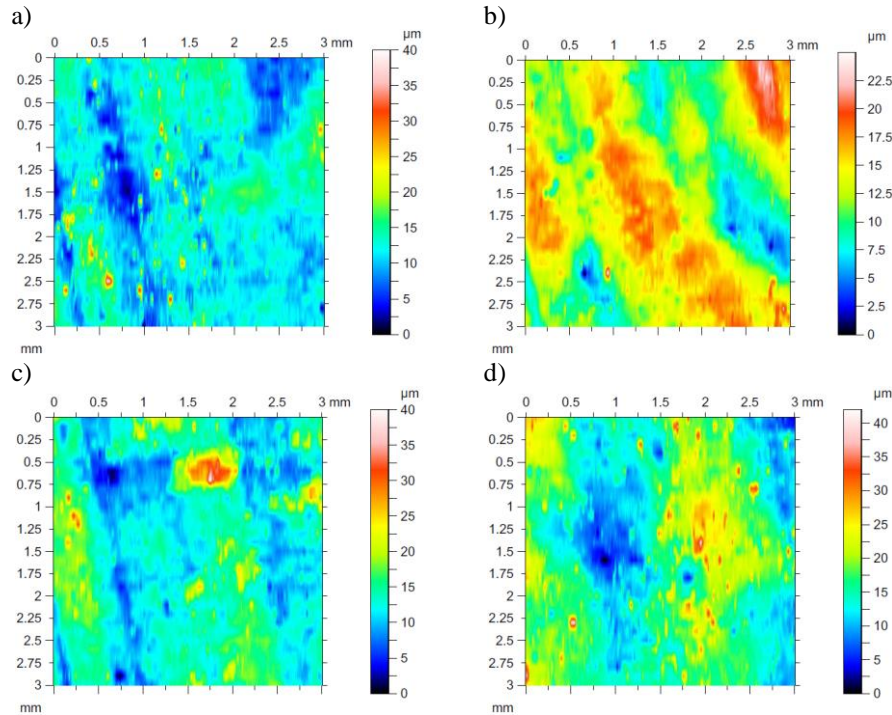
Fig. 2. Topography and basic surface roughness parameters of the countersamples: a) F1, b) F2, c) F3 and d) F4
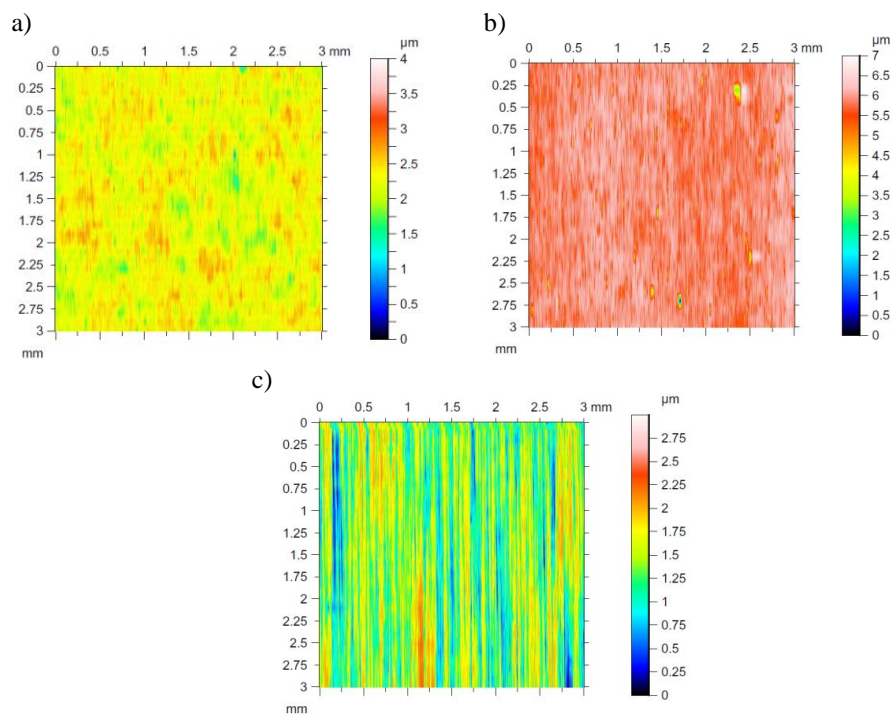
Fig. 3. Topography and basic surface roughness parameters of the sheets in their as-received state: a) AMS5599, b) AMS5510 and c) AMS6061-T4

Table 2. Basic surface roughness parameters of the sheets and countersamples

Material	Sq, µm	Ssk	Sku	Sp, µm	Sv, µm	Sa, µm
AMS5599	0.206	-0.385	4.06	0.825	2.28	0.162
AMS5510	0.246	-2.98	34.0	1.04	5.89	0.170
AMS6061-T4	0.383	-0.251	2.32	1.01	1.36	0.322
F1	3.05	0.587	6.42	26.4	11.8	2.25
F2	3.41	-0.116	2.55	12.0	13.0	2.80
F3	3.85	1.12	6.22	26.1	13.3	2.86
F4	4.73	0.293	3.21	25.1	16.0	3.81

2.2. Strip drawing test

The value of the coefficient of friction (COF) was determined using a tribotester to carry out the strip drawing test (SDT). The tribotester consists of a body in which cuboid-shaped countersamples are placed horizontally (Fig. 4). The SDT device is mounted in a Zwick/Roell Z100. During the tests, a strip of sheet metal approximately 400 mm long and 18 mm wide is placed between the counter-samples.
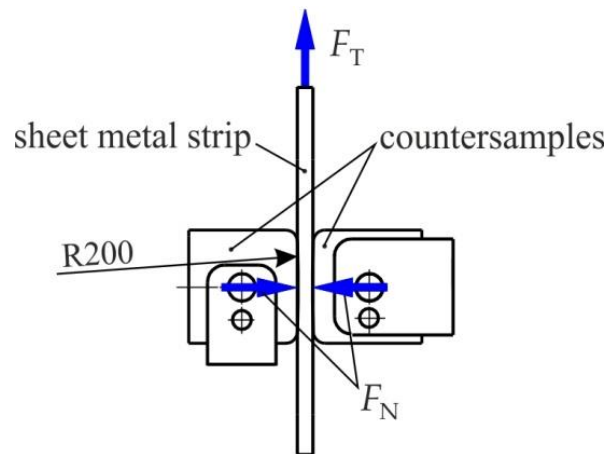
Fig. 4. Schematic diagram of the strip drawing test

The countersamples were pressed against the surface of the samples with a pressing force F_N equal to: 23, 46, 69, 92, 115, 138 and 160 N. During the movement of the sheet between the counter-samples, the measuring system of the testing machine registers the value of the tangential force (friction force) F_T. The value of the COF was determined on the basis of the value of the friction force F_T and the pressure force F_N from the relationship:

$$\mu = \frac{F_T}{2F_N} \tag{1}$$

The average value of the COF was separately determined according to Eq. (1) for each of the various levels of contact force applied.

3. Results and discussion

A tendency to decrease the value of the COF was observed with an increase in the value of the contact force. On the other hand, above the clamping force value of 100 N, stabilising effect occurs with regards to the value of the coefficient of friction. This may be due to the fact that after exceeding a certain load value, the relationship between the friction force and the normal force is nonlinear, and the coefficient of friction is not constant and changes with increasing pressure. The same phenomenon was observed by Kirkhorn et al. (2013), Murtagh et al. (1995) and ten Thije et al. (2008). As the friction force increases, it does not change proportionally to the normal force. As a result, the coefficient of friction varies nonlinearly with a change in contact pressure. The nonlinear relationship between the tangential force (friction force) and the normal force suggests that there are additional phenomena in certain load ranges that should be reflected in friction models.

The difference in the value of COF of AMS5599 sheet determined for individual sets of counter-samples ranges from 0.0122 (F_N = 138 N) to 0.0311 (F_N = 92 N). The smallest values of the coeffi-

cient of friction in the entire range of clamping forces were observed for countersamples fabricated from materials F1 and F2 (Fig. 5). The difference in the value of COF of AMS5510 sheet determined for individual variants of the countersamples ranges between 0.0159 (F_N = 69 N) and 0.0357 (F_N = 23 N). In the range of clamping forces exceeding F_N = 100 N, the lowest value of the coefficient of friction (about 0.175) is provided by the countersamples made of the base material F1 (Fig. 6). The COF reached the highest values over the entire range of clamping forces applied with the countersamples made of material F4.

In the entire range of clamping forces applied, the highest value of COF of AMS6061-T4 sheet was recorded for countersamples marked F4. The countersamples of the material F2 provided the lowest value of the friction coefficient, which stabilised on reaching a value of about 0.197 (Fig. 7). The difference in the value of COF of AMS5510 sheet determined for individual variants of countersamples ranges between 0.0129 (F_N = 138 N) and 0.0254 (F_N = 69 N).
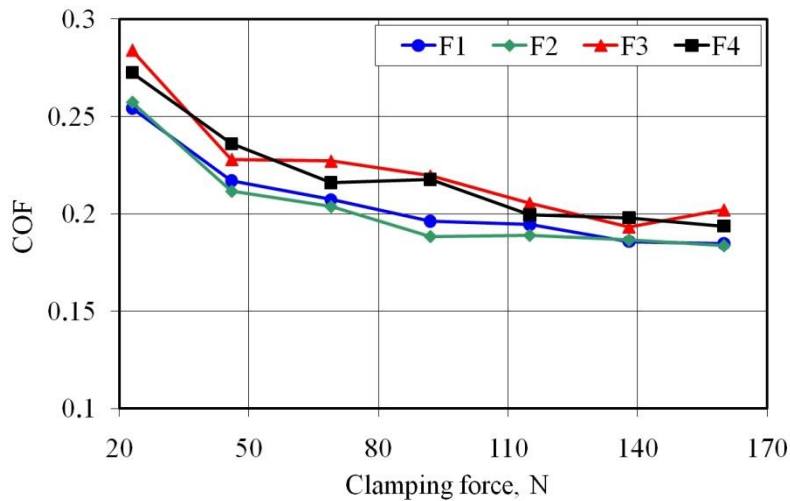
Fig. 5. Effect of clamping force on the value of COF of AMS5599 sheet
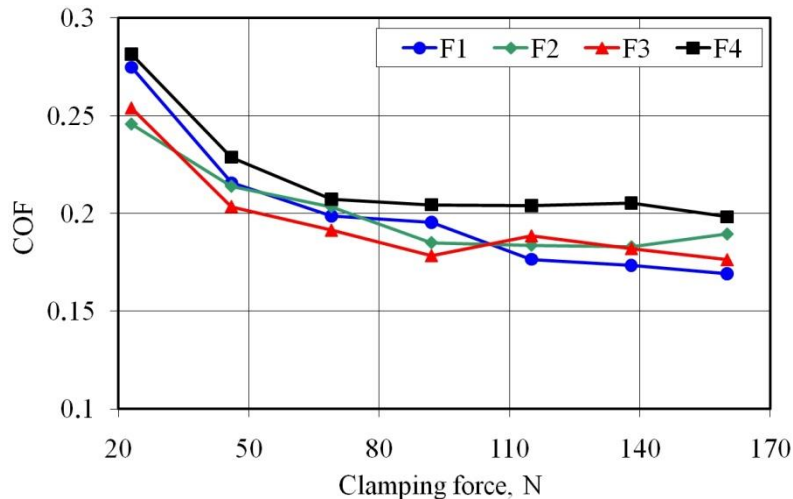
Fig. 6. Effect of clamping force on the value of COF of AMS5510 sheet

Figures 8, 9 and 10 show the percentage change in the value of the friction coefficient in relation to the unmodified base variant F1 of the countersample material. During the friction tests on the AMS5599 sheet, variants of countersamples containing aluminium powder at a rate of 10 wt.% resulted in an increase in the value of COF over the entire range of pressure forces tested, a difference even reaching about 12% (Fig. 8). Only the variant containing 5 wt% of roving fabric in the clamping force range of F_N = 46-115 N showed a noteworthy effect reducing the COF by about 2-4%.

When testing the AMS5510 stainless steel sheet in the clamping force range of F_N = 115-160 N, all the modified countersamples increased the COF by approximately 4-18% (Fig. 9). However, the most unfavourable friction conditions were observed when testing countersamples modified with aluminium powder (10 wt%) and roving fabric (5 wt%). This countersample showed an unfavourable effect on the friction conditions in the entire range of clamping forces tested. Countersamples modi-

fied only with the addition of 10wt.% of aluminium powder, in the clamping force range of $F_N = 23$-92 N, provided a decrease in the COF by about 3.9-8.4%.
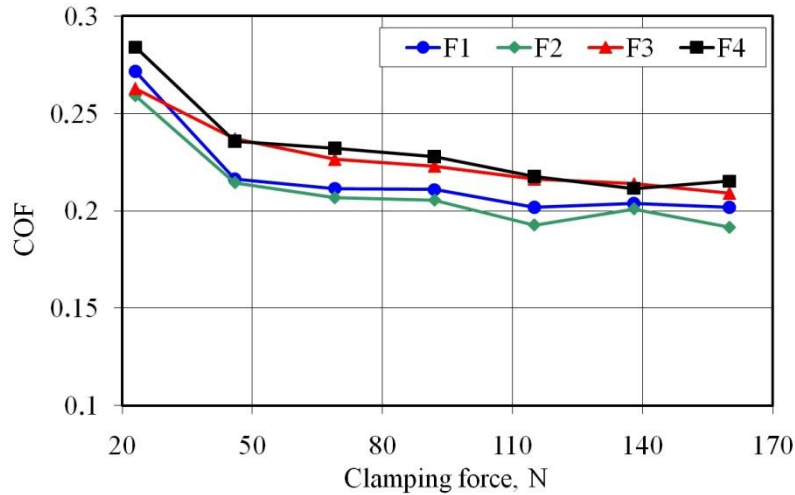
Fig. 7. Effect of clamping force on the value of COF of AMS6061-T4 sheet
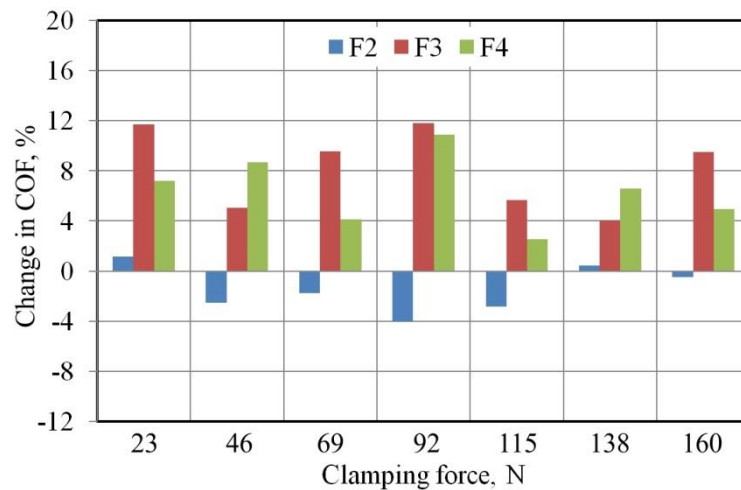
Fig. 8. Change of the value of COF of AMS5599 sheet in relation to the base variant F1

Countersamples modified only with roving fabric content are the most suitable for use with AMS6061-T4 aluminium alloy sheet. A reduction in the COF value was observed across the entire range of clamping forces tested. Countersamples modified with aluminium powder and roving fabric showed unfavourable friction values, increasing the value of the COF in the range of 3.6-9.7% (Fig. 10). There is a tendency for these materials to have a synergistic effect on the coefficient of friction with increasing clamping force.
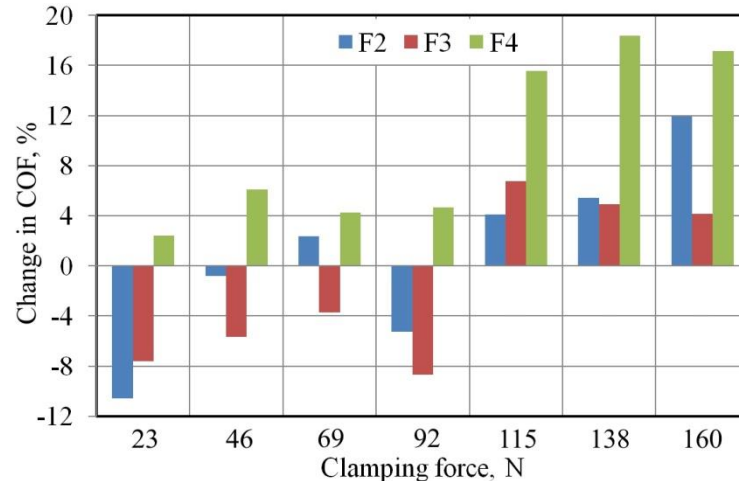
Fig. 9. Change of the value of COF of AMS5510 sheet in relation to the base variant F1

No visible change in the surface topography of the samples after the friction process was observed. This may be due to the much greater hardness of the materials of the tested samples in relation to the composite material of the countersamples. However, the specimens were tested at a distance of about 340 mm. Further studies are needed to determine the effect of the countersamples material on the surface roughness of the samples and vice versa.
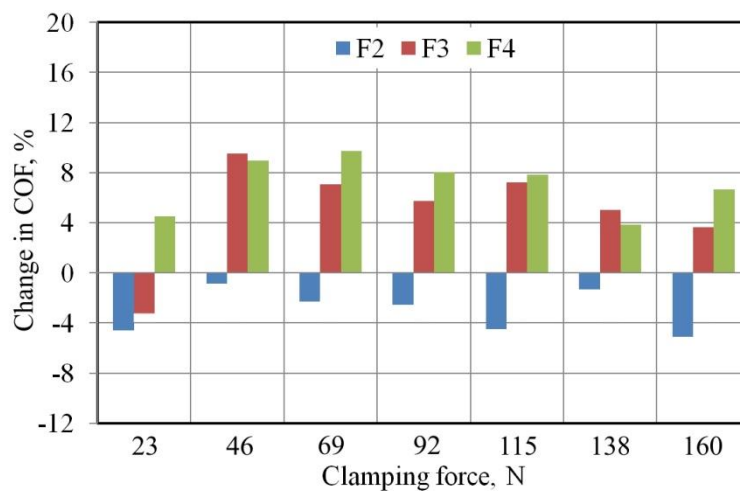
Fig. 10. Change of the value of COF of AMS6061-T4 sheet in relation to the base variant F1

4. Conclusions

Composite inserts in stamping dies are a promising method of changing the friction conditions in selected areas of the drawpiece. The aim of this work was to test the friction of selected composite materials using the strip drawing test, commonly used to simulate friction conditions in sheet metal forming. It was found that when testing AMS5599 nickel-based alloy sheets the smallest values of COF in the entire range of clamping forces were observed for countersamples fabricated from base material which was modified with aluminium powder and roving fabric. In the case of sample material AMS5510 the highest values of COF in the entire range of clamping forces applied were observed for the base variant of the countersamples. The most suitable material for forming AMS6061-T6 aluminium alloy sheets is found in countersamples modified only with the roving fabric content. Their application has the effect of reducing the COF value by 0.9-5.1% depending on the value of the pressing force.

Acknowledgements

References

Bergweiler, G., Fiedler, F., Kampker, A., & Lichtenthäler, K. (2019). Additively manufactured forming tools in prototype construction (in German). Umformtechnik Blech Rohre Profile.

Bergweiler, G., Fiedler, F., Shaukat, A., & Loffler, B. (2021). Experimental investigation of dimensional precision of deep drawn cups using direct polymer additive tooling. *Journal of Manufacturing and Materials Processing*, *5*(1), 3. https://www.mdpi.com/2504-4494/5/1/3

Birkhold, M., Pauli, F.B., Lechler, A., & Verl, A. (2013). On the development of transformable sheet metal forming tools. *IFAC Proceedings Volumes*, *46*(16), 391-396. https://doi.org/10.3182/20130825-4-US-2038.00040

Domitner, J., Silvayeh, Z., Shafiee Sebet, A., Öksüz, K.I., Pelcastre, L., & Hardell, J. (2021). Characterization of wear and friction between tool steel and aluminum alloys in sheet forming at room temperature. *Journal of Manufacturing Processes*, *64*, 774-784. https://doi.org/10.1016/j.jmapro.2021.02.007

Ersoy-Nürnberg, K., Nürnberg, G., Golle, M., & Hoffmann, H. (2008). Simulation of wear on sheet metal forming tools—An energy approach. *Wear*, *265*(11-12), 1801-1807. https://doi.org/10.1016/ j.wear.2008.04.039

Frank, C. (1999). Polymers as tooling material for deep drawing of sheet metal (in German). PhD thesis. Leibniz University Hannover.

Groche, P., Christiany, M., & Wu, Y. (2019). Load-dependent wear in sheet metal forming. *Wear*, *422-423*, 252-260. https://doi.org/10.1016/j.wear.2019.01.071

Hol, J., Cid Alfaro, M.V., de Rooij, M.B., & Meinders, T. (2012). Advanced friction modeling for sheet metal forming. *Wear*, *286-287*, 66-78. https://doi.org/10.1016/ j.wear.2011.04.004

Kirkhorn, L., Bushlya, V., Andersson, M., & Ståhl, J. E. (2013). The influence of tool microstructure on friction in sheet metal forming. *Wear*, *302*, 1268–1278. https://doi.org/10.1016/ j.wear.2013.01.050

Leal, R., Barreiros F., Alves L. (2017). Additive manufacturing tooling for the automotive industry. *International Journal of Advanced Manufacturing Technology*, *92*, 1671-1676. https://doi.org/10.1007/s00170-017-0239-8

Levy, G.N., Schindel, R., Schleiss, P., Micari, F., & Fratini, L. (2003). On the use of SLS tools in sheet metal stamping. *CIRP Annals*, *52*(1), 249-252. https://doi.org/ 10.1016/S0007-8506(07)60577-0

Liewald, M. & de Souza, J. H. C. (2008). New developments on the use of polymeric materials in sheet metal forming. *Production Engineering*, 2, 63-72. https://doi.org/10.1007/s11740-008-0077-5

Murtagh, A. M., Lennon, J. J., & Mallon, P. J. (1995). Surface friction effects related to pressforming of continuous fibre thermoplastic composites. *Composites Manufacturing*, *6*, 169–175. https://doi.org/10.1016/ 0956-7143(95)95008-M

Park, Y., & Colton, J.S. (2003). Sheet metal forming using polymer composite rapid prototype tooling. *Journal of Engineering Materials and Technology*, *125*(3), 247-255. https://doi.org/10.1115/1.1543971

Schell, T. (2005). Basic investigations of a new Rapid Tooling technique for sheet metal forming" (in German). PhD thesis. University of Erlangen-Nürnberg.

Schmoeckel, D., Frontek, H., & von Finckenstein, E. (1986). Reduction of wear on sheet metal forming tools. *CIRP Annals*, *35*(1), 195-198. https://doi.org/10.1016/S0007-8506(07)61869-1

Schuh, G., Bergweiler, G., Bickendorf, P., Fiedler, F. & Cong, C. (2020), Sheet metal forming using additively manufactured polymer tools. *Procedia CIRP*, *93*, 20-25. https://doi.org/10.1016/j.procir.2020.04.013

ten Thije, R. H. W., Akkerman, R., van der Meer, L., & Ubbink, M. P. (2008). Tool-ply friction in thermoplastic composite forming. *International Journal of Material Forming,* 1, 953–956. https://doi.org/10.1007/ s12289-008-0215-9

Vierzigmann, H.U., Merklein, M., & Engel, U. Friction conditions in sheet-bulk metal forming. *Procedia Engineering*, *19*, 377-382. https://doi.org/10.1016/j.proeng.2011.11.128

Analiza Właściwości Tribologicznych Nowych Wkładek Kompozytowych Tłoczników za Pomocą Testu Przeciągania Pasa Blachy

Streszczenie

Celem artykułu jest ocena właściwości tribologicznych nowych kompozytowych wkładek do tłoczników. Badaniom poddano cztery zestawy przeciwpróbek kompozytowych składających się z żywicy poliuretanowej z wypełniaczem mineralnym (wariant bazowy) oraz modyfikowanych proszkiem aluminiowym (10% mas.) i tkaniną rowingową (5% mas.). Próbki do testu przeciągania pasa blachy wycięto z blach AMS5599, AMS5510 i AMS6061-T4. Zaobserwowano wpływ rodzaju materiału przeciwpróbki na współczynnik tarcia. Najmniejsze wartości współczynnika tarcia w całym zakresie zmian siły docisku dla blach AMS5599 i AMS5510 zaobserwowano podczas badań z przeciwpróbkami wykonanymi z bazowego wariantu kompozytu. Podczas badania blachy ze stopu aluminium AMS6061-T4 przeciwpróbki modyfikowane tkaniną rowingową zapewniły najmniejszą wartość współczynnika tarcia, która w zakresie ustabilizowanym osiągnęła wartość około 0,197.

Słowa kluczowe: tarcie, współczynnik tarcia, narzędzie kompozytowe, tłocznik

Original Research

Crystal Plasticity Elastic-Plastic Rate-Independent Numerical Analyses of Pollycrystalline Materials

Marta Wójcik [1],* iD, Andrzej Skrzat [1] iD, Feliks Stachowicz [1] iD , Emil Spišák [2] iD

[1] Department of Materials Forming and Processing, Faculty of Mechanical Engineering and Aeronautics, Rzeszow University of Technology, 8 Powstańców Warszawy Ave., 35-959 Rzeszów, Poland

[2] Department of Technology, Materials and Computer Supported Production, Faculty of Mechanical Engineering, Technical University of Košice, 74 Mäsiarska St., 040 01 Košice, Slovakia

* Correspondence: m.wojcik@prz.edu.pl, tel.: +48 17 865 15 07

Abstract

Macroscopic analyses of plastic forming processes give only the overall description of the problem without the consideration of mechanisms of plastic deformation and the microstructure evolution. For the consideration of these processes, numerical simulations within crystal plasticity include the change of texture, anisotropy, and strain hardening of the material are used. In this paper, a crystal plasticity rate-independent model proposed by Anand and Kothari is applied for numerical analyses of polycrystalline materials. The slip was considered as the main mechanism of the plastic deformation. Basic constitutive equations of crystal plasticity for large deformation theories are presented. The selected results of elastic-plastic problems obtained using both macro- and micro- scales software for the explicit and implicit integration are featured here. The heterogeneous distribution of strain and stress in different grains are obtained, which is associated with the various crystal orientation. The crystal plasticity modelling of materials subject to plastic deformation involves not only the information about the change of a material's shape in a macro-scale, but also describes the phenomena occurring in material in a micro-scale.

Keywords: crystal plasticity, polycrystalline materials, plastic deformation, CPFEM, dislocation slip

1. Introduction

Numerical analyses of elastic-plastic problems of materials forming and processing can be solved on macroscopic level using the classical plasticity theory or on the microscopic one using crystal plasticity. This first approach describes the behaviour of materials under loading only in a macroscopic scale without taking into consideration its micromechanical changes. In such macroscopic analyses, a variety of models, e.g. Prager, Ziegler, Johnson-Cook, Ohno-Wang, Frederick-Armstrong, and Chaboche ones are commonly applied (Buljak et al., 2021; Genna, 1993; Remache et al., 2020; Chen et al., 2005; Schäfer, 2019; Sajjad et al., 2019). Material processing analyses including only the macroscopic behaviour of materials under cyclic loading were tested by authors in the past. Wójcik and Skrzat (2020) applied the Frederick-Armstrong model in order to predict the stress-strain response of a material subject to the cyclic loading test. Authors were also testing the application of both Frederick-Armstrong and Chaboche models in numerical analyses of the KOBO extrusion (Wójcik & Skrzat, 2022b; Wójcik & Skrzat, 2021). Although the good convergence between experimental and numerical results is obtained, only the macroscopic response of the material was considered. It gives the incomplete description of the material behavior, especially in the case of large deformation processes, Severe Plastic Deformation (SPD) processes in which the significant refinement of a microstructure is a very important feature.

The crystal plasticity (CP) theory presents a full explanation of a material plastic deformation under loading and includes both the change of the material shape in a macro scale, as well as, its microstructure evolution and grains anisotropy (Men & Meng, 2022). The CP models link different scales of the problem considered – from macro- to micro- and to nano- levels. The CP theory has been developed as a

useful tool to describe the mechanical response of polycrystalline materials on all scales from single crystals to whole engineering parts in last thirty years (Dabiri et al., 2018).

In the CP approach, materials are considered as polycrystals with a large number of grains in which each grain has a specific crystallographic orientation. The single crystal has the three-dimensional arrangement of atoms - FCC (face centered cubic), BCC (body centered cubic) or HCP (hexagonal close packed) (Ramos et al., 2020). The level of the plastic deformation in a polycrystalline material varies from one crystal to another, which depends on, e.g. the orientation, geometry, neighboring crystals and loading conditions (Yang & Park, 2003).

Contrary to the classical theory of plasticity, the CP takes into consideration the mechanisms of plastic deformation in materials – mainly slip and twinning. The CP models based on the slip are well-known and developed in the CP theory (Bridier et al., 2009; Messner et al., 2017; Alankar et al., 2011). Models assuming twinning are in the intensive development at present. Liu et al. (2021) proposed the coupled crystal plasticity finite element-phase field model with kinetics-controlled twinning. Abdolvand et al. (2011) developed the crystal plasticity model assuming the twinning reorientation. The numerical modelling of twinning-induced plasticity using crystal plasticity finite element method (CPFEM) is described in by Khan et al. (2016). Apart from the heterogeneity of plastic strain in crystalline materials caused by the anisotropy of grains, a lot of CP models available assume some simplifications. In the Taylor model, all grains have the same strain state common to the global strain (Pramanik, 2021). Every grain is deformed in the same way as the representative volume element (RVE) here. The Sachs model assumes the same stress state for all grains which is the same as the global stress state of the material (Romanova, 2022). It results in the discontinuity of displacements. In the self-consistent model, every grain is considered as an ellipsoidal heterogeneity placed in a uniform space representing the polycrystalline structure (Li et al., 2021).

Apart from popular models, there are also new approaches in order to simulate the behaviour of a material under loading based on the CP theory. The microstructure-based CP model in order to evaluate the shear deformation behavior of a material under cyclic load is described by Yang et al. (2022). The new twinning-induced crystal plasticity model in terms of the thermomechanical framework and with a new integration method, is developed by Khan and Alfozan (2019). The fully implicit integration procedure for a twinning-induced plasticity model based on the CP approach is also presented by Khan et al. (2022). The propositions of other new models using the CP theory in order to simulate the behaviour of material in a microscopic scale are also available in literature (Li et al., 2022; Ibragimova et al., 2021; Li et al., 2020; Jeong & Voyiadjis, 2022).

The plastic deformation due to the dislocation slip was considered in this paper. Anisotropic slip occurs only in selected directions and in selected crystalline planes which define slip systems (Nguyen, 2021). Additionally, the dislocation slip does not change the crystalline orientation of a material. All atoms in a lattice maintain the same distance with each other, therefore (Faul, 2021). Polycrystalline structures have a different number of slip systems determined by **n** and **m** vectors which describe the normal to the slip plane and the slip direction, respectively. For FCC structure considered here, four sets of slip planes {111} and three close packed slip directions <110> in each plane are determined, which gives a combination of twelve slip systems (Weinberger, 2013). The plastic deformation caused by the slip occurs more easily in crystals which have higher number of the slip systems and which are located more favorably against the a load direction (Wójcik & Skrzat, 2022a).

The activation of slip systems is described by Schmid's law. The yielding in a crystal takes place when the resolved shear stress (τ^{α}) of a selected slip system exceeds its critical resolved shear stress - τ_{CRSS} (Eq. 1) (Mlikota & Schmauder, 2018).

$$\tau^{\alpha} = \sigma cos\phi cos\lambda > \tau_{CRSS} \tag{1}$$

where: σ is a tensile stress, λ is an angle between tensile axis and the slip direction and ϕ is an angle between tensile angle and the slip plane normal. The $cos\varphi cos\lambda$ coefficient defines the Schmid factor.

Numerical elastic-plastic analyses of a copper alloy subjected to simple tension tests are presented here. The simulations were done for different shapes of samples. The material was modelled as a polycrystalline anisotropic material with the random distribution of grains. The CP analyses were performed using open-source NEPPER and FEPX, and commercial Simulia Abaqus softwares. The Anand and Kothari approach was applied here. It is a relatively simple, effective and efficient numerically model in order to calculate the stress increment. The main advantage of the method is that the Anand and Kothari procedure presents the way to choose the slip systems which is a long-lasting problem of the rate-independent CP theory. Additionally, the CP approach developed by Anand and Kothari is

implemented in the PRISMS commercial software which can be used as a reference solution in order to check the correctness of a solution. The results obtained presents the potential of CP as an effective numerical approach for solving engineering problems, including modeling of materials forming processes characterized by the large plastic deformation. The micromechanical analyses using CP theory give a more complete description of the material behavior under loading than classical macro-mechanical approaches.

2. Constitutive equations of Crystal Plasticity theory

The rate-independent CP constitutive model for a single crystal FCC structure developed by Anand & Kothari (1996) is used in this paper. Based on assumption of deformation decomposition into elastic and plastic parts CP constitutive equations are as follows:

1) Multiplicative decomposition of deformation gradient $\boldsymbol{F}$ into elastic $\boldsymbol{F}^e$ and plastic components $\boldsymbol{F}^p$ is the following (Eq. 2):

$$\boldsymbol{F} = \boldsymbol{F}^e \boldsymbol{F}^p \tag{2}$$

Elastic part includes the information about rotation and stretching, plastic part influences on plastic shearing on crystallographic slip systems and defines dislocations (Fig. 1) (Paudel et al., 2021).
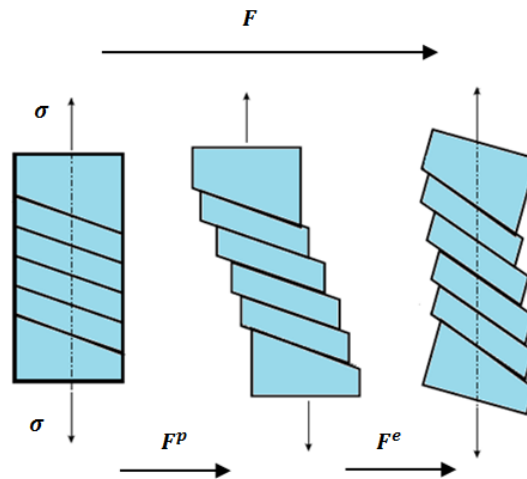
Fig. 1. Explanation of elastic and plastic parts of the deformation gradient tensor

2) The macroscopic velocity gradient $\boldsymbol{L}$ is decomposed additively into elastic and plastic parts (Eq. 3), as well as into symmetric and antisymmetric ones (Eq. 4):

$$\boldsymbol{L} = \boldsymbol{L}^e + \boldsymbol{L}^p = \dot{\boldsymbol{F}}^e (\boldsymbol{F}^e)^{-1} + \boldsymbol{F}^e \dot{\boldsymbol{F}}^p (\boldsymbol{F}^p)^{-1} (\boldsymbol{F}^e)^{-1} \tag{3}$$

$$\boldsymbol{L} = \boldsymbol{D} + \boldsymbol{\Omega} \tag{4}$$

where: $\boldsymbol{L}^e$ and $\boldsymbol{L}^p$ are elastic and plastic velocity gradient tensors, respectively; $\boldsymbol{D}$ is symmetric deformation velocity tensor and $\boldsymbol{\Omega}$ is an antisymmetric spin (Eq. 5-6). Similarly to tensor $\boldsymbol{L}$, tensors $\boldsymbol{D}$ and $\boldsymbol{\Omega}$ are additively decomposed into elastic and plastic parts in line with Eq. 7-8:

$$\boldsymbol{D} = sym(\boldsymbol{L}) = \frac{1}{2}(\boldsymbol{L} + \boldsymbol{L}^T) \tag{5}$$

$$\boldsymbol{\Omega} = asym(\boldsymbol{L}) = \frac{1}{2}(\boldsymbol{L} - \boldsymbol{L}^T) \tag{6}$$

$$\boldsymbol{D} = \boldsymbol{D}^e + \boldsymbol{D}^p \tag{7}$$

$$\boldsymbol{\Omega} = \boldsymbol{\Omega}^e + \boldsymbol{\Omega}^p \tag{8}$$

3) On the basis of the polar decomposition, the elastic part of the deformation gradient might be expressed as a multiplication of a rigid body tensor $\boldsymbol{R}^e$ and the right stretching tensor $\boldsymbol{U}^e$ (Eq. 9). Using the $\boldsymbol{R}$ tensor, the elastic part of a spin might be written as (Eq. 10):

$$\boldsymbol{F}^e = \boldsymbol{R}^e \boldsymbol{U}^e \tag{9}$$

$$\boldsymbol{\Omega}^e = \boldsymbol{R}^e \cdot \dot{\boldsymbol{R}}^{eT} \tag{10}$$

4) The macroscopic plastic velocity gradient links different scales of the problem considered (macro- and micro-) (Men & Meng, 2022; Ryś et al., 2022). It might be expressed as the superposition of shear deformation caused by the crystallographic slip (Eq. 11):

$$\boldsymbol{L}^p = \sum_{\alpha=1}^{n} \dot{\gamma}^\alpha \boldsymbol{S}^\alpha \tag{11}$$

where: $\dot{\gamma}^\alpha$ is the shearing rate on the α slip system, n is a total number of slip systems and $\boldsymbol{S}^\alpha$ is the Schmid tensor for the slip system α defined as follows (Eq. 12):

$$\boldsymbol{S}^\alpha = \boldsymbol{m}^\alpha \otimes \boldsymbol{n}^\alpha \tag{12}$$

where: $\boldsymbol{m}^\alpha$ is the slip direction and $\boldsymbol{n}^\alpha$ defines the slip plane normal, as well as, $\boldsymbol{m}^\alpha$ and $\boldsymbol{n}^\alpha$ are orthogonal (Nibur & Bahr, 2003). Assuming the microscopic level, the plastic deformation velocity gradient $\boldsymbol{D}^p$ and the plastic spin $\boldsymbol{\Omega}^p$ tensors are expressed in line with the following equations (Eq. 13-14) (Deng, 2014).

$$\boldsymbol{D}^p = \frac{1}{2}(\boldsymbol{L}^p + \boldsymbol{L}^{pT}) = \sum_{\alpha=1}^{n} \boldsymbol{p}^\alpha \cdot \dot{\gamma}^\alpha \tag{13}$$

$$\boldsymbol{\Omega}^p = \frac{1}{2}(\boldsymbol{L}^p - \boldsymbol{L}^{pT}) = \sum_{\alpha=1}^{n} \boldsymbol{\omega}^\alpha \cdot \dot{\gamma}^\alpha \tag{14}$$

where: $\boldsymbol{p}^\alpha$ and $\boldsymbol{\omega}^\alpha$ are symmetric and asymmetric tensors defining the Schmid tensor on the α slip system defined as follows (Eq. 15-16).

$$\boldsymbol{p}^\alpha = \frac{1}{2}(\boldsymbol{n}^\alpha \otimes \boldsymbol{m}^\alpha + \boldsymbol{m}^\alpha \otimes \boldsymbol{n}^\alpha) \tag{15}$$

$$\boldsymbol{\omega}^\alpha = \frac{1}{2}(\boldsymbol{n}^\alpha \otimes \boldsymbol{m}^\alpha - \boldsymbol{m}^\alpha \otimes \boldsymbol{n}^\alpha) \tag{16}$$

5) The resolved shear stress which causes the shear on a given crystallographic plane in a given crystallographic direction is defined as (Eq. 17) (Frydrych & Kowalczyk-Gajewska, 2016):

$$\tau^\alpha = \boldsymbol{\sigma} : \boldsymbol{S}^\alpha = \boldsymbol{\sigma} : (\boldsymbol{m}^\alpha \otimes \boldsymbol{n}^\alpha) \tag{17}$$

6) Based on Schmid's law, the CP hardening model of polycrystalline material and shear rate $\dot{\gamma}^\alpha$ for the α slip system evaluate as follows (Eq. 18):

$$\dot{\gamma}^\alpha = \dot{\gamma}_0 \left(\frac{|\tau^\alpha|}{g^\alpha}\right)^k sgn(\tau^\alpha) \tag{18}$$

where: $\dot{\gamma}_0$ is the reference shear strain rate on the α slip system, τ^α is the resolved shear stress on the α slip system, k is the rate sensitivity coefficient, g^α is the critical shear stress on the α activated slip system to govern the isotropic hardening of the crystal and sgn is a signum function. For a rate-independent CP, $k \to \infty$ (Yaghoobi et al., 2019).

7) The shear rate $\dot{\gamma}^\alpha$ which consists of the effect of a backstress related with the kinematic hardening is written by the following (Eq. 19):

$$\dot{\gamma}^\alpha = \dot{\gamma}_0 sgn(\tau^\alpha - x^\alpha) \left(\frac{|\tau^\alpha - x^\alpha|}{g^\alpha}\right)^k \tag{19}$$

where: x^α is a backstress describing the nonlinear kinematic (directional) hardening of the crystal on the α slip system.

8) The evolution of a slip resistance ($\dot{g}^\alpha$) for the α slip system is described as follows (Eq. 20):

$$\dot{g}^{\alpha} = \sum_{\beta} h^{\alpha\beta} \dot{\gamma}^{\beta} \tag{20}$$

where: $h^{\alpha\beta}$ is a hardening modulus defining the variation of slip resistance for the α slip system due to the slip rate on β slip system and might be defined as a relationship assuming both hardening and recovery (Eq. 21) (Asaro & Needleman, 1985):

$$h^{\alpha\beta} = \begin{cases} h_0^{\beta} \left[1 - \frac{g^{\beta}}{g_s^{\beta}} \right]^{\alpha\beta} & for\ \alpha = \beta \\ h_0^{\beta} q \left[1 - \frac{g^{\beta}}{g_s^{\beta}} \right]^{\alpha\beta} & for\ \alpha \neq \beta \end{cases} \tag{21}$$

where: q is a latent hardening ratio, h_0^{β} is a hardening parameter for β slip system, g_s^{β} defines the slip resistance at hardening saturation for β slip system, and α^{β} is a material constant for β slip system defining the sensitivity of the hardening moduli to the slip resistance (Khan & Alfozan, 2019). It is assumed that $h^{\alpha\beta}$ is a self-hardening modulus for $\alpha = \beta$ or for $\alpha \neq \beta$, $h^{\alpha\beta}$ is a latent hardening one (Yaghoobi et al., 2019).

The Anand & Kothari model presented above indicates very good compatibility with the experimental data in most cases. Acar et al. (2017) obtained a very good convergence between the microstructure measured experimentally and achieved in simulations using the Anand and Kothari model for a titanium-aluminum alloy. The research of Balasubramanian & Anand (2002) also confirmed the very good agreement between numerical and experimental stress-strain response, strain-rate history and temperature-history effect for aluminum with the use of Anand and Kothari model.

3. Numerical integration of Crystal Plasticity constitutive equations

The numerical calculations of elastic-plastic problems based on the CP theory with the use of equations presented in Section 2 are time-consuming and complex. A lot of computation steps are required in such analyses and the calculations are done iteratively in a loop. These steps are shown in Fig. 2.
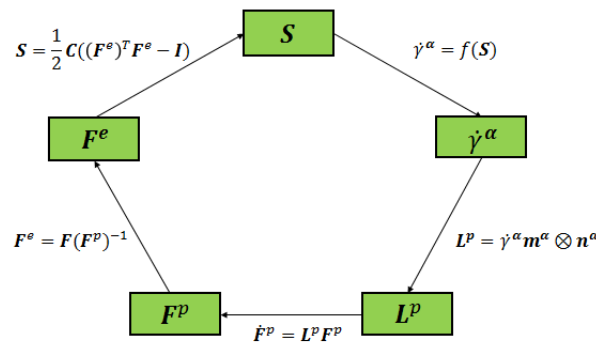
Fig. 2. Diagram showing the complexity of calculations using the CP theory

The implicit integration procedure of constitutive equations is presented here. Five state variables $\{ \boldsymbol{F}(t), \boldsymbol{F}^e(t), \boldsymbol{F}^p(t), \boldsymbol{\sigma}(t)$ Cauchy stress and $g^{\alpha}(t) \}$ at initial time t undergo the incremental deformation, and then they are updated for the time $t_1 = t + \Delta t$. The given data are $\boldsymbol{F}(t)$, $\boldsymbol{F}(t_1)$, stress $\boldsymbol{S}(t)$, $g^{\alpha}(t)$ and time-independent parameters defining the slip system ($\boldsymbol{m}_0^{\alpha}$ and $\boldsymbol{n}_0^{\alpha}$). The $\boldsymbol{F}^p(t_1)$, $\boldsymbol{T}(t_1)$ and $g^{\alpha}(t_1)$, as well as the information about the orientation of the slip system, are calculated. Unfortunately, there are only five independent plastic strain components available (six plastic strain components are constrained by the incompressibility condition, while potentially twelve slip systems should be determined. In this research we use the integration procedure proposed by Anand and Kothari which is summarized as follows.

1) Firstly, the trial elastic strain $E^e(t_1)^{tr}$ is calculated in line with the Eq. 22-24.

$$\boldsymbol{F}^e(t_1)^{tr} = \boldsymbol{F}(t_1)\boldsymbol{F}^p(t_1) \tag{22}$$

$$\boldsymbol{C}^e(t_1)^{tr} = (\boldsymbol{F}^e(t_1)^{tr})^T \boldsymbol{F}^e(t_1)^{tr} \qquad (23)$$

$$\boldsymbol{E}^e(t_1)^{tr} = \frac{1}{2}[\boldsymbol{C}^e(t_1)^{tr} - \boldsymbol{I}] \qquad (24)$$

where: $\boldsymbol{C}^e$ is elastic right Cauchy-Green strain tensor and $\boldsymbol{I}$ is the identity matrix.

2) Based on the trial elastic strain the $\boldsymbol{S}^*(t_1)^{tr}$ trial stress tensor is determined (Eq. 25).

$$\boldsymbol{S}^*(t_1)^{tr} = \ell[\boldsymbol{E}^e(t_1)^{tr}] \qquad (25)$$

where: ℓ *is* the fourth order elastic stiffness tensor.

3) The trial resolved shear stress $\tau^\alpha(t_1)^{tr}$ on each slip system expressed by the Schmid tensor is calculated as follows (Eq. 26-27):

$$\tau^\alpha(t_1)^{tr} = \boldsymbol{S}^*(t_1)^{tr} \cdot \boldsymbol{S}_0^\alpha \qquad (26)$$

$$\boldsymbol{S}_0^\alpha = \boldsymbol{m}_0^\alpha \otimes \boldsymbol{n}_0^\alpha \qquad (27)$$

In Eq. 26, $\boldsymbol{S}_0^\alpha$ Schmid tensor for α slip system is the same in both relaxed and undeformed configuration because plastic slip does not directly affect the crystallography of the underlying lattice (Faul, 2021).

4) Assuming some simplifications, the following relationship can be written as (Eq. 28):

$$sign[\tau^\alpha(t_1)^{tr}] = sign[\tau^\alpha(t_1)] \qquad (28)$$

The determination of active slip systems and shear increments require long-lasting computations in rate-independent CP theory. The following approach for the determination of active and inactive slip systems based on the plasticity condition (Eq. 29) might be applied.

$$f^\alpha = |\tau^\alpha| - g^\alpha \qquad (29)$$

According to the Kuhn-Tucker special consistency conditions, the slip system is inactive if $\dot{\gamma}_\alpha = 0$ and $|\tau^\alpha| < g^\alpha$ or if $|\tau^\alpha| = g^\alpha$ and the trial stress rate points to the inside of the yield surface. For active slip systems, $|\tau^\alpha| = g^\alpha$, $\dot{\gamma}_\alpha > 0$ and the trial stress rate points to the outside of the yield surface (Sundararaghavan & Zabaras, 2008). In order to determine the active slip systems and corresponding slip increments, the consistency condition in the form of linear equations (Eq. 30) is applied.

$$\sum_{\beta \epsilon A} A^{\alpha\beta} \dot{\gamma}^\beta = b^\alpha \qquad (30)$$

in which: A is a set of potentially active slip systems and matrix $A^{\alpha\beta}$ defines potentially active slip systems. At the end of calculations, the size of $A^{\alpha\beta}$ matrix is reduced to *m* by *m* where m means the number of active slip systems. The search for active slip systems relies on the solving of the system of linear equations above (see Eq. 30) until all systems meet the requirement $\dot{\gamma}^\beta > 0$. If the system is inactive, it is removed from the set of active slip systems and the size of matrix A is reduced, therefore (Li et al., 2021).

5) Next the plastic deformation gradient $\boldsymbol{F}^p(t_1)$ at time t_1 is updated (Eq. 31).

$$\boldsymbol{F}^p(t_1) = \{\boldsymbol{I} + \sum_{\alpha=1}^m sign(\tau^\alpha(t_1)^{tr}) \Delta\gamma^\alpha \boldsymbol{S}_0^\alpha\} \boldsymbol{F}^p(t) \qquad (31)$$

6) Then it is necessary to check if $det\boldsymbol{F}^p(t_1) = 1$. If this condition is not satisfied, $\boldsymbol{F}^p(t_1)$ is normalized as follows (Eq. 32).

$$\boldsymbol{F}^p(t_1) = [\det \boldsymbol{F}^p(t_1)]^{-1/3} \boldsymbol{F}^p(t_1) \qquad (32)$$

7) In the further step, the elastic deformation gradient $\boldsymbol{F}^e(t_1)$ and stress tensor $\boldsymbol{S}^*(t_1)$ are computed (Eq. 33-34).

$$\boldsymbol{F}^e(t_1) = \boldsymbol{F}(t_1)\boldsymbol{F}^{p-1}(t_1) \qquad (33)$$

$$\boldsymbol{S}^*(t_1) = \boldsymbol{S}^e(t_1)^{tr} - \sum_{\alpha=1}^m \{\Delta\gamma^\alpha sign(\tau^\alpha(t_1)^{tr})\} \ell[sym(\boldsymbol{C}^e(t_1)^{tr} \boldsymbol{S}_0^\alpha)] \qquad (34)$$

8) At the end of the integration procedure, the $S(t_1)$ and $g^\alpha(t_1)$ variables, as well as, parameters associated with the texture evolution - $m_{t_1}^\alpha$ and $n_{t_1}^\alpha$ are calculated (Eq. 35-38).

$$S(t_1) = F^e(t_1)\{[detF^e(t_1)]^{-1}S^*(t_1)\}F^{e^T}(t_1) \tag{35}$$

$$g^\alpha(t_1) = g^\alpha(t) + \sum_{\beta=1}^N h^{\alpha\beta}\Delta\gamma^\beta, \quad \alpha = 1, \dots, N \tag{36}$$

$$m_{t1}^\alpha = F^e(t_1)m_0^\alpha \tag{37}$$

$$n_{t1}^\alpha = F^e(t_1)n_0^\alpha \tag{38}$$

The integration procedure presented above has been implemented by authors in the form of the user material subroutine in ABAQUS program. The same approach is also used in PRISMS open software, which can be applied in solving benchmark tests treated as reference solutions. It is worth noting that static procedure requires the Jacobian matrix for the Newton-type iterative method in order to calculate the equilibrium configuration at the end of the time step (Deng, 2014). Contrary to this, the dynamic analysis does not require the determination of the Jacobian matrix.

4. Elastic-plastic numerical simulations using the CP theory

The CPFEM simulations presented in this paper were carried out using the following open-source programs: NEPER as pre- and post- processor, and FEPX as the solver. The geometry of models is prepared in NEPER as a polycrystalline structure using the 3D Voronoi tessellation. The finite element mesh is generated in the same program. The numerical calculations are executed in FEPX program assuming proper boundary conditions. The stages of the CP analysis are shown in Fig. 3.

Simulations were done for cube and paddy-shape samples. Different number of grains and different meshes were tested. The generic copper alloy with a FCC crystalline structure with 12 slip systems was included here for which elastic and plastic parameters (FEPX, 2008) are contained in Table 1.
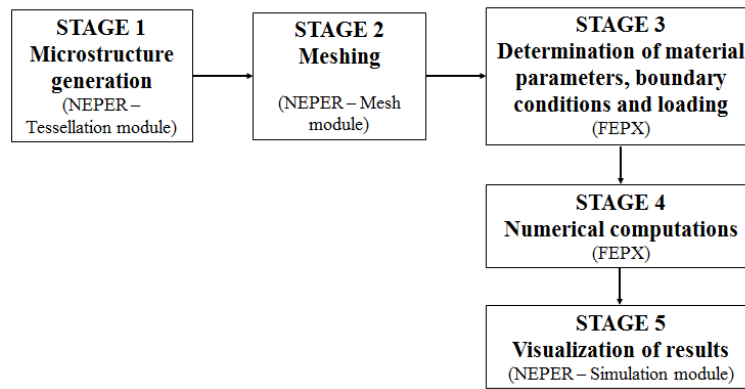
Fig. 3. Stages of CP analyses in NEPER and FEPX software

Table 1. Elastic parameters and other data associated with the strain hardening used in analyses

Parameter	Unit	Value
Elastic parameters		
Elastic constant C_{11}	MPa	$245\cdot10^3$
Elastic constant C_{12}	MPa	$155\cdot10^3$
Elastic constant C_{44}	MPa	$62.5\cdot10^3$
Plastic parameters		
material constant m	-	0.05
reference shear strain rate $\dot{\gamma}_0$	s^{-1}	1
fixed-state hardening rate scaling coefficient h_0	MPa	200
initial slip system strength g_0	MPa	210
initial slip system saturation strength g_{s0}	MPa	330
rate sensitivity coefficient k [-]	-	1

Although, the microstructural analyses of elastic-plastic problems using the CP theory give the better description of phenomena occurring in materials than the macroscopic ones, the computational cost of such calculations is very high.

In the further part of the research, the simple tension test of a plate with two holes is considered. The calculations are done in ABAQUS software using the user material procedure for the static analysis. The selected data applied in calculations are included in Table 2. On the basis of a macroscopic FEM analysis with the use of a UMAT, the information about stress and strain states, as well as, the deformation and velocity gradient tensors might be obtained. They can be then used in calculation based on the CP theory. So far, the UMAT material subroutine has been written for small strains only.

Table 2. Selected parameters used in the elastic-plastic analysis in ABAQUS

Parameter	Unit	Value
Young modulus E	MPa	$0.2 \cdot 10^5$
Poisson's ratio ν	-	0.33
Yield stress σ_p	MPa	200

5. Results

The CP analyses are usually done for a representative volume element (RVE) of a polycrystalline material in a cubic shape. Each grain in the RVE is considered as independent of other grains. The grain microstructure of the RVE might be represented by voxels with stair-stepped grain boundaries or using the smooth topology with a smooth flat grain boundaries (Fig. 4).
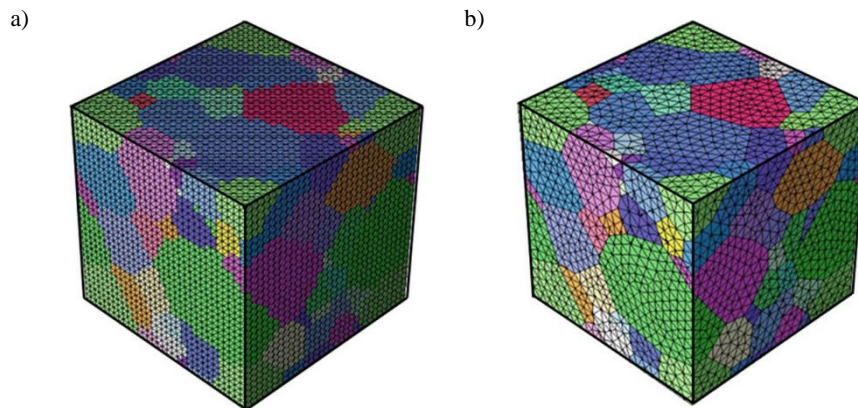
Fig. 4. The microstructure using a) the voxels and b) grains with a smooth topology

Some benchmark tests were conducted with NEPER and FEPX programs using the CP theory. In order to estimate the computation time, the non-isotropic polycrystalline sample of rectangular shape of dimensions 1 x 1 x 5 mm is subject to the tension with the strain rate $\dot{\varepsilon} = 0.02 \left[\frac{1}{s}\right]$. The material is modelled as an aggregate of 200 single crystals with crystals random orientations defined by the Euler angles (Fig. 5). The grain size was in the range of 50-200 μm. Each grain is discretized by several tetrahedral elements (Fig. 6). All elements in the single grain have the same crystal orientations.
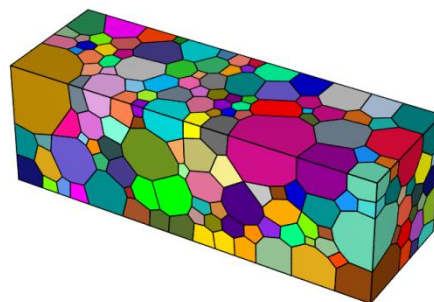
Fig. 5. The microstructure of a rectangular sample with 200 randomly orientated grains
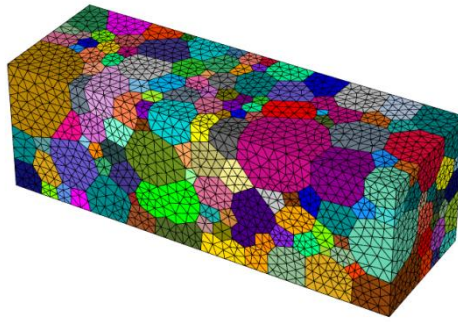
Fig. 6. FEM mesh for a rectangular sample with 200 grains

The σ_{zz} stress distribution acting on the loading direction is shown in Fig. 7. Heterogeneous distribution of stress inside the sample is noted, which is the result of grains anisotropy. The higher stress values in the range of 350-400 MPa are observed on the left and right faces. The heterogeneous stress distribution in the range of 50-200 MPa in the middle of a sample is also noted.
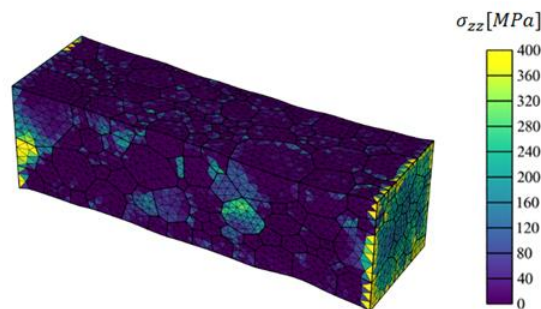
Fig. 7. Distribution of longitudinal σ_{zz} stress for a rectangular 200 grains sample

The distribution of strain in longitudinal direction ε_{zz} is presented in Fig. 8. The strain is mostly up to 0.006 and its distribution is heterogeneous. Some of grains show higher strains than others, which is associated with the anisotropy of the material.
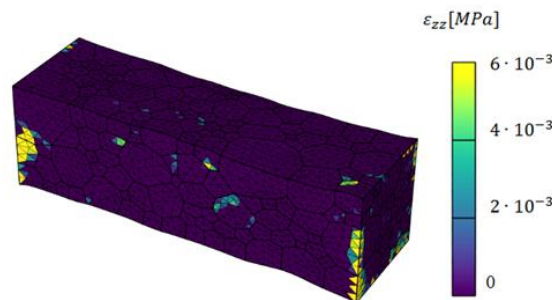
Fig. 8. Distribution of longitudinal strain ε_{zz} for a rectangular 200 grains sample

The microscopic analysis presented here allows predicting the macroscopic response of material. The macroscopic stress-stain curve for the tension test of rectangular sample with 200 grains was computed using the homogenization procedure (Fig. 9). The homogenized stress is computed as the total tensile force related to the actual cross-section (calculated with the assumption of the volume conservation).

In the second test a paddy shape sample with overall dimensions of 1.0 x 0.2 x 4.0 mm was subject to the tension load. The sample consists of 400 or 800 grains with random crystal orientations generated in the tessellation process (Fig. 10). The global coordinate system, material data, as well as, the boundary conditions are the same as in the previous test.
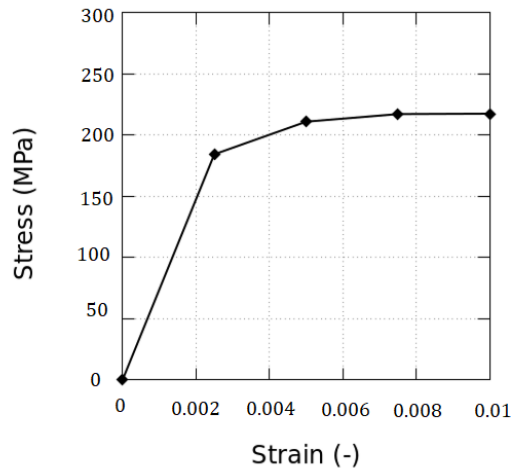
Fig. 9. Macroscopic stress-strain curve obtained with the use of the homogenization process
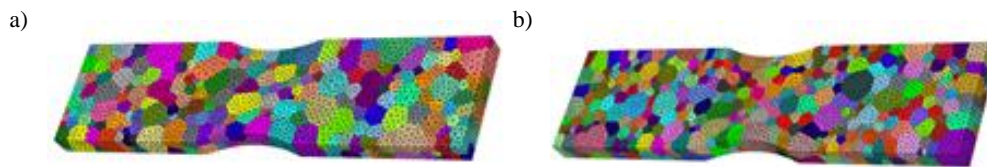
Fig. 10. The microstructure of a paddy-like shape; a) 400 and b) 800 grains

The effective stress and equivalent plastic strain distributions for the sample with 800 grains are presented in Fig. 11 and 12. The localization of strain near to the notch is noted. For both samples with different number of grains, shearing bands can be noted (contours sloped at 45˚ angle). The pole figures before and after the tensile load are presented in Fig. 13.
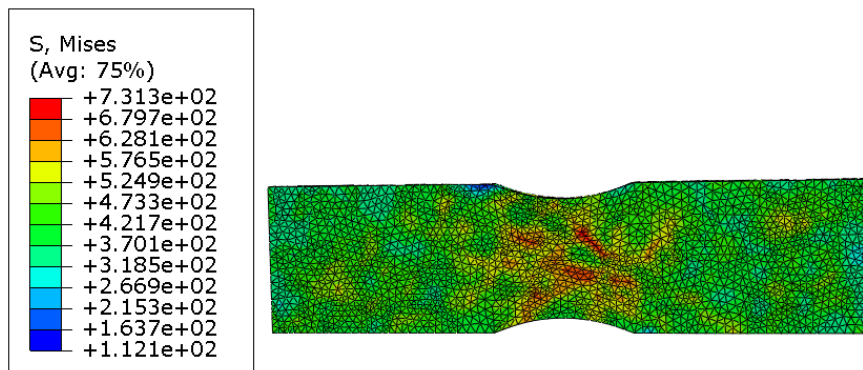
Fig. 11. The HMH (von Mises) stress distribution
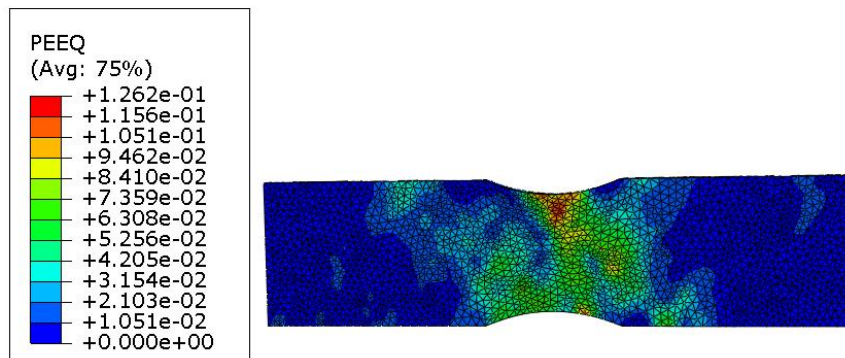
Fig. 12. The equivalent plastic strain (PEEQ) distribution
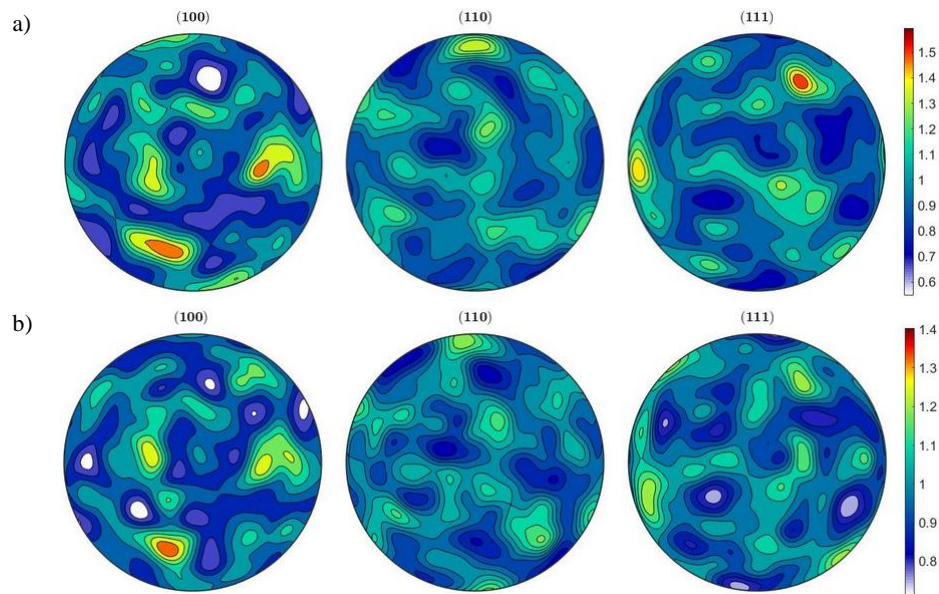
Fig. 13. Pole figures showing the microstructure of a copper alloy; a) before and b) after a tensile loading test

In the last test a flat plate with two holes fixed at one end is considered. The prescribed displacement is placed to the second end of this plate. The FE mesh consists of 1700 hexahedral elements (Fig. 14). The calculations are done as a static analysis for an isotropic material – all crystals have the same orientation. Using UMAT user material procedure developed for small displacements analysis, one can get stress and strain states, as well as, the velocity and deformation gradients, rotation tensors, etc.
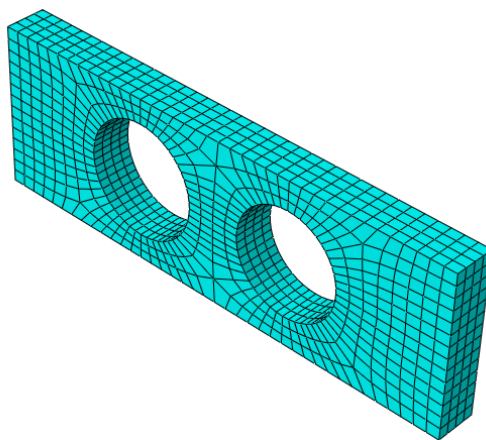
Fig. 14. The FEM mesh for plate with two holes example

The selected macroscopic results – the distribution of effective stress and the equivalent plastic strain are shown in Fig. 15. Because of the isotropic response of polycrystalline structure resulting from uniform crystal orientation, macroscopic stress and strain are coincident with the solution obtained within classical plasticity.
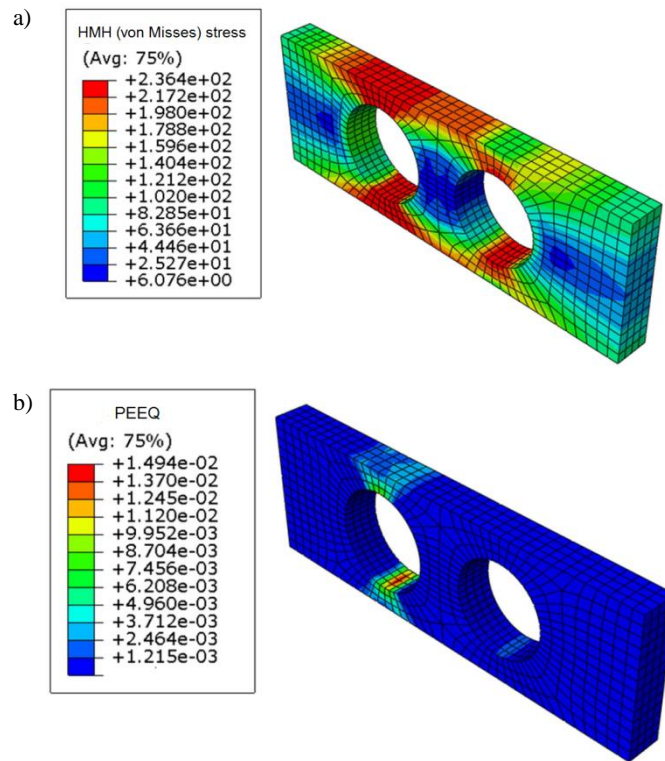
Fig. 15. The distribution of a) HMH (von Misses) stress and b) equivalent plastic strain in a plate with two holes

6. Discussion

Numerical tests presented in this paper show the potential of using crystal plasticity approach in solving elastic-plastic engineering problems. In this two-scale approach the macroscopic stress and strain are computed considering the dislocation slip as the source of the plastic deformation (Fig. 16).
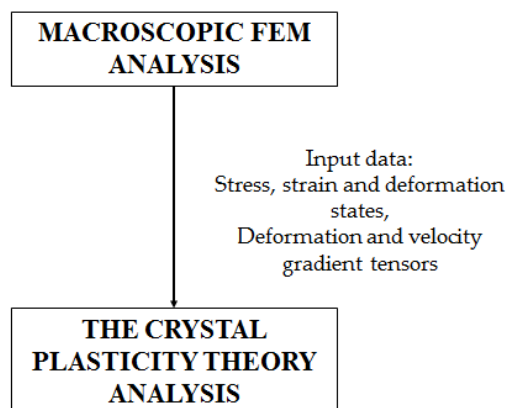
Fig. 16. The idea of the combined micro- and macromechanical analysis

The numerical CPFEM analysis is a complex and time-consuming. The following initial data are necessary for the microscopic analysis using the CPFEM model:
1) The elastic moduli of a material C_{ij}.
2) Number of potentially activated slip systems.
3) Initial crystallographic orientation in the sample coordinate system.
4) Shear strain rate which depends on the resolved shear stress.
5) Modulus of hardening.
6) Parameters for the iteration method.

The following steps of a combined micro- and macromechanical approach are used here:

1) Firstly, the orientation and slip systems are defined.
2) At the starting time of the increment, the information about stress, strain, rotation, time increment and solution dependent variable are necessary.
3) On the basis of the input parameters, the active slip systems and spin tensor are calculated.
4) After that, the slip normal and directions are determined.
5) The Jacobian matrix and other state variables are computed.
6) All the state variables and stress are updated at the end of the load increment.

The data obtained in numerical analyses using the CP theory shows anisotropic response of material under loading. Due to various orientation of crystals in polycrystalline materials the heterogeneous distribution of stress and strain is noted.

It is worth highlighting, that the user material subroutine UMAT used here should consider the rotation of the coordinate system. For this reason, the constitutive equations are written in the corotational frame. As a result of this objective stress rates should be used, namely Jaumann ($\boldsymbol{\sigma}^{\nabla J}$) and Green-Naghdi ($\boldsymbol{\sigma}^{\nabla G}$) stress (Eq. 39-40) (Okereke & Keates, 2018; Perez, 2017).

$$\boldsymbol{\sigma}^{\nabla J} = \dot{\boldsymbol{\sigma}} + \boldsymbol{\sigma}\boldsymbol{W} - \boldsymbol{W}\boldsymbol{\sigma} \tag{39}$$

$$\boldsymbol{\sigma}^{\nabla G} = \dot{\boldsymbol{\sigma}} + \boldsymbol{\sigma}\boldsymbol{\Omega} - \boldsymbol{\Omega}\boldsymbol{\sigma} \tag{40}$$

where: $\dot{\boldsymbol{\sigma}}$ is stress rate tensor in a corotational frame, $\boldsymbol{\sigma}$ is Cauchy stress tensor, $\boldsymbol{W}$ is spin tensor which comprises both the deformation and the rotation and $\boldsymbol{\Omega}$ is the angular velocity tensor resulting from a rigid body rotation. The parts $\boldsymbol{\sigma}\boldsymbol{W}$ and $\boldsymbol{W}\boldsymbol{\sigma}$ are associated with the rigid body rotation and the $\dot{\boldsymbol{\sigma}}$ term is associated with the material deformation (Wójcik & Skrzat, 2022c).

In ABAQUS program, the Jaumann stress rate is used for materials commercially implemented and for a user material subroutine. However, application of the Green-Naghdi stress rate can change the material response, especially for large shearing associated with the large rotations. It is possible to enforce using Green-Naghdi objective stress rate by adding two terms shown in Eq. 41.

$$\boldsymbol{\sigma}^{\nabla G} = \boldsymbol{\sigma}^{\nabla J} - \boldsymbol{\sigma}(\boldsymbol{W} - \boldsymbol{\Omega}) + (\boldsymbol{W} - \boldsymbol{\Omega})\boldsymbol{\sigma} \tag{41}$$

The rate-independent crystal plasticity approach based on dislocation slip as the only plastic response was used so far. In the further research the other models, e.g. viscoplastic ones will be considered and implemented in user material procedures. Further works will also focus on developing the VUMAT user material procedure for dynamic analyses. Other mechanisms of plastic deformations, e.g. the twinning phenomena will be also considered.

7. Summary and conclusions

The possibility of the use of a crystal plasticity (CP) theory to solve elastic-plastic problems is presented in this paper. The numerical calculations using the CP approach based on the Anand and Kothari model was done. The selected macro- and micro- scales software were applied here. The stress and plastic strain distributions within grains in the polycrystalline material were analyzed here. On the basis of results obtained, the main conclusions are as follows:

1) The CP theory gives the better interpretations of phenomena occurring in materials which are deformed plastically, especially in materials forming processes, e.g. SPD processes.
2) The numerical calculations on the microscale level are associated with the writing of a user material procedure which is a very time-consuming and difficult task.
3) The heterogeneous distribution of stress and strain in the polycrystalline material was noted which is a result of different orientation of crystals within grains. Some grains have higher stress and strain values than others, therefore.
4) In order to verify the correctness of the user material procedure written and results obtained, additional tests are necessary, e.g. shearing tests, equal channel angular processing (ECAP), extrusion test, etc.

Acknowledgments

References

Abdolvand, H., Daymond, M.R., & Mareau, C. (2011). Incorporation of twinning into a crystal plasticity finite element model: Evolution of lattice strains and texture in Zircaloy-2. *Int. J. Plast.*, *27,* 1721-1738. https://doi.org/10.1016/j.ijplas.2011.04.005

Acar, P., Ramazani, A., & Sundararaghavan, V. (2017). Crystal Plasticity Modeling and Experimental Validation with an Orientation Distribution Function for Ti-7Al Alloy. *Metals*, *7,* 459. https://doi.org/10.3390/met7110459

Alankar, A., Eisenlohr, P., & Raabe, D. (2011). A dislocation density-based crystal plasticity constitutive model for prismatic slip in α-titanium. *Acta Mater.*, *59*, 7003-7009. https://doi.org/10.1016/j.actamat.2011.07.053

Anand, L., & Kothari, M. (1996). A computational procedure for rate-independent crystal plasticity. *J. Mech. Phys. Solids*, *44,* 525-588. https://doi.org/10.1016/0022-5096(96)00001-4

Asaro, R.J., & Needleman, A. (1985). Texture development and strain hardening in rate dependent polycrystals. *Acta Metall.*, *33*, 923-953. https://doi.org/10.1016/0001-6160(85)90188-9

Balasubramanian, S., & Anand, L. (2002). Elasto-viscoplastic constitutive equations for polycrystalline fcc materials at low homologous temperatures. *J. Mech. Phys. Solids, 50(1),* 101-126. https://doi.org/10.1016/S0022-5096(01)00022-9

Bridier, F., McDowell, D.L., Villechaise, P., & Mendez, J. (2009). Crystal plasticity modeling of slip activity in Ti–6Al–4V under high cycle fatigue loading. *Int. J. Plast.*, *25,* 1066-1082. https://doi.org/10.1016/j.ijplas.2008.08.004

Buljak, V., Baivier-Romero, S., & Kallel, A. (2021). Calibration of Drucker–Prager Cap Constitutive Model for Ceramic Powder Compaction through Inverse Analysis. *Materials, 14,* 4044. https://doi.org/10.3390/ma14144044

Chen, X., Jiao, R., & Kim, K.S. (2005). On the Ohno–Wang kinematic hardening rules for multiaxial ratcheting modeling of medium carbon steel. *Int. J. Plast.*, *21,* 161-184. https://doi.org/10.1016/j.ijplas.2004.05.005

Dabiri, M., Lindroos, M., Andersson, T., Afkhami, S., Laukkanen, A., & Björk, T. (2018). Utilizing the theory of critical distances in conjunction with crystal plasticity for low-cycle notch fatigue analysis of S960 MC high-strength steel. *Int. J. Fatigue*, *117*, 257-273. https://doi.org/10.1016/j.ijfatigue.2018.07.042

Deng, G. (2014). Crystal plasticity finite element method simulation of equal channel angular pressing. University of Wollongong Press.

Faul, U. (2021). Dislocation structure of deformed olivine single crystals from conventional EBSD maps. *Phys Chem Minerals*, *48*, 35. https://doi.org/10.1007/s00269-021-01157-3

FEPX: Finite Element Polycrystal Plasticity (2008). https://fepx.info

Frydrych, K., & Kowalczyk-Gajewska, K. (2016). A three-scale crystal plasticity model accounting for grain refinement in fcc metals subjected to severe plastic deformations. *Mater. Sci. Eng. A*, *658*, 490-502. https://doi.org/10.1016/j.msea.2016.01.101

Genna, F. (1993). Integration of plasticity equations for the case of Ziegler's kinematic hardening. *Comput. Methods Appl. Mech. Eng.*, *109,* 111-130. https://doi.org/10.1016/0045-7825(93)90227-O

Ibragimova, O., Brahme, A., Muhammad, W., Lévesque, J., & Inal, K. (2021). A new ANN based crystal plasticity model for FCC materials and its application to non-monotonic strain paths. *Int. J. Plast.*, 144, 103059. https://doi.org/10.1016/j.ijplas.2021.103059

Jeong, J., & Voyiadjis, G.Z. (2022). A physic-based crystal plasticity model for the prediction of the dislocation densities in micropillar compression. *J. Mech. Phys. Solids.*, 167, 105006. https://doi.org/10.1016/j.jmps.2022.105006

Khan, R., & Alfozan, A. (2019). Modeling of twinning-induced plasticity using crystal plasticity and thermodynamic framework. *Acta Mech., 230*, 2687-2715. https://doi.org/10.1007/s00707-019-02419-6

Khan, R., Pervez, T., Alfozan, A., Qamar, S.Z., & Mohsin, S. (2022). Numerical Modeling and Simulations of Twinning-Induced Plasticity Using Crystal Plasticity Finite Element Method. *Crystals*, *12*, 930. https://doi.org/10.3390/cryst12070930

Khan, R., Zahedi, F.I., & Siddiqui, A.K. (2016). Numerical Modeling of Twinning Induced Plasticity in Austenite Based Advanced High Strength Steels. *Procedia Manuf.*, *5*, 772-786. https://doi.org/10.1016/j.promfg.2016.08.063

Li, C., Cao, F., Chen, Y., Wang, H., & Dai, L. (2022). Crystal Plasticity Model Analysis of the Effect of Short-Range Order on Strength-Plasticity of Medium Entropy Alloys. *Metals*, *12*, 1757. https://doi.org/10.3390/met12101757

Li, H., Larsson, F., Colliander, M.H., & Ekh, M. (2021). Elastic-viscoplastic self-consistent modeling for finite deformation of polycrystalline materials. *Mater Sci Eng. A.*, *799*, 140325. https://doi.org/10.1016/j.msea.2020.140325

Li, Y.L., Kohar, C.P., Mishra, R.K., & Inal, K. (2020). A new crystal plasticity constitutive model for simulating precipitation-hardenable aluminum alloys. *Int. J. Plast.*, 132, 102759. https://doi.org/10.1016/j.ijplas.2020.102759

Liu, G., Mo, H., Wang, J., & Shen, Y. (2021). Coupled crystal plasticity finite element-phase field model with kinetics-controlled twinning mechanism for hexagonal metals. *Acta Mater.*, *202*, 399-416. https://doi.org/10.1016/j.actamat.2020.11.002

Men, M., & Meng, B. (2022). Crystal Plasticity Simulation of Yield Loci Evolution of SUS304 Foil. *Materials*, *15*, 1140. https://doi.org/10.3390/ma15031140

Messner, M.C., Rhee, M., Arsenlis, A., & Barton, N.R. (2017). A crystal plasticity model for slip in hexagonal close packed metals based on discrete dislocation simulations. *Modelling Simul. Mater. Sci. Eng., 25,* 044001. https://doi.org/10.1088/1361-651X/aa687a

Mlikota, M., & Schmauder, S. (2018). On the Critical Resolved Shear Stress and Its Importance in the Fatigue Performance of Steels and Other Metals with Different Crystallographic Structures. *Metals*, *8,* 883. https://doi.org/10.3390/met8110883

Nguyen, K., Zhang, M., Amores, V.J., Sanz, M.A., & Montáns, F.J. (2021). Computational Modeling of Dislocation Slip Mechanisms in Crystal Plasticity: A Short Review. *Crystals*, *11*, 42. https://doi.org/10.3390/cryst11010042

Nibur, K.A., & Bahr, D.F. (2003). Identifying slip systems around indentations in FCC metals. *Comput. Mater. Sci.*, *49*, 1055-1060. https://doi.org/10.1016/j.scriptamat.2003.08.021

Okereke, M., & Keates, S. (2018). Finite Element Applications. A Practical Guide to the FEM Process. Springer.

Paudel, Y., Giri, D., Priddy, M.W., Barrett, C.D., Inal, K., Tschopp, M.A., Rhee, H., & El Kadiri, H. (2021). A Review on Capturing Twin Nucleation in Crystal Plasticity for Hexagonal Metals. *Metals*, *11*, 1373. https://doi.org/10.3390/met11091373

Perez, N. (2017). Theory of Elasticity. Springer.

Pramanik, S., Tasche, L., Hoyer, K.P., & Schaper, M. (2021). Correlation between Taylor Model Prediction and Transmission Electron Microscopy-Based Microstructural Investigations of *Quasi*-In Situ Tensile Deformation of Additively Manufactured FeCo Alloy. *J. Mater. Eng. Perform.*, *30,* 8048–8056. https://doi.org/10.1007/s11665-021-06065-9

Ramos, P.M., Herranz, M., Foteinopoulou, K., Karayiannis, N.Ch., & Laso, M. (2020). Identification of Local Structure in 2-D and 3-D Atomic Systems through Crystallographic Analysis. *Crystals*, *10*, 1008. https://doi.org/10.3390/cryst10111008

Remache, D., Semaan, M., Rossi, J.M., Pithioux, M., & Milan, J.L. (2020). Application of the Johnson-Cook plasticity model in the finite element simulations of the nanoindentation of the cortical bone. *J. Mech. Behav. Biomed. Mater.*, *101,* 103426. https://doi.org/10.1016/j.jmbbm.2019.103426

Romanova, V., Balokhonov, R., Zinovieva, O., Lychagin, D., Emelianova, E., & Dymnich, E. (2022). Mechanical Aspects of Nonhomogeneous Deformation of Aluminum Single Crystals under Compression along [100] and [110] Directions. *Metals*, *12*, 397. https://doi.org/10.3390/met12030397

Ryś, M., Stupkiewicz, S., & Petryk, H. (2022). Micropolar regularization of crystal plasticity with the gradient-enhanced incremental hardening law. *Int. J. Plast.*, *156,* 103355. https://doi.org/10.1016/j.ijplas.2022.103355

Sajjad, H.M., Hanke, S., Güler, S., ul Hassan, H., Fischer, A., & Hartmaier, A. (2019). Modelling Cyclic Behaviour of Martensitic Steel with J2 Plasticity and Crystal Plasticity. *Materials*, *12,* 1767. https://doi.org/10.3390/ma12111767

Schäfer, B.J., Song, X., Sonnweber-Ribic, P., ul Hassan, H., & Hartmaier, A. (2019). Micromechanical Modelling of the Cyclic Deformation Behavior of Martensitic SAE 4150—A Comparison of Different Kinematic Hardening Models. *Metals*, *9*, 368. https://doi.org/10.3390/met9030368

Sundararaghavan, V., & Zabaras, N. (2008). A multi-length scale sensitivity analysis for the control of texture-dependent properties in deformation processing. *Int. J. Plast.*, *24*, 1581–1605. https://doi.org/10.1016/j.ijplas.2007.12.005

Weinberger, C.R., Boyce, B.L., & Battaile, C.C. (2013). Slip planes in bcc transition metals. *Int. Mater. Rev., 58*, 296-314. https://doi.org/10.1179/1743280412Y.0000000015

Wójcik, M., & Skrzat, A. (2020). Fuzzy logic enhancement of material hardening parameters obtained from tension–compression test. *Continuum Mech. Thermodyn.*, *32,* 959-969. https://doi.org/10.1007/s00161-019-00805-y

Wójcik, M., & Skrzat, A. (2021). The Coupled Eulerian-Lagrangian Analysis of the KOBO Extrusion Process. *ASTRJ*, *15,* 197-208. https://doi.org/10.12913/22998624/131663

Wójcik, M., & Skrzat, A. (2022a). An Elastic-Plastic Analysis of Polycrystalline Structure Using Crystal Plasticity Modelling – Theory and Benchmark Tests. *ASTRJ*, *16*, 163-177. https://doi.org/10.12913/22998624/154025

Wójcik, M., & Skrzat, A. (2022b). Coupled Thermomechanical Eulerian-Lagrangian Analysis of the KOBO Extrusion Process. *Arch. Metall. Mater.*, *67,* 1185-1193. https://doi.org/10.24425/amm.2022.139719

Wójcik, M., & Skrzat, A. (2022c). Numerical modelling of the KOBO extrusion process using the Bodner–Partom material model. *Meccanica*, *57,* 2213–2230. https://doi.org/10.1007/s11012-022-01569-7

Yaghoobi, M., Ganesan, G., Sundar, S., Lakshmanam, A., Rudraraju, S., Allison, J.E., & Sundararaghavan, V. (2019). PRISMS-Plasticity: An open-source crystal plasticity finite element software. *Comput. Mater. Sci.*, *169*, 109078. https://doi.org/10.1016/j.commatsci.2019.109078

Yang, G., & Park, S.-J. (2003). Deformation of Single Crystals, Polycrystalline Materials, and Thin Films: A Review. *Materials*, *12,* 2003. https://doi.org/10.3390/ma12122003

Yang, G., Dayong, A., Fengbo, H., Liu, X., Guozheng, K., & Xu, Z. (2022). Multiple-mechanism and microstructure-based crystal plasticity modeling for cyclic shear deformation of TRIP steel. *Int. J. Mech. Sci.*, 222, 107269. https://doi.org/10.1016/j.ijmecsci.2022.107269

Sprężysto-plastyczne Analizy Numeryczne Niezależne od Prędkości Odkształcenia dla Materiałów Polikrystalicznych z Zastosowaniem Teorii Plastyczności Kryształów

Streszczenie

Analizy makroskopowe procesów przeróbki plastycznej prezentują jedynie ogólny zarys rozważanego problemu, bez uwzględnienia mechanizmów odkształcenia plastycznego oraz ewolucji mikrostruktury. W celu rozważania procesów przeróbki plastycznej stosowane są symulacje numeryczne w ramach teorii plastyczności kryształów uwzgledniające zmianę tekstury, anizotropię oraz umocnienie odkształceniowe. W artykule zaprezentowano zastosowanie modelu Ananda i Kothari w ramach teorii plastyczności kryształów niezależnej od prędkości odkształcenia do rozwiązywania analiz numerycznych dla materiałów polikrystalicznych. W badaniach uwzględniono poślizg dyslokacyjny jako główny mechanizm odkształcenia plastycznego. Zaprezentowano wybrane rezultaty dla problemów sprężysto-plastycznych uzyskane zarówno w skali makro, jak i mikro- dla całkowania typu *explicit* i *implicit*. Uzyskano niejednorodny rozkład naprężenia i odkształcenia w poszczególnych ziarnach, związany z różną orientacją kryształów. Modelowanie numeryczne z zastosowaniem teorii plastyczności kryształów dla materiałów poddanych plastycznemu odkształceniu dostarcza nie tylko informacje o zmianie kształtu materiału w skali makro, ale także opisuje zjawiska zachodzące w materiale w skali mikro-.

Słowa kluczowe: plastyczność kryształów, materiał polikrystaliczny, odkształcenie plastyczne, CPFEM, poślizg dyslokacyjny

Original Research

The Formation of Al-Si Aluminide Coatings by Pack Cementation Method on TNM-B1 Intermetallic Alloy

Mateusz Woźniak [1], Marek Góral [2,]* ID, Barbara Kościelniak [2] ID

[1] Doctoral School of Engineering and Technical Sciences at the Rzeszow University of Technology, Rzeszow University of Technology, Powstancow Warszawy 12, Rzeszow, 35-959, Poland

[2] Rzeszow University of Technology, Research and Development Laboratory for Aerospace Materials, Zwirki i Wigury 4, 35-959 Rzeszow, Poland

* Correspondence: mgoral@prz.edu.pl

Abstract

The TiAl intermetallics are the promising material for aerospace application. According to its insufficient oxidation resistance above 900oC the using of protective coatings is necessary. The diffusion aluminide coatings based on TiAl2 or TiAl$_3$ phases permits to formation of alumina scale on the surface of TiAl alloys. The pack cementation with Si doping is one of the most popular methods of this type of coatings production. In present article the influence of Si content in the pack, process time and temperature during pack cementation process were investigated. The thickness of obtained coating was in range 20-50 μm. When Si content was higher the formation of titanium silicide's was observed using almost all analysed values of process parameters. The results showed that using of 24 wt. % Si containing pack and process parameters: 4h/950ºC enables to obtain the coating characterized by optimal thickness and structure. The porosity and cracks in coatings according to TiAl phases brittleness was observed.

Keywords: pack cementation, TiAl, aluminide coatings, Al-Si coatings, oxidation

1. Introduction

The Ti-Al system includes intermetallic phases, which are characterized by high operating temperature (up to 800˚C), good oxidation resistance, high plasticity, high Young's modulus and low weight. Due to such properties of the intermetallics, they might be used in aerospace and automotive applications (Goral et al., 2007; Rubucha et al., 2022; Wu et al., 2006; Novak et al., 2009). For increase the operating temperature and oxidation resistance of the TiAl alloy, it is possible to introduce alloying elements into the base material by diffusion treatment (Jiang et al., 2008). The main elements modifying the surface layer of the Ti-Al intermetallics are: Si (Musi et al., 2022), Nb (Jiang et al., 2002), W (Wendler & Kaczmarek, 2005) or Mo (Chlupová et al., 2020). Above a temperature of 800˚C, the material begins to oxidize quickly, which leads to a reduction in mechanical properties. Mainly titanium and aluminium oxides mixture, are formed on the surface of TiAl alloy. Additionally, nitride oxides TiN / Ti$_2$AlN or Ti$_3$AlN might appear at the interface. The oxides of these elements do not protect the TiAl against oxygen, which causes a rapid weight gain (Knaislová, 2021; Locci, 2001; Swadźba et al., 2020a). Many methods and technologies were developed for increasing oxidation resistance of TiAl intermetallics. Wang at al. (2015) showed that a silicon-rich coating significantly inhibits oxygen diffusion into the layer, resulting in better oxidation resistance of the alloy. The silicon protective layer can be obtained by various processes. Goral M. (2011) and Moskal et al. (2009) proposed a slurry diffusion coating and Arc-PVD deposition of Al-Si and formation of Si-rich titanium silicides into aluminide coating (Bauer et al., 2022; Bobzin et al., 2018) investigated the HS-PVD rapid vapor deposition process in which the cathodic discharge (HCD) phenomenon occurs and gas sputtering (GFS), which allows to obtain thick coatings Earlier research shows the effect of silicon on TiAl material. Swadźba et al. (2020b) showed that silicon significantly affects the working time of the ma-

terial at the temperature of 850˚C. The substrate of the material without silicon modification after the oxidation process formed a thick oxide scale, which did not protect the substrate against corrosive gases. By modifying of the TiAl substrate with silicon, a continuous scale was formed, protecting the base material. Jiang et al. (2002) after high-temperature oxidation confirmed that silicon has a positive effect on the substrate. Studies have shown that dense Al_2O_3 is formed inside. Moreover, TiAl alloys produce a Ti_5Si_3 phase. In this phase, after the high-temperature oxidation process, the TiO_2 phase is formed. They used the pack cementation method to introduce silicon by inward diffusion to base material. A coating thickness of up to 30 µm was obtained. The coating consisted of two outer and inner layers. The inner layer contained $TiAl_3$ and the outer layer slilicide (Xiang et al., 2003). It has also been shown that during very long heating, two phases of $TiAl_3$ and $TiAl_2$ are formed. Additionally, silicon can bind titanium and niobium, where the aforementioned Ti_5Si_3 phase is formed on the thin phases of $TiAl_3$ and $TiAl_2$ (Swadźba et al., 2020b).

The pack cementation is the main method of Si-modification of TiAl aluminides (Novák et al., 2009) In present article the kinetics growth of Si-modified aluminide coatings on TNM-B1 alloy was presented.

2. Experimental

The TNM-B1 type intermetallic alloy with composition (wt. %): Al-28.6% Nb-9.2% Mo-2.3% and Ti-bal. was used as a base material. Samples were 10 mm × 20 mm. The samples were cut to rectangular from cylindrical bar. The surface was grinded using waterproof paper to gradation Mesh 500. The sample were put into metallic box and mounted into Ar-protective atmosphere tube furnace (Xerion, Germany). The two types of powder were prepared (wt. %):

- Si-14%, Al-14%, $AlCl_3$-2%, Al_2O_3- bal,
- Si-28% Al-14%, $AlCl_3$-2%, Al_2O_3- bal.

In experimental three values of temperature (900/950/1000ºC) any time (2/4/6h) were used. The duration of the aluminizing process and the temperature were selected from previously published scientific articles. Etching of metallographic samples was carried out in a solution of the following chemical composition: 30 cm^3 $C_3H_6O_3$, 15 cm^3 HNO_3 and 5 cm^3 HF. The process was conducted in Ar flow 0.5 NLPM (Normal litres per minute). The microstructure was analysed using Phenom XL scanning electron microscope equipped with EDS detector used for elemental mapping. The thicknesses of the coatings formed during aluminizing were also measured using a program built into the Phenom XL software. Qualitative phase analysis was performed from the surface of the samples by X-ray diffraction.

3. Results and discussion

3.1. The coating formed from powder containing 14 wt. % of Si

The temperature had strong influence on microstructure of Si aluminide coating formed after 4h of deposition time. In lower temperature (900ºC) the measured coating was about 30 µm (Fig. 1a). Thin (about 2 µm) layer was observed on the interface with base material. In higher temperature (950ºC) thicker (about 35 µm) with presence of small precipitation zone (about 5 µm thick) in the inner zone (Fig. 1b). According to Goral et al. (2007) the columnar titanium silicide grains were formed in $TiAl_3$ matrix. In highest analysed temperature (1000ºC) the coating's thickness decreased to about 20 µm (Fig. 1c) and silicide precipitations were not observed in the structure (Goral et al., 2011). It was connected probably with oxidation of surface layer and non-homogenized powder structure used for experimental.

After 2h of pack aluminizing process conducted at 950ºC the thin columnar inner zone was formed (Fig. 2a). Based on Goral et al. (2011) and Moskal et al. (2009) and elemental mapping (Fig. 2b-e) the titanium silicides in $TiAl_3$ matrix were formed. Extending the process to 6 hours resulted in the formation of a coating devoid of silicon precipitates (Fig. 3a). During aluminizing, oxidation of the coating surface was observed, which resulted in the appearance of titanium nitrides and oxides on the surface. On the elemental mapping (Fig. 3b-e) on the surface, an increased content of these elements was observed on the surface. The crack seen in Fig.1a may be caused by the pressure set too high when the samples were incubated. Further testing was corrected, and a lower pressure was set.

An analysis of a phase composition proved that the $TiAl_3$ phase in a main component of the aluminide coating formed from powder containing 14 wt. % of Si during 4h pack aluminizing (Fig. 4). In addition, a TiN phase was found to be present in the surface layer. The TiN phase may have been formed by oxygen access to the vacuum furnace during the aluminizing process. Phase analysis confirmed the presence of an AlN and Al_2O_3 phase. The Al_2O_3 phase increases oxidation resistance and improves the mechanical properties of the surface layer (Lu et al., 2020). Zhao et al. (2023) showed that the addition of Si significantly affects the formation of the Al_2O_3 phase (Yang et al. 2023). The AlN phase can significantly improve corrosion resistance. At 900°C, AlN can be oxidised to Al_2O_3 (Yang et al., 2023).
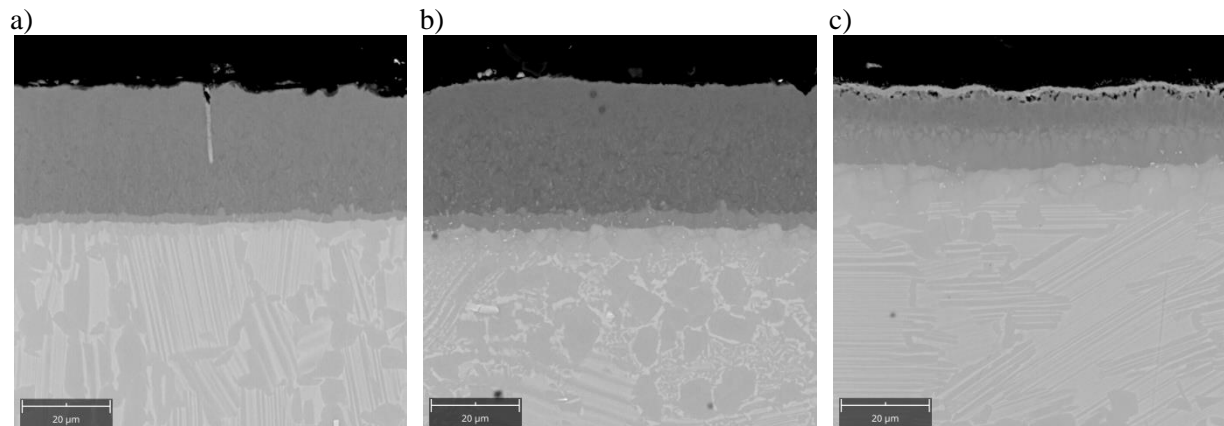
Fig. 1. The microstructure of aluminide coating formed using 14% Si containing pack at 900 (a), 950 (b) and 1000°C (c) during 4h diffusion process
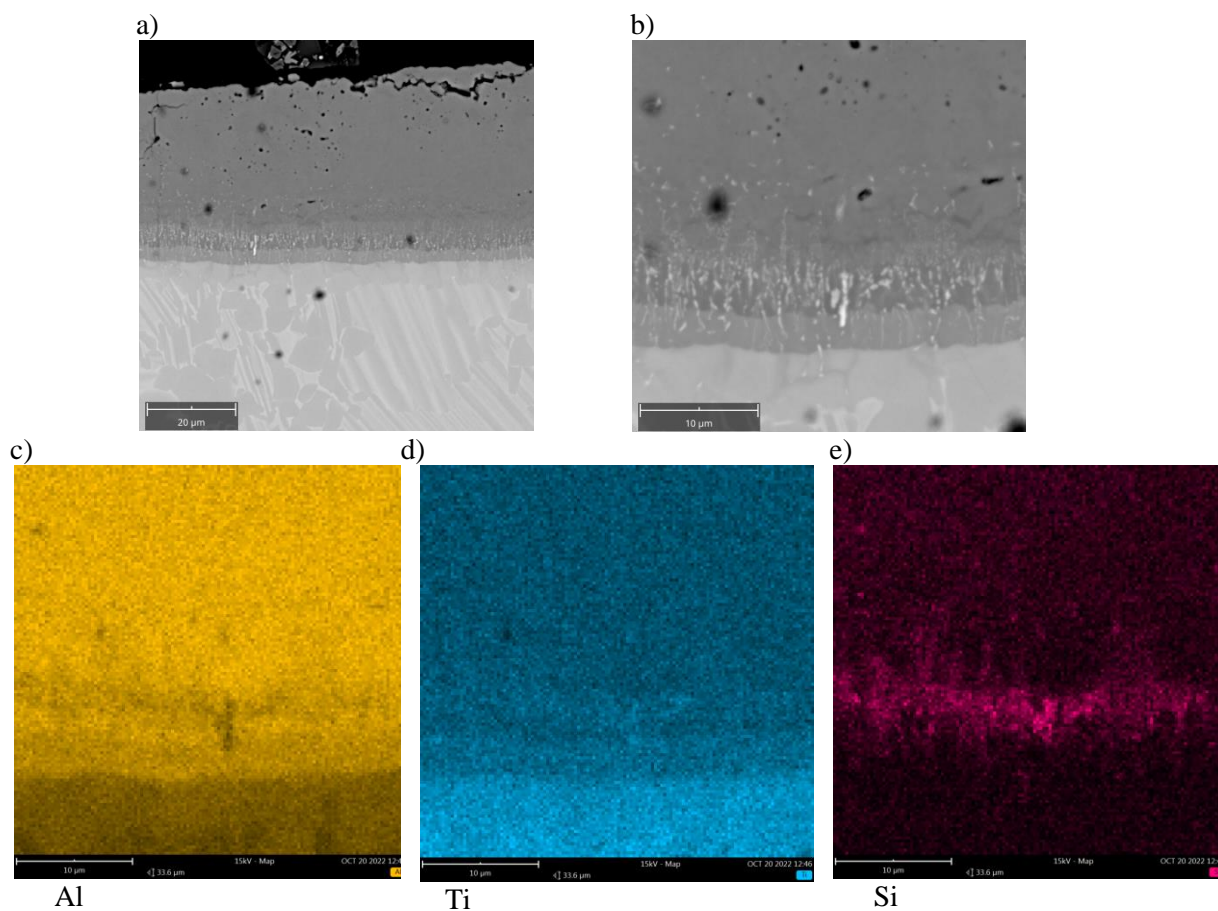
Fig. 2. The microstructure of whole coating (a) and inner zone (b) of aluminide coating formed from powder containing 14 wt. % of Si and elemental mapping of Al (c), Ti (d) and Si (e)
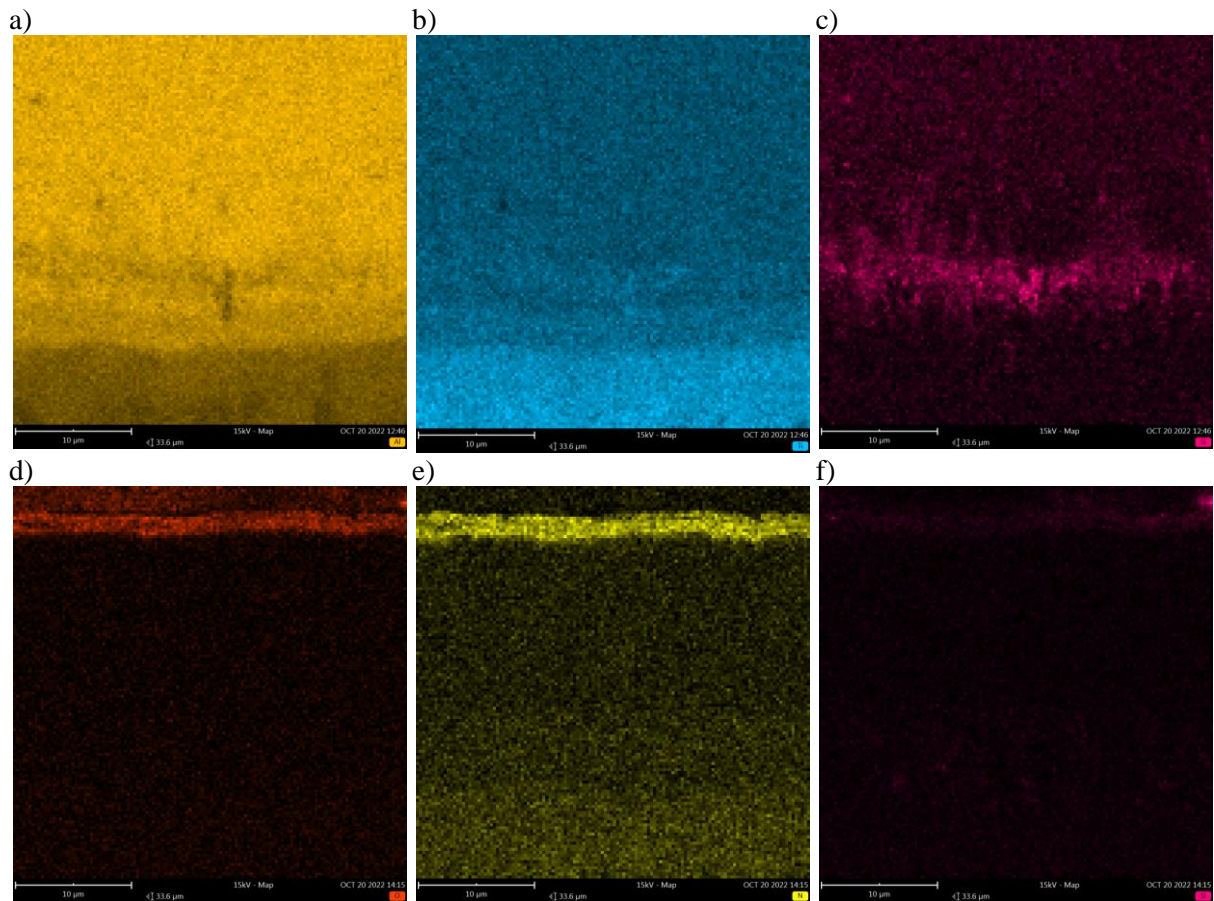
Fig. 3. The microstructure of aluminide coating formed from powder containing 14 wt% of Si (a) and elemental mapping of Al (b)., Ti (c) O (d), N (e) and Si (f)
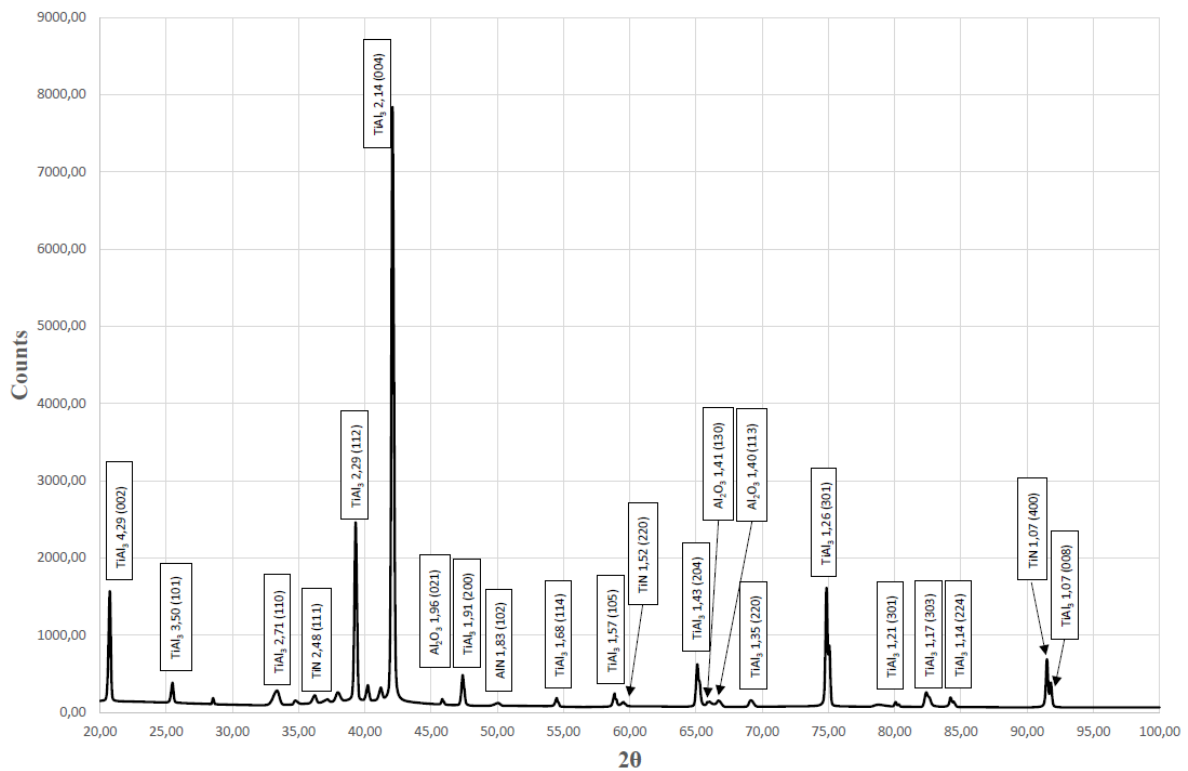
Fig. 4. Results of analysis of phase composition of a sample aluminide coating formed from powder containing 14 wt. % of Si after 4h

3.2. The coating formed from powder containing 28 wt.% of Si

The increase in the silicon content in the powder resulted in the formation of silicide precipitates in all the analysed coatings during pack aluminizing process (Fig. 5a-c). The temperature had a strong influence on coating thickness. In lowest temperature (900°C) the coating thickness did not exceed 30 μm (Fig. 5a). The presence of cracks in the coating is related to the high brittleness of the TiAl$_3$ phase from which it is composed. Increasing the aluminizing temperature to 950°C doubled the thickness of the coating (to over 40 μm, Fig. 5b). The microstructure showed not only cracks but also porosity, which might be caused by the Kirkendall effect. Similar phenomena were observed in the coatings studied by Rubacha et al. (2022). In the coating obtained at the highest temperature (1000°C) of similar thickness, a zone of columnar precipitations of titanium silicides was formed (Goral et al., 2007). Rich precipitates also appeared on the grain boundaries of the TiAl$_3$ phase – elemental mapping Fig. 5c-f. A similar structure was observed in coatings made of suspensions containing from 5 to 20% Si (Goral et al., 2007).
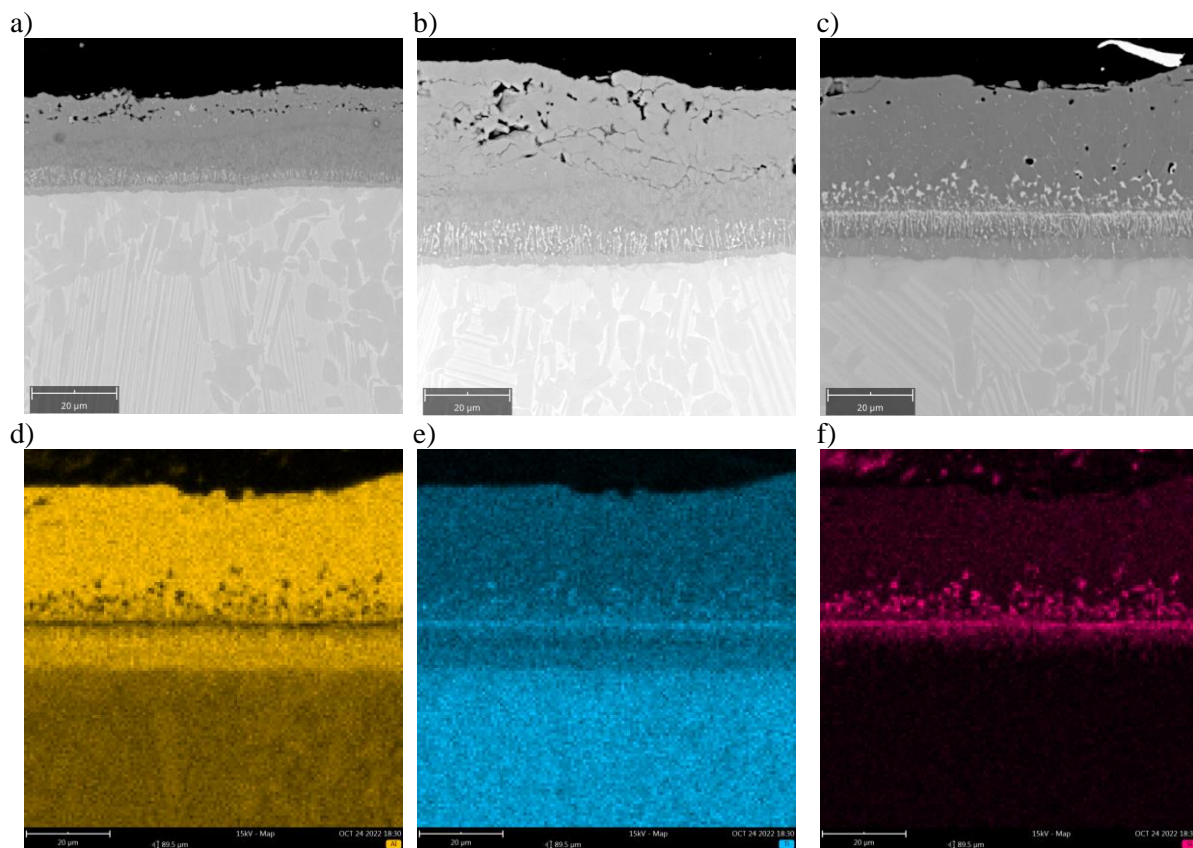
Fig. 5. The microstructure of aluminide coating formed from powder containing 28 wt% of Si at 900 (a)/950(b)/1000h(c) during 4h pack aluminizing and elemental mapping of Al (d), Ti (e) and Si (f) of coating produced at 1000°C

The influence of process time on structure of Si aluminide coating at 950°C was also observed. After 2 hours of pack aluminizing porous outer layer was formed (Fig. 6a). Below the titanium silicides formed on grain boundary of TiAl$_3$ phase and formed columnar layer on coating/base material interface which were visible on elemental mapping (Fig. 6d,e) When pack aluminizing time was extended to 4 hours the increasing of coating thickness above 40 μm was observed (Fig. 6b). In microstructure lower porosity and presence of cracks I inner layer were observed. The precipitations of titanium silicides on grain boundary were not detected probably as a result of their dissolution in TiAl$_3$ phase. In result of long-time pack aluminizing process the very small number of pores were observed (Fig. 6c). Additionally the smaller precipitations in inner zone were replaced the columnar zone formed during 2 and 4 h pack aluminizing process.

An analysis of a phase composition proved that the TiAl$_3$ phase in a main component of the aluminide coating formed from powder containing 28 wt% of Si during 4h pack aluminizing (Fig. 7). The diffractogram is like the X-ray diffraction shown for 14 wt% Si. The main phase present in the TiAl surface layer is TiAl$_3$. The appearance of titanium nitrides is also noted on the surface layer. TiN in the

present study is not the phase of interest. In addition, the formation of $TiSi_2$ and Ti_4O_7 phases was noted.
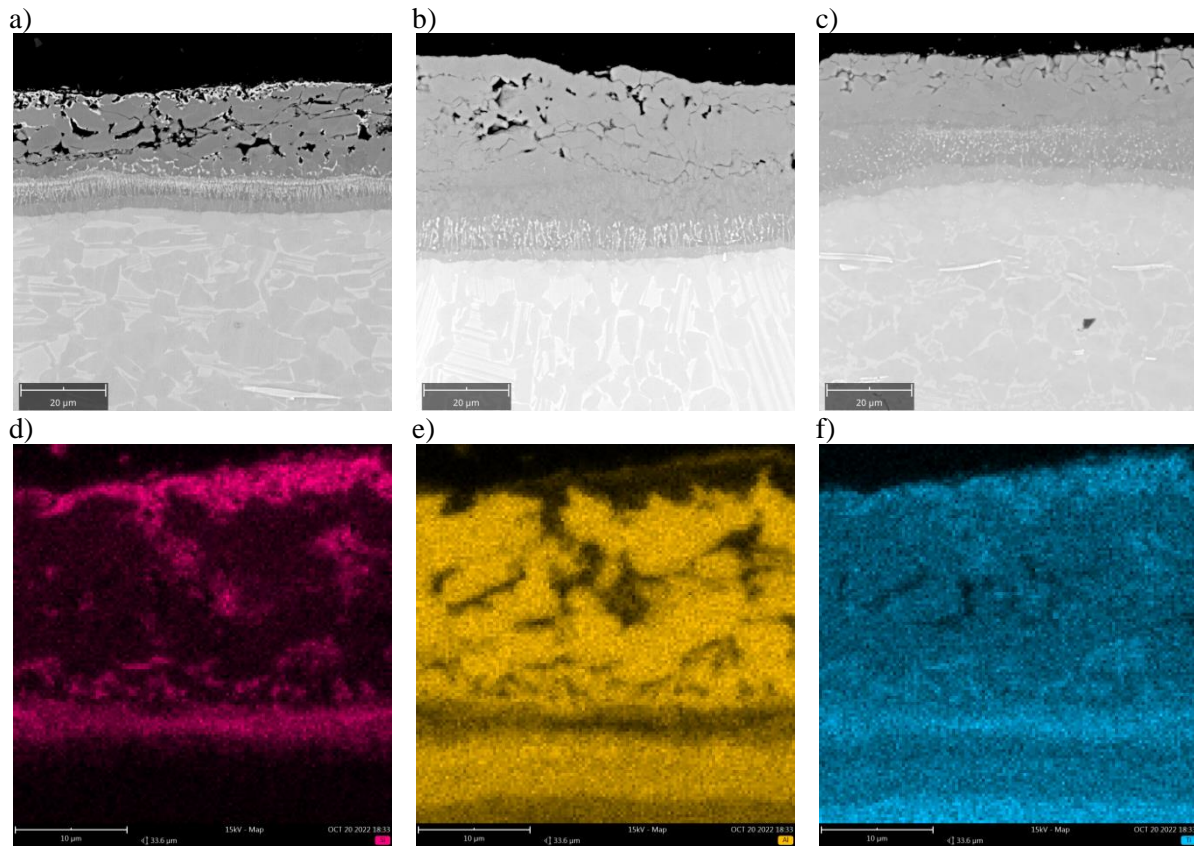
Fig. 6. The microstructure of aluminide coating formed from powder containing 28 wt. % of Si after 2 (a)/4(b)/6h(c) of pack aluminizing and elemental mapping of Al (d), Ti (e) and Si (f) of coating after 2h of the process
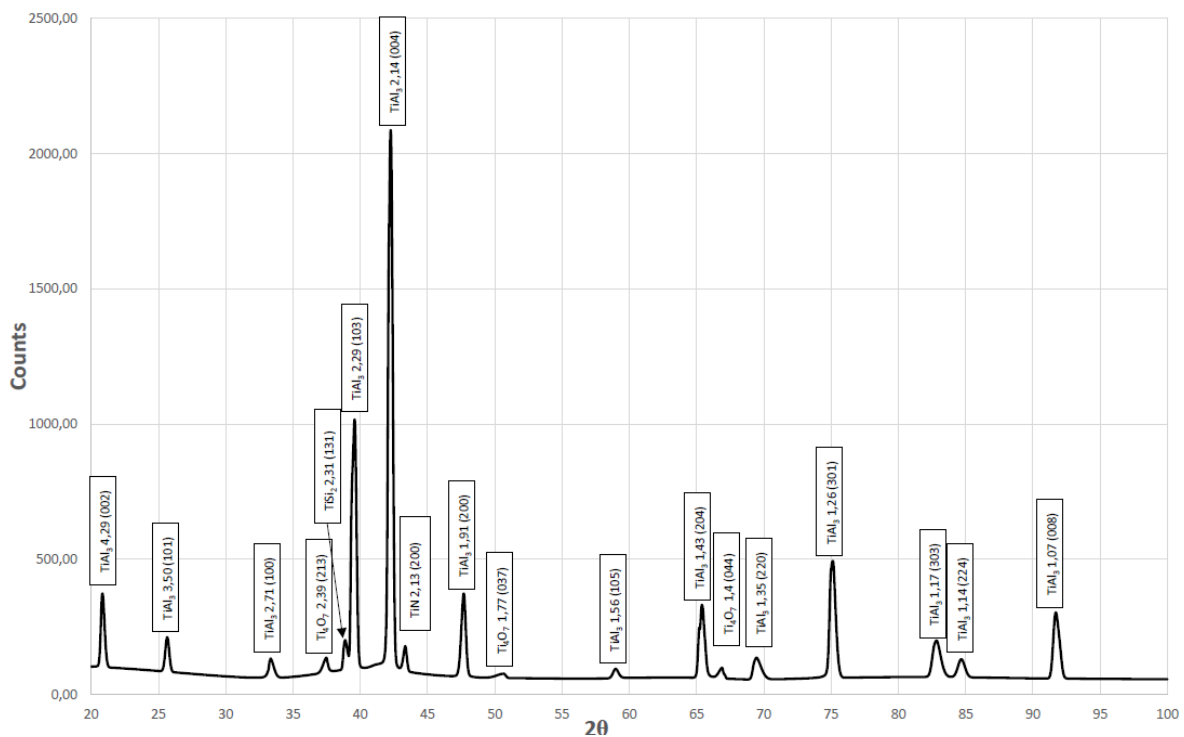
Fig. 7. Results of analysis of phase composition of a sample aluminide coating formed from powder containing 28 wt. % of Si after 4h

4. Conclusions

The conducted research showed large differences in kinetics growth of Si-modified aluminide coatings on TNM-B1 intermetallic alloy. Based on analysis of obtained results some conclusions were formed:

1) The Kirkendall effect with formation of pores was observed after short aluminizing time (2h, 4h using both types of powders).
2) There was no relationship between process time and thickness probably as a consequence of partial oxidation of coating during deposition, thin nitride layer was observed on the surface of selected sample.
3) The structure of coating was similar to formed using slurry method - columnar precipitations of titanium silicides were visible into inner area of coating.
4) The $TiAl_3$ and $TiAl$ phases were the main components of developed coatings.
5) The using of better types of furnaces with inert atmosphere are required for further pack cementation processes.
6) Diffraction analysis showed the formation of $TiSi_2$ titanium silicide and Ti_4O_7 oxide.
7) TiN phase formed by oxidation of the sample in a vacuum furnace.

References

Bauer, P.P., Klamann, L., Swadźba, R., & Laska, N. (2022). Effect of Si Content on Deposition and High Temperature Oxidation of Al-Si Coatings Obtained by Magnetron Sputtering PVD Method. *Coatings*, *12*(6), 859. https://doi.org/10.3390/coatings12060859

Bobzin, K., Brögelmann, T., Kalscheuer, C., & Liang, T. (2018). Al-Si and Al-Si-Y coatings deposited by HS-PVD for the oxidation protection of γ-TiAl. *Surface and Coatings Technology*, *350*, 587–595. https://doi.org/10.1016/j.surfcoat.2018.06.074

Chlupová, A., Heczko, M., Obrtlík, K., Dlouhý, A., Kruml, T. (2020). Effect of heat-treatment on the microstructure and fatigue properties of lamellar γ-TiAl alloyed with Nb, Mo and/or C. *Materials Science and Engineering A*, *786*, 139427. https://doi.org/10.1016/j.msea.2020.139427

Goral, M., Moskal, G., Swadzba, L., & Hetmańczyk, M. (2011). The Influence of Silicon Amount on Structure of Si Modified Aluminide Coating Deposited on Ti46Al7Nb Alloy by Slurry Method. *Key Engineering Materials*, *465*, 251–254. https://doi.org/10.4028/www.scientific.net/KEM.465.251

Goral, M., Moskal, G., Swadzba, L., & Tetsui, T. (2007), Si-modified aluminide coating deposited on TiAlNb alloy by slurry method. *Journal of Achievements in Materials and Manufacturing Processing*, 21(1), 75-78.

Jiang, H., Hirohasi, M., Lu, Y., & Imanari, H. (2002). Effect of Nb on the high temperature oxidation of Ti-(0-50 at.%)Al. *Scripta Materialia*, 46, 639–643. https://doi.org/10.1016/S1359-6462(02)00042-8

Jiang H.-R., Wang Z.-L., Ma W.-S., Feng X.-R., Dong Z.-Q., Liang Z., Yong L. (2008). Effects of Nb and Si on high temperature oxidation of TiAl. Transactions of Nonferrous Metals Society of China, 18(3), 512-517. https://doi.org/10.1016/S1003-6326(08)60090-4

Knaislová, A., Novák, P., Cabibbo, M., Jaworska, L., & Vojtěch, D. (2021). Development of TiAl–Si alloys—a review. *Materials*, *14*(4), 1030. https://doi.org/10.3390/ma14041030

Liu, Z. C., Lin, J. P., Li, S. J., & Chen, G. L. (2002). Effects of Nb and Al on the microstructures and mechanical properties of high Nb containing TiAl base alloys. *Intermetallics*, *10*(7), 653-659. https://doi.org/10.1016/S0966-9795(02)00037-7

Locci, I. E., Brady, M. P., & Smialek, J. L. (2000). Long Term Oxidation of Model and Engineering TiAl Alloys. *MRS Online Proceedings Library*, *646*, 444-449. https://doi.org/10.1557/PROC-646-N5.50.1

Lu, X., Li, J., Chen, X., Qiu, J., Wang, Y., Liu, B., Liu, Y., Rashad, M., & Pan, F. (2020). Mechanical, tribological and electrochemical corrosion properties of in-situ synthesized Al2O3/TiAl composites. *Intermetallics*, *120*, 106758. https://doi.org/10.1016/j.intermet.2020.106758

Moskal, G., Witala, B., & Rozmysłowska, A. (2009). Influence of heat treatment on microstructure of slurry aluminide coatings type TiAlSi obtained on TiAlCrNb alloy. J*ournal of Achievements in Materials and Manufacturing Processing*, *23*(2), 204-210.

Musi, M., Galy, B., Stark, A., Schell, N., Hantcherli, M., Monchoux, J. P., Couret, A., Clemens, H., & Spoerk-Erdely, P. (2022). How Si affects the microstructural evolution and phase transformations of intermetallic γ-TiAl based alloys. *Materialia*, 24, 101475. https://doi.org/10.1016/j.mtla.2022.101475

Novák, P., Michalcová, A., Šerák, J., Vojtěch, D., Fabián, T., Randáková, S., Průša, F., Knotek, V., & Novák, M. (2009). Preparation of Ti-Al-Si alloys by reactive sintering. *Journal of Alloys and Compounds*, 470(1–2), 123–126. https://doi.org/10.1016/j.jallcom.2008.02.046

Rubacha, K., Godlewska, E., Zawadzka, K., & Dąbrowa, J. (2022). Formation of silicide layers on a Ti-46Al-8Ta alloy in pack cementation and diffusion couple experiments. *Surface and Coatings Technology*, 429, 127860. https://doi.org/10.1016/j.surfcoat.2021.127860

Swadźba, R., Marugi, K., Pyclik, Ł. (2020a). STEM investigations of γ-TiAl produced by additive manufacturing after isothermal oxidation. *Corrosion Science*, 169, 108617. https://doi.org/10.1016/j.corsci.2020.108617

Swadźba, R., Swadźba, L., Mendala, B., Bauer, P. P., Laska, N., & Schulz, U. (2020b). Microstructure and cyclic oxidation resistance of Si-aluminide coatings on γ-TiAl at 850 °C. *Surface and Coatings Technology*, *403*, 126361. https://doi.org/10.1016/j.surfcoat.2020.126361

Swadźba, R., Swadźba, L., Mendala, B., Witala, B., Tracz, J., Marugi, K., & Pyclik, Ł. (2017). Characterization of Si-aluminide coating and oxide scale microstructure formed on γ-TiAl alloy during long-term oxidation at 950 °C. *Intermetallics*, *87*, 81–89. https://doi.org/10.1016/j.intermet.2017.04.015

Wang, J, Kong, L., Wu, J., Li, T., Xiong, T. (2015). Microstructure evolution and oxidation resistance of silicon-aluminizing coating on γ-TiAl alloy. Applied Surface Science, 356, 827-836. https://doi.org/10.1016/j.apsusc.2015.08.204

Wendler, B.G., & Kaczmarek, Ł. (2005). Oxidation resistance of nanocrystalline microalloyed γ-TiAl coatings under isothermal conditions and thermal fatigue. *Journal of Materials Processing Technology*, *164–165*, 947–953. https://doi.org/10.1016/j.jmatprotec.2005.02.158

Wu, X. (2006). Review of alloy and process development of TiAl alloys. *Intermetallics*, 14(10–1), 1114–1122. https://doi.org/10.1016/j.intermet.2005.10.019

Xiang, Z. D., Rose, S. R., & Datta, P. K. (2003). Codeposition of Al and Si to form oxidation-resistant coatings on γ-TiAl by the pack cementation process. *Materials Chemistry and Physics*, 80(2), 482–489. https://doi.org/10.1016/S0254-0584(02)00551-5

Yang, L., Gao, F., Zhou, Z., Jia, Y., Du, Y., Wang, J., Qiao, Y., Zhu, S., & Wang, F. (2023). Oxidation behavior of the AlN coatings on the TiAl alloy at 900 °C. *Corrosion Science*, *211*, 110891. https://doi.org/10.1016/j.corsci.2022.110891

Zhao, P. -X., Li, X. -B., Xing, W. -W., Chen, B., Ma, Y. -C., & Liu, K. (2023). Cyclic oxidation behavior of Nb/Mn/Si alloying beta-gamma TiAl alloys. *Transactions of Nonferrous Metals Society of China*, *33*(1), 128-140. https://doi.org/10.1016/S1003-6326(22)66095-3

Tworzenie się Powłok Aluminidkowych Al-Si Uzyskanych Metodą Kontaktowo-Gazową na Podłożu Stopu na Osnowie Fazy Międzymetalicznej Typu TNM-B1

Streszczenie

Fazy międzymetaliczne TiAl są obiecującym materiałem do zastosowań w lotnictwie. Ze względu na niedostateczną odporność na utlenianie powyżej 900°C konieczne jest stosowanie powłok ochronnych. Dyfuzyjne powłoki aluminidkowe na bazie faz $TiAl_2$ lub $TiAl_3$ pozwalają na tworzenie się zgorzeliny tlenku aluminium na powierzchni stopów TiAl. Aluminiowanie metodą kontaktowo gazową z wprowadzaniem Si jest jedną z najpopularniejszych technik wytwarzania tego typu powłok. W niniejszym artykule zbadano wpływ zawartości Si w powłoce w zależności od czasu trwania procesu oraz temperatury. Grubość otrzymanej powłoki zawierała się w przedziale 20-50 μm. Gdy zawartość Si była wyższa, obserwowano powstawanie krzemków tytanu przy prawie wszystkich analizowanych wartościach parametrów procesu. Wyniki pokazały, że użycie proszku zawierającego 24% wag. % Si oraz czasu i temperatury 4h/950°C pozwala na uzyskanie powłoki charakteryzującej się optymalną grubością i strukturą. Zaobserwowano porowatość i spękania powłok.

Słowa kluczowe: metoda kontaktowo-gazowa, TiAl, powłoki aluminidkowe, powłoki Al-Si, utlenianie

Original Research

The Influence of Natural Aging of the AW-2024 Aluminum Sheet on the Course of the Strain Hardening Curve

Stanisław Kut [1] [iD], Grzegorz Pasowicz [2],* [iD]

[1] Department of Materials Forming and Processing, Faculty of Mechanical Engineering and Aeronautics, Rzeszow University of Technology, al. Powst. Warszawy 8, 35-959 Rzeszów, Poland

[2] Doctoral School of the Rzeszow University of Technology, al. Powst. Warszawy 12, 35-959 Rzeszów, Poland

* Correspondence: d546@stud.prz.edu.pl

Abstract

Aluminum sheet drawpieces pressings with the ability to harden precipitation can be shaped from the sheet after annealing or heat treatment. In the second variant during the analysis and design of the technological proces, the change in the material properties of the shaped sheet due to natural aging should be additionaly taken into account. This article presents the results of research on the effect of the natural aging time after heat treatment of AW-2024 sheet material with a thickness of 1 mm on the course of the strain hardening curve. Strain hardening curves were determined on the basis of a uniaxial tensile test. The sheets were tested immediately after heat treatment and during natural aging, i.e. (20, 45, 90 and 120) minutes after heat treatment. The research showed a significant influence of natural aging in the tested range of times after heat treatment on the course of the deformation hardening curve of the sheet material. Based on experimentally determined in particular directions (0, 45 and 90 degrees to the rolling direction) the strain hardening curves, the values of material coefficients as a function of natural aging time were determined for four models of flow stress. Material coefficients in individual yield stress models were determined on the basis of approximation of strain hardening curves using the least squares method. On the basis of the analysis of approximation errors, the accuracy of the tested models of yield stress to describe the course of the hardening curve of the material of the tested sheet in the tested range of natural aging time was assessed.

Keywords: AW-2024 sheet, natural aging, strain hardening curves, strain hardening models, constitutive parameters

1. Introduction

Aluminum alloys, due to their properties (including high strength-to-weight ratio) and ease of production, are widely used in aviation and other areas of the transport industry (Polmear, 2006). They are the most widely used material in the production of aircraft. A practical example of this is AW-2024 (AlCu4Mg1) alloy. Its precipitation hardening ability is very often used to achieve the required mechanical properties (Davies, 2003; Kučera & Vojtěch, 2017). After solution treatment (heat treatment and aging), it shows relatively high strength and good fracture toughness (Miller et al., 2000; May et al., 2010; Sun et al., 2020). Aging after heat treatment may be natural or accelerated (artificial aging) (ASM International, 1991; Przybyłowicz, 2006). Natural aging gives better results in the form of increasing the strength of the drawpiece material than accelerated aging, but it lasts much longer, i.e., 4–5 days (Przybyłowicz, 2006). On the other hand, an increase in temperature causes a decrease in the accelerated aging time. Unfortunately, the material strength gets reduced after aging (ASM International, 1991; Przybyłowicz, 2006).

Aluminum sheet drawpieces pressings with the ability to harden precipitation can be shaped in two variants. In the first one, the sheets are shaped after softening annealing in the so-called "O" state, while the finished drawpieces undergo heat treatment and aging. On the other hand, in the second variant, the sheets are shaped after heat treatment. Forming the sheet after heat treatment is advantageous

because the drawpiece does not enter the furnace after forming, where it could deform during the heat treatment process by heating in the furnace followed by rapid cooling. Moreover, which is also very favorable, it is much easier to perform heat treatment of the sheets in the form of flat sheets than in the form of moldings formed therefrom with complex shapes.

However, after heat treatment during natural aging, there is an increase in strength and a decrease in deformability of the sheet material, which is unfavorable from the point of view of technological properties (Sobotka et al., 2018). The work (Fallah Tafti et al., 2018) presents the results of research on the variability of the microstructure as well as the strength and plastic properties of AW-2024 sheet 0.81 mm thick immediately after heat treatment and during natural aging for a specified time (0.5, 1.5, 4 and 24 hours) after heat treatment. The obtained results indicate that the greatest increase in strength properties occurred during natural aging up to 4 hours after heat treatment. For example, after 4 hours of aging, the yield point value increased by approx. 86% compared to the yield point immediately after heat treatment. However, in the tested time from 4 to 24 hours, the increase in the yield point was not so intense and amounted to only about 20% compared to the yield point after 4 hours of natural aging. Thus, the greatest increase in the strength properties, and the simultaneous decrease in deformability of the material occur in the first hours after heat treatment, i.e., the time when the drawpieces according to the second variant are formed, i.e., from sheet metal after heat treatment. Therefore, the parameters of the drawpieces shaping process (e.g., forming forces, susceptibility to plastic deformation) and the behavior of the material in this process (e.g., the amount of springback of the sheet) will significantly depend on the time after heat treatment in which a given technological operation will be carried out.

Due to the above, in engineering practice, forming sheet metal elements in the second variant, i.e., after heat treatment, requires taking into account the technological process called stamping. Changes in the properties of the sheet material (shaped in subsequent operations) occur as a result of natural aging. For this purpose, it is necessary to know the strength and plastic parameters as well as the material coefficients in the constitutive equations of the flow stress function depending on the natural aging time.

The aging process of the sheet material after heat treatment can be slowed down or delayed by lowering the temperature. The work (Sobotka et al., 2018). presents, inter alia, the results of research on the influence of the storage time in the freezer of sheet metal after heat treatment on its strength and plastic properties. The tests were carried out with the use of 2 mm thick AW-2024 sheet, which was stored in a freezer at -15 ˚C after heat treatment. Then, after (72, 120, 168 and 240) hours of storage in the freezer, uniaxial tensile tests were carried out in order to determine the strength and plastic properties. For the storage time in the freezer from 3 to 10 days, an almost 5% increase in the yield point was observed. At the same time, the elongation of Ag and A80 mm practically did not change. It is advantageous because storing the sheet in a freezer after heat treatment gives some possibilities related to the preparation and implementation of the entire technological and production process of sheet metal parts shaped in the second variant, i.e., after heat treatment. In industrial practice, the possibility of storing sheets after heat treatment in a freezer allows the process of forming a given batch of parts at a given production station at the same time after removal from the freezer, i.e., at the same stage of natural aging, which ensures repeatability of the technological properties of the charge sheet. For this reason, it is important when designing and analyzing the technological process of the drawpiece to determine at what stage of aging after heat treatment will be performed a specific operation of plastic forming of the part and to know the material parameters for this stage in the constitutive equations of yield stress.

As already mentioned, the analysis and design of the technological process of the sheet metal stamping after heat treatment requires, first of all, the knowledge of the material coefficients in the constitutive equations of flow stress as a function of natural aging time. Unfortunately, there are no studies in this field in the literature, which was the basis for the research presented in this article.

The aim of the research presented in this article was to determine the material coefficients for AW-2024 sheet with a thickness of 1 mm as a function of the natural aging time after heat treatment for four selected models of strain hardening. Knowing the values of these coefficients will make it possible to take into account the effect of changes in the properties of the sheet material resulting from natural aging after heat treatment in the analysis and design of technological processes and tooling in the stamping industry.

2. Test material and experimental procedure

The tested material was AW-2024 alclad sheet metal with a thickness of 1 mm. The chemical composition of the material of the tested sheet is presented in Table 1.

Table 1. Chemical composition of AW-2024 sheet material (European Committee for Standardization, 2007)

Si	Fe	Cu	Mn	Mg	Cr	Zn	Ti	Zr+Ti	Others		Aluminium min.
									Each	Total	
≤0.5	≤.5	3.8-4.9	0.3-0.9	1.2-1.8	≤0.1	≤0.25	≤0.15	≤0.2	0.05	0.15	Remainder

From this sheet as delivered, i.e., after softening annealing, samples were taken for uniaxial stretching in the directions (0, 45 and 90) degrees to the direction of sheet rolling. A total of 45 samples were prepared for the five aging time measurement points. The shape and dimensions of samples for testing in accordance with ISO 6892-1 are shown in Fig. 1.
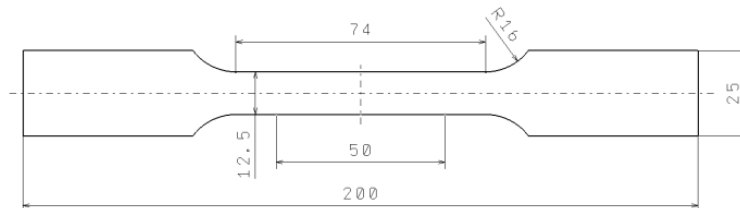
Fig. 1. Shape and dimensions of test specimens in mm

A solution heat treatment called heat treatment was carried out on the samples prepared in this way. The samples were successively heated in an oven to the temperature of 493 °C and kept at this temperature for 40 minutes (SAE International, 2015), and then subjected to rapid cooling in cold water. Then, uniaxial tensile tests were carried out successively immediately after heat treatment and during natural aging for 0, 20, 45, 90 and 120 minutes after heat treatment. The scope of aging time covered by the study was determined on the basis of an analysis of the range of manufactured drawpieces and engineering practice, taking into account the AMS2770 standard (SAE International, 2015). The time determined in this way was considered fully sufficient to complete the required technological operations of forming sheet metal parts. Such a time range was considered to be fully sufficient to carry out the required technological operations of shaping sheet metal parts. For each of the tested aging times after heat treatment, three samples were stretched in each direction. For this reason, in order to maintain the assumed time intervals between individual tests, solution heat treatment, and then uniaxial tensile tests were carried out in three rounds of 15 samples each. Static uniaxial tensile tests of individual samples were carried out successively on the Zwick / Roell Z030 testing machine with measurement of the elongation and change of the sample width using a multiextensometer (Fig. 2).

Fig. 2. An example of a sample during the uniaxial tensile test

3. Results and discussion

On the basis of the obtained results of experimental tests, the curves of strain hardening for particular directions (0˚, 45˚ and 90˚) and times after heat treatment were developed. Then, the values of material coefficients were determined for four selected constitutive models of flow stress with the determination of curve matching errors. The analysis of the influence of time after heat treatment on the value of the yield point and numerical values of the coefficients in selected constitutive equations was performed.

3.1. Influence of natural aging time on the yield point

The yield point is one of the basic strength parameters of the material, the numerical value of which significantly affects not only the forming forces and tool load, but also other parameters of the technological process, such as the amount of springback of the sheet. Therefore, it is important to know how this parameter changes with the aging time after heat treatment. The diagram (Fig. 3) shows the dependence of the yield strength of the tested sheet material as a function of the natural aging time after heat treatment. The numerical values for individual experimental points in the graphs present the arithmetic mean value obtained on the basis of three uniaxial stretching tests carried out in the same conditions. The obtained test results showed some differentiation of the strength and plastic properties of the tested sheet depending on the direction of sample collection (average normal anisotropy = 0.71 and its value practically did not depend on the aging time). The highest values of the yield point were in the 0˚ direction, slightly lower in the 90˚ direction, and the lowest in the 45˚ direction towards the rolling direction. In all directions, an almost linear increase in the yield strength was observed as a function of the natural aging time over the entire tested time range, i.e., (0–120) minutes. An approx. 40% increase in the yield point was observed. The position of the points on the graphs for the average value of individual parameters [$R_{p0.2\text{-AV}}$, $B_{d\text{-AV}}$, $n_{1\text{-AV}}$, $K_{2\text{-AV}}$, $n_{2\text{-AV}}$, $\sigma_{0\text{-AV}}$, $A_{3\text{-AV}}$, $K_{3\text{-AV}}$, $n_{3\text{-AV}}$, $A_{4\text{-AV}}$, $B_{4\text{-AV}}$, $K_{4\text{-AV}}$] described later in the article were calculated on the basis of the results for samples with different orientations in relation to the rolling direction according to the relationship:

$$X_{AV} = \frac{X_0 + 2X_{45} + X_{90}}{4} \tag{1}$$

where X is the parameter, and the subscripts denote the orientation of the specimen with respect to the rolling direction of the sheet.

As a result of the approximation of the experimental points, linear equations were obtained describing the increase in the yield point as a function of the natural aging time in particular directions. These equations for individual directions [$R_{p0.2\text{-}0}$ (t), $R_{p0.2\text{-}45}$ (t), $R_{p0.2\text{-}90}$ (t))] and for the average value [$Rp_{0.2\text{-AV}}$ (t)], were in the diagram (Fig. 3). In all cases, the correlation coefficient $R^2 > 0.99$.
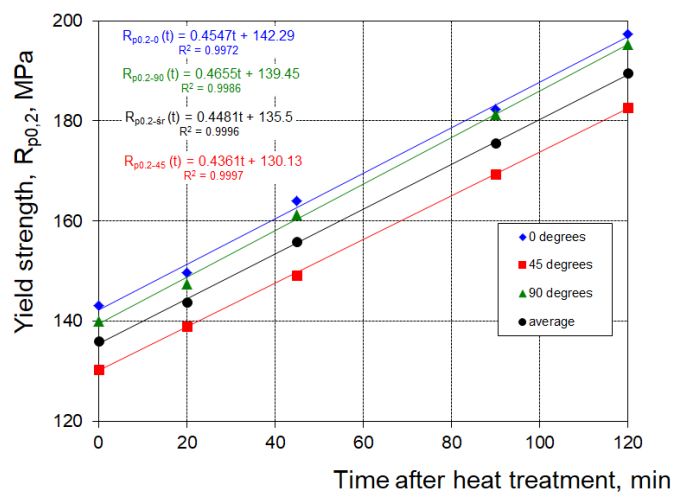
Fig. 3. Influence of aging time on the yield point

3.2. Influence of natural aging time on strain hardening curves

The hardening curves reflect the behavior of the material during plastic deformation. Their course describes the change in flow stress σ_p as a function of plastic strain ε_p. They are usually determined on the basis of uniaxial tensile, compression and torsion tests. Knowledge of the hardening curves is of great practical importance and is necessary for mathematical modeling of plastic forming processes.

The graph (Fig. 4) shows the experimentally determined curves of the material hardening of the tested sheet in the 0 ° direction for the tested times after heat treatment. On the other hand, in the graphs (Figs. 5 and 6), the curves of the strain hardening curve determined in the directions 45˚ (Fig. 5) and 90˚ (Fig. 6) for the same times after heat treatment. In all cases, a clear influence of the aging time on the course of the hardening curve was observed, with the aging time increasing the value of the flow stress σ_p proportionally over the entire range of plastic strain ε_p.
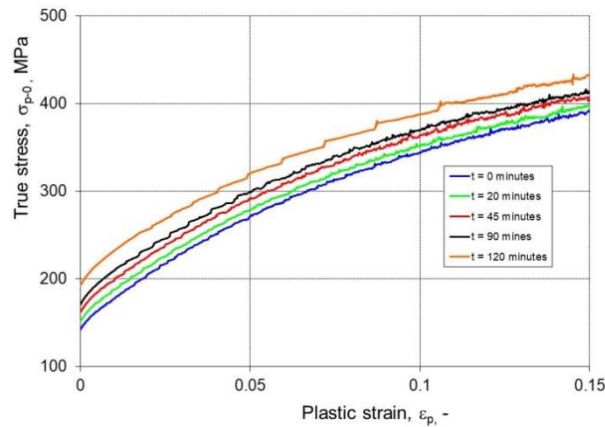
Fig. 4. Strain hardening curves in the direction of 0° for the five tested times after heat treatment
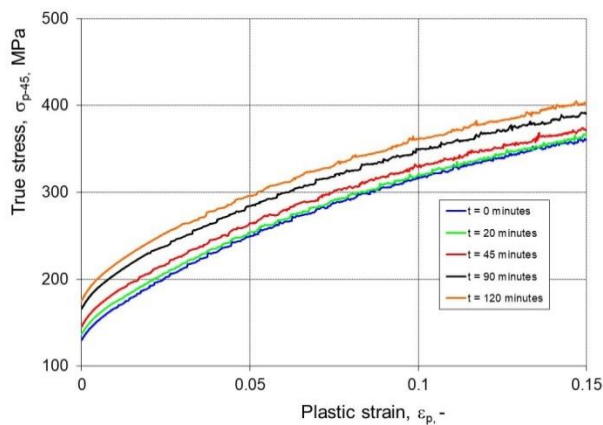
Fig. 5. Strain hardening curves in the direction of 45° for the five tested times after heat treatment
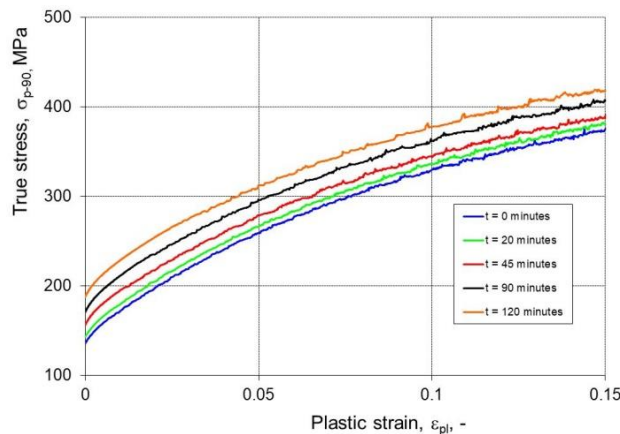
Fig. 6. Strain hardening curves in the direction of 90° for the five tested times after heat treatment

3.3. Selected functions of flow stress

For practical reasons, the curves of strain hardening are presented in the form of constitutive equations of the so-called function of flow stress. Such equations are used, inter alia, for the analysis and simulation of cold forming processes at relatively low strain rates, when their influence on the flow stress can be neglected. In this paper, four models of flow stress of various complexity levels were selected to describe the course of the material strain hardening of the tested sheet:

I. Hollomon (Hollomon, 1945)

$$\sigma_p(\varepsilon_p) = K_1 \varepsilon_p^{n_1} \tag{2}$$

II. Swift (Swift, 1952)

$$\sigma_p(\varepsilon_p) = K_2(\varepsilon_0 + \varepsilon_p)^{n_2} \tag{3}$$

III. Voce (Voce, 1948)

$$\sigma_p(\varepsilon_p) = A_3 + K_3\left(1 - \exp(-n_3 \varepsilon_p)\right) \tag{4}$$

IV. Extended Voce (Stiebler et al., 1991)

$$\sigma_p(\varepsilon_p) = A_4 + B_4 \varepsilon_p + K_4\left(1 - \exp(-n_4 \varepsilon_p)\right) \tag{5}$$

where: σ_p – flow stress, ε_p – equivalent plastic strain, $K_1 \div K_4$, A_3, A_4, B_4, ε_0, $n_1 \div n_4$ – material constants determined experimentally.

The Hollomon model is the simplest and most often used in engineering practice, the strain hardening model, which provides a good description of the hardening curve in a wide range of deformation, which is why it is willingly used in modeling plastic forming processes, especially those with large deformations, such as forging, extrusion, punching, etc. The Swift model, like the Hollomon model, due to its versatility but also greater accuracy in the description of the initial course of the strain hardening curve, is very often used in numerical modeling of a wide range of plastic forming processes in the field of small and large deformations. Voce is also often used to describe the course of the strain hardening curve, which, like the Swift model, requires knowledge of three material constants. The most complex of the selected models is the extended Voce model with an additional linear component. Determination of the extended Voce model requires as many as four material constants. The extended Voce model is also referred to in the literature as the El-Magd model (Sener & Yurci, 2017).

3.4. Influence of constitutive equation on the error of matching curves of strain hardening

The material constants in equations (2)–(5) were determined for the individual strain hardening curves using the least squares method using the Logger Pro program. The error of fit B_d was calculated by relating the root mean square error RMSE to the mean feature level σ_p from the relationship:

$$B_d = \frac{RMSE}{(\sigma_p)_{av}} \cdot 100\% \tag{6}$$

The graphs (Figs. 7–10) summarize the calculated values of the error of matching the course of the strain hardening curves for each constitutive model, taking into account the directions of 0°, 45° and 90° depending on the natural aging time after heat treatment. The numerical values in the individual columns were calculated as the arithmetic average of the matching error on the basis of three uniaxial tensile tests carried out under the same conditions. The Hollomon model showed the largest matching error (slightly above 2%), which was practically independent of the aging time in the studied range (Fig. 7). In the case of using models with three material factors, the obtained error of matching was less than half that. In the case of these models, the matching error was influenced by both the sampling direction and the natural aging time after heat treatment. The Swift model showed the largest

error of matching in the 0˚ direction, and the smallest in the 90˚ direction (Fig. 8). On the other hand, the Voce model showed the greatest error of alignment in the 45˚ direction, and the smallest in the 0˚ direction (Fig. 9). Comparing the results for the Voce model with the results for the extended Voce model (Fig. 10), practically the same trend of the matching error distribution was observed, but the error of matching itself in the extended Voce model was the smallest among all the tested models. The effectiveness of individual models for describing the course of the hardening curves of the material of the tested sheet in terms of the tested aging times after heat treatment is best presented in the diagram (Fig. 11). The average error of matching for individual models was calculated from the dependence (1) on the basis of the error values calculated in the 0˚, 45˚ and 90˚ directions. As already mentioned, the largest average error of fit in the range (1.97–2.3%) was shown by the Hollomon model. In the case of the Swift model, the average matching error immediately after heat treatment was 0.95% and it decreased with the aging time reaching the value of 0.69% for the 120 minutes of aging time. for the Voce model, only slightly lower values of the average error of matching were obtained, but the average error of matching after heat treatment was 0.67% and (unlike the Swift model) it increased to 0.87% for the time of 120 minutes. As already mentioned, the same trend occurred in the case of the extended Voce equation, except that the average matching error was at the lowest level, ranging from 0.49% after heat treatment to 0.7% for an aging time of 120 minutes after heat treatment.
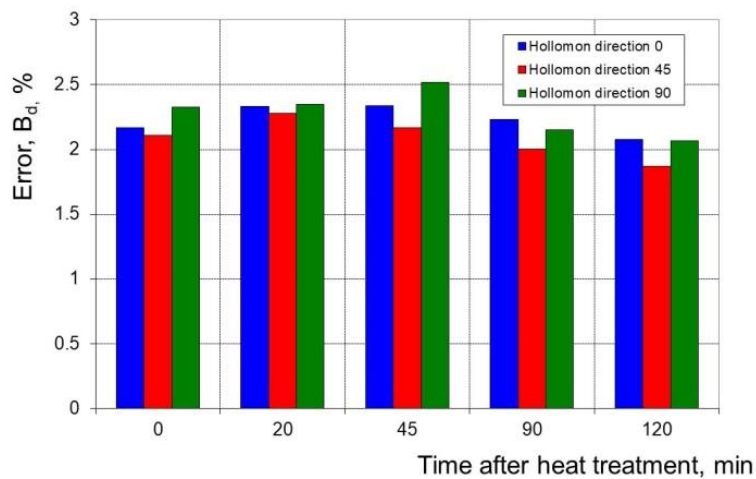
Fig. 7. The matching Error of the curve by the Hollomon equation
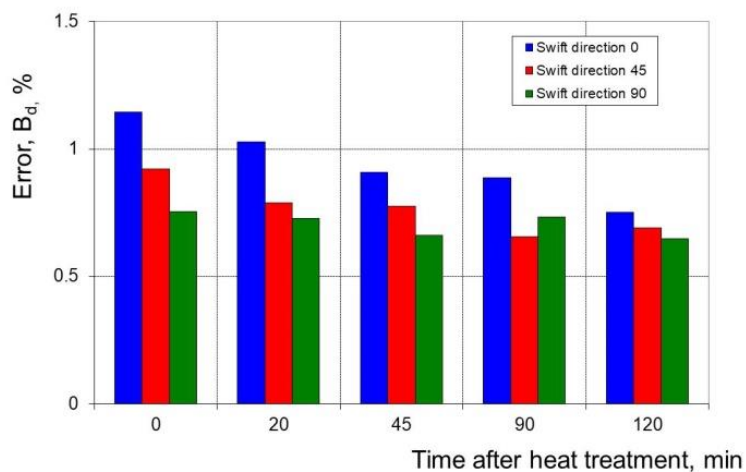
Fig. 8. The matching Error of the curve by the Swift equation
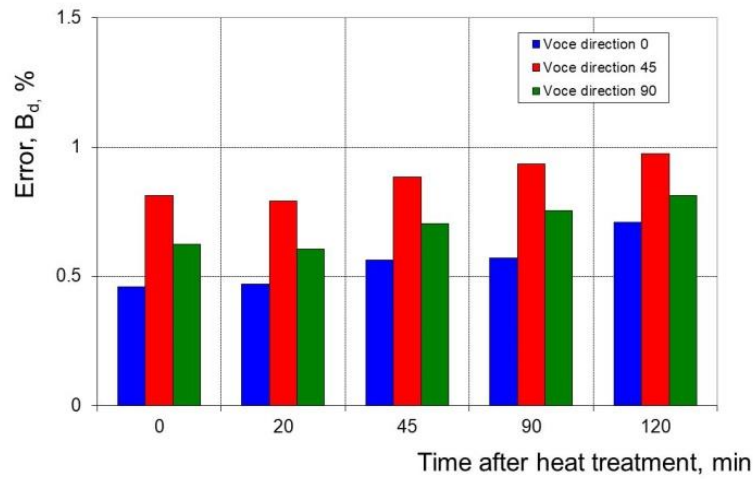
Fig. 9. The matching Error of the curve by the Voce equation
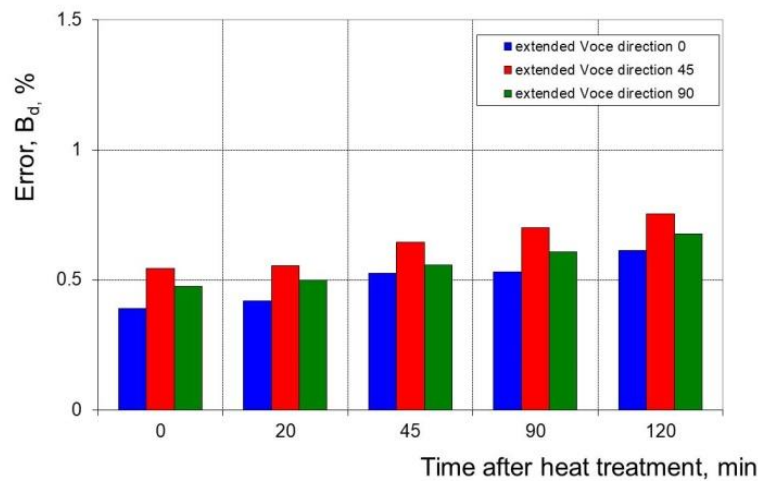
Fig. 10. The matching Error of the curve by the extended Voce equation
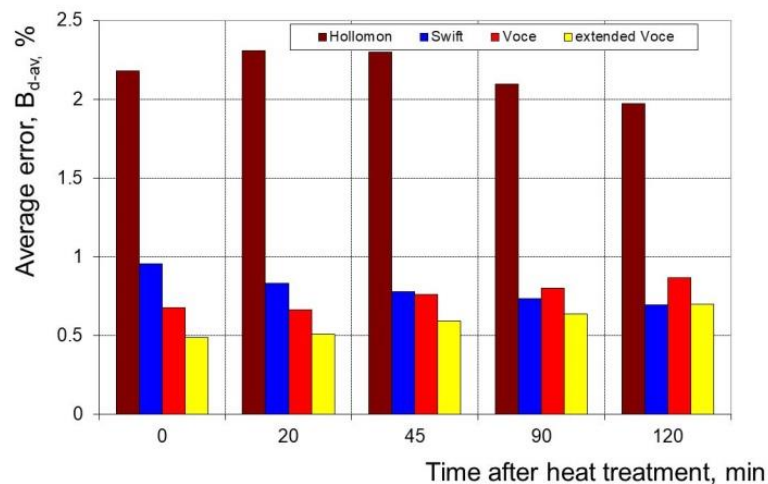
Fig. 11. Average matching error of curve for the tested models

3.5. Coefficients in constitutive equations as a function of aging time

In order to determine the dependence of the effect of the natural aging time after heat treatment on the value of the material coefficients in equations (2)–(5), graphs were prepared showing the dependence of individual coefficients as a function of the aging time after heat treatment. The points on the graphs for the 0˚, 45˚ and 90˚ directions (Fig. 12–23) present the arithmetic average value of

a given material factor, calculated on the basis of the approximation of the strain hardening curves for three tensile tests carried out under the same conditions. On the other hand, the location of the points for the average values of individual material parameters in these charts was calculated from the dependence (1).

In the case of the K_1 and K_2 coefficients in the Hollomon and Swift equations (Figs. 12 and 14), no specific trend was observed in aging after heat treatment in any of the directions. For this reason, the values of these coefficients were assumed to be constant in the range of the investigated heat treatment time, and their average value for each direction was calculated on the basis of five measurement points and presented in these graphs. On the other hand, a clear influence of the aging time was observed for the exponents of the strain hardening curves n_1 and n_2, respectively, in these equations (Figs. 13 and 15). In the case of these coefficients in all directions, a decrease in their value was observed with the aging time, and the trend was practically linear. As a result of the approximation of the experimental points with linear equations, the values of the coefficients in these equations were determined, which were presented in the graphs (Fig. 13 and 15) together with the values of the correlation coefficient R^2. In the case of the exponents n_1 and n_2, there was a high correlation, and the correlation coefficient for the average values of these coefficients was $R^2 > 0.99$. Among the respondents, only the coefficient ε_0 in the Swift equation did not show a typical linear trend. Therefore, in this case, the nonlinear equation presented in the graph was used for approximation (Fig. 16). In this case, the matching error for the average value $\varepsilon_{0\text{-AV}}$ calculated from the dependence (6) was 0.8%.
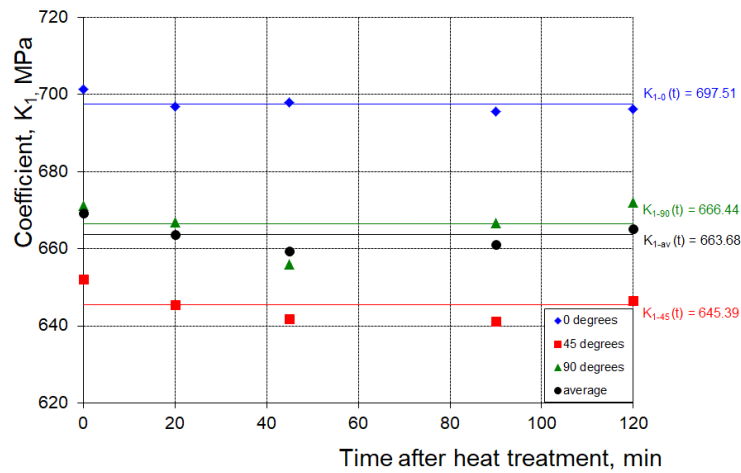
Fig. 12. Influence of aging time on the K_1 coefficient in the Hollomon equation
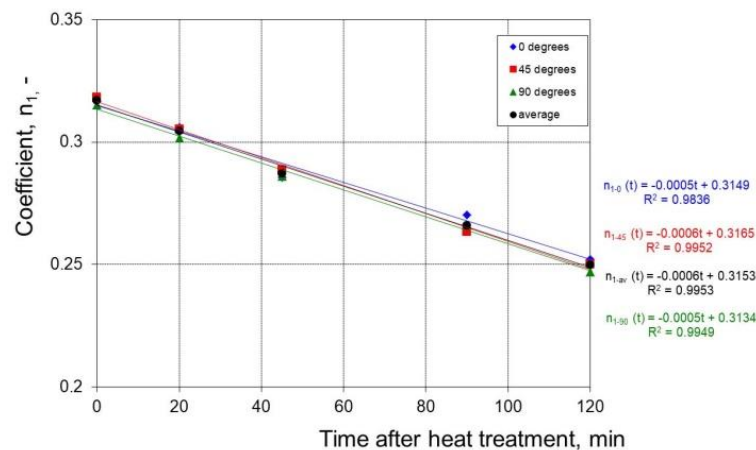
Fig. 13. Influence of aging time on the n_1 coefficient in the Hollomon equation
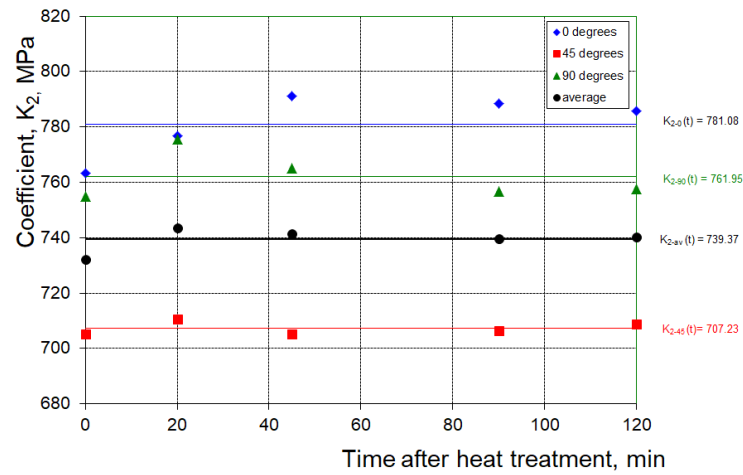
Fig. 14. Influence of aging time on the K_2 coefficient in the Swift equation
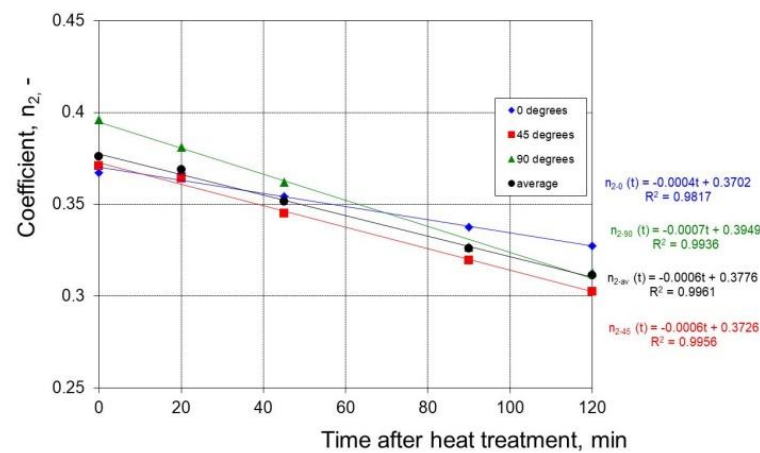
Fig. 15. Influence of aging time on the n_2 coefficient in the Swift equation
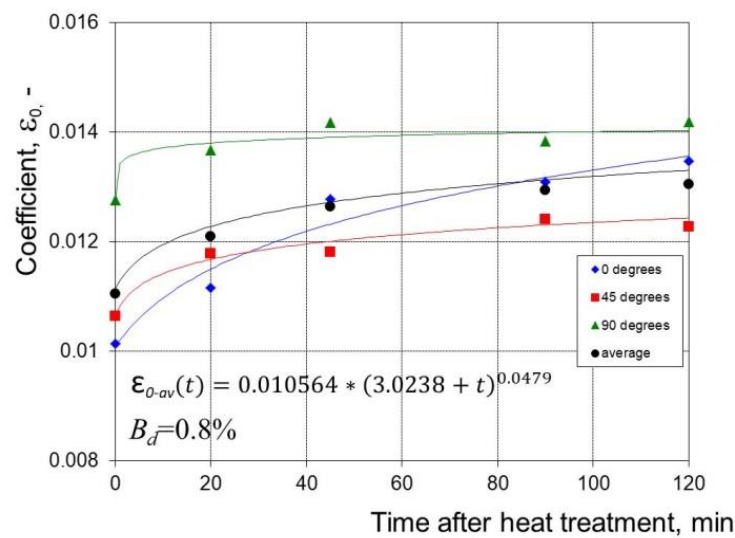
Fig. 16. Influence of aging time on the ε_0 coefficient in the Swift equation

In the case of the Voce model and the extended Voce model, practically all material coefficients showed an almost linear relationship in the tested aging time after heat treatment (Figs. 17–23). However, in the case of the A_3 and n_3 coefficients (Figs. 17 and 19), as well as A_4, B_4 and n_4 (Figs. 20, 21 and 23), an increase in their values was observed during aging after heat treatment. However, in the case of the remaining material coefficients K_3 (Fig. 18) and K_4 (Fig. 22), a decrease in their values was observed over time after heat treatment. As above, the calculated values of the coefficients in the line-

ar equations and the value of the correlation coefficient R^2 for each coefficient are presented in the form of equations in the graphs (Figs. 17–23).

The most important from the point of practical use of individual constitutive equations (e.g., in numerical modeling of the processes of forming the tested sheet metal after heat treatment) is the knowledge of the average value of material coefficients as a function of aging time after heat treatment. For this reason, the determined average values of the material coefficients for the tested strain hardening models as a function of the natural aging time after heat treatment are summarized in Table 2.
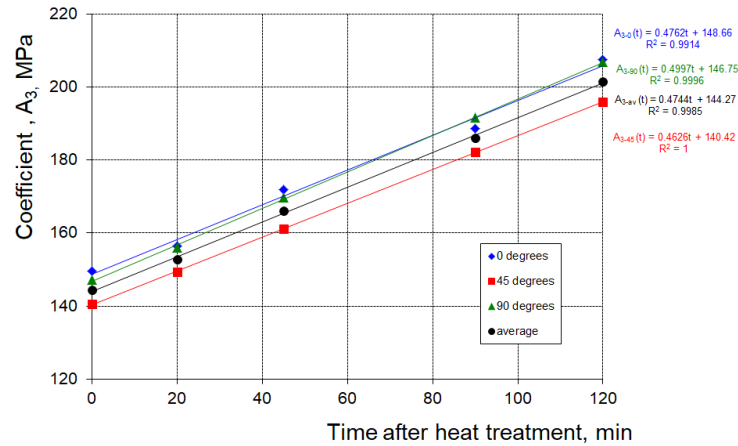
Fig. 17. Influence of aging time on the A_3 coefficient in the Voce equation
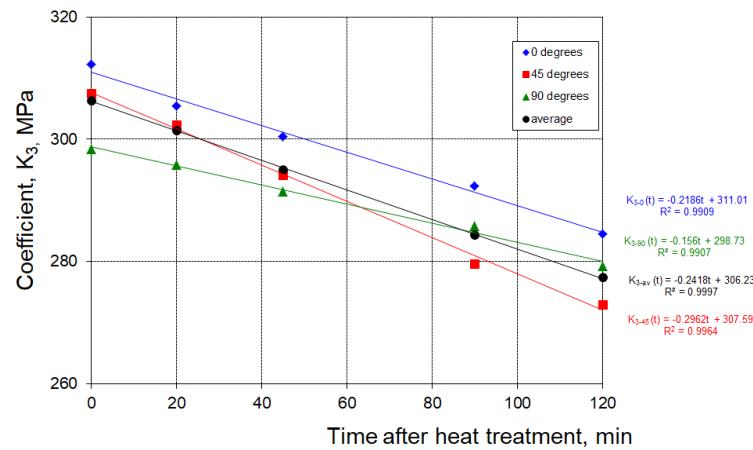
Fig. 18. Influence of aging time on the K_3 coefficient in the Voce equation
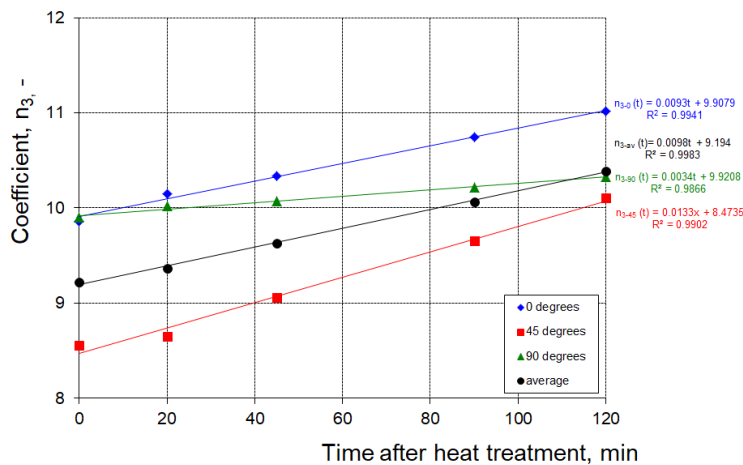
Fig. 19. Influence of aging time on the n_3 coefficient in the Voce equation
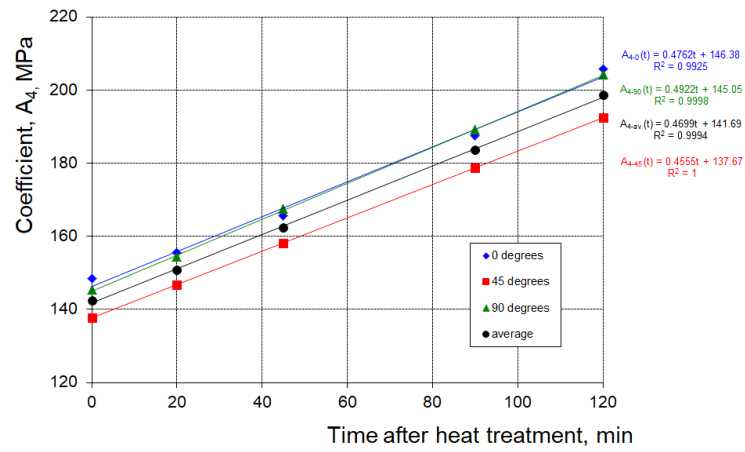
Fig. 20. Influence of aging time on the A_4 coefficient in the extended Voce equation
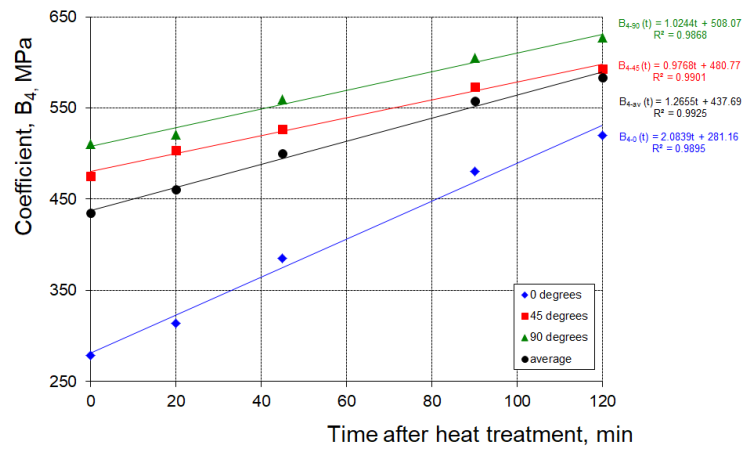
Fig. 21. Influence of aging time on the B_4 coefficient in the extended Voce equation
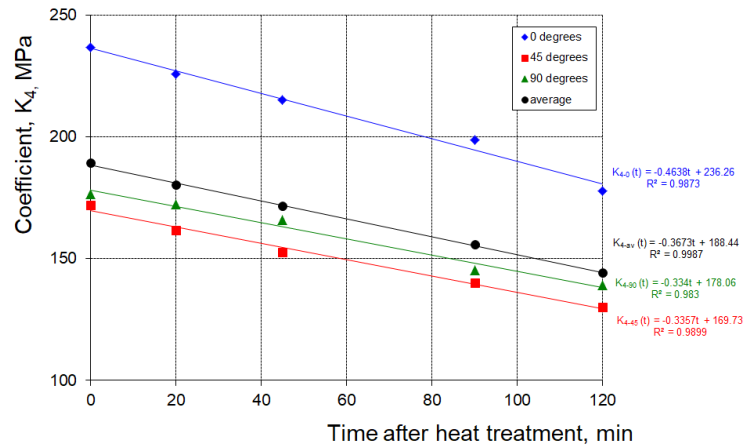
Fig. 22. Influence of aging time on the K_4 coefficient in the extended Voce equation
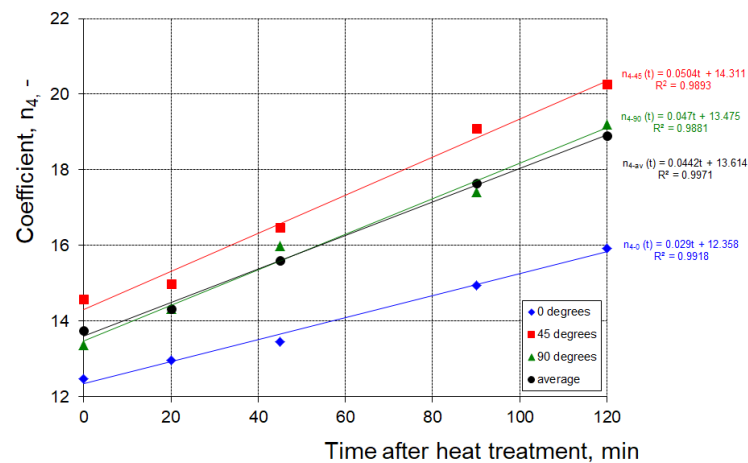
Fig. 23. Influence of aging time on the n_4 coefficient in the extended Voce equation

Table. 2. Experimentally determined material coefficients as a function of natural aging time in the range of 0–120 minutes after heat treatment for AW-2024 sheet with a thickness of 1 mm.

Strain hardening model		Coefficients as a function of aging time after heat treatment	Average value of the coefficient for the three directions	Correlation coefficient R^2
I	Hollomon	$K_1(t)$, MPa	663.68	-
		$n_1(t)$, -	$-0.0006t+0.3153$	0.9953
II	Swift	$K_2(t)$, MPA	739.37	-
		$\varepsilon_0(t)$, -	$0.0106*(3.0238+t)^{0.048}$	$B_d = 0.8\%$
		$n_2(t)$, -	$-0.0006t+0.3776$	0.9961
III	Voce	$A_3(t)$, MPa	$0.4744t+144.27$	0.9985
		$K_3(t)$, MPa	$-0.2418t+306.23$	0.9997
		$n_3(t)$, -	$0.0098t+9.194$	0.9983
IV	Extended Voce	$A_4(t)$, MPa	$0.4699t+141.69$	0.9994
		$B_4(t)$, MPa	$1.2655t+437.69$	0.9925
		$K_4(t)$, MPa	$-0.3673t+188.44$	0.9987
		$n_4(t)$, -	$0.0442t+13.614$	0.9971

4. Conclusions

In this article, on the basis of experimental tests for AW-2024 sheet with a thickness of 1 mm, material coefficients were determined in models of yielding stress as a function of natural aging time. Material coefficients were determined for four models: Hollomon, Swift, Voce and extended Voce. On the basis of the analysis of approximation errors, the usefulness of the tested models was assessed to describe the function of yielding stress of the tested sheet material after heat treatment and during natural aging in the examined time range. The range of aging time for which the tests were carried out and the values of material coefficients with excess were determined include the time during which individual operations of shaping the extrusions from heat-treated sheets are carried out. This ensures the possibility of analyzing and modeling individual stages of the molding process with the use of computer computational methods.

Based on the research, the following conclusions can be drawn:

1) In the scope of the tested aging time after heat treatment $0 \div 120$ min, an approx. 40% increase in the yield point of the material of the tested sheet was found. Moreover, in the examined period of natural aging, the increase in the yield point was almost linear (correlation coefficient $R^2 > 0.99$).

2) Among the examined models of strain hardening, the extended Voce model ($B_{d\ av} \approx 0.58\%$) and the Voce model ($B_{d\ av.} \approx 0.75\%$) turned out to be the most accurate. The popular Swift

model was comparable ($B_{d\,av.} \approx 0.79\%$). It was observed that in the case of the Voce models, the error of matching increased with the aging time, while in the case of the Swift model it was the other way round, i.e., it decreased with aging time. In the case of the Hollomon model, the average error of matching was the highest and amounted to $B_{d\,av} \approx 2\%$.

3) In the studied range of aging, no clear trends were found in the course of the strain hardening factor K_1 in the Hollomon model and K_2 in the Swift model as a function of the aging time. For this reason, the average value for these coefficients from individual trials was adopted. The remaining coefficients in the tested strain hardening models showed a clear change in the aging time function, and their course was described with the use of linear equations, except for the ε_0 coefficient in the Swift model, the course of which was described by a power equation.

4) The dependence of the coefficients in the equations of flow stress on the time after heat treatment allows to easily take into account the change in technological properties of the material as a result of aging during the analysis and design of the molding processes in the second variant, i.e., after heat treatment.

References

ASM International. (1991). *ASM Handbook. Volume 4: Heat Treating ASM Handbook Committee*, 841-879. https://doi.org/10.1361/asmhba0001205

Davies, G. (2003). *Materials for automobile bodies*. Butterworth-Heinemann.

European Committee for Standardization. (2007). Aluminium and aluminium alloys - Chemical composition and form of wrought products - Part 3: Chemical composition and form of products (Standard No. EN 573-3).

Fallah Tafti, M. Sedighi, M., & Hashemi, R. (2018). Effects of natural ageing treatment on mechanical, microstructural and forming properties of Al 2024 aluminum alloy sheets. *Iranian Journal of Materials Science & Engineering, 15* (4), 1-10. https://doi.org/10.22068/ijmse.15.4.1

Hollomon, J. H. (1945) Tensile deformation. *Transactions of the Metallurgical Society of AIME*, *162*, 268-290.

Kučera, V., & Vojtěch D. (2017). Influence of the heat treatment on corrosion behavior and mechanical properties of the AA 7075 alloy. *Manufacturing Technology*, *17*(5), 747-752. https://doi.org/10.21062/ujep/x.2017/a/1213-2489/MT/17/5/747

May, A., Belouchrani, M.A., Taharboucht, S., & Boudras, A. (2010). Influence of heat treatment on the fatigue behaviour of two aluminium alloys 2024 and 2024 plated. *Procedia Engineering, 2(1)*, 1795-1804. https://doi.org/10.1016/j.proeng.2010.03.193

Miller, W.S., Zhuang, L., Bottema, J., Wittebrood, A.J., Smet, P.D., Haszler, A., & Vieregge, A. (2000). Recent development in aluminium alloys forthe automotive industry. *Materials Science and Engineering: A, 280 (1),* 37-49. https://doi.org/10.1016/S0921-5093(99)00653-X

Polmear I. (2006). *Light alloy: From traditional alloys to nanocrystals.* Butterworth-Heinemann.

Przybyłowicz K. (2006). *Metaloznawstwo*. Wydawnictwa Naukowo-Techniczne. In Polish.

SAE International. (2015). *Heat treatment of wrought aluminum alloy parts* (Standard No. AMS 2770R). Retrieved from https://www.sae.org/standards/content/ams2770r/

Sener B., & Yurci M. E. (2017). Comparison of quasi-static constitutive equations and modeling of flow curves for austenitic 304 and ferritic 430 stainless steels. *Acta Physica Polonica A*, *131* (3), 605-607. https://doi.org/10.12693/APhysPolA.131.605

Sobotka, J., Solfronk, P., Kolnerova, M., & Korecek D. (2018). Influence of technological parameters on ageing of aluminium alloy AW-2024. *Manufacturing Technology, 18*(6), 1023-1028. https://doi.org/10.21062/ujep/218.2018/a/1213-2489/MT/18/6/1023

Stiebler, K., Kunze, H., & El-Magd, E. (1991). Description of the of behaviour of a high strength austenitic steel under biaxial loading by a constitutive equation. *Nuclear Engineering and Design 127*(1), 85-93. https://doi.org/10.1016/0029-5493(91)90041-F

Sun, S., Fang, Y., Zhang, L., Li, Ch., & Hu, S. (2020). Effects of aging treatment and peripheral coarse grain on the exfoliation corrosion behaviour of 2024 aluminium alloy using SR-CT. *Journal of Materials Research and Technology*, *9*, 3219-3229. https://doi.org/10.1016/j.jmrt.2020.01.069

Swift, H.W. (1952). Plastic instability under plane stress. *Journal of the Mechanics and Physics of Solids 1* (1), 1-18. https://doi.org/10.1016/0022-5096(52)90002-1

Voce, E. (1948). The relationship between stress and strain for homogeneous deformations. *Journal of the Institute of Metals 74*, 537-562.

Wpływ Starzenia Naturalnego Blachy Aluminiowej AW-2024 na Przebieg Krzywej Umocnienia Odkształceniowego

Streszczenie

Wytłoczki z blach aluminiowych mających zdolność do utwardzania wydzieleniowego mogą być kształtowane z blachy po wyżarzaniu zmiękczającym lub po przesycaniu. W drugim przypadku podczas analizy i projektowania procesu technologicznego należy dodatkowo uwzględnić zmianę właściwości materiału kształtowanej blachy w wyniku starzenia naturalnego. W tym artykule przedstawiono wyniki badań wpływu czasu starzenia naturalnego po przesycaniu materiału blachy AW-2024 o grubości 1 mm na przebieg krzywej umocnienia odkształceniowego. Krzywe umocnienia zostały wyznaczone na podstawie próby jednoosiowego rozciągania. Badaniom poddano blachy bezpośrednio po przesycaniu oraz w trakcie starzenia naturalnego tj. (20, 45, 90 oraz 120) minut po przesycaniu. Badania wykazały, istotny wpływ starzenia naturalnego w badanym zakresie czasów po przesycaniu na przebieg krzywej umocnienia odkształceniowego materiału blachy. W oparciu o wyznaczone doświadczalnie na poszczególnych kierunkach (0, 45 oraz 90 stopni do kierunku walcowania) przebiegi krzywych umocnienia odkształceniowego wyznaczono wartości współczynników materiałowych w funkcji czasu starzenia naturalnego dla czterech modeli naprężenia uplastyczniającego. Współczynniki materiałowe w poszczególnych modelach naprężenia uplastyczniającego zostały wyznaczone na podstawie aproksymacji przebiegu krzywych umocnienia odkształceniowego metodą najmniejszych kwadratów. Na podstawie analizy błędów aproksymacji dokonano oceny dokładności badanych modeli naprężenia uplastyczniającego do opisu przebiegu krzywej umocnienia materiału badanej blachy w badanym zakresie czasu starzenia naturalnego.

Słowa kluczowe: blacha AW-2024, starzenie naturalne, krzywe umocnienia, modele umocnienia, stałe materiałowe

Original Research

Experimental Study of Mechanical Properties of Selected Polymer Sandwich Composites

Paulina Zielińska * iD **, Waldemar Ziaja** iD

Faculty of Mechanical Engineering and Aeronautics, Rzeszow University of Technology, 12 Powstańców Warszawy ave., 35-959 Rzeszow, Poland

* Correspondence: paulina_wojcik25@wp.pl

Abstract

The aim of this work was to determine the influence of material and geometric factors of selected sandwich composites on their mechanical properties. The first pair of sandwich materials under consideration were made by the industrial infusion method and consisted of epoxy resin reinforced with 7 layers of glass fabric (skin) with core made of PVC foam or aramid honeycomb. The second pair of materials was prepared manually and consisted of polyester resin reinforced with glass mat (skin) with aramid honeycomb core of varying thicknesses. The aim of this work was to determine the influence of material and geometrical factors of selected sandwich composites on their mechanical properties. The mechanical properties were determined in static bending, compression and tensile tests. In each case, the method of destruction of the tested composite materials was assessed. In the case of composites with epoxy resin skins application of aramid honeycomb core resulted in higher tensile and edgewise compressive strength. For materials with polyester resin skins and honeycomb cores it was found that increase of core thickness yielded higher bending stiffness but the tensile and bending strength were reduced.

Keywords: sandwich composites, mechanical properties, static bending tests, static compression test, static tensile test

1. Introduction

Layered composites are usually made of several layers of fibers, in the form of roving, knitted fabrics, fabrics or mats, which are embedded in a polymer, ceramic or metal matrix (Woźniak & Kukiełka, 2014). Layered composites are classified into the two categories: laminates and sandwich composites.

Laminates are composite materials that consist of a polymer matrix and several layers of fabrics or mats. An example of a laminate is plywood, which, unlike the wood from which it is made, has isotropic properties in the plane of the sheet (Boczkowska et al., 2016).

Sandwich composites are materials consisting of rigid skin and a low-density core. They owe their unique properties by the combination of the best features of two materials with completely different properties. Sandwich structures are characterized by a high stiffness to weight ratio. An example of such composite can be a resonant panel, which consists of high-quality cardboard glued between the skins of a carbon fiber-reinforced polymer composite (Rajczyk & Stachecki, 2011). The core of the sandwich composite can be made of foamed polymer or honeycomb core (this is the most commonly used core). The honeycomb is formed as a result of local sticking of the tapes at specified intervals, and then stretching them in a direction perpendicular to the tape. The cellular disc created in this way is joined with skins on two sides. Skins are most often made of polymer composites, which are reinforced with carbon fibers or glass fabrics (Mayer & Kaczmar, 2008). The resulting sandwich panel is rigid, light and has high compressive and bending strength. Sandwich composites are most often used in the aerospace industry (mainly military), civil engineering (beams, girders) and automotive industry (Grabarski, 2001). Multilayer structures, despite their many advantages, have also a number of disad-

vantages associated with a variety of modes of destruction. Sandwich composites may be damaged as a result of: buckling, delamination of the core, shearing of the core and local surface depression or buckling of a single cell (Ochelski, 2004).

The properties of sandwich composites strongly depend on the materials used for their core and skins. A sandwich structure requires a specific distribution of internal forces and a system of masses which affect the stability, strength and rigidity of the designed structure. Skins of sandwich composites are usually made of steel, aluminum alloys or fiber reinforced polymer (FRP) composites. Organic materials such as balsa or cork tree were used to build the cores of the first sandwich composites (Sawal et al., 2015). These materials were replaced by artificial materials such as cellular cores or polymeric foams due to excessive cost of production. Today, there are 5 basic types of materials that are used to produce the core of sandwich structures: balsa, PU (polyurethane), PVC (polyvinyl chloride), PET (polyethylene terephthalate) foams and honeycomb cores.

Laminate with balsa is a sandwich composite characterized by very high stiffness, strength, and low weight. Balsa is perfectly compatible with all types of adhesives and resins and is suitable for most production processes.

Polymer foams are the cheapest and lightest types of cores. These include PU, PVC and PET foams. Their mechanical properties depend mainly on the density of the material used. Moreover, they are easy to manufacture and process. PU foam is a rigid foam with closed cells. It is used for sandwich elements produced industrially in large quantities. It is used in both simple and complex 3D structures, at room and elevated temperature. PVC foam is cross-linked polymer foam with closed cells. It is characterized by high rigidity, strength and low density. PVC foam is resistant to chemicals, is not brittle, and has very low water absorption. It is compatible with the majority of resins and ideally suits as a basic material for all lightweight sandwich structures which are subject to static or dynamic loads. PET foams are thermoplastic structural foams. They are used for all types of resin connections. Their big advantage is their ease of processing and thermoformability. Due to their beneficial properties – high compressive strength, creep and fatigue resistance – they are used in a wide range of composites.

Honeycomb cores are used in heavily loaded structural elements. They are manufactured from various materials, such as paper or aluminum alloys. Paper cores with a honeycomb structure consist of a series of hexagonal cells joined together. They form a sheet that contains about 95% free space. Due to the unique geometry of honeycomb cores, sandwich composites are characterized by high strength to weight ratio, high rigidity, good fatigue and acoustic properties, thermal and acoustic insulation, resistance to fire, moisture, corrosion, and many others. The unique geometric structure of the honeycomb cores combined with the properties of the materials used, provides unique properties.

The aim of this work was to determine the influence of material and geometrical factors of selected sandwich composites on their mechanical properties. The mechanical properties were determined in static bending, compression and tensile tests. In each case, the method of destruction of the tested composite materials was assessed.

2. Materials and methods

Four types of sandwich materials were adopted for the examination, which in the further part of the paper were marked with numbers from 1 to 4.

Materials 1 and 2: the skins were prepared from a laminate made of glass fabric with a plain weave. Each skin consisted of 7 layers of fabric. The laminate matrix was made of Hexion Epikote Resin L 1100 with a density of 1150 kg/m^3. The average thickness of one skin was 1.4 mm. The materials were made by the industrial infusion method. Infusion moulding is a modern process for manufacturing composite materials. It consists of placing dry reinforcements in a mould covered by a vacuum bag which will then be impregnated with the arrival of resin which is sucked up by the depression created in the mould. This technology allows the production of monolithic parts (low and high thickness), such as sandwich structures. The resin was hardened at 85°C for 2 h. In material number 1, the core was made of PVC foam – Airex C70.55 with a density of 60 kg/m^3, while in material number 2 aramid honeycomb core was used with a thickness of 4 mm and a density of 29 kg/m^3. The average total thickness of sandwich material no. 1 was 6.60 mm and material no. 2 was 6.92 mm.

Materials 3 and 4: the skins were made of glass mat reinforced polyester resin HAVELPOL 1 having a density of 1200 kg/m^3. The average thickness of one skin was 2.8 mm. The aramid honeycomb cores had various thickness: 3 mm in material number 3 and 8 mm in material number 4. The

skins were hand-bonded to the core with a two-component epoxy glue – Araldite. Total average thickness of the sandwich material number 3 was 9.10 mm and material number 4 – 14.25 mm.
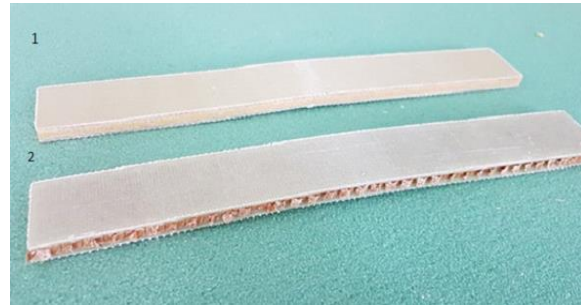
Fig. 1. Sandwich material no. 1 and 2
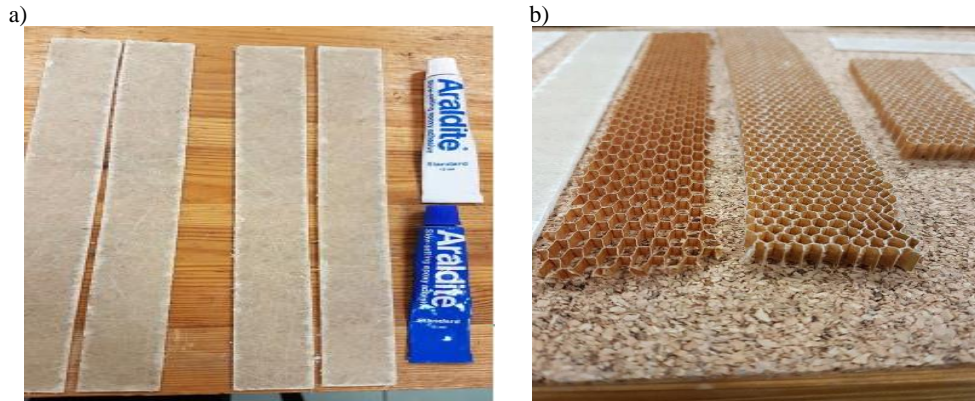
Fig. 2. Materials used to make the sandwich composite no. 3 and 4: a) glass mat reinforced polyester laminate, b) aramid cores, 3 and 8 mm in thickness

The three-point bending test was performed on an Instron 5982 testing machine in accordance with ASTM D7249/D7249M standard (American Society for Testing and Materials, 2012). The machine was equipped with a bending fixture and deflectometer. An extensometer, which measured the deflection, was attached to the deflectometer. During the test, the crosshead displacement [mm], load [N] and deflection of the specimen [mm] were recorded.

From the values recorded during the test, flexural modulus was calculated, using following formula:

$$E_b = \frac{Pl^3}{48fI} \tag{1}$$

where: P – force [N], l – spacing of supports [mm], f – mid-span deflection [mm]; I – moment of inertia of the specimen cross-section [mm^4], which is given by:

$$I = \frac{bh^3}{12} \tag{2}$$

where: b – specimen width [mm], h – specimen thickness.

To verify the values of flexural modulus and to determine the influence of the distance between supports on its value, a second variant of the bending test in terms of elastic deformation was performed, taking three support spacings: 60, 130 and 200 mm. The deflection of samples was measured with the Keyence LK-H052 laser measuring head at 100 Hz sampling frequency.

The static tensile test was carried out on a Zwick UTS 100 testing machine, at the crosshead speed of 2 mm/min (American Society for Testing of Materials, 2010). The values measured during the test were: crosshead displacement [mm], force [N], and elongation [%].

From the values recorded during the test, the ultimate tensile strength was calculated using equation:

$$Rm = \frac{Pmax}{A} \tag{3}$$

where: *Pmax* – maximum force during tensile test [N], *A* – initial cross-sectional area of the skins [mm^2].

The edgewise compression test was performed on an Instron 3382 testing machine according to ASTM C364/C364M standard at a crosshead speed of 2 mm/min (American Society for Testing and Materials, 2017). The values measured during the test were crosshead displacement [mm] and loading force [N] (the test was performed without an extensometer) (American Society for Testing and Materials, 2017). The edgewise compressive strength was calculated from the values recorded during the test using the equation:

$$R_\text{s} = \frac{Pmax}{b(2\,t)} \tag{4}$$

where: *Pmax* – maximum force [N], *b* – specimen width [mm], *t* – skin thickness [mm].

3. Results and discussion

On the basis of the results of the bending test, it was found that the greatest stiffness and ability to carry bending loads, regardless to the distance between supports, is characterized by material no. 4 and secondly by material no. 3 (Figs. 3a and 4a). This is a result of the higher thickness of these materials in comparison with materials 1 and 2 – the geometric factor is decisive in this case. In turn, the bending strength of materials 3 and 4, expressed as the maximum stress value in the skin, is the lowest, which results from the low strength of the skin reinforced with a glass mat (Figs. 3b and 4b) (Antony et al., 2012). The apparent flexural modulus values are lower for materials 3, 4 in comparison to materials 1 and 2, which confirms the crucial influence of the elastic modulus of the skin (Table 1).
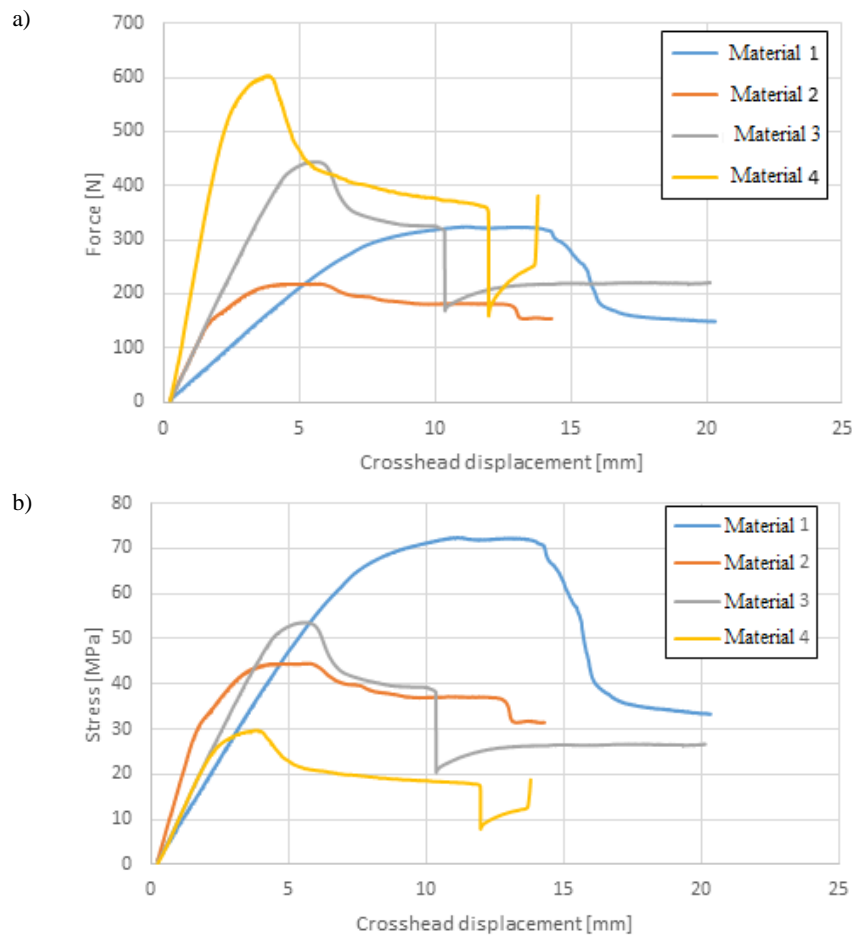
Fig. 3. Bending curves for support spacing of 200 mm: a) force – crosshead displacement, b) stress – crosshead displacement
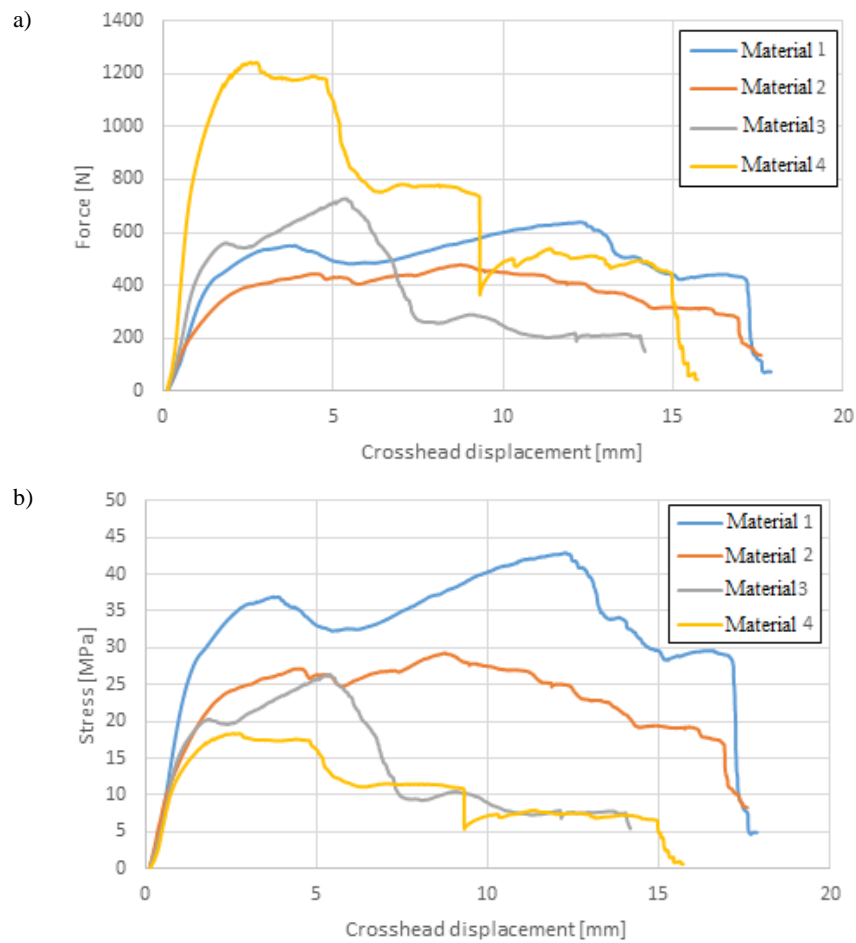
Fig. 4. Bending curves for support spacing of 60 mm: a) force – crosshead displacement, b) stress – crosshead displacement

Table 1. Flexural modulus of sandwich materials determined in two variants of the bending test

Material	Spacing of supports [mm]	Flexural modulus [GPa] (laser sensor measurement)	Flexural modulus [GPa] (deflectometer measurement)
1		3.05	3.05
2	60	2.39	2.32
3		3.88	1.56
4		1.06	0.81
1		7.44	-
2	130	6.21	-
3		4.74	-
4		2.53	-
1		10.63	12.05
2	200	9.63	11.80
3		5.04	5.31
4		3.46	2.63

The values of flexural modulus determined in the classical bend test with the deflection of the sample using a deflectometer were verified in the test during which the deflection was measured using a laser measuring head (Figs. 5a and 5b). In both cases, the determined values of flexural modulus were slightly different (Królicka & Trębacki, 2017). The use of a laser measurement system allows results to be obtained more reliably than in the case of a deflectometer coupled with an extensometer.

It was found that as the distance between supports increases, apparent flexural modulus value also increases. This is due to a change in the ratio between the normal bending and shear stresses, with a change in support spacing (Fig. 6). Calculation of the value of the modulus elasticity in bending requires the use of specimens with a sufficiently large proportion of their length to thickness, which

results in minimizing the effect of shear on specimen deformation (Lu et al., 2015). The dominant specimen failure mode in a bending test was the cracking of the skin subjected to tension (Fig. 7).

a)

b)
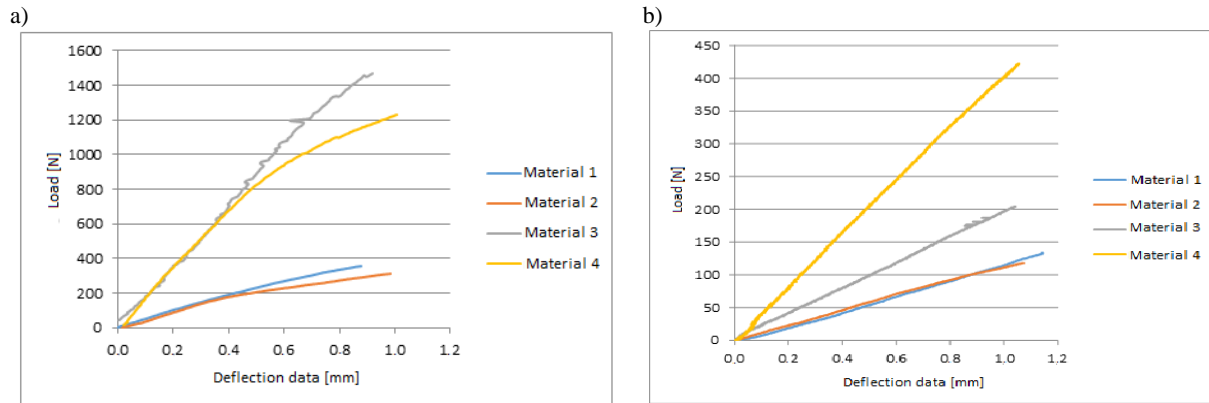
Fig. 5. Load – deflection bending curves measured using laser measuring head for the support spacing of a) 60 mm, b) 130 mm
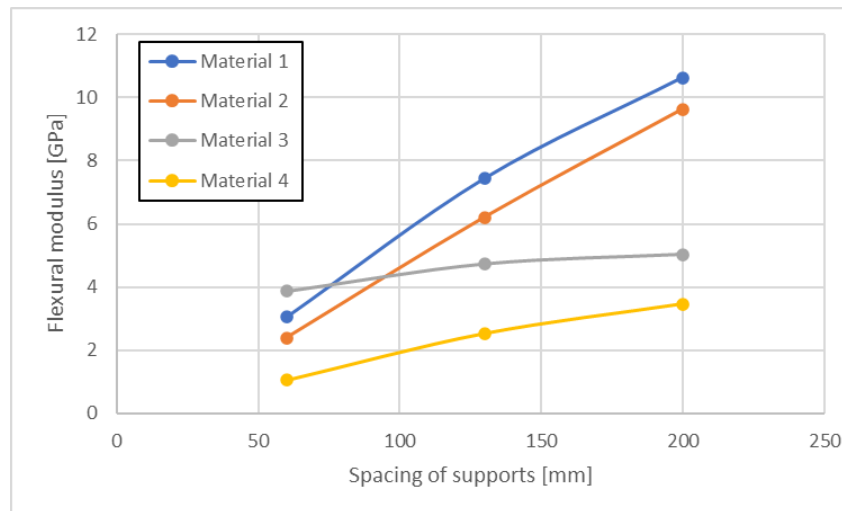
Fig. 6. The influence of supports spacing in the bending test on the value of the flexural modulus of elasticity

It was found that skin material and connection between cores and skin have significant influence on flexural modulus (Arbaoui et al., 2014). Higher values of flexural modulus for materials 1 and 2, which were increasing markedly with increasing supports spacing, resulted mainly from the higher stiffness of the reinforcement applied. More firm and stronger connection between skin and core obtained in industrial process was an additional factor enhancing flexural modulus of these materials.
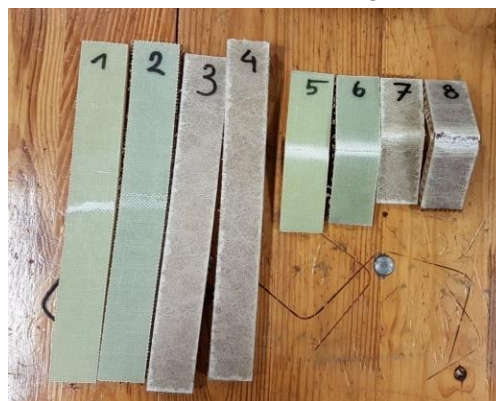
Fig. 7. Samples after three-point bending test

As a result of the tensile and compression tests, the tensile strength and compressive strength (Table 2) were determined for materials 1-4, referring the load values to the cross-section of the skins themselves. It was assumed that the direct contribution of the core to the carrying of such loads is minimal. However, it may affect the deformation of the skin, which causes differences in the stiffness of

individual materials (e.g., 1 and 2 in tension) despite the use of the same skin material. In both tests, the highest tensile and compressive strength was obtained for materials 1 and 2 and the lowest for material 4 (Figs. 8, 9). This is due to the decisive influence of the skin material properties on the resultant properties of the sandwich material in this loading mode. Although the skin material of sandwich materials 1 and 2 was the same, different tensile and compressive strength values were obtained. This is related to the different materials of their cores: the material with a honeycomb core has a higher load-carrying capacity than the material with a foam core, which makes it more resistant. Material 4, with the highest thickness, had the lowest compression and tensile strength, which may be caused by the irregular distribution of the glue between the skin and the core and by not gluing them together precisely. The particularly large difference in tensile strength between materials 3 and 4, despite the use of the same skin material, is due to the difficulty in implementing the right way to introduce the load into a thick specimen. The specimen slipped out of the grip of the testing machine and the increase in gripping force caused crushing of the specimen, so the stress distribution in the specimen was different from the uniaxial tensile state, which caused its earlier failure.

Table 2. Tensile strength and edgewise compressive strength of the materials 1-4

Material	Maximum tensile force [N]	Tensile strength [MPa]	Maximum compressive force [N]	Edgewise compressive strength [MPa]
1	23163	268	22358	133
2	32579	379	23595	140
3	9222	54.9	21007	62.5
4	6141	36.6	16464	49.0
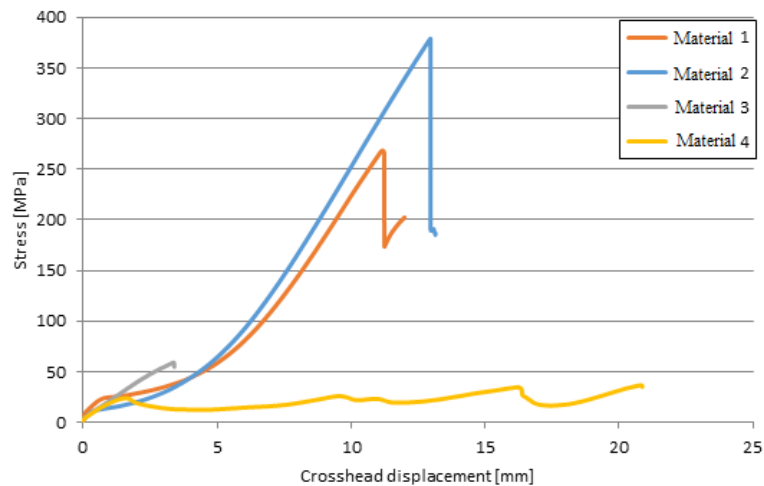
Fig. 8. Tensile stress – crosshead displacement curve
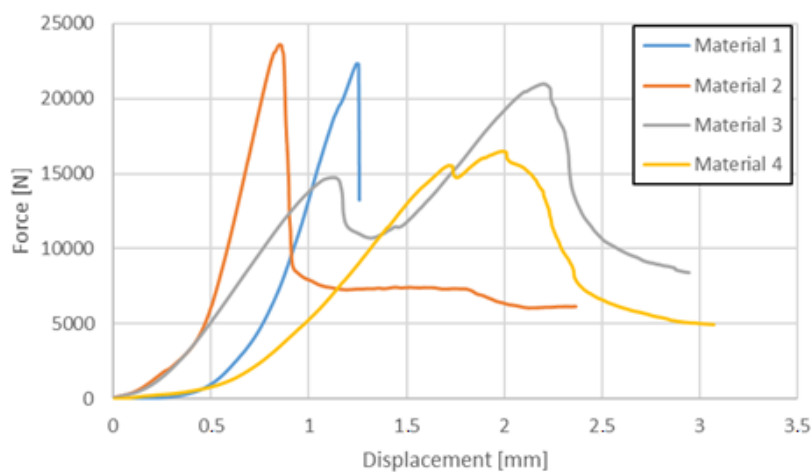
Fig. 9. Force – displacement curves in edgewise compression test

Materials 1, 2, and 4 in the tensile test were damaged by breaking the skin at a short distance from the machine grips (Fig. 10a). Only material 3 was damaged in the gauge length. In the edgewise com-

pression test, the specimens failed by cracking the skin (ASTM C364 code F) (Fig. 10b) (Muc & Nogowczyk, 2005; Greń et al., 2008). The results of the tensile and edgewise compression tests of the sandwich materials in the direction parallel to the plane of the element showed that the type of core material has some influence on the resulting stiffness of the sandwich element, especially in tension (materials 1 and 2). On the other hand, the effect of the core thickness with the same skin material and core material is insignificant (materials 3 and 4) (Banghai et al., 2015).

a)   b)
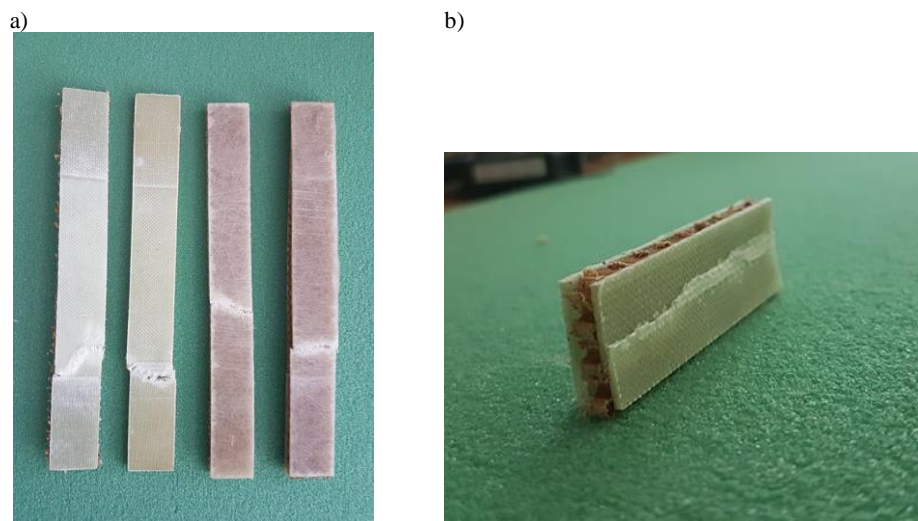
Fig. 10. a) Samples after the tensile test (from the left - material 1, material 2, material 3, material 4), b) specimen of the material no. 2 after compression test – cracked skin

4. Summary and conclusions

Based on the analysis of the obtained results of own research, the following observations and conclusions were formulated:

- Based on the results of the bending test, it was found that the highest stiffness and ability to carry bending loads, regardless of the distance between supports, is characterized by material no. 4, and secondly by material no. 3 – the thickness of the sandwich material is decisive in this case.
- Skins reinforced with glass fabric can carry much higher stress than skins reinforced with glass mats.
- The result values of flexural modulus of sandwich materials, calculated in a classical bend test and a bend test during which the deflection arrow was measured with a laser measuring head, differs slightly.
- As the distance between supports increases, the apparent flexural bending modulus value for all materials increases, due to reduced effect of shear stresses.
- As a result of the bending test, the samples were damaged due to cracking of the stretched skin
- The highest compressive and tensile strength was obtained for material 2 (laminate reinforced with glass fabric/cell core), while the lowest for material 4 (laminate reinforced with glass mat/thicker cell core).
- The honeycomb cell core material has a higher load-bearing capacity in the plane of the sandwich element than the polymer foam core material.
- The lowest tensile and compressive strength of material 4 was probably due to the uneven sticking of the core and skin. The sample slid out of the strength machine's grip, and the increase of pressure force in the grip caused its crushing, hence the stress distribution in the sample deviated from the uniaxial, causing its earlier destruction.
- In the edgewise compression test, the samples were damaged by cracking of the facesheets.

References

Antony, M.D., Prakash, A., Jagannatha Guptha, V.L., Sharma, R.S., & Mohan, B. (2012). Influence of cell size on the core shear properties of FRP honeycomb sandwich panels. *Materials and Manufacturing Processes, 27,* 169-176. https://doi.org/10.1080/10426914.2011.560227

Arbaoui, J., Schmitt, Y., Pierrot, J.L., & Royer, F.X. (2014). Effect of core thickness and intermediate layers on mechanical properties of polypropylene honeycomb multi-layer sandwich structures. *Archives of Metallurgy and Materials, 59,* 11-16. https://doi.org/10.2478/amm-2014-0002

American Society for Testing and Materials. (2010). *Standard test method for flatwise tensile strength of sandwich constructions* (Standard No. C297/C297M–04). Retrieved from https://doi.org/10.1520/C0297_C0297M-04

American Society for Testing and Materials. (2012). *Standard test method for facing properties of sandwich constructions by long beam flexure* (Standard No. D7249/D7249M-06). Retrieved from DOI: https://doi.org/10.1520/D7249_D7249M-06

American Society for Testing and Materials. (2017). *Standard test method for edgewise compressive strength of sandwich construction* (Standard No. C364/C364M–07). Retrieved from https://doi.org/10.1520/C0364-99

Banghai, J., Zhibin, L., & Fangyun, L.(2015). Failure mechanism of sandwich beams subjected to three-point bending. *Composite Structures, 133,* 739-745. https://doi.org/10.1016/j.compstruct.2015.07.056

Boczkowska, A., Kapuściński, J., Lindemann, Z., Witenberg-Perzyk, D., & Wojciechowski, S. (2016). *Kompozyty*. Oficyna Wydawnicza Politechniki Warszawskiej.

Grabarski, J. (2001). *Materiały i kompozyty niemetalowe*. Oficyna Wydawnicza Politechniki Warszawskiej.

Greń, K., Szatkowski, P., & Chłopek, J. (2008). Characteristics of failure mechanisms and shear strength of sandwich composites. *Composites Theory and Practice, 16*(4), 255-259.

Królicka, A., & Trębacki, K. (2017). Próby wytrzymałościowe kompozytów polimerowych. *Autobusy : technika, eksploatacja, systemy transportowe, 18*(9), 97-100.

Lu, C., Zhao, M., Jie, L., Wang, J., Gao, Y., Cui, X., & Ping Chen, P. (2015). Stress distribution on the composite honeycomb sandwich structure suffered from bending load. *Procedia Engineering, 99*, 405-412. https://doi.org/10.1016/j.proeng.2014.12.554

Mayer, P., & Kaczmar, W. (2008). Właściwości i zastosowania włókien węglowych i szklanych. *Tworzywa Sztuczne i Chemia, 6*, 52-56 .

Muc, A., & Nogowczyk, R. (2005). Formy zniszczenia konstrukcji sandwiczowych z okładzinami wykonanymi z kompozytów. *Kompozyty, 5*(4), 31-35.

Ochelski, S. (2004). *Metody doświadczalne mechaniki kompozytów konstrukcyjnych*. Wydawnictwo Naukowo-Techniczne.

Rajczyk, M., & Stachecki, B. (2011). Współczesne materiały kompozytowe wybrane kierunki rozwoju technologii. *Budownictwo o Zoptymalizowanym Potencjale Energetycznym, 8*, 202-211.

Sawal, N., Nazr, A., & Akil, H. (2015). Effect of cell size material on the mechanical properties of honeycomb core structure. *International Journal of Science and Research, 4*(2), 80-84.

Woźniak, D., & Kukiełka, L. (2014). Kompozyty w technice w aspektach materiałów nowej generacji. A*utobusy: technika, eksploatacja, systemy transportowe, 15*(6), 292-296.

Badania Właściwości Mechanicznych Wybranych Polimerowych Kompozytów Przekładkowych

Streszczenie

Celem pracy było określenie wpływu czynników materiałowych i geometrycznych wybranych kompozytów przekładkowych na ich właściwości mechaniczne. Pierwsza badana para materiałów przekładkowych została wykonana metodą infuzji przemysłowej i składała się z żywicy epoksydowej wzmocnionej 7 warstwami tkaniny szklanej (okładki) z rdzeniem z pianki PVC lub aramidowego plastra miodu. Druga para materiałów została przygotowana ręcznie i składała się z żywicy poliestrowej wzmocnionej matą szklaną (okładki) z rdzeniem aramidowym o strukturze plastra miodu o różnej grubości. Celem pracy było określenie wpływu czynników materiałowych i geometrycznych wybranych kompozytów przekładkowych na ich właściwości mechaniczne. Właściwości mechaniczne określono w próbach statycznych zginania, ściskania i rozciągania. W każdym przypadku oceniono sposób niszczenia badanych materiałów kompozytowych. W przypadku kompozytów z okładkami z żywicy epoksydowej zastosowanie rdzenia aramidowego o strukturze plastra miodu spowodowało zwiększenie wytrzymałości na rozciąganie i ściskanie. W przypadku materiałów z okładkami z żywicy poliestrowej i rdzeniami o strukturze plastra miodu stwierdzono, że zwiększenie grubości rdzenia dawało większą sztywność zginania, ale wytrzymałość na rozciąganie i zginanie uległy zmniejszeniu.

Słowa kluczowe: kompozyty przekładkowe, właściwości mechaniczne, próby statyczne zginania, próby statyczne ściskania, próby statyczne rozciągania

Original Research

Influence of Input Parameters on the Coefficient of Friction during Incremental Sheet Forming of Grade 5 Titanium Alloy Sheets

Marcin Szpunar [1,*] iD **, Paulina Szawara** [2] iD **, Piotr Myśliwiec** [2] iD **, Robert Ostrowski** [2] iD

[1] Doctoral School of Engineering and Technical Sciences at the Rzeszow University of Technology, Rzeszow University of Technology, al. Powst. Warszawy 12, 35-959 Rzeszów, Poland

[2] Department of Materials Forming and Processing, Rzeszow University of Technology, al. Powst. Warszawy 8, 35-959 Rzeszów, Poland; p.szawara@prz.edu.pl (P. Szawara); p.mysliwiec@prz.edu.pl (P. Myśliwiec); rostrows@prz.edu.pl (R. Ostrowski)

* Correspondence: d547@stud.prz.edu.pl

Abstract

This research paper focuses on investigating the influence of input parameters on the coefficient of friction (COF) during incremental sheet forming (ISF) of grade 5 titanium alloy sheet. Titanium alloys are widely used in various industries due to their corrosion resistance and strength to weight ratio. ISF is a flexible and cost effective process for producing complex shapes. The aim of this study was to gain insight into the frictional conditions during ISF that affect formability, surface quality, and overall process performance. The experiments were carried out using a combination of MoS_2 lubrication and friction stir rotation-assisted heating. COF was measured using a high precision piezoelectric dynamometer, taking into account axial and horizontal components of forming force. A split-plot design was used and 25 runs were performed to obtain the COF for each run. The results of the study provide valuable information on the relationship between input parameters and COF, contributing to the understanding of the frictional conditions in the ISF.

Keywords: ANOVA, coefficient of friction, incremental sheet forming, titanium alloys

1. Introduction

Titanium alloys are widely used in a variety of industries, including aerospace, automotive, orthopaedic, and dental, because of their exceptional corrosion resistance and impressive strength-to-weight ratio. Among the various techniques used to form titanium and its alloys, incremental sheet forming (ISF) stands out as a flexible and advantageous process compared to traditional sheet forming methods. It plays an important role in modern manufacturing by enabling the production of complex shapes at reduced cost (Oleksik et al., 2021). Using a universal set of tools, ISF allows the creation of a wide variety of shapes, resulting in increased production flexibility and reduced tooling costs. It also makes it easier to achieve higher levels of stress. However, it is most economically viable for low-volume production. This includes metal (Trzepieciński et al., 2022a), polymer (Rosca et al., 2021) and composite (Harhash & Palkowski, 2021) sheets. The main advantages associated with ISF include the ability to form elements on conventional CNC machines such as lathes or milling machines (Cheng et al., 2020; Jadhav et al., 2003).

In the ISF process, a circular forming tool gradually shapes the sheet by executing a coordinated motion around the stationary workpiece, The tool then performs a depth movement with a specified step size, forming the component by traversing the next horizontal trajectory at a feed rate (Harfoush et al., 2021; Patel and Gandhi, 2022). In ISF, friction plays a critical role in the interaction between the tool and the workpiece (Duflou et al., 2017). Friction not only influences the forming limit, but also the surface quality of the resulting parts (Szewczyk and Szwajka, 2023; Więckowski et al., 2023). As

surface quality has a significant impact on the aesthetics, performance and service life of metal structures, it warrants serious attention.

The lubricants used in ISF are the same as those used in conventional sheet metal forming processes and are selected mainly on the basis of factors such as pressure values, material grade of the workpiece/tool material pair and tool speed (Najm et al., 2021). Several factors come into play when considering the potential use of the ISF method and ensuring forming accuracy. These include technological parameters (e.g., tool diameter, step size, tool rotational speed, friction conditions), product design factors (e.g., sheet thickness, die geometry) and mechanical parameters of the workpiece (e.g., work hardening, material anisotropy, Young's modulus) (Najm and Paniti, 2020). Higher tool rotational speeds allow greater plastic deformation to be applied to the sheet material without the risk of cracking, making them ideal for forming thin sheets with limited plasticity (Martins et al., 2008; Sbayti et al., 2020).

The challenge of achieving suitable forming conditions arises from the contact between relatively low strength materials and high hardness, high strength tools (Pepelnjak et al., 2022). Najm and Paniti (2021) used an artificial neural network to investigate and determine the formability of the workpiece and the geometry of the forming tools. They also derived an analytical equation for each output based on the weight and bias of the most accurate network prediction. Tooling characteristics were found to play an essential role in all predictions and to have a significant impact on the final products. Najm et al. (2021) investigated the effect of forming tool diameter, tool rotational speed, feed rates and coolant type on the hardness of EN AW-1100 aluminium alloy sheets in ISF. Various coolant oils and greases were analysed at the same feed rates and the study showed that the use of coolant oil increased hardness whereas the use of grease decreased hardness. Milutinović et al. (2021) fabricated a X6Cr17 stainless steel denture base plate for a full maxillary prosthesis using a lost wax technique. An ordinary form of mineral oil was selected as the lubricating agent in this particular case. Experimental tests on the surface roughness of the inner surface of the cup showed that the step size had a significant influence on the surface quality. Machine learning based procedure to predict result of surface roughness parameters (Ra, Rz) for heat assisted ISF titanium grade 5 was proposed by Bautista-Monsalve et al. (2021). The authors confirmed algorithm prediction potential with an experiment results. Sbayti et al. (2022) investigated the ISF process of a Ti6Al4V titanium alloy acetabular cup at high temperatures using finite element based simulations and an optimisation procedure. The effects of four key process parameters – coefficient of friction (COF), processing temperature, step depth and tool diameter - on the final part were analysed. The computational results showed that moth-flame optimisation, multiverse optimisation and Harris Hawk optimisation provided highly competitive geometry optimisation results. Popp et al. (2021) investigated the sheet bending mechanism in the ISF of Al-Cu4PbMgMn aluminium alloy blanks using finite element based analysis. The study showed that the shape of the retaining rings significantly influenced the final geometric accuracy of the parts produced by ISF. A novel method was presented by McPhillimy et al. (2022). The authors applied laser metal deposition to thicken locally titanium grade 2 sheet before incremental forming process. Such a treatment allowed them to improve drawpiece thickness homogeneity, but also caused early fracture phenomenon especially at high wall angles.

Numerous research studies have focused on parameter optimisation for incremental sheet forming of pure titanium sheets. Hussain et al. (2008) found that increasing the feed rate or incremental step depth reduced the formability, while increasing the tool diameter improved it. Ajay (2020) also confirmed that these input factors had the most significant influence on process parameters such as, wall angle, surface roughness and thickness. The increased relative tool speed was found to be critical to generate forming forces and ensuring successful forming commercially pure titanium sheets without cracking (Zwolak et al., 2022). However an elevated tool rotation causes increase in surface roughness Rz parameter of the formed sheets, while step size is a key factor affecting axial and in-plane forming force components (Szpunar et al., 2021). Trzepieciński et al. (2022b) studied input parameters of ISF titanium grade 5 sheets to find optimal one. The authors found that proper feed rate and tool rotational speed setup allows to achieve greater deformation. Kim et al. (2022) developed an CPB06ex2 anisotropic and asymmetric yield function for the titanium grade 5 sheet. The excellence was presented by the correlation with the experiment and finite element method results of the surface profile. Naranjo et al. (2017) conducted the analysis of ISF titanium grade 5 at elevated temperatures. They found not significant correlation between the temperature and surface quality. Ambrogio et al. (2018) investigated super plastic forming and ISF to obtain titanium protests without failure. On the other hand Racz et al. (2018) presented decision-making method to select the most favourable manufacturing method for

titanium Ti6Al4V alloy dedicated for medical devices with forming at room temperature inclusion. Other studies have investigated the microstructural effects after ISF of pure titanium sheets. Kumar et al. (2020) investigated the magnitude and state of residual stresses in commercially pure grade 2 titanium after forming. They observed that increasing wall angles and incremental step depth resulted in higher residual tensile stresses. Li et al. (2023) carried out and experiment with titanium grade 1 perforated sheets. The authors found the limit for the wall angle as 60°, while with 45° good thickness distribution and geometric accuracy can be obtained. Mishra et al. (2021) analysed the evolution of microstructure and texture and found that prismatic slip dominated in the ISF of pure titanium, while twinning occurrence varied with several parameters and was heterogeneous. Yoganjaneyulu et al. (2021) analysed the effect of tool rotation on mechanical properties and microstructure and found that grain elongation and orientation followed the incremental step depth. They also found that tool rotation did not affect grain size, but higher rotation rates induced an effect of strain hardening by denser in dislocations.

A review of the literature indicates that research into the ISF of titanium sheets has focused primarily on investigating the influence of input parameters on geometric accuracy and mechanical properties. However, studies that specifically investigate friction conditions, quantified by COF, are relatively limited. Therefore, the aim of this research is to investigate the influence of the ISF input parameters: cavity pressure, tool rotational speed, feed rate and step size on the COF between a hemispherical solid carbide tool and a grade 5 titanium alloy sheet. By analysing the COF, this study aims to gain insight into the frictional conditions during the ISF process, which play a crucial role in the formability limits, surface quality and overall process performance.

2. Materials and Methods

The experimental material used was a 0.8-mm-thick Ti-6Al-4V titanium alloy sheet. At room temperature, the microstructure of this alloy is predominantly hexagonal closed packed (HCP) for the α phase and body centred cubic (BCC) for the β phase. The chemical composition of the sheets material presents Table 1.

Table 1. Chemical composition of the sheets material within % weight content (Titanium, 2023).

Component	Al	V	Fe	O	C	N	H	Ti
Wt. %	5.5−6.75	3.5−4.5	<0.4	<0.2	<0.08	<0.03	<0.015	remainder

This Ti-based alloy, known as a two-phase (α-β) alloy, is widely used in various fields such as turbine blades, discs, rings and structural components in the aerospace industry. Furthermore, Ti-6Al-4V is widely used as a biocompatible implant in medical applications. It has desirable properties such as high corrosion resistance, good weldability, excellent strength and a low modulus of elasticity. However, due to its complex microstructure at room temperature, this alloy is typically formed at elevated temperatures. Mechanical properties of the sheets material is presented in Table 2.

Table 2. Basic mechanical properties of the sheets material (Titanium, 2023).

Density	Ultimate Tensile Strength	Yield Tensile Strength	Elastic modulus	Hardness
4.43 g/cm^3	950 MPa	880 MPa	113.8 GPa	349 HV

The experiments involved the forming of drawpieces using a combination of ISO 6743/12 QB oil-based lubrication and friction stir rotation-assisted heating in a warm ISF. A die consisting of a housing and a blank holder were used to secure the displacement of the workpiece flange. Figure 1 shows the experimental setup. The blank holder was securely mounted with screws. An electric oil heater was placed within the die cavity and the oil pressure was maintained at a constant level during the forming process through a valve. The forming device was mounted on the bed of a PS95 CNC vertical milling machine. A 100 mm diameter workpiece was used to form conical truncated cones with varying wall angle from (Fig. 2). A tungsten carbide material was selected for the tool with a rounded tip with a radius of 4 mm. The tool was mounted in the face mill using an ER32 collet. To minimise friction, in the experiments a dry grease-free antifriction spray containing MoS_2 was used. This lubricant is temperature resistant from −185°C up to 400°C. Before applying the lubricant, the surfaces were thoroughly cleaned and degreased. During the process, the tool followed a spiral path as

it indented into the workpiece. The path of the tool (Fig. 1), was generated using NX CAM software. The tool path was generated based on a numerical model that represents the desired shape of the part.
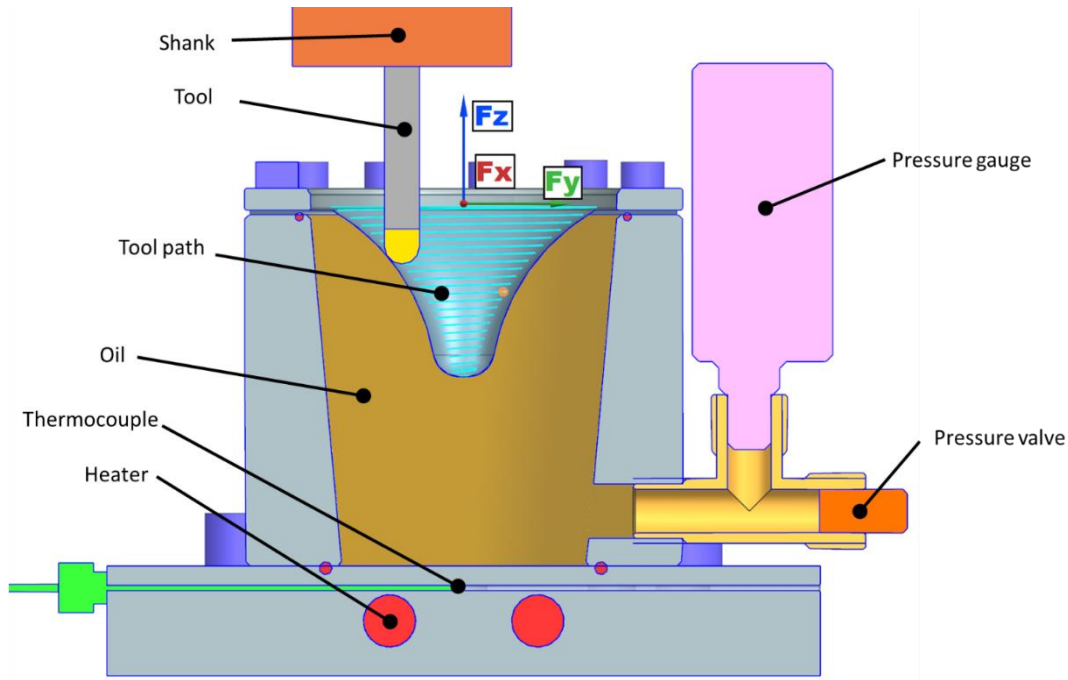
Fig. 1. Heat assisted incremental forming device.
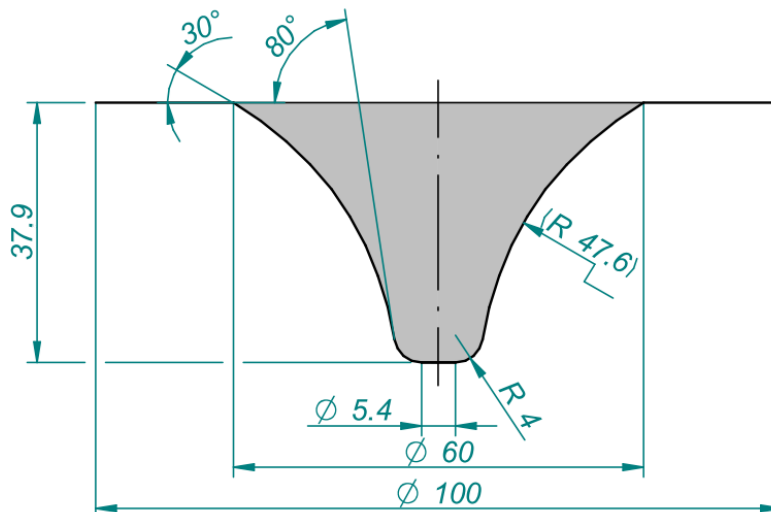
Fig. 2. Desired drawpice shape with varying wall angle from 30° to 80°.

A high-precision piezoelectric dynamometer from Kistler Holding AG in Winterthur, Switzerland, was used to measure the axial force (F_z) and the horizontal components of the forming force (F_x and F_y). This dynamometer has a maximum sampling rate of 200 kHz per channel.

The value of the COF was determined using the following equation (Decultot, 2011; Saidi et al., 2015):

$$\mu = \frac{\sqrt{F_x{}^2 + F_y{}^2}}{\sqrt{F_z{}^2}} \tag{1}$$

Equation (1) is a commonly used method for predicting the COF by considering the axial and horizontal forces experienced during the ISF process. This equation has been widely used by many researchers in this field. Shin (2021) in his thesis, carried out a finite element analysis (FEA) and found that the coefficient of friction had a minimal effect (less than 10%) on the axial force. However,

higher COF values were associated with increased horizontal forces. Durante et al. (2009) also used this equation to determine the COF in sliding tests between an ISF tool and 20 mm wide specimens. Hamilton (2010) used the same equation in his thesis, which was subsequently validated by FEM analysis by Li et al. (2014).

The experiment used a split-plot design with a I-optimal criterion. There were 25 runs, carefully selected to optimise the design and efficiently capture relevant information. The factors in the experiment were coded to facilitate analysis. The low level of each factor was coded as −1, while the high level was coded as +1. The factors and their respective units were as shown in Table 3. The range of input factors was selected by initial tests while cavity pressure was limited by valve and gauge restrictions.

Table 3. The input factors range with equivalent coded values.

Factor	Name	Units	Min.	Max.	Coded Low	Coded High	Mean	Standard deviation
a	cavity pressure	bar	1	4	−1 ↔ 1	+1 ↔ 4	2.40	1.04
B	tool rotational speed	rpm	100	1000	−1 ↔ 100	+1 ↔ 1000	550.17	363.50
C	feed rate	mm/min	500	2000	−1 ↔ 500	+1 ↔ 2000	1274	619.85
D	step size	mm	0.1	0.5	−1 ↔ 0.1	+1 ↔ 0.5	0.3031	0.1632

3. Results and Discussion

In this experiment, a total of 25 consecutive runs were performed, allowing the researchers to obtain the COF for each run. The COF response was measured as the output variable of interest. Table 4 shows the input factors for each run along with the corresponding COF response.

Table 4. Plan of the experiment with input factors and COF response.

Run	Factor 1 (a: cavity pressure, bar)	Factor 2 (B: tool rotational speed, rpm)	Factor 3 (C: feed rate, mm/min)	Factor 4 (D: step size, mm)	Response (COF)
1	2	1000	1475	0.10	0.12
2	2	100	2000	0.10	0.17
3	2	514	1370	0.31	0.11
4	2	1000	500	0.10	0.1
5	2	590	1175	0.35	0.12
6	2	100	2000	0.50	0.14
7	2	100	500	0.50	0.12
8	2	122	1108	0.10	0.09
9	2	1000	1145	0.33	0.14
10	2	559	2000	0.26	0.11
11	4	100	2000	0.30	0.22
12	4	595	620	0.50	0.2
13	4	100	883	0.14	0.14
14	4	757	1550	0.10	0.13
15	4	1000	2000	0.37	0.18
16	1	581	538	0.50	0.11
17	1	550	500	0.10	0.08
18	1	1000	2000	0.50	0.07
19	1	100	1423	0.32	0.15
20	1	762	2000	0.12	0.11
21	3	1000	2000	0.50	0.1
22	3	100	500	0.27	0.1
23	3	680	500	0.20	0.12
24	3	1000	500	0.50	0.2
25	3	343	1565	0.50	0.13

The coefficient of friction was estimated by calculating the mean value from the stabilised region of the forming process (Fig. 3). This approach ensured that the COF measurement captured the representative behaviour of the system by focusing on a consistent and reliable part of the forming process. By considering the stabilised region, any transient or initial variations were minimised, providing a more accurate estimate of the COF for each run.

For the purposes of the experiment a level of significance $\alpha = 0.05$ has been selected. The summary (Table 5) provides an overview of the sequential p-values, adjusted R^2 and predicted R^2 for different types of model terms. In your case, the quadratic model was selected and a backward elimination algorithm was applied to remove model terms with p-values greater than 0.05, following the model hierarchy. Based on the p-values and the model hierarchy, the quadratic model was selected as the most appropriate model type. The backward elimination algorithm was then used to remove model terms with p-values greater than 0.05, resulting in a refined model.

Analysis of the experimental data revealed important findings (Table 6). The model used in the study showed a significant fit, as indicated by the low p-value (less than 0.0001) and the high F-value (39.47), with a sum of squares of 0.034. This suggests that the model effectively captures the relationship between the factors and the response variable.
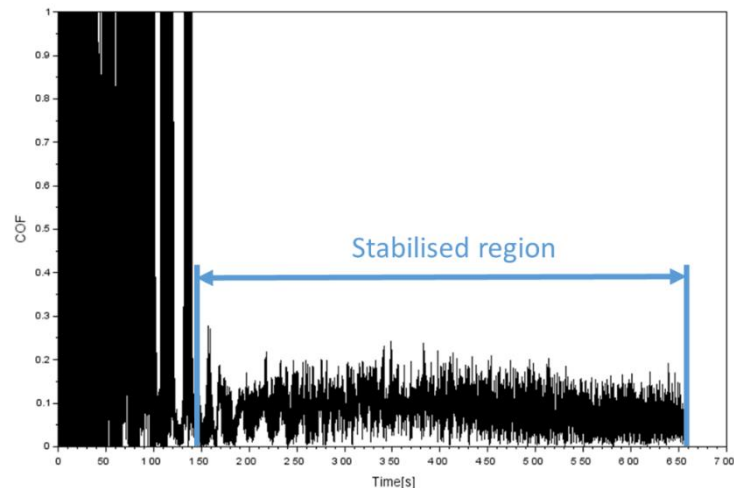
Fig. 3. Stabilised range of the COF selected for analysis.

Table 5. Criteria of model selection.

Source	Sequential p-value	Adjusted R²	Predicted R²	Decision
Linear	0.0252	0.2947	0.0282	Rejected
2FI	0.0048	0.6919	0.3119	Rejected
Quadratic	0.0006	0.9299	0.7922	Selected

Table 6. Analysis of variance (ANOVA) table for the reduced quadratic model.

Source	Sum of Squares	Degrees of freedom	Mean Square	F-value	p-value	
Model	0.0339	10	0.0034	39.47	< 0.0001	significant
a - cavity pressure	0.0083	1	0.0083	97.06	< 0.0001	
B - tool rotational speed	8.823E-07	1	8.823E-07	0.0103	0.9207	
C – feed rate	0.0002	1	0.0002	2.61	0.1283	
D - step size	0.0026	1	0.0026	30.52	< 0.0001	
aD	0.0017	1	0.0017	19.35	0.0006	
BC	0.0082	1	0.0082	95.12	< 0.0001	
CD	0.0054	1	0.0054	62.70	< 0.0001	
a²	0.0029	1	0.0029	33.45	< 0.0001	
B²	0.0026	1	0.0026	30.68	< 0.0001	
D²	0.0015	1	0.0015	17.20	0.0010	
Residual	0.0012	14	0.0001			
Correlation Total	0.0351	24				
				R²	0.9657	
Standard deviation	0.0093			**Adjusted R²**	0.9413	
Mean	0.1304			**Predicted R²**	0.8872	
C.V. %	7.11			**Adeq Precision**	25.3212	

Among the individual factors, a - cavity pressure had a highly significant effect on the response variable, with a large sum of squares (0.0083) and a high F-value (97.06). This means that variations in cavity pressure have a significant effect on the COF response. On the other hand, the tool rotational speed (B) had a negligible effect on the response, with a very small sum of squares ($8.823 \cdot 10^{-7}$) and

a low F-value (0.0103). The p-value of 0.9207 further confirms that changes in tool speed do not significantly affect the response variable. Similarly, the feed rate (C) had little effect on the response as indicated by its relatively low sum of squares (0.0002) and F-value (2.61). The p-value of 0.1283 suggests that changes in feed rate have a relatively small effect on the response. In contrast, the step size (D) had a significant effect on the response, with a substantial sum of squares (0.0026) and a high F-value (30.52). The low p-value (less than 0.0001) further supports the importance of this factor in influencing the response variable. The interactions between the factors were also examined. The interactions aD, BC and CD showed significant effects on the response, as evidenced by their large sum of squares and high F-values. These results highlight the importance of considering the combined influence of multiple factors rather than analysing them individually. In addition, the quadratic terms a^2, B^2 and D^2 also showed a significant influence on the response, with substantial sums of squares and high F-values. This suggests that the relationship between these factors and the response variable is nonlinear. The overall fit of the model was evaluated using the R^2 value, which measures the proportion of variability in the response that is explained by the model. In this case, the R^2 value was determined to be 0.9657, indicating that the model explains approximately 96.57% of the variation in the response variable.
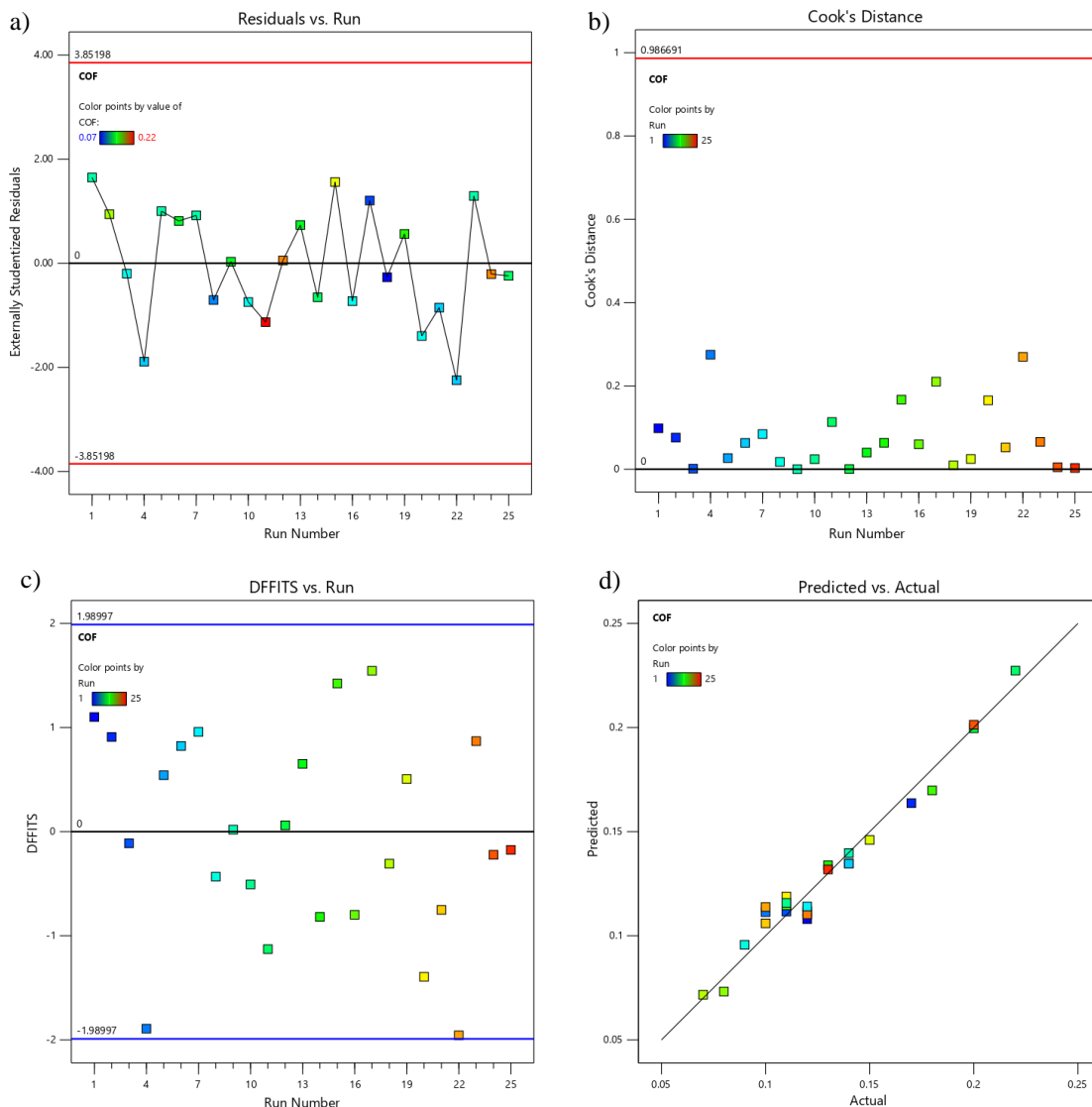
Fig. 4. Diagnostic plots: a) residuals vs. run, b) Cook's distance, c) DFFITS vs. run, d) predicted vs. actual.

The plot of the externally studentized residuals versus the order of the trials (Fig. 4a) is used to identify any lurking variables that may have influenced the response during the current trials. In this graph, a random scatter pattern is desirable, indicating that there are no systematic influences or time-related variables affecting the response. Cook's distance is a measure of the influence of each data

point in a regression model. It takes into account both the leverage (how extreme the predictor variables are) and the residual (the difference between the observed and predicted values) of each observation. Cook's distance provides a summary of how much the regression model would change if a particular observation were removed from the data set (Fig. 4b). The difference in fit(s) (DFFITS) statistic measures the influence of each observation on the predicted values of the regression model. Quantifies the change in the predicted value if the i-th observation is removed from the analysis. A larger value of DFFITS indicates that the observation has a greater influence on the predicted values within its neighbourhood in the design space (Fig. 4c). The predicted vs. actual graph compares the predicted response values from the regression model with the actual response values obtained during the experiment. This graph helps to assess the accuracy of the model by examining how closely the predicted values match the actual values. It can reveal any discrepancies or patterns that may indicate areas where the model's predictions differ from the observed data (Fig. 4d). The diagnostic plots contain no outliers and they are in line with expectations for the chosen model.
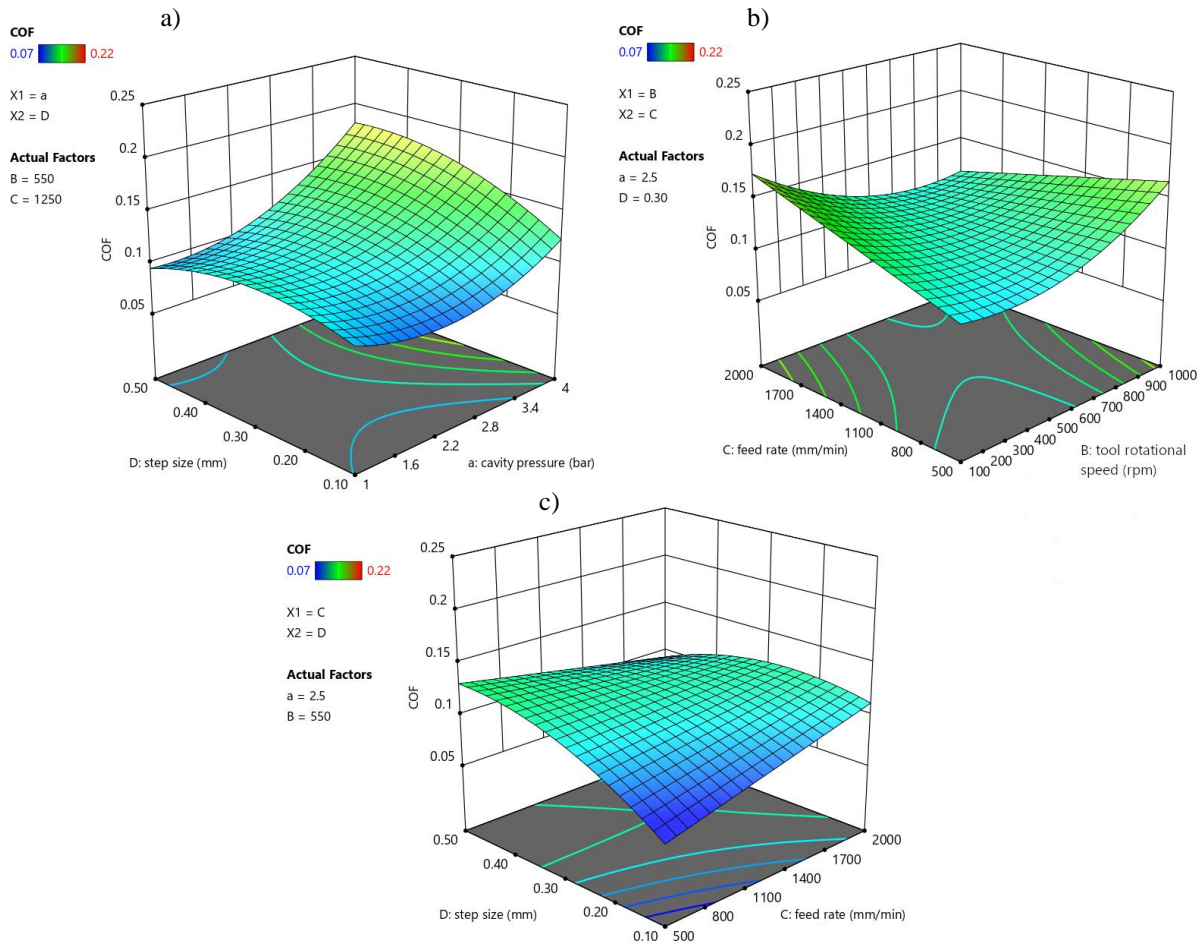
Fig. 5. Response surfaces characterise COF values for the obtained model by the inputs: a) cavity pressure and step size, b) feed rate and tool rotational speed, c) step size and feed rate.

Response surfaces provide valuable information on the relationship between the input factors and coefficient of friction. By analysing these surfaces, we can observe the effect of different input factors on the COF. One notable finding is that higher cavity pressure has a positive effect on COF, indicating that increased pressure leads to higher friction levels. This suggests that careful control and optimisation of cavity pressure are critical in managing friction during the forming process. Furthermore, the response surfaces show that the combination of the correct tool speed and feed rate can effectively reduce friction. This highlights the importance of selecting appropriate tool speeds and feed rates to minimise frictional forces and improve overall system performance. To further illustrate the influence of step size and feed rate on COF, a graphical representation is shown in Fig. 5. This figure provides a visual understanding of how variations in step size and feed rate affect the COF. By examining the trends and patterns in Fig. 5, valuable information can be gained about the optimal values of step size and feed rate that will result in the desired COF levels. Overall, response surface analysis provides valuable information about the relationship between input factors and COF, allowing engineers and

researchers to make informed decisions and optimise the forming process to achieve the desired friction characteristics.

4. Conclusions

In this research article, the influence of input parameters on the COF during the ISF process of a grade 5 titanium alloy sheet was investigated. The goal was to gain insight into the frictional conditions which allows for better understanding of contact conditions between tool and workpiece. Results obtained in this research are helpful for process modelling with finite element method. The main findings and conclusions of this study are summarised as follows:

- ANOVA was performed to determine the significance of each input parameter and their interactions on the COF. It was found that all four input parameters contributed significantly to the variation in COF. Furthermore, interactions between these parameters also have a significant effect on the COF.
- The input parameters, including cavity pressure, tool rotational speed, feed rate and step size, have a significant influence on the COF during the ISF process. These parameters play a crucial role in determining the frictional conditions.
- A reduced quadratic model was chosen to represent the relationship between the input parameters and the COF. This model accurately captures the nonlinear behaviour and interactions between the input factors. The obtained model, incorporating the input parameters, exhibited a high coefficient of determination R^2 (0.9657), indicating that approximately 96.57% of the variability in the coefficient of friction was explained, with further validation through adjusted R^2 (0.9413) and predicted R^2 (0.8872) values. The coefficients of the model can be used to predict the COF within the investigated parameter range.
- Cavity pressure has a significant effect on COF. Higher cavity pressure values tend to increase the COF, indicating a higher friction between the tool and the titanium alloy sheet. This finding suggests that controlling the cavity pressure can help to optimise frictional conditions and improve overall process performance.
- The tool rotational speed is another critical factor that affects COF. Higher tool speeds result in higher COF values, indicating increased friction during the forming process. This means that the adjustment of the tool speed can be used to control frictional conditions and achieve the desired surface quality and formability.
- Feed rate has a marked effect on COF. Higher feed rates tend to reduce the COF, indicating a lesser friction between the tool and the sheet. This suggests that adjusting the feed rate can help to optimise the frictional conditions and improve the overall performance of the ISF process.
- The step size plays an important role in determining the COF. Larger step sizes are associated with higher COF values, indicating increased friction during the forming process. Therefore, controlling the step size can be a critical parameter in achieving the desired frictional conditions and improving the formability and surface finish of the formed components.

The results of this study provide information on the frictional behaviour of the grade 5 titanium alloy sheet during ISF. Understanding the COF can help to optimise process parameters to improve formability limits, surface quality and overall process performance. Although this study investigated the influence of input parameters on the COF, more research is needed to investigate the effects of other factors, such as lubricant type and tool geometry, on frictional conditions during ISF. In addition, investigating the relationship between COF and other performance indicators, such as surface roughness and forming forces, would contribute to a comprehensive understanding of the ISF process.

References

Ajay, C.V. (2020). Parameter optimization in incremental forming of titanium alloy material. *Transactions of the Indian Institute of Metals,* 73(9), 2403–2413. https://doi.org/10.1007/s12666-020-02044-1

Ambrogio, G., Palumbo, G., Sgambitterra, E., Guglielmi, P., Piccininni, A., Napoli, L.D., Villa, T., & Fragomeni, G. (2018). Experimental investigation of the mechanical performances of titanium cranial prostheses manufactured by super plastic forming and single-point incremental forming. *The International Journal of Advanced Manufacturing Technology, 98*, 1489–1503. https://doi.org/10.1007/s00170-018-2338-6

Bautista-Monsalve, F., García-Sevilla, F., Miguel, V., Naranjo, J., & Manjabacas, M.C. (2021). A novel machine-learning-based procedure to determine the surface finish quality of titanium alloy parts obtained by heat assisted single point incremental forming. *Metals*, *11*(8),1287. https://doi.org/10.3390/met11081287

Cheng, Z., Li, Y., Xu, C., Liu, Y., Ghafoor, S., & Li, F. (2020). Incremental sheet forming towards biomedical implants: A review. *Journal of Materials Research and Technology, 9*(4), 7225–7251. https://doi.org/10.1016/j.jmrt.2020.04.096

Decultot, N. (2011). *Formage incrémental de tôle d'aluminium: Étude du procédé à l'aide de la mesure de champs et identification de modèles de comportement.* Universite de Toulouse.

Duflou, J.R., Habraken, A.M., Cao, J., Malhotra, R., Bambach, M., Adams, D., Vanhove, H., Mohammadi, A., & Jeswiet, J. (2017). Single point incremental forming: state-of-the-art and prospects. *International Journal of Material Forming, 11*, 743–773. https://doi.org/10.1007/s12289-017-1387-y

Durante, M., Formisano, A., Langella, A., & Minutolo, F. (2009). The influence of tool rotation on an incremental forming process. *Journal of Materials Processing Technology, 209*, 4621–4626. https://doi.org/10.1016/j.jmatprotec.2008.11.028

Hamilton, K.A.S. (2010). *Friction and External Surface Roughness in Single Point Incremental Forming: A study of surface friction, contact area and the 'orange peel' effect*. Master of Applied Sciences Thesis, Queen's University, Kingston, Ontario, Canada. Retrieved from https://qspace.library.queensu.ca/handle/1974/5425 (accessed on 19 May 2023).

Harfoush, A., Haapala, K.R., & Tabei, A. (2021). Application of artificial intelligence in incremental sheet metal forming: A review. *Procedia Manufacturing*, *53*, 606–617. https://doi.org/10.1016/j.promfg.2021.06.061

Harhash, M., & Palkowski, H. (2021). Incremental sheet forming of steel/polymer/steel sandwich composites. *Journal of Materials Research and Technology*, *13*, 417–430. https://doi.org/10.1016/j.jmrt.2021.04.088

Hussain, G., Gao, L., & Zhang, Z. Y. (2008). Formability evaluation of a pure titanium sheet in the cold incremental forming process. *The International Journal of Advanced Manufacturing Technology*, *37*(9), 920–926. https://doi.org/10.1007/s00170-007-1043-7

Jadhav, S., Goebel, R., Homberg, W., & Kleiner, M. (2003). Process optimization and control for incremental forming sheet metal forming. *Proceedings of the Conference of the International Deep Drawing Research Group*, Bled, Slovenia, 11-15 May 2003, pp. 165–171.

Kim, M., Lee, H., & Park, N. (2022). Evaluation of deformation for titanium alloy sheet in single point incremental forming based on asymmetric yield function. *International Journal of Material Forming*, *15*(5), 66. https://doi.org/10.1007/s12289-022-01712-5

Kumar, R., Kumar, G., & Singh, A. (2020). An assessment of residual stresses and micro-structure during single point incremental forming of commercially pure titanium used in biomedical applications. *Materials Today: Proceedings*, *28*, 1261–1266. https://doi.org/10.1016/j.matpr.2020.04.147

Li, Y., Liu, Z., Daniel, W.J.T. (Bill), & Meehan, P.A. (2014). Simulation and experimental observations of effect of different contact interfaces on the incremental sheet forming process. *Materials and Manufacturing Processes*, 29(2), 121–128. https://doi.org/10.1080/10426914.2013.822977

Li, R., Wang, T., & Li, F. (2023). The formability of perforated TA1 sheet in single point incremental forming. *Materials*, *16*(8), 3176. https://doi.org/10.3390/ma16083176

Martins, P. A.F., Bay, N., Skjoedt, M., & Silva, M.B. (2008). Theory of single point incremental forming. *CIRP Annals*, 57(1), 247–252. https://doi.org/10.1016/j.cirp.2008.03.047

McPhillimy, M., Yakushina, E., & Blackwell, P. (2022). Tailoring titanium sheet metal using laser metal deposition to improve room temperature single-point incremental forming. *Materials*, *15*(17), 5985. https://doi.org/10.3390/ma15175985

Milutinović, M., Lendjel, R., Baloš, S., Zlatanović, D.L., Sevšek, L., & Pepelnjak, T. (2021). Characterisation of geometrical and physical properties of a stainless steel denture framework manufactured by single-point incremental forming. *Journal of Materials Research and Technology*, *10*, 605–623. https://doi.org/10.1016/j.jmrt.2020.12.014

Mishra, S., Yazar, K. U., Kar, A., Lingam, R., Reddy, N. V., Prakash, O., & Suwas, S. (2021). Texture and microstructure evolution during single-point incremental forming of commercially pure titanium. *Metallurgical and Materials Transactions A*, *52*(1), 151–166. https://doi.org/10.1007/s11661-020-06000-y

Najm, S.M., & Paniti, I. (2020). Study on effecting parameters of flat and hemispherical end tools in SPIF of aluminium foils. *Tehnicki Vjesnik - Technical Gazette*, *27*(6), 1844–1849. https://doi.org/10.17559/TV-20190513181910

Najm, S.M., & Paniti, I. (2021). Artificial neural network for modeling and investigating the effects of forming tool characteristics on the accuracy and formability of thin aluminum alloy blanks when using SPIF. *The International Journal of Advanced Manufacturing Technology*, *114*(9), 2591–2615. https://doi.org/10.1007/s00170-021-06712-4

Najm, S.M., Paniti, I., Trzepieciński, T., Nama, S.A., Viharos, Z.J., & Jacso, A. (2021). Parametric effects of single point incremental forming on hardness of AA1100 aluminium alloy sheets. *Materials*, *14*(23), 7263. https://doi.org/10.3390/ma14237263

Naranjo, J., Miguel, V., Martínez, A., Coello, J., Manjabacas, M.C., & Valera, J. (2017). Influence of temperature on alloy Ti6Al4V formability during the warm SPIF process. *Procedia Engineering*, *207*, 866–871. https://doi.org/10.1016/j.proeng.2017.10.843

Oleksik, V., Trzepieciński, T., Szpunar, M., Chodoła, Ł., Ficek, D., & Szczęsny, I. (2021). Single-point incremental forming of titanium and titanium alloy sheets. *Materials*, *14*(21), 6372. https://doi.org/10.3390/ma14216372

Patel, D., & Gandhi, A. (2022). A review article on process parameters affecting Incremental Sheet Forming (ISF). *Materials Today: Proceedings*, *63*, 368–375. https://doi.org/10.1016/j.matpr.2022.03.208

Pepelnjak, T., Sevšek, L., Lužanin, O., & Milutinović, M. (2022). Finite element simplifications and simulation reliability in single point incremental forming. *Materials*, 15(10), 3707. https://doi.org/10.3390/ma15103707

Popp, M., Rusu, G., Racz, S.G., & Oleksik, V. (2021). Common defects of parts manufactured through single point incremental forming. *MATEC Web of Conferences*, *343*, 04007. https://doi.org/10.1051/matecconf/202134304007

Racz, S.G., Breaz, R.E., Tera, M., Gîrjob, C., Biriș, C., Chicea, A.L., & Bologa, O. (2018). Incremental forming of titanium Ti6Al4V alloy for cranioplasty plates—decision-making process and technological approaches. *Metals*, *8*(8), 626. https://doi.org/10.3390/met8080626

Rosca, N., Oleksik, M., & Oleksik, V. (2021). Experimental study regarding PA and PE sheets on single point incremental forming process. *MATEC Web of Conferences*, *343*, 03009. https://doi.org/10.1051/matecconf/202134303009

Saidi, B., Boulila, A., Ayadi, M., & Nasri, R. (2015). *Prediction of the friction coefficient of the incremental sheet forming SPIF*. Proceedings of the 6th International Congress Design and Modelling of Mechanical Systems CMSM'2015, Hammamet, 23-25 March 2015, Tunisia, pp. 1–2.

Sbayti, M., Bahloul, R., & Belhadjsalah, H. (2020). Efficiency of optimization algorithms on the adjustment of process parameters for geometric accuracy enhancement of denture plate in single point incremental sheet forming. *Neural Computing and Applications*, *32*(13), 8829–8846. https://doi.org/10.1007/s00521-019-04354-y

Sbayti, M., Ghiotti, A., Bahloul, R., BelhadjSalah, H., & Bruschi, S. (2022). Effective strategies of metamodeling and optimization of hot incremental sheet forming process of Ti6Al4Vartificial hip joint component. *Journal of Computational Science*, 60, 101595. https://doi.org/10.1016/j.jocs.2022.101595

Shin, J. (2021). *Investigation of Incremental Sheet Forming (ISF) using Advanced Numerical and Analytical Approaches*. PhD Thesis, University of Michigan, MI, USA. https://doi.org/10.7302/2657

Szewczyk, M., & Szwajka, K. (2023). Assessment of the tribological performance of bio-based lubricants using analysis of variance. *Advances in Mechanical and Materials Engineering*, *40*, 31–38. https://doi.org/10.7862/rm.2023.4

Szpunar, M., Ostrowski, R., Trzepieciński, T., & Kaščák, Ľ. (2021). Central composite design optimisation in single point incremental forming of truncated cones from commercially pure titanium Grade 2 sheet metals. *Materials*, *14*(13), 3634. https://doi.org/10.3390/ma14133634

Titanium. (2023). Titanium Ti-6Al-4V (Grade 5), Annealed. [WWW Document]. Retrieved from: https://www.matweb.com/search/DataSheet.aspx?MatGUID=a0655d261898456b958e5f825ae85390&ckck=1 (accessed on 23 July 2023).

Trzepieciński, T., Szpunar, M., Dzierwa, A., & Żaba, K. (2022a). Investigation of surface roughness in incremental sheet forming of conical drawpieces from pure titanium sheets. *Materials, 15*(12), 4278. https://doi.org/10.3390/ma15124278

Trzepieciński, T., Szpunar, M., & Ostrowski, R. (2022b). Split-Plot I-Optimal design optimisation of combined oil-based and friction stir rotation-assisted heating in SPIF of Ti-6Al-4V titanium alloy sheet under variable oil pressure. *Metals*, *12*(1), 113. https://doi.org/10.3390/met12010113

Więckowski, W., Adamus, J., Dyner, M., & Motyka, M. (2023). Tribological aspects of sheet titanium forming. *Materials*, *16*(6), 2224. https://doi.org/10.3390/ma16062224

Yoganjaneyulu, G., Vigneshwaran, S., Palanivel, R., Alblawi, A., Rasheed, M. A., & Laubscher, R. F. (2021). Effect of tool rotational speed on the microstructure and associated mechanical properties of incrementally formed commercially pure titanium. *Journal of Materials Engineering and Performance*, *30*(10), 7636–7644. https://doi.org/10.1007/s11665-021-05900-3

Zwolak, M., Szpunar, M., Ostrowski, R., & Trzepieciński, T. (2022). Research on forming parameters optimization of incremental sheet forming process for commercially pure titanium Grade 2 sheets. *Archives of Metallurgy and Materials, 67*(4), 1411–1418. https://doi.org/10.24425/amm.2022.141068

Wpływ Parametrów Wejściowych na Współczynnik Tarcia podczas Formowania Przyrostowego Blach ze Stopu Tytanu Grade 5

Streszczenie

Niniejszy artykuł badawczy koncentruje się na badaniu wpływu parametrów wejściowych na współczynnik tarcia podczas przyrostowego formowania blach tytanowych grade 5. Stopy tytanu są szeroko stosowane w różnych gałęziach przemysłu ze względu na ich odporność na korozję i korzystny stosunek wytrzymałości do masy. Kształtowanie przyrostowe to elastyczny i opłacalny proces produkcji elementów o złożonych kształtach. Celem tego badania była analiza warunków tarcia podczas kształtowania przyrostowego, które wpływają na formowalność blachy, jakość powierzchni i ogólną wydajność procesu. Eksperymenty przeprowadzono przy użyciu kombinacji smarowania MoS_2 i ogrzewania materiału blachy wspomaganego obrotami narzędzia. Wartość współczynnika tarcia wyznaczono na podstawie składowych siły kształtowania (siły osiowej i sił poziomych), które mierzono za pomocą precyzyjnego dynamometru piezoelektrycznego. Zastosowano plan split-plot i wykonano 25 prób w celu uzyskania wartości współczynnika dla każdej z nich. Wyniki badania dostarczają cennych informacji na temat związku między parametrami wejściowymi a współczynnikiem tarcia, przyczyniając się do zrozumienia warunków tarcia występujących podczas kształtowania przyrostowego.

Słowa kluczowe: ANOVA, współczynnik tarcia, kształtowanie przyrostowe, stopy tytanu

Original Research

Exploring the Performance, Simulation, Design, and Construction of a Closed Solar Swimming Pool in Kirkuk City

Fayadh M. Abed [1,*] iD **, Hussein Hayder Mohammed Ali** [2] iD **, Nursan Bayraktar** [2] iD

[1] Mechanical Engineering Department, Faculty of Engineering, Tikrit University, 34001 Tikrit, Iraq
[2] Northern Technical University/Technical College of Engineering, 36001 Kirkuk, Iraq; hussein_kahia@ntu.edu.iq (H. H. M. Ali); nursanbayrakdar@ntu.edu.iq (N. Bayraktar)

* Correspondence: Fayadh_moahmed@tu.edu.iq

Abstract

Indoor swimming pools are sports or entertainment facilities that require substantial energy to heat the pool water and maintain a comfortable atmosphere in compliance with international standards. However, traditional methods of heating swimming pools using fuels or electricity often result in high operational costs and environmental pollution. To address these challenges, solar water heating has emerged as the most significant and environmentally friendly technology. Consequently, the construction of solar-powered swimming pools has become a prominent issue, drawing considerable attention from governments worldwide. Solar energy is currently being utilized in various applications, with water heating in residential settings being one of the most popular ones. Iraq, known for its high solar energy potential, stands to benefit greatly from adopting and designing solar swimming pools. The proposed design incorporates essential components such as the swimming pool, pump, filter, control valves, and the solar collector. This study explores the influence of flow rate on the solar collector's performance and its relationship with pool size under varying weather conditions in Kirkuk city. The month of February, characterized by lower solar radiation intensity and air temperature, was selected for the investigation. This study provides insights into heating indoor swimming pools using solar energy, examining the types of solar collectors, filters, and pumps involved. By offering guidance in the system design process, our research can be instrumental in facilitating the installation of such systems.

Keywords: indoor swimming pools, solar energy, swimming pool heating, thermal calculations

1. Introduction

Swimming pools are a widely enjoyed leisure activity worldwide, and it is crucial to have indoor pool structures with efficient heating systems for use during winter months, ensuring a pleasant experience for swimmers. The energy required to heat indoor swimming pools is significant, given their role as major sports and recreational facilities. Heating the pool area and providing hot water for other services necessitate addressing heat loss. Therefore, finding a heat source that meets requirements is essential, as traditional heating systems, fueled by either electricity or conventional fuels, are environmentally unfriendly and economically inefficient (Haddy et al., 2021). Moreover, these traditional systems contribute to climate change and dependence on fossil fuels (Li et al., 2021). Recognizing these issues, there is a growing focus on exploring potential renewable energy solutions that can reduce the impact of traditional systems, such as solar techniques, while minimizing carbon dioxide emissions (Natali et al., 2020).

According to the International Swimming Federation, the water temperature in Olympic swimming pools is regulated to 25–28 °C (FINA, 2017). The American Red Cross recommends a temperature between 25 and 28 °C for sports swimming and 27 °C for recreational swimming. Although setting water temperature limits in residential pools is a good practice, these values serve as guidelines for individual preferences and considerations related to human health, well-being, and comfort (Starke et al., 2017).

In indoor swimming pools, a common challenge is not only to maintain an acceptable water temperature but also to ensure comfortable indoor conditions. Water evaporation increases indoor humidity, requiring additional ventilation (Rajagopalan & Jamei, 2015). The primary issue with heating enclosed swimming pools lies in the high expenses associated with conventional heating approaches, such as electrical heaters (Mousia & Dimoudi, 2015). The Spanish National Sports Council recommends a water temperature of 26 ± 1 °C (Consejo Superior de Deportes, 2005). In practice, many public swimming pools operate at 28 °C, which is the temperature considered in this study.

Various technologies are employed to heat indoor pools during winter, including passive and active approaches. Passive solutions utilize thermal insulating covers to minimize heat loss when the pool is covered. Active heat-saving strategies are designed to meet the pool's thermal requirements. Studies on passive strategies have shown that using a cover significantly reduces heat loss in the pool (Yadav & Tiwari, 1987). Additionally, research has demonstrated that transparent covers are more effective than opaque covers in raising water temperature by allowing for increased solar radiation absorption (Francey et al., 1980).

Active approaches include the use of air source heat pumps for pool heating, as demonstrated in a hotel in Hong Kong. The study analyzed the energy savings and life cycle costs of the system, revealing an average energy savings and economic savings ratio of 72.8% and 81.1%, respectively, compared to traditional heating systems (Chan & Lam, 2003; Lam & Chan, 2001). Water evaporation is the primary cause of heat loss in pool heating, accounting for over 60% of the total energy requirement (Zuccari et al., 2017). Even when the facility is closed and not in use, evaporation continues to occur, necessitating a readily accessible power source throughout the year. Furthermore, given that the pool area needs to be warmer than the water, including the pool surroundings, there is a significant demand for heating and domestic hot water for showers. Due to the complexity of thermal mechanisms in indoor pools, specialized expertise is required to enhance energy efficiency and reduce costs (Marín & García-Cascales, 2020).

To determine the impact of different solar collector types on the solar fraction factor for heating an indoor swimming pool in Baghdad, Iraq (located at 33.32° N, 44.32° E), various flat-plate solar collectors were used, including black and selective absorber covers, as well as a pool absorber (polyvinyl chloride - PVC) type (Haddy & Hassen, 2021). The results indicated that the highest solar fraction factor values were obtained when using two selective absorber covers, while the lowest values were achieved with the pool absorber. The experiments were conducted during the winter season (November, December, January, and February). Simulation results for a 10,000 m^2 pool surface area and a mass storage tank with 25 kg/m^2 showed a solar fraction factor of 84% in November using two selective absorber covers, and 50% in February using the pool absorber.

Numerous recent studies have focused on solar swimming pool development, including research on solar heat pumps, thermal losses in solar heated pools, the impact of flow rates on solar collector performance, and the financial feasibility of solar-powered swimming pools. Other studies have aimed to improve the efficiency and performance of solar collectors for both indoor and outdoor pool heating. This current study encompasses the design and construction of a solar heated swimming pool, considering the climatic conditions in the city of Kirkuk, as well as the design and operational factors affecting the system, such as atmospheric temperature, solar radiation, wind speed, wind direction, relative humidity, and sky clarity. The design specifies the type and size of the solar collector necessary to meet the water heating requirements of the pool. It also involves calculating heat loss rates from the pool, selecting the appropriate pump type and size for water circulation, and determining the type, size, and number of filters required for water purification, all tailored to the specific climate conditions of the study site. This paper aims to investigate the economic feasibility, improve, and design a solar heating system for indoor swimming pools. The essay is organized as follows: Section 2 describes the approach used in this study, followed by a description of the system. Section 3 presents the findings and discussions, including the results. Finally, Section 4 concludes the paper by providing a summary of the key points discussed.

2. Methodology

The aim of this research is to design and develop an indoor solar swimming pool for Kirkuk city (latitude 35.5° N, longitude 44.4° E) that utilizes a specialized solar collector to enhance the heating system. To achieve this objective, a solar flat plate with a rotated plastic (flexible) pipe connected to a pump and filter, as depicted in Figure 1, is utilized. This collector transfers heat to two water-filled

tanks. The flow rate of water inside the plastic pipe is carefully chosen, and the flat plate is painted black to maximize solar radiation absorption.

To evaluate the heating performance, three different flow rates were selected, and six thermocouple sensors were strategically placed at various locations to monitor temperature profiles. The pump flow rate and filter type and size were chosen in accordance with international swimming pool standards. The effectiveness of the solar collector system was assessed through an experimental investigation conducted in Kirkuk (Iraq), using real-time data.
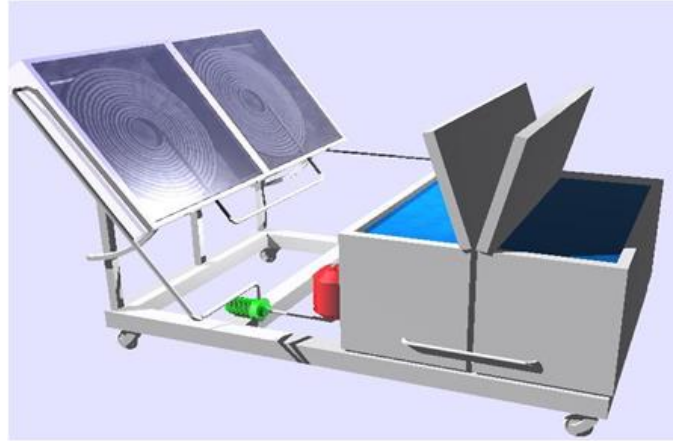
Fig. 1. Schematic drawing of solar swimming pool prototype.

2.1. Description of the system

Figure 2 illustrates the schematic view of the concentrating solar collector integrated with the swimming pool tank, as well as the accompanying equipment such as the pump and filter. A circular flexible pipe is securely attached to the flat plate and covered with transparent nylon to enhance energy absorption within the pipe and minimize thermal resistance in the gap area between the plate and the cover. Aluminum was chosen as the material for the plate due to its favorable physical properties. The distance between the plate and the absorbent cap should range between 0.5% and 2% of the collecting area (Dymond & Kutscher, 1997).
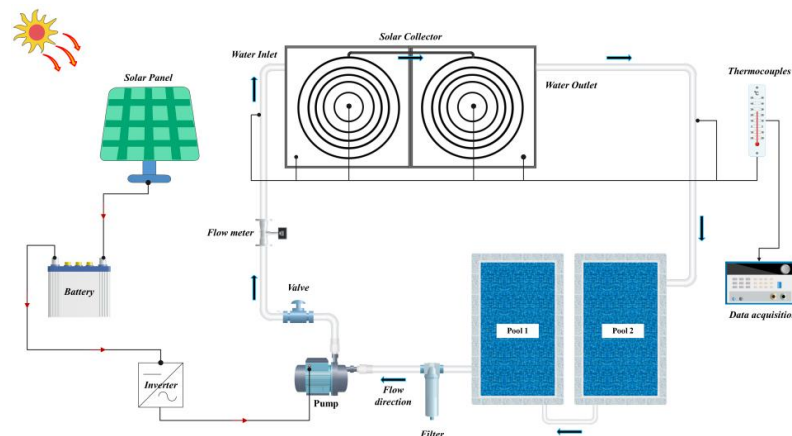
Fig. 2. Schematic representation of solar swimming pool systems.

2.1.1. Solar collector

The choice and design of a solar collector for heating pool water are influenced by two factors: the size of the pool and the amount of energy required, which also depend on the desired design temperature. The design temperature should be selected based on the type of pool usage and in accordance with standard criteria, as outlined in Table 1.

The solar collector comprises a 2 cm diameter flexible plastic tube that can be shaped into concentric rings, as depicted in Figure 3. Depending on the site's latitude, the solar collector is installed facing south, inclined at a 45° angle from the horizon, and positioned 40 cm above the ground. The plastic tube, readily available in the local market at an affordable price, possesses efficient heat ab-

sorption properties through its walls. The tube's length is 100 meters, a crucial factor in maximizing heat absorption and raising the temperature of the pool water.

The rings of the tube are affixed to a wooden base with dimensions of 260 cm in length and 120 cm in width, painted black to enhance heat absorption. To minimize heat losses, a layer of glass wool insulation is applied on all sides, except for the front exposed to solar radiation. The second layer above the insulation, where the coiled tube is fixed, consists of aluminum foil, matching the dimensions of the wooden box. The aluminum foil is painted with a dark black coating to maximize solar radiation absorption. Aluminum was chosen due to its lightweight nature and relatively low cost.

A polyethylene nylon cover is placed on the inclined surface of the solar collector, with a confined distance of 5 cm between the cover and the absorption surface. This distance is chosen to provide optimal insulation for heat transfer through convection and radiation from the relatively hot absorption surface. The components of the solar collector, including the plastic pipe, insulation, case, aluminum plate, and the method of fixation, are illustrated in Figures 4 and 5.

Table 1. Standards temperature of swimming pool (Garnysz-Rachtan & Zapałowicz, 2018).

Relative humidity, %	Water temperature, °C	Air temperature, °C	Type of pool
Recreational	24 to 29	24 to 29	50 to 60
Therapeutic	27 to 29	29 to 35	50 to 60
Competition	26 to 29	24 to 28	50 to 60
Diving	27 to 29	27 to 32	50 to 60
Elderly swimmers	29 to 29	29 to 32	50 to 60
Hotel	28 to 29	28 to 30	50 to 60
Whirlpool/Spa	27 to 29	36 to 40	50 to 60

a)   b)
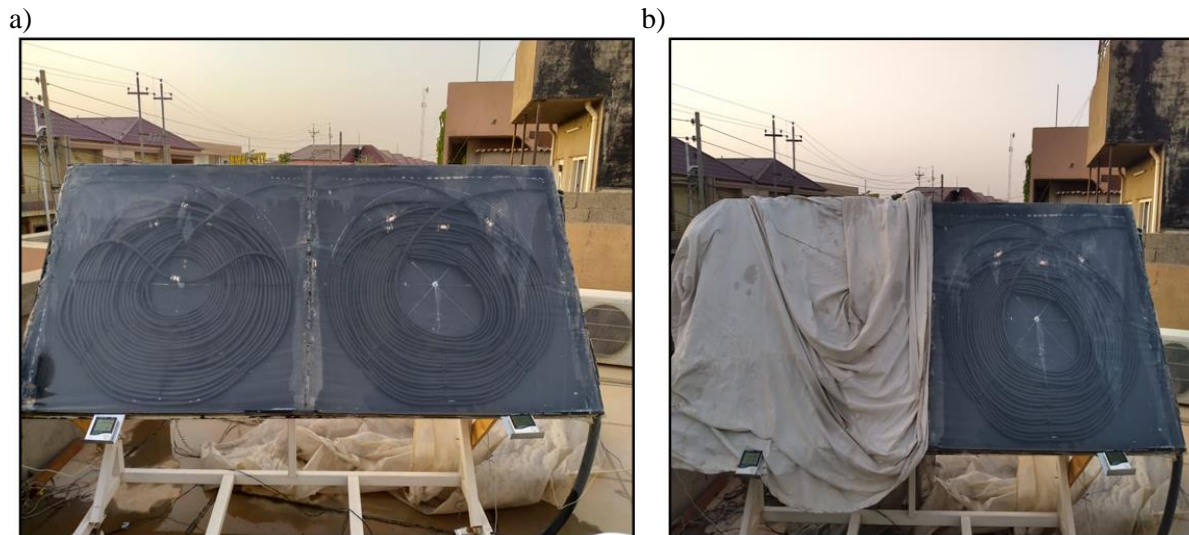
Fig. 3. Solar collector cases: a) 100% used, b) 50% is used.
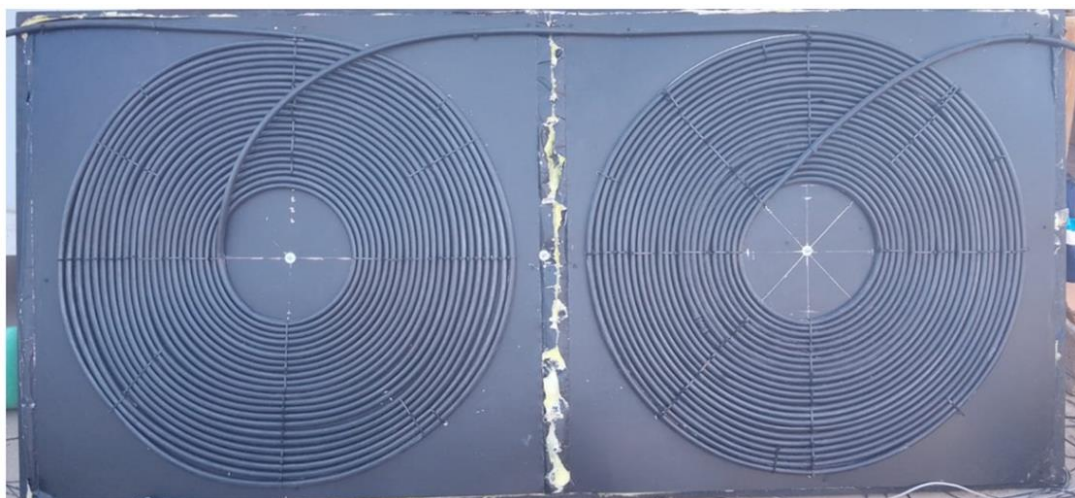
Fig. 4. Type of solar collector (plastic pipe, aminume plate and the way of installing).
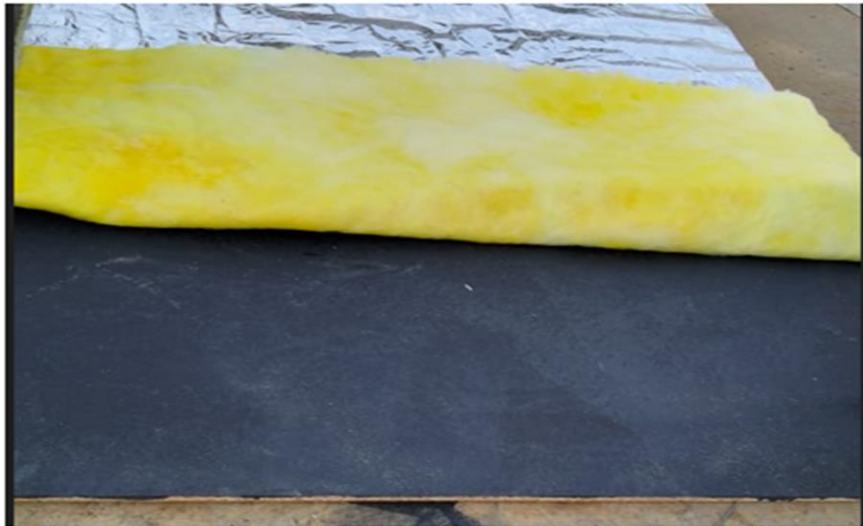
Fig. 5. Case of solar collector, insulation and aluminum plate.

2.1.2. Design calculations for swimming pools

When designing a swimming pool, it is essential to determine its volume, perimeter, and average depth. Additionally, the selection of the turnover period depends on the type of pool, as indicated in Table 2. The subsequent calculations aim to establish the design parameters for operating a swimming pool in accordance with international standards. This includes selecting the appropriate type of solar collectors based on the study area's weather conditions and determining the operational variables. The required collector area is calculated based on the energy needed for heating, followed by determining the operational duration, pump type, filter size, and filter type. The design of the swimming pool takes into account the specific weather conditions of the study area, incorporating measurements such as hourly solar radiation, air temperature, relative humidity, number of cloudy days, and wind speed, as outlined in Table 3.

Table 2. Swimming pool type and turnover period (ASHRAE, 2017).

Type of pool	Turnover period, hr.
Spa	0.1 – 0.25
Leisure water bubble pools	0.1 – 0.33
Teaching pools	0.5 – 1.0
Waterslide splash pools	0.5 – 1.0
Hydrotherapy pools	0.5 – 1.0
Leisure water up to 0.5 m deep	0.2 – 0.6
Leisure water up to 0.5–1 m deep	0.6 – 1.2
Leisure water over 1.5 m deep	1.8 – 2.5
Conventional public pools up to 25 m long with a 1 m shallow end	2.5 – 3.0
Competition pools 50 m long	3.0 – 4.5
Diving pools	4.0 – 8.0
Domestic pools	4.0 – 8.0

Table 3. Weather conditions at Kirkuk city 2021 (RH – relative humidity, Ta – air temperature, GH – hourly solar radiation).

Month	RH, %	Ta, °C	GH, kWh	Black day	Wind speed, km/h
January	69	9.9	2.66	11	11
February	65	11.9	3.15	8	9
March	65	13.7	3.9	9	12
April	61	17.9	5.18	8	13
May	32	28.9	6.98	6	11
June	19	36.5	8.2	0	8
July	19	36.7	8.3	0	9
August	19	37.7	6.4	0	8
September	20	32.6	5.5	2	12
October	32	26.6	3.6	6	10
November	33	17.2	2.6	5	11
December	66	13.1	1.6	8	13

The energy required for heating $Q_{\text{reg.}}$ is calculated based on the mathematical equation for heating as follows (Al Aboushi & Raed, 2015):

$$Q_{\text{req.}} = \frac{\text{volume} \cdot \text{density} \, (T_{\text{final}} - T_{\text{initial}})}{860 \cdot \text{hr.}} \tag{1}$$

According to the pool volume and turnover period the pump flow rate is estimated as:

$$\text{Pump flow rate (m}^3\text{/h)} = \frac{\text{Volume of Pool (m}^3)}{\text{Pool turnover rate(h)}} \tag{2}$$

2.1.3. Sizing filtration and circulation systems

The selection of the filter type and size depends on the circulating rate of the pool system and the filtration velocity. The cross-sectional area of the filter is calculated accordingly, considering the chosen diameter. The filter specifications can be determined based on the pool flow rate and the load surface factor. It is recommended that this factor does not exceed 40 m^3/m$^2 \cdot$hr. The pool flow rate Q can be calculated as follows:

$$Q = \frac{\text{volume of pool}}{\text{turnover period}} \tag{3}$$

and the surface load factor is:

$$\text{Surface load} = \frac{Q \, (\frac{\text{m}^3}{\text{h}})}{\text{filter area } A_{\text{f}} (\text{m}^2)} \tag{4}$$

Once the filter area A_{f} has been calculated, the corresponding filter diameter is determined, and the appropriate filter type is selected.

2.1.4. Pump

Solar pool heaters are typically integrated with the plumbing systems of the pool. The heater, as well as lint, hair, and leaf filters, are commonly installed before the pump. This configuration allows the pump to draw water from the skimmer and main drains, pass it through the filter, and return it to the pool. While manual flow control or time clock control methods are simple and affordable, they do have their disadvantages. Therefore, automatic flow controls are often employed. The selection of the pump is determined based on factors such as swimming pool size, filter size, and the turnover period specified in international standards, as illustrated in Table 4.

Table 4. Technical specifications of pump.

Type	Total head, m	Engine net power, kW	Maximum output capacity, L/min	Engine speed, rpm	Maximum operation temperature, °C
QB60	27	0.41	30	2850	45

3. Real-time experimental investigation

3.1. Meteorological conditions of experimental site

All tests were conducted during sunny winter days in the Kirkuk city region (latitude 35.5° N, longitude 44.4° E), Iraq. Six thermocouples were strategically placed in different locations, as depicted in Figure 6. These locations include the inlet and outlet of the pipe, the surface, middle, and bottom of the tank water, as well as before the pump and after the filter. Ambient conditions such as temperature, relative humidity, and irradiation were recorded from 8:00 a.m. to 5:00 p.m. local time throughout the month of February 2022. Temperature and humidity readings were recorded at 30-minute intervals.

Fig. 6. Solar collector and thermocouple sensor location.

3.2. Experimental error and uncertainty analysis

A digital data logger was connected to a computer to automatically record all the data. The water temperature at various points and weather conditions such as air temperature, relative humidity, and solar radiation were recorded. Solar intensity was measured using a calibrated pyrometer, while capacitive sensors were used for relative humidity measurements. K-type calibrated thermocouples were utilized for temperature measurements. Each modification was calibrated according to the established protocol. The uncertainties of the measuring instruments are provided in Table 5. Through the aforementioned approach, the greatest uncertainty was determined to be less than 5% for all parameters. Assuming that the measured parameters T_1, T_2, T_3, T_m, T_{m+1}, T_n are measured with uncertainties δT_1, δT_2, δT_3, ..., δT_m, δT_{m+1}, δT_n, where n is the total number of measurements. The fractional uncertainty of T can be expressed as (Abed et al., 2014; Islam et al., 2021):

$$\frac{\delta T}{T} = \sqrt{\left(\frac{\delta T_1}{T_1}\right)^2 + \left(\frac{\delta T_2}{T_2}\right)^2 + \left(\frac{\delta T_3}{T_3}\right)^2 + \cdots + \left(\frac{\delta T_n}{T_n}\right)^2 + \left(\frac{\delta T_{n+1}}{T_{n+1}}\right)^2 + \left(\frac{\delta T_m}{T_m}\right)^2} \tag{5}$$

The trustworthiness of the measured data is indicated by uncertainty values in this range.

Table 5. Accuracy of instruments, measurement ranges and maximum error margin.

Instrument	Operational range	Max. error	Accuracy
Thermocouple (K-type)	0 to 1250 °C	3.08%	±1.1
Digital data logger	−250 to 1000 °C	6.19%	±2%
Solar power meter TM-207	0-1999 W/m²	0.10 W/m²·°C	±5%
Anemometer testo 425	0-20 m/s	6.58%	±5%

4. Results and discussion

Practical tests were conducted under the weather conditions of Kirkuk city, located at 35.4656° N, 44.3804° E. The experiments took place during the months of February, March, and April. During the summer season, temperatures exceeded 35 °C, resulting in intense solar radiation. The objective of the design was to heat the water in the swimming pool and raise its temperature to the desired limit. This allows for a thorough evaluation of the proposed design's performance. The following sections discuss the impacts of operational weather conditions.

4.1. Ambient condition

Based on data from various sources (Abed, 2018; Al-Douri & Abed, 2016), Iraq's deserts experience a peak power density of 2310 kW/m^2/year. Regarding the geographical location of Kirkuk city, measurements indicate that the average solar radiation ranges from 3.0 to 6.4 kWh/m^2/day. Additionally, the average air temperature falls within the range of 10 to 45 °C, with atmospheric humidity levels ranging from 13% to 44%. Considering these environmental parameters at the experimental study location, all calculations and tests were conducted, as depicted in Figure 7.
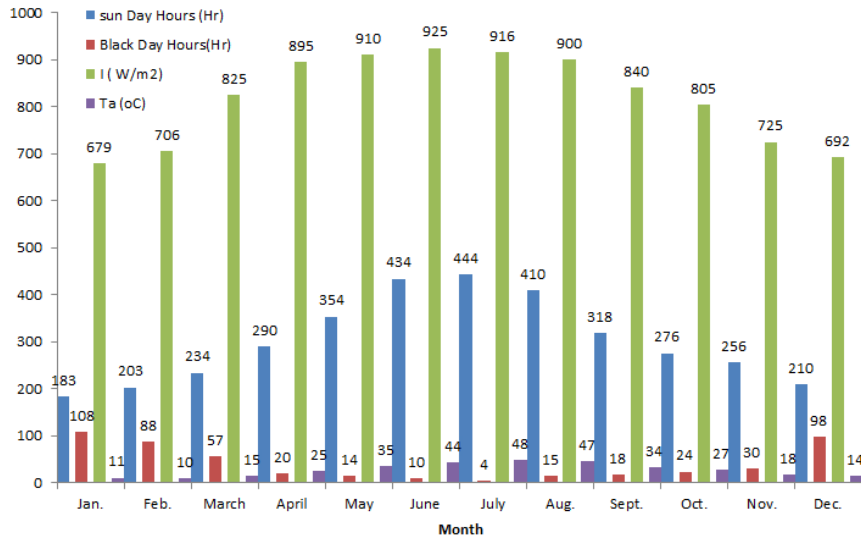
Fig. 7. Yearly data of average weather conditions at site of test 2021.

4.2. The global solar radiation and ambient temperature effects

The year-round ambient temperature and solar radiation data for the test site are obtained from Abed et al. (2014). In September, the maximum daily radiation reaches 25 MJ/m^2, while in January, the minimum daily radiation is 10 kJ/m^2. The maximum and minimum temperatures in September and January are 39 °C and 15 °C, respectively. Figure 8 illustrates the average test data profile of air temperature and humidity in Kirkuk city.
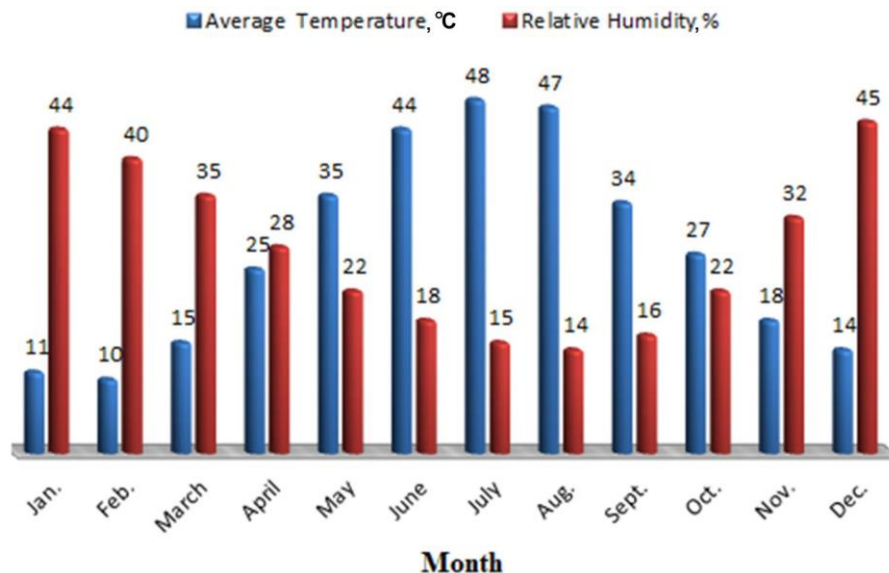
Fig. 8. The Kirkuk area's average monthly temperature and relative humidity.

To assess the impact of operational conditions on the performance of the proposed design for a solar indoor swimming pool, considering the size, type, and area of the solar collector, three cases were examined. The first case involved using both collectors, the second case used only one collector, and the third case utilized both collectors but with coverings. The flow rates tested in all cases were 1, 3, and 7 liters per minute (LPM). The experiments were conducted over a three-month period (Febru-

ary, March, and April) in accordance with the environmental conditions of the study area. These months were chosen to represent suitable conditions for operating winter swimming pools, allowing for an investigation of the amount of thermal energy required to heat the pool water according to international standards for indoor swimming pools.

The study primarily focused on evaluating the performance of the proposed solar collector. Three cases were tested, with the first case fully exposed to solar radiation, the second case partially exposed, and the third case completely blocked. The variables of air temperature and solar radiation significantly influenced the heat gained from the solar collector to warm the water flowing through the pipes installed on the collector plate. To achieve the desired level of pool water heating based on the proposed design, operational variables such as the water flow rate through the pump played a crucial role in achieving this objective.

4.3. The effect of flow rate on the heating of swimming pool water

A series of tests were conducted to examine the impact of flow rate on heating the aquarium water to the desired temperature under the weather conditions specific to the study area. The month of February was selected due to its lower temperatures and solar radiation levels, allowing for an assessment of the heat required to warm the pool water and the efficiency of the proposed solar collector design.

Three flow rate values of 1, 3, and 7 liters per minute were chosen, taking into consideration the relationship between circulation rate, pump volume, purification filter, swimming pool purification criteria, and the water volume in the basin. The collector design plays a vital role in the system, consisting of two interconnected centers as illustrated in Figure 4. For each flow rate, two test cases were conducted: one with both centers uncovered, and the other with a 50% cover placed on the collector. The purpose was to control the rise in heating temperature above the design limit.

Figure 9 demonstrates the effect of different flow rates (1, 3, and 7 LPM) using both collectors on increasing the pool water temperature. The volume of the pool was 685 liters, and the relationship with solar radiation intensity was observed over a 10-hour period throughout the day. The results revealed that the flow rate of 1 LPM achieved the highest increase in pool temperature, followed by the flow rates of 3 LPM and 7 LPM, respectively.
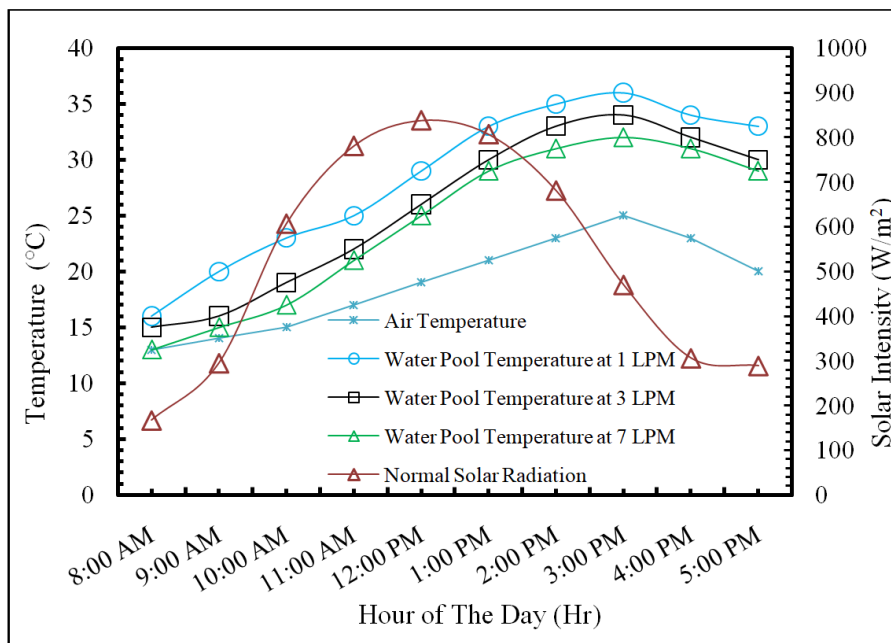
Fig. 9. Profile of the temperature change of the water swimming pool with time at different flow rates (1,3 and 7 LPM), in February 2022, with average solar radiation rate of 550 W/m^2 and an average ambient temperature of 20 °C.

4.4. The effect of the flow rate on the amount of heat gained for the swimming pool water

Figure 10 illustrates the heat capacity needed to warm the pool water using both collectors. The results indicated that lower flow rates corresponded to lower heat capacity requirements for achieving the desired temperature in the swimming pool water. This finding aligns with previous research by

Cunio and Sproul (2012). It is worth noting that the energy requirement is inversely proportional to the decrease in solar radiation intensity and the temperature of the swimming pool.
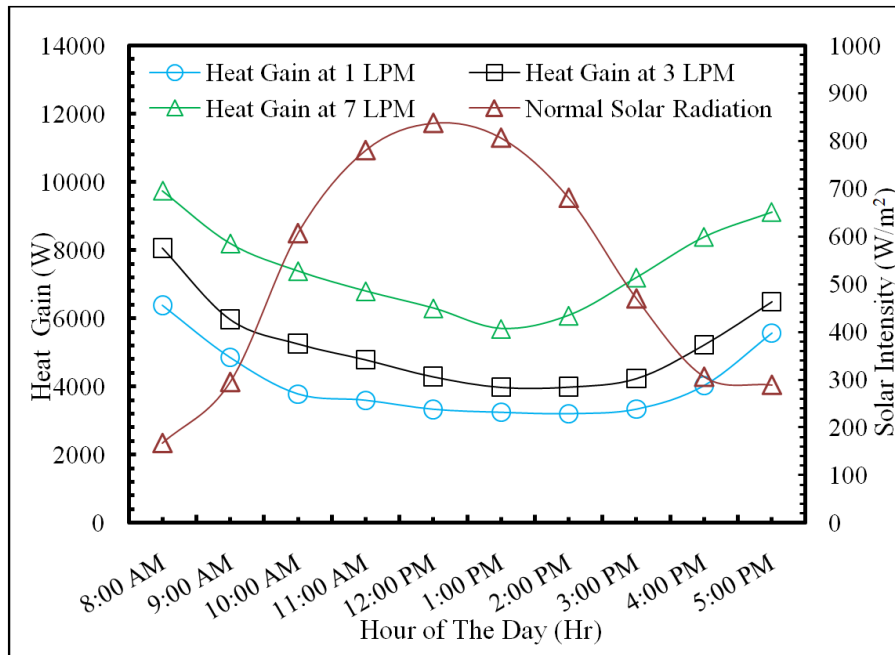
Fig. 10. Profile of heat gain water swimming pool with time at different flow rates (1,3 and 7 LPM), in February 2022, with average solar radiation rate of 550 W/m² and an average ambient temperature of 20 °C.

4.5. The effect of the flow rate on the amount of heat lost from the pool water

Figure 11 displays the heat losses experienced by the swimming pool water when utilizing both collectors, with a volume of 685 liters, and its relationship with solar radiation intensity over a 10-hour period. The results demonstrated that the magnitude of heat losses is dependent on the intensity of solar radiation absorbed by the collectors, decreasing as solar radiation decreases. This aligns with the understanding that losses tend to increase with rising temperatures, as observed by Tarrad (2017). Heat loss to the surrounding environment occurs when the pool temperature exceeds the ambient temperature.
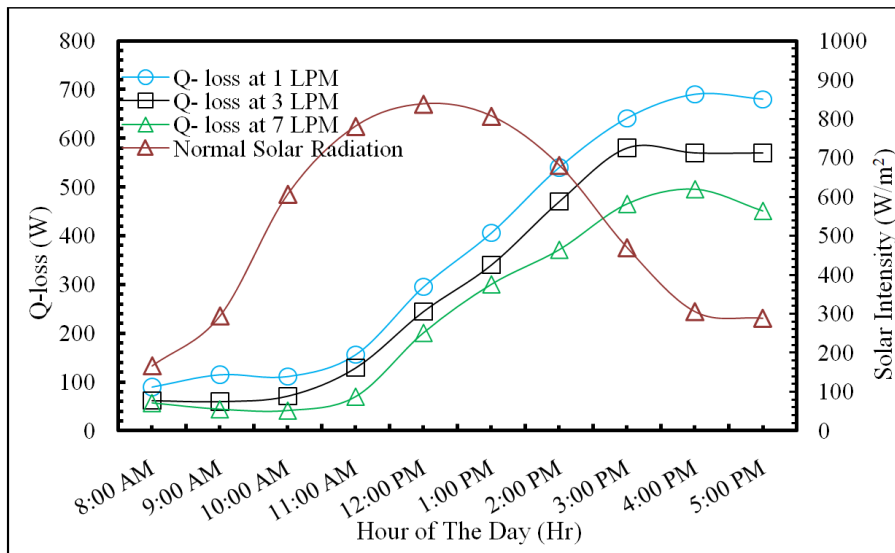
Fig. 11. Profile of heat losses of water swimming pool with time at different flow rates (1,3 and 7 LPM), in February 2022, with average solar radiation rate of 550 W/m² and an average ambient temperature of 20 °C

Figures 12a, 12b, and 12c present a comparison between the heat energy gained and lost from a swimming pool water with a volume of 685 liters under specific weather and operational conditions. By examining the curves of these two variables, we can observe the relationship between the quantities. This relationship is influenced by the temperature rise, where a smaller flow rate corresponds to

a greater temperature increase but less heat gain. Conversely, a larger flow rate leads to less temperature rise but greater heat loss.
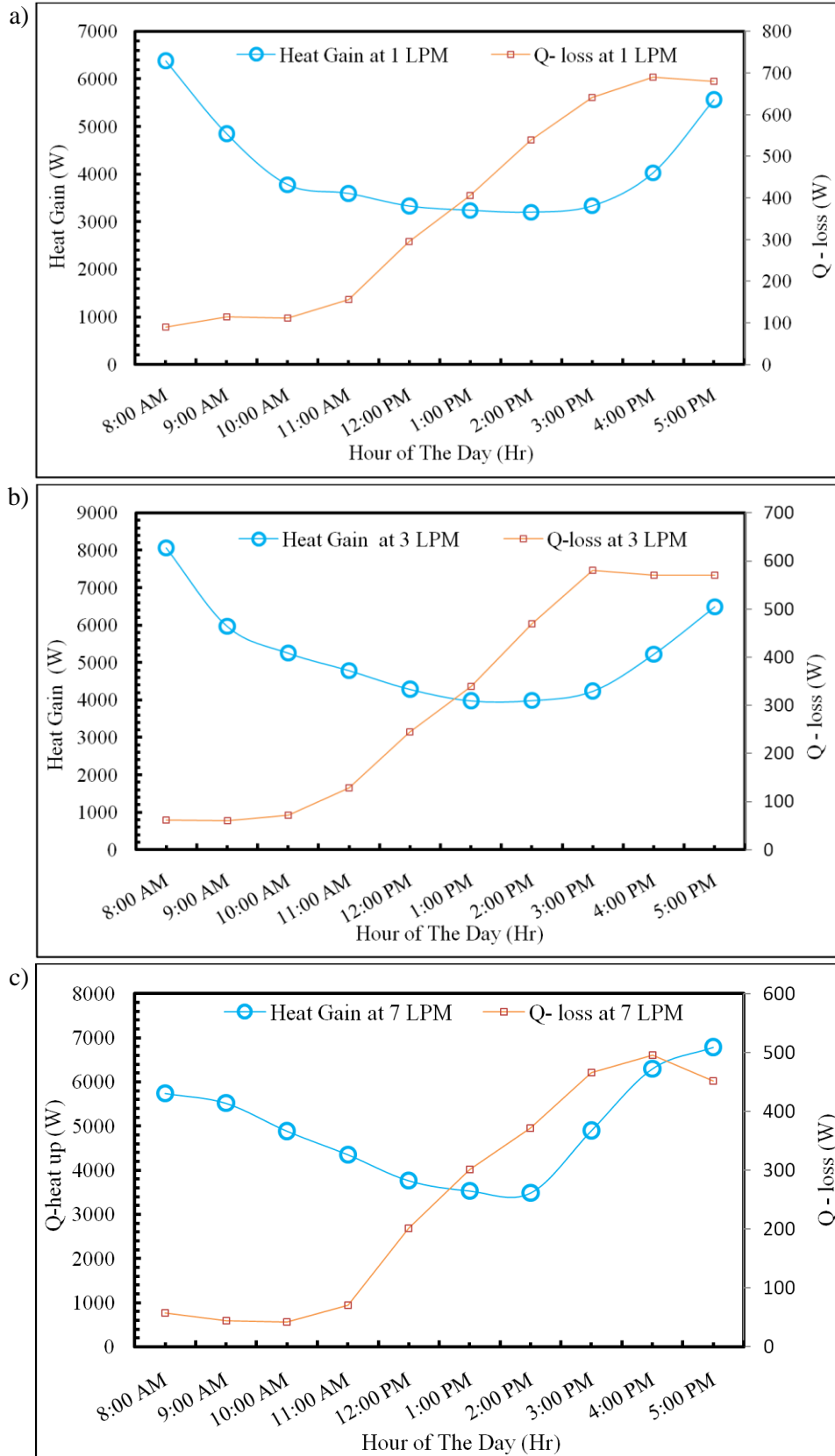
Fig. 12. Comparison of heat gain and losses with time at different flow rates: a) 1 LPM, b) 3 PM and c) 7 LPM, in February 2022, with average solar radiation rate of 550 W/m² and an average ambient temperature of 20 °C, without cover.

4.6. The effect of flow rate on the efficiency of solar collectors in heating the water of the swimming pool

Figure 13 illustrates that the efficiency of solar collectors rises with the increase in solar radiation intensity, peaking at 66% between the hours of 1 to 12 in the afternoon. The results also indicate that the efficiency of the solar collector increases as the flow rates decrease, aiming to raise the water temperature. This observation is consistent with the findings of researchers Aldeen et al. (2023), Amroune et al. (2021), Berkache et al. (2022), Poudyal and Bhattarai (2014) and Quader et al. (2023).

On the other hand, with the same conditions but 50% of collector is covered from the sun, the results show that the efficiency is 63% at flow rate 1 LPM and 59% at 7 LPM. As shown in Fig. 14.
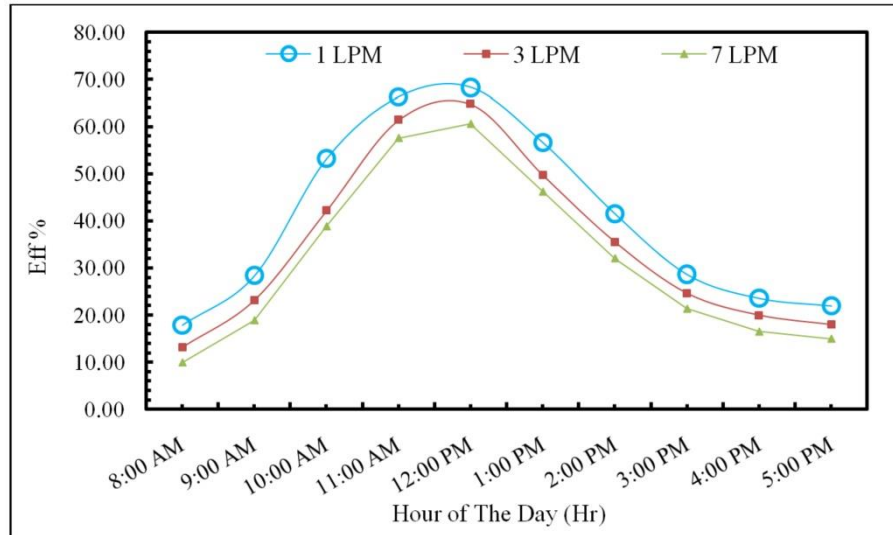
Fig. 13. Profile of collector efficiency time at different flow rates (1,3 and 7 LPM), in February 2022, with average solar radiation rate of 550 W/m^2 and an average ambient temperature of 20 °C, without cover.
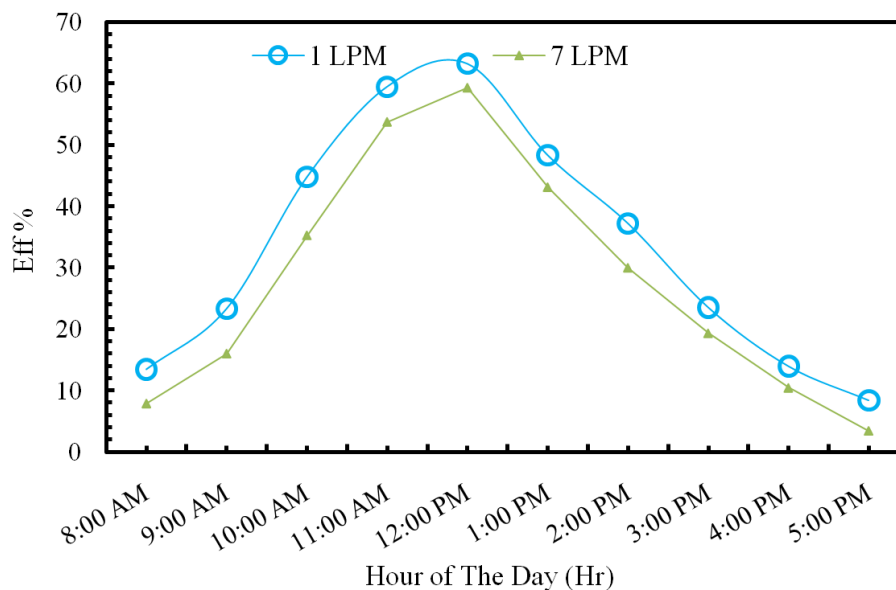
Fig. 14. Profile of collector efficiency time at different flow rates (1 and 7 LPM), in February 2022, with average solar radiation rate of 550 W/m^2 and an average ambient temperature of 20 °C, 50% covered.

5. Conclusion

The proposed design of the solar collector system can effectively fulfill the requirements for heating a swimming pool, offering additional advantages such as ease of construction, affordability, and reliability. When it comes to maintaining warm swimming pools, passive methods are the simplest and most cost-effective approach.

References

Abed, F. M. (2018). Design and fabrication of a multistage solar still with three focal concentric collectors. *Journal of Solar Energy Engineering*, *140*(4), 041003. https://doi.org/10.1115/1.4039351

Abed, F. M., Al-Douri, Y., & Al-Shahery, G. M. Y. (2014). Review on the energy and renewable energy status in Iraq: the outlooks. *Renewable and Sustainable Energy Reviews*, *39*, 816–827. https://doi.org/10.1016/j.rser.2014.07.026

Al Aboushi, A. R. & Raed, A. A. (2015). Heating indoor swimming pool using solar energy with evacuated collectors. Proceedings of the International Conference on Advances in Environment Research, Republic of Korea, 90–94. https://doi.org/10.7763/IPCBEE.2015.V87.17

Aldeen, A., Mahdi, D., Zhongwei, C., Disher, I., & Mohamad, B. (2023). Effect of isothermal and isochronal aging on the microstructure and precipitate evolution in beta-quenched N36 Zirconium alloy. *Facta Universitatis-Series Mechanical Engineering*, 1-15. https://doi.org/10.22190/FUME230405019A

Al-Douri, Y., & Abed, F. M. (2016). Solar energy status in Iraq: Abundant or not—Steps forward. *Journal of Renewable and Sustainable Energy*, *8*, 025905. https://doi.org/10.1063/1.4947076

Amroune, S., Belaadi, A., Zaoui, M., Menaseri, N., Mohamad, B., Saada, K., & Benyettou, R. (2021). Manufacturing of rapid prototypes of mechanical parts using reverse engineering and 3D Printing. Journal of the Serbian Society for Computational Mechanics, *15*(1), 167–176. https://doi.org/10.24874/jsscm.2021.15.01.11

ASHRAE. (2017). *2017 ASHRAE Handbook – Fundamentals* (I-P ed.). American Society of Heating, Refrigerating and Air-Conditioning Engineers, Inc.

Berkache, A., & Amroune, S., Golbaf, A., & Mohamad, B. (2022). Experimental and numerical investigations of a turbulent boundary layer under variable temperature gradients. *Journal of the Serbian Society for Computational Mechanics*, *16*(1), 1–15. https://dx.doi.org/10.24874/jsscm.2022.16.01.01

Chan, W. W., & Lam, J. C. (2003). Energy-saving supporting tourism sustainability: a case study of hotel swimming pool heat pump. *Journal of Sustainable Tourism*, *11*(1), 74–83 . https://doi.org/10.1080/09669580308667194

Consejo Superior de Deportes. (2005). Normas NIDE. Normativa sobre instalaciones deportivas y parael esparcimiento. Madrid: Ministerio de Educación y Ciencia. Consejo Superior de Deportes.

Cunio, L. N., & Sproul, A. B. (2012). Performance characterization and energy savings of uncovered swimming pool solar collectors under reduced flow rate conditions. Solar Energy, 86(5), 1511–1517. https://doi.org/10.1016/j.solener.2012.02.012

Dymond, C., & Kutscher, C. (1997). Development of a flow distribution and design model for transpired solar collectors. *Solar Energy 60*(5), 291–300. https://doi.org/10.1016/S0038-092X(96)00157-0

FINA. (2017). FINA Facilities rules 2017–2021. Fédération Internationale de Natation.

Francey, J., Golding, P., & Clarke, R. (1980). Low-cost solar heating of community pools using pool covers. *Solar Energy*, *25*(5), 407–416. https://doi.org/10.1016/0038-092X(80)90447-8

Garnysz-Rachtan, A., & Zapałowicz, Z. (2018). Effect of air parameters, water temperature, and number of pool occupants on moisture gains. *E3S Web of Conferences*, *70*, 02006. https://doi.org/10.1051/e3sconf/20187002006

Haddy, L. M., & Hassen, A. S. D. M. (2021). Thermal Performance Prediction of Indoor Swimming Pool Solar Heating System Using Different Types of Flat-Plate Solar Collectors. *Association of Arab Universities Journal of Engineering Sciences, 28*(2), 8–18. https://doi.org/10.33261/jaaru.2021.28.2.002

Islam, M. M., Hasanuzzaman, M., Rahim, N. A., Pandey, A. K., Rawa, M., & Kumar, L. (2021). Real time experimental performance investigation of a NePCM based photovoltaic thermal system: an energetic and exergetic approach. *Renewable Energy*, *172*, 71–87. https://doi.org/10.1016/j.renene.2021.02.169

Lam, J. C., & Chan, W. W. (2001). Life cycle energy cost analysis of heat pump application for hotel swimming pools. *Energy Conversion and Management*, *42*(11), 1299-1306. https://doi.org/10.1016/S0196-8904(00)00146-1

Li, Y., Nord, N., Huang, G., & Li, X. (2021). Swimming pool heating technology: A state-of-the-art review. *Building Simulation*, *14*(3), 421–440. https://doi.org/10.1007/s12273-020-0669-3

Marín, J. P. D., García-Cascales, J. R. (2020). Dynamic simulation model and empirical validation for estimating energy demand in indoor swimming pools. *Energy Efficiency*, *13*, 955–970. https://doi.org/10.1007/s12053-020-09863-7

Mousia, A., & Dimoudi, A. (2015). Energy performance of open air swimming pools in Greece. Energy and Buildings, 90, 166–172. https://doi.org/10.1016/j.enbuild.2015.01.004

Natali, A., Bottarelli, M., & Fausti, P., (2020). A Methodology of Energy Optimization in Indoor Swimming Pool. *Tecnica Italiana-Italian Journal of Engineering Science*, *64*(2–4), 135–142. https://doi.org/10.18280/ti-ijes.642-402

Poudyal, A., Bhattarai, R. N. (2014). Design and Analysis of a Solar Swimming Pool Heating System" Proceedings of IOE Graduate Conference, 131–139. Available online: http://conference.ioe.edu.np/publications/ioegc2014/IOE-CONF-2014-16.pdf (Accessed on 3 August 2023).

Qader, F., Hussein, A., Danook, S., Mohamad, B., & Khaleel, O. (2023). Enhancement of double-pipe heat exchanger effectiveness by using porous media and TiO2 water. *CFD Letters*, 15(4), 31–42. https://doi.org/10.37934/cfdl.15.4.3142

Rajagopalan, P., & Jamei, E. (2015). Thermal comfort of multiple user groups in indoor aquatic centres. *Energy and Buildings*, *105*, 129–138. https://doi.org/10.1016/j.enbuild.2015.07.037

Starke, A. R., Cardemil, J. M., Escobar, R., & Colle, S. (2017). Thermal analysis of solar-assisted heat pumps for swimming pool heating. *Journal of the Brazilian Society of Mechanical Sciences and Engineering*, *39*(6), 2289–2306. https://doi.org/10.1007/s40430-016-0671-y

Tarrad, A. (2017). A Perspective Numerical Step by Step Thermal Modeling for Over-Ground Outdoor Swimming Pool Design Optimization. *International Journal OF Engineering Sciences & Management Research*, 4(8), 1–20.

Yadav, Y., & Tiwari, G. (1987). Analytical model of solar swimming pool: transient approach. *Energy Conversion and Management*, *27*(1), 49–54. https://doi.org/10.1016/0196-8904(87)90052-5

Zuccari, F., Santiangeli, A., & Orecchini, F. (2017). Energy analysis of swimming pools for sports activities: cost effective solutions for efficiency improvement. *Energy Procedia*, *126*, 123–130. https://doi.org/10.1016/j.egypro.2017.08.131

Badanie Wydajności, Symulacja, Projektowanie i Budowa Zamkniętego Basenu Słonecznego w Mieście Kirkuk

Streszczenie

Kryte pływalnie to obiekty sportowe lub rozrywkowe, które wymagają znacznej energii do podgrzania wody w basenie i utrzymania komfortowej atmosfery zgodnie z międzynarodowymi standardami. Tradycyjne metody ogrzewania basenów za pomocą paliw lub energii elektrycznej często wiążą się z wysokimi kosztami eksploatacji i zanieczyszczeniem środowiska. Aby sprostać tym wyzwaniom, słoneczne ogrzewanie wody stało się najbardziej znaczącą i przyjazną dla środowiska technologią. Budowa basenów zasilanych energią słoneczną stała się ważną kwestią, przyciągając znaczną uwagę rządów na całym świecie. Energia słoneczna jest obecnie wykorzystywana w różnych zastosowaniach, a ogrzewanie wody w budynkach mieszkalnych jest jednym z najpopularniejszych. Irak, znany ze swojego wysokiego potencjału energii słonecznej, może odnieść ogromne korzyści z budowy basenów słonecznych. Proponowany projekt obejmuje podstawowe elementy takie jak basen, pompa, filtr, zawory regulacyjne i kolektor słoneczny. Zbadano wpływ natężenia przepływu na wydajność kolektora słonecznego i jego związek z wielkością basenu w różnych warunkach pogodowych w mieście Kirkuk. Do badań wybrano miesiąc luty, charakteryzujący się niskim natężeniem promieniowania słonecznego i temperaturą powietrza. Wyniki badań dostarczyły informacji na temat ogrzewania basenów krytych za pomocą energii słonecznej z uwzględnieniem różnych rodzajów kolektorów słonecznych, filtrów i pomp. Opracowane wskazówki w zakresie projektowania systemu ogrzewania basenowego mogą odegrać kluczową rolę w ułatwieniu instalacji takich systemów.

Słowa kluczowe: kryte pływalnie, energia słoneczna, ogrzewanie basenu, obliczenia cieplne

Review

A Review of Enhancement of Thermal Performance of Flat–Plate Solar Collectors through Nanofluid Implementation

Zahraa H. Mohammed Ali * (iD), **Adnan M. Hussein** (iD)

Northern Technical University/Technical College of Engineering, 36001 Kirkuk, Iraq; dradnan@ntu.edu.pl (A.M. Hussein)

* Correspondence: zahraa.h.m@ntu.edu.iq

Abstract

Nanofluids have found widespread practical applications in heat transfer, including cooling oils for diverse uses like automobile radiators, solar and nuclear power systems, biomedical devices, ventilation, heating, air conditioning, refrigeration, engine cooling, and transformers. Extensive scientific studies have investigated the impact of exotic fluids when combined with traditional heat transfer fluids, revealing that this combination enhances heat transfer performance beyond that of conventional working fluids. Collectively, these studies demonstrate the impressive heat transfer abilities of nanofluids. To optimize the efficiency of flat plate solar collectors, a comprehensive approach integrating theory and experimentation is essential. The results of such research highlight that increasing both the mass flow rate and concentration of nanofluids can lead to significant efficiency improvements, with potential enhancements ranging from 20% to 85%. The aim of this article is to present scientific achievements in the field of the implementation of nanofluids to increase the thermal performance of flat-plate solar collectors.

Keywords: nanofluids, solar collector, flat plate, thermal performance, solar energy

1. Introduction

To meet the heating requirements of various industrial processes, flat-plate heaters are employed, operating at temperatures below 150 °C. These solar collectors have the remarkable capacity to elevate the working fluid's temperature by 30 to 100 °C above the ambient environment. The underlying principle involves harnessing the sun's radiation and efficiently transferring it to the working fluid flowing through the collector's tubes. In pursuit of improved thermal efficiency, nanofluids have emerged as promising candidates for solar collector fluids or operating fluids, offering the potential for significant energy and cost savings.

The advantages of renewable energy systems, such as reduced pollutants, have become increasingly vital as pollution worsens and the depletion of fossil fuels accelerates. Consequently, there is an urgent need for alternative, clean, and cost-effective energy sources (Ali et al. 2023; Berkache et al., 2022; Hussein et al. 2014; Kalogirou, 2004; Natarajan & Sathish, 2009; Qader et al., 2023). Addressing these challenges, Yousef et al. (2012) conducted a study on a 2 m² flat solar collector, augmenting its performance through the use of MWCNT-H$_2$O nanofluids. By varying the mass flow rate (ranging from 0.0167 to 0.05 kg/s), nanofluid concentration (ranging from 0.2 vol% to 0.4 vol%), and nanoparticle diameter (10 to 30 nm), they achieved a remarkable 83% increase in the efficiency of the flat solar collector.

Dutta et al. (2019) investigated magnetohydrodynamic natural convection and entropy generation in rhombic enclosures filled with Cu-water nanofluids. Numerical simulations cover various Rayleigh (*Ra*) and Hartmann (*Ha*) numbers, along with enclosure inclinations and nanofluid volume fractions. Findings reveal that magnetic fields notably affect heat transfer at high *Ra*, while the interaction of Hartmann number and nanofluid fraction influences thermal behavior and entropy generation. Same researcher investigates the impact of natural convection using Cu-water nanofluid in a two-

dimensional recto-trapezoidal enclosure for absorber plate fin applications. The enclosure has an inclination angle of 60°, with cold temperature maintained on the vertical walls, a hot temperature at the bottom, and an adiabatic top wall. Numerical simulations, utilizing finite element methods, analyze streamlines, isotherms, and heat transfer rates across a range of Rayleigh numbers ($10^3 \leq Ra \leq 10^6$) and solid volume fractions ($0 \leq \varphi \leq 0.1$) of Cu-water nanoparticles. Results reveal intensified streamlines at higher Rayleigh numbers for greater nanoparticle volume fractions, demonstrating heat transfer rate enhancements of over 20% at $Ra = 10^6$ and 30% enhancements using Cu-water nanofluid at $Ra = 10^3$ (Dutta & Biswas, 2019).

These findings underscore the immense potential of nanofluids to revolutionize solar collectors, offering a pathway towards more efficient and sustainable energy utilization. As research in this area progresses, nanofluids hold the promise of playing a pivotal role in our transition towards a cleaner and greener energy future.

2. Models of useful energy gain (Q_u) and efficiency of the flat–plate solar collectors (FPSC)

The most basic prerequisite for studying the thermal performance of flat plate solar collectors through nanofluid implementation model. This model's mathematical formula was reported in publications of (Ali et al., 2023; Hussein et al., 2014; Vijayakumaar et al., 2013) and it is as follows:

The density and specific heat capacity can be estimated as:

$$\rho_{nf} = (1 - \varphi)\rho_w + \varphi \times \rho_p \tag{1}$$

$$C_{P_{nf}} = \frac{(1 - \varphi)(\rho c_p)_w + \varphi(\rho c_p)_p}{(1 - \varphi)\rho_w + \varphi \times \rho_p} \tag{2}$$

The useful energy gain (Q_u) of the FPSC determined by:

$$Q_u = \dot{m} * Cp_w * (T_{ws.co} - T_{ws.cin}) = \tau\alpha * I(t) * A_{sc} - U_L * A_{sc} * (T_{pm} - T_a) \tag{3}$$

where $\dot{m}$, Cp_w $T_{ws.cin}$ and $T_{ws.co}$ are fluid mass flow rate, fluid specific heat, fluid inlet the solar collector and fluid outlet from the solar collector, respectively. τ is transmittance coefficient of cover glass, α is the absorption coefficient of the absorbent plate, $I(t)$ is solar radiation intensity instantious, A_{sc} is the flat plate solar water collector area, U_L is total heat loss coefficient, T_{pm} is absorption plate mean temperature, T_a is ambient temperature.

The hourly efficiency, η_{sc}, for the flat plate solar water collector is (Dutta et al., 2019):

$$\eta_{sc} = \frac{Q_u}{I(t) * A_{sc} * \Delta t} * 100\% = F_R\tau\alpha - F_R U_L \left(\frac{T_{ws.cin} - T_a}{I(t)}\right) \tag{4}$$

where F_R is heat removal factor, and Δt is time period.

In a study conducted by Vijayakumar et al. (2013), a carbon nanotube (CNT) nanofluid with a diameter of 1 nm and varying weight proportions (0.6%, 0.5%, and 0.4%) was applied to an area-based solar collector with a deployed area of 0.34 m². The data from this investigation revealed a significant 39% increase in efficiency during a focused effort at 0.5%.

Another controlled experiment, carried out by Chaji et al. (2013), involved the utilization of TiO₂ nanofluid mixed with water as the base fluid with a diameter of 20 nm. Various ratios of weight (0.3%, 0.2%, 0.1%, and 0%) and volumetric flow rates of 36, 72, and 108 dm³/h were employed on a 1 m² flat solar collector as shown in Figure 1. The introduction of nanoparticles in this setup resulted in a commendable 15.7% boost in collector efficiency, particularly at a flow rate of 108 dm³/h.

On a flat solar collector with an area of 0.67 m², Zamzamian et al. (2014) investigated Cu nanofluids mixed with ethanol, featuring diameters of 10 nm. The volumetric concentrations ranging from 0.2% to 0.3%. At specific flow rates of 0.016-0.050 kg/s and a concentration of 0.3 vol%, the highest efficiency was obtained, highlighting the favorable impact of these conditions on the collector's performance.

Additionally, Nasrin and Alim (2014) conducted an experiment involving nanoparticles of various sizes (Al₂O₃, CuO, and TiO₂) mixed with distilled water for a 1.51 m² solar collector as shown in

Figure 2. Three different concentrations of nanoparticles (0.2 vol%, 0.4 vol%, and 0.8 vol%) were used, along with a mass flow rate of 4 kg/min, creating a laminar flow environment. The results of the experiment indicated that enhancing the rate of heat transfer is greatly facilitated when nanoparticles are uniformly dispersed throughout the base liquid. These research endeavors demonstrate the immense potential of nanofluids in enhancing the efficiency of solar collectors, offering valuable insights into optimizing energy utilization and promoting sustainable practices.
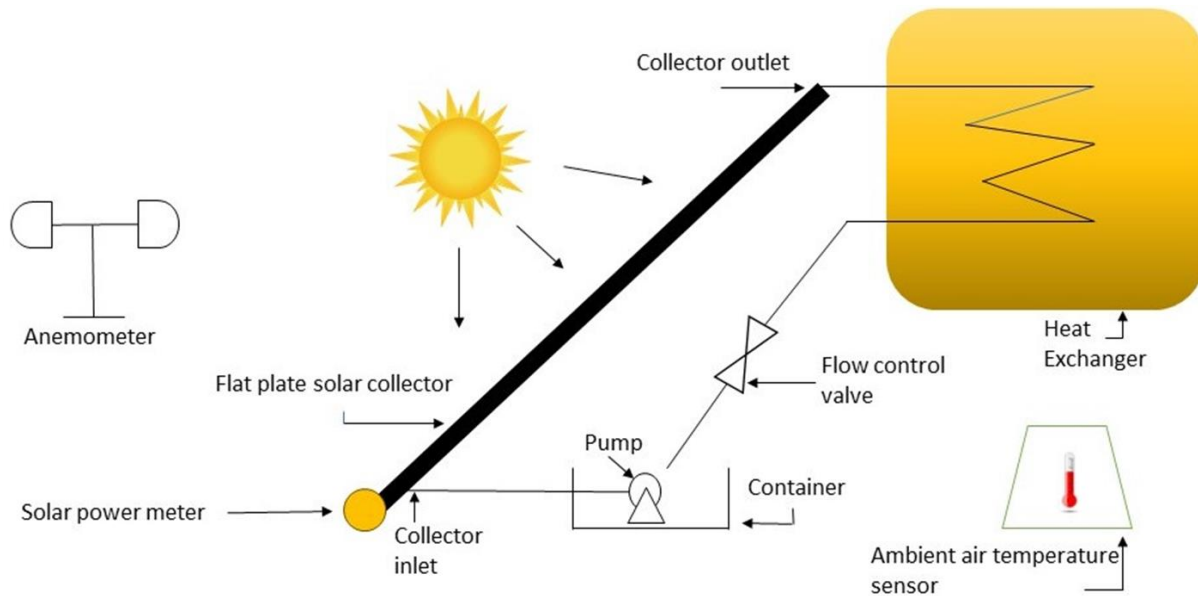
Fig. 1. The experimental set up schematic, prepared on the basis of Chaji et al. (2013).
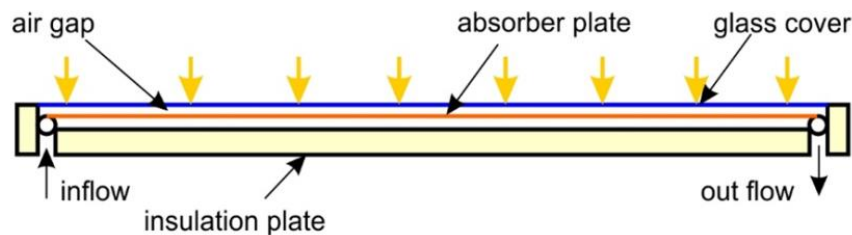
Fig. 2. The experimental set up schematic, prepared on the basis of Nasrin and Alim (2014).

The surface temperature gradient varies depending on the type of particle used, and copper particles exhibit a higher heat transfer rate compared to aluminum oxide and titanium oxide particles. The greatest improvement in efficiency, reaching 87.8%, is observed when using a combination of copper oxide and distilled water, surpassing the efficiency of distilled water alone by 52.5%.

Moghadam et al. (2014) examined the impact of CuO–water nanofluid in a flat-plate solar collector for domestic solar water heating. Nanofluid with 0.4 vol% CuO nanoparticles boosts collector efficiency by 21.8% compared to water alone at a 1 kg/min mass flow rate. The study suggests nanofluids can enhance thermal characteristics and improve collector performance in solar water heating systems.

During a separate experiment, a solar collector with an area of 2.184 m^2 was employed by Michael and Iniyan (2015). They have been used a CuO nanofluid with a diameter of 0.3-0.4 nm combined with water as the base fluid. The volumetric concentration was set at 0.05%, and the resulting efficiency of 57.98% at 0.1 kg/min for natural thermal load outperformed the forced thermal load.

Shojaeizadeh et al. (2015), researched on a 1.51 m^2 flat solar collector involving Al_2O_3 nanofluid mixed with distilled water, featuring a diameter of 15 nm and volumetric concentrations ranging from 0.090696 to 0.1423%, showed varying effects on combined energy by manipulating other factors. This study emphasized the potential for enhancing the available energy efficiency of nanofluids mixed with water.

Said et al. (2015) conducted an experiment on a solar collector with a flat surface area of 1.84 m^2 as shown in Figure 3. They utilized a TiO_2 nanofluid with a diameter of 21 nm and volumetric concentrations of 0.1% and 0.3%, employing a laminar flow with a mass flow rate of 0.5 kg/min. The per-

centage of efficiency increased by an impressive 76.6% compared to water as the base fluid, and the researchers used surfactants such as polyethylene clay and pentaethylene glycol (PEG) in the liquid.
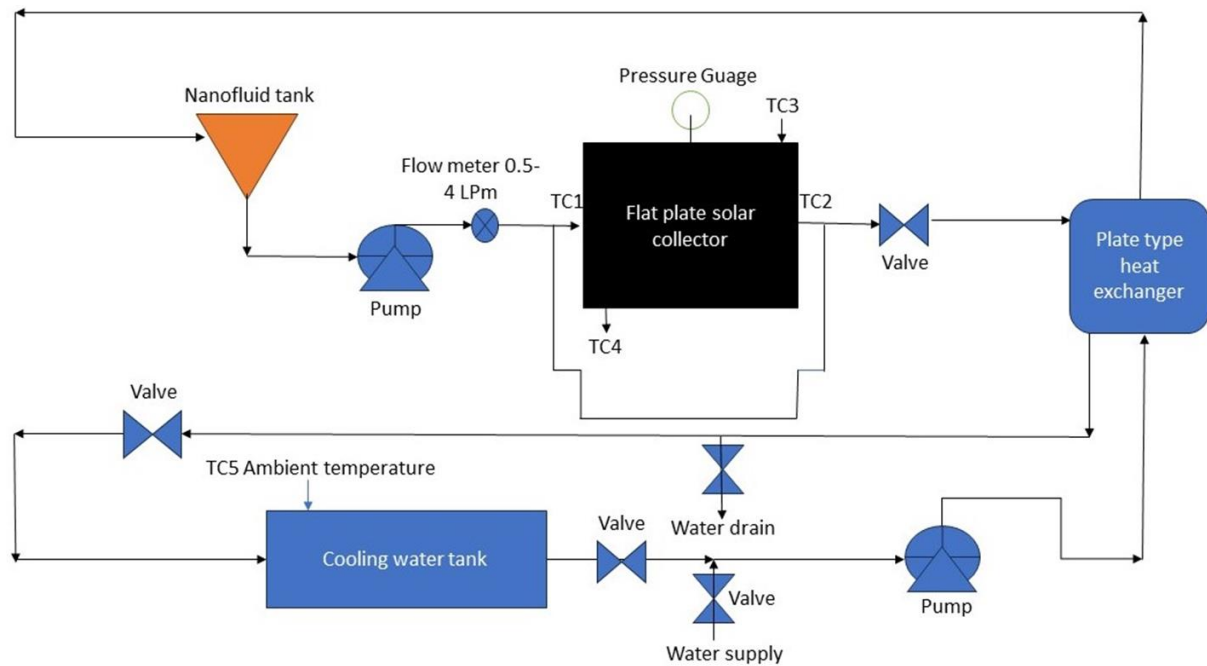
Fig. 3. Schematic presentation of the experimental setup, prepared on the basis of Said et al. (2015).

In the same year, Meibodi et al. (2015) conducted two experimental studies. The first study involved a flat solar collector of 1.59 m^2, using a nanofluid SiO$_2$/EG-water with a diameter of 10 nm and volumetric concentrations of 0.5%, 0.75%, and 1%. They operated with a turbulent flow and a mass flow rate of 2.7 kg/min. The results demonstrated a notable improvement in efficiency percentage, ranging from 4% to 8%, when compared to using water as the base fluid. In this study, the researchers utilized a flat solar collector with an area of 2 m^2, employing a SiO$_2$ nanofluid with a diameter of 10 nm and volumetric concentrations of 0.2%, 0.4%, and 0.6%. The flow condition was set to turbulent, and the mass flow rate was maintained at 3 kg/min. Remarkably, the findings revealed a substantial 23.5% increase in efficiency percentage as compared to using water as the base fluid.

Vakili et al. (2016) focused on enhancing the efficiency of solar collectors through a study on a 0.36 m^2 solar collector used for residential water heating. The results unveiled a noteworthy trend: the augmentation of collector efficiency in direct correlation to the increase in nanofluid weight fraction. Strikingly, the pinnacle of collector efficiency was achieved at the 0.015 kg/s flow rate, applying to both the base fluid and nanofluids alike. The efficiencies were quantified with exceptional precision: zero-loss efficiencies using nanofluids at weight fractions of 0.0005, 0.001, and 0.005 emerged at 83.5%, 89.7%, and 93.2%, respectively, while the base fluid yielded a comparatively modest 70% zero-loss efficiency.

Similarly, Verma et al. (2016) conducted an experiment on a 0.375 m^2 flat solar collector to investigate the impact of varying volumetric concentrations of MgO nanofluid mixed with water on the collector's efficiency. The results demonstrated a considerable 9.34% increase in heat efficiency at a concentration of 0.75% and a volumetric flow rate of 1.5 dm^3/min. Furthermore, the utilization of nanofluid as a base fluid resulted in a significant 32.23% improvement in the collector's availability efficiency at the same volumetric concentration and mass flow rate when compared to using water. Notably, the entropy generated at a concentration of 0.75 percent was lower, measuring 0.0611 W/K, as opposed to the concentration of 1.5 percent (0.071 W/K) with a flow rate of 0.1394 W/K.

Verma et al. (2017) conducted a research study aimed at enhancing the efficiency of solar collectors. They performed experiments on a flat solar collector with an area of 0.375 m^2, exploring various nanoparticles mixed with water at different concentrations and sizes. The volumetric concentration used in their study was 0.75%, with a mass flow rate of 0.025 kg/s, and the available energy was assessed. The research team found that employing TiO$_2$-H$_2$O, SiO$_2$-H$_2$O, CuO-H$_2$O, Al$_2$O$_3$-H$_2$O, Graphene-H$_2$O, and MWCNTs-H$_2$O as primary and subordinate liquids led to noteworthy improvements in thermal efficiency, showing percentage enhancements of 5.74, 6.97, 10.86, 16.67, 21.46, and 29.32, respectively, compared to water. Additionally, the entropy generated by the solar collector was lower

for each of the mentioned combinations, ranging from 4.08% to 5.09%, from 8.28% to 12.64%, and from 16.97% to 23.4%.

In another study, Jouybari et al. (2017) evaluated the thermal efficiency of a 0.8 m^2 solar collector, aiming to enhance the collector's performance by using a SiO$_2$ nanofluid with a diameter of 7 nm mixed with a water-based carrier fluid. The researchers assessed three different nanoparticle concentrations (0.2%, 0.4%, and 0.8%) and a flow velocity of 1.5 kg/min to create a laminar flow environment. The study findings indicated that heat transfer was directly proportional to the nanoparticle concentration in the base liquid, and the type of particle used had a notable impact on the flat surface collector's performance. There was a notable 8% increase in productivity compared to using water as the base fluid. In another experiment, Sundar et al. (2018) conducted a study on a 2 m^2 flat solar collector with turbulent flow, utilizing Al$_2$O$_3$ nanofluid at 0.1% and 0.3% by volume, and a flow rate of 5 kg/s. This resulted in an impressive 18% efficiency increase in contrast to using H$_2$O as the primary medium.

Kiliç et al. (2018) evaluated the impact of a TiO$_2$ Triton X-100 nanofluid, with a 44 nm diameter, 0.2% volumetric concentration, and 2 kg/min mass flow rate, on the efficiency of a flat solar collector with an area of 1.82 m^2. According to their findings, the use of CeO$_2$ nanofluid in water, at varying mass flow rates and volumetric concentrations, can improve the performance of a flat solar collector by up to 34.43% compared to using water alone. Sharafeldin and Gróf (2018) discovered a linear relationship between the collector's thermal efficiency and the concentration of nanoparticles in the mass flow.

In another study by Tong et al. (2019), nanofluids with varying concentrations were used to assess their impact on the efficiency of a 2 m^2 flat solar collector. The best efficiency was achieved with a volumetric concentration of 0.1% Al$_2$O$_3$ nanofluid, resulting in a remarkable 21.9% efficiency rating. Moreover, the use of nanofluids, particularly with a volumetric concentration of 0.1 vol% Al$_2$O$_3$ or 0.5 vol% CuO, significantly increased the available energy by 56% and 49.6%, respectively, when compared to water as the base fluid. Additionally, the highest level of entropy was observed when using water, whereas the lowest was observed with a nanofluid containing 0.1 vol% Al$_2$O$_3$.

According to these findings, the incorporation of nanofluids into water can effectively enhance the performance of flat plate solar collectors, particularly with a 0.1% volumetric concentration of Al$_2$O$_3$ nanofluid. In an experimental study conducted by Choudhary et al. (2020) to optimize the performance of a 2.1 m^2 flat solar collector, they used ZnO nanofluid in EG&H Blend (ethylene glycol and water) with a 50 nm diameter and a volumetric flow rate of 30-150 dm^3/h. As the flow rate increased, the collector's thermal efficiency improved, reaching a maximum of 69.24% at a flow rate of 60 dm^3/h and a 1% volumetric concentration of nanofluid. This translated to a significant 19.24% boost in productivity compared to using distilled water alone.

Okonkwo et al. (2020) conducted an evaluation using single and hybrid nanofluids (Al$_2$O$_3$ and Al$_2$O$_3$-Fe) combined with water as the base fluid in a flat solar collector with a surface area of 1.51 m^2. The study revealed that nanofluid usage resulted in a more sensitive measurement of produced entropy compared to using water. The lowest percentage of entropy created was 5.541% W/K, and the highest percentage was 5.725% W/K, both achieved with nanofluid. Utilizing a nanofluid containing Al$_2$O$_3$ with a concentration of 0.1 vol% as the base fluid improved the thermal efficiency of the flat solar collector by 2.16%, while a hybrid nanofluid decreased it by 1.79%. However, the hybrid nanofluids were found to improve availability efficiency by 6.9% when compared to a single nanofluid.

To enhance the heat transfer process over a 3 m^2 area and increase efficiency, Alklaibi et al. (2021) conducted an experiment using a flat solar collector with a nanofluid containing diamond particles mixed with water as the base fluid. Different volume concentrations of 0.2, 0.4, 0.6, 0.8, and 1% were tested at a mass flow rate of 0.02 kg/s. The study found that using a 1 vol% concentration of nano-diamond fluid in water increased the flat solar collector's effectiveness by an impressive 69.8% compared to using water alone as the base fluid.

In the research by Hawwash et al. (2018), flat solar collectors with a surface area of 2.1 m^2 were evaluated, utilizing nanofluid Al$_2$O$_3$ with a diameter of 20 nm and a mass flow rate of 5.51 kg/min at volume concentrations ranging from 0.1 to 0.3% in distilled water. The study demonstrated that in the hot climate of Egypt, this research improved efficiency by 0.18% over water. The theoretical work was performed using ANSYS 17 program, and it was found that nanoparticles in the fluid reduced pressure, enhanced efficiency, and cooled the collector output. Two nanofluids were generated, one with TiO$_2$ and the other with Al$_2$O$_3$.

Farajzadeh et al. (2018) conducted a theoretical and experimental investigation to explore how nanofluids could enhance the efficiency of a flat 2 m^2 solar collector. Nanofluids with 20 nm particles and cetyltrimethylammonium bromide (CTAB) surfactant enhancer were used, with different volumetric flow rates (2.0, 2.0, and 1.5 dm^3/min) for different groups. The use of nanofluids instead of water increased the flat solar collector efficiency by 19%, 21%, and 26% for the respective flow rate groups. The study found that nanoparticle concentration had a positive effect on efficiency, with a 5% improvement. Both computational fluid dynamics (CFD) and numerical calculations yielded equivalent results, confirming the findings.

In the evaluation by Alawi et al. (2021), a flat solar collector with varying concentrations of graphene powder in distilled water was investigated. Different variables were assessed, such as mass flows (0.5, 1, and 1.5 kg/min), temperatures (30, 40, and 50 °C), and radiation intensities (500, 750, and 1000 W/m^2). The study consistently showed that mass flow increased heat transfer, circulation, and graphene nanoplatelets (GrNPs) percent. Nanofluids significantly influenced the thermal performance of flat-plate solar collectors, with CeO_2 nanofluid addition to varying mass flow rates and volumetric concentrations resulting in an efficiency increase of 34.43%. Flat solar collectors using nanofluids outperformed water-based ones, with efficiency improvements of 19%, 21%, and 26% for different flow rates. Concentrations of 0.075 wt.% and 0.1 wt.% at 0.025 kg/s achieved efficiencies of 13% and 12.5% respectively compared to water. MATLAB calculations were used to verify and validate the efficiency of the flat solar collector, demonstrating that introducing nanofluids led to an overall rise in efficiency in conjunction with water flow. Dutta et al. (2021) examines magnetohydrodynamic buoyancy-driven thermal energy transport within a copper-water nanofluid-filled quadrantal enclosure. The enclosure's base experiences constant temperature heating, while the vertical wall maintains a uniform cold temperature and the curved wall is insulated. Across the parameter range of $10^3 \leq$ Rayleigh number $(Ra) \leq 10^6$, $0 \leq$ Hartmann number $(Ha) \leq 100$, and $0 \leq$ volume fraction of nanoparticles $(\phi) \leq 0.05$, the research indicates that the average Nusselt number increases with ϕ and decreases with Ha, particularly at higher Ra (10^5 and 10^6) values. Moreover, altering the enclosure's sector angle affects the heat transfer rate alongside Ra, ϕ, and Ha, emphasizing the combined role of geometry and influencing factors in heat transfer alterations.

Keerthi et al. (2022) investigates convective-radiative heat exchange with a radial-profile wet porous fin exposed to a hybrid nanofluid flowing at a constant velocity. The analysis considers various nanoparticle shape combinations and employs the mixture model to assess thermophysical attributes. By applying numerical techniques, the effects of multiple parameters on energy distribution, thermal gradient profiles, and thermal fin efficiency are graphically analyzed. Notably, nanoparticle volume fraction and shape factor significantly influence efficiency, with the highest value observed for the spherical-platelet combination, highlighting potential in extended surface technology enhanced by nanotechnology. Mohamad and Zelentsov (2022) employed a range of optimization techniques, starting from 1D simulations and extending to full 3D CFD simulations. These methods are also combined, utilizing a hybrid approach that integrates a 1D model with 3D tools.

3. Nanofluids

Nanofluids, composed of nanoparticles dispersed in base fluids, have emerged as a potential solution for enhancing the efficiency of flat plate solar collectors. By incorporating nanoparticles with high thermal conductivity, such as metal or oxide nanoparticles, these nanofluids can significantly enhance heat absorption and transfer within the collector, ultimately improving overall energy conversion. Various types of nanofluids, including metal-based (e.g., copper, silver), oxide-based (e.g., alumina, titania), and hybrid nanofluids, offer versatile options for tailoring the performance of flat plate solar collectors to specific operational conditions and requirements. Farhana et al. (2019) conducted a meticulous investigation aimed at evaluating the state of three distinct flow parameters concerning nanofluids and hybrid nanofluids as they traverse the internal header and riser tubes of a flat plate solar collector. The study employed CFD modeling, employing nanofluids such as Al_2O_3, TiO_2, and ZnO, as well as hybrid nanofluids like Al_2O_3+TiO_2, TiO_2+ZnO, and ZnO+Al_2O_3.

The modeling approach adopted a three-dimensional framework, utilizing the k-epsilon turbulence model configured with the Standard and Standard Wall Functions. The research maintained an absolute reference frame and a predetermined calculative intensity percentage throughout the modeling. The base fluid utilized in the study was water, with a consistent volume fraction of 0.1% for both nanofluids and hybrid nanofluids. The research methodology involved a single-phase viscous model accompanied by an energy equation. Three distinct design models (referred to as Model A, Model B,

and Model C) were employed, featuring fixed inlet and outlet diameters. While the number of header tubes was consistently set at two, the number of riser tubes varied across three scenarios: two, seven, and twelve.

The findings from Farhana et al. (2019) study yielded noteworthy results. In Model B, both nanofluids and hybrid nanofluids experienced a considerable increase in maximum dynamic pressure, with approximately 48% and 16% increments, respectively. Furthermore, Model B showcased the most significant enhancement in velocity magnitude for both nanofluids and hybrid nanofluids. The study also highlighted that the highest turbulence kinetic energy was achieved in Model A (5.5%) for nanofluids and in Model B (18%) for hybrid nanofluids. Ultimately, Farhana et al. (2019) work underscored the superior performance of Model B when compared to both Model A and Model C.

These findings provide evidence that nanofluids have the potential to enhance solar collector performance. However, the choice of nanoparticle and model can impact the extent of improvement. The details of the finding from selected references are presented in Table 1.

Table 1. Summary of the main findings on analysis of thermal performance of solar collectors through nanofluid implementation

Reference	Type of the study	Nanoparticle type	Used liquid	Findings
Yousef et al. (2012)	Experimental	MWCNT	H_2O	Increased mass flow rate and nanofluid concentration resulted in an 83% improvement in the planar solar collector's efficiency.
Vijayakumar et al. (2013)	Experimental	CNT	H_2O	At a volume fraction of 0.5%, the results showed a 39% increase in efficiency.
Chaji et al. (2013)	Experimental	TiO_2	H_2O	The effectiveness of the solar collector rose in proportion to the volumetric rate of flow.
Zamzamian et al. (2014)	Experimental	Cu	C_2H_6O	Nanofluids boost collector efficiency and absorb power factor.
Nasrin and Alim (2014)	Experimental	TiO_2, CuO, Al_2O_3	H_2O	Copper oxide with distilled water had the largest efficiency gain (87.8%), while aluminum oxide and titanium oxide had lower numbers (71%). in contrast to pure water.
Moghadam et al. (2014)	Experimental	CuO	H_2O	The efficiency rate was 21.8% higher in comparison to water.
Michael and Iniyan (2015)	Experimental	CuO	H_2O	At flow rate of 0.1 kg/s, the solar collector is 57.98% efficient compared to a forced load.
Shojaeizadeh et al. (2015)	Experimental	Al_2O_3	H_2O	Change other parameters and increase nanofluids mixed with water energy efficiency to affect combined energy.
Said et al. (2015)	Experimental	TiO_2	H_2O	The results proved a 76.6% efficiency gain compared to when water was the starting point.
Meibodi et al. (2015)	Experimental	SiO_2/EG	H_2O	In contrast to working with water, in contrast to working with water, the findings revealed a percentage efficiency gain of 4-8%.
Meibodi et al. (2015)	Experimental	SiO_2	H_2O	Compared to water, efficiency was 23.5% greater.
Vakili et al. (2016)	Experimental	Graphene nanoplatelets	H_2O	A mass flow rate of 0.015 kg/s is optimal for the planar solar collector.
Verma et al. (2016)	Experimental	MgO	H_2O	The collector's heat efficiency increased 9.34% at flow rate 1.5 dm^3/min and 0.75% concentration.
Verma et al. (2017)	Experimental	(MWCNTs, graphene, CuO, SiO_2, TiO_2, Al_2O_3)	H_2O	Highest possible solar collector efficiency.
Jouybari et al. (2017)	Experimental	SiO_2	H_2O	The rate of heat transmission increased as nanoparticle concentration in the base liquid increased.

Table 1. *Cont.*

Reference	Type of the study	Type of nanofluid used	Used liquid	Findings
Sundar et al. (2018)	Experimental	Al_2O_3	H_2O	Compared to water, efficiency was 18% greater.
Kiliç et al. (2018)	Experimental	TiO_2 Triton X-100	H_2O	In contrast to working with water, the findings showed a 34.43% efficiency increase.
Sharafeldin and Gróf (2018)	Experimental	CeO_2	H_2O	Collector thermal efficiency is a function of the volumetric concentration of nano-particles and the mass flow rate.
Tong et al. (2019)	Experimental	CuO, Al_2O_3	H_2O	Nanofluids in water improved solar collector performance.
Choudhary et al. (2020)	Experimental	ZnO	mixed with a mixture of ethylene clay col with distilled	At flow rate of 150 dm^3/h, a flat solar collector's thermodynamic efficiency rises, and its exit temperature is 45.47 ºC.
Okonkwo et al. (2020)	Experimental	Al_2O_3-Fe, Al_2O_3	H_2O	A hybrid nanofluid enhances the availability efficiency by 6.9% relative to the size of a single nanofluid.
Alklaibi et al. (2021)	Experimental	Diamond	H_2O	Nanofluid generated greater entropy than water.
Hawwash et al. (2018)	Theoretical and experimental	Al_2O_3	H_2O	Increased water nanoparticle concentrations enhanced solar collector efficiency and exit temperature.
Farajzadeh et al. (2018)	Numerical and experimental	TiO_2-Al_2O_3	H_2O	Nanofluids instead of water increased flat solar collector efficiency by 19- 26%. Nanoparticle concentration between 0.1 vol% and 0.2 vol% increases performance by 5%.
Alawi et al. (2021)	Theoretical and experimental	Graphene	H_2O	By raising volumetric concentration of GrNPs and fluid mass flow rate, heat transmission was improved. At 0.075 wt.% and 0.1 wt.%, the flat solar collector was 13% efficient, whereas at 0.025 wt.%, it was only 12.5% efficient.
Alim et al. (2013)	Theoretical	TiO_2, SiO_2, CuO, Al_2O_3	H_2O	CuO nanofluid potentially decreases entropy creation by 22.15% compared to water.
Farhana et al. (2019)	Theoretical	ZnO, TiO_2, Al_2O_3 and hybrid nanofluids ZnO+ ZnO, TiO_2+TiO_2, Al_2O_3+Al_2O_3	H_2O	Utilizing three scenarios: two, seven, and twelve of riser tubes to enhance thermal performance of flate plate solar collector

4. Conclusions

Numerous researchers have found that incorporating nanofluids in a solar collector can significantly enhance its efficiency, leading to the following improvements:

- Enhanced flow rate in a volumetric medium: when nanofluids are used as the working fluid in a solar collector, the flow rate within the collector increases. This increase in flow rate contributes to the overall improvement in the collector's efficiency.
- Increased efficiency with higher fluid concentration and absorbed power: as the concentration of nanofluids in the solar collector rises, along with the absorbed power factor, the efficiency of the collector is further improved. Higher concentrations of nanofluids lead to better thermal performance and energy absorption, resulting in enhanced overall efficiency.

By leveraging nanofluids mixed with water, researchers have identified these key factors that positively impact the efficiency of solar collectors, paving the way for more efficient and effective solar energy utilization.

References

Alawi, O.A., Kamar, H.M., Mallah, A.R., Mohammed, H.A., Sabrudin, M.A.S., Newaz, K.M.S., Najafi, G., & Yaseen, Z.M. (2021). Experimental and theoretical analysis of energy efficiency in a flat plate solar collector using monolayer graphene nanofluids. *Sustainability*, *13*, 5416. https://doi.org/10.3390/su13105416

Ali, H. H. M., Hussein, A. M., Allami, K. M. H., & Mohamad, B. (2023). Evaluation of shell and tube heat exchanger performance by using ZnO/water nanofluids. *Journal of Harbin Institute of Technology (New Series),* 30, 1–13 https://doi.org/10.11916/j.issn.1005-9113.2023001

Alim, M. A., Abdin, Z., Saidur, R., Hepbasli, A., Khairul, M. A., & Rahim, N. A. (2013). Analyses of entropy generation and pressure drop for a conventional flat plate solar collector using different types of metal oxide nanofluids. Energy and Buildings, 66, 289–296. https://doi.org/10.1016/j.enbuild.2013.07.027

Alklaibi, A. M., Sundar, L. S., & Sousa, A. C. M. (2021). Experimental analysis of exergy efficiency and entropy generation of diamond/water nanofluids flow in a thermosyphon flat plate solar collector. I*nternational Communications in Heat Mass Transfer*, *120*, 105057. https://doi.org/10.1016/j.icheatmasstransfer.2020.105057

Berkache, A., Amroune, S., Golbaf, A., & Mohamad, B. (2022). Experimental and numerical investigations of a turbulent boundary layer under variable temperature gradients. *Journal of the Serbian Society for Computational Mechanics*, 16(1), 1–15. https://doi.org/10.24874/jsscm.2022.16.01.01

Chaji, H., Ajabshirchi, Y., Esmaeilzadeh, E., Heris, S. Z., Hedayatizadeh, M., & Kahani, M. (2013). Experimental study on thermal efficiency of flat plate solar collector using TiO2/water nanofluid. *Modern Applied Science*, *7*(10), 60–69. https://doi.org/10.5539/mas.v7n10p60

Choudhary, S., Sachdeva, A., & Kumar, P. (2020). Investigation of the stability of MgO nanofluid and its effect on the thermal performance of flat plate solar collector. *Renewable Energy*, *147*, 1801–1814, https://doi.org/10.1016/j.renene.2019.09.126

Dutta, S., Biswas, A. (2019). A numerical investigation of natural convection heat transfer of copper-water nanofluids in a rectotrapezoidal enclosure heated uniformly from the bottom wall. *Mathematical Modelling of Engineering Problems*, *6*, 105–114. https://doi.org/10.18280/mmep.06011

Dutta, S., Goswami, N., Biswas, A. K., & Pati, S. (2019). Numerical investigation of magnetohydrodynamic natural convection heat transfer and entropy generation in a rhombic enclosure filled with Cu-water nanofluid. *International Journal of Heat and Mass Transfer*, *136*, 777–798. https://doi.org/10.1016/j.ijheatmasstransfer.2019.03.024

Dutta, S., Pati, S., & Baranyi, L. (2021). Numerical analysis of magnetohydrodynamic natural convection in a nanofluid filled quadrantal enclosure. *Case Studies in Thermal Engineering*, *28*, 101507. https://doi.org/10.1016/j.csite.2021.101507

Farajzadeh, E., Movahed, S., & Hosseini, R. (2018). Experimental and numerical investigations on the effect of Al2O3/TiO2–H2O nanofluids on thermal efficiency of the flat plate solar collector. *Renewable Energy*, *118*, 122–130. https://doi.org/10.1016/j.renene.2017.10.102

Farhana, K., Kadirgama, K., Noor, M. M., Rahman, M. M., Ramasamy, D., & Mahamude, A. S. F. (2019). CFD modelling of different properties of nanofluids in header and riser tube of flat plate solar collector. *IOP Conference Series: Materials Science and Engineering*, *469*(1), 012041. https://doi.org/10.1088/1757-899X/469/1/012041

Hawwash, A. A., Abdel Rahman, A. K., Nada, S. A., & Ookawara, S. (2018). Numerical investigation and experimental verification of performance enhancement of flat plate solar collector using nanofluids. *Applied Thermal Engineering*, *130*, 363–374. https://doi.org/10.1016/j.applthermaleng.2017.11.027

Hussein, A. K., Ashorynejad, H. R., Shikholeslami, M., & Sivasankaran, S. (2014). Lattice Boltzmann simulation of natural convection heat transfer in an open enclosure filled with Cu–water nanofluid in the presence of a magnetic field. *Nuclear Engineering and Design*, *268*, 10–17. https://doi.org/10.1016/j.nucengdes.2013.11.072

Jouybari, H. J., Saedodin, S., Zamzamian, A., Nimvari, M. E., & Wongwises, S. (2017). Effects of porous material and nanoparticles on the thermal performance of a flat plate solar collector: An experimental study. *Renewable Energy*, *114*, 1407–1418. https://doi.org/10.1016/j.renene.2017.07.008

Kalogirou, S. (2004). Solar thermal collectors and applications. *Progress in Energy and Combustion Science*, *30*, 231–295. https://doi.org/10.1016/j.pecs.2004.02.001

Keerthi, M. L., Gireesha, B. J., & Sowmya, G. (2022). Numerical investigation of efficiency of fully wet porous convective-radiative moving radial fin in the presence of shape-dependent hybrid nanofluid. *International Communications in Heat and Mass Transfer*, *138*, 106341. https://doi.org/10.1016/j.icheatmasstransfer.2022.106341

Kiliç, F., Menlik, T., & Sözen, A. (2018). Effect of titanium dioxide/water nanofluid use on thermal performance of the flat plate solar collector. *Solar Energy*, *164*, 101–108. https://doi.org/10.1016/j.solener.2018.02.002

Meibodi, S. S., Kianifar, A., Niazmand, H., Mahian, O., & Wongwises, S. (2015). Experimental investigation on the thermal efficiency and performance characteristics of a flat plate solar collector using SiO2/EG-water nanofluids. *International Communications in Heat and Mass Transfer*, *65*, 71–75. https://doi.org/10.1016/j.icheatmasstransfer.2015.02.011

Michael, J. J., & Iniyan, S., (2015). Performance of copper oxide/water nanofluid in a flat plate solar water heater under natural and forced circulations. *Energy Conversion and Management*, *95*, 160–169. https://doi.org/10.1016/j.enconman.2015.02.017

Moghadam, A. J., Farzane-Gord, M., Sajadi, M., & Hoseyn-Zadeh, M. (2014). Effects of CuO/water nanofluid on the efficiency of a flat-plate solar collector. *Experimental Thermal and Fluid Science*, *58*, 9–14. https://doi.org/10.1016/j.expthermflusci.2014.06.014

Mohamad, B., & Zelentsov, A. (2022). Methode hybride pour la conception et l'optimisation d'un echappement silencieux de voitures de course formula. *Canadian Acoustics / Acoustique canadienne, 50(4)*, 5-11.

Nasrin, R., & Alim, M. A. (2014). Semi-empirical relation for forced convective analysis through a solar collector. *Solar Energy*, *105*, 455–467. https://doi.org/10.1016/j.solener.2014.03.035

Natarajan, E., & Sathish R. (2009). Role of nanofluids in solar water heater. *International Journal of Advanced Manufacturing Technology*, *43*, 6082–6087. https://doi.org/10.1007/s00170-008-1876-8

Okonkwo, E. C., Wole-Osho, I., Kavaz, D., Abid, M., & Al-Ansari, T. (2020). Thermodynamic evaluation and optimization of a flat plate collector operating with alumina and iron mono and hybrid nanofluids. *Sustainable Energy Technology and Assessments*, *37*, 100636. https://doi.org/10.1016/j.seta.2020.100636

Qader, F., Hussein, A., Danook, S., Mohamad, B., & Khaleel, O. (2023). Enhancement of Double-Pipe Heat Exchanger Effectiveness by Using Porous Media and TiO2 Water. *CFD Letters*, *15*(4), 31–42. https://doi.org/10.37934/cfdl.15.4.3142

Said, Z., Saidur, R., Sabiha, M. A., Rahim, N. A., & Anisur, M. R. (2015). Thermophysical properties of single wall carbon nanotubes and its effect on exergy efficiency of a flat plate solar collector. *Solar Energy*, *115*, 757–769. https://doi.org/10.1016/j.solener.2015.02.037

Sharafeldin M. A., & Gróf, G. (2018). Experimental investigation of flat plate solar collector using CeO$_2$-water nanofluid. *Energy Conversion and Management*, *155*, 32–41. https://doi.org/10.1016/j.enconman.2017.10.070

Shojaeizadeh, E., Veysi, F., & Kamandi, A. (2015). Exergy efficiency investigation and optimization of an Al$_2$O$_3$-water nanofluid based Flat-plate solar collector. *Energy and Buildings*, *101*, 12–23. https://doi.org/10.1016/j.enbuild.2015.04.048

Sundar, L. S. Singh, M. K. Punnaiah, V. Sousa, A. C. M. (2018). Experimental investigation of Al$_2$O$_3$/water nanofluids on the effectiveness of solar flat-plate collectors with and without twisted tape inserts. *Renewable Energy*, *119*, 820–833. https://doi.org/10.1016/j.renene.2017.10.056

Tong, Y., Lee, H., Kang, W., & Cho, H. (2019). Energy and exergy comparison of a flat-plate solar collector using water, Al$_2$O$_3$ nanofluid, and CuO nanofluid. *Applied Thermal Engineering*, *159*, 113959. https://doi.org/10.1016/j.applthermaleng.2019.113959

Vakili, M., Hosseinalipour, S. M., Delfani, S., Khosrojerdi, S., & Karami, M. (2016). Experimental investigation of graphene nanoplatelets nanofluid-based volumetric solar collector for domestic hot water systems. *Solar Energy*, *131*, 119–130. https://doi.org/10.1016/j.solener.2016.02.034

Verma, S. K., Tiwari, A. K., & Chauhan, D. S. (2016). Performance augmentation in flat plate solar collector using MgO/water nanofluid. *Energy Conversion and Management*, *124*, 607–617. https://doi.org/10.1016/j.enconman.2016.07.007

Verma, S. K., Tiwari, A. K., & Chauhan, D. S. (2017). Experimental evaluation of flat plate solar collector using nanofluids. *Energy Conversion and Management*, *134*, 103–115. https://doi.org/10.1016/j.enconman.2016.12.037

Vijayakumaar, S. C. R., Shankar, L., & Babu, K. (2013). Effect of CNT-H$_2$O nanofluid on the performance of solar flat plate collector-an experimental investigation. Proceedings of the International Conference on Advanced Nanomaterials & Emerging Engineering Technologies ICANMEET 2013, India, pp. 197–199. https://doi.org/10.1109/ICANMEET.2013.6609275

Yousefi, T., Shojaeizadeh, E., Veysi, F., & Zinadini, S. (2012). An experimental investigation on the effect of pH variation of MWCNT-H 2O nanofluid on the efficiency of a flat-plate solar collector. *Solar Energy*, *86*(2), 771–779. https://doi.org/10.1016/j.solener.2011.12.003

Zamzamian, A., KeyanpourRad, M., KianiNeyestani, M., & Jamal-Abad, MAZZ. T. (2014). An experimental study on the effect of Cu-synthesized/EG nanofluid on the efficiency of flat-plate solar collectors. *Renewable Energy*, *71*, 658–664. https://doi.org/10.1016/j.renene.2014.06.003

Przegląd Doskonalenia Wydajności Cieplnej Płaskich Kolektorów Słonecznych poprzez Zastosowanie Nanocieczy

Streszczenie

Nanociecze znalazły szerokie praktyczne zastosowanie w wymianie ciepła. Oleje chłodzące w tym oleje stosowane są w różnych zastosowaniach, takich jak chłodnice samochodowe, systemy energii słonecznej i jądrowej, urządzenia biomedyczne, wentylacja, ogrzewanie, klimatyzacja, chłodnictwo, chłodzenie silników i transformatorów. Celem szeroko zakrojonych badań naukowych było zbadanie wpływu egzotycznych cieczy w połączeniu z tradycyjnymi cieczami przenoszącymi ciepło, ujawniając, że ta kombinacja poprawia wydajność wymiany ciepła w porównaniu z konwencjonalnymi cieczami roboczymi. Badania wykazały imponujące zdolności przenoszenia ciepła przez nanociecze. Optymalizacja wydajności płaskich kolektorów słonecznych polega na kompleksowym podejściu łączącym metody teoretyczne oraz badania eksperymentalne. Wyniki takich badań podkreślają, że zwiększenie zarówno masowego natężenia przepływu, jak i stężenia nanocieczy może prowadzić do potencjalnej poprawy wydajności w zakresie od 20% do 85%. Celem tego artykułu jest zaprezentowanie osiągnięć naukowych w zakresie implementacji nanocieczy do zwiększenia efektywności cieplnej płaskich kolektorów słonecznych.

Słowa kluczowe: nanociecze, kolektor słoneczny, płaska płyta, sprawność cieplna, energia słoneczna

Original Research

Effect of Heating and Cooling of Aluminium-Based Fibre Metal Laminates on Their Tensile Strength

Kamil Boczar [1] , **Karol Wasłowicz [2]** , **Andrzej Kubit [3]** , **Dorota Chodorowska [4]** ,
Romuald Fejkiel [4],*

[1] Nowy Styl sp. z o.o., ul. Pużaka 49, 38-400 Krosno, Poland; kamil.boczar12344@gmail.com
[2] Eba Sp. z o.o. Artykuły Metalowe, ul. Popiełuszki 86, 38-400 Krosno, Poland; karol.waslowicz@gmail.com
[3] Department of Manufacturing Processes and Production Engineering, Rzeszow University of Technology, al. Powst. Warszawy 8, 35-959 Rzeszów, Poland; akubit@prz.edu.pl
[4] Department of Mechanics and Machine Building, The State Academy of Applied Sciences, Rynek 1, 38-400 Krosno, Poland; dorota.chodorowska@kpu.krosno.pl (D. Chodorowska)

* Correspondence: romuald.fejkiel@kpu.krosno.pl

Abstract

The widespread use of composite materials in the construction of machines encourages to better understand their properties and the impact of various external factors on these properties. Fibre metal laminates (FMLs) consist of alternating layers of metal and a polymer matrix laminate reinforced with continuous fibres. The aim of this work was to investigate the effect of cyclical temperature changes and thermal shocks (heating the sample to a high temperature in a short time) on the strength properties of glass fibre and carbon fibre-reinforced AW-1050A aluminium laminates. The research concerns the determination of how cyclical temperature changes affect the tensile strength of FMLs. The results indicate that temperature changes have little effect on the tensile strength of the composites tested, with carbon fibre-reinforced aluminium laminates showing a tendency to delaminate.

Keywords: fibre metal laminates, FML, mechanical properties, tensile strength, thermal shocks

Nomenclature

c   specific heat [J/kgK]
E   Young's modulus [MPa]
R_m tensile strength [MPa]

Greek symbols

α   coefficient of linear expansion [μm/mK]
ν   Poisson's ratio
ρ   density [kg/m^3]

1. Introduction

A composite material as a combination of two or more insoluble materials differing in species or chemical composition are usually produced to produce a structural material with suitable mechanical, electrical, thermal, tribological or other properties (Chandrasekar et al., 2017).They usually contain fibres or phase particles that are stiffer and more durable than the matrix. Many reinforcement materials also provide good thermal and electrical conductivity, a low coefficient of thermal expansion or good wear resistance (Costa et al., 2023). Fibre metal laminates (FMLs) consist of alternating layers of metal and a polymer matrix composite reinforced with continuous fibres. FMLs as hybrid materials are characterised by improved properties compared to the component materials. Due to their attractive

properties, FMLs are widely used in the automotive industry (Kumar et al., 2022), aerospace (Etri et al., 2022), military (Pai et al., 2023) and marine applications (Raheem & Subbaya, 2023).

Fibre-reinforced composite materials are most commonly used to provide increased static and fatigue strength, including specific strength and stiffness (Yelamanchi et al., 2020), which is achieved by incorporating stiff fibres into a ductile matrix. The matrix transfers the applied load to the fibres (Dobrzański, 2016).

The characteristics of FMLs are excellent stiffness and strength in relation to density, high fatigue strength (Alderiesten, 2019), resistance to dynamic loads (Li et al., 2023; Vieira et al., 2022), compression (Kalfountzos et al., 2022) and stretching (Sun et al., 2023). In addition, they are characterized by high resistance to environmental conditions including corrosion. They can also be fire-resistant and highly durable (Bieniaś, 2018). A prerequisite for meeting the requirements for the fibre metal laminates is a sufficiently strong connection between the matrix and the reinforcing layer and a good adhesive joint between the metal and the composite (Fontes at al., 2023; Kabir et al., 2023). The selection of a composite material should begin with defining the requirements for its construction. Each material has different physical, chemical or mechanical properties. Not all materials can cooperate with each other, which results, among others, from their different electrical potentials or different values of thermal expansion coefficients. If the potential difference between the components of the composite is large, the galvanic cell phenomenon occurs, which may result in electrochemical corrosion inside the composite (Hamill et al., 2018; Verma et al., 2022). In the case of materials with different thermal expansion, delamination may occur, resulting in separation of the reinforced layer and the reinforcing layer (Kumaran et al., 2023; Sarfraz et al., 2021). The appropriate selection of fabrication method and the selection of individual components are largely responsible for increasing the laminate's resistance to destruction (Chen et al., 2023).

This article presents the results of strength tests of aluminium-based FMLs. The FMLs were made of AW-1050A aluminium sheet coated with a L285 resin matrix. The aluminium sheers were reinforced with one layer of twill weave glass fabric or one layer of twill weave carbon fabric. Lamination was done using the vacuum bag method. The samples were exposed to cyclical heating and cooling in the temperature range from −30°C to 90°C. Samples exposed to single heating and then slow cooling to temperatures of 150°C, 200°C and 250°C were also tested.

2. Materials and methods

2.1. Test material

Two types of the FMLs were used in the investigations. A 1-mm-thick AW-1050A aluminium sheet covered with a L285 resin reinforced with one layer of twill weave glass fabric of 190 g/m^2 (Fig. 1a) was used as test material. The second type of aluminium-based samples was reinforced with one layer of twill weave carbon fabric of 160 g/m^2 (Fig. 1b). Selected physical properties of AW-1050A aluminium sheet are presented in Table 1. Selected properties of the fabrics used are shown in Tables 2 and 3.
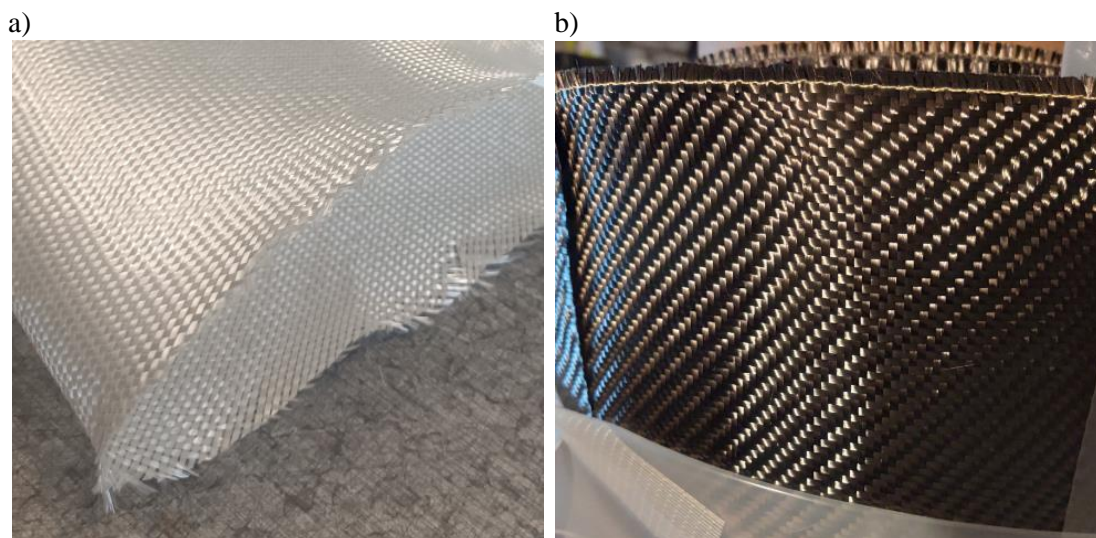
Fig. 1. a) twill weave glass fabric and b) twill weave carbon fabric.

Table 1. Physical properties of AW-1050A aluminium, prepared on the basis of AW-1050A (2023).

Density ρ, g/cm³	Young's modulus E, MPa	Poisson's ratio ν	Specific heat c, J/kg·K	Coefficient of linear expansion α, μm/m·K	Resistivity ρ , nΩm	Heat conductivity λ, W/m·K	Conductivity, %IACS
2.70	69000	0.33	899	23.5	29	229	59.5

Table 2. Geometrical and physical properties of glass fibre (E-glass, 2023).

Type of fibre	Shape of fibre	Length	Diameter μm	Cross section	Coefficient of linear expansion α, μm/m·K	Tensile strength R_m, MPa	Young's modulus E, GPa
glass fibre	straight glass fibre	continuous fibres-	φ9 ±1.5	round	5.00	3450	72 GPa

Table 3. Geometrical and physical properties of carbon fibre (Toray, 2023).

Type of fibre	Shape of fibre	Length	Diameter μm	Cross section	Coefficient of linear expansion α, μm/m·K	Tensile strength R_m, MPa	Young's modulus E, GPa
carbon fibre	straight glass fibre	continuous fibres	φ7±1	round	0.41	3530	230 GPa

L285 (MGS) epoxy resin with relatively low reactivity polyamide hardener was used in the lamination process. Before lamination, the sheet was sandblasted and washed with isopropyl alcohol. Lamination was done using the vacuum bag method. After applying a layer of resin on the surface of the aluminium sheet using a sponge paint roller, the fabric was applied and carefully pressed in order to evenly distribute the resin. A transverse-longitudinal arrangement of the fabric fibres relative to the lateral edges of the laminated sheets was used. A seepage mat was then placed over the applied fabric. The composites prepared in this way were placed in a vacuum bag, which was sealed with butyl tape. After starting the vacuum pump (Fig. 2) the composites were left for 24 hours until the resin was cured.

Fig. 2. Lamination of glass fibre-reinforced aluminium laminates.

2.2. Experimental test

To determine the strength properties of AW-1050A-based FMLs, a static tensile test was carried out on flat specimens with dimensions 20 mm (width) × 280 mm (length). Tensile stresses are a representative type of loading on FML composites, in both tension and flexural elements. The samples were prepared using a KIMLA milling plotter equipped with a shank cutter. The diameter of the cutter was 3 mm.

Composite samples were divided into six groups. The samples of the first group were prepared for a static tensile test. These samples were not heat treated. The samples of the second group were exposed to cyclic heating and cooling in the temperature range between −30°C and 90°C, and the number of cycles was 100. The samples of the third group were exposed to cyclic heating and cooling

in the temperature range between 30°C and 90°C, and the number of cycles was 400. The fourth, fifth and sixth groups were heated once and then slowly cooled down to 150°C, 200°C, and 250°C, respectively. Cyclical heating and cooling of FML samples was carried out using the TSE-12-A thermal shock chamber. All samples without heat treatment and after heat treatment were exposed to a uniaxial tensile test. A Zwick/Roell Z100 tensile testing machine was used to perform the uniaxial tensile test. Three replicates were used to obtain statistically significant results.

3. Results and discussion

Figure 3 shows the results of tensile test of aluminium sheets. Initially, there is a large increase in the tensile force until the yield point is reached. The plastic flow range is characterized by increasing strain with a constant or slightly decreasing amount of tensile force. Sample failure occurs at a sample elongation of approximately 5.5%. This graph shows the response of an aluminium sample exposed to a static tensile test taking into account the work hardening effect. The average ultimate tensile strength R_m was equal to 107.8 MPa.
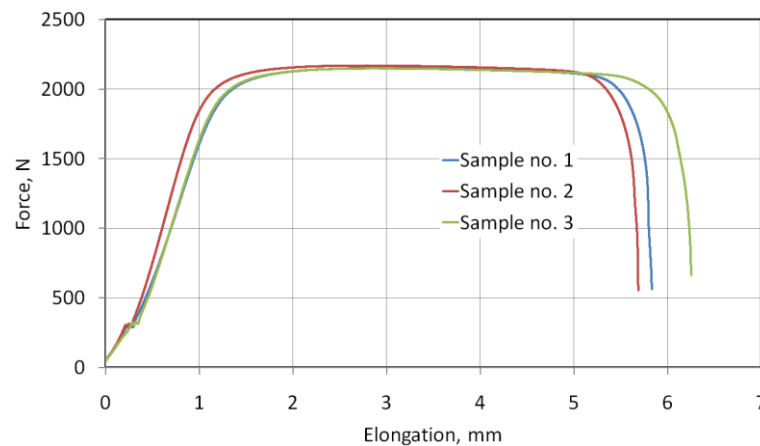
Fig. 3. Tensile curves of the AW-1050A aluminium sheets.

Figure 4a shows the results of the tensile test of glass fibre-reinforced aluminium laminates that have not been exposed to thermal shocks or heating and cooling cycles. Comparing these tests to the testing of aluminium sheet samples, a much higher maximum force can be observed. At the elongation value of about 4.5%, the fabric breaks without delamination of the composite (Fig. 5a). Gradual tearing of the fibres (breaking of individual fibres of the glass fabric) was observed. This translated into a sudden reduction in the force acting on the sample. In this way, the total tensile force was transmitted through the aluminium sheet until the necking was initiated and then the tensile force suddenly decreased. The force causing the breaking of the glass fibres is about 3600 N. With further stretching of the sample, the change in tensile force is typical for an aluminium sample.

a)

b)
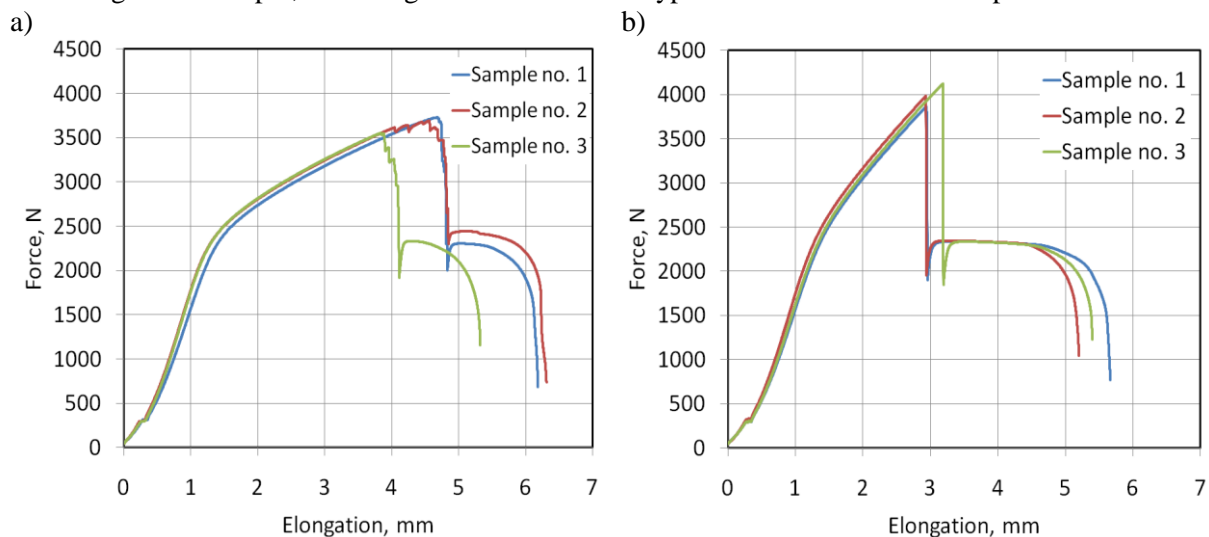
Fig. 4. Tensile curves of a) glass fibre-reinforced aluminium laminates and b) carbon fibre-reinforced aluminium laminates non exposed to thermal shocks and cycles

Figure 4b shows the tensile test results of carbon fibre-reinforced aluminium laminates that have not been exposed to thermal shocks or heating and cooling cycles. Comparing these results with the results for glass fibre-reinforced aluminium laminates (Fig. 4a), an increase in the maximum tensile force (3800-4100 N) can be observed. The delamination of carbon fibre-reinforced aluminium laminates (Fig. 5b) occurs at a much lower elongation (3 mm) compared to the elongation of glass fibre-reinforced aluminium laminates (min. 3.8 mm) (Fig. 4a). The breaking force of the carbon fibre fabric is almost twice as high as that of the aluminium sheet (Fig. 3).

Figure 6a shows the results of the tensile test of the glass fibre-reinforced aluminium laminates, which were exposed to one hundred thermal cycles. These tests, compared to the samples not exposed to thermal cycles (Fig. 4a), are characterized by very similar results for the maximum tensile force. The use of heat treatment resulted in an increase in the elongation corresponding to the maximum tensile force, compared to the samples not exposed to heat treatment (Fig. 4a). This proves that the stiffness of the composites is reduced as a result of thermal treatment.
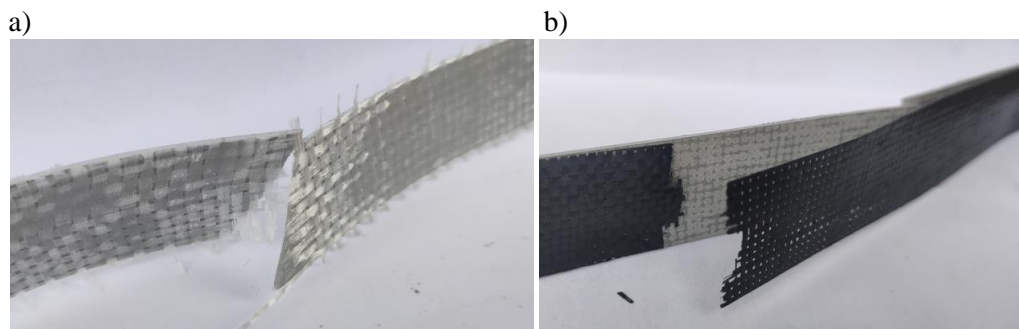
Fig. 5. Samples after tensile test a) tearing of glass fibre-reinforced aluminium laminate and b) delamination of carbon fibre-reinforced aluminium laminate.

Tensile test results of carbon fibre-reinforced aluminium laminates exposed to 100 cycles of thermal shocks show less stable results compared to samples not exposed to thermal shocks (Fig. 6b). In the elongation range between 2 and 5 mm, the carbon fibre fabric breaks. The degree of delamination of the samples due to the cyclic heating and cooling may have an impact on a large variation in maximum tensile force. In the case of sample no. 3, it is difficult to distinguish any differences from the test of samples not exposed to thermal cycling. Sample no. 1 was particularly weakened after heating and cooling cycles. The destruction of the carbon fibre fabric in the case of this sample occurred at a maximum force of 2500 N.

Fig. 6. Tensile curves of a) glass fibre-reinforced aluminium laminates and b) carbon fibre-reinforced aluminium laminates exposed to 100 cycles of thermal shocks.

Fig. 7a shows the results of the tensile test of glass fibre-reinforced aluminium laminates that were exposed to 400 thermal cycles. These tests, compared to the samples not exposed to thermal cycles (Fig. 4a) and to the samples exposed to 100 thermal cycles (Fig. 6a), show very similar results of the maximum tensile force. For samples exposed to 400 cycles, a high repeatability of results can be

observed, especially in the case of samples 1 and 2. In this case, the breaking force of the fabric is about 3700 N, while for sample 3 the maximum tensile force is about 3500 N. Tests of samples exposed to 100 thermal cycles (Fig. 6a) showed a slightly lower elongation of the samples corresponding to the maximum tensile force, compared to the samples exposed to 400 thermal cycles (Fig. 7a).

The samples of carbon fibre-reinforced aluminium laminates exposed to 400 cycles of thermal shocks (Fig. 7b) showed a very similar maximum force needed to break the fabric compared to glass fibre-reinforced aluminium laminates (Fig. 7a). The elongation of the sample corresponding to the failure of the fabric is much smaller in the case of carbon fibre-reinforced aluminium laminates compared to glass fibre-reinforced aluminium laminates (Fig. 7a).

Figure 8a shows the results of tensile test of the glass fibre-reinforced aluminium laminates exposed to soaking in an oven for 5 minutes at a temperature of 150°C. The samples behave in a similar manner to previous tests showing a maximum fabric breaking force of approximately 3600 N. The elongation at maximum tensile force is approximately 6.3 mm (samples no. 2 and 3 in Fig. 8a). The increased elongation in the graph showing the results for sample number 1 is due to slippage of the sample in the grippers of the testing machine. Therefore, this test cannot be considered significant.

Fig. 7. Tensile curves of a) glass fibre-reinforced aluminium laminates and b) carbon fibre-reinforced aluminium laminates exposed to 400 cycles of thermal shocks.
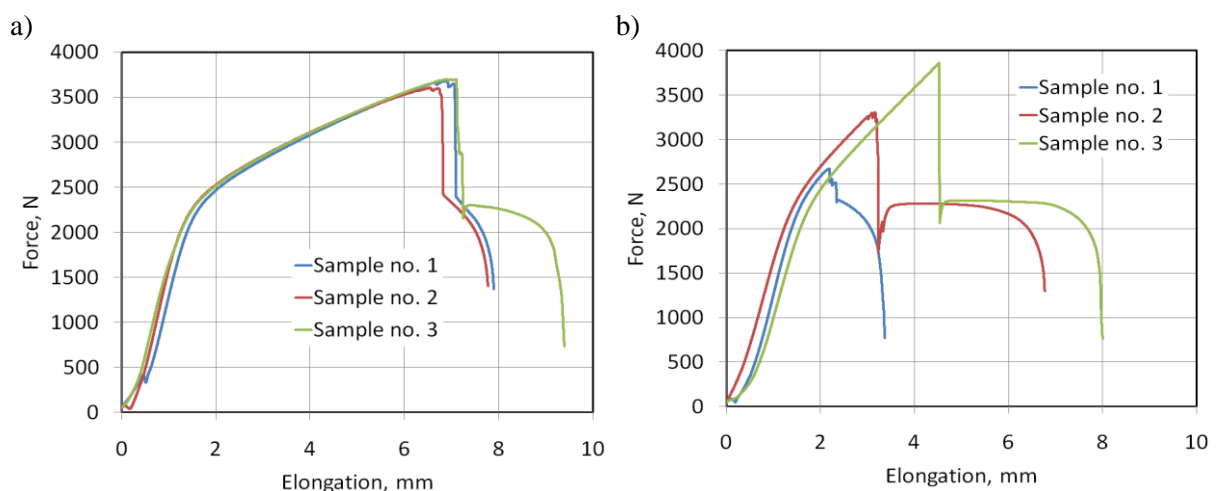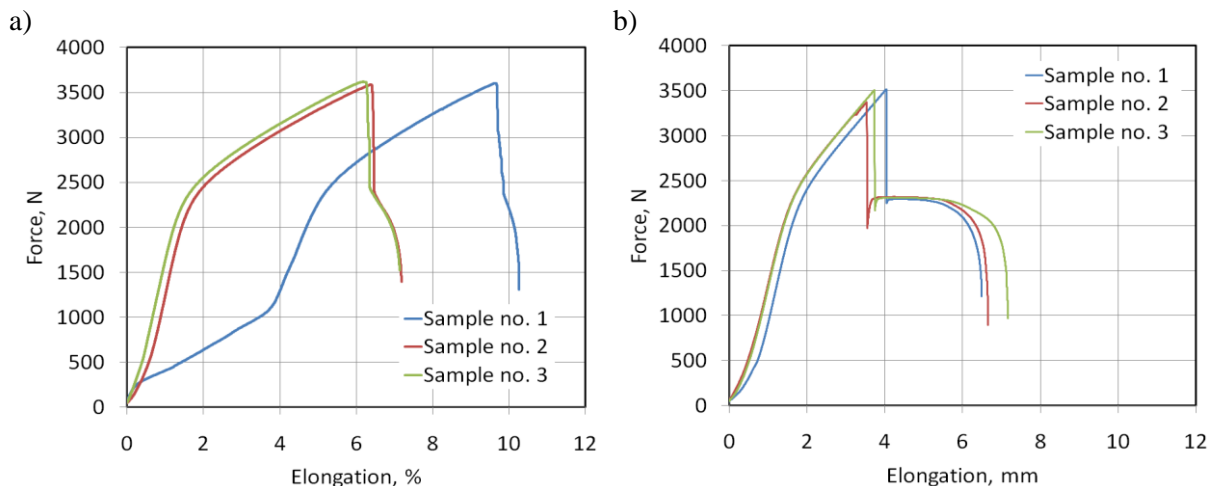

Fig. 8. Tensile curves of a) glass fibre-reinforced aluminium laminates and b) carbon fibre-reinforced aluminium laminates exposed to soaking at 150°C.

In the case of carbon fibre-reinforced aluminium laminates exposed to soaking at 150°C, the maximum force was lower compared to the untreated samples (Fig. 4b). The force reaches a maximum of 3500 N (Fig. 8b), which is a result similar to the samples exposed to 400 cycles of heating and cooling (Fig. 7b).

The tensile results of the glass fibre-reinforced aluminium laminates exposed to soaking for 5 min at 200°C indicate breakage of the glass fabric at a force of 3700-3800 N (Fig. 9a) and at an elongation

similar to the results of tests of samples processed at other temperatures. After breaking the glass fibres, the aluminium alloy sheet is not strengthened again, as shown in Figs. 4a, 6a and 7a.

The maximum tensile force of carbon fibre-reinforced aluminium laminates exposed to soaking at 200°C is similar to that of carbon fibre-reinforced aluminium laminates exposed to soaking at 150°C (Fig. 8b). In the case of the sample no. 2 slipping of the sample in the gripper of the testing machine was observed (Fig. 9b).

Test results of glass fibre-reinforced aluminium laminates exposed to heating in an oven for 5 minutes at 250°C indicate breaking of the glass fabric at a force of 3700-3800 N (Fig. 10a). The behaviour of carbon fibre-reinforced aluminium laminates exposed to soaking at 250°C was similar to the previously presented results for this type of samples (Fig. 10b). However, the elongation of the samples corresponding to fabric failure was almost two times lower compared to glass fibre-reinforced aluminium laminates exposed to soaking at 250°C (Fig. 10a). The deformation of the aluminium sheet takes place practically at a constant value of the tensile force, which corresponds to a weak work hardening of the material. A similar effect was observed in the case of carbon fibre-reinforced aluminium laminates exposed to soaking at 200°C (Fig. 9b).

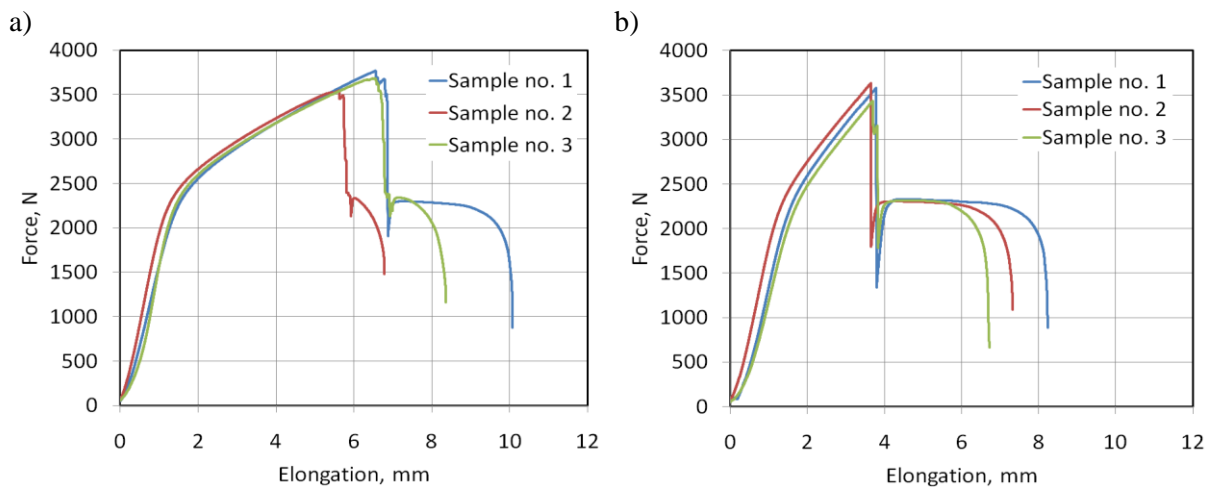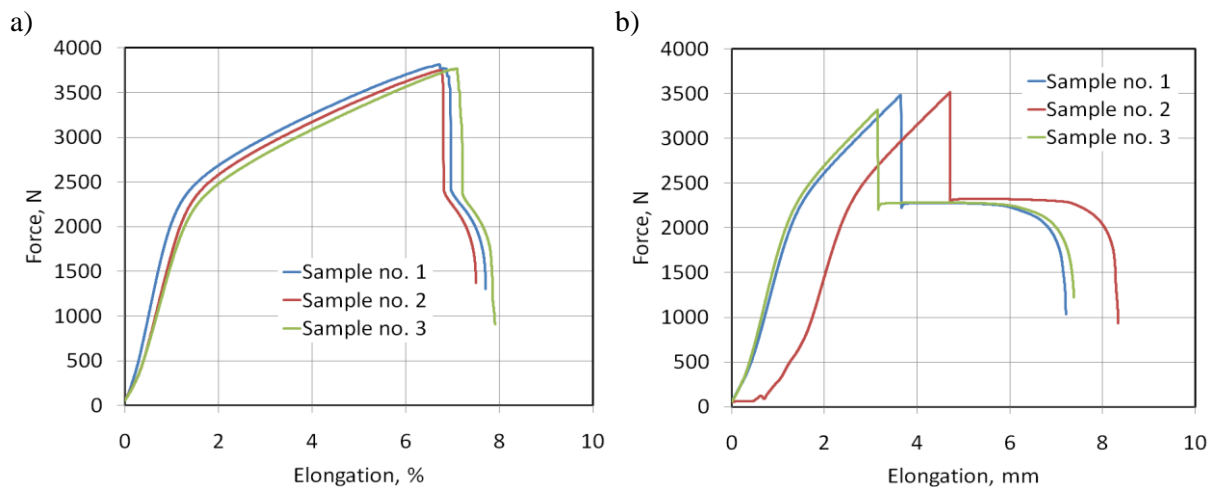**Fig. 9.** Tensile curves of a) glass fibre-reinforced aluminium laminates and b) carbon fibre-reinforced aluminium laminates exposed to soaking at 200°C.
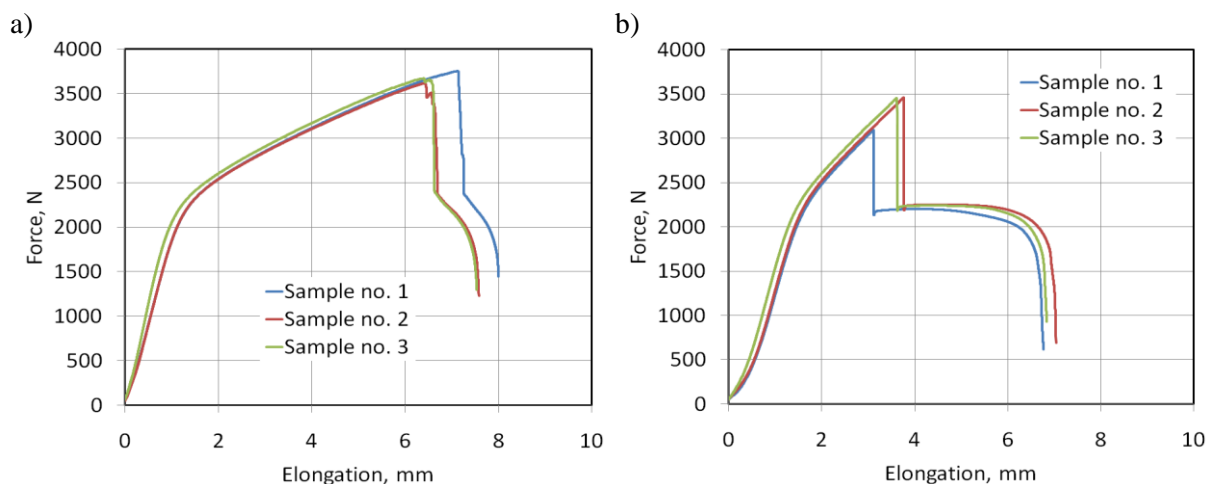
Fig. 10. Tensile curves of a) glass fibre-reinforced aluminium laminates and b) carbon fibre-reinforced aluminium laminates exposed to soaking at 250°C.

4. Summary and conclusions

Based on the results of uniaxial stretching FMLs the following conclusions can be drawn:
- Carbon fibre fabric exhibits a completely different thermal expansion than AW-1050A aluminium. When when the aluminium sheet expands under the influence of temperature, the fibre does not change its dimensions and the sample delaminates due to difference in the length of individual materials. The second reason for avoiding this carbon fibre-reinforced

composites is the phenomenon of the galvanic cell, which leads to the formation of oxide layers on the metal-carbon fibre interface. This phenomenon occurs due to the different corrosion potentials of these materials. In the case of glass fibres, this problem does not occur, these fibres are characterized by greater flexibility than carbon fibres.

- Glass fibre-reinforced aluminium laminates showed high resistance to delamination. The glass fibre samples did not delaminate even after they were broken - the glass fabric was very firmly connected to the matrix.
- The soaking of the samples also had an impact on their strengthening. It is assumed that the resin hardened even more during the soaking process and this process became responsible for the strengthening of the samples compared to non treated specimens.
- For the glass fibre reinforced specimens, the maximum destructive force of the laminate reinforcement after each heat treatment increased from 3600 N to 3700-3800 N.
- For the carbon fibre reinforcement after heat treatment, a decrease in the maximum breaking force was observed from 3800 N to 3700 N for 100 cycles of temperature variation down to 3500 N after the specimens were heated to 250ºC.
- An increase in the elongation of the heat-treated specimens was observed until the maximum failure force occurred. In the case of glass fibre reinforcement, 2-3 mm, and for carbon fibre reinforcement, 1-1.5 mm.
- The tests were aimed at presenting the influence of alternating heating and cooling cycles and thermal shocks on the properties of selected types of FMLs. Subsequently, the same tests should be carried out, but for sandwich composites consisted additional layers of carbon and glass fabric. It should be analysed whether the phenomenon of delamination of the metal at the metal/fabric interface occurs with a larger number of laminate layers. Another aspect is the use of fibres with a different density and a different type of weave. The use of an electrochemical method of surface processing should be explored, which would translate into a better bonding of the laminate.

References

Alderiesten, A. (2019). Fatigue in fibre metal laminates: The interplay between fatigue in metals and fatigue in composites. *Fatigue & Fracture of Engineering Materials & Structures, 42*(11), 2414-2421. https://doi.org/10.1111/ffe.12995

AW-1050A. (2023, June 20). *AW-1050A*. https://www.kronosedm.pl/aluminium-a1-aw-1050a/

Bieniaś, J. (2018). *Kształtowanie stanu powierzchni rozdziału metal-kompozyt w laminatach metalowo-włóknistych z włóknami węglowymi*. Politechnika Lubelska.

Chandrasekar, M., Ishak, M.R., Jawaid, M., Leman, Z., & Sapuan, S.M. (2017). An experimental review on the mechanical properties and hygrothermal behaviour of fibre metal laminates. *Journal of Reinforced Plastics and Composites*, *36*(1), 72-82. https://doi.org/10.1177/0731684416668260

Chen, Y., Yang, Y., Wang, Z., Wang, H., Li, J., & Hua, L. (2023). Accurate simulation on the forming and failure processes of fiber metal laminates: A review. *International Journal of Lightweight Materials and Manufacture, 6*(3), 344-356. https://doi.org/10.1016/j.ijlmm.2023.02.003

Costa, R.D.F.S., Sales-Contini, R.C.M., Silva, F.J.G., Sebbe, N., & Jesus, A.M.P. A. (2023). Critical review on fiber metal laminates (FML): From manufacturing to sustainable processing. *Metals*, *13*, 638. https://doi.org/10.3390/met13040638

Dobrzański, L.A. (2016). *Podstawy nauki o materiałach i metaloznawstwo*. Wydawnictwa Naukowo-Techniczne.

E-Glass. (2023, September 1). *E-Glass Fiber*, *Generic*. MatWeb. https://www.matweb.com/search/DataSheet.aspx?MatGUID=d9c18047c49147a2a7c0b0bb1743e812&ckck=1

Etri, H.E., Korkmaz, M.E., Gupta, M.K., Gunay, M., & Xu, J. (2022). A state-of-the-art review on mechanical characteristics of different fiber metal laminates for aerospace and structural applications. *International Journal of Advanced Manufacturing Technology*, *123*, 2965–2991. https://doi.org/10.1007/s00170-022-10277-1

Fontes, A., & Shadmehri, F. (2023). Data-driven failure prediction of fiber-reinforced polymer composite materials. *Engineering Applications of Artificial Intelligence*, *120*, 105834. https://doi.org/10.1016/j.engappai.2023.105834

Hamill, L., Hofann, D.C., & Nutt, S. (2018). Galvanic corrosion and mechanical behavior of fiber metal laminates of metallic glass and carbon fiber composites. *Advanced Engineering Materials, 20*(2), 1700711. https://doi.org/10.1002/adem.201700711

Kabir, S., Shahed, C.A., Ador M.S.H., Choudhyry, I.A., & Ahmad, F. (2023). Review of the developments in composite materials over the last 15 years. *Reference Module in Materials Science and Materials Engineering*. https://doi.org/10.1016/B978-0-323-96020-5.00044-3

Kalfountzos, C.D., Bikakis, G.S.E., & Theotokoglou, E.E. (2022). Postbuckling and secondary buckling of rectangular fiber-metal laminates and glass-fiber reinforced composites under uniaxial compression. *Engineering Structures, 267*, 114663. https://doi.org/10.1016/j.engstruct.2022.114663

Kumar, K.A., Prabu, R., & Arulraj, R. (2022). Development and characterization of fiber metal laminates (FML) using aluminium and Kevlar fibre for automobile applications. AIP Conference Proceedings 2413(1), 050002. https://doi.org/10.1063/5.0091668

Kumaran, D., Antony, J.M.; Lokeshwaran, G., Srinivasan, P.S., Vigneshwar, S.R.M., Ramnath, B.V., & Kumar, R.S. (2023). Investigation of flexural, inter delamination and impact behaviour of fiber metal laminate composite. *Materials Today: Proceedings*. https://doi.org/10.1016/j.matpr.2023.05.624

Li, K., Qin, Q., Cui, T., Han, Q., Peng, J., Sha, Z., & Zhang, W. (2023). Soft impact of GLARE fiber metal laminates. *International Journal of Impact Engineering*, *178*, 104607. https://doi.org/10.1016/j.ijimpeng.2023.104607

Mohammad-Zaheri, F., Mohammadi, B., & Taheri-Behrooz, F. (2023). Prediction of stress distribution and stiffness degradation in fiber metal laminates containing matrix cracking. *Composite Structures*, *311*, 116820. https://doi.org/10.1016/j.compstruct.2023.116820

Pai, A., Kini, C.R. Hegde, S., & Satish, S.B. (2023). Thin fiber metal laminates comprising functionally graded ballistic-grade fabrics exposed to mechanical and damping characterization. *Thin-Walled Structures, 185*, 110628. https://doi.org/10.1016/j.tws.2023.110628

Raheem, A., & Subbaya, K.M. (2023). Performance evaluation of hybrid polymer composite materials in marine applications: A review. *Materials Today: Proceedings*. https://doi.org/10.1016/j.matpr.2023.01.346

Sarfraz, M.S., Hong, H., & Kim, S.S. (2021). Recent developments in the manufacturing technologies of composite components and their cost-effectiveness in the automotive industry: A review study. Composite Structures, 266, 113864. https://doi.org/10.1016/j.compstruct.2021.113864

Sun, J., Xu, S., Lu, G., Ruan, D., & Wang, Q. (2023). Mechanical response of fibre metal laminates (FMLs) under low to intermediate strain rate tension. *Composite Structures*, *305*, 116493. https://doi.org/10.1016/j.compstruct.2022.116493

Toray. (2023, September 1). *Toray T300 Carbon Fiber*. MatWeb. https://www.matweb.com/search/datasheet.aspx?matguid=86d0be5b80514c66b2c91e3357c57a1f&ckck=1

Verma, E., Gajera, H., Ramani, D., Bist, N., Sircar, A. (2022). Corrosion in the light of electrochemistry. *Materials Today: Proceeding*s, *62*, 7057-7061. https://doi.org/10.1016/j.matpr.2022.01.138

Vieira, L.M.G., Dobah, Y., dos Santos, J.C., Panzera, T.H., Campos Rubio, J.C., & Scarpa, F. (2022). Impact properties of novel natural fibre metal laminated composite materials. *Applied Sciences*, *12*, 1869. https://doi.org/10.3390/app12041869

Yelamanchi, B., MacDonald, E., Gonzalez-Canche, N.G., Carrillo, J.G., & Cortes, P. (2020). The mechanical properties of fiber metal laminates based on 3D printed composites. *Materials*, *13*, 5264. https://doi.org/10.3390/ma13225264

Wpływ Nagrzewania i Chłodzenia Laminatów Metalowo-Włóknistych na Bazie Blachy Aluminiowej na ich Właściwości Wytrzymałościowe

Streszczenie

Coraz powszechniejsze zastosowanie materiałów kompozytowych w konstrukcji maszyn skłania do podejmowania działań mających na celu lepsze poznanie ich właściwości, oraz wpływu różnych czynników zewnętrznych na te właściwości. Kompozyty metalowo-włókniste (ang. Fibre Metal Laminates) składają się z naprzemiennie ułożonych warstw metalu oraz laminatu o osnowie polimerowej wzmacnianego włóknami ciągłymi. Celem pracy było zbadanie wpływu cyklicznych zmian temperatury oraz szoków termicznych (nagrzanie próbki do wysokiej temperatury w krótkim czasie) na właściwości wytrzymałościowe laminatów metalowo-włóknistych wykonanych na bazie blachy aluminiowej AW-1050A pokrytej jednostronnie laminatem wzmocnionym włóknem szklanym lub włóknem węglowym. Badania dotyczyły ustalenia jak zmiany temperatury, w tym przede wszystkim zmiany cykliczne, wpływają na właściwości wytrzymałościowe laminatów. Wyniki wykazały mały wpływ liczby cykli obciążeń cieplnych na wytrzymałość kompozytów na rozciąganie. Laminaty wzmocnione włóknem węglowym wykazywały tendencję do rozwarstwienia.

Słowa kluczowe: kompozyty metalowo-włókniste, FML, właściwości mechaniczne, wytrzymałość na rozciąganie, szoki termiczne

Original Research

Enhancing the Efficiency of the Double-Tube Heat Exchanger by using a Twisted Inner Tube

Hussein Hayder Mohammed Ali 🆔**, Fatima A. Tahir** * 🆔

Northern Technical University/Technical College of Engineering, 36001 Kirkuk, Iraq; hussein_kahia@ntu.edu.iq (H. H. M. Ali)

* Correspondence: fatimaawni89@gmail.com

Abstract

This study utilized two double tube-type heat exchangers. The first exchanger employed a smooth inner tube, while the second one utilized a twisted inner tube. The shell was constructed of poly(vinyl chloride) (PVC), while the tube was made of copper with a length of 1000 mm, an outer diameter of 62.24 mm, a smooth tube inner diameter of 14.2 mm, and an equivalent diameter of 11.8 mm for the twisted tube. To minimize heat loss, the shell was insulated externally with a thermal insulator. A flow rate of 3 liters per minute of hot water was passed through a ring-shaped tunnel, with an inlet temperature of 63 °C, to enhance the heat exchanger's performance. The experimental results of the two heat exchangers (smooth and twisted inner tubes) were compared, and the use of water as the primary fluid led to improved performance. The twisted inner tube-type heat exchanger achieved a maximum efficiency of 0.33 at a volumetric flow rate of 5 liters per minute, while the maximum improvement in effectiveness was 65.71% at a volume flow rate of 3 liters per minute in the twisted inner tube-type heat exchanger.

Keywords: heat exchanger efficiency, heat transfer coefficient, double-tube heat exchangers, twisted tube.

1. Introduction

In numerous industrial and practical applications, the transfer of heat is necessary between two flowing fluids through a solid surface (barrier) that separates them. To accomplish this, "heat exchangers" are utilized as devices. Heat exchangers enable the transfer of heat between fluids without mixing them. However, larger heat transfers require more space and higher costs. Therefore, researchers continue to focus not only on performance attributes but also on considering the size, capacity of the designated space, and cost-effectiveness of manufacturing the exchanger. Improving the heat transfer rate can be achieved through two steps: (a) improving heat exchanger design and (b) enhancing the thermal conductivity of the working fluid (Holman, 2008).

Heat exchanger tubes are often made of metals with high heat conductivity, such as copper and aluminum. Various updates have been made to exchanger designs, aiming to improve their thermal performance. Heat exchangers can be classified in several ways, each contributing to enhancing their efficiency in terms of heat transport and practical application. The classifications of heat exchangers are as follows:

- classification based on heat transfers,
- classification based on the number of liquids,
- classification based on surface compactness,
- classification based on building characteristics,
- classification based on flow arrangements,
- classification based on heat transfer mechanism.

A double tube heat exchanger typically consists of two concentric tubes, with a smooth inner tube maximizing the available area. One fluid flows through the inner tube, while the other flows in the

opposite direction through the annular space created between the two tubes (Shah, 1986; Pardhi & Baredar, 2012).

If the application requires relatively constant wall temperatures, fluids can flow in parallel flow direction as seen in Fig. 1. This type of exchanger is considered the simplest, with no flow distribution issues and easy disassembly for maintenance cleaning. Twin-tube exchangers are often preferred when one or both fluids are under high pressure, as it is more cost-effective to accommodate narrow corridor tubes compared to large cylindrical structures. For low-volume applications where the total heat exchange area is small, usually a few square feet, two-tube heat exchangers are commonly used. However, they are expensive per unit surface area, typically requiring around 50 square meters or less (Walker, 1982).

The performance of a pulsating heat pipe (PHP) (presumably referring to a heat pipe) is influenced by various factors, including the number of turns, pipe diameter, tube shape, length of the condenser and evaporator sections, overall length of the PHP, heat input, inclination, physical properties of the working fluid, and the volumetric filling ratio (Barrak et al., 2022).

The arrangement of flow direction in a two-tube exchanger generally depends on the desired exchanger efficiency, pressure drop, limitations on maximum and minimum velocities, fluid flow path, allowable thermal pressures, temperature levels, and other design criteria. Cold and hot fluids can flow in opposite or the same direction (Bergman et al., 2011; Bergies, 1999).
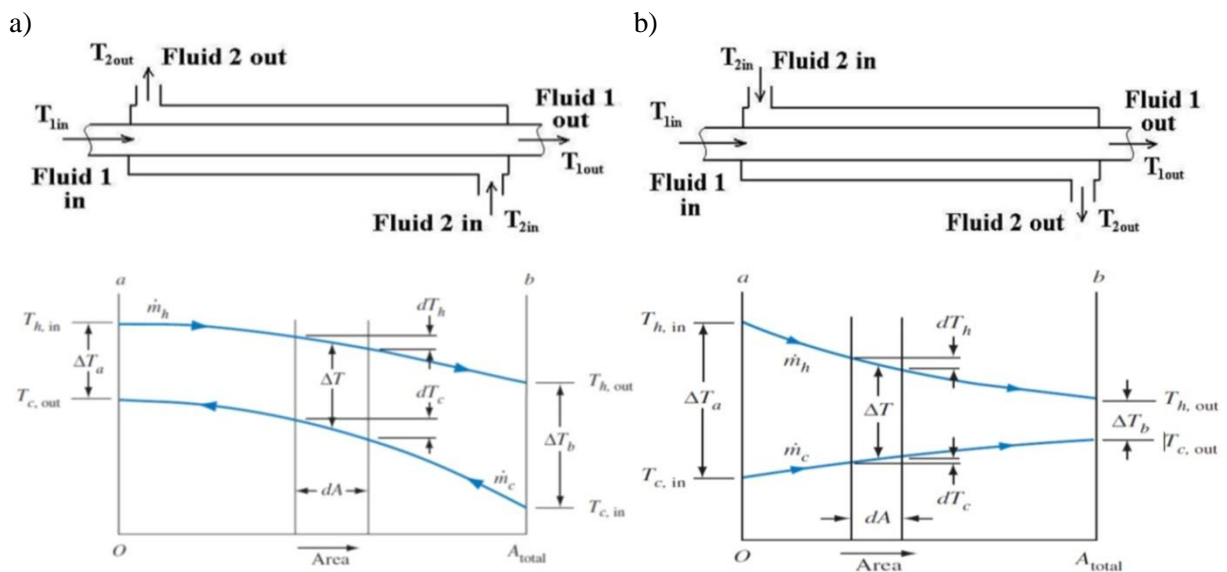
Fig. 1. Single-pass dual-flow heat exchange: a) reverse flow arrangement, b) parallel flow arrangement.

2. Features of the twisted tube

Twisted tubes are vortex flow generators utilized to enhance thermal performance. The impact of twisted tubes on heat transfer, pressure drop, and thermodynamic efficiency of thermal exchangers has been studied (Samruaisin et al., 2019). In many thermal applications, twisted tubes are employed to improve heat dissipation by increasing the available surface area (Abbas et al., 2021). Figure 2 illustrates that twisted tubes have gained attention due to their constructable shape, lower cost, and superior thermal performance compared to smooth tubes. The potential improvement mechanisms for this technique include: (1) expanding the surface area and length of the flow path through circuitous routes, (2) increasing fluid velocity due to flow obstacles and specific geometric curvatures, and (3) intensifying the fluid mixing process through centrifugal forces and vortex flows (Yan et al., 2017).

For highly viscous fluids, the heat transfer coefficient is typically low at low Reynolds numbers to prevent a significant increase in pressure drop. Using a convoluted tube is an effective method to enhance heat transport capacity without significantly raising the pressure drop (Yan et al., 2017). Experiments were conducted to observe the changes in pressure drop and heat transmission in a twisted oval tube with varying axis orientations and twist ratios, comparing it to a perfectly circular tube. The pressure drop inside the twisted oval tubes was greater, while the heat transmission rate was higher. Additionally, extensive studies established that as the twist ratios increased, pressure loss and heat transmission decreased, whereas the opposite was true for axis ratios (Wang et al., 2000).
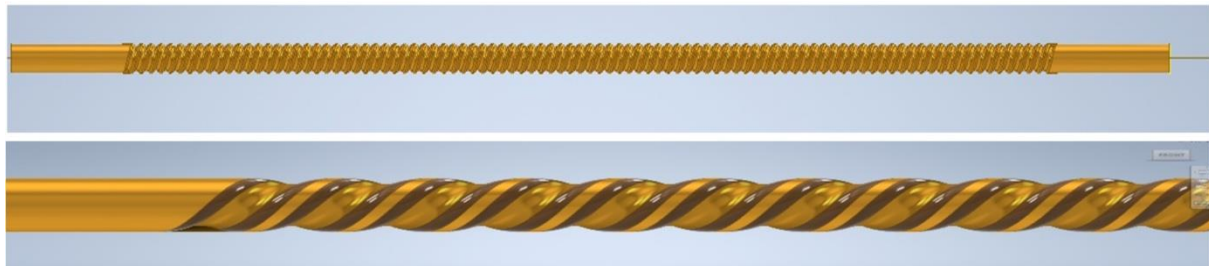
Fig. 2. The twisted tube.

In a study conducted by Samruaisin et al. (2019), a twisted trapezoidal tube and twisted bars with different winding ratios (y/w = 2.0, 3.0, 4.0, and 5.0) were used. Water was employed as the working fluid to simulate a turbulent system with Reynolds numbers ranging from 4,500 to 16,000. The research focused on temperature and velocity profiles as well as variations in local Nusselt numbers to gather information about fluid flow and heat transfer. A comparison was made between the combined devices and the individual use of either a smooth circular tube or a twisted tube. The experimental findings indicated that, for a given Reynolds number (Re), the Nusselt number (Nu), friction factor (f), and thermal performance of the twisted tube reinforced with a twisted bar were consistently higher than those of the twisted tube alone or the simple round tube. Additionally, the thermal performance factor, frictional loss, and heat transfer all improved with a decrease in the torsion ratio (y/w) because a bar with a smaller y/w provided a more regular and robust flow.

In another study conducted by Eltaweel et al. (2020), the performance of an exchanger using a flat plate solar collector was investigated. Two different mediums were used: purified water and multi-walled carbon nanotubes (MWCNTs)/aqueous nanofluids. Both types of heat exchangers were tested in the same location under similar environmental conditions. The use of convoluted tubes in the system improved performance by 12.8% and 12.5% in distilled water and MWCNT/water nanofluid, respectively, compared to employing circular tubes. Furthermore, when using MWCNTs, convoluted tubes resulted in a 34% improvement compared to standard pipes with distilled water.

In a numerical study conducted by researcher Khoshvaght-Aliabadi and Feizabadi (2020), liquid heat transfer properties were investigated using a composite method to compare various pitch ratios and five Reynolds values for laminar flow in tubular heat exchangers. The results showed that both the degree of torsion and the Reynolds number significantly influenced the dependence of transport properties on the optimized models. It was observed that the pressure drop in the twisted tube (TT) with torsion was generally higher than that in the twisted tube alone (TT), which contrasted with the heat transfer performance. However, the TT-minor TT and the TT-major TT exhibited the highest values. The secondary TT-TT configuration achieved the best overall hydrothermal performance, while the straight-tube (ST) equipped with twisted-tape (ST-TT) and the primary TT-TT performed similarly. The findings demonstrated that increasing both the degree of torsion and the Reynolds number led to improved performance across the board. In a numerical investigation conducted by researcher Eiamsa-Ard et al. (2016), the addition of a twisted bar with three channels to a spirally twisted tube was studied to enhance heat transmission. The effects of tube/tape designs (belly-to-belly and belly-to-neck) and the width ratio of the tape (w/D = 0.1, 0.25, 0.34, and 0.5) were examined. The study revealed that the width-to-thickness ratio of the tape has a significant impact on the heat transmission coefficient and friction. Comparing two systems with the same bandwidth, the belly-to-neck configuration was found to promote heat transmission more effectively than the belly-to-abdomen arrangement. At w/D = 0.1, 0.25, and 0.34, the Nusselt numbers for three-indented convoluted tubes with convoluted bands in a belly-to-neck configuration were up to 1.2%, 21%, and 36% higher compared to convoluted tubes without bands. Similarly, the Nusselt numbers of contorted tubes with a three-channel convoluted band in a belly-to-abdominal layout were up to 1.23%, 6.7%, 10%, and 17% higher than those of similar tubes without a band. The increased heat transmission in the belly-to-neck configuration (especially in the large w/D range) can be attributed to the enhanced engagement between the eddy flows induced by tubes and those induced by the tape. Additionally, the friction loss caused by the subsystems in the belly-to-neck layout was lower compared to the belly-to-bottom arrangement. Consequently, thermal efficiency characteristics improved when the systems were arranged with their bellies touching. With a Reynolds number of 5000, the maximum achievable thermal performance was observed to be 1.32 in a twisted tube with a three-channel twisted bar in a belly-to-neck configuration and a tape thickness of 0.34 inches.

In a study conducted by Farnam et al. (2021), it was observed that the wavy walls in a spiral twisted tube constantly alter the orientation and strength of the secondary flows and velocity lines, preventing the growth of thermal layer boundaries in the flow direction and leading to a more uniform temperature distribution. At moderate levels of design parameters, the Nusselt number increased by 14.2% within the investigated Reynolds number range ($600 \leq Re \leq 1200$), while the friction factor increased by 7.7%. The study performed a parameter analysis to understand the interaction of various design variables (helical diameter, helical pitch, and pitch torsion). It was found that the diameter of the spiral had the most significant effect on the thermo-hydraulic properties of the spiral twisted tube, followed by the convexity and step of the spiral. Minimizing both the helical diameter and torsional angle resulted in improved hydrothermal performance. With a Reynolds number of 900 and a spiral diameter of 50 mm, the model achieved a maximum performance index of 1.98.

In a study conducted by Thantharate (2013), four pipe passes were examined, each with a diameter of 0.3 meters, and four different flow rates of liters per minute (LPM) of 1.5 dm^3/min, 1.37 dm^3/min, 0.5 dm^3/min, and 0.24 dm^3/minwere tested, resulting in a Reynolds number range of 625 to 7000. Analytical, experimental, and numerical analyses of turbulent and laminar flow patterns were conducted. The findings showed that the plain tube performed better than the convoluted tube at low flow rates and high inlet temperatures, primarily due to the flow characteristics inside the tubes. The study concluded that when setting up a multi-path design, the use of convoluted tubing is necessary to achieve the desired flow rate. The study aimed to improve the efficiency of a double pipe counterflow heat exchanger using water as the hot and cold fluid, comparing the heat transfer results of twisted and smooth tubes. The experiments were conducted using water to achieve better performance at different flow rates (3, 5, 7, 9, 12 dm^3/min) for the cold fluid and a constant flow rate of 3 dm^3/minfor hot water.

3. Methodology for experiments

The test system depicted in Fig. 3 comprises two double tube-type heat exchangers. It includes two stainless steel basins with a capacity of 10 dm^3 each. One basin is used in the first stage as a reservoir for cold water with a temperature of 18±1ºC, which flows through the inner tube of both the smooth tube exchanger and the twisted tube exchanger. This circulation is facilitated by a pump with a horsepower capacity of 0.5 HP and a maximum head of 40 meters. The water exiting the inner tubes (smooth and twisted) at a higher temperature than that of the inner tubes returns to the same basin. The second basin supplies water at ambient temperature to an electric heater through another pump with a capacity of 0.5 HP and a maximum head of 40 meters. Upon entering the heater, the water temperature rises to 63±1ºC. The same basin is used to collect the return water from the outer tube of both exchangers, which has a lower temperature than the outer tubes. To maintain temperature consistency throughout the process, the heat exchangers and the plastic inlet and outlet pipes are covered with thermal asbestos.

4. Test configuration

This study aims to investigate improvements in the performance of a circular double-tube exchanger. This section provides a detailed explanation of the experimental procedure conducted for the tests. The experiments were carried out using cold water flowing in the opposite direction to the hot water in the dual pipe exchanger as seen in Fig. 3. Once the device was manufactured, the experiments were initiated to collect the necessary data for the calculations related to the research. The first experiment involved heating the water to a temperature of 63±1ºC using an electric heater. The cold water was set at a temperature of 18±1 ºC. The flow rate for both hot water (3 dm^3/min) and cold water (3 dm^3/min) was determined. Readings were taken after monitoring the temperature gauges until they reached a steady state to record the temperature values. Following this, the experiment was repeated by maintaining a fixed flow rate for hot water (3 dm^3/min) and varying the flow rate for cold water. Three different flow rates for cold water (3, 4, 5 dm^3/min) were tested. and the temperature values were recorded after reaching to a steady state.
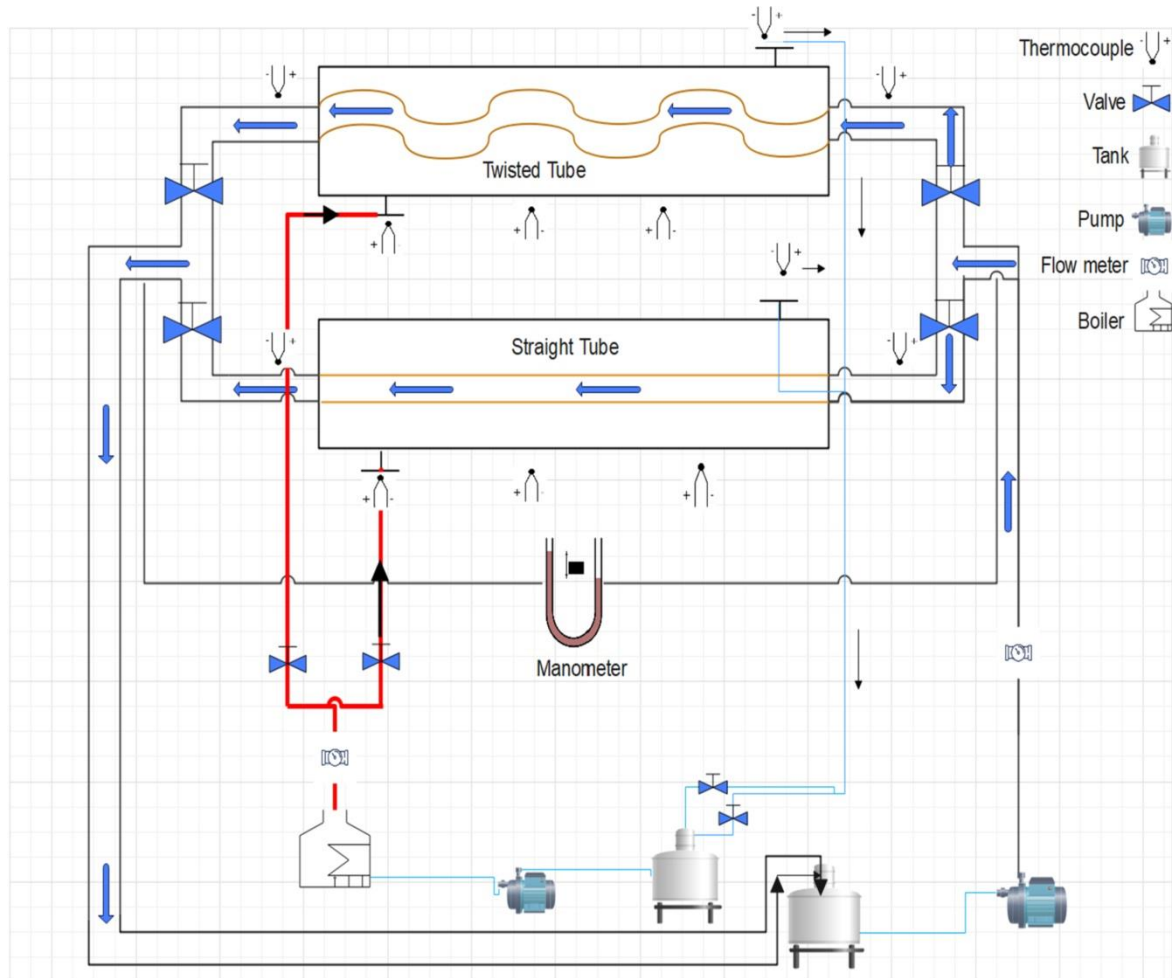
Fig. 3. Test diagram.

The water has been pumped out from the tanks, and all pipe connections have been tested. The pumps are now operating to circulate the working fluid in the exchanger.

The control valve was appropriately set to regulate the flow rate at the required level. The flow rate was monitored using the flowmeters installed in the test device. Cold water is flowing into the inner tube of the exchanger, while the electric heater in the hot tank is turned on to regulate the temperature. The hot water flows through the shell of the heat exchanger. The flow rate for the hot water is fixed at 3 dm³/min, while three different flow rates (3, 4, 5 dm³/min) were tested for the cold fluid.

After reaching a steady state, thermocouples were used to monitor the temperatures of the incoming and outgoing flows of the working fluid. The constant measurements were recorded using the Data Loader device. The hot water temperature was maintained at 63±1ºC, while the wall temperatures were measured. An electronic pressure gauge was utilized to measure the pressure drop (ΔP) across the inlet and outlet areas of the test section simultaneously.

The total heat transfer coefficient, the amount of heat transferred, and the heat exchanger efficiency were calculated using the following equations (Lee, 2022; Hayder, 2023).
Hot water mass flow rate:

$$\dot{m}h = \frac{V}{60000} \times \rho \tag{1}$$

where $\dot{m}h$ is mass flow rate for hot water, V is volumetric flow rate and ρ is density.
Cold water mass flow rate:

$$\dot{m}c = \frac{V}{60000} \times \rho \tag{2}$$

where $\dot{m}c$ is stand for mass flow rate for cold fluid.

The heat transferred from hot to cold water:

$$q_h = mh \times C_{ph} \times (T_{hi} - T_{ho}) \tag{3}$$

where q_h is stand for heat transfer for hot water, C_{ph} is specific heat for hot fluid, T_{hi} is temperature for hot fluid that inter the shell and T_{ho} is temperature for hot fluid at the end of the tube.
The amount of heat gained (qc) by cold water:

$$q_c = mc \times C_{pc} \times (T_{c0} - T_{ci}) \tag{4}$$

where C_{pc} is specific heat for cold fluid, T_{ci} is temperature for cold fluid that inter the tube and T_{c0} is temperature for cold fluid that end of the tube.
The average amount of heat transferred (q_{avg}):

$$q_{avg} = \frac{q_h + q_c}{2} \tag{5}$$

The inner portion of a twisted tube has a complex form, thus volume-driven diameters are used instead of the more commonplace metric diameters. It is determined as (Rousseau et al., 2003):

$$Dv_i = \sqrt{\frac{4V_{ol}}{\pi L}} \tag{6}$$

where Dv_i is the twisted tube inner diameter which is volume driven diameter, V_{ol} is volume occupied by the fluid in the tube and L is length of the exchanger.
The inner surface area (A_i) of the inner tube of inner fluid (di,ip):

$$A_i = \pi \times di,ip \times L \tag{7}$$

Logarithmic Mean Temperature Difference (LMTD) for counter flow arrangement is determined according to Eq. (8):

$$LMTD = \frac{(T_{hi} - T_{c0}) - (T_{h0} - T_{ci})}{ln\ (T_{hi} - T_{c0})/(T_{h0} - T_{ci})} \tag{8}$$

The efficient overall heat transfer coefficient U_i is calculated using the inner pipe surface area (Shah & Sekulic. 2003):

$$U_i = \frac{q_{avg}}{Ai,ip \times LMTD \times F} \tag{9}$$

Heat capacity for cold water:

$$C_c = \dot{m}_C \times Cp_c \tag{10}$$

Heat capacity for hot water:

$$C_h = \dot{m}_h \times Cp_h \tag{11}$$

C_{min} is minimum value out of C_c and C_h, C_{max} is maximum value out of C_c and C_h. The maximum heat transfer q_{max} can be found as below equation:

$$q_{max} = C_{min}(T_{hi} - T_{ci}) \tag{12}$$

The Nusselt number (Nu) in the inner tube is calculated by determining the temperature of the inner surface of the tube, which is assumed to be equal to the outer surface temperature (for small wall thickness). This is done by measuring the temperature along the outer surface of the inner tube and then calculating the internal heat transfer coefficient:

$$T_{w_c} = \frac{T_1 + T_2}{2} \tag{13}$$

T_{w_c} is the temperature of wall of the tube for cold fluid and T_1, T_2 are temperatures that are taken from thermocouples fixed at the wall of the tube.

$$T_{c,avg} = \frac{T_{c_o} + T_{c_i}}{2} \tag{14}$$

$T_{c,avg}$ is the average temperature for cold fluid and T_{co}, T_{ci} are temperatures for cold fluid at entrance and end of the tube, respectively.

Internal heat transfer coefficient (h_i) can be calculated from equation below:

$$h_i = \frac{q_{avg}}{A_i(T_w - T_{c,avg})} \tag{15}$$

$$Nu_c = \frac{h_i d_i}{k_i} \tag{16}$$

where Nu_c is Nusselt number for cold fluid, d_i is tube diameter and K_i is thermal conductivity for inner fluid (cold fluid).

The pressure difference (Δp) was calculated from the digital manometer. The coefficient of friction for the inner tube was calculated from the following equation (Thulikkanam, 2000):

$$f = \frac{2 * \Delta P * g_c * d_i}{L * \rho * u^2} \tag{17}$$

where f is coefficient of friction, $\Delta P = (P_2 - P_1)$ is pressure difference, g_c is constant and u^2 is velocity of the cold fluid entering the tube.

The heat exchanger performance evaluation coefficient (PEC) was calculated from the following equation (Ali et al., 2023; Ali & Mohamad, 2022; Berkache et al., 2022; Quader et al., 2023; Shrirao et al., 2013):

$$PEC = \frac{\left(\frac{Nu_{TT}}{Nu_{ST}}\right)}{\left(\frac{f_{TT}}{f_{ST}}\right)^{\frac{1}{3}}} \tag{18}$$

where Nu_{TT} represents the Nusselt number for twisted tube heat exchangers, Nu_{ST} denotes the Nusselt number for smooth tube heat exchangers, f_{TT} signifies the coefficient of friction for twisted tube heat exchangers and f_{ST} corresponds to the coefficient of friction for smooth tube heat exchangers.

5. Discussion of results

From the results shown in Fig. 4, it is observed that the use of a heat exchanger with a twisted inner tube enhances the temperature difference between the inlet and outlet for both cold and hot water. Additionally, it is noted that the temperature difference decreases with an increase in the volumetric flow rate. This is due to the increased mass flow rate, which leads to an increase in thermal storage. A twisted tube is an effective way to improve heat transfer in heat exchangers. The percentage increase in the temperature difference for the twisted tube compared to the smooth tube is 66.7% at a flow rate of 5 dm³/min.

Fig. 5 depicts the total internal heat transfer coefficient (U_i), which increases with the flow rate and reaches its highest value at a flow rate of 5 dm³/min for water in the heat exchanger with a twisted inner tube. The increase in volumetric flow rate leads to an increase in convective heat transfer coefficient.
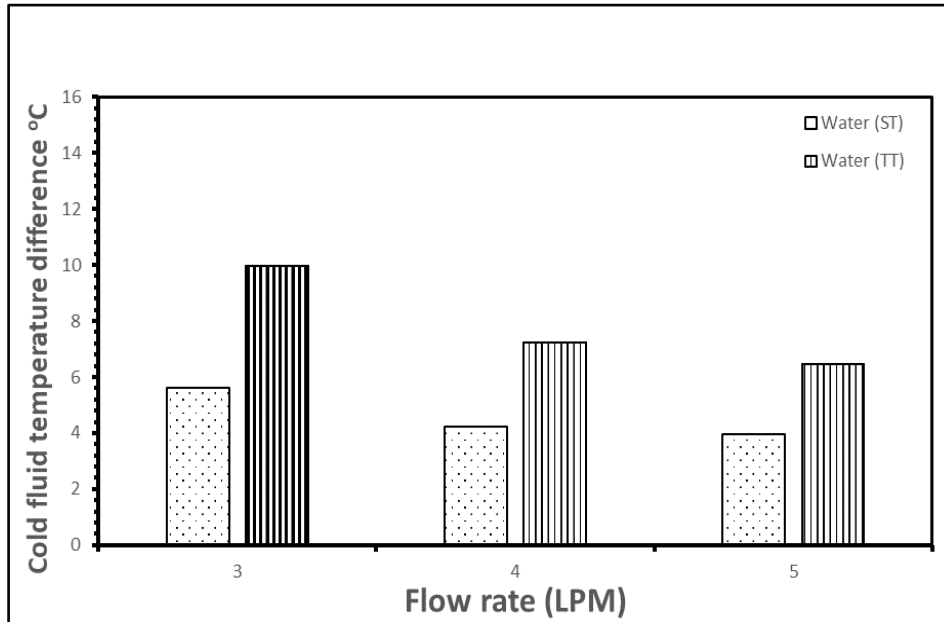
Fig. 4. Difference between the entry and exit temperatures of the fluid passing through the (smooth) and (twisted) inner tube.
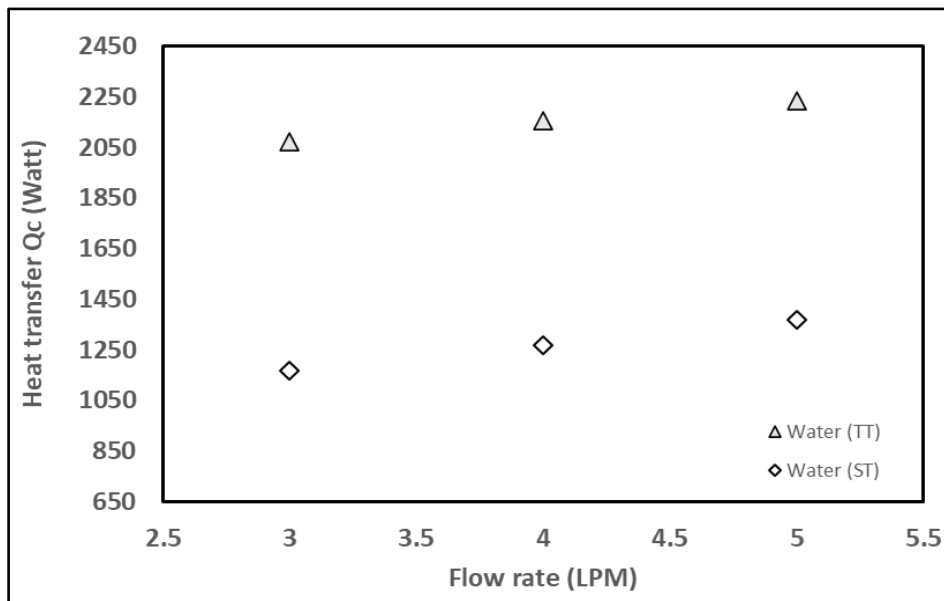
Fig. 5. The effect of changing the three flow rates on the heat transfer rate of the two exchangers.

In Fig. 6, it is observed that there is a direct relationship between the heat transfer rate and the flow rate, as well as an increase in heat transfer when using the twisted inner tube. The highest heat transfer rate (Q_c) is achieved with the flow model that reduces the thickness of the boundary layer. This reduction is due to the random movement and swirling motion generated by the twisted tube, along with the random movement of water, resulting in increased heat transfer.

Fig. 7 illustrates the change in the effectiveness of the heat exchanger using water in the inner tube for both exchangers and at the three flow rates. The highest exchanger efficiency is obtained at a flow rate of 5 dm^3/min in the heat exchanger with the twisted inner tube. According to the Eq. (11), when the heat capacity of the hot water is smaller, the temperature difference is greater, leading to an increase in exchanger effectiveness. The highest improvement in effectiveness (65.71%) is achieved at a flow rate of 3 dm^3/min in the heat exchanger with the twisted inner tube.

Fig. 8 presents the Nusselt number, which increases with the flow rate and reaches its highest value in the heat exchanger with the twisted inner tube at a flow rate of 5 dm^3/min when using water. The Nusselt number, as per Eq. (18), demonstrates the change in the Nusselt number with an increasing flow rate.
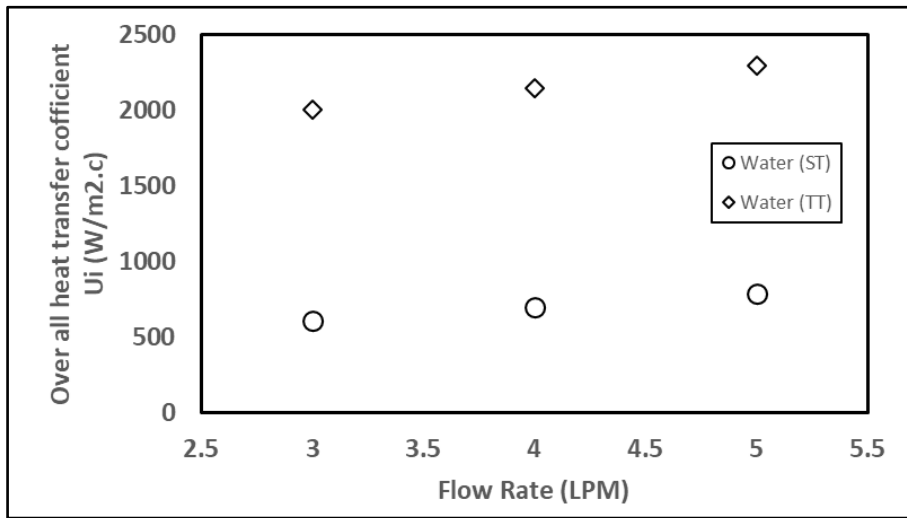
Fig. 6. Changing the coefficient of heat transfer and the rate of flow for the smooth (ST) and twisted (TT) inner tube exchange.
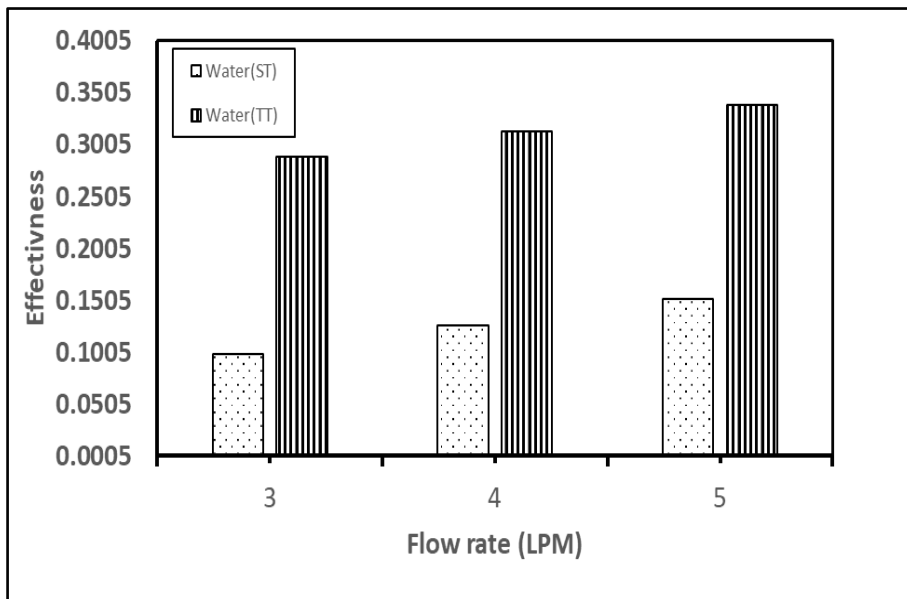
Fig. 7. Changing the effectiveness of the exchanger and the three flow rates for the two exchangers.
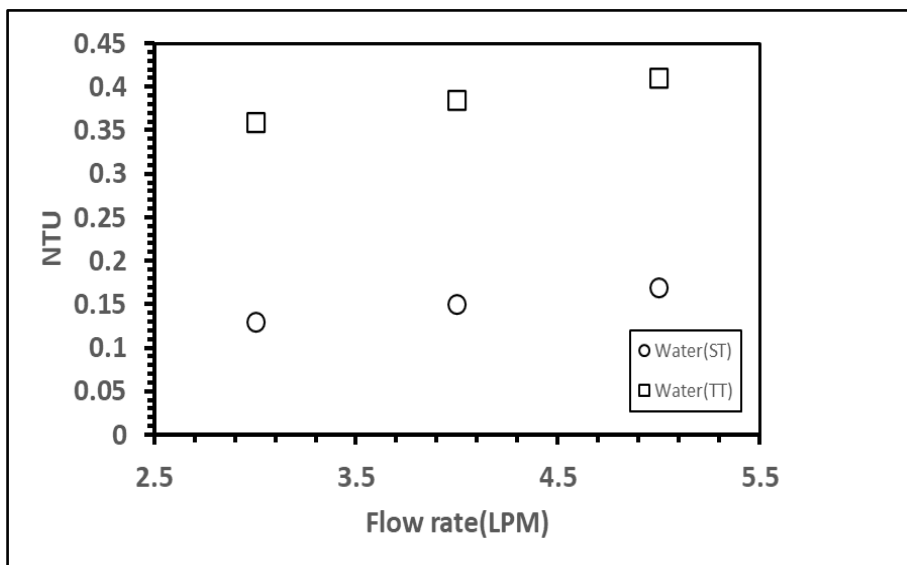
Fig. 8. Changing the Nusselt number with changing the flow rate.

Fig. 9 demonstrates the effect of the Reynolds number (*Re*) on the friction coefficient of water at the three flow rates (3, 4, 5 dm³/min). It is observed that the friction coefficient decreases with an increase in the Reynolds number. For water, the highest value of the friction coefficient is obtained in the heat exchanger with the twisted inner tube at a flow rate of 3 dm³/min.

Fig. 10 shows the performance evaluation coefficient at the three flow rates, as we notice that the performance evaluation coefficient decreases with the increase in the volumetric flow rate, as it reached its lowest value at the flow rate (5 dm³/min). The performance evaluation coefficient decreases after the flow rate (3 dm³/min) and that is based on the values of the Nusselt number and the friction coefficient, where the highest value of the performance evaluation coefficient is at the flow rate (3 dm³/min), where the value of the transferred heat and the internal heat transfer coefficient are the highest possible, and therefore the Nusselt number increases according to Eq. 18, and thus we get the highest value of the performance evaluation coefficient (3.28).
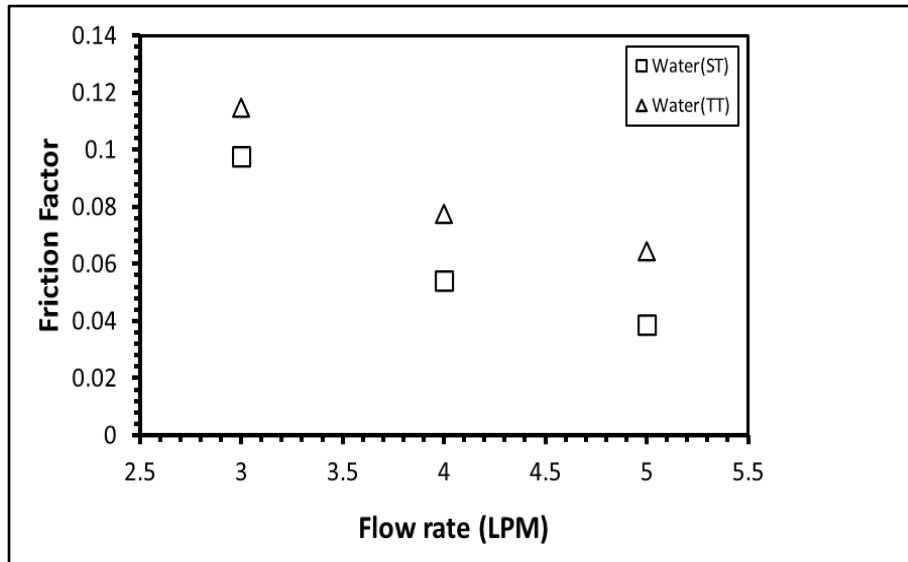
Fig. 9. Comparing the friction coefficient of water at the three flow rates.
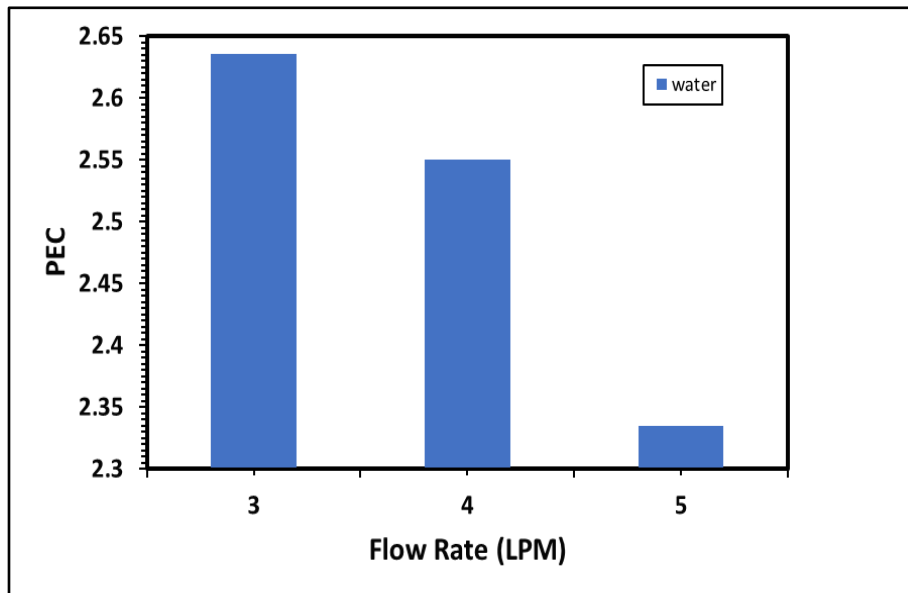
Fig. 10. Performance evaluation coefficient (PEC) using water at the three flow rates.

6. Conclusions

The overall heat transfer coefficient increased with an increase in the average amount of heat transferred in the heat exchanger with a twisted inner tube. However, the value decreased with increasing flow rates since there is not enough time for efficient heat exchange to occur in both exchangers. The highest efficiency of the exchanger was achieved at a flow rate of 5 dm³/min in the

heat exchanger with the twisted inner tube. According to Eq. 11, this is due to the smallest heat capacity of the hot water resulting in a greater temperature difference, thus increasing the exchanger efficiency. It was observed that the friction coefficient decreased with an increase in the flow rate, reaching its highest value at a flow rate of 3 dm^3/min in the heat exchanger with the twisted inner tube. The highest value of the performance evaluation coefficient (PEC) for the heat exchanger was observed at a flow rate of 3 dm^3/min.

References

Abbas, E. F., Ali, H. H. M., & Mahmood, N. J. (2021). Comparison between numerical study and experimental work on heat transfer from heat sink under transient conditions. *Journal of Mechanical Engineering Research and Developments*, *44*(7), 141-150.

Ali, H.H.M., Hussein, A.M., Allami, K.M.H., & Mohamad, B. (2023). Evaluation of shell and tube heat exchanger performance by using ZnO/water nanofluids. *Journal of Harbin Institute of Technology (New Series)*. https://doi.org/10.11916/j.issn.1005-9113.2023001.

Ali, M.Q., & Mohamad, B. (2022). A review of the design and control using computational fluid dynamics of gasoline direct injection engines. *Diagnostyka*, *23*(3), 1-8. https://doi.org/10.29354/diag/153373.

Barrak, A. S., Ali, N. M., & Ali, H. H. M. (2022). An effect of binary fluid on the thermal performance of pulsation heat pipe. *International Journal of Applied Mechanics and Engineering*, 27(1), 21–34. https://doi.org/10.2478/ijame-2022-0002.

Bergies, E.A. (1999). *The imperative to enhance heat transfer* (S. Kakaç, A.E. Bergles, F. Mayinger, H. Yüncü, Eds). Heat Transfer Enhancement of Heat Exchangers. Nato ASI Series, 355. Springer, Dordrecht. https://doi.org/10.1007/978-94-015-9159-1_2.

Bergman, T. L., Incropera, F. P., Dewitt, D. P., & Lavine, A. S. (2011). *Fundamentals of heat and mass transfer*. John Wiley & Sons.

Berkache, A., Amroune, S., Golbaf, A., & Mohamad, B. (2022). Experimental and numerical investigations of a turbulent boundary layer under variable temperature gradients. *Journal of the Serbian Society for Computational Mechanics*, *16*(1), 1-15. https://doi.org/10.24874/jsscm.2022.16.01.01.

Eiamsa-Ard, S., Promthaisong, P., Thianpong, C., Pimsarn, M., & Chuwattanakul, V. (2016). Influence of three-start spirally twisted tube combined with triple-channel twisted tape insert on heat transfer enhancement. *Chemical Engineering and Processing: Process Intensification*, *102*, 117–129. https://doi.org/10.1016/j.cep.2016.01.012.

Eltaweel, M., Abdel-Rehim, A. A., & Hussien, H. (2020). Indirect thermosiphon flat-plate solar collector performance based on twisted tube design heat exchanger filled with nanofluid. *Interntional Journal of Energy Research*, *44*(6), 4269–4278. https://doi.org/10.1002/er.5146.

Farnam, M., Khoshvaght-Aliabadi, M., & Asadollahzadeh, M. J. (2021). Intensified single-phase forced convective heat transfer with helical-twisted tube in coil heat exchangers. *Annals of Nuclear Energy*, *154*, 108108. https://doi.org/10.1016/j.anucene.2020.108108.

Hayder, H. Ali, M. Hussein, A. M. Mohammed, K. Allami, H. & Mohamad, B. (2023). Evaluation of shell and tube heat exchanger performance by using ZnO/water nanofluids. *Journal of Harbin Institute of Technology (New Series)*. https://doi.org/10.11916/j.issn.1005-9113.2023001.

Holman, J. P. (2008). *Heat transfer*. 6th Ed. Tata McGraw-Hill Education.

Khoshvaght-Aliabadi, M., & Feizabadi, A. (2020). Performance intensification of tubular heat exchangers using compound twisted-tape and twisted-tube. *Chemical Engineering and Processing - Process Intensification*, *148*, 107799. https://doi.org/10.1016/j.cep.2019.107799.

Lee, H. (2022). *Thermal design: heat sinks, thermoelectrics, heat pipes, compact heat exchangers, and solar cells*. John Wiley & Sons.

Pardhi C. K., & Baredar, P. (2012). Performance improvement of double pipe heat exchanger by using turbulator. *International Journal of Engineering Science & Advanced Technology*, 2(4), 881–885.

Qader, F., Hussein, A., Danook, S., Mohamad, B., & Khaleel, O. (2023). Enhancement of double-pipe heat exchanger effectiveness by using porous media and TiO2 water. *CFD Letters*, *15*(4), 31-42. https://doi.org/10.37934/cfdl.15.4.3142.

Rousseau, P. G., Van Eldik, M., & Greyvenstein, G. P. (2003). Detailed simulation of fluted tube water heating condensers. *International Journal of Refrigeration*, *26*(2), 232–239. https://doi.org/10.1016/S0140-7007(02)00077-4.

Samruaisin, P., Kunlabud, S., Kunnarak, K., Chuwattanakul, V., & Eiamsa-Ard, S. (2019). Intensification of convective heat transfer and heat exchanger performance by the combined influence of a twisted tube and twisted tape. *Case Studies in Thermal Engineering*, *14*, 100489. https://doi.org/10.1016/j.csite.2019.100489.

Shah, R.K. (1986). *Classification of heat exchangers h* (S. Kakac, A.E. Bergles, F. Mayinger, Eds.). Heat exchangers: Thermal Hydraulic Fundamentals and Design. Hemisphere Publishing Corp., Washington, DC.

Shah, R. K., & Sekulic, D. P. (2003). *Fundamentals of heat exchanger design*. John Wiley & Sons.

Shrirao, P. N., Sambhe, R. U., & Bodade, P. R. (2013). Experimental investigation on turbulent flow heat transfer enhancement in a horizontal circular pipe using internal threads of varying depth. *IOSR Journal of Mechanical and Civil Engineering*, *5*(3), 23–28.

Thantharate, V., & Zodpe, D. B. (2013). Experimental and numerical comparison of heat transfer performance of twisted tube and plain tube heat exchangers. *International Journal of Scientific & Engineering Research*, *4*(7), 1107–1113.

Thulukkanam, K. (2000). *Heat exchanger design handbook*. CRC Press. https://doi.org/10.1201/9781420026870.

Walker, G. (1982). *Industrial heat exchangers: a basic guide*. Hemisphere Publishing Corporation.

Wang, L., Sun, D.W., Liang, P., Zhuang, L., & Tan, Y. (2000). Heat transfer characteristics of carbon steel spirally fluted tube for high pressure preheaters. *Energy Conversion and Management*, *41*(10), 993–1005. https://doi.org/10.1016/S0196-8904(99)00159-4.

Yan, W., Gao, X., Xu, W., Ding, C., Luo, Z., & Zhang, Z. (2017). Heat transfer performance of epoxy resin flows in a horizontal twisted tube. *Applied Thermal Engineering*, *127*, 28–34. https://doi.org/10.1016/j.applthermaleng.2017.08.013.

Zwiększanie Wydajności Dwururowego Wymiennika Ciepła oprzez Zastosowanie Skręconej Rury Wewnętrznej

Streszczenie

W badaniach wykorzystano dwa dwururowe wymienniki ciepła. W pierwszym wymienniku zastosowano gładką rurę wewnętrzną, natomiast w drugim zastosowano rurę skręconą. Płaszcz wykonano z poli(chlorku winylu) (PVC), natomiast rura wykonana z miedzi charakteryzowała się następującymi wymiarami: długość 1000 mm, średnica zewnętrzna 62,24 mm, średnica wewnętrzna 14,2 mm i średnica zastępcza dla rury skręconej 11,8 mm. Aby zminimalizować straty ciepła, rura została zaizolowana od zewnątrz izolatorem termicznym. Aby poprawić wydajność wymiennika ciepła, przez tunel w kształcie pierścienia przepuszczano gorącą wodę z szybkością 3 dm³/min., a temperatura na wlocie wynosiła 63°C. Porównano wyniki eksperymentalne dwóch wymienników ciepła (gładkiego i o skręconej rurze wewnętrznej) i stwierdzono, że zastosowanie wody jako płynu roboczego doprowadziło do poprawy wydajności wymiennika. Wymiennik ciepła wykonany ze skręconej rury wewnętrznej osiągnął maksymalną wydajność 0,33 przy objętościowym natężeniu przepływu 5 dm³/min., natomiast maksymalna poprawa efektywności wyniosła 65,71% przy objętościowym natężeniu przepływu 3 dm³/min.

Słowa kluczowe: sprawność wymiennika ciepła, współczynnik przenikania ciepła, dwururowe wymienniki ciepła, skręcona rura.

Original Research

„Above the Pack" Diffusion Aluminizing of Turbine Compressor Blades made of EI867 in the Aerospace Industry

Anna Pytel [1,2,*] , **Andrzej Nowotnik [2]** , **Agnieszka Nalborczyk-Kazanecka [1,2]**

[1] Pratt&Whitney Rzeszów S.A, ul. Hetmańska 120, 35-078, Rzeszów, Poland

[2] Faculty of Mechanical Engineering and Aeronautics, Rzeszów University of Technology, al. Powstańców Warszawy 12, 35-959, Rzeszów, Poland; nowotnik@prz.edu.pl (A. Nowotnik), d484@stud.prz.edu.pl (A. Nalborczyk-Kazanecka)

* Correspondence: anna.tomczak@prattwhitney.com

Abstract

In the publication, tests were conducted on compressor turbine working blades made of EI-867 material, in accordance with the TU 14-1-402-72 standard, which were subjected to the gas non-contact aluminizing process. Metallographic analyses of the produced aluminide layer were undertaken, and the phase components of the aluminide layer microstructure were identified. This identification was achieved by analyzing the chemical composition in micro-areas using the EDS attachment in a scanning electron microscope and using X-ray diffraction. Additionally, hardness and creep resistance tests of the blades, after undergoing solution and aging processes, were performed over different durations. The research was aimed at exploring the feasibility of the aluminizing process using the "above the pack" method on parts made of EI-867 material and understanding the process's impact on the creep resistance of the part. Experimental research have shown that aluminizing turbine blades with EI-867 using the "above the pack" method to obtain a layer thickness in the range of 0.03-0.06 mm is possible within 10 hours at 950ºC. Aluminizing with the analyzed method results in the formation of an aluminized layer with a three-phase structure that ensures the appropriate strength of the coating. However, it has been shown that the aluminizing process using the "above the pack" method with the applied time of 10 hours causes a significant reduction in the creep resistance of the material. Based on the obtained results, it was shown that the non-contact aluminizing method for turbine blades made of EI 867 material does not meet aviation requirements for safe operation due to a significant reduction in mechanical properties.

Keywords: diffusion aluminizing, compressor turbine blades, EI867 alloy, turbine engine, compressor turbine

1. Introduction

Various types of damage to turbine components may occur during operation. The most vulnerable element of the turbine is the blades. The technical condition of which significantly influences the durability and operational reliability of both the turbine and the entire engine (Albrecht, 2017). According to literature, the primary causes of blade damage are creep, overheating, and thermal fatigue of the material (Błachnio et al., 2014; Szczepankowski & Szymczak, 2016). This can be attributed to manufacturing defects, such as using insufficiently durable heat-resistant coatings or improperly applying them to the blade material (Błachnio et al., 2014). The selection of the protective coating and the material to manufacture the blade with the desired durability must consider its mechanical and thermal properties in the highest temperature zones (Błachnio, 2011).

Heat-resistant alloys, especially those used for turbine components in aerospace production, endure very high temperatures (around 1000ºC) (Golewski, 2015; Zasada et al., 2016). To augment their resistance to atmospheric and gas corrosion at these temperatures, thermo-chemical treatments, which involve diffusion saturation of the surface layer with aluminum, are used. Applying the aluminum coating enhances the parts' heat resistance, extending their service life (Godzimirski, 2011). In modern metallurgy, there are numerous aluminizing methods. It is crucial that the chosen method not only

achieves the desired results after the aluminizing process but also maintains the mechanical properties of the base material. The EI 867 material is a heat-resistant nickel-based superalloy melted and casted in vacuum furnaces. Its chemical composition should adhere to standard TU 14-1-402-72 for EI 867 or TU 14-1-223-72 for EI 867 WD (Table 1). The EI-867 WD alloy falls within the group of nickel matrix superalloys that do not contain titanium. Notably, this alloy has a lower chromium content than other superalloys, rendering it more susceptible to corrosion. Consequently, components made from these alloys necessitate protective coatings, specifically aluminum layers.

Table 1. The chemical composition of the EI867 alloy (МЧМ, 1972).

Element	Min, wt.%	Max, wt.%
C	-	0.10
Si	-	0.60
Mn	-	0.30
Cr	8.5	10.5
Ni	remainder	
Al	4.2	4.9

In order to obtain the highest possible properties of the EI867 alloy, the alloy is subjected to heat treatment, i.e. precipitation hardening. This treatment consists in solution solution at 1220±10ºC for 4 to 6 hours and aging at 950±15ºC for 8 hours (МЧМ, 1972). Solution solution causes dissolution of some carbides and intermetallic phases in the matrix. On the other hand, in the aging process, dispersion precipitates of the above-described γ' coherent phase and carbides are formed, evenly distributed in the matrix. The annealing is carried out in an inert atmosphere or sometimes in a vacuum. The purpose of precipitation hardening is to obtain a structure in which the size, shape and arrangement of the phases strengthening the alloy will ensure optimal mechanical properties and maximum stability of the structure at the operating temperature. In order to obtain a heat-resistant coating on the EI867 alloy, a powder aluminization process is used. The parts are covered directly with a powder consisting of a mixture of ferroaluminum and ammonium chloride. The standard process is carried out at a temperature of 950ºC for 2 to 4 hours, depending on the requirements of the depth of the aluminized layer. Due to the guidelines of the TU 14-1-402-72 standard for EI 867, the technological process should be arranged in such a way that it does not last longer than 8 hours at 950ºC. The use of protective coatings provides more effective protection against heat loads and protection against the influence of the environment (Golewski, 2015). At the same time, it affects the possibility of increasing the operating temperature of the most thermally loaded engine components. These coatings should be characterized primarily by low thermal conductivity and high structural stability (Godzimirski, 2011). In order to reduce the brittleness of the aluminized layer caused by the formation of intermetallic phases and to increase the thickness of the layer, additional diffusion annealing is applied after aluminizing at 900÷1050°C for 3 to 5 hours.

Due to the continuous development of the aviation industry and the ever-higher guidelines for the acceptance of parts subject to thermal stress during operation, trials of diffusion aluminizing using the "above the pack" method of the EI 867 material were carried out. A semi-finished product (forgings) used for the production of working blades of the compressor turbine made of the EI 867 alloy was used for the tests.

2. Methodology and results

The initial phase of the research involved aluminizing samples, specifically blades made of the EI-867 (HN62MWKJu) alloy, using the non-contact gas process, also known as "above the pack." The objective was to achieve an aluminized layer thickness within the range of 0.03 to 0.06 mm. This thickness range would ensure a heat-resistant coating that is operationally safe. Three aluminizing experiments were conducted, with their parameters detailed in Table 2. For each experiment, two samples (blades) and 20 additional blades (serving as ballast) were used.

The conventional aluminizing process operates at 1000ºC. However, due to the restriction of not exceeding the 950ºC parameter (as mandated by the TU 14-1-402-72 standard aging temperature) for the EI867 material, the aluminization experiments were performed at 950ºC. Because of this temperature reduction, the process duration had to be extended to 10 hours to achieve the desired thickness for the aluminized layer. The microstructure of the obtained layer is shown in Figures 1 and 2.

Table 2. Parameters of the EI 867 aluminizing tests with the results of the main aluminized layer.

Test	Temperature, ºC	Heating time, ºC/min	Hold time, h	Layer depth, mm
1	950	2÷6	4	0.010÷0.048
2	950	2÷6	8.5	0.028÷0.040
3	950	2÷6	10	0.033÷0.044
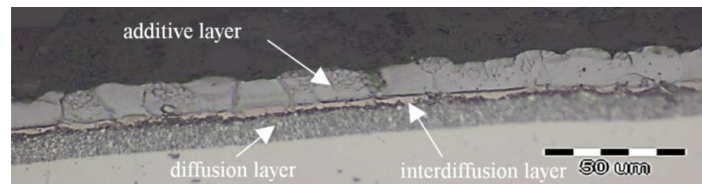
Fig. 1. Microstructure of the aluminized layer showing the in gray and orange; non-etched microsection of the blade's suction side.

Fig. 2. Microstructure of the aluminized layer; non-etched microsection treated with Kalling's reagent (blade's suction side).

Analyses of the aluminized layer were conducted using the OLYMPUS GX51 microscope, serial no. 8R14922, with a ×500 magnification. A sample for analysis was sourced from a cross-section of a blade. This metallographic specimen was etched using Kalling's reagent. The structure of the aluminum layer is influenced by various factors, including the aluminum's activity in the mixture, the substrate's chemical composition, and the aluminizing temperature and duration. Aluminide layers formed on a nickel based alloy's substrate (rich in other alloying elements that enhance heat and high-temperature corrosion resistance) typically exhibit a triphasic structure. This is attributed to two opposing diffusion flows: a flow of aluminum atoms from the atmosphere and another of atoms, including nickel, moving from the substrate. The diffusion of nickel and certain alloying elements from the substrate towards the surface leads to their depletion, culminating in the creation of what is known as the interdiffusion layer (Fig. 3). Concurrently, nickel diffusion encourages the development of intermetallic phases and carbides in the intermediary layer, establishing a barrier against aluminum's diffusion into the substrate. The depth of the obtained layer is shown in Figure 4.
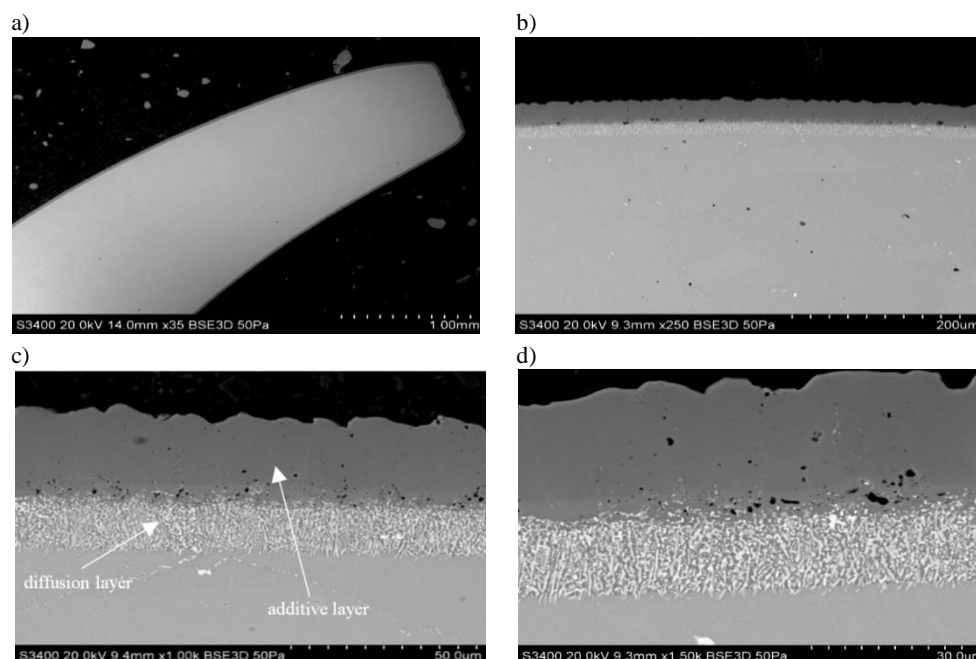
Fig. 3. a)-f) Microstructure of the aluminide layer formed in the thermochemical non-contact gas process ("above the pack") on the surface of an EI-867 alloy blade.

e)

f)

Fig. 3. *Cont.*

a)

b)
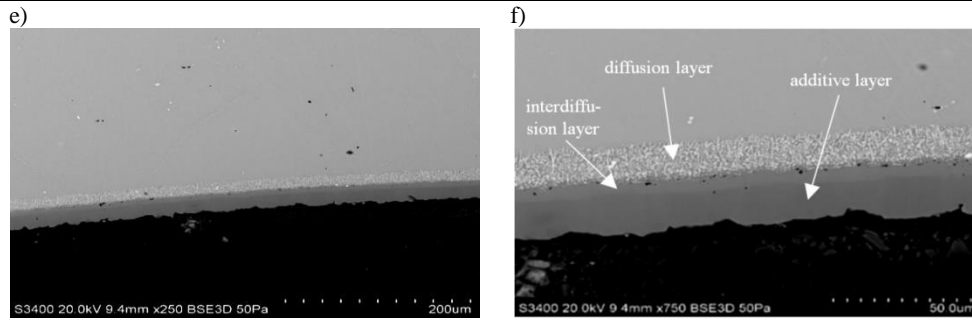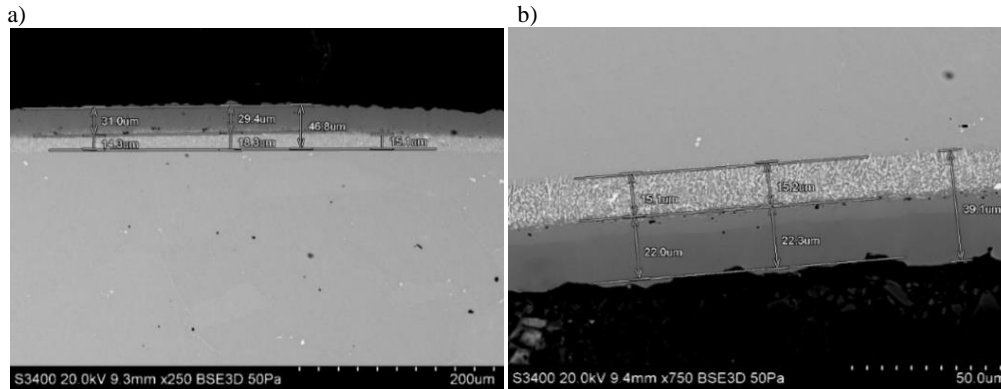
Fig. 4. Microstructure of the aluminide layer formed in the thermochemical process ("above the pack" method): a) suction side, b) pressure side – leading edge. The depth of the layer is indicated.

Table 3. Chemical composition of micro cross-sectional areas of the aluminide layer produced on the base of the blade in the thermochemical process using the "above the pack" method

Point	Al-K	Si-K	Cr-K	Co-K	Ni-K	Mo-L	W-L
1	32.3	2.6	1.8	2.5	60.8		
2	14.4	2.2	18.4	3.2	45.9	9.8	6.1
3	10.5	1.6	13.9	5.5	43.9	15.7	9.0
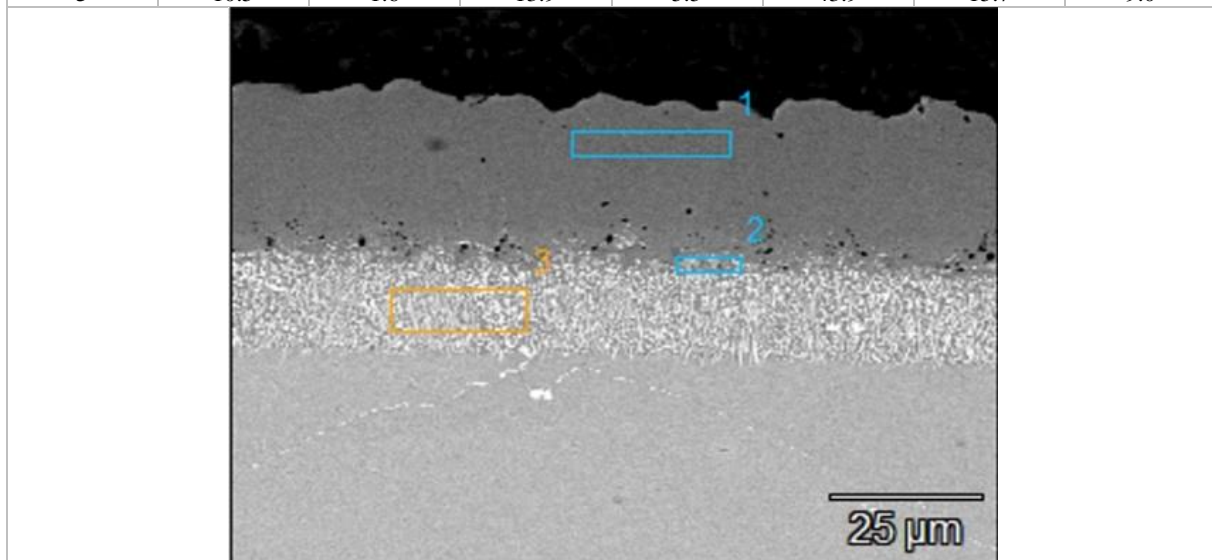
The phase components of the microstructure of the aluminide layer after the gas-free contact aluminizing process were identified by analyzing the chemical composition in micro-areas using the EDS attachment in a scanning electron microscope and by X-ray diffraction. The results of quantitative and qualitative (Fig. 5, Table 3) tests allow to conclude that, in accordance with the assumptions made, an aluminide layer consisting of the expected NiA phase was formed on the blade surface from the EI 867 superalloy substrate, ensuring its good heat resistance properties. XRD studies confirmed the presence of a stable β-NiAl phase in the aluminide layer (Fig. 6).

a)
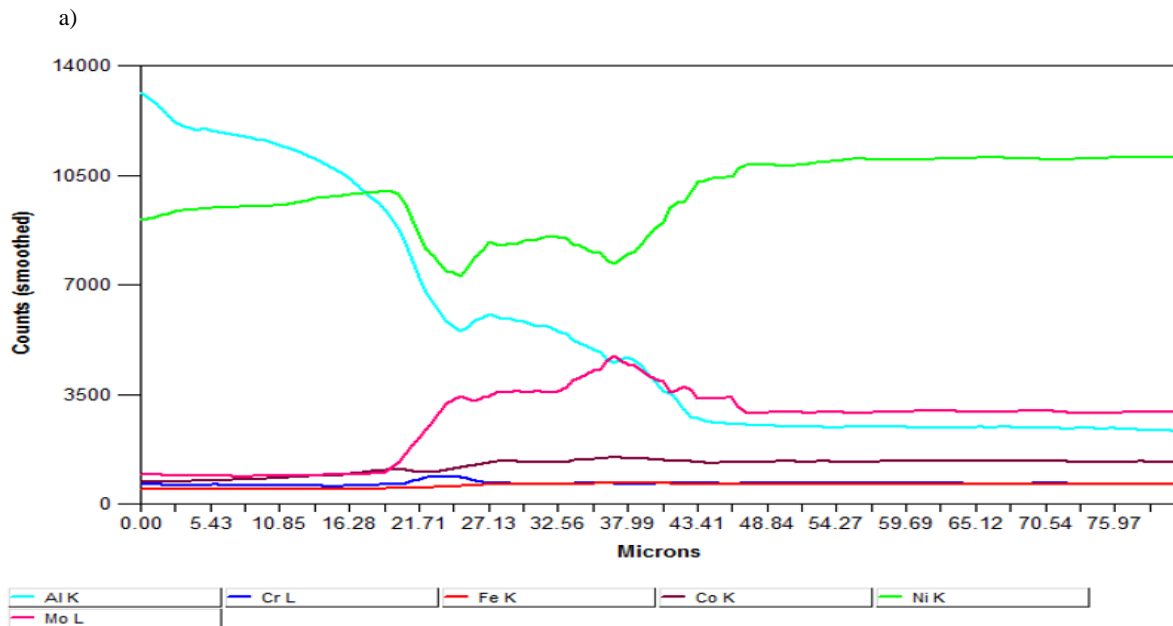
b)
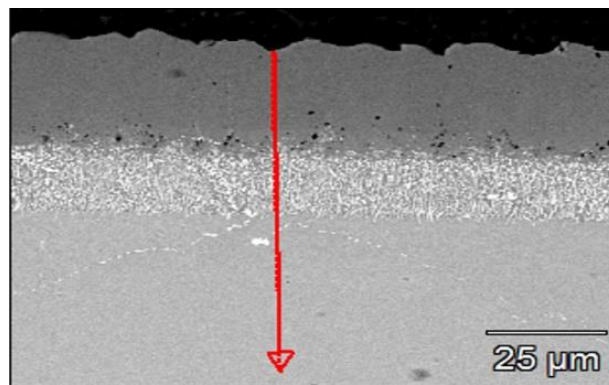
Fig. 5. a) Linear profile of changes in the content of elements along a given scanning line on b) the cross-section of a blade with an aluminide layer produced in the aluminizing process using the "above the pack" method.
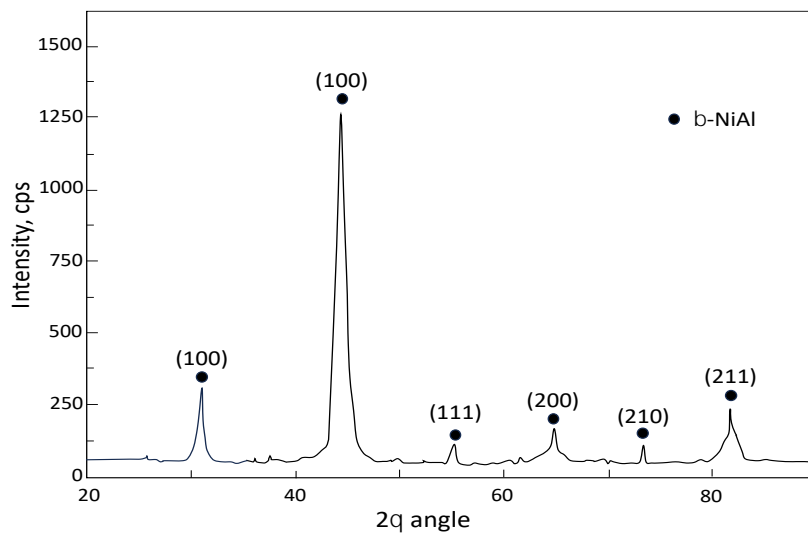
Fig. 6. XRD pattern of the aluminide layer deposited on the examined blades.

Extending the holding time at 950ºC affects the strength properties of the material working at elevated temperatures. Therefore, it was necessary to carry out control tests confirming the effect of extending the time on the creep resistance of the EI867 material. In the case of the turbine blades analyzed in the publication, apart from the need to have a heat-resistant layer, the parts must have a creep

resistance of at least 50 hours due to aviation requirements for safe operation. 10 samples (semi-finished product in the form of forgings for turbine blades) were used for the tests. All samples underwent the solution treatment process for 4 h at 1220±10ºC. Then, the aging process was carried out within the endurance range of 9 to 18 hours (according to the TU 14-1-402-72 standard, the endurance time is 8 hours).

The assumptions of the creep resistance test assumed conducting the test until the sample broke. The requirement of the test was not to break the sample before the period of 50 hours. According to the assumptions of the Technical Conditions, this time was sufficient for the safe operation of the turbine blades. All samples (Fig. 7) were tested on the same creep test machine. The test parameters are presented in Table 4. Results of research are shown in Table 5 and Figure 8.

Fig. 7. Appearance of the sample used for creep resistance testing.

Table. 4. Creep resistance test parameters

Cross-section of the sample	circular
Nominal sample diameter, d0 nom,mm	4
Nominal test temperature, ºC	900
Nominal test stress, MPa	216

Table. 5. The course of the aging test and the results of creep resistance and hardness tests.

Sample number	Hold time, h	Creep resistance, h	Hardness, HBW
P10	18	the sample failed	302
P9	17	56.2	302
P8	16	56.1	317
P7	15	42.1	302
P6	14	45.9	206
P5	13	52.6	302
P4	12	46.2	302
P3	11	45.4	302
P2	10	45	302
P1	9	43.9	302
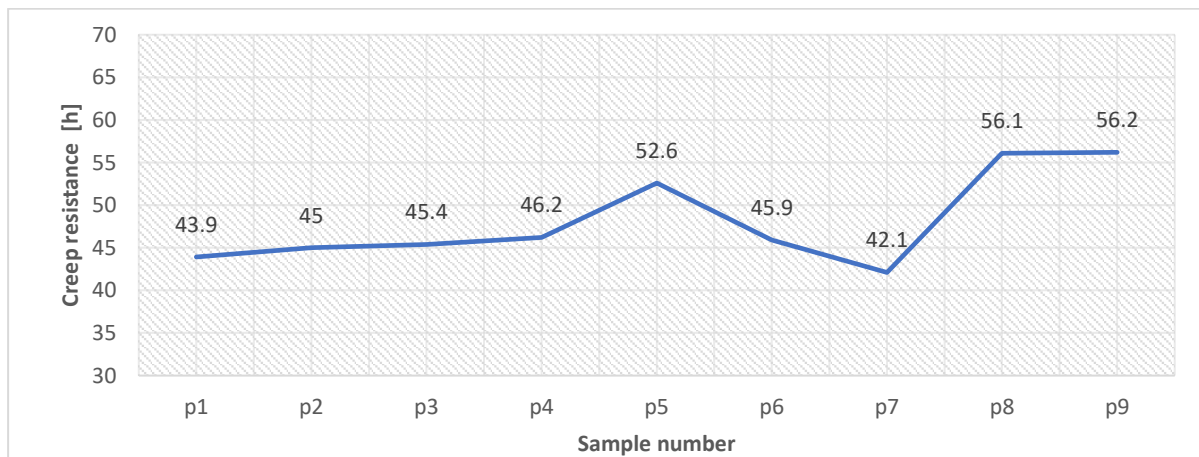
Fig. 8. Creep resistance results [h].

In addition, the hardness of the core of the samples was measured using the Manometer PBM No. 249 hardness tester according to PN-EN ISO 6506-1:2004-12 standard. The measurement was made on the HBW scale. Results are shown in figure 9.
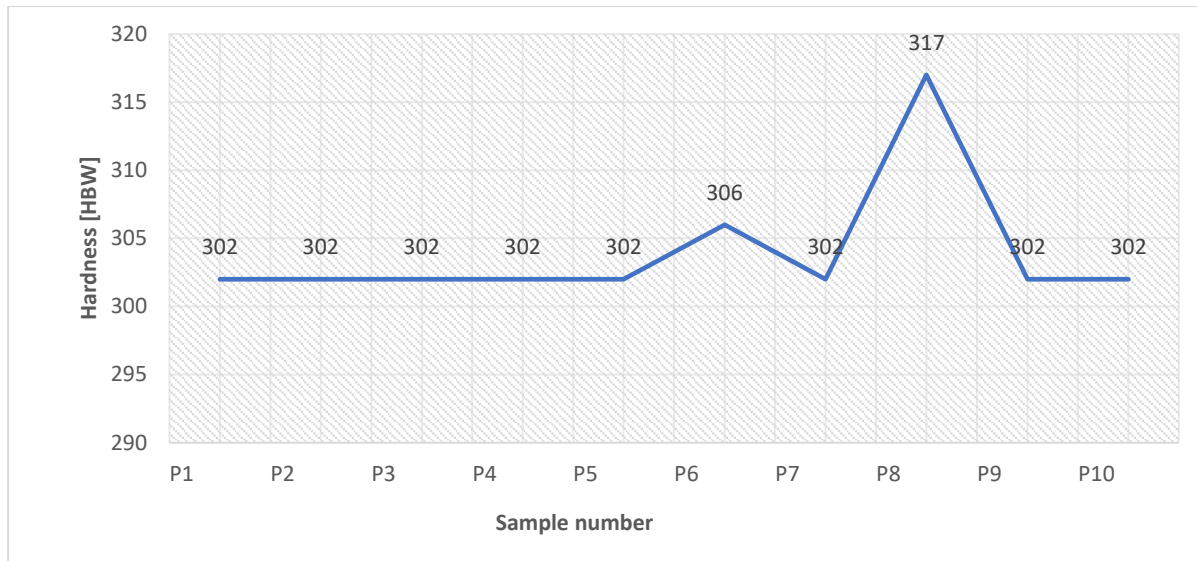
Fig. 9. Hardness results [HBW].

Additional tests on the samples subjected to the creep-strength test assessed the nature of the fracture and the place of initiation of the loss of cohesion by the material and the microstructure of the cross-section of the samples, and determining the grain size. Two samples broken during the creep resistance test were used for the tests (Figs. 10 and 11). The samples were labeled as P4 and P9. In both cases, the fracture has the characteristics of an intercrystalline fracture. No defects (inclusions, crimps, etc.) that could affect the initiation and development of cracks were observed on the samples. Grain distribution on the cross-section of both samples is shown in Fig. 12. In the case of sample P4, decohesion probably started along the grain boundaries from the left side, ending with an oblique fracture (tears are visible), while for sample P9, it can be seen that decohesion could have occurred evenly along the entire cross-section, ending with a fracture perpendicular to the axis of the sample.

The fracture surfaces of the broken samples were observed using SEM (Fig. 13). The SEM HITACHI SU3500 microscope equipped with the EDS/EDX micro-analyzer (Thermo Fisher model NS7; SN; 0914065) was used. Grain size checks were made by comparison using ASTM E112-13 Table 1 standards which cover grain sizes from 1 to 8.

Fig. 10. Sample cut from the P4 blade - the sample after the creep resistance test broke after 42.6 h.

Fig. 11. Sample cut from the P9 blade - the sample after the creep resistance test broke after 52.6 h.
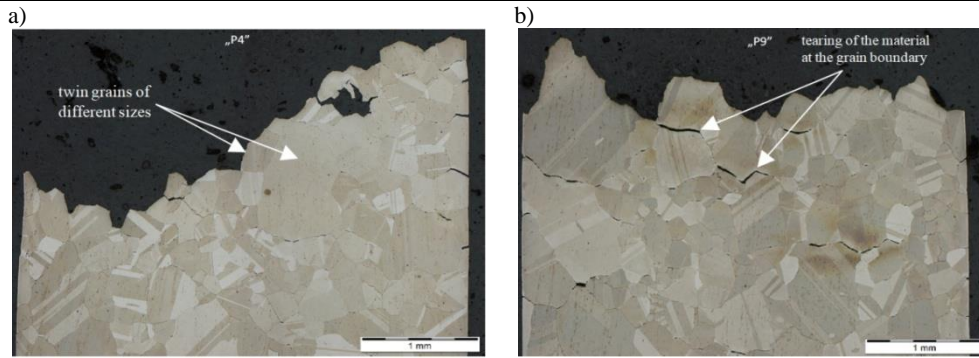
Fig. 12. Cross-sectional view of the zone adjacent to the fracture of the a) P4 sample b) P9 sample. In the structure, twin grains of different sizes and typical effects of the creep process (tearing of the material at the grain boundary) are visible. Etchant: Kalling's reagent.
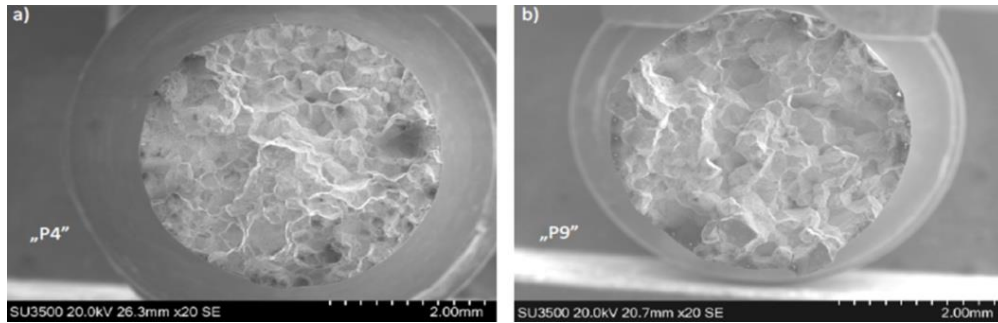
Fig. 13. SEM image (SE mode) of the fracture surface of two samples a) P4 blade, b) P9 blade.

3. Conclusions

Experimental research have shown that:

1) Aluminizing the Turbine Blades with the EI-867 material using the "above the pack" method to obtain a layer depth in the range of 0.03-0.06 mm is possible within 10 hours at 950ºC.

2) During the aluminizing of the EI-867 material, a layer with a three-phase structure is formed due to oppositely directed diffusion streams (from the surface and from the atmosphere). During the aluminizing of the EI-867 material, it has been observed that a layer with a three-phase structure forms. This is believed to be a result of oppositely directed diffusion streams, originating both from the surface of the material and from the surrounding atmosphere. This observation aligns with the results from multiple research teams, wherein similar material interactions exhibited the formation of multiphase structures under comparable conditions. The consistency in these findings across varied studies suggests that this behavior is not an anomaly, but rather a characteristic response of the EI-867 material to aluminizing processes.

3) Quantitative and qualitative analysis of the aluminized layer allowed to conclude that, in accordance with the adopted assumptions, an aluminide layer consisting of the expected NiA phase was formed on the blade surface from the EI 867 superalloy substrate, ensuring its good heat resistance properties. After a rigorous quantitative and qualitative analysis of the aluminized layer, we can deduce that the formation process aligns with our initial assumptions. An aluminide layer, predominantly consisting of the anticipated NiA phase, was identified on the blade surface derived from the EI 867 superalloy substrate. This specific phase composition is known in the research community to endow materials with enhanced heat resistance properties. Furthermore, comparable studies and examinations of similar superalloys have consistently shown the emergence of such layers when subjected to analogous aluminizing conditions, further strengthening our conclusion.

4) EI-867 forgings aged for 9, 10, 11, 12, 14, 15 h did not meet the limit value of creep resistance (assumed min. 50 h).

5) Forgings aged for 13, 16, 17 h met the requirement of the limit value of creep resistance (assumed min. 50 h).

6) The hardness of almost all forgings (except P8) remained at a constant level of 302-306 HBW.

7) During the metallographic tests, no defects of forging origin (inclusions, forging) were observed on the samples, which could affect the initiation and development of the crack.

8) The average grain size on the tested samples no. P4 and P9 was 1 on a scale from 1 to 8 according to ASTM E112-13 for nickel alloys. At the same time, in both tested blades, both much larger grains (several times) and clusters of smaller grains (grain no. 3 and a single smaller grain) are observed. The largest grain observed on blade P4 measured about 0.17 mm, while on blade P9 about 0.23 mm.

9) In both cases of the tested creep resistance samples, the fracture had the characteristics of intercrystalline fracture after rupture.

References

Albrecht, R. (2017). *Defekty strukturalne oraz ich związek z krystalizacją monokrystalicznych łopatek silników lotniczych* [Rozprawa doktorska, Uniwersytet Śląski]. Katowice.

Błachnio, J. (2011). Analysis of causes of decohesion of a gas turbine blade made of EI 867-WD alloy. *Aircraft Engineering and Aerospace Technology*, *83*(1), 14-20. https://doi.org/10.1108/00022661111119874

Błachnio, J., Dzięgielewski, W., Kułaszka, A., & Zasada, D. (2014). Wpływ czynników eksploatacyjnych na stan żaroodpornej powłoki łopatek turbiny gazowej. Studies & Proceedings of Polish Association for Knowledge Management. 68, 17-31.

Godzimirski, J. (2011). Nowe technologie lotniczych silników turbinowych. *Prace Instytutu Lotnictwa*, *213*, 22-36.

Golewski, P. (2015). *Obciążenia cieplno-mechaniczne łopatek silników turbinowych z ceramicznymi powłokami ochronnymi* [Rozprawa doktorska, Politechnika Lubelska]. Lublin.

МЧМ. (1972). Министерство черной металлургии СССР, Москва. Прутки из жаропрочных сплявов. (Norma materiałowa TU 14-1-402-72).

Szczepankowski, A., & Szymczak, J. (2016). Uszkodzenia cieplne lotniczych silników turbinowych. *Prace Naukowe Instytutu Technicznego Wojsk Lotniczych*, *38*, 21-32.

Zasada, D., Bogdan, M., & Błachnio, J. (2016). Increased temperature impact on durability of gas turbine blades. *Eksploatacja i Niezawodnosc - Maintenance and Reliability*, *19*(1), 48-53. http://dx.doi.org/10.17531/ein.2017.1.7

Aluminiowanie dyfuzyjne metodą „above the pack" łopatek roboczych turbiny sprężarki z materiału EI867 stosowanych w lotnictwie

Streszczenie

W pracy przeprowadzono badania łopatek roboczych turbiny sprężarki wytwarzanych z materiału EI-867 wg normy TU 14-1-402-72 poddawanych procesowi gazowego bezkontaktowego procesu aluminiowania. Wykonano badania metalograficzne wytworzonej warstwy aluminiowanej oraz poddano identyfikacji składniki fazowe mikrostruktury warstwy aluminidkowej za pomocą analizy składu chemicznego w mikroobszarach z użyciem przystawki EDS w skaningowym mikroskopie elektronowym oraz metodą dyfrakcji rentgenowskiej. Ponadto wykonano badania twardości oraz żarowytrzymałości łopatek poddawanych procesowi przesycania i starzenia w różnych czasach wytrzymania. Praca miała na celu określenie możliwości prowadzenia procesu aluminiowania metodą „above the pack" części z materiału EI-867 przy jednoczesnym określeniu wpływu procesu na zmianę żarowytrzymałości części. Na podstawie badań eksperymentalnych wykazano, że aluminiowanie łopatek turbin materiałem EI-867 metodą „above the pack" do uzyskania grubości warstwy w zakresie 0.03-0.06 mm możliwe jest w ciągu 10 godzin w temperaturze 950˚C. Aluminiowanie analizowaną metodą powoduje powstanie warstwy aluminiowanej o strukturze trójfazowej zapewniającej odpowiednią wytrzymałość powłoki. Wykazano jednak, że proces aluminiowania metodą "above the pack" z zastosowanym czasem 10 godzin powoduje znaczne obniżenie żarowytrzymałości materiału. Na podstawie uzyskanych wyników wykazano iż metoda bezkontaktowego aluminiowania w przypadku łopatek turbiny z materiału EI 867 nie spełnia wymogów lotniczych dla bezpiecznej eksploatacji ze względu na znaczne obniżenie własności mechanicznych.

Słowa kluczowe: aluminiowanie dyfuzyjne, łopatki turbiny sprężarki, stop EI867, silnik turbinowy, turbina sprężarki

Original Research

Performance of a Single Cylinder Direct Injection 4-Stroke Diesel Engine Under Effect of Using Diesel and Naphtha Blends

Marwah E. Basas * (iD)**, Rafeq A. Khalefa** (iD)

Department of Fuel and Energy, Technical College–Kirkuk, Northern Technical University, 36001 Kirkuk, Iraq; rafeqahmed42@ntu.edu.iq (R. A. Khalefa)

* Correspondence: marwaez2023@gmail.com

Abstract

The demand for diesel fuel in the transport industry is expected to rise due to greenhouse gas laws and global economic expansion, necessitating the search for alternative energy sources. If light distillate fuels can match diesel fuel's efficiency and cleanliness at a more affordable cost, they could potentially enter the market. The aim of the investigations was to assess a single cylinder, four stroke diesel engine's performance using various blends of diesel (D) and heavy naphtha (N): D100%, D97.5%N2.5%, D95%N5%, D92.5%N7.5%, and D90%N10%. Tests were conducted at 3000 rpm and variable loads, revealing that the maximum permissible naphtha content in diesel oil (D100%) is 10%. Higher naphtha proportions led to misfire and instability under heavy loads. 100% diesel demonstrated the lowest brake-specific fuel consumption and higher thermal efficiency, while mixture of 90% diesel and 10% naphtha showed the highest fuel consumption and lower thermal efficiency.

Keywords: internal combustion engine, diesel engine, additives, engine performance, engine efficiency

1. Introduction

Diesel engines offer superior fuel efficiency, lower CO_2 emissions, and excellent driving performance compared to gasoline engines, mainly due to their lower fuel consumption per unit of output power (Chang et al., 2012; Gupta, 2012). Moreover, diesel engines boast the highest heat efficiency among internal combustion engine types, thanks to their high compression ratio, making them versatile for various applications and sizes. However, with the increasing global population and automobile usage, there is a growing need to reduce fossil fuel consumption (Pan et al., 2020; Yilmaz, 2020).

To address this challenge, researchers are exploring new technologies, combustion modes, alternative fuels, vehicle technology, and additives. One promising substitute for diesel (D) fuels is inexpensive refinery product naphtha (N), which emits fewer CO_2 and NOx during combustion and refinement. Several studies have been conducted on the use of naphtha in compression ignition engines (Mohamad et al., 2018; Mohamad & Zelentsov, 2019; Zhang et al., 2016a).

Ashour et al. (2020) examined the impact of adding 5%, 10%, and 15% naphtha to conventional diesel fuel D100 and biodiesel B30 in a four-stroke, single-cylinder, air-cooled diesel engine under different loads. They found a slight increase in brake specific fuel consumption with D95N5 compared to conventional diesel, and this consumption increased with higher naphtha content. Naphtha had a slight effect on the specific fuel consumption of the B30N5 mixture. Additionally, naphtha reduced nitrogen oxide emissions for the B30N5 mixture under all loads, and CO_2 emissions decreased for the diesel-naphtha blend, while CO2 emissions increased for the B30N5 mixture. The study determined that the maximum permissible percentage of naphtha was 10% for D100 and 5% for B30. Akihama et al. (2009) investigated the limitations of naphtha in achieving the greatest engine power due to significant ignition delay, leading to increased premixed combustion impact, noise levels, and peak in-

cylinder pressure. Wang et al. (2014) studied the impact of gasoline and naphtha on multi-premixed combustion igniting mode in a diesel engine with a single-cylinder and 16.7 compression ratio. Multiple premixed compression ignition (MPCI) fuelled with both gasoline and naphtha demonstrated low combustion noise and high efficiency with low exhaust gas recirculation (EGR) ratio and high load. Zhang et al. (2016b) examined how heavy and light naphtha fuels affected combustion and performance in a 6-cylinder diesel engine, showing relatively low soot and NO_x emissions compared to extremely low sulfur diesel. Javed et al. (2016) investigated the auto-ignition properties of low-octane fuel light naphtha, finding that the multi-component surrogate closely matched the light naphtha ignition delay under specific conditions. Vallinayagam et al. (2018) analyzed combustion uniformity and its impact on soot production for partially premixed combustion (PPC) and dieseline fuels in compression ignition (CI) and naphtha modes. Naphtha enhanced combustion uniformity, resulting in almost negligible soot emissions in PPC mode and reduced soot emissions in CI mode compared to dieseline. The use of naphtha as a fuel for typical CI engines presents significant disadvantages, primarily due to its low flash temperature and poor ignition quality, which can result in fire hazards during handling and storage. Additionally, naphtha's low lubricity and kinematic viscosity necessitate the use of lubricity additives to ensure proper fuel pump lubrication.

This study aimed to explore the impact of naphtha-diesel fuel blends on diesel engine performance and compare it with pure diesel fuel. The experiments were conducted at a fixed engine speed of 3000 rpm. Engine operating limitations were established based on factors such as power output, brake-specific fuel consumption and brake thermal efficiency.

2. Experimental setup

This section provides an overview of the experimental setup, test fuels, and the test engine used in the study. The investigation utilized a single cylinder, four stroke, normally aspirated diesel engine with direct injection. The tests were carried out at the Internal Combustion Machinery Laboratory located within the Department of Fuel and Energy Technologies Engineering Techniques at the Technical College of Kirkuk.

2.1. Test engine

The experimental tests utilized a single-cylinder, four-stroke diesel engine operating on conventional diesel fuel. This engine was coupled with an electric generator and various measuring instruments to monitor crucial parameters. These instruments measured the incoming air flow, fuel consumption rate, current, voltage of electric loads, and engine rotational speed. Figure 1 depicts the test setup with the mentioned devices and measuring instruments.
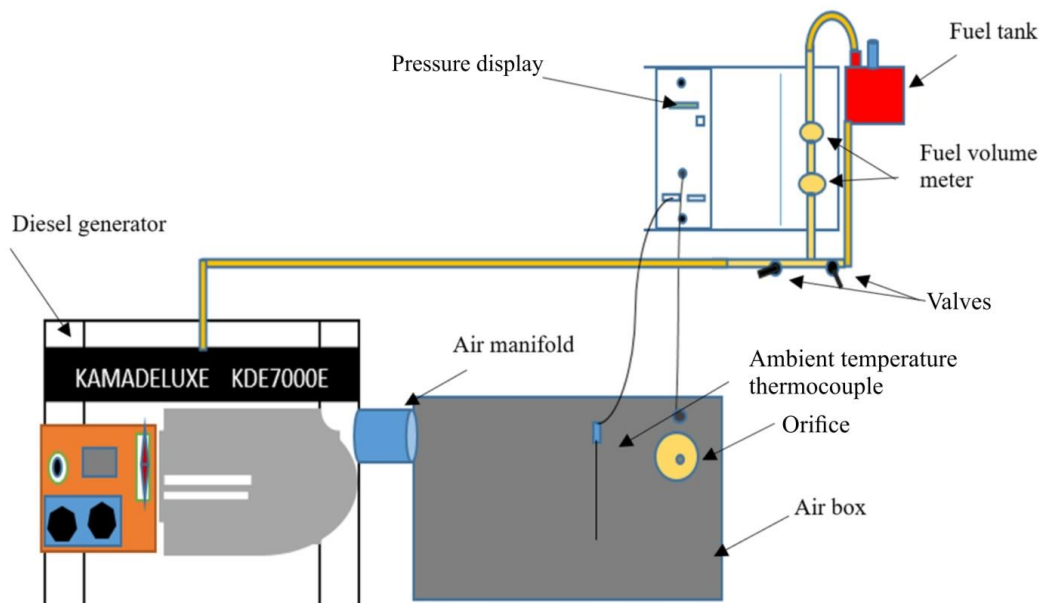

Fig. 1. Test stand.

The engine is manually started by delivering the fuel at a higher level than the engine to ensure a smooth flow towards the mechanical fuel pump. The fuel is then compressed and transformed into a mist to facilitate ignition inside the combustion chamber. The high pressure within the combustion

chamber leads to automatic combustion. Table 1 provides an overview of the characteristics of the diesel engine utilized in the laboratory tests.

Table 1. Test engine specification.

Parameter	Value
Cylinder diameter	86 mm
Cylinder number	1
Stroke (s)	72 mm
Connecting rod length (L)	125 mm
Compression ratio	14
Intake valve closing	30 aBDC
Exhaust valve opening	50 bBDC

In an experimental setup, maintaining a consistent and controlled diesel fuel supply is essential for accurate testing of various aspects of diesel engine performance. This is achieved through an automatic regulation system, which ensures that the desired fuel flow rate is maintained. A sensors of system begins by incorporating sensors that monitor critical parameters. In this context, a flow rate sensor is used to measure the actual fuel flow rate. Setpoints used as target fuel flow rate, known as the setpoint, is established. This is the value the control system aims to achieve and maintain throughout the experiment. An appropriate controller, which can be a microcontroller or a programmable logic controller (PLC), is employed. Its primary function is to compare the actual fuel flow rate (sensed by the sensor) with the setpoint.

A controller algorithm utilizes a control algorithm, often a proportional-integral-derivative (PID) controller. This algorithm calculates necessary adjustments required to align the actual fuel flow rate with the desired setpoint. It does this by considering the error, which is the difference between the setpoint and the actual value, as well as historical error information. An actuator, such as a fuel injector or a valve, is connected to the output of the controller. The actuator is responsible for physically adjusting the fuel supply to the diesel engine, based on the instructions provided by the controller.

Continual monitoring of the fuel flow rate via the sensor is done by feedback loop. The sensor data is fed back to the controller in real-time. In response, the controller makes immediate adjustments to the actuator to bring the actual fuel flow rate back in line with the setpoint.

The control system's parameters, including proportional, integral, and derivative gains in a PID controller, are finely tuned to ensure stable and precise regulation of the fuel supply. Rigorous testing of the setup is carried out, and the system is calibrated to ensure it accurately responds to changes in the setpoint, maintaining a consistent and controlled fuel supply.

2.2. Fuels and additives

The fuel that this research investigates includes diesel fuel and naphtha, which is produced by distilling crude oil without any additional processing. The choice of naphtha is intended to take into account a significant portion of naphtha fuels generated by refineries around the world. In this study, the different ratios of diesel fuel and naphtha have been utilize to find out the effect of these ratios of additives on performance parameters such as power, efficiency and specific fuel consumption of a single cylinder four stroke diesel engine. The properties of the diesel and naphtha utilized in this study are shown in Table 2.

Table 2. Physical propertise of diesel and naphtha blends.

Fuel	Density, kg/cm^3	Low heating value, MJ/kg
D100%	853.0	44.8
N100%	671.0	42.2
D97.5%N2.5%	848.3	44.75
D95%N5%	843.6	44.70
D92.5%N7.5%	839.3	44.65
D90%N10%	835.7	44.59

The test engine operates initially on conventional diesel fuel (D100%) without any load, allowing a 30-minute stabilization period to ensure accurate readings, which are sensitive to load changes. The required data, including engine speed, fuel consumption, and pressure difference, are then recorded.

To apply loads, an electric heater is activated, raising exhaust gas temperature, increasing fuel consumption, and causing a slight decrease in electrical voltage while elevating electrical current. With each increase in applied load, data across all parameters change accordingly.

After recording data for conventional diesel (D100%), the tank is emptied, and a mixture of naphtha and conventional diesel is used as a fuel (D97.5%N2.5%). The engine is run without load, and data for this mixture are recorded. Subsequently, the applied load is gradually increased. The same procedure is repeated for mixtures (D95%N5%, D92.5%N7.5%, D90%N10%), and all relevant data are collected. Diesel engines often operate with a relatively high excess air coefficient across a wide range of loads. This is due to the nature of diesel combustion, which relies on spontaneous ignition caused by high compression ratios.

As load increases in diesel engines, the excess air coefficient may decrease slightly to optimize combustion efficiency, but it generally remains higher than in gasoline engines.

The brake power (BP) is calculated by multiplying the current (I) and voltage (V) of the electric generator connected to the engine, taking into account a generating efficiency of 80% as per the equation provided by (Chang et al., 2013).

$$BP = \frac{I \times V}{1000} \, kW \tag{1}$$

The brake specific fuel consumption (BSFC) is obtained by calculating the mass flowrate of the fuel ($\dot{m}_f$) measured in units like kilograms per second (kg/s) and brake power that was previously found. The mass flowrate of fuel $\dot{m}_f$ can be calculated using the following equation (Lata et al., 2012):

$$\dot{m}_f = \rho_f \times Q_f \tag{2}$$

where ρ_f symbolizes the density of the fluid and is measured in units like kilograms per cubic meter (kg/m³) and Q_f represents the volumetric flow rate of the fluid and is typically measured in units like cubic meters per second (m³/s). The brake specific fuel consumption calculated from the following equation:

$$BSFC = \frac{\dot{m}_f}{BP} \times 3600 \tag{3}$$

Air (A) to fuel (F) ratio (A/F) is calculated from dividing mass of air ($\dot{m}_a$) by mass of fuel from the following equation (Mohamad et al., 2020):

$$\frac{A}{F} = \frac{\dot{m}_a}{\dot{m}_f} \tag{4}$$

Then the braking thermal efficiency (BTE) monitored, which is the ratio of the brake power generated by the engine to the thermal energy of the fuel from the following equation (Heywood, 2018):

$$BTE = \frac{BP}{\dot{m}_f \times Q_{H.V}} \times 100\% \tag{5}$$

where Q_{HV} symbolizes the heating value of the fuel, often referred to as the lower heating value (LHV) or higher heating value (HHV). It is typically measured in units like joules per kilogram (J/kg).

3. Results and discussion

The results of the practical tests conducted on a single cylinder, four stroke diesel engine, using different volumetric ratios of mixtures consisting of conventional diesel fuel and medium-density naphtha, are presented and discussed in Table 2. The engine was operated under various loads and the same operating conditions. Performance parameters, such as power, brake specific fuel consumption (BSFC), and braking thermal efficiency, were studied for each volumetric ratio (D97.5%N2.5%, D95%N5%, D92.5%N7.5%, D90%N10%).

Figure 2 illustrates the relationship between brake power and brake thermal efficiency for diesel fuel and the various mixtures of diesel and naphtha. The results reveal that brake thermal efficiency increases with increased brake power at low and moderate loads. However, at high loads where the

brake power is increased, the brake thermal efficiency decreases. The highest brake thermal efficiency is achieved with conventional diesel fuel, followed by D97.5%N2.5%, D95%N5%, D92.5%N7.5%, and D90%N10%, respectively.

For instance, at a power output of 3.740 kW, it is observed that the brake thermal efficiency of pure diesel fuel surpasses that of all mixtures (D97.5%N2.5%, D95%N5%, D92.5%N7.5%, D90%N10%) with the following ratios: 4%, 7.9%, 12.09%, and 16.24%, respectively.
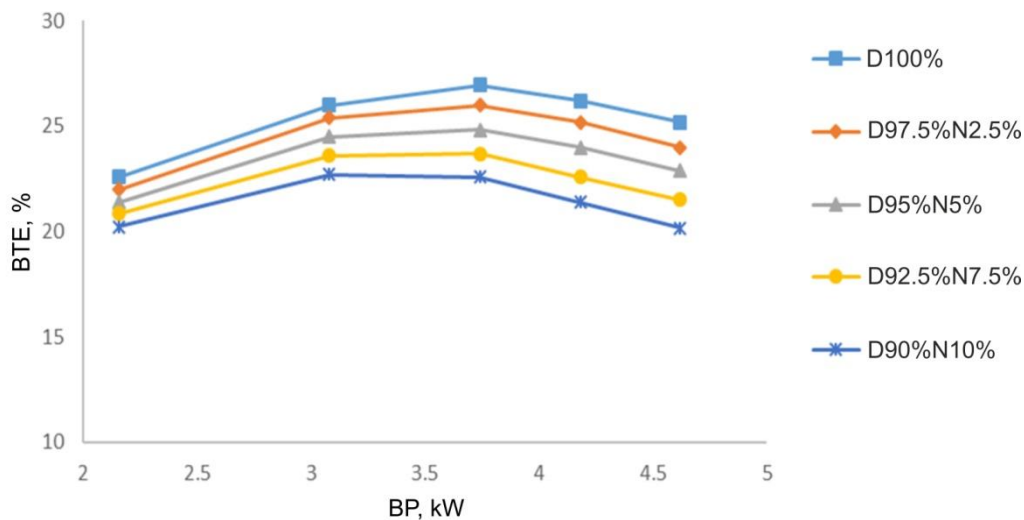
Fig. 2. The relation between brake power and BTE.

Figure 3 illustrates the relationship between BSFC and brake power for both conventional diesel fuel and diesel-naphtha mixtures. It is evident that BSFC decreases with increasing brake power at low loads, but it increases as the brake power is applied at high loads. Moreover, specific fuel consumption rises with higher proportions of naphtha added to diesel fuel, with conventional diesel fuel (D100%) exhibiting the lowest specific fuel consumption compared to all diesel-naphtha mixtures. Notably, D90%N10% has the highest specific fuel consumption among the mixtures (D100%, D97.5%N2.5%, D95%N5%, D92.5%N7.5%). To understand the specific reasons for the significant difference in BTE between the fuels with similar calorific values, detailed testing and analysis of the combustion process, engine parameters, and fuel properties are necessary. Adjustments to the engine's operating parameters and fuel delivery may be needed to optimize BTE for each fuel type.
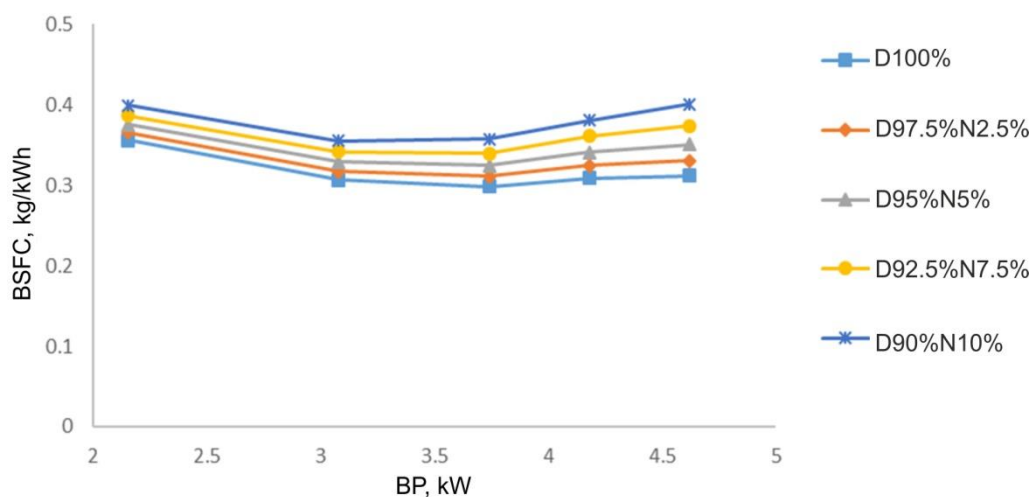
Fig. 3. The relation between brake power and BSFC.

Analyzing the data from the figure, it can be observe that at a power output of 4.180 kW, the specific fuel consumption of pure diesel fuel (D100%) is lower than the mixtures (D97.5%N2.5%, D95%N5%, D92.5%N7.5%, D90%N10%) in the following proportions: 4.77%, 9.36%, 14.46%, and 19.46%, respectively. This is primarily due to conventional diesel fuel's higher density and calorific value compared to all the diesel-naphtha mixtures.

Figure 4 displays the relationship between the air-to-fuel ratio and brake power. A comparison between conventional diesel fuel and diesel-naphtha mixtures reveals that the highest air-to-fuel ratio is achieved when using pure D100% at the lowest load. At the lowest load (2.156 kW), the air-to-fuel ratio shows an increase of (2.38%, 4.76%, 7.45%, 10.36%) compared to all diesel-naphtha mixtures (D97.2%N2.5%, D95%N5%, D92.5%N7.5%, D90%N10%) respectively, and this ratio increases with higher loads. Conversely, the lowest air-to-fuel ratio is observed when using D90%N10% at the highest load. Consequently, the brake-specific fuel consumption increases with higher loads and the percentage of added naphtha.
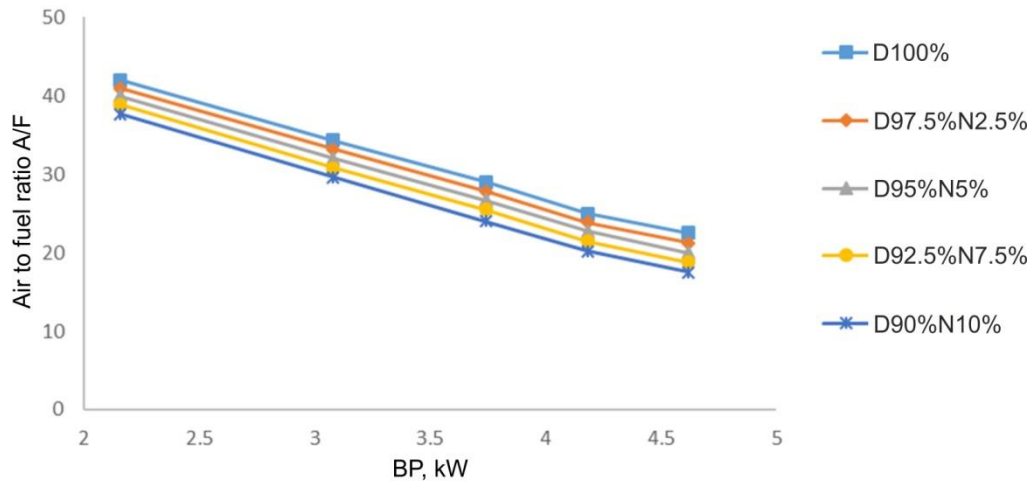
Fig. 4. The relation between A/F and brake power.

4. Conclusions

In this research, the effect of adding naphtha to conventional diesel fuel was studied, and the impact of this addition on brake specific fuel consumption, thermal efficiency, and the air-to-fuel (A/F) ratio was examined at a constant speed of 3000 rpm. The results obtained indicate that 10% was the highest proportion that could be added to D100%. Further increasing the percentage of naphtha caused the engine to misfire and operate unstably under heavy loads. It became evident that the brake specific fuel consumption and air-to-fuel ratio decrease with the increase of the load applied to the engine. Moreover, the increase in the percentage of naphtha added to diesel fuel led to an increase in the brake specific fuel consumption rate. The results of this study concluded that the lowest specific consumption rate and highest air-to-fuel ratio and thermal efficiency are observed when using diesel fuel, followed by D95%N5%, and then D90%N10%, respectively. Numerous experiments that fall outside the purview of this paper's discussion can help understand how to use naphtha in CI engines when blended with diesel. In order to enhance the proportion of naphtha added to diesel fuel D100% that is permitted, it may be beneficial to investigate the impact of increasing injection time.

References

Akihama, K., Kosaka, H., Hotta, Y., Nishikawa, K., Inagaki, I., Fuyuto, T., Iwashita, Y., Farrell, J., & Weissman. W. (2009). An investigation of high load (compression ignition) operation of the 'naphtha engine'– a combustion strategy for low well-to-wheel CO2 emissions. *SAE International Journal of Fuels and Lubricants*, *1*(1), 920–932. https://doi.org/10.4271/2008-01-1599

Ashour, M. K., Eldrainy, Y. A., & Elwardany, A. E. (2020). Effect of cracked naphtha/biodiesel/diesel blends on performance, combustion and emissions characteristics of compression ignition engine. *Energy*, *192*, Articloe 116590. https://doi.org/10.1016/j.energy.2019.116590

Chang, J., Kalghatgi, G., Amer, A., & Viollet, Y. (2012). Enabling high efficiency direct injection engine with naphtha fuel through partially premixed charge compression ignition combustion. *SAE Techical Paper*, Article 2012-01-0677. https://doi.org/10.4271/2012-01-0677

Chang, J., Kalghatgi, G., Amer, A., Adomeit, P., Rohs, H., & Heuser, B. (2013). Vehicle demonstration of naphtha fuel achieving both high efficiency and drivability with EURO6 engine-out NOx emission. *SAE International Journal of Engines*, *6*(1), 101–119. https://doi.org/10.4271/2013-01-0267

Gupta, H. N. (2012). *Fundamentals of internal combustion engines*. PHI Learning Pvt. Ltd.

Heywood, J. B. (2018). *Internal combustion engine fundamentals*. McGraw-Hill Education.

Javed, T., Nasir, E. F., Ahmed, A., Badra, J., Djebbi, K., Beshir, M., Ji, W., Sarathy, S. M., & Farooq, A. (2016). Ignition delay measurements of light naphtha: A fully blended low octane fuel. *Proceedings of the Combustion Instute*, *36*(1), 315–322. https://doi.org/10.1016/j.proci.2016.05.043

Lata, D. B., Misra, A., & Medhekar. S. (2012). Effect of hydrogen and LPG addition on the efficiency and emissions of a dual fuel diesel engine. *International Journal of Hydrogen Energy*, *37*(7), 6084-6096, https://doi.org/10.1016/j.ijhydene.2012.01.014

Mohamad, B., Karoly, J., Zelentsov, A., & Amroune, S. (2020). A hybrid method technique for design and optimization of Formula race car exhaust muffler. *International Review of Applied Sciences and Engineering, 11*(2), 174–180. https://doi.org/10.1556/1848.2020.20048

Mohamad, B., Szepesi, G. L., & Bollo, B. (2018). Effect of Ethanol-Gasoline Fuel Blends on the Exhaust Emissions and Characteristics of SI Engines. In K. Jármai, & B. Bolló (Eds.) *Vehicle and automotive engineering 2* (pp. 29-41). Springer. https://doi.org/10.1007/978-3-319-75677-6_3

Mohamad, B., Zelentsov, A. (2019). 1D and 3D modeling of modern automotive exhaust manifold. *Journal of the Serbian Society for Computational Mechani*cs, *13*(1), 80-91. https://doi.org/10.24874/jsscm.2019.13.01.05

Pan, S., Liu, X., Cai, K., Li, X., Han, W., & Li, B. (2020). Experimental study on combustion and emission characteristics of iso-butanol/diesel and gasoline/diesel RCCI in a heavy-duty engine under low loads. *Fuel*, *261*, Article 116434. https://doi.org/10.1016/j.fuel.2019.116434

Vallinayagam, R., An, Y., Vedharaj, S., Sim, J., Chang, J., & Johansson, B. (2018). Naphtha vs. dieseline–The effect of fuel properties on combustion homogeneity in transition from CI combustion towards HCCI. *Fuel*, *224*, 451–460. http://dx.doi.org/10.1016/j.fuel.2018.03.123

Wang, B., Wang, Z., Shuai, S., Yang, H., & Wang. J. (2014). Combustion and emission characteristics of Multiple Premixed Compression Ignition (MPCI) fuelled with naphtha and gasoline in wide load range. *Energy Conversion and Management*, *88*, 79–87. https://doi.org/10.1016/j.enconman.2014.08.045

Yilmaz. E. (2020). A Comparative Study on the Usage of RON68 and Naphtha in an HCCI Engine. *International Journal of Automotive Science and Technology*, *4*(2), 90–97. https://doi.org/10.30939/ijastech..721882

Zhang, Y., Kumar, P., Traver, M., & Cleary, E. D. (2016a). Conventional and low temperature combustion using naphtha fuels in a multi-cylinder heavy-duty diesel engine. *SAE International Journal of Engines*, *9*(2), 1021–1035. https://doi.org/10.4271/2016-01-0764

Zhang, Y., Voice, A., Tzanetakis, T., Traver, M., & Cleary, D. (2016b). An evaluation of combustion and emissions performance with low cetane naphtha fuels in a multicylinder heavy-duty diesel engine. *Journal of Engineering for Gas Turbines and Power*, *131*(10), Article GTP-16-1042. https://doi.org/10.1115/1.4032879

Wydajność Jednocylindrowego 4-Suwowego Silnika Wysokoprężnego z Bezpośrednim Wtryskiem Paliwa Zasilanego Mieszaniną Oleju Napędowego i Benzyny Ciężkiej

Streszczenie

Oczekuje się, że zapotrzebowanie na olej napędowy w branży transportowej będzie zwiększało się ze względu na przepisy dotyczące gazów cieplarnianych i globalną ekspansję gospodarczą, co wymusza poszukiwanie alternatywnych źródeł energii. Jeżeli lekkie destylaty będą w stanie dorównać wydajności i czystości olejowi napędowemu, przy bardziej przystępnej cenie, mogłyby potencjalnie zostać wprowadzone na rynek. Celem badań była ocena osiągów jednocylindrowego, czterosuwowego silnika wysokoprężnego stosując różne mieszanki oleju napędowego (D) i benzyny ciężkiej (N): D100%, D97.5%N2.5%, D95%N5%, D92.5%N7.5% i D90%N10%. Badania przeprowadzono przy 3000 obr/min i zmiennym obciążeniu. Wykazano, że maksymalna dopuszczalna zawartość benzyny ciężkiej w oleju napędowym wynosi 10%. Większa zawartość benzyny w oleju napędowym prowadziła do przerw w zapłonie i niestabilności pod dużym obciążeniem. 100% olej napędowy wykazał najniższe zużycie paliwa przy hamowaniu i wyższą sprawność cieplną, podczas gdy mieszanina 90% oleju napędowego and 10% benzyny ciężkiej wykazała najwyższe zużycie paliwa i niższą sprawność cieplną.

Słowa kluczowe: silnik wewnętrznego spalania, silnik wysokoprężny, dodatki, osiągi silnika, sprawność silnika

Investigating Mechanical and Physical Properties of Stir Casted Al6061/Nano Al₂O₃/Quartz Hybrid Composite

Dagim Tirfe [1,2] iD **, Abraham Woldeyohannes** [1] iD **, Bonsa Hunde** [1] iD **,
Temesgen Batu** [2, *] iD **, Eaba Geleta** [2] iD

[1] Mechanical Engineering Department, College of Engineering, Addis Ababa Science and Technology University, Addis Ababa P.O. Box 16417, Ethiopia; dagimasegidtirfe0286@gmail.com (D. Tirfe), abraham.debebe@aastu.edu.et (A. Woldeyohannes), bonsa.regassa@aastu.edu.et (B. Hunde)

[2] Center of Armament and High Energy Materials, Institute of Research and Development, Ethiopian Defence University, Bishoftu P.O. Box 1041, Ethiopia; beyene.eaba@yahoo.com (E. Geleta)

* Correspondence: temesgen.batu@kiot.edu.et, tel.: +25 190 004 6019

Abstract

Aluminum alloys are widely used in different engineering application areas, such as aerospace, automotive, and marine industries. However, their properties need some improvement in order to enlarge their application area. Thus, the objective of the study was to improve the physical and mechanical properties of Al6061 aluminum alloy by reinforcing it with nano-Al₂O₃ and micro-quartz particles. The investigation primarily was focused on studying the impact of quartz particles on the mechanical and physical properties of an Al6061/nano-Al₂O₃/quartz hybrid composite. The hybrid composite was developed using a stir casting technique, by varying the weight percentage of quartz particles at 3%, 6%, and 9%, while maintaining a constant weight percentage of nano-Al₂O₃ at 3.5%. To evaluate the composite's properties, test samples were prepared according to ASTM E9-09 and ASTM E23 standards for hardness, compressive strength, creep, and impact energy absorption, respectively. The results of the investigation demonstrate that, with the addition of 9 wt.% of micro-quartz particles and 3.5 wt.% of nano-Al₂O₃ nanoparticles, all mechanical and physical properties of the matrix were improved, except for the impact strength. Based on these results, the developed hybrid composite material can be recommended for light weight automotive spare parts such as brakes and clutch discs.

Keywords: Al6061 aluminium alloy, hybrid aluminium matrix composite, nano-Al₂O₃, quartz (SiO₂), stir casting

1. Introduction

The evolution of materials has played a pivotal role in advancing human civilization from the Stone Age to the modern era. Materials are indispensable in our day-to-day activities, and without them, our current way of life would be nearly impossible to imagine. Researchers continuously strive to develop new materials that meet the evolving needs of society and industry, ensuring safety and comfort in our world. Industries such as automobile, defense, marine, and aerospace demand materials with higher resistance, strength, weldability, and corrosion resistance (Virinchy et al., 2019; Yang et al., 2004).

One class of materials that has shown significant promise in meeting these requirements is the third generation of aluminum metal matrix composites (AMMCs). These composites offer an excellent strength-to-weight ratio, low thermal expansion coefficients, and improved mechanical properties, making them ideal for various applications (Parhiban et al., 2017; Sun et al., 2014). Aluminum composites, including AMMCs, have found widespread use in the manufacturing of automotive components, electronics, defense systems, and aerospace components (Baradeswaran et al., 2013).

To fabricate composite materials, several methods such as stir casting, compo-casting, and powder metallurgy are available. Among these techniques, stir casting stands out as a cost-effective and

versatile process for composite manufacturing (Chen & Hoshi, 1992; Poornachandiran et al., 2020). The process involves blending the matrix alloy with reinforcement materials using a friction stir casting setup. Stir casting allows for easy fabrication of large quantities of composite materials, and it ensures a minimal chemical reaction between the matrix alloy and reinforcements, resulting in low porosity (Caracostas et al., 1997; Pugazhenthi et al., 2019). The uniform distribution of reinforcement particles within the composite is achieved through the optimization of the process parameters (Baradeswaran & Perumal, 2013). Considering its cost-effectiveness and favorable outcomes, stir casting has become a preferred method for producing composite materials (Jino et al., 2017).

In the quest to enhance the hardness and strength of aluminum alloys, researchers have incorporated various reinforcement particles, such as silicon carbide (SiC) and boron carbide (B_4C), through the stir casting process (Das et al., 2014; Sankarlal & Kuppusamy, 2018). These additions significantly improve the mechanical properties of the composite materials, particularly hardness and tensile strength (Mishra et al., 2019a). The chemical analysis of the composite materials confirms the composition of the aluminum alloy, such as Al6061, using techniques like optical emission spectrometry.

Aluminum alloys, including Al6061, have demonstrated their suitability across a wide range of applications, including automobiles, aircraft, spacecraft, ships, biomedical devices, household appliances, industrial equipment, electrical components, and electronic instruments (Mishra et al., 2019b). The advantages of Al6061 alloy include high strength-to-weight ratio, resilience under static and dynamic loading, excellent corrosion resistance, and durability at low temperatures. To further enhance the mechanical properties, researchers have developed and formulated composite materials based on alloy matrices. Composites consist of a matrix in the continuous phase and reinforcements in the discontinuous phase, where the matrix can be metallic, ceramic, or polymer, and the reinforcement can be particulate fillers or fibrous materials (Marques et al., 2021; Nieberle et al., 2021).

Composite materials, such as metal matrix composites (MMCs), ceramic matrix composites (CMCs), and polymer matrix composites (PMCs), exhibit superior properties compared to their individual constituents. By formulating the composition, specific properties can be modified or improved (Gangwar et al., 2013; Mehara et al., 2021; Singh et al., 2012; Singh et al., 2013). Aluminum matrix composites (AMCs), comprising aluminum or its alloys as the matrix and fillers or fibers as reinforcements, are widely used due to their remarkable mechanical and wear properties (Bodunrin et al., 2015; Manigandan et al., 2015; Singh et al., 2011). Among them, Al6061 alloy-based composites have gained attention in automotive, aircraft, and ship components due to their lightweight nature, strength, formability, corrosion resistance, and weldability (Breval, 1995; Kamat et al., 1989). The addition of alumina ceramic fillers to Al6061 alloy composites has been observed to increase the ultimate tensile strength and yield strength (Kumar et al. 2016). Additionally, the size, shape, and surface treatment of the filler materials influences the performance of the composite materials (Arif et al., 2018; Ezatpour et al., 2014).

While previous research has focused on the incorporation of nanoparticles, such as nano-alumina, nano-silica, and SiC, into Al alloy-based materials, however, there is a scarcity of published articles on the effect of adding micro quartz particles on the mechanical and physical properties of Al6061/nano-Al_2O_3 (Kareem et al., 2021). While previous research has focused on the incorporation of nanoparticles, such as nano-alumina, nano-silica, and SiC, into Al alloy-based materials, there is a lack of comprehensive studies on their physical and detailed mechanical properties (Kareem et al., 2021). Therefore, this research aims to investigate the effects of micro quartz particles on the physical and mechanical properties of Al6061-based composite materials. By exploring the behavior of these hybrid composites, valuable insights can be gained for further optimization and applications. The novelty of the current research work is that no one has ever developed this hybrid composite material. Furthermore, there might be some research that tries to study different mechanical properties and physical properties of hybrid aluminum alloy-based metal matrix composites, but there is no published study that is conducted on studying the creep properties of Al6061/nano Al_2O_3/quartz hybrid composites, so this also makes this research novel.

In summary, the present study focuses on the investigation of the mechanical and physical properties of Al6061/nano Al_2O_3/quartz hybrid composite. By examining the effects of micro-quartz particles combined with nano-Al_2O_3 on the composite, valuable insights can be gained to enhance the performance and durability of these materials.

2. Materials and methods

2.1. Materials

For the current research work, aluminum alloy 6061 is selected as a matrix material as it has better wear resistance and mechanical properties than other aluminum alloys because Si and Mg are the main alloying elements in this alloy (Alnaqi et al., 2016; Arif et al., 2018) as shown in Table 1. The reason behind selecting aluminum as a matrix is due to its light weight from other metals. Various companies use different aluminum alloys in automotive parts such as clutches and brake rotors, especially for light duty vehicles (Alnaqi et al., 2016). Aluminum alloy 6061 has better wear resistance properties than the other aluminum alloy groups (Sabry et al., 2001).

Table 1. Nominal chemical composition (in wt.%) of the matrix Al6061 alloy used in the study in the ASTM standard (Sabry et al., 2001).

Elements of Al6061	Si	Fe	Cu	Mn	Mg	Cr	Zn	Ti	Al	other
Content	0.4-0.8	0.7	0.15-0.4	0.15	0.8-1.2	0.04-0.35	0.25	0.15	94.0	0.15

In order to identify the major and minor oxides which are present within the quartz particle, a complete silicate analysis was performed in Ethiopian Geological survey laboratory, and the report was presented in the appendix section of this article. Furthermore, Table 2 presents the report of complete silicate analysis of the micro quartz particles.

Table 2: Major and minor oxides which are present with in quartz particles.

Oxides	SiO_2	Al_2O_3	Fe_2O_3	CaO	MgO	Na_2O	K_2O	MnO	P_2O_5	TiO_2	H_2O	LOI
Percentage	96.68	<0.01	0.74	0.36	0.16	0.54	<0.01	<0.01	<0.01	0.02	0.22	0.31

Micro quartz and nano-Al_2O_3 (aluminum oxide) were used as reinforcement particles. Al_2O_3 is the second wear-resistance material next to silicon carbide. Due to the oxide it has the highest corrosion resistance properties than any other ceramic reinforcement agent. Furthermore, it has better thermal conductivity which is 20–30 W/mK. If the material has good thermal conductivity, then heat will be easily removed from it (Kala et al., 2014). Furthermore, quartz is the second material that has the highest impact resistance (toughness), whenever any material becomes tough it improves the wear resistance and high temperature performance of the composite (Sayuti et al., 2012). Particle sizes of 45 μm quartz particles are prepared by ball milling and 50 μm of Al_2O_3 reinforcing particles are bought from the shelf to develop the composite. Table 3 shows the details of the mixture design during casting.

Table 3. Mixture proportion design of matrix and reinforcement materials in one sample composite material.

Exp. run	% mass of Al6061	% mass of nano-Al_2O_3	% mass of quartz
1	100% = 1382 g	0% = 0 g	0% = 0 g
2	96.5%= 1333.63 g	3.5%= 48.37 g	0% = 0 g
3	93.5% = 1292.17 g	3.5% = 48.37 g	3% = 41.46 g
4	90.5% = 1250.71 g	3.5% = 48.37 g	6% = 82.92 g
5	87.5% = 1209.25 g	3.5% = 48.37 g	9% = 124.38 g

2.2. Methods

2.2.1. Experimental design for sample preparation

The mass amount of the matrix required for a single run of casting was determined by calculating the volume of each test sample using simple formulas based on density times volume. For all samples, it is calculated in similar ways. For this study, 6.5 kilograms of Al6061 alloy matrix, 300 grams of quartz, and 320 grams of nano aluminum oxide were used to prepare the hybrid composite specimen. Overall, the passage effectively explains the methodology used to determine the mass amount of the components for the hybrid composite specimen, providing clarity and context for the study.

2.2.2. Sample preparation

The stir casting method of fabrication was utilized to develop the hybrid metal matrix composite. Due to the fact that whenever ceramic particles are added to melted metals, since the density of the ceramic is higher than that of aluminum, the ceramic particles will segregate at the bottom of the melt

(Arunachalam et al., 2019; Kumar, 2017). In order to prevent this scenario, stir casting is used. The four-blade stirrer was made from chrome-plated stainless steel in order to prevent the melting of the stirrer blade and was powered by a Nama 21 steeper motor, the stirring speed and time of which were controlled by the Arduino Mega microcontroller.

The preheated Al_2O_3 particles were first sintered at 500°C for activation and to remove any moisture if present in the particles in order to prevent porosity and added to the molten metal at a constant feed rate in the order of 5% in each cast, and after the addition of nano aluminum oxide, the 45 μm particle size quartz powderwas added to the aluminum and aluminum oxide mixture at a constant feed rate in the order of 3%, 6%, and 9% by weight of the Al alloy matrix. The molten aluminum alloy matrix composite was stirred continuously for 5 minutes at a stirring speed of 400 rpm to distribute the reinforcements uniformly inside the matrix phase using a especially speed-controlled stirrer. Then the molten metal is poured immediately into the metallic mold. After solidification, the mold is splinted and the specimen is taken out. finally different machining operations such as turning, milling and drilling were performed to produce ASTM standard sample for testing. The procedure was repeated three times in the same manner to get a different percentage of the reinforcement. Figure 1 depicts fabrication of the composite starting from preheating the reinforcement to machining of the sample to standard ASTM samples.
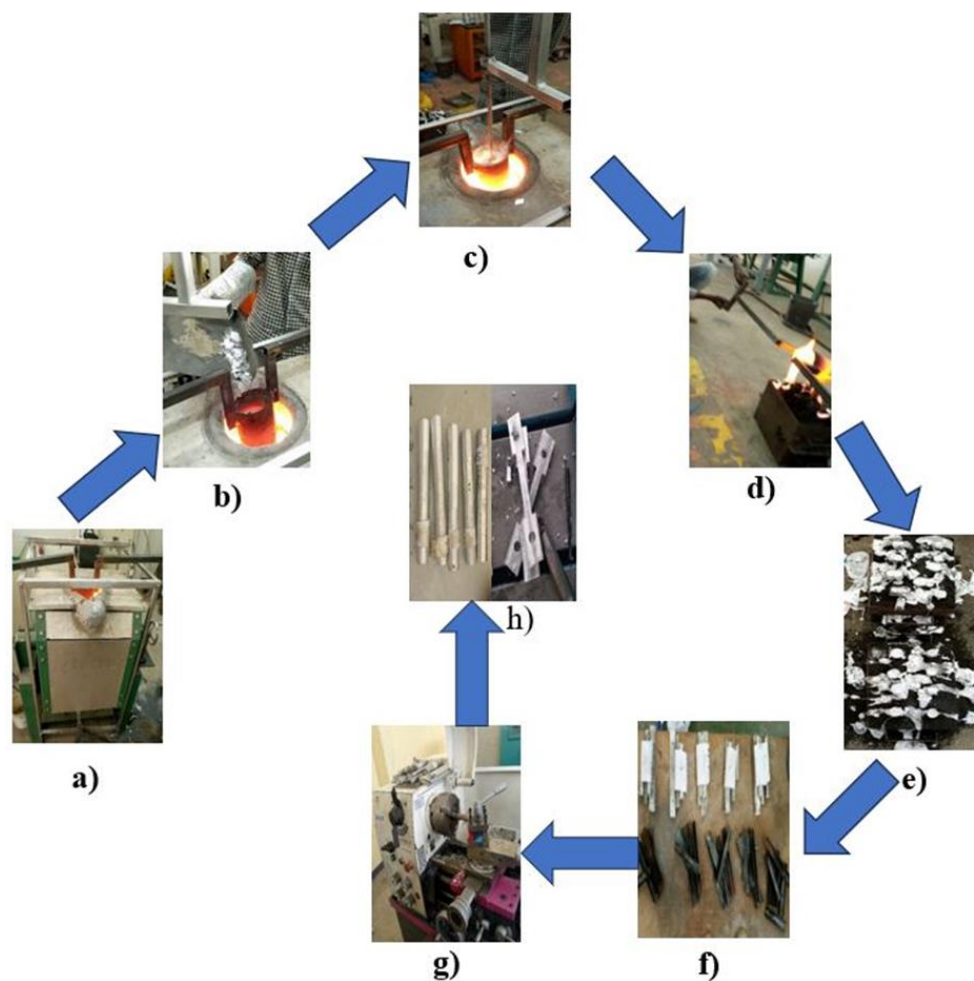
Fig. 1. Fabrication of the metal matrix composite: a) heating the empty crucible in the furnace at 500˚C, b) adding the aluminum matrix in the crucible, c) after adding the reinforcement on molten Al 6061 alloy then stirring of the melt, d) pouring of the melt in to the mold, e) cooling of the melt in the mold, f) removing the cast from the mold, g) machining, h) machined samples.

Both physical and mechanical property characterizations are performed to investigate the effect of the reinforcing ceramic particles on the developed hybrid metal matrix composite, which is presented below.

2.2.3. Physical property characterization

The physical property test includes density (theoretical and experimental) and porosity calculation.

1. Theoretical density

The theoretical density of composite can be calculated from the rule of mixture (Kala et al., 2014) as given in equation (1).

$$\rho_c = \rho_r \times V_r + \rho_m \times V_m \tag{1}$$

For hybrid reinforced composite the theoretical density can be re written as in equation (2).

$$\rho_c = (\rho_{r1} \times V_{r1} + \rho_{r2} \times V_{r2}) + (\rho_m \times V_m) \tag{2}$$

where: ρ_c is density of the composite, ρ_r is density of the reinforcement, ρ_m is density of the matrix, V_{r1} is volume fraction of the first reinforcement, V_{r2} is volume fraction of the second reinforcement, V_m is volume fraction of the matrix.

2. Experimental approach

The experimental approach to density computation was performed by using the Archimedes principle. According to the Archimedes principle, the density of the material will be determined by measuring the mass of the specimen in air and submerging the specimen in distilled water, and then the mass of the displaced fluid will be measured. The density of the material will be computed from the given formula (Kala et al., 2014; Singh & Chauhan, 2018). That is shown by equation (3).

$$\rho_c = \frac{M_a}{M_a - M_l} \times \rho_d \tag{3}$$

where ρ_c is density of the composite, M_a is mass of the specimen in air, M_l is mass of the displaced fluid and ρ_d is density of distilled water at 20°C (0.998 g/cm^3).

3. Percent porosity analysis

The basic objective of density computation is in order to investigate the porosity level in the manufactured composite specimen. It can be estimated by comparing the experimental density with the theoretical density. Porosity in cast metal matrix composite play crucial role in controlling the mechanical properties of the fabricated composite material. Percent porosity (*P*) of a composite can be calculated by the help of equation (4) (Singh & Chauhan, 2018).

$$P = \frac{\rho_{actual} - \rho_{theoretical}}{\rho_{theoretical}} \times 100\% \tag{4}$$

2.2.4. Mechanical property characterization

The mechanical property test includes hardness test, impact test, compression test and high temperature creep test.

1. Hardness test

The hardness of a material is usually determined by pressing an indenter into its surface that is precisely dimensioned and loaded, and then the depth of the indentation gives the hardness of that specific material. But the depth of indentation is inversely proportional to the hardness of the material. For the current study, the hardness of the material is measured using Rockwell hardness testing machine as per scale B because the material is soft compared to other materials such as steel and cast iron (Prasad et al., 2014). To get a well-defined indentation, the aluminum matrix composite surface should be flat and smooth. Smooth cylindrical samples are prepared as per the ASTM E23 standard with a specimen diameter of 15 mm and a 25 mm length. During the test, the load is kept constant for a specified time of 15 seconds. The prepared composite samples for the hardness test are shown in Fig. 2a.

2. Compression test

A compressive strength test is a method used for determining the behavior of the aluminum metal matrix composite material under a compressive load. It is one of the basic properties of a material, which is the ability to resist deformation by applied compressive load. In this experiment, the material specimen was subjected to a gradual increasing compressive loading that was applied uniaxial along the long axis of the specimen at a constant compressive strain rate until failure. The compressive specimen was made according to ASTM E9-09 standard. The experimental test was conducted on universal

testing machine (UTM) at room temperature with a deformation rate of 2 mm/min. Square and circular cross-section specimens were used with different volume fractions of the reinforcement material. The specimen for the compressive test has a diameter of 13 mm and a height of 22 mm and has an aspect ratio of 1.7, which is machined from the cast specimen. The test samples are shown in Fig. 2b.

3. Impact test

The impact resistance of a material determines the ability of the material to absorb energy without cracking. This test is very important for automotive brake disc material because the brake disc should absorb the energy during the braking action by the brake pad without cracking. The impact test for the current experimental investigation is carried out using a Charpy impact testing machine. The specimens were prepared from the casting materials and machined as per ASTM E-23 standard size. The specimens have a square cross section which is prepared as per ASTM E-23 standard size (Muraliraja et al., 2019). The dimension of the V-notch is 2 mm depth with angle of 45°. The prepared composite samples for impact test are shown in Fig. 2c.

4. High temperature creep test

Creep resistance of a material determines its ability to withstand the highest operating loads at elevated temperatures (Singh & Chauhan, 2018). The high temperature creep resistance property of a material is a significant index to determine the elevated temperature performance of the material or part (Prasad et al., 2014). Creep resistant materials are used in machine parts and facilities operated at higher temperatures, such as automotive engine parts and brake system components. A constant stress tensile creep technique was performed on the metal matrix composite sample to quantify the macro-creep behavior of the aluminum alloy on a SUST-D5 creep testing machine (SUST, Zhuhai, China) with an assisting furnace. The creep specimen was machined to a gauge length of 50 mm. The creep test samples were shown in Fig. 2d. The creep temperature was 360°C to obtain an aluminum alloy with high strength and fine precipitates.
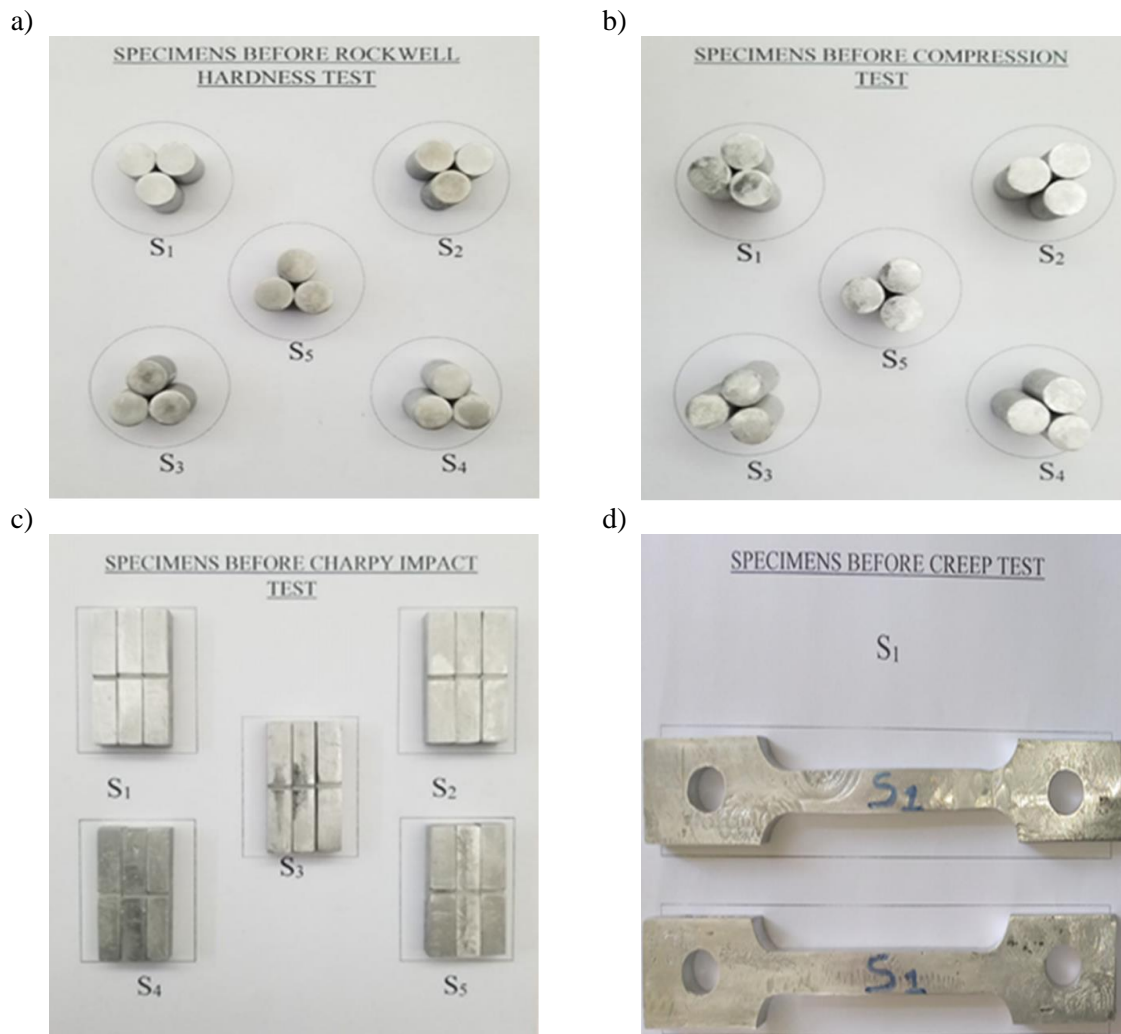
Fig. 2. Composite samples for: a) hardness test, b) compression test, c) impact test, d) creep test.

3. Results and discussion

This section of the study presents the result obtained from the different mechanical and physical tests as well as the discussion behind each test result in separate sections.

3.1. Results

3.1.1. Physical property test

The results of the physical tests, such as density and porosity, are shown in Fig. 3. The percentage porosity demonstrates an increase as the weight percentage of the reinforcement rises. This increase in porosity can be attributed to several factors, including the presence of reinforcing powder in molten aluminum and poor nucleation at Al_2O_3 particulate sizes. These factors are primarily responsible for the increment in porosity. The minimum porosity was obtained for the 0% reinforcing composite, i.e., the unreinforced aluminum alloy.

a)   b)
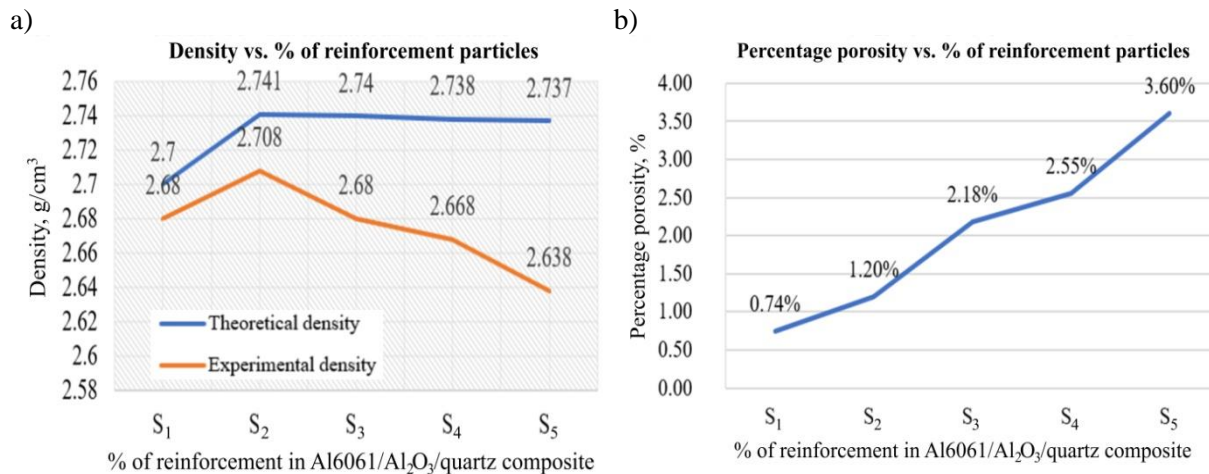
Fig. 3. a) density vs. % of reinforcement, b) percentage porosity vs. % of reinforcement.

Based on the analysis of Fig. 3, it can be concluded that the porosity level of the composite specimen increases as the volume fraction of the reinforcement particulates increases.

3.1.2. Mechanical property

In this section, hardness, compressive strength, impact, and creep tests were discussed.

1. Hardness

The results of the Rockwell hardness test are presented in Table 4 and Figure 4a. During the test, a minor load is applied to overcome the film thickness on the material's surface.

Table 4. Hardness result of the fabricated composite as a function of reinforcement.

Designation	Composite description	Rockwell hardness (HRB)			Average Rockwell hardness (HRB)
		Test 1	Test 2	Test 3	
S1	Al6061 alloy	40.5	39.2	41.4	40.36
S2	Al6061 + 3.6% Al_2O_3	47.6	48.4	46.9	47.63
S3	Al6061 + 3.6% Al_2O_3 + 5% quartz	54.7	53.2	52.7	53.6
S4	Al6061 + 3.6% Al_2O_3 + 10% quartz	57.2	57.9	58.4	57.83
S5	Al6061 + 3.6% Al_2O_3 + 15% quartz	60.7	59.1	61.5	60.43

As observed in Fig. 4a, the hardness of the composite improves with increasing weight fraction of reinforcing particles. The addition of 3.5% nano-Al_2O_3 to the Al6061 alloy enhances the hardness from 40.36 HRB to 47.63 HRB, a 18.01% increase. Further, the inclusion of quartz particles in the Al6061/nano-Al_2O_3 composite boosts the hardness from 47.63 HRB (sample S2) to 60.43 HRB (sample S5). Similar results were reported by Bhat et al. (2021), where the addition of 10% and 15% Al_2O_3 in the Al6061 matrix improved hardness from 90 HV to 140 HV, attributed to the incorporation of very hard Al_2O_3 particles into the soft aluminum alloy.

a)

b)

c)

d)
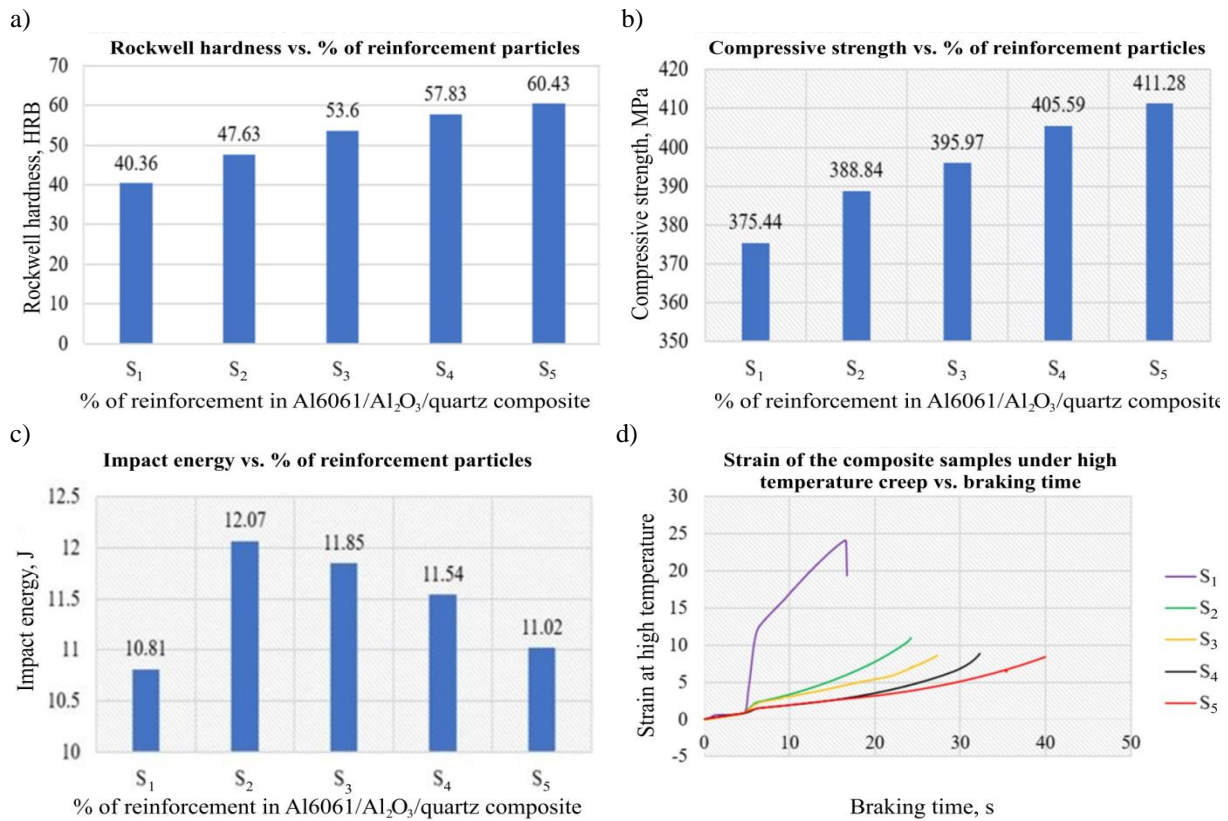
Fig. 4. The effect of percentage weight fraction of the reinforcement on: a) hardness, b) compressive strength, c) impact energy and d) high temperature strain of the hybrid composite sample.

4. Compressive strength

The compressive strength test results of the hybrid composites were displayed in Table 5 and Fig. 4b. As observed from both the table and the graphical representation, the compressive strength of the composite material improves with an increase in the percentage weight fraction of nano-Al_2O_3 and quartz particulates within the fabricated composite. Moreover, the compressive strength of the composite surpasses that of the unreinforced aluminum alloy.

Table 5. Compression test result of the fabricated composite as a function of reinforcements.

Designation	Composite description	Compressive strength, N/mm^2			Average strength, N/mm^2
		Test 1	Test 2	Test 3	
S1	Al6061 alloy	375.42	374.68	376.21	375.44
S2	Al6061 + 3.6% Al_2O_3	389.81	387.30	390.22	388.84
S3	Al6061 + 3.6% Al_2O_3 + 5% quartz	396.32	395.51	396.07	395.97
S4	Al6061 + 3.6% Al_2O_3 + 10% quartz	405.51	407.54	403.72	405.59
S5	Al6061 + 3.6% Al_2O_3 + 15% quartz	411.02	409.72	413.11	411.28

5. Impact energy

The values of impact energy absorbed by the individual specimens, along with their corresponding trials, are listed in Table 6 and Fig. 4c. The impact strengths, presented in the table below, were calculated as the impact energy per unit contact area of the specimens.

6. Creep properties

The addition of reinforcing ceramic particles enhances the composite's high-temperature strain, as seen in Fig. 4d. The applied stress during the creep test was 10 MPa, equivalent to 250 percent of the maximum compressive pressure that would be produced under difficult braking conditions in an automobile at a maximum temperature of 360°C. In comparison to the other composite samples tested, sample S5 exhibits the optimum material properties for various automotive applications, such as clutch and brake discs. Furthermore, this sample shows the minimum high-temperature strain compared to other composite samples.

Table 6. Impact energy absorbed by the fabricated composite as a function of reinforcements.

Designation	Composite description	Impact energy, J			Average impact energy, J
		Test 1	Test 2	Test 3	
S$_1$	Al6061 alloy	10.82	10.46	11.15	10.81
S$_2$	Al6061 + 3.6% Al$_2$O$_3$	12.55	11.62	11.85	12.07
S$_3$	Al6061 + 3.6% Al$_2$O$_3$ + 5% quartz	11.77	11.90	11.88	11.85
S$_4$	Al6061 + 3.6% Al$_2$O$_3$ + 10% quartz	11.60	11.71	11.31	11.54
S$_5$	Al6061 + 3.6% Al$_2$O$_3$ + 15% quartz	10.08	10.18	9.82	10.02

The same result was reported by Sivaram et al. (2015), who fabricated LM25 reinforced with zirconium dioxide particles to investigate the creep behavior of the composite. The test's results demonstrate that the addition of reinforcing ceramic particles improves the creep property of the composite, with the author concluding that this improvement was achieved due to the uniform distribution of the reinforcing particles in the matrix phase.

3.2. Discussion

The finding of the porosity study aligns with the results reported by Prasad et al. (2014), who observed a similar increase in porosity with an increase in the volume fraction of reinforcing particulates. Bhat et al. (2021) reported that the formation of porosity in aluminum metal matrix composites is mainly due to hydrogen gas in the melt, the higher amount of reinforcing particles in the melt, and the stirring process, which leads to an increment of air bubbles in the contact surface area between the matrix alloy and the reinforcement particulates. According to Shankar et al. (2018), the acceptable limit of porosity level in metal matrix composites is between 2% and 4%. As observed in the current study, the percentage porosity varies from 0.74% to 3.6%, which falls within the accepted limit. According to AnandhaKumar et al. (2021) the incorporation of a hard ceramic phase in an aluminum metal matrix composite always improves its hardness by hindering dislocation movement in the matrix. However, the current experimental investigation suggests that the addition of quartz particulate in the Al6061/nano Al$_2$O$_3$ composite initially improves hardness with a higher percentage increment. However, as more quartz particulate is added, the hardness value reaches a certain point and then declines due to the formation of brittle phase in the matrix as a result of the quartz reinforcement. Similar improvements in compressive strength were reported by Gnaneswaran et al. (2022) and Kumar et al. (2018), who stated that the addition of 9% Al$_2$O$_3$ to Al7075 improved the alloy's compressive strength by 70.61%. The author attributed this enhancement to the Al$_2$O$_3$ particles acting as barriers to dislocation in the microstructure of the composite, effectively resisting deforming stress and increasing the compressive strength. Likewise, Kaviyarasan et al. (2018) fabricated an aluminum metal matrix composite with an Al6061 matrix and Al$_2$O$_3$ as reinforcement. The author reported that adding 3% Al$_2$O$_3$ by mass to the matrix alloy enhanced the compressive strength from 554 N/mm^2 to 644 N/mm^2. This improvement indicates a transformation of the ductility behavior of the Al6061 matrix aluminum alloy to a more brittle nature, resulting from the incorporation of reinforcing hard ceramic Al$_2$O$_3$ particles into the soft ductile aluminum alloy. As observed from Table 6 and Figure 3(c), the impact energy absorbed by some of the fabricated composites (S$_2$, S$_3$, S$_4$, S$_5$) is slightly higher than that of the base alloy, but the improvement is marginal. Interestingly, sample S$_5$ exhibits the lowest impact energy among all the composite samples due to the fact that incorporation of more ceramic particles with in a matrix phase result in the formation of brittle phase. The maximum percentage improvement in impact energy is 11.65%, observed for sample S$_2$, attributed to the addition of 3.5% nano-Al$_2$O$_3$. The improvement is achieved due to uniformly distribution of small amount of reinforcing particles within the matrix phase. The high temperature creep strength of the developed composite show an increase with increase in reinforcing particles, same result was reported by Sivaram et al. (2015), who fabricated LM25 reinforced with zirconium dioxide particles to investigate the creep behavior of the composite. The test's results demonstrate that the addition of reinforcing ceramic particles improves the creep property of the composite, with the author concluding that this improvement was achieved due to the uniform distribution of the reinforcing particles in the matrix phase.

4. Conclusions

Al6061/nano Al_2O_3/quartz hybrid composite materials samples were prepared using stir casting methods for the first time. Then, mechanical properties (hardness, compressive strength, creep, and impact energy absorption) and physical properties (porosity and density) were studied. From the study, the following points are concluded.

- The porosity level of the composite specimen increases as the volume fraction of the reinforcing particulates increases, due to the increment of air bubbles in the contact surface area between the matrix alloy and the reinforcement particulates.
- The Rockwell hardness of the hybrid composite was found to increase linearly with the addition of hard ceramic reinforcing particles. Furthermore, the results reveal that the addition of quartz particles improves the material's resistance to indentation, with the maximum hardness value of 60.43 HRB recorded for sample S_5 (3.5% nano-Al_2O_3 + 9% quartz).
- The compressive strength test of the hybrid composite shows that the addition of quartz particles linearly increases the compressive strength of the composite, similar to the hardness test. However, as the weight percentage of the reinforcing particles increases within the composite, the percentage increase in compressive strength decreases. The maximum compressive strength value of 411.283 N/mm^2 was recorded for sample S_5 (3.5% nano-Al_2O_3 + 9% quartz).
- Upon adding reinforcing quartz particles up to 6%, the impact energy absorption capacity of the hybrid composite improves. However, adding quartz above 6% drastically reduces the impact energy-absorbing capacity of the composite material. For 9% quartz particle addition, the impact energy of the composite is even lower than that of the base aluminum alloy matrix.
- The addition of reinforcing ceramic particles improves the high-temperature strain of the composite samples. Sample S_1 shows the minimum elongation with short braking or deformation time compared to the other samples. However, sample S_5 (3.5% nano-Al_2O_3 + 9% quartz) reveals the maximum long braking or deformation time. Based on the results of the mechanical property tests, the developed hybrid composite sample S_5 (3.5% nano-Al_2O_3 + 9% quartz) can replace the Al6061 matrix in different engineering applications with improved properties. The creep property of the developed new hybrid metal matrix composite (Al6061/nano Al_2O_3/quartz) was studied for the first time; there is no published research article on studying the high-temperature creep property of Al6061/nano Al_2O_3/quartz. This research provides new insight into studying the creep properties of hybrid metal matrix composites for different engineering applications.

References

Alnaqi, A. A., Kosarieh, S., Barton, D. C., Brooks, P. C., & Shrestha, S. (2016). Material characterisation of lightweight disc brake rotors. *Proceedings of the Institution of Mechanical Engineers, Part L: Journal of Materials: Design and Applications*, *232*(7), 555-565. https://doi.org/10.1177/1464420716638683

AnandhaKumar, C., Gopi, S., Kumar, S. S., & Mohan, D. G. (2021). Mechanical, metallurgical and tribological properties of friction stir processed aluminium alloy 6061 hybrid surface composites. *Surface Topography: Metrology and Properties*, *9*(4), Article 045019. https://doi.org/10.1088/2051-672X/ac3120

Arif, S., Aziz, T., & Ansari, A. H. (2018). Characterization and mechanical behaviour of zirconia reinforced aluminium matrix nanocomposites fabricated through powder metallurgy technique. *Materials Focus*, *7*(6), 1-5. https://doi.org/10.1166/mat.2018.161

Arunachalam, R., Krishnan, P. K. & Muraliraja, R. (2019). A review on the pro-duction of metal matrix composites through stir casting–Furnace design, properties, challenges, and research opportunities. *Journal of Manufacturing Processes*, *42*, 213-245. https://doi.org/10.1016/j.jmapro.2019.04.017

Baradeswaran A., & Perumal, A. E. (2013). Influence of B_4C on the tribological and mechanical properties of Al 7075–B_4C composites. *Composites Part B: Engineering*, *54*, 146-152. https://doi.org/10.1016/j.compositesb.2013.05.012

Baradeswaran, A., Elayaperumal, A., & Issac, R. F. (2013). A statistical analysis of optimization of wear behaviour of Al-Al_2O_3 composites using Taguchi technique. *Procedia Engineering*, *64*, 973-982. https://doi.org/10.1016/j.proeng.2013.09.174

Bhat, A., Kakandikar, G., Deshpande, A., Kulkarni, A., & Thakur, D. (2021). Characterization of Al2O3 reinforced Al 6061 metal matrix composite. Materials Science, Engineering and applications, 1(1), 11-20. https://doi.org/10.21595/msea.2021.22028

Bodunrin, M. O., Alaneme, K. K., & Chown, L. H. (2015). Aluminium matrix hybrid composites: a review of reinforcement philosophies; mechanical, corrosion and tribological characteristics. *Journal of Materials Research and Technology*, *4*(4), 434-445. https://doi.org/10.1016/j.jmrt.2015.05.003

Breval, E. (1995). Synthesis routes to metal matrix composites with specific properties: A review. *Composites Engineering*, *5*(9), 1127-1133. https://doi.org/10.1016/0961-9526(95)00048-R

Caracostas, C. A., Chiou, W., Fine, M. E., Cheng, H. S. (1997). Tribological properties of aluminum alloy matrix TiB₂ composite prepared by in situ processing. *Metallurgical and Materials Transactions A*, *28*, 491-502. https://doi.org/10.1007/s11661-997-0150-2

Chen P., & Hoshi, T. (1992). High-performance machining of SiC whisker-reinforced aluminium composite by self-propelled rotary tools. *CIRP Annals*, *41*(1), 59-62. https://doi.org/10.1016/S0007-8506(07)61152-4

Das, D. K., Mishra, P. C., Singh, S., & Pattanaik, S. (2014). Fabrication and heat treatment of ceramic-reinforced aluminium matrix composites - a review. *International Journal of Mechanical and Materials Engineering*, *9*, Article 6. https://doi.org/10.1186/s40712-014-0006-7

Ezatpour, H. R., Sajjadi, S. A., Sabzevar, M. H. & Huang, Y. (2014). Investigation of microstructure and mechanical properties of Al6061-nanocomposite fabricated by stir casting. *Materials & Design*, *55*, 921-928. https://doi.org/10.1016/j.matdes.2013.10.060

Gangwar, S., Kukshal, V., Patnaik, A., & Singh, T. (2013). Mechanical and fracture toughness behavior of TiO₂-filled A384 metal alloy composites. *Science and Engineering of Composite Materials*, *20*(3), 209-220. https://doi.org/10.1515/secm-2012-0143

Gnaneswaran, P., Hariharan, V., Chelledurai, S. J. S., Rajeshkumar, G., Gnanasekaran, S., Sivananthan, S., & Debtera, B. (2022). Investigation on mechanical and wear behaviors of LM6 aluminium alloy-based hybrid metal matrix composites using stir casting process. *Advances in Materials Science and Engineering*, *2022*, Article 4116843. https://doi.org/10.1155/2022/4116843

Jino, R. Pugazhenthi, R., Ashok, R., Ilango, K. G., Chakravarthy, T., & Kalyana, P. R. (2017). Enhancement of mechanical properties of Luffa fiber/epoxy composite using B₄C. *Journal of Advanced Microscopy Research*, *12*(2), 89-91. https://doi.org/10.1166/jamr.2017.1324

Kala, H., Mer, K. K. S., & Kumar, S. (2014). A review on mechanical and tribological behaviors of stir cast aluminum matrix composites. *Procedia Materials Science*, *6*, 1951-1960. https://doi.org/10.1016/j.mspro.2014.07.229

Kamat, S. V., Hirth, J. P., & Mehrabian, R. (1989). Mechanical properties of particulate-reinforced aluminum-matrix composites. *Acta Metallurgica*, *37*(9), 2395-2402. https://doi.org/10.1016/0001-6160(89)90037-0

Kareem, A., Qudeiri, J. A., Abdudeen, A., Ahammed, T., & Ziout, A. (2021). A review on AA 6061 metal matrix composites produced by stir casting. *Materials*, *14*(1), Article 175. https://doi.org/10.3390/ma14010175

Kaviyarasan, K., Pridhar, T., Sureshbabu, B., Boopathi, C., & Srinivasan, R. (2018). Fabrication of Al6061-Al₂O₃ composite through liquid metallurgy technique. *IOP Conference Series: Materials Science and Engineering*, *402*, Article 012148. https://doi.org/10.1088/1757-899X/402/1/012148

Kumar, U. K. G. B. A. V. (2017). Method of stir casting of aluminum metal matrix composites: a review. *Materials Today: Proceedings*, *4*(2), 1140-1146. https://doi.org/10.1016/j.matpr.2017.01.130

Kumar, S. R., Patnaik, A., & Bhat, I. K. (2016). The in vitro wear behavior of nanozirconia-filled dental composite in food slurry condition. *Proceedings of the Institution of Mechanical Engineers, Part J: Journal of Engineering Tribology*, *231*(1), 23-40. https://doi.org/10.1177/1350650116641329

Kumar, V. M., & Venkatesh, C. V. (2018). Effect of ceramic reinforcement on mechanical properties of aluminum matrix composites produced by stir casting process. *Materials Today: Proceedings*, *5*(1), 2466-2473. https://doi.org/10.1016/j.matpr.2017.11.027

Manigandan, K., Srivatsan, T. S., Ren, Z., & Zhao, J. (2015). Influence of reinforcement content on tensile response and fracture behavior of an aluminum alloy metal matrix composite. In T. Sano, & T. S. Srivatsan (Eds.) *Advanced composites for aerospace, marine, and land applications II* (pp. 345-359). Springer. https://doi.org/10.1007/978-3-319-48141-8_8

Marques, C. L. M., Kumar, S. R., Goswami, C. & Verma, R. (2021). Numerical simulation of armor materials and optimization using gray relational analysis. *Materials Today: Proceedings*, *44*, 4717-4730. https://doi.org/10.1016/j.matpr.2020.10.942

Mehara, M., Goswami, C., Kumar, S. R., Singh, G. & Wagdre, M. K. (2021). Performance evaluation of advanced armor materials. *Materials Today: Proceedings*, *47*, 6039-6042. https://doi.org/10.1016/j.matpr.2021.04.611

Mishra, S., Patnaik, A., & Kumar, S. R. (2019a). Comparative analysis of wear behavior of garnet and fly ash reinforced Al7075 hybrid composite. *Materials Science & Engineering Technology*, *50*(1), 86-96. https://doi.org/10.1002/mawe.201800121

Mishra, S., Patnaik, A., & Kumar, S. R. (2019b). Physico-mechanical characterization of garnet and fly ash reinforced Al7075 hybrid composite. *Materials Science & Engineering Technology*, *50*(6), 731-741. https://doi.org/10.1002/mawe.201800133

Muraliraja, R., Arunachalam, R., Al-Fori, I. Al-Maharbi, M., & Piya, S. (2019). Development of alumina reinforced aluminum metal matrix composite with enhanced compressive strength through squeeze casting process. *Proceedings of the Institution of Mechanical Engineers, Part L: Journal of Materials: Design and Applications, 233*(3), 307-314. https://doi.org/10.1177/1464420718809516

Nieberle, T., Kumar, S. R., Patnaik, A., & Goswami, C. (2021). Review: Composite materials for armour appli-

cation. In: P. K. Rakesh, A. K. Sharma, & I. Singh (Eds.), *Advances in engineering design* (pp. 239-248). Springer. https://doi.org/10.1007/978-981-33-4018-3_22

Parthiban, A., Pugazhenthi, R., Ravikumar, R., & Vivek, P. (2017). Experimental investigation of turning parameters on AA 6061-T6 material. *IOP Conference Series: Materials Science and Engineering*, *183*, Article 012013. https://doi.org/10.1088/1757-899X/183/1/012013

Poornachandiran, N., Pugazhenthi, R., Vijay Ananth, S., Krishnan, T. G. & Vairavel, M. (2020). Investigation of mechanical properties of Al6061 with reinforcement of SiC/B$_4$C metal matrix composites. A*IP Conference Proceedings*, *2283*, Article 020113. https://doi.org/10.1063/5.0025004

Prasad, D. S., Shoba, C., & Ramanaiah, N. (2014). Investigations on mechanical properties of aluminum hybrid composites. *Journal of Materials Research and Technology*, *3*(1), 79-85. https://doi.org/10.1016/j.jmrt.2013.11.002

Pugazhenthi, R., Sivaganesan, S., Dhansekaran, C. & Parthiban, A. (2019). Morphological and mechanical characteristics of hybrid aluminium matrix composites. *International Journal of Vehicle Structures & Systems*, *11*(2), 173-175. https://doi.org/10.4273/ijvss.11.2.11

Sabry, I., Ghafaar, M. A., Mourad, A. H. I., & Idrisi, A. H. (2001). Stir casted SiC-Gr/Al6061 hybrid composite tribological and mechanical properties. *AN Applied Sciences*, *2*, Article 943. https://doi.org/10.1007/s42452-020-2713-4

Sankarlal, S., & Kuppusamy, V. (2018). Fabrication of aluminium 6061-SiC-Al$_2$O$_3$ MMC and HMMC by stir casting technique and comparing the mechanical properties. *International Journal of Mechanical and Production Engineering Research and Development, 8*(1), 635-642.

Sayuti, M., Sulaiman, S., Vijayaram, T. R., Baharudin, B. T. H. T., & Arifi, M. K. A. (2012). Manufacturing and Properties of Quartz (SiO$_2$) Particulate Reinforced Al-11.8%Si Matrix Composites. In N. Hu (Ed.), *Composites and their properties*. InTechOpen. doi: https://doi.org/10.5772/48095

Shankar, M. C. G., Shettar, M., Sharma, S. S., Kini, A., & Jayashree. (2018). Enhancement in hardness and influence of artificial aging on stir cast Al6061-B$_4$C and Al6061-SiC composites. *Materials Today Proceedings*, *5*(1), 2435-2443. https://doi.org/10.1016/j.matpr.2017.11.023

Singh, J., & Chauhan, A. (2018). A review of microstructure, mechanical properties and wear behavior of hybrid aluminium matrix composites fabricated via stir casting route. *Sādhanā*, *44*, Article 16. https://doi.org/10.1007/s12046-018-1025-5

Singh, T., Patnaik, A. & Satapathy, B. K. (2011). Effect of Carbon Nanotubes on Tribo-Performance of Brake Friction Materials. *AIP Conference Proceedings*, *1393*(1), 223-224. https://doi.org/10.1063/1.3653690

Singh, T., Patnaik, A., & Satapathy, B. K. (2013). Friction braking performance of nano-filled hybrid fiber reinforced phenolic composites: Influence of nanoclay and carbon nanotubes. *Nano*, *08*(03), Article 1350025. https://doi.org/10.1142/S1793292013500252

Singh, T., Patnaik, A., Satapathy, B. K. & Kumar, M. (2012). Performance analysis of organic friction composite materials based on carbon nanotubes-organic-inorganic fibrous reinforcement using hybrid AHP-FTOPSIS approach. *Composites: Mechanics, Computations, Applications: An International Journal*, *3*(3), 189-214. https://doi.org/10.1615/CompMechComputApplIntJ.v3.i3.10

Sivaram, A., Krishnakumar, K., Rajavel, D. R., & Sabarish, R. (2015). Experimental investigation of creep behaviour of aluminium alloy (LM25) and zirconium DI-oxide (ZR0$_2$) particulate MMC. *International Journal of Mechanical Engineering and Technology, 6*(8), 126-138.

Sun, Y., Lyu, Y., Jiang, A. & Zhao, J. (2014). Fabrication and characterization of aluminum matrix fly ash cenosphere composites using different stir casting routes. *Journal of Materials Research*, *29*, 260-266. https://doi.org/10.1557/jmr.2013.372

Virinchy, C. S., Vijayarangan, J., Asif, A. H., & Pugazhenthi, R. (2019). Experimental investigation of Al-Mg-SiC-fly ash composites for automotive alloy wheel rims. *International Journal of Vehicle Structures & Systems*, *11*(2) 121-124. http://dx.doi.org/10.4273/ijvss.11.2.01

Yang, J. B., Lin, C. B., Wang, T. C., & Chu, H. Y. (2004). The tribological characteristics of A356.2Al alloy/Gr$_{(p)}$ composites. *Wear*, *257*(9-10), 941-952. https://doi.org/10.1016/j.wear.2004.05.015

Badanie Właściwości Mechanicznych i Fizycznych Hybrydowego Kompozytu Al6061/Nano Al$_2$O$_3$/Kwarc Wytwarzanego Metodą Odlewania z Mieszaniem

Streszczenie

Stopy aluminium są szeroko stosowane w różnych obszarach zastosowań inżynieryjnych, takich jak przemysł lotniczy, motoryzacyjny i morski. Właściwości stopów aluminium wymagają udoskonaleń, aby zwiększyć zakres ich zastosowań. Celem badań była poprawa właściwości fizycznych i mechanicznych stopu aluminium Al6061 poprzez wzmocnienie nanocząstkami Al$_2$O$_3$ i cząstkami mikrokwarcu. Badania skupiały się przede wszystkim na badaniu wpływu cząstek kwarcu na właściwości mechaniczne i fizyczne kompozytu hybrydowego Al6061/nano Al$_2$O$_3$/kwarc. Kompozyt hybrydowy opracowano techniką odlewania z mieszaniem,

zmieniając udział wagowy cząstek kwarcu na 3%, 6% i 9%, utrzymując natomiast stały udział wagowy nano-cząstek Al$_2$O$_3$ (3,5%). Do oceny właściwości kompozytu, przygotowano próbki testowe zgodnie z normami ASTM E9-09 i ASTM E23 dotyczącymi odpowiednio twardości, wytrzymałości na ściskanie, pełzania i pochłaniania energii uderzenia. Wyniki badań wykazały, że dodatek 9% kwarcu i 3,5% nanocząstek Al$_2$O$_3$ spowodował poprawę wszystkich właściwości mechanicznych i fizycznych osnowy, z wyjątkiem udarności. Na podstawie uzyskanych wyników, opracowany hybrydowy materiał kompozytowy może być zalecany do lekkich części zamiennych do samochodów, takich jak tarcze hamulcowe i sprzęgła.

Słowa kluczowe: stop aluminium Al6061, kompozyt hybrydowy, nano Al$_2$O$_3$, kwarc (SiO$_2$), odlewanie z mieszaniem

Original Research

Design of Newly Developed Burner Rig Operating with Hydrogen Rich Fuel Dedicated for Materials Testing

Wojciech J. Nowak [1],* [ID]**, Marcin Drajewicz [1]** [ID]**, Marek Góral [1]** [ID]**, Robert Smusz [2]** [ID]**, Piotr Cichosz [3]** [ID]**, Andrzej Majka [4]** [ID]**, Jarosław Sęp [5]** [ID]

[1] Department of Materials Science, Faculty of Mechanical Engineering and Aeronautics, Rzeszow University of Technology, Al. Powstancóv Warszawy 12, 35-959 Rzeszów, Poland; drajewic@prz.edu.pl (M. Drajewicz), mgoral@prz.edu.pl (M. Góral)

[2] Thermodynamics Department, Rzeszow University of Technology, Al. Powstańców Warszawy 12, 35-959 Rzeszow, Poland; robsmusz@prz.edu.pl

[3] PROXIMO AERO SP. Z O.O., ul. Dębicka 221 A, 35-213 Rzeszów, Poland; piotr.cichosz@proximo.aero

[4] Department of Aircrafts and Aircraft Engines, Rzeszow University of Technology, Al. Powstańców Warszawy 12, 35-959 Rzeszów, Poland; andrzej.majka@prz.edu.pl

[5] Faculty of Mechanical Engineering and Aeronautics, Rzeszow University of Technology, Al. Powstańców Warszawy 12, 35-959 Rzeszów, Poland; jsztmiop@prz.edu.pl

* Correspondence: wjnowak@prz.edu.pl

Abstract

The main purpose of present article is to present the burner rig station newly developed at the Rzeszow University of Technology in Poland. The burner rig is dedicated to operate on fuels rich in hydrogen. The burner rig is able to operate with fuels with hydrogen content up to 50 volume %. A detailed description of burner rig construction is presented. Moreover a mathematical model predicting temperature distribution within the combustion chamber is presented. The obtained results showed a good insulation of burner rig construction leading to the temperature gradient from 1674°C in the burner rig to 214°C on steel housing.

Keywords: hydrogen-rich fuel, burner rig, high temperature oxidation, water vapour, high temperature materials
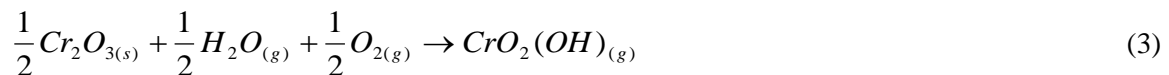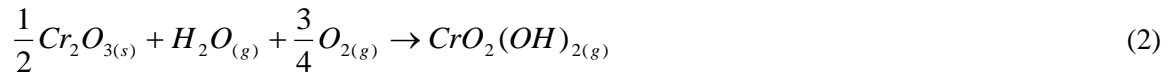
1. Introduction

Alloys used in aircraft engines or in stationary gas turbines (SGT) face harsh conditions, such as high temperature, aggressive gases and cyclic thermal loading. Thus, they need to possess good combinations of mechanical strength, microstructural stability and oxidation resistance. Ni-based alloys are the most common materials used in the hottest part of the gas turbines nowadays. However, the constant need of increase in gas turbines efficiency demands increasing of inlet gases temperature (Schütze & Quadakkers, 2017). Also a strong need of limitation of pollutions from jet engines exhaust exists. This can be achieved by using a hydrogen rich fuel despite gasoline. Combustion of hydrogen rich fuel results in an increase in exhaust gases temperature and higher water vapor content in the exhaust gases. Therefore, the materials used in the gas turbines face not only the higher temperature but also water vapor. It is known from the literature, that water vapor presence in the atmosphere significantly alters oxidation kinetics of the alloys. It was found for pure chromium, that the water vapor presence causes increase of oxidation kinetics accompanied with better chromia scale adherence and formation of blade-shaped oxide (Quadakkers et al., 1996; Michalik et al., 2005; Hänsel et al., 1998; 2003). Differences in oxidation kinetics and the oxide scale morphology formed on Ni-Cr binary alloy during exposure in dry and wet oxygen was found by Essuman et al. (2008) and Żurek et al. (2008), namely oxidation rate was found to be higher in wet atmosphere as compared to dry one. Similar observation on Ni-base alloys during oxidation in dry and humid atmosphere was found by e.g. England and Virkar (1999, 2001). The authors found the oxidation rates in wet hydrogen to be higher by a fac-

tor varying between 8 and 30 compared to air, while at 1100°C the effect of water vapour decreased and the growth rate in wet hydrogen was higher than in dry air by a factor of 1.5 to 13.
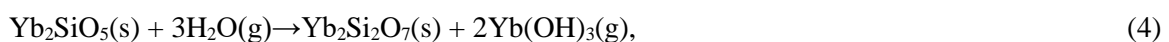
One of the effect of water vapor is enhanced chromium evaporation from the surfaces of chromia forming alloys at high temperatures. This phenomenon was extensively investigated e.g. by Opila et al. (2007) and Stanislowski et al. (2007) in high pO_2-gas, e.g. wet air. Chromium oxide can evaporate according to the following reactions:

$$\frac{1}{2}Cr_2O_{3(s)} + \frac{3}{4}O_2 \rightarrow CrO_{3(g)} \tag{1}$$

$$\frac{1}{2}Cr_2O_{3(s)} + H_2O_{(g)} + \frac{3}{4}O_{2(g)} \rightarrow CrO_2(OH)_{2(g)} \tag{2}$$

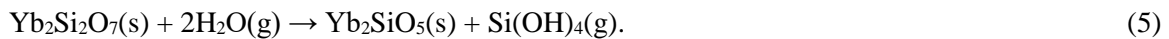$$\frac{1}{2}Cr_2O_{3(s)} + \frac{1}{2}H_2O_{(g)} + \frac{1}{2}O_{2(g)} \rightarrow CrO_2(OH)_{(g)} \tag{3}$$

Volatilization of chromium species during high temperature exposure of Ni-base alloys was investigated by many researchers, like e.g. Deodeshmukh (2013a, 2013b), Holcomb (2008) or Pujilaksono et al. (2008). The authors found mass loss of the exposed specimen without oxide scale spallation (Deodeshmukh, 2013b) and formation of blade-shaped oxides (Pujilaksono et al., 2008). It was also claimed, that not only temperature, but also amount of water vapor in the atmosphere has detrimental effect on the rate of volatilization of chromium species (Holcomb, 2008). It was also found by Nowak et al. (2016) that the water vapour suppresses nitrides formation below the external chromia scale on Ni-base superalloy Rene 80. The authors correlated the latter with preferential adsorption of water vapor molecules on the surface and suppressing the nitrogen transport through the oxide scale.

In case of an alumina forming alloys it was found by Maris-Sida et al. (2003) that presence of water vapor in the test atmosphere, strongly enhance spallation of the oxide scale. Onal et al. (2004) found that for alumina forming alloys water vapour adversely affects the selective oxidation of aluminium. The authors concluded that suppression of external oxidation of aluminium may be the result of a more rapid growth of the transient oxides caused by the presence of water vapour. Enhanced spallation of an alumina scale was observed as well. Janakiraman et al. (1999) found that 2 to 4 times increase in weight loss in the presence of water vapor in the atmosphere during cyclic oxidation of Ni-base superalloys. Smialek et al. (2010) found so called desktop spallation (DTS) and moisture-induced delayed spallation (MIDS). In both proposed mechanisms moisture has been postulated to serve as a source of interfacial hydrogen embrittlement. Hydrogen, in this particular case, is derived from reaction with aluminium in the alloy at an exposed interface.

Considering all findings mentioned above there is a strong need to find a materials exhibiting better performance at elevated temperature and increased water vapor content. Such materials can be e.g. high entropy alloys (e.g. NiCoCrAlFe) or materials covered by protective coatings, like e.g. thermal barrier coatings (TBC) or environmental barrier coatings (EBC). Typically for conventional fuel gas turbines the thermal barrier coatings are used for protection of Nickel-superalloys surface material (Grilli et al., 2021; Suzuki et al., 2022). The outer ceramic layer contains usually yttria stabilized zirconia oxide (YSZ) (Golewski and Sadowski, 2019) or pyrochlores (Pędrak et al., 2021; 2022). The bond coat protects surface against oxidation and hot corrosion and might be formed from MCrAlY-type alloys (Zakeri et al., 2022) or by production of aluminide coatings (Góral et al., 2021; Kopec et al., 2021). For production of TBCs different method might be uses such as diffusion aluminizing (Cocojaru et al., 2022), atmospheric plasma spraying (Girolamo et al., 2014) or electron beam physical vapour deposition (EB—PVD) (Qiu et al., 2021). In new Environmental Barrier Coatings (EBC) the outer ceramic layer might contain different ceramic materials such as Y_2SiO_5-YS, $Yb_2Si_2O_7$-YDS, $Gd_2Zr_2O_7$, $Y_3Al_5O_{12}$, $Yb_2Si_2O_7$-YDS, Y_2O_3 produced using different thermal spraying processes (Vassen et al., 2019). In the case of hydrogen application as a fuel the water vapor formed during hydrogen burning is formed during reactions (Wang et al., 2020):

$$Yb_2SiO_5(s) + 3H_2O(g) \rightarrow Yb_2Si_2O_7(s) + 2Yb(OH)_3(g), \tag{4}$$

$$Yb_2Si_2O_7(s) + 2H_2O(g) \rightarrow Yb_2SiO_5(s) + Si(OH)_4(g). \hspace{2cm} (5)$$

The silicon is usually used for protection against water vapour in this application (Chen et al., 2021).

However, most of aforementioned materials were examined using mixture of air and water vapor. Investigations of these materials in direct exhaust coming from burning of hydrogen rich fuel is very limited. Thus in the present work a burner rig operating with mixture of fuel and hydrogen is introduced. In this equipment a testing of various materials inside the burner rig is possible, which gives the unique opportunity of testing in real exhaust originating from burning a hydrogen fuel in real operating conditions. Such equipment is installed at the Rzeszow University of Technology (Poland, Subcarpathian region).

The hydrogen is considered as an alternative fuel for Industrial Gas Turbines. Leading IGT manufacturers such as MHI (*Decarbonization technology*, 2023), Siemens (*Zero emission hydrogen turbine center*, 2023), General Electric (*Hydrogen fueled gas turbines*, 2023) are planning the using of fully hydrogen powered gas turbines. The first industrial scale experimental gas turbine fueled by mixture of natural gas and up to 20 % of hydrogen was successfully validated in Plant McDonough-Atkinson facility (USA) on MHI gas turbine (*Southern Co.,* 2023). In Norway the first micro turbine powered by 100% hydrogen fuel was demonstrated in 2022 by Banihabib and Assadi (2022). The small hydrogen power generator based on small gas turbine was developed by Turbotec Company (*Hydrogen gas turbine*, 2023). This type of gas turbines might be connected with renewable energy power plants (wind turbines, photovoltaics (PV)) and used as energy storage unit (Grilli et al., 2021; Pyo et al., 2021). From many years the design and manufacturing research are conducted in the case of gas turbine design (Najjar, 1990; Marin et al., 2021) and materials (Stefan et al., 2022).

The hydrogen might be also used in aeroengines. The B-57 was the first plane, which was tested in 50s for using of hydrogen as a fuel in Curtiss Wright J-65 jet engine. In this solution two independent fuel systems were used, namely one using kerosene and another using hydrogen (Winter, 1990). The using of hydrogen was considered for application of high-speed reconnaissance plane Lockheed CL-400 (Rich, 1973). The Tupolev (Soviet Union) converted the civil Tu-154 for using of hydrogen (Tupolev, 1994). Since 1991 the design of airplane using hydrogen fuel was considered in international cooperation (Westenberger, 2002). Finally the CRYOPLANE European project was run in 2000 (Westenberger, 2003). The other solutions for using of hydrogen for aeroengine applications is using for petrol-powered engines (Boeing, 2010) as well as for fuel-cells proposed (Renouard-Vallet et al., 2011). The application of fuel cells is planned by leading aircraft manufacturers such as Airbus (Airbus, 2023). Hydrogen is a promising fuel for hypersonic planes and was tested on X-43 experimental plane (Moses et al., 2004).

Hydrogen from decades are used for rocket propulsion applications. In the United States the M-1 was the first hydrogen-powered rocket engine (Report 2555-M-1-F, 1967). The J-2 engine was successfully used in Saturn family of rocked used in Apollo program (NASA, 1968). The next generation of cryogenic hydrogen-oxygen (LH/LOX) powered rocket engines R-2S was applied in Space Shuttle as a unit with highest trust in the history (Wilhelm, 1972). Currently the Blue Origin developing the cryogenic BE-3 engine (Cowing, 2012). The similar development of LH/LOX rocket engines took splace in Russia which designed the RD-0120 engine as an equivalent for R-23S engine (Rachuk et al., 1996). This types of engines were also developed in other countries: Japan (Negoro et al., 2007),China (Tan, 2013) and applied in EU - Ariane 5 (Chopinet et al., 2011), and India in GSLV-family rockets (Lele, 2014).

2. Materials and methods

Construction of burner rig dedicated for operation with fuels rich in hydrogen, which is able to operate with fuels with hydrogen content up to 50 volume % was described in details. A schematic pictures showing dimensions and cross-sections of burner rig was presented and explained. Moreover a mathematical model predicting temperature distribution within the combustion chamber is presented. The modelling is done according to algorithm shown in ASTM C 680-08 (2010).

3. Results

3.1. Burner rig description

For a purpose of research activities, new test bench has been designed, a functional research stand for combustion of hydrogen-based mixtures. Combustion chamber allows research of the impact of hydrogen flames on the structure of base materials structure and coatings. The thermodynamical and mechanical design was performed to maximize technical capabilities of the rig, which is able to be feed of a mixture of hydrogen with an oxidant, i.e. air and/or oxygen in the desired proportions up to 50% H_2. Fuel and oxidants are supply to the burner through independent installations controlling pressure, temperature and flow for each medium. An overview of the burner rig is shown in Figure 1.


(a)	(b)
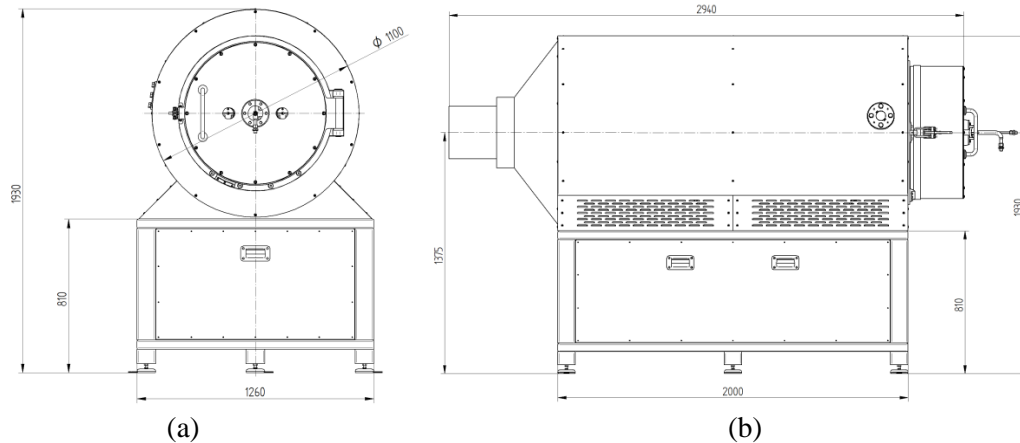
Fig. 1. Front view (a) and side view (b) of burner rig.

The combustion chamber is a cylinder with a base diameter of about 0.15 m and a length of about 0.5 m with a burner and a multi-position mounting bracket for the tests item. It is equipped with an inspection window that allows the observation of the combustion process using cameras as well as temperature measurement for the non-contact method. The chamber enabling simple and quick assembly of the test pieces in the holder and placing it together with the holder in the chamber. In addition to thermal resistance, the chamber must also ensure mechanical strength, as well as must be thermally insulated and protected against accidental contact with hot elements by technical personnel. The combustion chamber is made of refractory concrete (1) (Runcast BWM1), next thermal shock absorbing and sealing compound (Promix ZOR), high temperature insulation (Promaform 1430), medium temperature insulation (Promaform 1260) (4) and steel casing. Inspection window (5) and thermocouple port (6) (Figure 2).
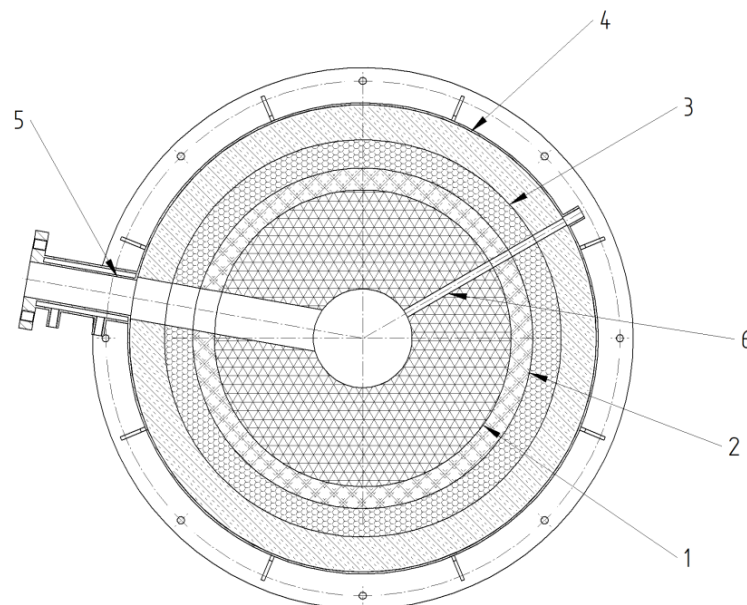

Fig. 2. Cross-section of combustion chamber: 1 – refractory concrete, 2 –insulating concrete layer 1, 3 –insulating concrete layer 2, 4 – medium temperature insulation, 5 – inspection window, 6 – thermocouple port.

The thicknesses and order of the layers have been determined in such a way as to reduce heat loss as much as possible on the one hand, and to minimize thermal stresses that may cause damage to the concrete on the other hand. Burner rig is built up from several segments, including burner, combustion chamber, adiabatic, transition, flue gases cooling and exhaust outlet (Figure 3) and can easily be expanded by adding additional segments in the future depending on demands.

The burner system placed in the chamber have an ignition system and a flame detection system cooperating with the leak control system and automatic fuel cut-off. Flue gas outlet led outside the room to the chimney with measurement of flue gas parameters. The outlet is thermally insulated and ensure tightness. The control system of the stand has been designed and made in a way that allows the preparation of an appropriate mixture for combustion, its control (composition, temperature, flow, pressure, etc.), safe combustion, control of the temperature of the test item and parameters in the combustion chamber itself. The key parameters of the test are register by the data acquisition system (DAQ) and enable data export. The process control is based on the software run on industrial PLC controller. In the future additional capabilities will be incorporated into research rig, therefore some possibility of expanding its functionality in the future has been secured. The control system ensures the ability to remotely conduct the full test cycle and the key element of the control system is an independent safety system guarantees the safety of its operators. The rig is control by HMI (Human Machine Interface), which allows the staff to determine the process parameters and visualize the process itself as well as all measured parameters. Additionally process parameters and measured data can be broadcast using a communication protocol.
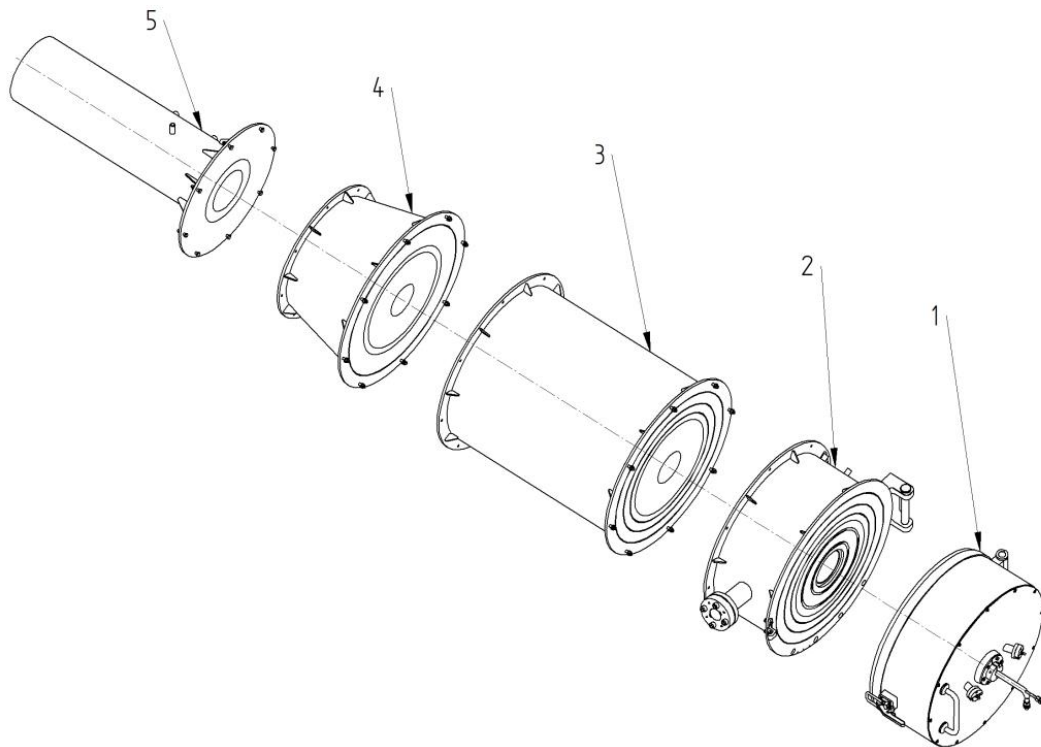
Fig. 3. Modules of combustion chamber: burner (1), combustion chamber (2), adiabatic (3), transition (4), flue gases cooling and exhaust outlet (5).

Research stand is equipped with pressure reducers on each of the connected media along with leakage detection and has the measurement stubs allowing additional measurement of process parameters not resulting from the requirements of the control system and the process safety system.

Main process parameters:
- Burner: 7.5 kW,
- H_2 level: up to 50%,
- Max temp in combustion chamber: 1750°C,
- Max fuel flow: 1.54 m³/h,
- Max oxidant flow: 11.8 m³/h,
- Temperature measurement points: 3,
- Total weight: 1300 kg.

Figure 4 depicts the existing burner rig placed in the Hydrogen Laboratory within the Research and Development Laboratory for Aerospace Materials structure. The device is currently being tested.

Fig. 4. Images showing the existing burner rig (a) and the control panels (b).

3.2. Modelling of temperature distribution

Based on the mathematical model and algorithm presented in the standard ASTM C 680-08 (2010) the temperature distribution for all layers was calculated. The calculations take into account the variable value of the thermal conductivity coefficient. Perfect contact between materials was established. The heat flux conditions for internal and external surfaces were given by Newton's law of convection.

For the internal side:

$$-k(T)\frac{\partial T}{\partial n} = h_{si}(T_i - T_{si}) \tag{6}$$

where: h_{si} − heat transfer coefficient on the internal boundary, T_i − fluid temperature at the inside boundary, T_{si}—surface temperature on the internal boundary, $k(T)$ − thermal conductivity.

$$-k(T)\frac{\partial T}{\partial n} = h_{se}(T_{se} - T_e) \tag{7}$$

where: h_{se} − heat transfer coefficient, T_e − fluid temperature at the outside boundary, T_{se} − surface temperature on the external boundary of the model. Radiative heat exchange was taken into account on the outer surface.

$$h_{se} = h_{ce} + h_{re} \tag{8}$$

where: h_{re} − component of the heat transfer coefficient due to radiation, h_{ce} − component of the heat transfer coefficient due to convection.

$$h_{re} = \frac{\sigma\varepsilon(T_{se}^4 - T_o^4)}{T_{se} - T_o} \tag{9}$$

where: $\sigma = 5.67 \cdot 10^{-8}$ W/(m²K⁴) is the Stefan-Boltzmann constant, ε − is the emissivity of the surface, T_o − surrounding temperature.

To determine the heat transfer coefficient on the internal boundary, the Gnielinski correlation was used, taking into account the influence of the thermophysical properties of the fluid and the thermal entrance region (Gnielinski, 1976):

$$Nu = \frac{\left(\frac{f_D}{8}\right) \cdot (Re - 1000) \cdot Pr}{1 + 12.7 \cdot \left(\frac{f_D}{8}\right)^{0.5} \cdot \left(Pr^{\frac{2}{3}} - 1\right)} \cdot \left[1 + \left(\frac{D_h}{L}\right)^{\frac{2}{3}}\right] \cdot \left(\frac{\eta}{\eta_{wall}}\right)^m \tag{10}$$

where: f_D − Darcy friction factor, D_h −hydraulic diameter of the combustion chamber, L − length of the combustion chamber, Pr − Prandtl number, η − dynamic viscosity of the fluid, Re − Reynolds number, Nu − Nusselt number.

$$m = 0.11 \; if \; \frac{\eta}{\eta_{wall}} < 1 \tag{11}$$

$$m = 0.25 \; if \; \frac{\eta}{\eta_{wall}} > 1 \tag{12}$$

On the other hand, to determine the component of the heat transfer coefficient due to convection on the external boundary, the Churchill and Chu correlation was used (Churchill and Chu, 1975):

$$Nu = \left\{0.6 + \frac{0.387 Ra^{1/6}}{\left[1 + \left(\frac{0.559}{Pr}\right)^{9/16}\right]^{8/27}}\right\}^2 \tag{13}$$

where: Ra − Rayleigh number.

The calculated temperature distribution in the combustion chamber is shown in the Figure 5 and Table 1.
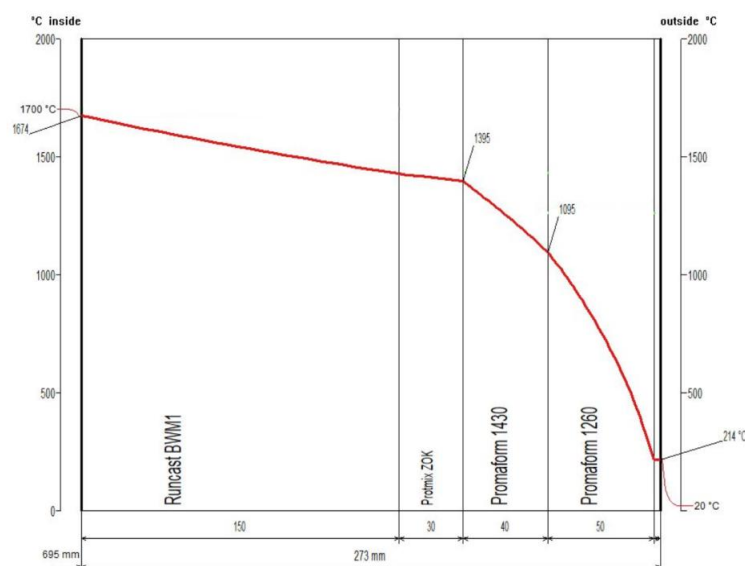
Fig. 5. Calculated temperature distribution in combustion chamber.

Table 1. Layer mean and surface temperature in combustion chamber (NASA, 1968).

Material	Thickness, mm	Surface temp., °C	Layer mean temp., °C
Runcast BWM1	150	1674	1536
Protmix ZOR	30	1426	1410
Promaform 1430	40	1395	1249
Promaform 1260	50	1096	720
Steel	3	214.5	214

As can be seen from the Figure 5 high temperature resistant alumina based refractories have low thermal conductivity values (Table 2) which result in deep penetration of temperature into the furnace wall. This requires thick walls of refractory materials to reduce the temperature to an acceptable value for strictly insulating materials. This is a significant limitation that makes it impossible to minimize the dimensions and weight of the furnace. This results in a high heat capacity of the kiln, and thus a large time constant during kiln start-up (Figure 6).

Table 2. Materials thermal properties of furnace (NASA, 1968).

Material	Density, kg/m³	Layer mean temp., °C	Mean thermal conductivity, W/m°C
Runcast BWM1	2600	1536	1.98
Protmix ZOR	170	1410	2.6
Promaform 1430	270	1249	0.34
Promaform 1260	390	720	0.14
Steel	7850	214	49
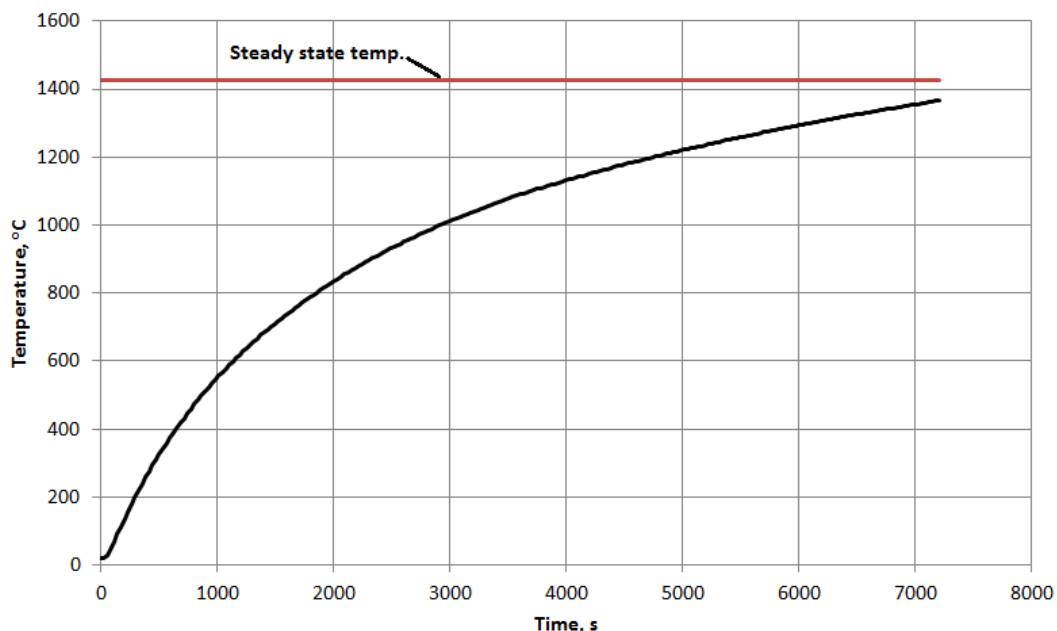
Fig. 6. Temperature at the boundary of Runcast BWM1 and Protmix ZOR layers.

4. Conclusions

Burning of hydrogen enriched fuel leads to increase in operating temperature (comparing to "traditional fuels") as well as in increase in water vapor content in the exhaust gases. The description of burner rig allowed to make a following conclusions:

- The design of used burner allows for using a mixture of traditional fuels (e.g. methane, LPG) and hydrogen with the H_2-content up to 50 volume %,
- Due to specific design of burner rig a strict control of temperature at each stage of the burner rig, flame shape and exhaust gases chemical composition is possible,
- The technological solutions applied in the burner rig allows for testing of the materials at different stages of it, i.e. inside the flame and behind it as well as in the zone of exhaust gases originated from burning of H_2-rich fuels. This in turn allows for better simulation of materials behavior used at different parts of the turbines and makes the newly developed equipment very flexible,
- Numerical modelling of temperature distribution showed significant decrease of temperature from 1674°C in the inside of burner rig to 214°C on steel housing.

References

Airbus (2023). *Could hydrogen fuel-cell systems be the solution for emission-free aviation?* Retrieved September 15, 2023, from https://www.airbus.com/en/newsroom/stories/2022-11-could-hydrogen-fuel-cell-systems-be-the-solution-for-emission-free

ASTM C 680–08 (2010). American Society for Testing and Materials. Standard practice for estimate of the heat gain or loss and the surface temperatures of insulated flat, cylindrical, and spherical systems by use of computer programs.

Banihabib, R., & Assadi, M. A. (2022). Hydrogen-fueled micro gas turbine unit for carbon-free heat and power generation. *Sustainability*, *14*, Article 13305. https://doi.org/10.3390/su142013305

Boeing (2010, July 14). Boeing's phantom eye ford fusion powered stratocraft. https://www.theregister.com/2010/07/13/phantom_eye_rollout/

Chen, K., Seo, D., & Canteenwalla, P. (2021). The effect of high-temperature water vapour on degradation and failure of hot section components of gas turbine engines. *Coatings*, *11*, Article 1061. https://doi.org/10.3390/coatings11091061

Chopinet, J. N., Lassoudière, F., Fiorentino, C., Alliot, P., Guedron, S., Supié, P., et al., (2011, October 3-7). Results of the Vulcain X technological demonstration. Proceedings of the 62nd International Astronautical Congress, 8, (pp. 6289-6298). International Astronautical Federation.

Churchill, S.W., & Chu, H. H. S. (1975). Correlating equations for laminar and turbulent free convection from a horizontal cylinder. *International Journal of Heat and Mass Transfer*, *18*(9), 1049-1053. https://doi.org/10.1016/0017-9310(75)90222-7

Cojocaru, M. O., Branzei, M., & Druga, L.N. (2022). Aluminide diffusion coatings on IN 718 by pack cementation. *Materials*, *15*, Article 5453. https://doi.org/10.3390/ma15155453

Cowing, K. (2012, October 16). Blue origin tests 100 k lb LOX/LH2 engine in commercial crew program. NewSpace Watch. http://archive.is/XtDg5

Decarbonization technology. Hydrogen gas turbine. (2023, September 11). https://solutions.mhi.com/power/decarbonization-technology/hydrogen-gas-turbine/

Deodeshmukh, V. P. (2013a). Long-term performance of high-temperature foil alloys in water vapor containing environment. Part I: Oxidation behavior. *Oxidation of Metals*, *79*, 567-578. https://doi.org/10.1007/s11085-012-9343-1

Deodeshmukh, V. P. (2013b). Long-term performance of high-temperature foil alloys in water vapor containing environment. Part II: Chromia vaporization behavior. *Oxidation of Metals*, *79*, 579-588. https://doi.org/10.1007/s11085-012-9344-0

England, D. M., & Virkar, A. V. (1999). Oxidation kinetics of some nickel-based superalloy foils and electronic resistance of the oxide scale formed in air part I. *Journal of The Electrochemical Society*, *146*(9), 3196–3202. https://doi.org/10.1149/1.1392454

England, D. M., & Virkar, A. V. (2001). Oxidation kinetics of some nickel-based superalloy foils in humidified hydrogen and electronic resistance of the oxide scale formed part II *Journal of The Electrochemical Society*, *148*(4), A330–A338. https://doi.org/10.1149/1.1354611

Essuman, E., Meier, G. H., Zurek, J., Hänsel, M., Norby, T., Singheiser, L., & Quadakkers, W. J. (2008). Protective and non-protective scale formation of NiCr alloys in water vapour containing high- and low-pO_2 gases. *Corrosion Science*, *50*(6), 1753–1760. https://doi.org/10.1016/j.corsci.2008.03.001

Girolamo, G. D., Brentari, A., & Serra, E. (2014). Morphology and microstructure of NiCoCrAlYRe coatings after thermal aging and growth of an Al_2O_3-Rich oxide scale. *Coatings*, *4*(4), 701-714. https://doi.org/10.3390/coatings4040701

Gnielinski, V. (1976). New equations for heat and mass transfer in the turbulent pipe and channel flow. International Chemical Engineering, 16(2), 359-368.

Golewski, P., & Sadowski, T. (2019). The Influence of TBC aging on crack propagation due to foreign object impact. *Materials*, *12*(9), Article 1488. https://doi.org/10.3390/ma12091488

Góral, M., Pytel, M., Ochal, K., Drajewicz, M., Kubaszek, T., Simka, W., & Nieuzyla, L. (2021). Microstructure of aluminide coatings modified by Pt, Pd, Zr and Hf formed in low-activity CVD process. *Coatings*, 11(4), Article 421. https://doi.org/10.3390/coatings11040421

Grilli, M. L., Valerini, D., Slobozeanu, A. E., Postolnyi, B. O., Balos, S., Rizzo, A., & Piticescu, R. R. (2021). Critical raw materials saving by protective coatings under extreme conditions: a review of last trends in alloys and coatings for aerospace engine applications. *Materials*, *14*(7), Article 1656. https://doi.org/10.3390/ma14071656

Hänsel, M., Quadakkers, W. J., Singheiser, L., & Nickel, H. (1998). Report Forschungszentrum Julich, Jul-3583, ISSN 0944-2952.

Hänsel, M., Quadakkers, W. J., & Young, D. J. (2003). Role of water vapor in chromia-scale growth at low oxygen partial pressure. *Oxidation of Metals*, *59*(3/4), 285-301. https://doi.org/10.1023/A:1023040010859

Holcomb G. R. (2008). Calculation of reactive-evaporation rates of chromia. *Oxidation of Metals*, *69*, 163-180. https://doi.org/10.1007/s11085-008-9091-4

Hydrogen fueled gas turbines. (2023, September 12). https://www.ge.com/gas-power/future-of-energy/hydrogen-fueled-gas-turb-nes?utm_campaign=h2&utm_medium=cpc&utm_source=google&utm_content=rsa&utm_term=Ge%20hydrogen%20turbines&gclid=CjwKCAiAheacBhB8EiwAItVO2z_lfkno6CHBFQBoXnpvzF9GlALjzAhJouUzlArw-J2vuC-Ncb_XsBoCKlsQAvD_BwE

Hydrogen gas turbine. The Turbotec HyTG-550. (2023, September 14). https://www.turbotec.be/hydrogen-gas-turbine/

Janakiraman, R., Meier, G. H., & Petit, F. S. (1999). The effect of water vapor on the oxidation of alloys that develop alumina scales for protection. *Metallurgical and Materials Transactions A*, 30, 2905-2913. https://doi.org/10.1007/s11661-999-0128-3

Kopec, M., Kukla, D., Yuan, X., Rejmer, W., Kowalewski, Z. L., & Senderowski, C. (2021). Aluminide thermal barrier coating for high temperature performance of MAR 247 nickel based superalloy. *Coatings*, *11*(1), 48. https://doi.org/10.3390/coatings11010048

Lele, A. (2014). GSLV-D5 success: a major "booster" to India's space program. *The Space Review*. http://www.thespacereview.com/article/2428/1

Marin, G. E., Mendeleev, D. I., & Osipov, B. M. (2021). A study on the operation of a gas turbine unit using hydrogen as fuel. Journal; of Physics: Conference Series, 1891, Article 012055. https://doi.org/10.1088/1742-6596/1891/1/012055

Maris-Sida, M. C., Meier, G. H., & Petit F. S. (2003). Some water vapor effects during the oxidation of alloys that are α-Al_2O_3 formers. *Metallurgical and Materials Transactions A*, *34*, 2609-2619. https://doi.org/10.1007/s11661-003-0020-5

Michalik, M., Hänsel, M., Zurek, J., Singheiser, L., & Quadakkers, W. J. (2005). Effect of water vapour on growth and adherence of chromia scales formed on Cr in high and low pO_2-environments at 1000 and 1050°C. *Materials and High Temperatures*, *22*(3-4) , 213-221. https://doi.org/10.1179/mht.2005.025

Moses, P. L., Rausch, V. L., Nguyen, N. T., & Hill, J. R.. (2004). NASA hypersonic flight demonstrators-overview, status, and future plans. *Acta Astronautica*, *55*(3-9), 619-630. https://doi.org/10.1016/j.actaastro.2004.05.045

Najjar, Y. S. H. (1990). Hydrogen fueled and cooled gas turbine engine. *International Journal of Hydrogen Energy*, *15*(11), 827-832. https://doi.org/10.1016/0360-3199(90)90019-U

NASA (1968) J-2 Engine fact sheet. *Saturn V News Reference*. Retrieved September 17, 2023, from http://www.nasa.gov/centers/marshall/pdf/499245mainJ2Enginefs.pdf

Nazari, M. A., Alavi, M. F., Salem, M., & El Haj Assad M. (2022). Utilization of hydrogen in gas turbines: acomprehensive review. *International Journal of Low-Carbon Technologies*, *17*, 513–519. https://doi.org/10.1093/ijlct/ctac025

Negoro, N., Ogawara, A., Onga, T., Manako, H., Kurosu, A., Yamanishi, N., Miyazaki, K., Hari, S., & Okita, K. (2007, July 8-11). Next booster engine LE-X in Japan. Proceedings of the 43rd AI-AA/ASME/SAE/ASEE Joint Propulsion Conference & Exhibit, Article AIAA 2007-5490. https://doi.org/10.2514/6.2007-5490

Nowak, W. J., Wierzba, P., Naumenko, D., Quadakkers, W. J., & Sieniawski, J. (2016). Water vapour effect on high temperature oxidation behaviour of superalloy Rene 80. Advances in Manufacturing Science and Technology, 40, 41-52. https://doi.org/10.2478/amst-2016-000

Onal, K., Maris-Sida, M. C., Meier, G. H., & Pettit, F. S. (2004). The effects of water vapor on the oxidation of nickel-base superalloys and coatings at temperatures from 700°C to 1100°C. *Superalloys*, 607-615.

Opila, E. J., Mayers, D. L., Jacobson, N. S., Nielsen, I. M. B., Johnson, D. F., Olminsky, J. K., & Allendorf, M. D. (2007). Theoretical and experimental investigation of the thermochemistry of $CrO_2(OH)_2(g)$. *Journal of Physical Chemistry A*, *111*(10), 1971-1980. https://doi.org/10.1021/jp0647380

Pędrak, P., Dychtoń, K., Drajewicz, M., & Góral, M. (2021). Synthesis of $Gd_2Zr_2O_7$ coatings using the novel reactive PS-PVD Process. *Coatings*, *11*(10), Article 1208. https://doi.org/10.3390/coatings11101208

Pędrak, P., Góral, M., Dychton, K., Drajewicz, M., Wierzbinska, M., & Kubaszek, T. (2022). The influence of reactive PS-PVD process parameters on the microstructure and thermal properties of $Yb_2Zr_2O_7$ thermal barrier coating. *Materials*, *15*(4), Article 1594. https://doi.org/10.3390/ma15041594

Pujilaksono, B., Jonsson, T., Halvarsson, M., Panas, I., Svensson, J. E., & Johansson, L. G. (2008). Paralinear oxidation of chromium in O_2 + H_2O environment at 600-700°C. *Oxidation of Metals*, *70*, 163-188. https://doi.org/10.1007/s11085-008-9114-1

Pyo, M.-J., Moon, S.-W., & Kim, T.-S. (2021). A comparative feasibility study of the use of hydrogen produced from surplus wind power for a gas turbine combined cycle power plant. *Energies*, *14*(24), Article 8342. https://doi.org/10.3390/en14248342

Qiu, S.-Y., Wu, C.-W., Huang, C.-G., Ma, Y., & Guo, H.-B. (2021). Microstructure dependence of effective thermal conductivity of EB-PVD TBCs. *Materials*, *14*(8), 1838. https://doi.org/10.3390/ma14081838

Quaddakers, W. J., Norton, J. F., Canetoli, S., Schuster, K., & Gil, A. (1996). In S. B. Newcomb, J. A. Little, (Eds.); 3rd International Conference on Microscopy of Oxidation (pp. 609-619). The Institute of Materials.

Rachuk, V., Goncharov, N., Martinyenko, Y., & Fanciullo, T. (1996, July 1-3). Evolution of the RD-0120 for future launch systems. Proceedings of the 32nd Joint Propulsion Conference and Exhibit Article 96-3004. https://doi.org/10.2514/6.1996-3004

Renouard-Vallet, G., Kallo. J., Saballus, M., Schmithals, G., Schirmer, J., & Friedrich, K.A. (2011). Fuel cells for aircraft applications. *ECS Transactions*, *30*, 271-280. https://doi.org/10.1149/1.3562482

Report 2555-M-1-F. (1967). *Development of a 1,500,000-lb-thrust (nominal vacuum) liquid hydrogen/liquid oxygen engine.* (August 1967). Retrieved September 16, 2023, from http://alternatewars.com/BBOW/Space_Engines/1967_M-1_Final_Report.pdf

Rich, B.R. (1973, May 15-16). Lockheed CL-400 liquid hydrogen fueled Mach 2.5 reconnaissance vehicle. Symposium on hydrogen fueled aircraft.

Schütze, M., & Quadakkers, W. J. (2017). Future directions in the field of high-temperature corrosion research. *Oxidation of Metals*, *87*, 681–704. https://doi.org/10.1007/s11085-017-9719-3

Smialek, J. L. (2010). Moisture-induced alumina scale spallation: The hydrogen factor. Report NASA/TM-2010-216260 (pp. (1-31).Retrieved September 4, 2023, from https://ntrs.nasa.gov/api/citations/20100021167/downloads/20100021167.pdf

Southern Co. Gas-fired demonstration validates 20% hydrogen fuel blend. (2023, September 13). https://www.powermag.com/southern-co-gas-fired-demonstration-validates-20-hydrogen-fuel-blend/

Stanislowski, M., Froitzheim, J., Niewolak, L., Quadakkers, W. J., Hilpert, K., Markus, T., & Singheiser L. (2007). Reduction of chromium vaporisation from SOFC interconnectors by highly effective coatings. *Journal of Power Sources*, *164*(2), 578-589. https://doi.org/10.1016/j.jpowsour.2006.08.013

Stefan, E., Talic, B., Larring, Y., Gruber, A., & Peters, T. A. (2022). Materials challenges in hydrogen-fuelled gas turbines, International Materials Reviews, 67(5), 461-486. https://doi.org/10.1080/09506608.2021.1981706

Suzuki, M., Shahien, M., Shinoda, K., & Akedo, J. (2022) The current status of environmental barrier coatings and future direction of thermal spray process. *Materials Transactions*, 63(8), 1101-1111. https://doi.org/10.2320/matertrans.MT-T2021003

Tan, Y.H. (2013). Research on large thrust liquid rocket engine. *Yuhang Xuebao/Journal of Astronautics*, *34*(10), 1303-1308. http://dx.doi.org/10.3873/j.issn.1000-1328.2013.10.002

Tupolev, A.A., (1994). Utilization of liquid hydrogen or liquid natural gas as an aviation fuel. In R. E. Billings, E. Dayton (Eds.). *Conference proceedings, Project Energy* (p. 104). International Academy of Sciences.

Vassen, R., Bakan, E., Gatzen, C., Kim, S., Mack, D.E., & Guillon, O. (2019). Environmental barrier coatings made by different thermal spray technologies. *Coatings*, *9*(12), Article 784. https://doi.org/10.3390/coatings9120784

Wang, C., Liu, M., Feng, J., Zhang, X., Deng, C., Zhou, K., Zeng, D., Guo, S., Zhao, R., & Li, S. (2020). Water vapor corrosion behavior of Yb_2SiO_5 environmental barrier coatings prepared by plasma spray-physical vapor deposition. *Coatings*, *10*(4), 392. https://doi.org/10.3390/coatings10040392

Westenberger, A. (2002). Liquid hydrogen fuelled aircraft-system analysis. Final technical report 2002.

Westenberger, A. (2003). Liquid hydrogen fuelled aircraft-system analysis. Final technical report (publishable version). Cryoplane project, 2003.

Wilhelm, W. F. (1972). Space shuttle orbiter main engine design. *Society of Automotive Engineers Transactions*, *81*, Article 72 0807.

Winter, C. J. (1990). Hydrogen in high speed air transportation. *International Journal of Hydrogen Energy*, *15*(8), 579-595. https://doi.org/10.1016/0360-3199(80)90006-3

Zakeri, A., Bahmani, E., & Ramazani, A. (2022). A review on the enhancement of mechanical and tribological properties of MCrAlY coatings reinforced by dispersed micro and nanoparticles. *Energies*, *15*(5), 1914. https://doi.org/10.3390/en15051914

Zero emission hydrogen turbine center. (2023, September 12). https://www.siemens-energy.com/global/en/priorities/future-technologies/hydrogen/zehtc.html

Żurek, J., Young, D. J., Essuman, E., Hänsel, M., Penkalla, H. J., Niewolak, L., & Quadakkers, W. J. (2008). Growth and adherence of chromia based surface scales on Ni-base alloys in high- and low-pO_2 gases. *Materials Science and Engineering A*, *477*(1-2), 259-270. https://doi.org/10.1016/j.msea.2007.05.035

Charakterystyka badawczego stanowiska palnikowego zasilanego paliwem wodorowym dedykowanego do badań materiałów

Streszczenie

Głównym celem niniejszego artykułu jest przedstawienie stanowiska palnikowego nowo opracowanego na Politechnice Rzeszowskiej. Palnik przeznaczony jest do pracy na paliwach bogatych w wodór. Palnik może pracować z paliwami o zawartości wodoru do 50% obj. Przedstawiono szczegółowy opis budowy stanowiska palnika. Zaprezentowano także model matematyczny przewidujący rozkład temperatury w komorze spalania. Uzyskane wyniki wykazały dobrą izolację konstrukcji palnika, co doprowadziło do powstania gradientu temperatury od 1674°C w korpusie palnika do 214°C na obudowie stalowej.

Słowa kluczowe: paliwo wodorowe; stanowisko badawcze; korozja gazowa, para wodna, materiały żaroodporne.

Original Research

Analysis of High Temperature Oxidation Characteristic of Chrome-Plated, Nickel-Plated and Non-Plated Mild Steels

Atalay Alemayehu [1] , Eaba Beyene [2] , Temesgen Batu [2,*] , Dagim Tirfe [2]

[1] Centre of Biotechnology, Institute of Research and Development, Ethiopian Defence University, Bishoftu, Hora Lake Bishoftu, 1041, Ethiopia; atalayalemayehu@gmail.com

[2] Centre of Armament and High Energy Materials, Institute of Research and Development, Ethiopian Defence University, Bishoftu, Hora Lake Bishoftu, 1041, Ethiopia; beyene.eaba@yahoo.com (E. Beyene), dagimasegidtirfe0286@gmail.com (D. Tirfe)

* Correspondence: temesgen.batu@kiot.edu.et

Abstract

Metals are the best engineering materials owing to their superior conductivity, mechanical properties, and formability. However, they can be highly affected by environmental elements like oxygen, chlorine, etc. This reaction of metals with the environmental elements will indeed alter their electrical, chemical, and mechanical properties. To protect against corrosion, various protection methods such as electroplating have been established. The presence of anodic or cathodic films on the substrate surface protects steel from corrosion damage at ambient atmospheric temperature. This work focuses on the effect of temperature on the oxidative (corrosion) rate of non-plated, nickel-plated, and chrome-plated ASTM A283GC mild steel samples. A temperature range of 200–800 °C and a total heating time of 120 min were considered in this experiment. A temperature-regulated muffle furnace with a maximum heating capacity of 1000 °C has been used. Weight changes were determined every 30 minutes of heating using a digital weight balance with a precision of 0.001 g. The obtained experimental results of non-plated, nickel-plated, and chrome-plated mild steel samples were analyzed and compared with each other. The effect of oxidation on the surface hardness has also been studied with the help of a Vickers hardness testing machine. Changes in the physical nature of the samples caused by oxidation were also observed and pictured.

1. Introduction

Corrosion is surface degradation of metals which damages its properties and performance. It is a major operating problem that takes place in gas turbines, diesels engines, furnaces and other machinery components that come in contact with hot gas containing oxygen and other contaminants (Frankel, 1998). The metal atoms that are exposed to the corrosive environment are the ones that will encounter the damage along with the atoms surrounding them to undergo chemical reaction which will result corroded surface. Some of the reacting elements that can cause corrosion may go deep into the substrate through porous surface film to a limited thickness beneath the surface and react with the subsurface atoms of the substrate. This surface deterioration of metals may depend on the type of the metal substrate and the reacting elements (Maurice & Marcus, 2018). The exposure of metals to corrosive environment results to an appreciable mass loss, which increases with increasing duration of exposure (Apostolopoulos & Papadakis, 2008).

Some metals, like aluminium by nature have higher corrosion resistance. But huge volumes of metals notably iron and steel, used in designs and structures are damaged by various forms corrosion, including dry and wet corrosion (Lu, 2010). Because of this developed nations are yearly investing billions of dollars to protect metals from oxidative damage by developing and applying various prevention methods such as (Aliofkhazraei, 2014; Hou et al., 2017). Protection methods are applied to

increase the working life of the metals and are assumed to play a great role at an ambient atmospheric temperature in dry as well as wet season (McMahon, 2019).

The average pace at which a certain material will degrade owing to corrosion in a given environment is the definition of a substance's corrosion rate. This rate is influenced by the material's characteristics as well as the environment it is subjected to. Corrosion rate might be facilitated or speed up by environmental conditions such as temperature and humidity. Different materials have different resistance and susceptibility to corrosion. The rate of oxidation of metals may depend on the type of metals (Andrade & Alonso, 2001).

Corrosion can be influenced by various parameters including: strength and concentration of the reactants as well as temperature. For a given type of metal, the rate of corrosion is assumed to increase with concentration of the reactants and temperature. These protective coating however are assumed to play a greater protection role at an ambient atmospheric temperature in dry as well as wet season. At higher working temperature, it is deemed that these coatings may also play a role in protecting the substrate surface from corrosion. But the ability of the coating in protecting corrosion at a higher working temperature is not assumed to be the same with that of the lower working temperature. The methods will reduce to some extent the corrosion rate, if not like that of lower temperature case (North & MacLeod, 1987; Young, 2008).

For various coating applications, a wide range of coating techniques and materials are available with the shared objective of shielding a component or structure from mechanical or chemical harm. One of the dominant coating techniques is electroplating. Electroplating is the process of applying a metallic coating to an article by passing an electric current through an electrolyte in contact with the metal to be plated, thereby forming a surface having properties different from the substrate. The process is considered as one of the largely used electro deposition processes and is essentially used to electroplate any electrically conductive surface and nonconductive surfaces, such as plastic by making conductive layer through coating with metallic-loaded paints or silver-reduced spray. Both the cathode and the anode components are immersed in a solution called electrolyte containing one or more dissolved metal salts as well as other ions that permit the flow of electricity. The electrodes are immersed in the electrolyte with the anode connected to the positive leg of the power supply and the cathode to the negative leg. As the current is increased from zero, a point is reached where metal plating begins to occur on the cathode (Fotovvati et al., 2019; Kanani, 2004; Ojo & Dharmadasa, 2018). A desired metal's cations are reduced in solution by the electroplating method, which uses an electrical signal from an external power source to create a metallic coating (Chen et al., 2013). An electrolyte is a compound which forms ions in solution. Electrolytes include water solutions of acids, bases, or metal salts, certain pure liquids, and molten salts. Gases may act as electrolytes under conditions of high temperature or low pressure. In addition to metal salts, electrolytes usually contain a number of additives for various purposes for example: to increase electrolyte conductivity, to increase bath stability, to activate the surface, to improve leveling or metal distribution, or to optimize the chemical, physical, or technology properties of the coating (Samui & Sivaraman, 2010; Zhang et al., 2016).

A study done by Wang et al. (2015) analyzed the coating of copper surfaces with a single-phase Ni_2Al_3 by electrodepositing nickel, followed by slurry pack aluminizing at 800 °C for 12 hours. The oxidation resistance of the coating was identified by examining the fluctuations in mass gain vs. time. After slow oxidation of the coated copper for 250 hours at 1000 °C, there was no exfoliation of the protective Al_2O_3 scale, and the mass gain was 10.108 mg/cm^2. This study follows the same characterizing technique to analyze the oxidation property.

Hardness testing is usually performed to evaluate the mechanical characteristics of thin surface. This test procedure uses a single-point contacts, a diamond pyramid for measuring micro-hardness, and typically a diamond cone for measuring scratch resistance by causing plastic deformation on the substrate and coating's surface (Burnett & Rickerby, 1987). The relationship between relative indentation depth and the hardness of a coated system during indentation has been extensively investigated that the penetration should be less than 10% of the coating thickness to obtain coating hardness independent of the substrate (Burnett & Rickerby, 1987).

The high-temperature oxidation behavior of iron and steel alloys has been a subject of extensive research (Chen & Yeun, 2003). Studies have explored the kinetics and mechanisms of oxidation, shedding light on the formation of oxide scales and their impact on the material's performance at elevated temperatures (Chen & Yeun, 2003; Ma et al., 2023). Nickel, recognized for its intrinsic corrosion resistance, is often alloyed with iron to improve the oxidation resistance of steels in aggressive environments (Klapper et al., 2017). Furthermore, nickel-plated surfaces have been investigated for

their ability to provide an additional layer of protection against high-temperature oxidation (Weinstein et al., 2021).

Chromium, another essential alloying element, exhibits remarkable resistance to oxidation, forming a stable and adherent chromium oxide layer on the surface (Mehtani et al., 2021). Chrome-plated mild steels have demonstrated enhanced resistance to high-temperature oxidation, making them valuable in applications where prolonged exposure to elevated temperatures is a concern (Akhtar et al., 2023). Research efforts have been directed towards understanding the nuances of chromium's role in mitigating oxidation and its effectiveness in diverse environmental conditions (Lunk, 2015).

The following work was performed to study the high temperature oxidation characteristics of nickel-plated, chrome-plated and non-plated mild steel.

2. Materials and methods

2.1. Materials

This study utilized ASTM A283GC mild steel, nickel, and chromium samples, along with an electroplating device under specific operational conditions. The electrolyte, hardness furnace, tester, and spark emission spectroscopy were obtained from the Dejen Aviation Engineering Industry (Ethiopia).

2.2. Methods

The samples utilized in this experiment were prepared, electroplated, and examined at the Dejen Aviation Engineering Industry (Ethiopia). The mild steel substrates were also collected from the same industry, ensuring uniform thickness and coating thickness for all samples. Each sample had dimensions of 4 mm × 25 mm × 25 mm. In this study, the oxidation behavior of chrome-plated, nickel-plated, and non-plated mild steel was investigated at elevated temperatures. The oxidation tests were conducted at 200, 400, 600, and 800 °C using a muffle furnace with a maximum heating capacity of 1000 °C. The increase in weight, considered as a reference for oxidation behavior, was measured during the experiment using a precision weight balance with an accuracy of 0.001 g. The weight of each sample was recorded every 30 minutes, and the resulting increase in weight (Δw) was documented and analyzed.

2.2.1. Elemental analysis

The elemental analysis of the initial sample (ASTM A283GC mild steel) used in the oxidation study was conducted using spark emission spectroscopy at the Dejen Aviation Complex (Ethiopia). The obtained results have been tabulated in Table 1.

Table 1. Chemical composition of mild steel.

Element	C	Si	Mn	P	S	Cr	Mo	Ni	Cu	W	Fe
Composition in wt.%	<0.05	0.02	0.29	0.02	0.013	0.043	0.012	0.032	0.051	0.10	99.03

As presented in the web page Mild Steel (2023), the chemical compositions of mild steel in the standard value are listed as follows: carbon (0.16–0.18%), silicon (0.40% max.), manganese (0.70-0.90%), sulfur (0.040% max.), and phosphorus (0.040% max.).

The three elements are phosphorus and sulfur, and the major element is iron (Fe). The percentage composition of the test sample of mild steel is given in Table 1. As can be observed from the Table, the composition of the steel is generally different from the standard value. The standard value of carbon is 0.16–0.18%. The practical chemical composition analysis of mild steel shows that C is < 0.05% or dead steel, and other elements are reduced, like phosphorus (0.02%), manganese (0.02%), and silicon (0.013%).

2.2.2. Samples preparation method

The first step is to prepare mild steel samples of size 4 mm × 25 mm × 25 mm using a cutting machine. The second step involves cleaning the samples to remove dust, oil, and grease by degreasing and using other removal methods like polishing. After cleaning, the mass of each steel sample was determined using a weight measurement balance. A total of 12 samples were prepared for the experi-

ment. Subsequently, mild steel was chrome-plated and nickel-plated. Parameters of the plating process are listed in Tables 2 and 3. The experiments were carried out at the Dejen Aviation Engineering Industry in Ethiopia. Initial weight of chrome-plated, nickel-plated and non-plated samples is listed in Table 4.

Following the plating process, the samples were subjected to high-temperature oxidation to investigate their behavior. The change in weight of the samples was then measured. Additionally, the microstructure of the samples was observed, and a hardness test was performed.

Table 2. Parameters of the chrome plating process.

S/N	Chemical name / Parameter	Molecular formula	Concentration and specification
1	Anyhdride chromic acid	CrO_3	• Composition of solution 140–180 g/dm³, • Red dark flakes (plates form).
2	Sulphuric acid	H_2SO_4	• Composition of solution 1.5–2.2 g/dm³, • Specific gravity 1.84, • Density 1840 g/m³.
3	PH	-	3.8-4.2
4	Bath cathodic current density	-	10-25 A/dm²
5	Parameters Temperature	-	55-68 °C
6	Voltage	-	4-12 V
7	Preheating time	T	10 min

Table 3. Parameters of the nickel plating process.

S/N	Chemical name /Parameter	Molecular formula	Value
1	Sodium hydrated	NaOH	46.212
2	Nickel sulfate	$NiSO_4.H_2O$	89 g/dm³
3	Boric acid	H_3BO_3	45 g/dm³
4	Wetting agent	-	0.3 %vol./dm³
5	Total solution volume	-	70 dm³
6	Plating bath temperature	-	50 °C
7	PH	-	4.5–5.0
8	Bath cathodic current density	-	7–40 mA/cm²

Table 4. Initial weight of chrome-plated, nickel-plated and non-plated samples.

Samples	Weight of chrome-plated sample, g	Weight of nickel-plated sample, g	Non-plated sample weight, g
Sample 1	19.400	19.000	17.623
Sample 2	19.223	19.222	17.524
Sample 3	19.348	19.129	17.591
Sample 4	19.185	18.890	17.278

2.3. Oxidation process

The oxidation properties of the samples were measured based on the work by a Wang et al. (2015). In this study, we measured the initial thickness of the samples and studied the change in weight that occurred in non-plated, chrome-plated, and nickel-plated mild steel due to oxidation when heat-treated at 200 °C, 400 °C, 600 °C, and 800 °C at discrete intervals of time.

The tests were conducted at the Dejen Aviation Engineering Industry using micro test, a versatile and sophisticated thickness tester capable of measuring almost all electroplated metals on ferrous, non-ferrous, and non-metallic substrates. It can measure multiple coatings and provide individual readings. Table 5 displays the initial thickness of the samples.

Table 5. Thickness of plating.

Chrome-plated sheet	Thickness of plating, µm	Nickel-plated sheet	Thickness of plating, µm
Sample 1	12.5	Sample 1	11
Sample 2	12	Sample 2	9.5
Sample 3	9	Sample 3	9
Sample 4	11.5	Sample 4	10

2.4. Hardness measurement

The Vickers hardness test is a widely used method to determine the hardness of materials. To perform the test, first, ensure that the Vickers hardness tester is properly calibrated and in good working condition. The procedure of the hardness measurement was as follows:

1) Place the specimen on a flat and stable surface and select the appropriate scale based on the material's hardness.
2) Gently lower the indenter onto the material's surface to make initial contact, then zero the scale using the zero-adjustment dial.
3) Apply the initial minor load, followed by the main or major load specific to the scale being used.
4) Allow the major load to dwell for about 15 seconds, then release it while keeping the minor load applied.
5) Read the hardness value directly from the Vickers hardness tester's scale.
6) Take multiple measurements at different locations on the material for accuracy, and calculate the average hardness value.
7) Follow the manufacturer's instructions for your specific Vickers hardness tester model to ensure accurate and reliable results.

3. Result and Discussion

3.1. Microstructure

The original non-plated mild steel sample has been polished to achieve its mirror finish using various grades of polishing papers. Subsequently, the polished sample was examined using inter-phased optical microstructure analysis (Fig. 1), revealing the absence of phases other than ferrite.


**Fig. 1.** Microstructure of mild steel.

An attempt was also made to observe the changes in their physical states, such as color changes that may appear after the samples were heated to various temperatures for a total time of 120 minutes. Camera pictures were taken in both post-heating and pre-heating conditions. As can be seen in Figs. 2–5, a radical change in color was observed on the non-plated mild steel surface at temperatures beyond 600 °C and above. The color changed from grey (before heating) to dark brown (after heating). Notably, at 800 °C, the oxide layer of the mild steel sample was observed to flake off easily even by touch. However, this flaking-off problem was not observed in the nickel-plated and chrome-plated mild steel samples.
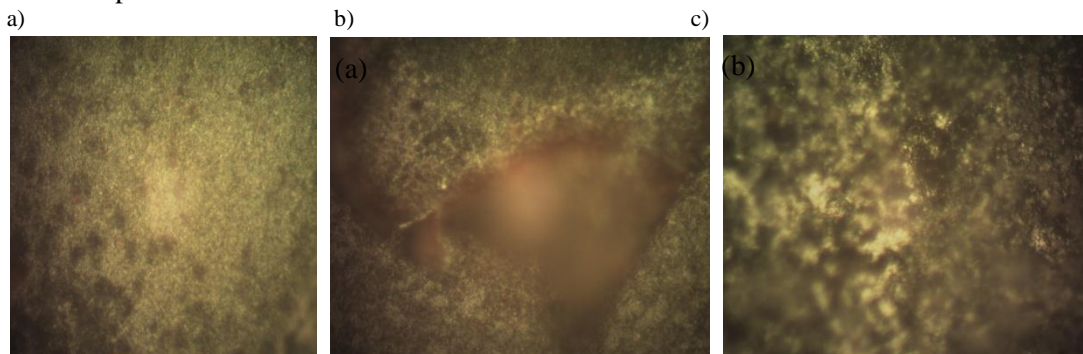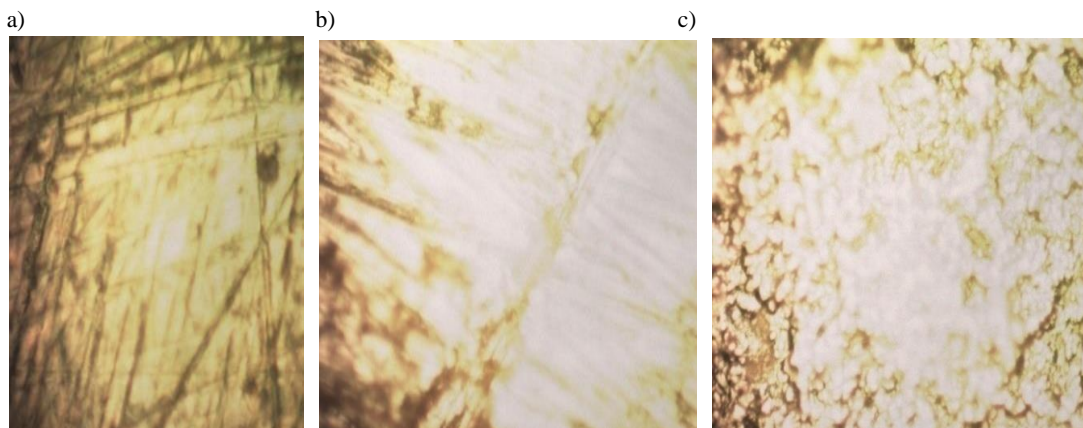

Fig. 2. Surface morphology of a) nickel-plated and b) chrome-plated and c) non-plated mild steel, oxidized at 800 °C for 120 min in unpolished condition.

a)   b)   c)
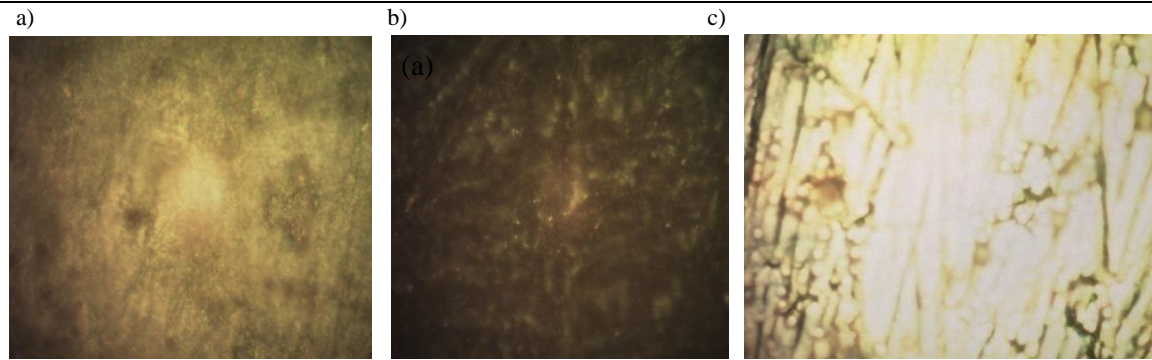
Fig. 3. Surface morphology of a) nickel-plated, b) chrome-plated and c) non-plated mild steel, oxidized at 600 °C for 120 min in unpolished condition.

a)   b)   c)
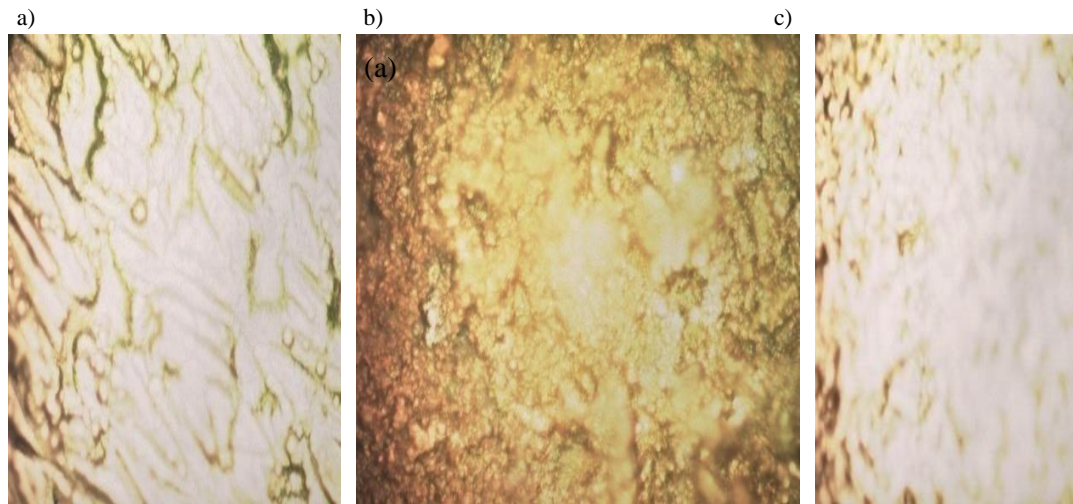
Fig. 4. Surface morphology of a) nickel-plated, b) chrome-plated and c) non-plated mild steel, oxidized at 400 °C for 120 min in unpolished condition.

a)   b)   c)

Fig. 5. Surface morphology of a) nickel-plated, b) chrome-plated and c) non-plated mild steel, oxidized at 200 °C for 120 min in unpolished condition.

3.2. Effect of change in weight in high temperature oxidation

Various temperatures, i.e., 200 °C, 400 °C, 600 °C, and 800 °C, have been selected for conducting oxidation studies on non-plated, chrome-plated, and nickel-plated mild steel samples. A total time of 120 minutes was considered for all three samples, including both plated and non-plated ones. Weight measurements were conducted every 30 minutes, and the variations of oxidation with respect to temperature and time are presented graphically for the three mentioned samples.

For the hot temperature corrosion studies, four samples from each type (non-plated, nickel-plated, and chrome-plated) were considered, and these samples were prepared to have similar surface areas. Before heating, the original weight of each sample was measured using a 0.1 mg precision balance.

All the mentioned samples were heated at various holding temperatures (200 °C, 400 °C, 600 °C, 800 °C) for a total heating time of 120 minutes. To determine the weight changes, the heating was interrupted every 30 minutes, during which the hot sample was gently removed from the muffle furnace using stainless steel tongs. The hot samples were allowed to cool to ambient atmospheric temperature before measuring their weight. The weight measurements of the samples are presented in Table 5.

Table 5. Experimental results for high temperature oxidation.

Materials	T, °C	w_0, g	w_1, g	ΔW_1, %	w_2, g	ΔW_2, %	w_3, g	ΔW_3, %	w_4, g	ΔW_4, %
Non-plated mild steel		17.6256	17.6258	0.0008	17.6261	0.0023	17.6266	0.0036	17.6273	0.0075
Chrome-plated	200	19.3987	17.3987	0	19.3991	0.00206	19.3993	0.00309	19.3995	0.0041
Nickel-plated		18.9986	18.9986	0	18.9993	0.0037	18.9998	0.0063	19.0001	0.0079
Non-plated mild steel		17.5241	17.5243	0.001	17.5252	0.0063	17.5260	0.0108	17.5261	0.011
Chrome-plated	400	19.2229	19.2230	0.00052	19.2235	0.00312	19.2236	0.0036	19.2238	0.0047
Nickel-plated		19.2224	19.2226	0.00104	19.2233	0.00468	19.2237	0.00676	19.2241	0.00884
Non-plated mild steel		17.5907	17.6008	0.057	17.6025	0.067	17.6038	0.0745	17.6054	0.08356
Chrome-plated	600	19.3470	19.3477	0.0036	19.3483	0.00672	19.3491	0.0108	19.3497	0.0139
Nickel-plated		19.1285	19.1290	0.0026	19.1299	0.00732	19.1307	0.0115	19.1313	0.0146
Non-plated mild steel		17.2780	19.3920	0.659	17.4183	0.812	17.4308	0.8843	17.4405	0.9405
Chrome-plated	800	19.1853	19.1877	0.0125	19.1881	0.0146	19.1884	0.016	19.1887	0.0177
Nickel-plated		18.8897	18.9068	0.0905	18.9139	0.127	18.9199	0.1598	18.9240	0.1799

Weight increase ΔW_1–ΔW_4 has been determined according to Eqs. (1)–(4):

$$\Delta W_1 = \frac{w_1 - w_0}{w_o} \times 100\% \tag{1}$$

$$\Delta W_2 = \frac{w_2 - w_0}{w_o} \times 100\% \tag{2}$$

$$\Delta W_3 = \frac{w_3 - w_0}{w_o} \times 100\% \tag{3}$$

$$\Delta W_4 = \frac{w_4 - w_0}{w_o} \times 100\% \tag{4}$$

where: w_0 is weight of non-plated sheet, w_1 is weight of sample after heating for 30 minutes, w_2 is weight of sample after heating for 60 minutes, w_3 is weight of sample after heating for 90 minutes and w_4 is weight of sample after heating for 120 minutes.

3.3. Oxidation behavior of non-plated mild steel

As shown in Figs. 6a)-6d) for the non-plated steel sample under constant given temperatures, oxidation increases with time. This increase in oxidation is manifested by an increase in the weight of the sample. The effect of temperature on weight change is presented graphically in Fig. 7. It is evident from this graph that temperature has a significant influence on corrosion. Upon comparison, it is observed that for any given time, higher temperatures result in greater weight change (oxidation) of the non-plated steel sample.
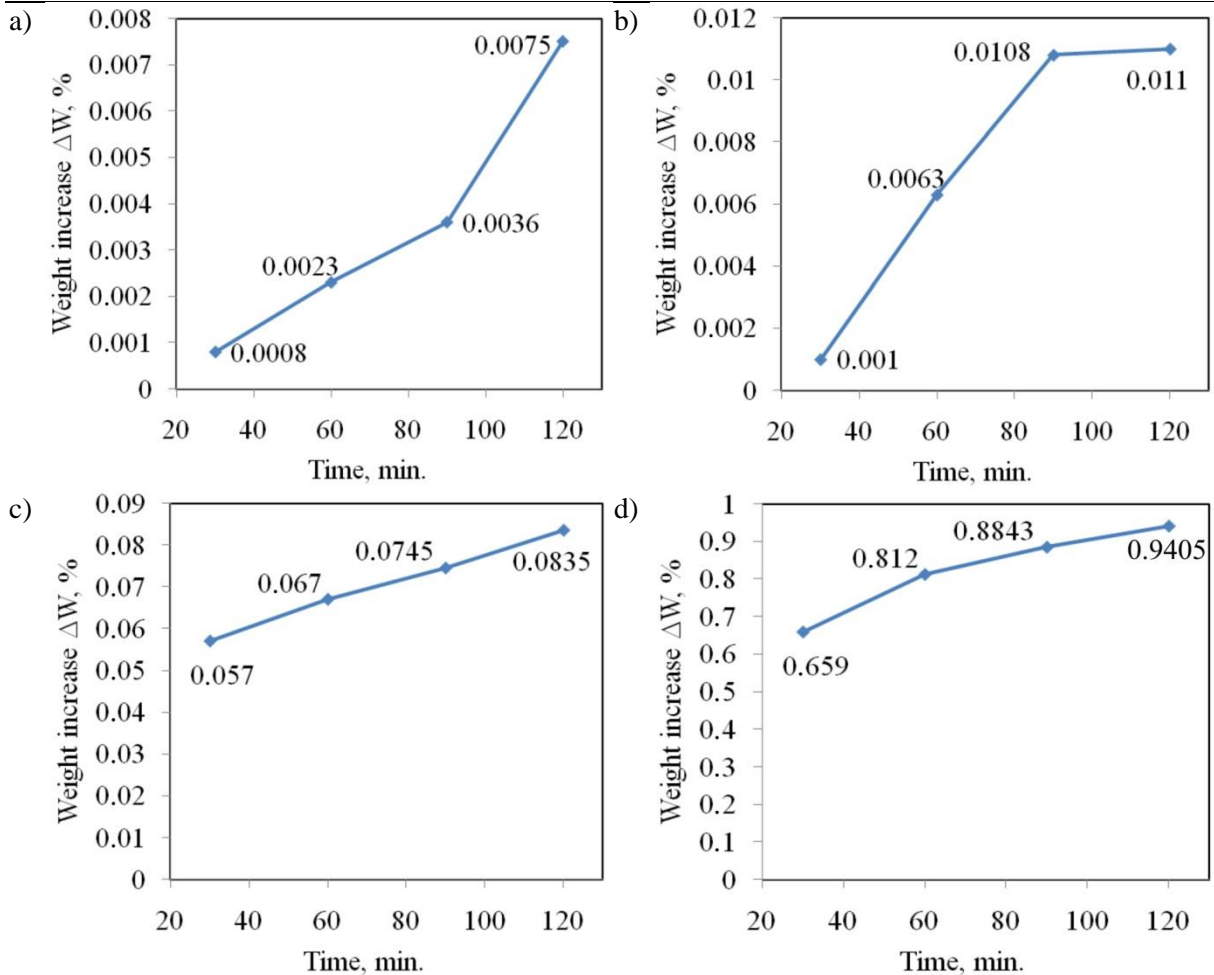
Fig. 6. Variation of oxidation with time for non-plated mild steel: a) T = 200 °C, b) T = 400 °C, c) T = 600 °C and d) T = 800 °C.
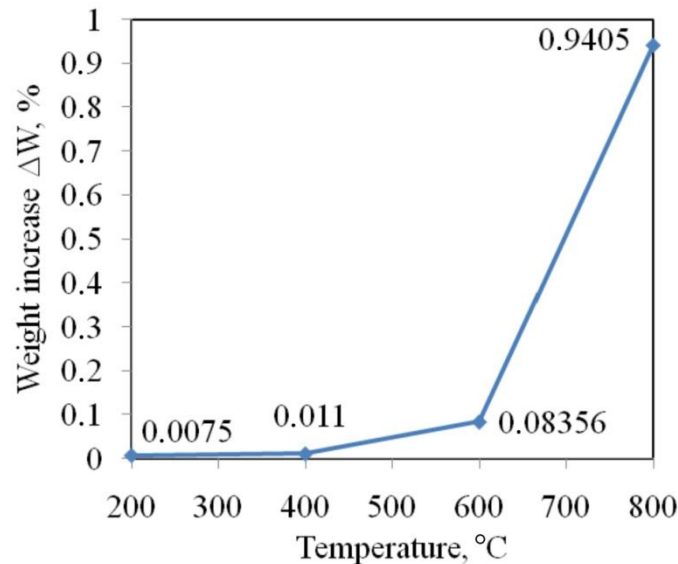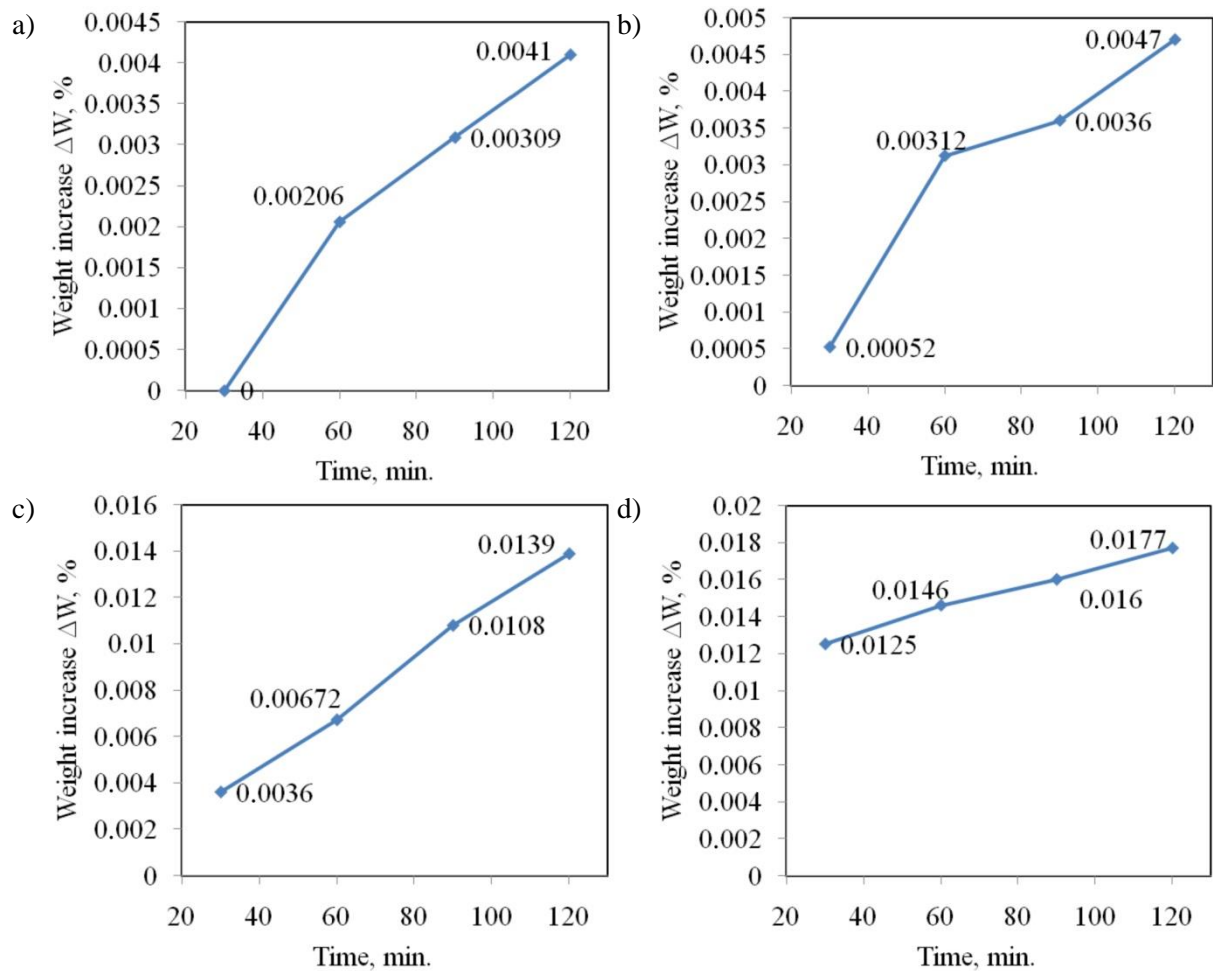

Fig. 7. Variation of oxidation with temperature for non-plated steel (time t = 120 min.).
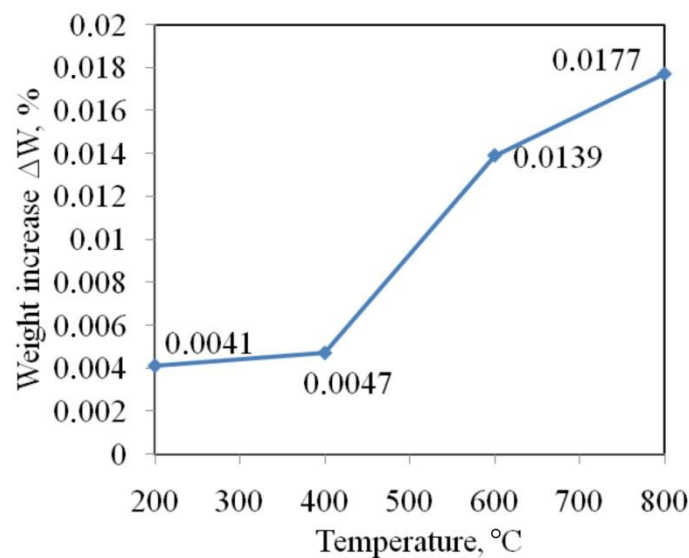
3.3.1. Oxidation behavior of chrome-plated mild steel

Effect of time and temperature on oxidation behaviour of chrome-plated mild steel sample is shown graphically in Figs. 8a)-8d). The experimental result indicates that oxidation behaviour of chrome-plated mild steel increases with time. The experimental result also testifies the strong dependence of oxidation rate on temperature. Moreover, the rate of oxidation increases with temperature Fig. 9.
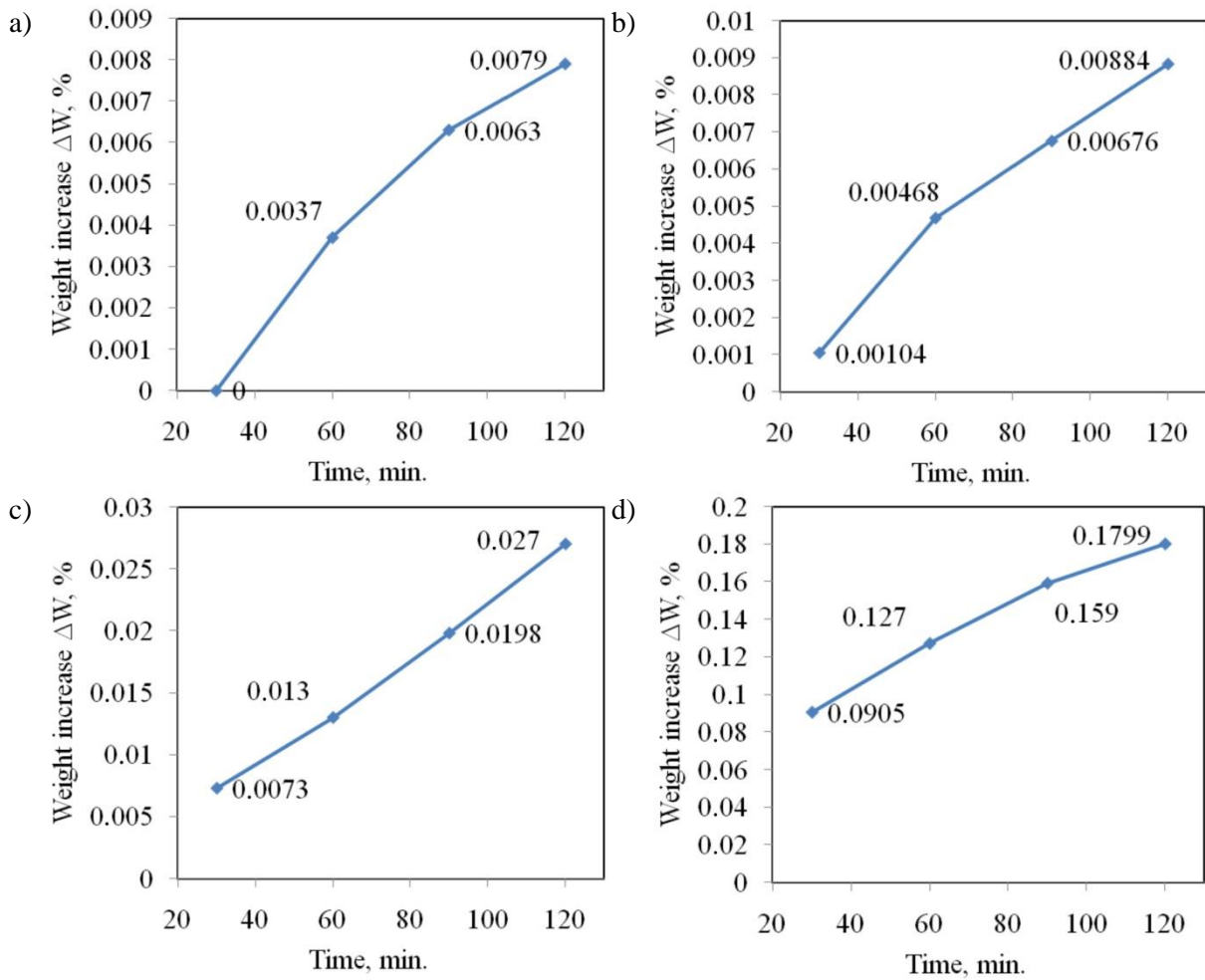
Fig. 8. Variation of oxidation with time for chrome-plated steel: a) T = 200 °C, b) T = 400 °C , c) T = 600 °C and d) T = 800 °C.
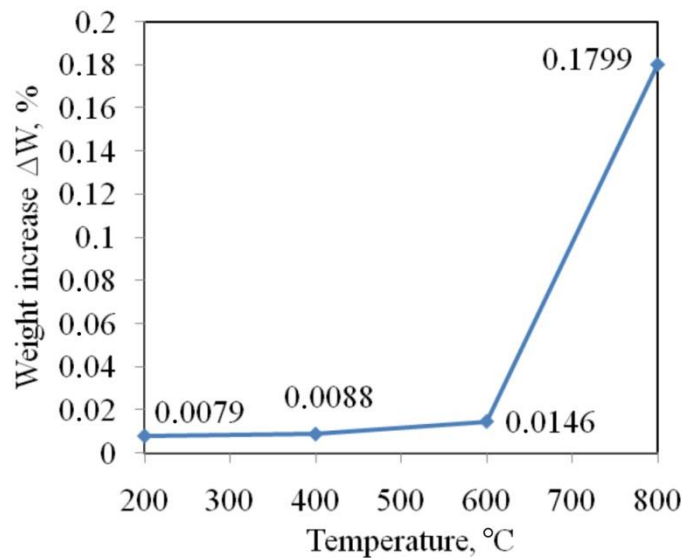

Fig. 9. Variation of oxidation with temperature for chrome-plated steel (time t = 120 min.).

3.3.2. Oxidation behavior of nickel-plated mild steel

The experimental results of the high-temperature oxidation study of nickel-plated mild steel are presented graphically in Figs. 10a)-10d). The oxidation behavior in nickel-plated mild steel is analogous to that of chrome-plated mild steel. The graphical results demonstrate that the oxidation behavior of nickel-plated steel increases with both time and temperature, as shown in Fig. 11.

Fig. 10. Variation of oxidation with time for nickel-plated steel: a) T = 200 °C, b) T = 400 °C , c) T = 600 °C and d) T = 800 °C.

Fig. 11. Variation of oxidation with temperature for nickel-plated steel (time t = 120 min.).

3.3.3. Comparison of oxidation behavior of samples

The oxidation behaviors of the three samples, heated at the same temperature and for the same duration, have been compared with each other. The oxidation versus time relationship for all three samples (non-plated, chrome-plated, and nickel-plated samples) at a given temperature has been plotted in one graph, as shown in Figs. 12a)-12d).
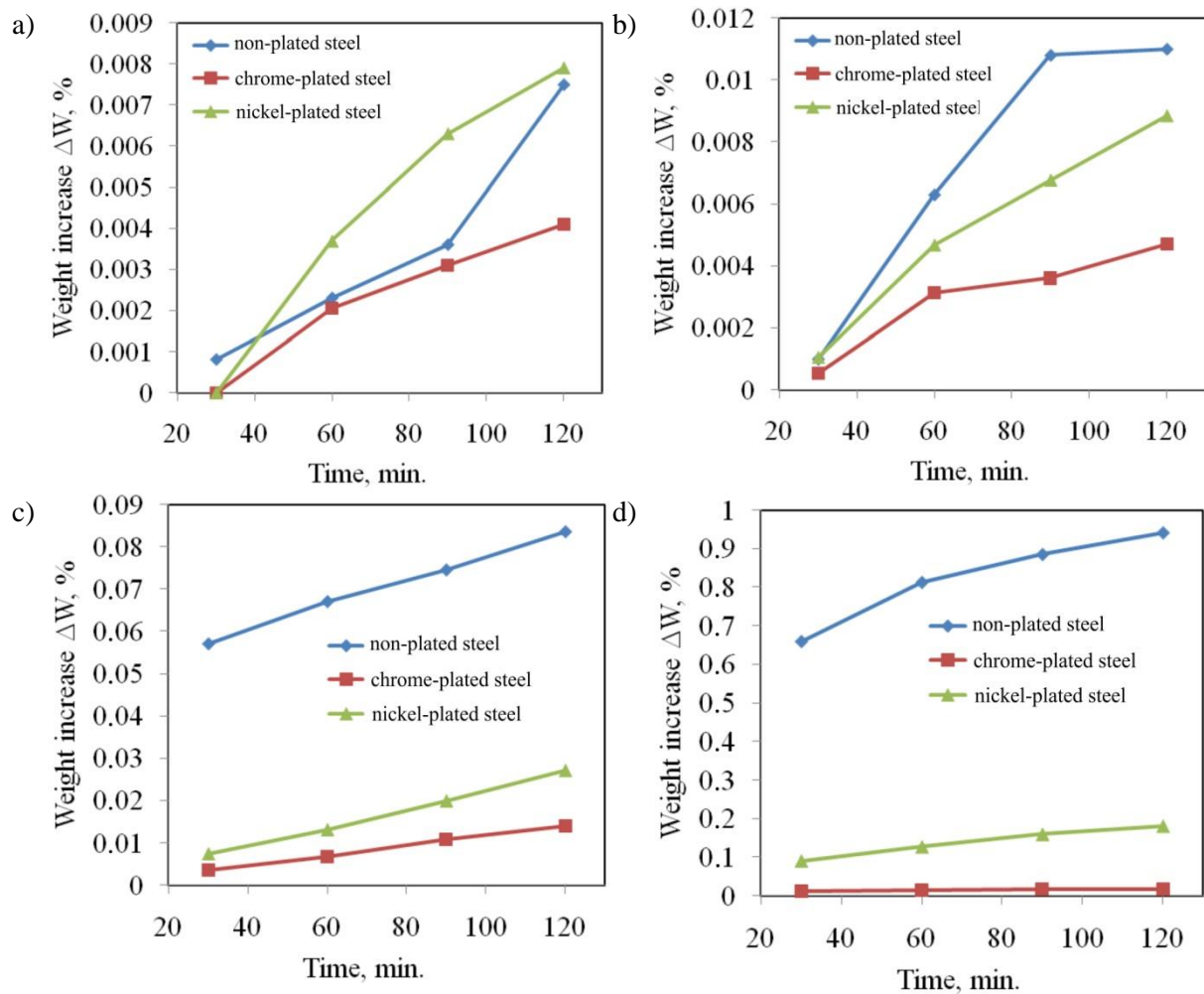
Fig. 12. Variation of oxidation behavior of non-plated and plated mild steel with time: a) T= 200 °C, b) T= 400 °C, c) T= 600 °C and d) T= 800 °C,
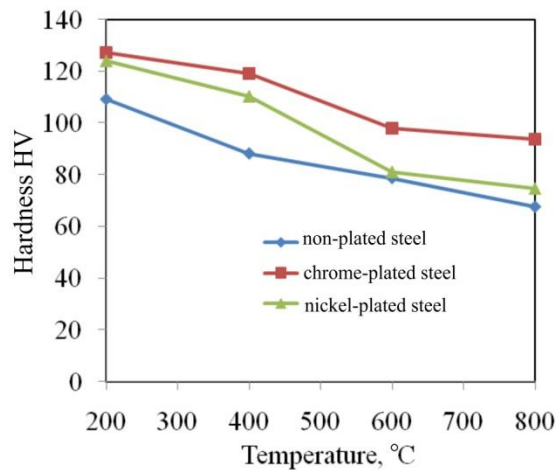
Fig. 13. Variation of oxidation behavior of non-plated and plated mild steel with temperature (time t = 120 min.).

As shown in Fig. 13, at any given temperature, the weight change (due to oxidation) of non-plated mild steel is higher than that of chromium or nickel-plated mild steel. This indicates that nickel-plated or chrome-plated mild steels exhibit higher corrosion resistance than non-plated mild steel. When comparing the performance of Ni and Cr in terms of corrosion resistance across various temperatures, it is observed that chrome-plated mild steel has higher corrosion resistance (lower corrosion rate) than nickel-plated mild steel.

3.4. Hardness

The hardness values of non-plated, chrome-plated and nickel-plated samples, heated for a total time of 120 minutes, were determined using a Vickers hardness tester. The aim of this test was to understand whether the formed oxide layers improve the hardness values of the surface or not. The hardness of the non-plated and unheated original mild steel sample is 133.4 HV.

The hardness of the heated mild steel sample was observed to be lower (Table 6 and Fig. 14) than that of the unheated one. When the results were correlated with temperature, it was found that the hardness of non-plated mild steel samples decreases with increasing temperature. The same trend was observed for the chrome-plated and nickel-plated mild steel samples.

Table 6. Variation of hardness with temperature of heating for non-plated, chrome-plated and nickel-plated mild steel.

T, ºC	Non-plated mild steel	Chrome-plated mild steel	Nickel-plated mild steel	Total heating time
200	109	127	124	
400	88	119	110.3	
600	78.5	98	81	120 min
800	67.4	93.8	74.5	
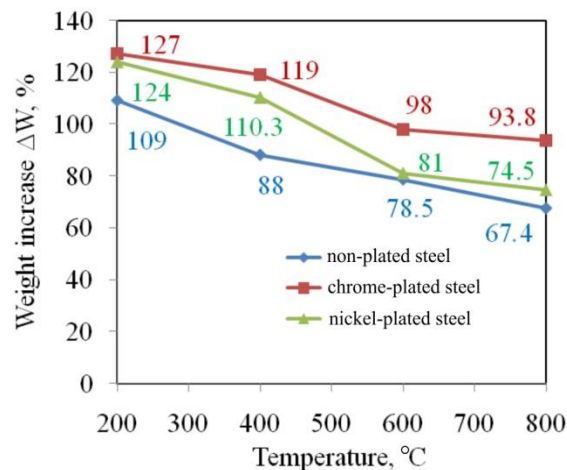
Fig. 14. Variation of hardness with temperature for non-plated, nickel-plated and chrome-plated mild steel (time t = 120 min.).

The same trend was observed for chrome-plated and nickel-plated mild steel samples. The surface hardness results of chrome-plated and nickel-plated samples are also affected by the heating temperature. As the holding temperature increases, the hardness of these plated samples becomes less and less. However, the rate of reduction in hardness of nickel-plated mild steel is observed to be higher than that of chrome-plated or non-plated mild steel.

4. Conclusions

In conclusion, the study shows that as the temperature increases, the three ASTM A283GC mild steel samples (non-plated, nickel-plated, and chrome-plated) experience higher rates of oxidation. Non-plated mild steel is the most vulnerable to corrosion, while chrome-plated mild steel demonstrates the best resistance to hot corrosion at all tested temperatures. The surface hardness of all samples decreases with increasing temperature and oxidation. Additionally, oxide scale easily peels off from the non-plated mild steel surface at 800 °C, but this issue is not observed in the plated samples. These findings emphasize the importance of temperature and plating in determining the corrosion behavior of mild steel. The study contributes valuable insights for selecting appropriate materials in applications requiring corrosion resistance in high-temperature environments.

References

Akhtar, M., Lohchab, A., Singh, D., Kumar, R., Gaur, P., & Yadav, B. (2023). Experimental studies on the effect of chromium plating on the mechanical properties of SAE 4140 steel. *Materials Today: Proceedings*, *72*, 2488–2496. https://doi.org/10.1016/j.matpr.2022.09.527

Aliofkhazraei, M. (2014). *Developments in corrosion protection*. IntechOpen. https://doi.org/10.5772/57010

Andrade, C., & Alonso, C. (2001). On-site measurements of corrosion rate of reinforcements. *Construction and Building Materials*, *15*(2-3), 141-145. https://doi.org/10.1016/S0950-0618(00)00063-5

Apostolopoulos, C. A., & Papadakis, V. G. (2008). Consequences of steel corrosion on the ductility properties of reinforcement bar. *Construction and Building Materials*, *22*(12), 2316-2324. https://doi.org/10.1016/j.conbuildmat.2007.10.006

Burnett, P. J. & Rickerby, D. S. (1987). The relationship between hardness and scratch adhesion. *Thin Solid Films*, *154*(1-2), 403-416. https://doi.org/10.1016/0040-6090(87)90382-8

Chen, R., & Yeun, W. (2003). Review of the high-temperature oxidation of iron and carbon steels in air or oxygen. *Oxidation of Metals*, *59*, 433–468. https://doi.org/10.1023/A:1023685905159

Chen, X. B., Easton, M. A., Birbilis, N., Yang, H. Y. & Abbott, T. B. (2013). Corrosion-resistant electrochemical plating of magnesium (Mg) alloys. In Song, G. L. (Ed.), *Corrosion prevention of magnesium alloys* (pp. 315-346). Woodhead Publishing Limited. https://doi.org/10.1533/9780857098962.3.315

Fotovvati, B., Namdari, N., & Dehghanghadikolaei, A. (2019). On coating techniques for surface protection: A review. *Journals of Manufacturing and Materials Processing*, *3*, 28. https://doi.org/10.3390/jmmp3010028

Frankel, G. S. (1998). Pitting corrosion of metals: a review of the critical factors. *Journal of The Electrochemical Society*, *145*(6), 2186-2198. https://doi.org/10.1149/1.1838615

Hou, B., Li, X., Ma, X., Du, C., Zhang, D., Zheng, M., Xu, W., Lu, D., & Ma, F. (2017). The cost of corrosion in China. *npj Materials Degradation*, *1*(1), Article 4. https://doi.org/10.1038/s41529-017-0005-2

Kanani, N. (2004). *Electroplating: basic principles, processes and practice*. Elsevier Ltd. https://doi.org/10.1016/B978-1-85617-451-0.X5000-3

Klapper, H. S., Zadorozne, N. S., & Rebak, R. B. (2017). Localized corrosion characteristics of nickel alloys: A review. *Acta Metallurgica Sinica* (*English Letters*), *30*, 296–305. https://doi.org/10.1007/s40195-017-0553-z

Lu, K. (2010). The future of metals. *Science*. *328*(5976), 319-320. https://doi.org/10.1126/science.1185866

Lunk, H. J. (2015). Discovery, properties and applications of chromium and its compounds. *ChemTexts*, *1*, Article 6. https://doi.org/10.1007/s40828-015-0007-z

Ma, E., Yang, X., Su, Y., Bi, Z., Sun, H., Wang, B., Ma, C., & Zhang, D. (2023). High temperature oxidation behavior of Fe–3.0%Si steel with non-equilibrium reaction. *Journal of Materials Research and Technology*, *23*, 2587–2600. https://doi.org/10.1016/j.jmrt.2023.01.163

Maurice, V., & Marcus, P. (2018). Progress in corrosion science at atomic and nanometric scales. *Progres in Materials Science*, *95*, 132-171. https://doi.org/10.1016/j.pmatsci.2018.03.001

McMahon, M. E., Santucci Jr., R. J., Glover, C. F., Kannan, B., Walsh, Z. R. & Scully, J. R. (2019). A review of modern assessment methods for metal and metal-oxide based primers for substrate corrosion protection. *Frontiers in Materials*, *6*, Article 190. https://doi.org/10.3389/fmats.2019.00190

Mehtani, H., Khan, M., Jaya, B. N., Parida, S., Prasad, M., & Samajdar, I. (2021). The oxidation behavior of iron-chromium alloys: The defining role of substrate chemistry on kinetics, microstructure and mechanical properties of the oxide scale. *Journal of Alloys and Compounds*, *871*, Article 159583. https://doi.org/10.1016/j.jallcom.2021.159583

Mild Steel. (2023, August 1). *Chemical composition - Mechanical properties*. https://kvsteel.co.uk/steel/mild-steel.html

North, N. A., & MacLeod, I. D. (1987). Corrosion of metals. In C. Pearson (Ed.), *Conservation of marine archaeological objects* (pp. 68-98), Elsevier. https://doi.org/10.1016/B978-0-408-10668-9.50010-1

Ojo, A. A., & Dharmadasa, I. M. (2018). Electroplating of semiconductor materials for applications in large area electronics: A review. *Coatings*, *8*, 262. https://doi.org/10.3390/coatings8080262

Samui, A. & Sivaraman, P. (2010). 11 - Solid polymer electrolytes for supercapacitors. In Sequeira, C., & Santos, D. (Eds.), *Polymer electrolytes fundamentals and applications* (pp. 431-470). Woodhead Publishing Limited. https://doi.org/10.1533/9781845699772.2.431

Wang, H. X., Zhang, Y., Cheng, J. L., & Li, Y. S. (2015). High temperature oxidation resistance and microstructure change of aluminized coating on copper substrate. *Transactions of Nonferrous Metals Society of China*, *25*(1), 184–190. https://doi.org/10.1016/S1003-6326(15)63594-4

Weinstein, M., Falconer, C., Doniger, W., Bailly-Salins, L., David, R., Sridharan, K., & Couet, A. (2021). Environmental degradation of electroplated nickel and copper coated SS316H in molten FLiNaK salt. *Corrosion Science*, *191*, Article 109735. https://doi.org/10.1016/j.corsci.2021.109735

Young, D. J. (2008). *High temperature oxidation and corrosion of metals* (2nd ed.), Elsevier. https://doi.org/10.1016/C2014-0-00259-6

Zhang, Q., Wang, Q., Zhang, S., Lu, X., & Zhang, X. (2016). Electrodeposition in ionic liquids. *ChemPhysChem*, *17*(3), 335-351. https://doi.org/10.1002/cphc.201500713

Analiza Charakterystyki Utleniania Wysokotemperaturowego Chromowanych, Niklowanych i Nieplaterowanych Stali Miękkich

Streszczenie

Metale są najlepszymi materiałami konstrukcyjnymi ze względu na ich doskonałą przewodność właściwą, właściwości mechaniczne i odkształcalność. Jednakże wpływ czynników środowiskowych takich jak tlen i chlor może zmienić ich właściwości elektryczne, chemiczne i mechaniczne. W celu ochrony metali przed korozją opracowano różne metody ochrony, m.in. w procesie galwanizacji. Obecność filmów anodowych lub katodowych na powierzchni podłoża chroni stal przed uszkodzeniami korozyjnymi w temperaturze otoczenia. Niniejszy artykuł skupia się na wpływie temperatury na szybkość utleniania (korozji) próbek stali miękkiej nieplaterowanej, platerowanej niklem i chromowanej. W badaniach uwzględniono zakres temperatury 200-800 °C i całkowity czas ogrzewania 120 minut. Zastosowano piec muflowy z regulowaną temperaturą o maksymalnej wydajności grzewczej 1000 °C. Zmiany masy mierzono co 30 minut w trakcie nagrzewania przy użyciu cyfrowej wagi z dokładnością do 0,001 g. Uzyskane wyniki eksperymentalne próbek ze stali miękkiej ASTM A283GC nieplaterowanej, platerowanej niklem i chromowanej poddano analizie i porównano ze sobą. Badano także wpływ utleniania na twardość powierzchni za pomocą twardościomierza Vickersa. Zaobserwowane zmiany w zachowaniu próbek spowodowane utlenianiem zostały sfotografowane.

Słowa kluczowe: metale, korozja, temperatura, twardość powierzchni, powlekanie galwaniczne